

© Copyright 2016

Samantha A. Byrnes

An Integrated System for Large Volume Sample Processing at the Point of Care

Samantha A. Byrnes

A dissertation

submitted in partial fulfillment of the

requirements for the degree of

Doctor of Philosophy

University of Washington

2016

Reading Committee:

Paul Yager (Chair)

Daniel Ratner

Kim Woodrow

Lisa Frenkel (GSR)

Program Authorized to Offer Degree:

Bioengineering

University of Washington

Abstract

An integrated system for large volume sample processing at the point of care

Samantha A. Byrnes

Chair of Supervisory Committee:

Dr. Paul Yager

Department of Bioengineering

The emergence of rapid, user-friendly, point-of-care (POC) diagnostic systems is paving the way for better disease diagnosis and control. Lately, there has been a strong emphasis on developing molecular-based systems due to their potential for greatly increased sensitivity and specificity. One of the most critical aspects of designing practical diagnostic devices is the ability to perform sample preparation at the POC. Many sensitive systems have been developed, but few have successfully translated out of the laboratory and into clinical use, often due to the lack of testing and compatibility with realistic samples. Therefore, diagnostic devices that can process complex samples such as blood, urine, or environmental water are rarely available at the POC.

Urine is simple to collect, making it an ideal sample for untrained users. A major challenge to processing urine for diagnostic tests, however, is the diluted nature of the sample. For accurate diagnosis, large volumes of urine (1–10 mL) are often required. Processing these volumes often relies on sample pre-treatment techniques that necessitate expensive equipment and highly trained personnel. To address these gaps, this dissertation details the development and integration of multiple sample preparation modules for large volume sample processing. The majority of this work will focus on urine-based diagnosis of chlamydia and gonorrhea, but these assays and the integrated device can serve as a platform for multiple sample types.

Table of Contents

List of Figures	v
List of Tables.....	vii
1. Introduction	1
2. Background	3
3. Specific Aim 1: POC-compatible pathogen lysis and urine specimen characterization.....	14
3.1. Background	14
3.2. Methods	17
3.3. Results and Discussion.....	22
3.4. Conclusions and Future Work.....	39
4. Specific Aim 2: Develop a POC-compatible gDNA fragmentation method.....	40
4.1. Background	41
4.2. Methods	51
4.3. Results and Discussion.....	57
4.4. Conclusions and Future Work.....	78
5. Specific Aim 3: Develop a method to purify and concentrate DNA in porous membranes.....	79
5.1. Background	79
5.2. Methods	82
5.3. Results and Discussion.....	87
5.4. Conclusions and Future Directions.....	108
6. Specific Aim 4: Automation of large volume sample processing through controlled fluid movement in multi-material porous networks	110
6.1. Background	110
6.2. Methods	119
6.3. Results and Discussion.....	127
6.4. Conclusions and Future Work.....	139
7. Overall Conclusions and Future Directions	140
8. Abbreviations and Acronyms	142
9. Acknowledgements.....	143
10. Literature Cited	144
11. Appendices	163
11.1. Appendix 1: Amplification sequence details.....	163
11.2. Appendix 2: Urine characterization.....	164
11.3. Appendix 3: Amplification interference studies	165
11.4. Appendix 4: MPH summary	182

List of Figures

Figure 1. A flooded road in Matlab, a rural region of Bangladesh, August 2013.....5

Figure 2. Procurement of HIV diagnostics around the world from 1999-20095

Figure 3. Examples of paper-based devices for POC diagnostics.....7

Figure 4. Schematic of long chains of DNA moving through porous membranes.11

Figure 5. Current MAD NAAT device for small volumes (~180 µL).13

Figure 6. Classification of bacteria by outer structure..16

Figure 7. Schematic of experiment to quantify E. coli movement through glass fiber membranes.19

Figure 8. Standard curve to determine the salinity of patient urine samples.20

Figure 9. Effect of pH on ACP activity for bacterial lysis.24

Figure 10. Effect of buffer composition and concentration on MSSA treatment with ACP.25

Figure 11. MSSA lysis with ACP in increasing dilutions of patient urine samples.....26

Figure 12. ACP lysis performance in urine samples grouped by salinity.....26

Figure 13. Effect of buffers on E. coli lysis methods.27

Figure 14. Effect of buffer and pH on bead beating lysis of E. coli.28

Figure 15. Comparing the effects of pH, temperature, and time on thermal lysis of E. coli.29

Figure 16. Thermal lysis of E. coli in undiluted human urine samples.....30

Figure 17. Comparing lysis pH values, times, and urine samples with NG direct from culture.....31

Figure 18. Comparing multiple lysis methods for CT+ cells.32

Figure 19. E. coli movement through a glass fiber membrane.34

Figure 20. Translating E. coli lysis from tube to membrane.....35

Figure 21. Comparing amplifiable DNA from in-tube and in-membrane lysis experiments.....36

Figure 22. ACP treatment for bacterial lysis.....36

Figure 23. Example of urine variability from discarded human specimens37

Figure 24. Protein gel of concentrated human urine samples.....37

Figure 25. Lysis efficiency of N. gonorrhoeae and C. trachomatis with and without pH modulation39

Figure 26. Enzymatic DNA fragmentation44

Figure 27. Fenton reaction with Fe(II)EDTA, H₂O₂, and ascorbic acid for DNA fragmentation.....45

Figure 28. Example of the COMET assay for visualizing DNA fragmentation.48

Figure 29. Pulsed field gel electrophoresis.....49

Figure 30. Experimental schematic to assess fragmentation of DNA and transport paper53

Figure 31. Schematic of DNA fragmentation experiments.55

Figure 32. PFGE to determine range of fragment sizes that flowed through paper.....59

Figure 33. Methods for analyzing thermal gDNA fragmentation and transport through paper61

Figure 34. Fragmentation of E. coli gDNA in tube from the Fenton reaction.62

Figure 35. Adsorption of DNA in porous membranes64

Figure 36. Effect of proteinase K (PK) treatment on samples post lysis and thermal fragmentation65

Figure 37. Lysis efficiencies for various methods and heating times at 95 °C.67

Figure 38. Effect of heating time on DNA fragmentation and transport through paper.....68

Figure 39. Example PFGE for varying <i>E. coli</i> heating time at 95 °C.	68
Figure 40. Extended <i>E. coli</i> heating times at 95 °C.	69
Figure 41. Lysis efficiencies for various methods and heating temperatures for 10 minutes.	71
Figure 42. Effect of heating temperature on DNA fragmentation and transport through paper	71
Figure 43. Example PFGE for varying <i>E. coli</i> heating temperatures for 10 minutes	72
Figure 44. Effect of gDNA size on transport through porous membranes.	73
Figure 45. Fragmentation and transport of mixed samples through porous membranes.	75
Figure 46. Comparing fragmentation methods of <i>E. coli</i> gDNA in tube and in membrane.	77
Figure 47. Gel from fragmentation experiments in tube v. in membrane.	77
Figure 48. Chitosan structure in protonated and unprotonated forms.	80
Figure 49. DNA purification in porous membranes using chitosan.	88
Figure 50. Membrane capacity for chitosan.	91
Figure 51. Chitosan retention during flow	92
Figure 52. Capacity of chitosan for DNA in nitrocellulose and glass fiber.	93
Figure 53. Calculation of less than a monolayer of DNA coverage when chitosan capacity is reached. ...	95
Figure 54. Dispersion of sequentially delivered fluids in nitrocellulose and glass fiber.	96
Figure 55. DNA concentration effects in nitrocellulose and glass fiber	98
Figure 56. Recovery of DNA using chitosan-modified membranes is concentration independent.	99
Figure 57. Effect of pH on DNA purification in nitrocellulose with chitosan.	100
Figure 58. DNA purification in porous membranes by chitosan capture.	101
Figure 59. DNA purification in porous membranes from samples containing blood.	103
Figure 60. Effect of increasing NaCl concentration on chitosan purification of DNA	104
Figure 61. Effect of increasing ionic strength and ion valence on Debye length	105
Figure 62. DNA purification from large volumes in Fusion 5 and standard 17.	106
Figure 63. Simultaneous purification of <i>E. coli</i> and MSSA DNA in membranes with chitosan.	106
Figure 64. Chitosan storage studies in Fusion 5	107
Figure 65. RNA purification in chitosan-patterned Fusion 5.	108
Figure 66. Paper diodes for controlling reagent flow in porous networks.	111
Figure 67. Controlling fluid flow through paper-actuated expanding elements.	112
Figure 68. Models and experiments predicting flow through porous membranes.	114
Figure 69. Multi-material porous network.	114
Figure 70. Wetting of porous membranes based on membrane capillary pressures.	115
Figure 71. Example water retention curves	116
Figure 72. P-switch: pressure-controlled flow through multi-material networks.	117
Figure 73. Schematic of waste pad configurations for large volume sample processing experiments. ...	121
Figure 74. Schematic of linear purification and p-switch purification.	121
Figure 75. Automating the p-switch for the large volume sample concentration.	123
Figure 76. Optimizing p-switch geometry to improve elution of DNA from the junction.	124
Figure 77. Schematic of device and individual component testing	125
Figure 78. Schematic of in-membrane amplification tests.	126
Figure 79. Comparing total flow time of stacked and single large waste reservoirs	127

Figure 80. DNA purification comparing a p-switch device to a linear geometry in Fusion 5.....	129
Figure 81. The p-switch for DNA purification and concentrated from 1 mL of human urine samples.....	130
Figure 82. Improving elution from the overlap region of p-switch networks.....	131
Figure 83. Comparing DNA recovery for devices with varying overlap geometries.	132
Figure 84. Automating the p-switch for the large volume sample concentration.....	133
Figure 85. Testing increasing amounts of urine non-target NA in the p-switch device.....	134
Figure 86. In-membrane NAAT comparing purified and non-purified samples.....	136
Figure 87. Lateral flow detection of in-membrane iSDA.....	138

List of Tables

Table 1. Summary of commercially available POC NAATs	8
Table 2. Summary of the effects of buffer, pH, and salinity on ACP lysis of MSSA in tube.	27
Table 3. Summary of the effects of buffer, pH, and time on thermal lysis of E. coli in tube.....	30
Table 4. Comparison of different methods to analyze gDNA fragmentation.	49
Table 5. Summary of gDNA fragmentation in tube.....	63
Table 6. Final chitosan concentration in each membrane after accounting for losses	91
Table 7. Chitosan capacity in nitrocellulose and glass fiber.....	94
Table 8. Comparison of polyamines for DNA purification in porous membranes.....	109
Table 9. Summary of the operational characteristics for chlamydia and gonorrhea diagnosis	118
Table 10. Summary of the integrated sample preparation device.	135
Table 11. Summary of device results for urine samples spiked with pathogens.....	135
Table 12. Comparing device output measured by qPCR to the clinical Aptima Test.....	139
Table 13. Characterization data for 35 de-identified, discarded human urine samples	164

1. Introduction

1.1. Significance of the Problem

Molecular diagnostics have a high potential for increased sensitivity and specificity, but many technologies cannot process large-volume samples, like urine, at the POC. Chlamydia and gonorrhea are two common sexually transmitted infections (STIs) that accounted for a combined 3.5 million cases in the US alone in 2012¹. Many of these infections go undiagnosed, and therefore untreated, due to insufficient screening, especially in underserved populations. The availability of a sensitive and specific POC-compatible combination chlamydia/gonorrhea test would help overcome access barriers and reduce disease transmission. Additionally, a new test should use nucleic acids as the diagnostic biomarker in order to identify infection from antibiotic-resistant strains. The US Centers for Disease Control and Prevention (CDC) has reported a rapid rise in antibiotic-resistant strains of gonorrhea. In 2006, there were five viable drugs for treating all gonorrhea infections; as of 2013 only one remained that was able to treat all strains of gonorrhea². It is a necessity that new diagnostic platforms are capable of directly testing for the resistant strains through the use of molecular diagnostics to guide effective treatment and curb further development of resistance.

1.2. Proposed Solution

The CDC recommends urine as an appropriate sample type for chlamydia and gonorrhea diagnosis³ using nucleic acid amplification tests (NAATs). Since these pathogens commonly cause co-infections of chlamydia and gonorrhea⁴, a useful test would diagnose both. Currently-available POC tests have sensitivities and specificities as low as 23% and 60%⁵ and none of these tests use NAATs, which can be challenging to perform outside the laboratory. Paper-based NAATs translate laboratory assays to POC devices⁶, but few, if any, have developed methods to automate large volume (mL) processing for samples such as urine. To address these gaps, this project describes the development of an automated, simple-to-use paper-based device for processing urine and extracting DNA to diagnose chlamydia and gonorrhea.

1.3. Summary of Specific Aims

This work has been divided into four specific aims. A summary of each is provided below.

- 1.3.1. **Aim 1:** Demonstrate POC-compatible pathogen lysis and urine specimen characterization
Main Deliverable: methods integrated into a manuscript with data from Aim 4 (in preparation)

Aim 1 of this work included three subsections aimed at designing a simple-to-use sample preparation system for pathogen lysis in urine samples. The system is intended for use in POC-compatible devices, so it was specifically developed to integrate with porous membrane substrates. The three subsections were: (i) evaluating lysis methods for bacterial pathogens in order to release amplifiable DNA; (ii) characterizing the range of variability in human urine samples; (iii) developing a simple method to modulate the pH of urine. The overall goal of this work was to investigate the underlying principles that govern NA sample preparation from urine. This knowledge was used to develop a POC sample preparation system for improved chlamydia and gonorrhea diagnosis, but *E. coli* was used as a simulant pathogen for initial experiments.

1.3.2. **Aim 2:** Develop a POC-compatible DNA fragmentation method

Main Deliverable: Manuscript for *Lab on a Chip* (ready for submission)

Aim 2 of this work was development and characterization of a method that combined cell lysis with DNA fragmentation to allow for lateral transport of genomic DNA through commonly-used porous membranes. This work included four subsections: (i) demonstrating that varying heating times and temperatures allowed for control of both lysis and fragmentation; (ii) evaluating these methods for multiple cell types and genome sizes; (iii) matching the experimental data to previously published models that describe both DNA denaturation and thermal scission; and (iv) using this method for semi-selective transport of pathogenic DNA over human DNA, which reduced the amount of interference in downstream applications. This method can be easily automated and is rapid, requiring less than 10 minutes and only one user step. Initial assay validation was done with *S. aureus* and *E. coli* bacteria; studies were then expanded to include mixed samples with *N. gonorrhoeae* and human epithelial cells. This assay was also integrated with the other components of the dissertation to develop an automated device for multiplexed detection of chlamydia and gonorrhea from urine samples.

1.3.3. **Aim 3:** Develop a method to purify and concentrate DNA in porous membranes

Main Deliverable: "One-step purification and concentration of DNA in porous membranes" – Byrnes *et al.* *Lab on a Chip*, 2015

Aim 3 of this work included three subsections: (i) investigation of polyamine interaction with common porous substrates; (ii) utilizing polyamine modified membranes to simultaneously purify and concentrate NA from complex samples; and (iii) testing the

efficacy of these modified membranes after long-term storage. The combination of these capabilities can be used on a wide range of sample types, which are ready for use in downstream processes, such as NAATs, without additional purification. Further, this purification system used a novel, one-step, sequential reagent delivery mechanism designed in the Yager and Lutz labs that directly translated to a simple, one-step user experience.

1.3.4. **Aim 4:** Automation of large volume sample processing through controlled fluid movement in multi-material porous networks

Main Deliverables: Manuscript for *PNAS* detailing the p-switch system (ready for submission)

Manuscript for *Nature Methods* describing the integrated sample preparation device for large volume urine processing (in preparation)

The final aim of this work included five subsections: (i) enhancing flow through porous membranes to reduce processing time of large volume samples; (ii) controlling fluid flow direction to sequence reagent delivery; (iii) automating multiplexed purification and concentration of *C. trachomatis* (CT) and *N. gonorrhoeae* (NG) DNA directly from pathogens in human urine; (iv) demonstrating platform compatibility with in-membrane NAAT and lateral flow readout; and (v) comparing device results to a clinical system used to detect CT/NG. This work linked the sample preparation modules developed in Aims 1–3.

2. Background

General background for the entire proposal is provided below and more detailed backgrounds can be found at the start of each aim.

2.1 Diagnosing infectious disease around the world

According to the 2010 Global Burden of Disease study, four of the top ten causes of death worldwide are attributed to communicable diseases, which disproportionately affect low resource settings (LRS)⁷⁻⁹. Number four is lower respiratory infections and number seven is diarrhea¹⁰. These infections have known and available treatments, but often lack accurate diagnosis, especially in low resource settings (LRS) where there is severely reduced availability of healthcare^{11,12}. In many settings, including the US and other developed countries, symptomatic diagnosis is commonly used by healthcare providers. Although symptoms are important, they can vary between individuals and are often shared by multiple infections. Diarrhea, for example, can be caused by different

pathogens including viruses, bacteria, and parasites¹³⁻¹⁶. Each of these classes of pathogens requires different treatments and within classes, treatments can vary due to potential resistances to common drugs.

Antimicrobial resistance has been on a constant rise around the world^{2,17}; one method for curbing this trend is accurate molecular diagnosis which can lead to identification of specific pathogens and potential drug resistances. Molecular diagnostics refer to the use of DNA or RNA for disease diagnosis, as apposed to immune-based diagnostics which commonly use protiens as the diagnostic target. A common method for molecular-based pathogen identification is nucleic acid amplification tests (NAATs), which uniquely identify a pathogen's DNA or RNA. Of the currently available NAATs, polymerase chain reaction (PCR) is the most common. The use of NAATs for disease diagnosis offers multiple advantages over symptomatic-based diagnosis and some immune-based tests, including increased sensitivity, the ability to multiplex, and epidemiological tracking of disease transmission and drift *via* nucleic acid (NA) sequencing. Molecular-based approaches, however, often require expensive equipment and highly trained personnel.

When someone is sick in the US, they can make an appointment with their healthcare provider, travel to the nearest clinic, have samples taken, and either wait at the clinic for their results or head home. Traditionally, results sent to a laboratory are ready in less than a week. With the development of POC tests, many patients have results on the same day as their visit¹⁸. This process is simple and direct, for some individuals. For others, however, the requirement of getting to a clinic costs time and money they may not have available.

Under-served populations in the developed world can live far from reliable healthcare¹⁹⁻²². For example, Archibald *et al.* mapped the availability of substance abuse treatment centers to the socio-economic status (SES) and race of a population. They found large clusters of regions with high poverty levels, high percentages of minorities, and limited access to healthcare¹⁹. These healthcare deserts require persons seeking medical care to travel long distances, often on public transit²⁰. The cost of public transportation, lost income for time off of work, and provider fees, especially without insurance, can add up even for routine visits. In addition, there can be laboratory and prescription fees once someone is diagnosed. These barriers often prevent people from seeking treatment which extends the burden of disease and increases the potential for transmission.



Figure 1. A flooded road in Matlab, a rural region of Bangladesh, August 2013. Image from Samantha A. Byrnes.

The situation is even more challenging in developing countries. In many remote regions, most populations only have access to tertiary healthcare facilities^{23–25}; in the global public health literature these centers are often defined as small, rural clinics with limited services. A recent study in rural Kenya found that for every 5 km increase in distance from a hospital, admissions [and therefore the potential for diagnosis and treatment] fell by 11% for men and 20% for women²³. If a patient requires assistance beyond standard care or if they need a laboratory for accurate diagnosis, they may need to travel to a major city. In Bangladesh, for example, most people travel to the capital, Dhaka, for reliable diagnosis and treatment. Due to poor infrastructure and constantly deadlocked traffic, a trip to Dhaka can take an entire day. If it is the rainy season, travel can take even longer because many roads are flooded and may be impassable without a boat, **Figure 1**.

Instead of requiring patients to travel to a healthcare center for diagnosis and treatment, solutions are being developed that bring these services to the POC. According to the WHO, the types of diagnostics used around the world have been shifting from traditional laboratory-based tests, such as the enzyme-linked immunosorbent assay (ELISA) and qPCR, to rapid test formats. From 1999 to 2009, the proportion of HIV rapid tests procured globally increased from ~35% to over 80%²⁶. This trend reached a peak in 2007 with over 95% of procurements being of the rapid test variety²⁶, **Figure 2**.

POC testing can also be highly cost-effective and time-saving, as reviewed by Loubiere *et al.* Overall, the authors recommended the use of POC tests due to the savings in time, for both patient and healthcare provider, and the reduced number of visits to the clinic²⁷. Additionally, they cited studies that showed reduced costs for POC STI testing in LRS. Using a \$4 combined chlamydia/gonorrhea

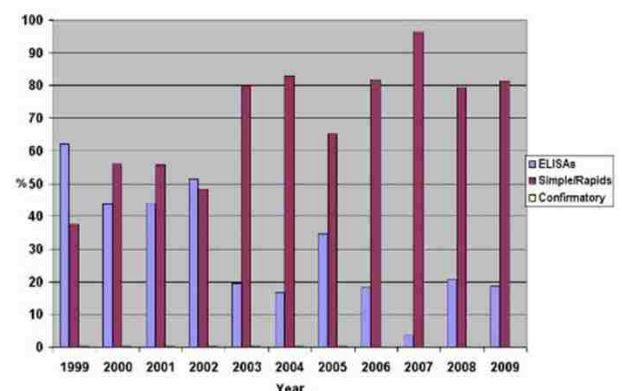


Figure 2. Procurement of HIV diagnostics around the world from 1999-2009²⁶

test, the researchers were able to avert 10% of the expected chlamydia/gonorrhea infections. With respect to HIV, they were able to avert 6% of infections and an average of \$292 dollars per person for future testing²⁸. Although this trend is encouraging, there is still a gap in the availability of accurate NAAT-based diagnostics for the POC that can more accurately diagnosis disease and identify antibiotic resistance, qualities that are lacking in many immunoassay-based tests. To overcome this limitation, research has focused on developing automated microfluidic platforms to diagnosis disease.

2.2 The evolution of microfluidics for disease diagnosis

Over the last 20 years, the field of microfluidics has aimed to address and overcome the gap between laboratory capabilities and POC systems through the development of single-use, plastic microfluidic chips²⁹. There have been numerous publications about the wide range of applications for these chips including cell lysis and NA purification^{30,31}, sample concentration³², immunoassays³³⁻³⁵, and NA amplification^{36,37}. Gubala *et al.* extensively reviewed many of these pioneering applications³⁸.

Although many of the above microchip-based systems show promise for translation to realistic POC settings, there is a drawback to their implementation due to the use of potentially expensive equipment for operation (e.g., syringe pumps). Devices that require this type of equipment have limited usability in POC settings such as a patient's home or rural health clinics in the developing world. Due to these constraints, many groups have begun to focus on an alternative platform for diagnostics: porous membranes.

The use of porous membranes, or paper-based substrates, as a platform for bioassays dates back to the 1930s with the development of paper chromatography³⁹⁻⁴¹. In the mid to late-1970s the home-based pregnancy test brought paper-based diagnostics to the POC⁴²⁻⁴⁴. More recently, George Whitesides' group began patterning cellulose paper to simultaneously detect glucose and proteins in urine samples⁴⁵. The field has also evolved to include systems which offer advantages such as the ability to perform complex, multi-step processes^{46,47}, the sequential timed delivery of reagents^{46,48}, and compatibility with various amplification and detection techniques^{6,49-51}. **Figure 3** shows an example of a traditional, one-dimensional lateral flow test (LFT) and a 2 dimensional paper network (2DPN) developed in the Yager group.

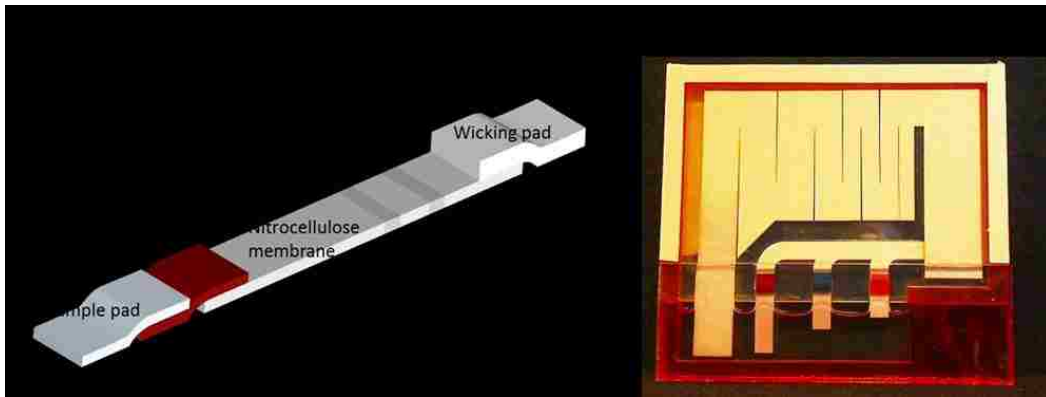


Figure 3. Examples of paper-based devices for POC diagnostics. **A.** One-dimensional lateral flow test, similar in format to the common pregnancy test. **B.** Two-dimensional paper network developed in the Yager laboratory for more sophisticated reactions⁴⁷.

Porous membrane-based assays do not require mechanical pumps because capillarity wicks fluids into and through the paper⁵². These devices are also inexpensive, easy to manufacture, and disposable, making them ideal candidates for POC tests. Recent reviews detail the use of porous membrane-based microfluidics for diagnostic devices^{53,54} and the translation of multi-step processes from laboratory gold-standard techniques to paper-based systems⁵⁵. Although this field of work is constantly growing with recent demonstrations of integrated paper-based NAATs^{56,57}, there is still a significant gap in translating nucleic acid tests to paper platforms as noted in the review by Mariella *et al.*⁵⁸ and as discussed below.

2.3 NAATs for the Point-of-Care

Plastic microfluidic chips were the first inexpensive and disposable devices developed to perform NAATs at the POC. The Klapperich group demonstrated on-device thermocycling for PCR⁵⁹ and coupled it to nucleic acid purification⁶⁰. Bau *et al.* designed a plastic microfluidic device that purified NA, performed PCR, and detected amplicons using an integrated lateral flow strip⁶¹. Lafleur *et al.* developed the stand-alone platform to NAAT-based tested at the POC⁶². Although these systems showed promising results, they all suffered from the thermal complexity of PCR; namely the requirement for strict control of temperature cycling. Due to this challenge, a large field of research has focused on developing isothermal NAATs⁶³ that could help reduce the time, cost, and equipment requirements of PCR-based devices. One of the most common isothermal NAATs is loop mediated isothermal amplification (LAMP)⁶⁴ which operates at ~65 °C.

Multiple devices have been constructed to run LAMP in LRS. Many of these devices use exothermic chemical reactions to provide heat without mains electricity⁶⁵⁻⁶⁷. An example by Huang *et al.* used a simple Styrofoam cup and commercially available hand-warmers to provide heat to an

isothermal amplification for the detection of *Clostridium difficile*, a common cause of diarrhea⁶⁸. An overview of NAAT-based microchip advances was recently published⁶⁹.

Due to small channel sizes and the need for precision fluidic control, many microfluidic chips rely on syringe pumps for operation. To help combat the need for this expensive equipment, research has begun to move toward an alternative reaction matrix: porous membranes. The first reports of an isothermal NAAT performed in a porous matrix demonstrated in-membrane reagent storage for amplification of HIV DNA and detailed the effects of overwhelming the system with non-target nucleic acids^{6,70}. Multiple groups have expanded on this work by integrating upstream assays with paper-based isothermal NAAT^{50,56,57,71}.

In 2011, Niemz *et al.* evaluated 13 commercially available POC NAAT-based systems, **Table 1**. All of these systems include an expensive, non-disposable component that requires mains electricity and, likely, a service contract. Additionally, less than half of these include on-device sample preparation thereby increasing the overall time and costs required for operation⁷². The most successful of these systems is the GeneXpert developed by Cepheid⁷³. This system integrates filters for cell isolation and ultrasonic lysis to expose nucleic acids⁷⁴.

Table 1. Summary of commercially available POC NAATs from Niemz *et al.*⁷² ^aTime to result depends upon the particular assay. Longer times may be required for assays with a reverse transcriptase step. ^bDevice sold by BioHelix in the USA; manufactured and sold by Ustar Biotech in China. Abbreviations: RTB real-time bioluminescence; RFT real-time fluorescence; RT real-time turbidimetry.

Platform	Manufacturer	Sample prep included?	Amplification	Detection	Time to result (min) ^a	Website
GeneXpert	Cepheid	Y	PCR	RTF	<120	www.cepheid.com
Liat Analyzer	IQuum	Y	PCR	RTF	<60	www.iquum.com
MDx	Biocartis	Y	PCR	RTF	Unknown	www.biocartis.com
FL/ML	Enigma	Y	PCR	RTF	<45	www.enigmadiagnostics.com
FilmArray	Idaho technologies	Y	PCR	RTF	60	www.idahotech.com
Razor	Idaho technologies	N	PCR	RTF	<60	www.idahotech.com
R.A.P.I.D.	Idaho technologies	N	PCR	RTF	<30	www.idahotech.com
LA-200	Eiken	N	Isothermal (LAMP)	RTT	< 60	www.eiken.co.jp
Twista	TwistDX	N	Isothermal (RPA)	RTF	< 20	www.twistdx.co.uk
BART	Lumora	N	Isothermal (LAMP)	RTB	< 60	lumora.co.uk/
Genie II	Optigene	N	Isothermal (LAMP)	RTF	< 20	www.optigene.co.uk
SAMBA	Diagnostics for the Real World	N	Isothermal (similar to NASBA)	NALF	> 60	Not available
BES ^t Cassette ^b	BioHelix/ Ustar Biotech	N	Not included, but typically isothermal	NALF	N/A	www.biohelix.com; www.bioustar.com

For a device to be useful in the home or LRS, it is imperative that sample preparation be fully integrated and require limited user intervention. Many diagnostic approaches do not include sample preparation components due to the high complexity of these processes, as discussed below.

2.4 Sample Preparation for NAATs

In 2008, Mariella *et al.* published the aptly named review *Sample Preparation: the weak link in microfluidics-based biodetection*⁵⁸. As a follow-up in 2009, Brehm-Stecher *et al.* published *Sample Preparation: the forgotten beginning*⁷⁵. Both of these reviews highlighted the necessity and real limitation of sample preparation outside of traditional laboratory settings. Although many microfluidic assays are extremely sensitive, they often require highly purified, small volume samples for proper performance. Unfortunately, real-world samples are far more complex. Protein identification from blood requires multiple purification steps to remove interfering biomolecules⁷⁶. Nucleic acid purification from urine can be complicated by high salinity and extreme dilution factors. Additionally, the salt, pH and overall concentration of samples from individuals can vary greatly from patient to patient.

In a clinical or research laboratory, nucleic acid sample preparation can include multiple processes depending on the input sample type. The most common first step involves cell lysis to make the NAs inside of a cell available for manipulation. The main mechanisms that exist for cell lysis are mechanical, enzymatic, chemical, electrical, and thermal lysis. Most often, many protocols use a combination of these mechanisms. The gold standard for mechanical lysis is the bead beater which applies a mechanical force to tear or puncture a cell membrane⁷⁷. Other mechanical lysis systems exist³¹, but are used less frequently. There are dozens of enzymes used for cell lysis to target NAs in the laboratory. Some are highly specialized for a specific cell type while others are more generally applied. Two of the most commonly used are lysozyme, which cleaves a linkage site between peptidoglycans in bacterial cell walls causing the cell walls to lose structure⁷⁸, and proteinase K which digests proteins⁷⁹. Chemical lysis often involves the use of detergents or chaotropic agents, such as the guanidinium ion, to disrupt the hydrogen bonding in cell membranes causing them to break open⁸⁰. This mechanism has an additional benefit for nucleic acid sample preparation because it also denatures proteins⁸¹. Urea and sodium dodecyl sulfate are two other commonly used reagents for disrupting cell membranes. Electrical lysis involves exposing cells to strong electric fields causing the non-covalent interactions of the cell membrane to become destabilized and break. Although effective, electrical lysis can be challenging to implement because some reports note an applied voltage of up to 20 kV cm⁻¹ is required³¹. Thermal lysis is the most simple mechanism and involves heating cells to destabilize the proteins in the cell membrane causing the membrane to lose structure and break⁷⁹. Unfortunately, heat-based lysis is not effective

on all cell types; thermal lysis is ineffective for pathogens with more structured coatings such as some gram-positive bacteria, mycobacteria (most notably *M. tuberculosis*), and spores⁸².

Common methods of NA purification used in laboratory settings often rely on one of three general mechanisms: solid-phase extraction, electrostatic interactions, or sequence-specific capture. One of the most widely used techniques is solid-phase extraction (SPE) with silica particles. Pioneering work by Boom *et al.* demonstrated a “rapid and simple” method for nucleic acid purification using chaotropic agents, ethanol, and an acidic silica slurry. Their method cited a total assay time of less than one hour for greater than 50% recovery of DNA⁸³. The current gold standard Qiagen kit utilizes a similar technique with silica particles embedded in a centrifugal filter for NA isolation from complex samples. Other common laboratory techniques rely on NA precipitation in the presence of solutions with high alcohol content⁸⁴. Another widely used technique for DNA purification exploits the negative charge of DNA molecules; DNA can associate with coated magnetic beads^{85,86}, cationic polymers^{87–89}, and can be separated through electrophoretic methods^{90–92}. There has also been initial work published on the use of sequence-specific capture for isolating NA targets^{93,94}. Many of these laboratory-based cell lysis and NA purification techniques have been translated into plastic microfluidic systems³¹, but few have been translated to paper-based devices^{71,95–97}.

Two additional sample preparation steps that are less commonly addressed, but can be vital when handling realistic samples are DNA fragmentation and sample concentration. Genomic DNA (gDNA) from bacterial pathogens is often greater than one million bases pairs (1 Mbp) in length. The width of a DNA double helix is ~2 nm while the average length of a DNA base is 0.34 nm; therefore, a 1 Mbp bacterial genome would be ~340 μm (3.4×10^5 nm) long, not accounting for secondary structure. For many paper membranes, the pore diameter ranges from 10’s to 100’s of microns; DNA molecules may be too large to flow through the pores, **Figure 4A**. Additionally, membranes are non-uniform, with highly tortuous pore structures; if a DNA molecule is not tightly compacted or small enough to fit through the pores, it may become tangled and unable to move through a membrane, **Figure 4B**.

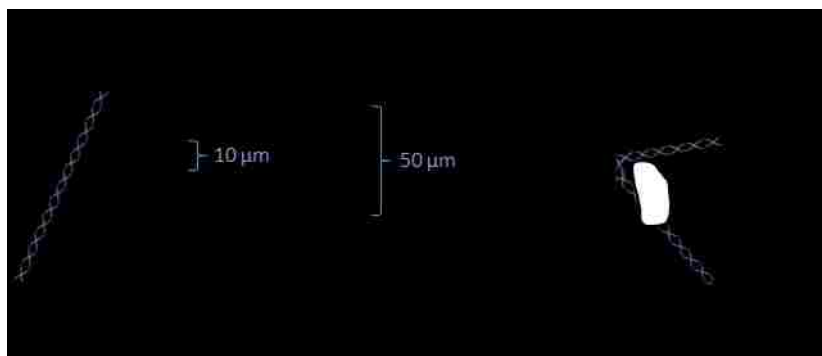


Figure 4. Schematic of long chains of DNA moving through porous membranes. **A.** Long DNA molecules may be too long to flow through small pore features. **B.** DNA molecules may become entangled in the tortuous pore structure of paper materials.

Fragmentation of DNA can result from a variety of processes including breaking through mechanical shearing, enzymatic methods, chemical methods, and thermal scission⁹⁸. Depending on the membrane and the distribution of pore features, even partially fragmented DNA may be too long to easily flow through paper membranes.

A final consideration for DNA preparation is sample concentration. Many laboratory techniques, such as the Qiagen kit, use concentration as a means to increase the sensitivity of their assays. Collecting larger volume samples from patients increases the potential number of collected pathogens that are available for detection. Concentration is especially important for highly dilute samples such as urine which serves as a reliable sample type for diagnosing multiple infections, including chlamydia and gonorrhea.

2.5 Chlamydia and gonorrhea

Chlamydia and gonorrhea are two common STIs that present in the urine. In 2012, these infections accounted for a combined 3.5 million cases in the US alone¹. Many of these infections go undiagnosed, and therefore untreated, due to insufficient screening, especially in underserved populations. The availability of a sensitive and specific POC-compatible chlamydia/gonorrhea test would help overcome access barriers and reduce disease transmission.

The US Centers for Disease Control and Prevention recommends urine as an appropriate sample type for chlamydia and gonorrhea diagnosis³ using NAATs. These pathogens commonly cause co-infection of CT and NG⁴; a useful test would diagnose both. Urine is simple to collect at the POC compared to self-swabbing, especially for men^{99,100}. Within a urine sample, the first 5-10 mL, also known as the first void urine (FVU), contains the highest concentration of pathogen biomarkers¹⁰¹. In women, FVU is acceptable as a sample for chlamydia diagnosis, but may detect up to 10% fewer

infections compared to vaginal swabs³. The clinical ranges of an ongoing chlamydia infection have been reported between 3×10^2 – 2×10^6 elementary bodies (EB)/mL^{102–104} and 2.0 – 2.2×10^5 EB/mL^{103,105} in men and women, respectively. Elementary bodies are the infectious unit of *C. trachomatis*. For gonorrhea, studies that have tracked the clinical range of an ongoing infection report 3.7×10^4 – 2.6×10^7 colony forming units (CFU)/mL¹⁰⁶ in men and 1×10^2 – 1×10^7 CFU/mL in women. A major drawback to some reported ranges, however, is that they are often measured by culture and not the more quantitative qPCR.

These infections can also be costly. In the US in 2008, the direct medical costs (diagnosis and treatment) for chlamydia and gonorrhea were \$516.7 [\$258.3–\$775.0 USD] million and \$162.1 [\$81.1–\$243.2 USD], respectively¹⁰⁷. These costs assume uncomplicated diagnosis with no additional testing for antibiotic resistance strains. In recent years, gonorrhea resistance to azithromycin, a common first-line antibiotic, has increased from 1.8% to 4.1% due to over-use or misuse⁴. In 2006, there were five viable drugs for treating all gonorrhea infections, as of 2013 only one remained that was able to treat all strains of gonorrhea².

Chlamydia is the most common STI in many developed countries¹⁰⁸ and is often highest for youth populations (under 25)^{1,109,110} with reported rates as high as 20%¹¹¹. Population-based studies have shown that in men and women, respectively, up to 88.5% and 68.3% of chlamydia infections were asymptomatic¹¹¹. On average, about 7% of these cases are chlamydia/gonorrhea co-infections. For high-risk populations such as female sex workers and men who have sex with men, the co-infection rates have been measured at up to 40%¹¹².

There is limited published data about the prevalence of chlamydia and gonorrhea in developing countries. In a 2013 meta-review of 25 studies focusing on chlamydia prevalence and diagnosis, only two were identified for low resource settings¹¹¹. There are some country-specific studies. In the Philippines, chlamydia prevalence rates in women were measured between 17.9–32%¹¹³; in Vanuatu, the average prevalence for men and women was reported as 18.6% and 27.8%, respectively¹¹⁴. A review by Mullick *et al.* detailed chlamydia and gonorrhea prevalence rates of 2.7–21.5% and 1.7–20% across multiple low-resource countries¹¹⁵. Similar to developed countries, the co-infection rate has been reported at 7.4% in some developing countries¹¹⁶. A common theme for reported prevalence rates in all settings is the poor performance of currently available rapid diagnostic tests for chlamydia and gonorrhea.

For chlamydia, current POC diagnostic methods have moderate to poor sensitivities ranging from 52–80%¹¹⁷. For gonorrhea, available tests are very inaccurate⁵ with sensitivities averaging 71% (23–

86%) for leucocyte esterase dipsticks, 70% (60–94%) for immunochromatographic tests, and 38-89% using microscopy. Additionally, these rapid tests cannot identify antibiotic resistant strains of gonorrhea. Because of the high prevalence and poor performance of currently available POC methods, there is an immediate need for an accurate and reliable bplexed POC test (POCT).

In 2014, Howick *et al.* conducted a study of over 2700 primary care providers across five countries; an average of 62% (49–75%) noted that a top priority was an accurate and reliable POCT for chlamydia. From this same survey, 55% (34–65%) called for a gonorrhea POCT. Of the 19 tests listed, chlamydia was the third and gonorrhea the sixth most sought after¹¹⁸. None of the commercially available rapid diagnostic tests utilize NAAT for pathogen identification. NAATs are specifically vital to identify molecular characteristics of gonorrhea because according to WHO “Treatment failures due to resistance to treatments of last resort for gonorrhoea (third-generation cephalosporins) have been reported from 10 countries. Gonorrhoea may soon become untreatable as no vaccines or new drugs are in development”¹⁷. For improved sensitivities, future tests, such as those being developed in the Yager Laboratory, should take advantage of NAAT-based technology.

2.6 Multiplexable Autonomous Disposable for Nucleic Acid Amplification Tests (MAD NAAT)

In order to address the lack of sensitive molecular-based tests available for POC usage, the Yager lab and collaborators have been developing a paper-based platform called MAD NAAT (Multiplexable Autonomous Disposable for Nucleic Acid Amplification Tests). This device will only require the user to introduce sample and close the lid. Once the lid has been closed, the internals of the device automate sample preparation, any required heating steps, assay timing, NA amplification, and detection. The final user step will involve taking a picture of the device readout for cell-phone based analysis.

The current iteration of the MAD NAAT device collects sample on a swab, which is then introduced to ~180 μ L of lysis solution and then heated for 10 minutes. Next, the lysate flows into an amplification region, **Figure 5**. This system works very well for swab-based samples⁵⁶, but the current device is unable to process larger volumes such as urine or diluted blood.

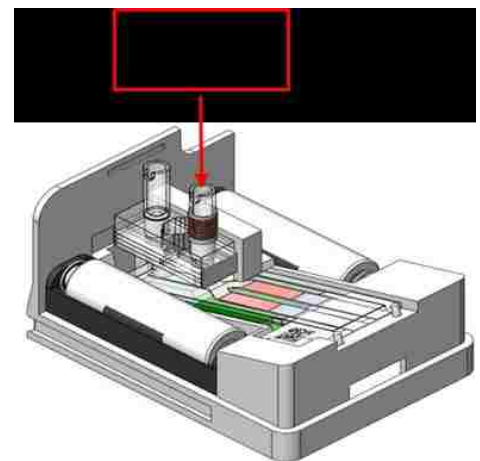


Figure 5. Current MAD NAAT device for small volumes (~180 μ L).

The work presented here will provide new tools for future iterations of the MAD NAAT platform for large volume sample processing.

3. Specific Aim 1: POC-compatible pathogen lysis and urine specimen characterization

Many common human pathogens, especially STIs, are present in the urine. For POC diagnostic devices, urine represents an easy sample type for untrained users to collect. However, urine samples also come in large volumes and with high complexity. Thus, it can be challenging to design simple-to-use devices that can process this large, complex sample for subsequent detection of pathogens.

Urine volume can range from 5–200 mL during urination and is dependent on patient hydration, time since the last bladder voiding, and dietary intake^{104,119}. Urine pH can vary between 4.5–8 depending on the time of day¹²⁰ and urine salinity is highly dependent on patient hydration. McCance *et al.* showed that during a dehydrated state, urine salinity increased by an average of nearly 40%; the highest observed increase from a hydrated to dehydrated state was 164 mM to 371 mM of chloride, equivalent to an increase of 126%¹²¹. This variation in samples requires diagnostic devices with pre-processing capabilities to perform equally well over large pH and salinity ranges.

This chapter of my dissertation includes three subsections aimed at designing a simple-to-use sample preparation system for pathogen lysis in urine samples. The system was designed for use in POC-compatible devices, so it was specifically developed to integrate with porous membrane substrates. The three subsections are (i) evaluating lysis methods for bacterial pathogens in order to release amplifiable DNA; (ii) characterizing the range of variability in human urine samples; (iii) developing a simple method to modulate the pH of urine. The overall goal of this work was to investigate the underlying principles that govern NA sample preparation from urine. This knowledge was also used to develop a POC sample preparation system for improved chlamydia and gonorrhea diagnosis, but *E. coli* was used as a simulant pathogen for initial experiments.

3.1. Background

In many settings, diseases are diagnosed based on a patient's symptoms, which can lead to inaccurate diagnosis because multiple infections present with similar symptoms. In the case of STIs, many infections may be asymptomatic. For example, Dielissen *et al.* systematically reviewed population-based studies that screened for chlamydia infection and found that 88.5% and 68.3% of cases were asymptomatic in men and women, respectively¹¹¹. Further, many bacterial infections

have pathogen-specific considerations that need to be made when treating a patient. Not all bacteria are susceptible to the same antibiotics. Without proper identification, treatments can be sub-optimal or even ineffective leading to prolonged illness and a higher potential for disease transmission. Inaccurate bacterial identification has also led to a rise in antibacterial resistance¹⁷ making treatment and infection control more challenging and costly¹⁷. Antibiotic resistance is steadily increasing for gonorrhea infections; in August 2016, the CDC noted that 30% of new infections are resistant to at least one antibiotic².

One strategy for curbing this trend is to rely on molecular diagnostics that use DNA/RNA to uniquely identify pathogens and any potential drug resistances. These nucleic acid tests are highly sensitive and specific, but require multiple pre-processing steps to isolate NA from a pathogen.

Pathogen and antibiotic resistance identification in a laboratory setting can be a time-consuming and expensive process. When translating these capabilities to the POC, there are additional constraints that need to be considered including costs, operational simplicity, timing, and equipment requirements¹²². Based on these constraints, this work focused on developing methods for processing samples that require less than 20 minutes, one user-step, no additional equipment, and porous networks as a low-cost diagnostic platform.

Overview of bacterial structure. Most often, the first step in sample pre-processing involves pathogen lysis to expose the NA. Multiple laboratory-based methods have been developed to reliably lyse bacteria, but effectiveness can vary based on bacterial structure, which can be generally classified as Gram-positive or Gram-negative based on the cell's ability to take up Gram stain. Gram-positive bacteria have a thick cell wall composed of peptidoglycan which retains the Gram stain, **Figure 6A**. Gram-negative bacteria have a far thinner cell wall with about eight times less peptidoglycan causing the Gram stain to be removed upon washing, **Figure 6B**⁷⁸. Peptidoglycans are linear repeating units of small peptides and disaccharides. The linear chains also covalently crosslink with tetrapeptide units which further increases their strength and structural integrity, **Figure 6C**⁷⁸.

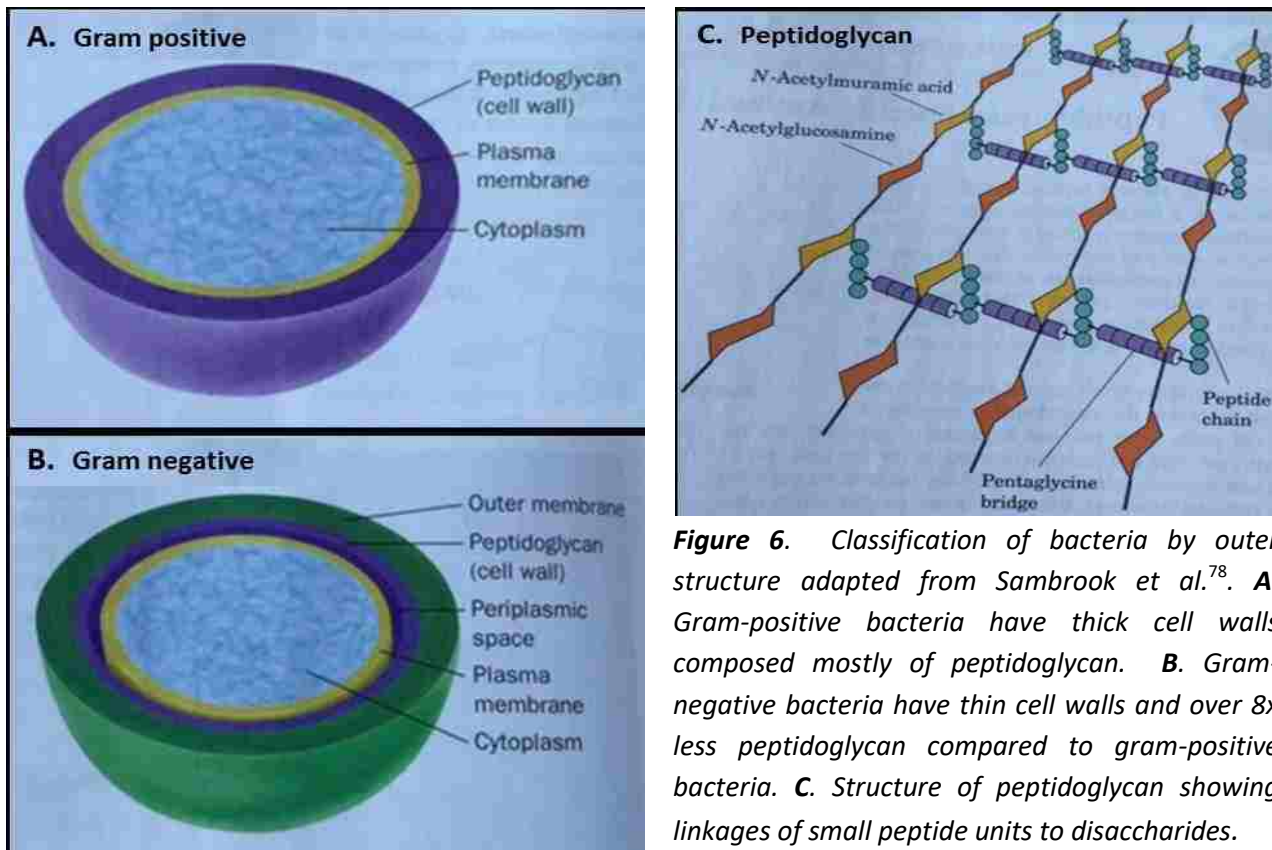


Figure 6. Classification of bacteria by outer structure adapted from Sambrook et al.⁷⁸. **A.** Gram-positive bacteria have thick cell walls composed mostly of peptidoglycan. **B.** Gram-negative bacteria have thin cell walls and over 8x less peptidoglycan compared to gram-positive bacteria. **C.** Structure of peptidoglycan showing linkages of small peptide units to disaccharides.

The thick cell wall of Gram-positive bacteria makes them more challenging to lyse than Gram-negative bacteria. Research has reported that heat is often sufficient to lyse Gram-negative bacteria because it can denature the thin cell wall; Gram-positive bacteria, on the other hand, are typically resistance to thermal lysis¹²³. Both chlamydia and gonorrhoeae are caused by Gram-negative bacteria, *Chlamydia trachomatis* and *Neisseria gonorrhoeae*. *N. gonorrhoeae* is an extracellular pathogen, while *C. trachomatis* is an obligate, intracellular pathogen; it resides inside of human epithelial cells. This presents another level of required lysis: both the eukaryotic human cell and the bacterial cell must be lysed to expose NA from *C. trachomatis*.

Methods for bacterial lysis. The main mechanisms that exist for bacterial lysis are mechanical, enzymatic, chemical, electrical, and thermal-based. Most often, protocols use a combination of these methods. This work focused on enzymatic and thermal lysis because these have been deemed the most compatible for POC use.

Enzymatic lysis can describe a large number of enzymes. Some lytic enzymes are highly specialized for a specific cell type, such as lysostaphin, which targets *Staphylococcus* bacteria¹²⁴, while others are more generally applied. The most commonly used and well understood lytic enzyme is lysozyme, which cleaves the peptide-disaccharide linkage of peptidoglycans in bacterial cell walls, causing them to denature⁷⁸. Many Gram-negative bacteria are not susceptible to

lysozyme because their thick outer membrane prevents the enzyme from interacting with the inner cell wall; additionally, some Gram-positive bacteria, such as *S. aureus*, are also resistant to lysozyme treatment¹²⁵. Achromopeptidase (ACP) is a broad-spectrum lytic mixture of enzymes^{80,125}. Some research suggests its primary mechanism of lysis involves cleaving the link between disaccharides in the peptidoglycan¹²⁶. Work in the Yager lab by Dr. Xiaohong Zhang, Dr. Paula Ladd, and Dr. Erin Heiniger has revealed that most commercially available ACP solutions are actually a mixture of at least a dozen agents. Some of these components target peptide-peptide bonds, some break down glycoside bonds between monosaccharides, and others hydrolyze the peptide-disaccharide linkage of the peptidoglycan (unpublished data). According to one vendor, the optimal conditions for ACP performance are in low salt buffers (under 50 mM), at moderate temperatures (near 37 °C), and in near-neutral pH (near pH 8)¹²⁷. These conditions are similar to the optimal specifications for many enzymes because enzymes are typically prone to denaturation in high salinity, high temperature, and non-neutral pH conditions^{78,128,129}.

Thermal lysis is a simple lysis method to implement. It involves heating cells to destabilize the outer membranes, causing them to lose structure and break⁷⁹. Thermal lysis is also referred to as boiling lysis because most protocols heat cells to 95–100°C. However, Zhu *et al.* showed rapid thermal lysis of *E. coli* at temperatures ranging from 70–80°C¹³⁰. Few studies have explicitly tested lower temperatures and there is also a lack of published data detailing the effect of pH, salinity, and choice of buffer on the effectiveness of thermal lysis. As already noted, lysis of pathogens in urine must be robust against wide ranges of many of these conditions.

The main objective of this chapter of my dissertation was to investigate the effect of realistic sample conditions on bacterial cell lysis. Although there are many demonstrations of lysis in the literature, few study lysis in varying sample conditions with wide ranges of pH, salinity, or sample volumes. Additionally, this work evaluated the more complex situation of chlamydia-infected mammalian cells as well as samples containing multiple types of pathogens. These principles were then be used to develop techniques that are compatible with porous membrane substrates for POC use. Urine was the primary sample type of interest; therefore, this work also characterized human urine samples to better understand and control for sample complexity.

3.2.Methods

Bacterial culture. Methicillin-resistant *Staphylococcus aureus* (*S. aureus*, strain 1770) was cultured in TSB and *Escherichia coli* (*E. coli*, strain K12) was cultured in LB. Both cultures were heated to 37°C with shaking (250 rpm). Secondary cultures were prepared from overnight cultures diluted 1:100 in fresh medium and grown to mid-log phase ($OD_{600} = \sim 2$). After three hours of secondary culture, cells were pelleted by centrifugation at 13000 $\times g$ for 3 minutes. The supernatant was decanted and the cells were resuspended in 1 \times volume of 10 mM Tris buffer, pH 8.

Neisseria gonorrhoeae (*N. gonorrhoeae*, strain 19424) was cultured directly from frozen stock on chocolate agar plates at 36°C in a 5% CO₂ environment. After 24-48 hours, colonies were collected from the plate and resuspended in 10 mM Tris buffer, pH 8.

Mammalian Cell Culture. Freshly cultured HeLa cells (ATCC CCL-2) or McCoy cells (ATCC CLR-1696) infected with *C. trachomatis* serovar L2 (LGV 434) were obtained from collaborators in either the Hybiske Lab in the Department of Microbiology at the University of Washington or the Harborview STI Clinic in Seattle, WA. To prepare the cells for experiments, culture media was removed and cells were washed with an equal volume of PBS, followed by treatment with 0.25% trypsin with shaking at 37°C for 15 minutes. Detached cells were pelleted by centrifugation at 13000 $\times g$ for 3 minutes. The supernatant was decanted and the cells were resuspended in 1 \times volume of 10 mM Tris buffer, pH 8.

In-tube bacterial lysis with ACP. Freshly cultured bacteria or infected mammalian cells were diluted in buffer to a final concentration of 10⁴ to 10⁵ bacteria per μL . The samples were added into a tube followed by ACP to a final concentration of 0.5 Units/ μL . The solutions were incubated at room temperature for up to 2 minutes followed by heating to 95°C for up to 10 minutes to deactivate the enzyme. The buffers tested were HEPES, Tris, Bis-tris, and MES, ranging in pH values between 5 and 8. The concentrations of the buffers ranged from 10 mM to 150 mM. Some experiments also included the addition of up to 150 mM of NaCl. Lysis was quantified as the amount of amplifiable DNA measured by qPCR. Additional samples were prepared for plating and CFU counting by diluting 50x in saline solution.

Thermal lysis of bacteria in tube. Freshly cultured bacteria or infected mammalian cells were diluted in buffer to a final concentration of 10⁴ to 10⁵ bacteria per μL . The solutions were incubated at between 49–95°C for up to 10 minutes. The buffers tested were Tris, HEPES, and MES ranging in pH values between 5 and 8. Sample volume was also varied between 100–1000 μL . Lysis was quantified as the amount of amplifiable DNA measured by qPCR. Additional samples were prepared for plating and CFU counting by diluting 50x in saline solution.

Bead beater for bacterial lysis. 800 μL of the diluted bacteria were added to a 2 mL screw top tube with 800 mg of 0.1 mm diameter glass beads. The samples were placed in the bead beater machine which was set to “homogenize” at full power. The samples were cycled through 3x cycles of 1 minute on followed by 1 minute off. Lysis was quantified as the amount of available amplifiable DNA measured by qPCR.

E. coli cell movement through paper membranes. To test the ability of *E. coli* to move through porous membranes, 80 μL of freshly cultured cells diluted in 10 mM Tris at pH 8 were added to a 1 cm wide by 5 cm long piece of glass fiber (pore diameter $\sim 10\text{-}100\ \mu\text{m}$, Standard 17, GE Global Research). This membrane was chosen because it is currently used in the MAD NAAT device. The sample solution was then chased with 120 μL of 10 mM Tris buffer. The glass fiber membrane was cut into five 1 cm by 1 cm sections and the fluid was removed by centrifugation at 10,000g for 3 minutes. Cells in each fraction were lysed with 2 μL of ACP (20 units/ μL) at room temperature for two minutes followed by heating to 95°C for 5 minutes, **Figure 7**. The percentage of *E. coli* bacteria in each paper section was then quantified by qPCR.

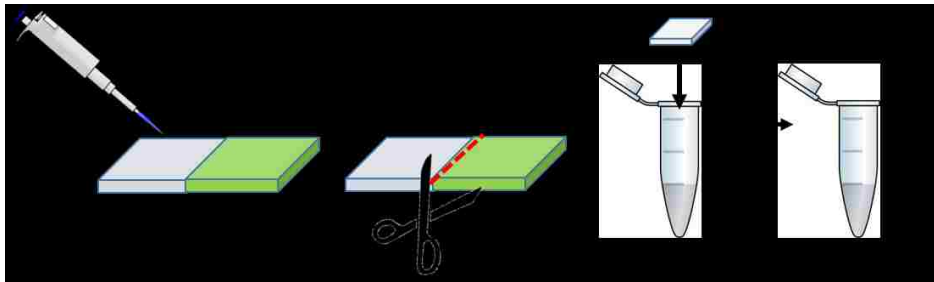


Figure 7. Schematic of experiment to quantify *E. coli* movement through glass fiber membranes. The green portion represents the solution containing cells and the blue is the chase buffer.

Bacterial lysis in porous membranes. Freshly cultured *E. coli* cells were diluted in 10 mM Tris buffer at pH 8 to a final concentration of 10^4 to 10^5 bacteria per μL . For enzymatic lysis, 38 μL of the diluted bacteria were mixed with either 2 μL of ACP (20 U/mL) or 2 μL of 10 mM Tris buffer in tube or in a Standard 17 glass fiber member (1 x 1 cm). The samples mixed in tube were then added to the porous membrane. All membrane samples were subjected to one of four lysis conditions: (i) no lysis, (ii) heat only lysis at 95°C for 5 minutes, (iii) ACP treatment at room temperature for 2 minutes followed by 1 minute of heat deactivation at 95°C (ACP needs to be deactivate before qPCR analysis), and (iv) ACP treatment at room temperature for 2 minutes followed by heat deactivation for 5 minutes at 95°C.

After treatment, half of the samples were prepared for plating to assess bacterial killing by placing the membranes in 500 μL of saline solution and vortexing for 30 seconds. The other half of the membrane samples were prepared for qPCR to analyze the recovery of amplifiable DNA. If the membranes were dry post-heating, they were re-wet with 40 μL of 10 mM Tris buffer. Liquid was collected by placing the membranes in a 0.6 mL Eppendorf tube modified with a small hole in the bottom. The 0.6 mL tube was placed in a 1.7 mL Eppendorf tube and centrifuged for 3 minutes at 10,000g.

Urine sample characterization. A total of 35 de-identified, discarded human urine samples were received from our collaborators at the Harborview STI Clinic in Seattle, WA. These samples were negative for both *C. trachomatis* and *N. gonorrhoeae*, but otherwise were uncharacterized. In order to better understand the sample variations and their potential effects on our assays, samples were characterized by measuring pH, salinity, total dissolved solids, total NA content, and protein content.

Measuring sample pH: Sample pH was measured with a standard laboratory pH meter.

Measuring sample salinity: Sample salinity was measured using a standard laboratory conductivity meter and prepared concentrations of NaCl to serve as a standard curve. Urine sample conductivity was compared to the NaCl standard curve to determine the salinity. The conductivity measurements are influenced by dissolved salts, but not buffers (such as Tris), **Figure 8**.

Measuring total dissolved solids: Total dissolved solids were measured by weighing a known sample volume before and after total liquid evaporation. Screw top tubes were weighed before and after addition of 500 μL of a urine sample. Samples were then stored overnight in an incubator set to 95°C in order to evaporate the liquid component of the urine. Tubes were re-weighed and compared to the empty tube weight to determine the total dissolved solids.

Measuring total NA content: To determine the total NA in each urine sample, 500 μL samples were used. Intact cells were lysed at 95°C for 10 minutes followed by ethanol precipitation using

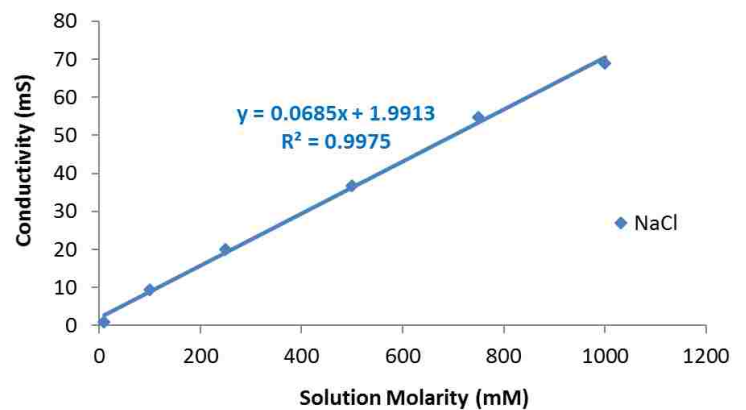


Figure 8. Standard curve to determine the salinity of patient urine samples.

glycogen. Purified NA were resuspended in 50 μ L sterile water and quantified using a Nanodrop. This method accounts for both DNA and RNA in a sample.

Measuring proteins: This work was done in collaboration with Dr. Paula Ladd. To qualitatively measure the total proteins in each sample, 500 μ L of urine was concentrated using a protein concentration kit (Vivaspin 500, 5000 Da molecular weight cut off). The concentrated samples were then run on a protein gel.

Modulation of sample pH. Urine sample pH was modulated by adding dry buffer to a sample prior to lysis. Buffer was added to 1 mL of urine to achieve final buffer concentrations between 10–500 mM. The pH of each sample was measured before and after modulation. A subset of samples was spiked with freshly cultured *N. gonorrhoeae* and *C. trachomatis* before and after pH modulation. These spiked samples were heated to 95°C for 10 minutes to test the effects of pH modulation on cell lysis. Lysis efficiency was quantified by qPCR; 10–500 mM MES buffer was also added to qPCR standards to ensure the addition of buffer did not impact the quantification.

qPCR. *S. aureus* DNA was quantified with a qPCR kit for the *ldh1* gene provided by the ELITech Group (ELITech Group Molecular Diagnostics, Bothell, WA, USA). The 20 μ L reactions were run on a Bio-Rad CFX real-time PCR instrument (Hercules, CA, USA) using the following protocol: 50°C hold for 2 minutes, 93°C hold for 2 minutes, 45 cycles of 93°C for 10 seconds, 56°C for 30 seconds, and 72°C for 15 seconds, ending with final elongation step at 72°C for 5 minutes. Fluorescence data were collected during the 56°C annealing step in the Texas Red channel. The qPCR results were analyzed using the automated threshold cycle (C_T) value calculation in the Bio-Rad software (Hercules, CA, USA). This assay was sensitive down to \sim 10 copies of the target sequence. Assay primer and probe sequences can be found in **Appendix 1**.

E. coli DNA recovery was quantified with qPCR for the *rodA* gene¹³¹ and *N. gonorrhoeae* DNA recovery was quantified with qPCR for the *porA* gene¹³² using the SensiFAST probe No-Rox kit from Bioline (Taunton, MA, USA). The 20 μ L reactions were run on a Bio-Rad CFX real-time PCR instrument (Hercules, CA, USA) using the following protocol: 95°C hold for 3 minutes, 40 cycles of 95°C for 10 seconds, 60°C for 30 seconds. Fluorescence data were collected during the 60°C annealing step in the FAM channel. The qPCR results were analyzed using the automated threshold cycle (C_T) value calculation in the Bio-Rad software (Hercules, CA, USA). These assays were sensitive down to \sim 10 copies of the target sequences. Assay primer and probe sequences can be found in **Appendix 1**.

C. trachomatis DNA recovery was quantified with qPCR for the *omcB* gene¹³³ using the SensiFAST Probe No-Rox kit from Bioline (Taunton, MA, USA). The 20 μ L reactions were run on a Bio-Rad CFX

real-time PCR instrument (Hercules, CA, USA) using the following protocol: 95°C hold for 3 minutes, 40 cycles of 95°C for 10 seconds and 60°C for 30 seconds. Fluorescence data were collected during the 60°C step in the FAM channel. The qPCR results were analyzed using the automated threshold cycle (C_T) value calculation in the Bio-Rad software (Hercules, CA, USA). This assay was sensitive down to ~10 copies of the target sequence. Assay primer and probe sequences can be found in Appendix 1.

Bacterial plating and CFU counting. 10 μ L of a sample from tube or membrane-based lysis were spread onto LB-agar plates. The plates dried at room temperature for 10 minutes followed by overnight incubation at 37°C. Colony forming units (CFUs) were manually counted to compare lysis treatment methods.

3.3. Results and Discussion

The main objectives of this work was to quantify the effects of buffer, pH, time, and salinity on two lysis mechanisms and apply the best performing method to lysis of *C. trachomatis* and *N. gonorrhoeae* in human urine samples. A simple metric was selected for evaluating the performance of lysis methods in the context of diagnostic NAATs. This metric was the percent of amplifiable DNA recovered from the lysate, without additional DNA purification, as measured by qPCR. For each method, bead beating (BB) was used as the gold standard lysis method (set to 100% recovery of amplifiable DNA), (**Equation 1**).



(Equation 1)

This work began by first testing enzymatic lysis followed by thermal-based lysis. Although *C. trachomatis* and *N. gonorrhoeae* were the pathogens of interest, initial experiments were conducted with MSSA and *E. coli*, because they were already available in the laboratory.

1.3.1 Evaluating lysis methods for bacterial pathogens

Effect of buffer, pH, and salinity on ACP lysis of bacteria in tube. Both the pH and salinity of urine vary widely within and between individuals^{120,134}. Therefore, diagnostic systems relying on urine as the input sample must be robust across a wide range of physiological values. As such, the effect of buffers, pH, salinity, and reaction time on ACP, a common enzymatic lysis method used in our lab, was evaluated. Although there are studies available in the literature that use ACP for cell lysis, none

are available that detail the effects of these conditions over these ranges. These parameters were chosen because they are highly variable across patient samples and often influence enzymatic performance.

According to the manufacturer, ACP is optimally active in 10 mM Tris with 10 mM NaCl at pH 8¹²⁷. Previous work performed by Dr. Xiaohong Zhang and Dr. Erin Heiniger in the Yager lab optimized the use of ACP for MSSA lysis from mock nasal swabs in 10 mM Tris. Their results showed equal or better recovery of amplifiable DNA, compared to bead beating, with ACP treatment for 30 seconds to 2 minutes at room temperature followed by 1 to 5 minutes of heating at 95°C.

In the context of this dissertation, the early work described above has been expanded to include testing the effects of buffer composition, pH, and salinity on ACP lysis activity. The amount of amplifiable DNA recovered from each test condition was compared to the amount recovered from the bead beating, a gold standard method for general cell lysis.

The first set of experiments aimed to isolate the effect of pH on ACP lysis. The standard ACP buffer, Tris, has a relatively narrow buffering range of pH 7.0–9.0, and is also highly sensitive to reaction temperature¹³⁵. Due to these limitations, HEPES buffer, pH range of ~6.8–8.2, and MES buffer, pH range ~5.5–6.7, were used to mimic the urine pH spectrum (4.5–8¹²⁰). MSSA cells were diluted in 10 mM Tris at pH 8, 20 mM HEPES at pH 6.5, 7, 7.5, or 8, or 40 mM MES at pH 5, 5.5, 6, 6.2, or 6.5. For each comparison, **Figure 9A**.

To isolate the effects of heat from the buffer composition, samples treated with ACP were compared to samples without ACP, which served as heat-only controls (95°C for 5 minutes). For each of the buffers tested, the heat-only controls resulted in little to no recovery of amplifiable DNA supporting the hypothesis that ACP is causing MSSA lysis, **Figure 9B**. Additionally, the limited recovery of DNA from heat-only lysis is supported by the literature; MSSA is a Gram-positive pathogen which is not susceptible to thermal lysis¹²³.

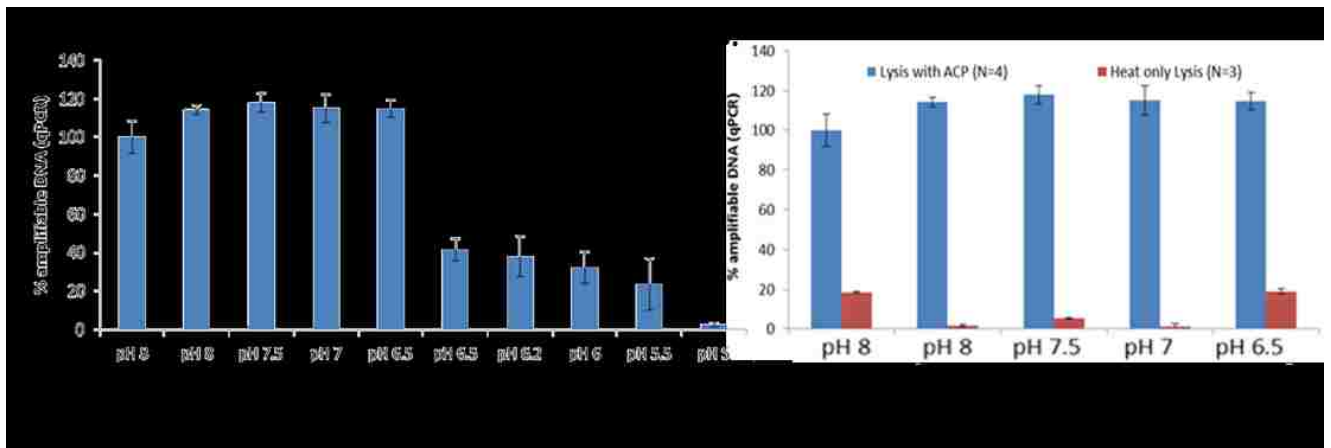


Figure 9. Effect of pH on ACP activity for bacterial lysis. Results were normalized to samples treated by bead beating. An average of at least N=3 +/- one standard deviation is reported for each condition. **A.** Testing a range of buffers and pH values. **B.** Samples lysed in the presence of ACP compared to samples lysed with only heat.

Even though ACP is reported to be most active at pH 8, the samples in HEPES buffer show equivalent lysis performance across all pH values tested. Lysis of MSSA cells in 40 mM MES buffer, however, showed a significant decrease in recovery of amplifiable DNA. Even though both species are Goods buffers which are relatively insensitive to modest temperature fluctuations¹³⁶, the extreme temperature changes in this system, ~22°C to 95°C, have an effect on the solution pH. At room temperature, ~25°C, the pH of both the 20 mM HEPES and 40 mM MES solutions is 6.5. The 20 mM HEPES solution decreases in pH by 0.12 units for each 10°C increase in temperature¹³⁷. This temperature sensitivity means that a pH 6.5 solution at room temperature would drop to a pH of ~5.7 at 95°C. These temperature effects are very similar for the 40 mM MES buffer; the pH decreases by 0.09 pH units per 10°C¹³⁷. At room temperature, a solution with a pH of 6.5 would drop to a pH of ~5.9 at 95°C. Based on these calculations, the effective pH of the solution does not appear to be the only driving factor in ACP performance.

The next set of experiments isolated the effects of buffer composition and concentration on ACP lysis. MSSA cells were treated with ACP in either Tris or HEPES at buffer concentrations ranging from 20 mM to 150 mM, **Figure 10A**. Additionally, ACP treatment was performed in 10 mM Tris buffer with increasing amounts of NaCl to mimic urine salinity, **Figure 10B**.

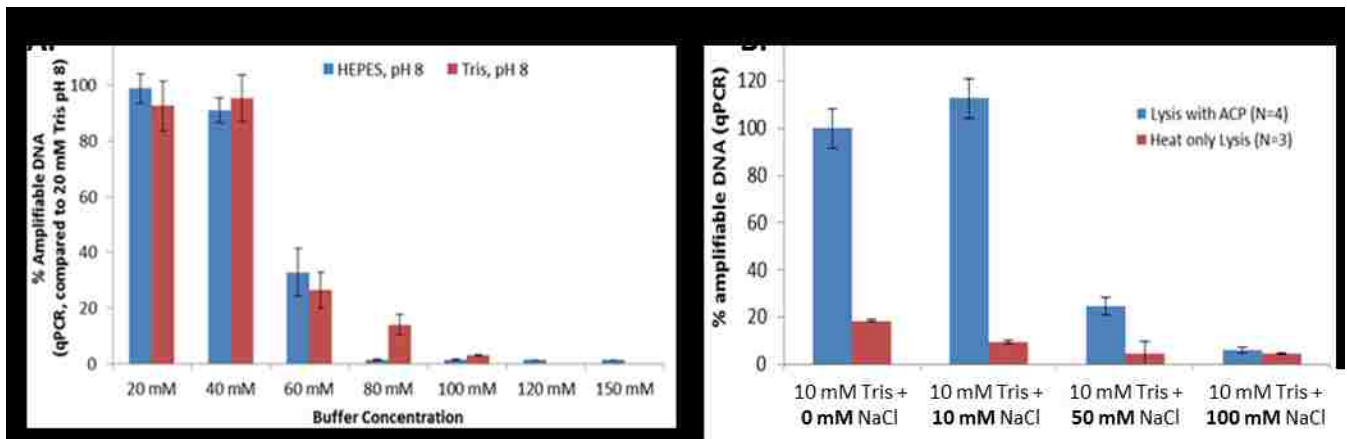


Figure 10. Effect of buffer composition and concentration on MSSA treatment with ACP. An average of at least N=3 +/- one standard deviation is reported for each condition. **A.** Increasing buffer concentration above 50 mM significantly impaired ACP function resulting in decreased availability of amplifiable DNA. **B.** Increasing NaCl concentration in the lysis buffer also significantly inhibited ACP function.

ACP was inactive in buffer or salinities above 50 mM. This effect was seen for both buffers tested, Tris and HEPES. ACP treatment also appears to be sensitive to the choice of buffer, HEPES vs. MES, and less sensitive to the pH of the solution, HEPES at 6.5 vs. MES at 6.5.

Collaborators in the Harborview STI Clinic provided 10 de-identified, discarded human urine specimens for initial testing. The salinities of these samples ranged from 11–416 mM, and based on the results presented above, 8/10 salinities would inhibit ACP function. One option to reduce the effect of salinity, is to dilute the initial sample. To test this effect, MSSA cells were spiked into increasing dilutions of urine samples (stock, 1/2 dilution, 1/5 dilution, 1/10 dilution, or 1/20 dilution). Urine was diluted with 10 mM Tris, pH 8. Following dilution, samples were treated with ACP for 2 minutes at room temperature followed by heat deactivation for 5 minutes at 95°C. Recovery of amplifiable DNA was quantified qPCR, **Figure 11.**

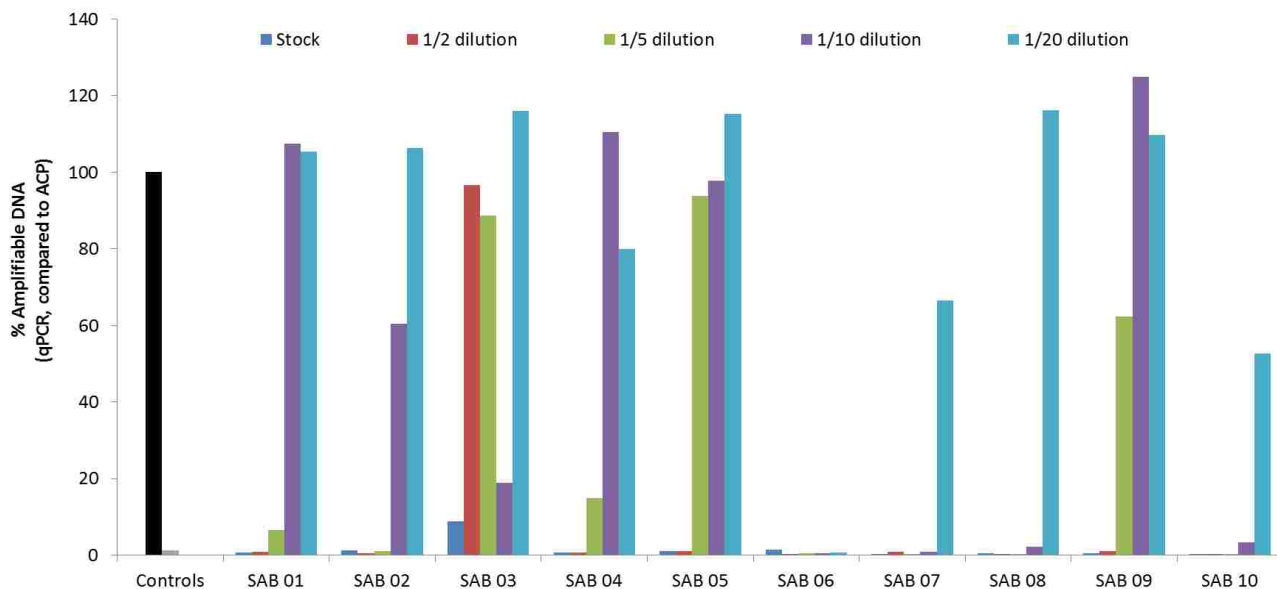


Figure 11. MSSA lysis with ACP in increasing dilutions of patient urine samples. Input $\sim 10^5$ bacteria/ μL , positive control was ACP treatment in 10 mM Tris (pH 8) followed by heat deactivation at 95°C for 5 minutes, negative control was no lysis.

All samples required at least a $\frac{1}{2}$ dilution of the stock urine to restore ACP performance (arbitrarily set to at least 80% performance compared to the positive control in 10 mM Tris, pH 8). SAB 03 had the lowest salinity, 11 mM. The majority of the urine samples required between 1/5 and 1/20 dilution to restore ACP performance. Three of the ten samples did not achieve restored ACP performance (at least 80% of the control) at any of the tested dilutions. These conditions were further evaluated by separating the samples into bins based on salinity, **Figure 12**.

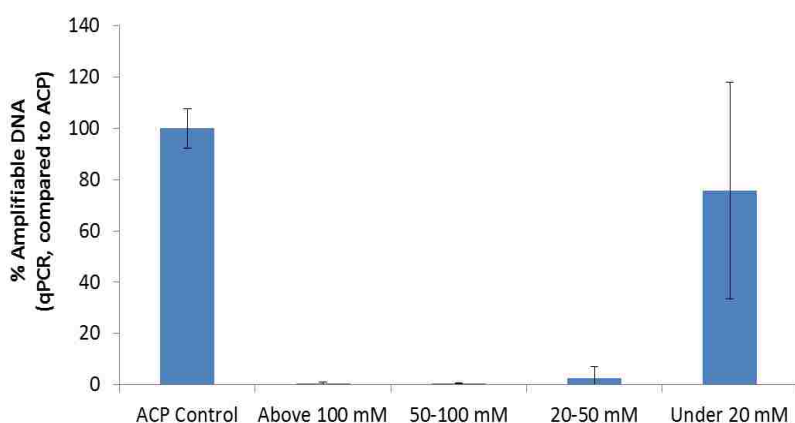


Figure 12. ACP lysis performance in urine samples grouped by salinity. Input $\sim 10^5$ bacteria/ μL , positive control was ACP treatment in 10 mM Tris followed by heat deactivation at 95°C for 5 minutes, negative control was no lysis. Restored ACP performance was arbitrarily set to at least 80% performance compared to the positive control.

These results are summarized with the effects of buffer, pH, and lysis time in **Table 2**. Overall, these data suggest that ACP treatment is not an effective lysis method for complex solutions, such as urine, without additional dilution or pathogen-specific concentration prior to lysis.

Table 2. Summary of the effects of buffer, pH, and salinity on ACP lysis of MSSA in tube.

Buffer	Concentration (mM)	pH	Salinity (mM)
Good lysis performance (near 100% compared to control, by qPCR)			
Tris	10–40 mM	8	0–10 mM
HEPES	10–40 mM	6.5 – 8	n/a
Human urine	< 20 mM	varies	n/a
Poor lysis performance (compared to control, by qPCR)			
Tris	60–150 mM	8	0–100 mM
HEPES	60–150 mM	8	n/a
MES	40 mM	5 – 6.5	n/a
Human urine	> 20 mM	varies	11–416 mM

Effect of buffer, pH, salinity, and time on thermal lysis in tube. The ACP-based experiments were performed with MSSA cells, which are Gram-positive bacteria and do not lyse efficiently with heat. This proposal focuses on two Gram-negative pathogens that commonly present in urine, *C. trachomatis* and *N. gonorrhoeae*. Next, lysis experiments were performed primarily with *E. coli*, a Gram-negative bacterium, to better represent effects on the pathogens of interest. Due to the sensitivity of ACP treatment to biologically relevant pH values and salinities, thermal based lysis procedures were explored.

Figure 13 compares the efficiency of thermal lysis of *E. coli* to bead beating in three buffers: 10 mM Tris at pH 8, 40 mM HEPES at pH 6.5, and 50 mM MES at pH 5. All values were normalized to the percent of amplifiable DNA recovered from bead beating *E. coli* in 10 mM Tris at pH 8. Thermal lysis in tube at 95°C for 5 minutes recovered about 50% of the DNA compared to beat beating. On average, thermal lysis of *E. coli* in 10 mM Tris at pH 8 resulted in more amplifiable DNA than the other two buffers but, statistically, there is no significant difference.

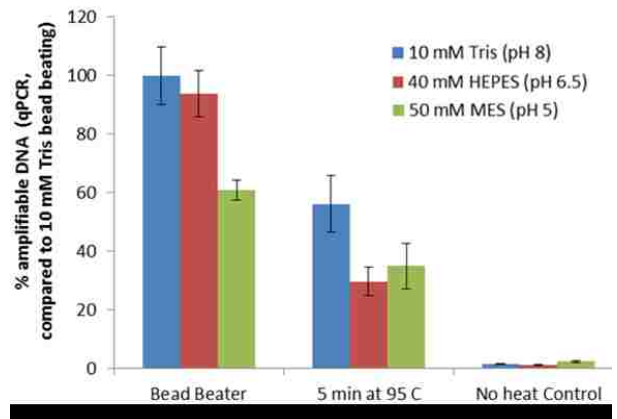


Figure 13. Effect of buffers on *E. coli* lysis methods. An average of N=4 +/- one standard deviation is presented for each condition.

The effect of pH and lysis time was further evaluated by testing thermal lysis of *E. coli* in HEPES and MES buffers at two different pH values. First, the effect of these buffers on the laboratory standard beat beating protocol was tested. The buffer choice did not appear to alter the performance of the bead beater, but low pH values, pH 5, did significantly reduce the amount of amplifiable DNA recovered after beat beating, **Figure 14**. The low pH and high heat generated

during bead beating may damage the DNA, leading to a loss in signal. All values were normalized to the percent of amplifiable DNA recovered from bead beating *E. coli* in 20 mM HEPES at pH 8, because previous studies have shown no significant difference in lysis and DNA recovery using 10 mM Tris or 20 mM HEPES, pH 8. Additionally, aliquots of these buffers were added to qPCR standards to verify that the different conditions did not significantly alter the amplification.

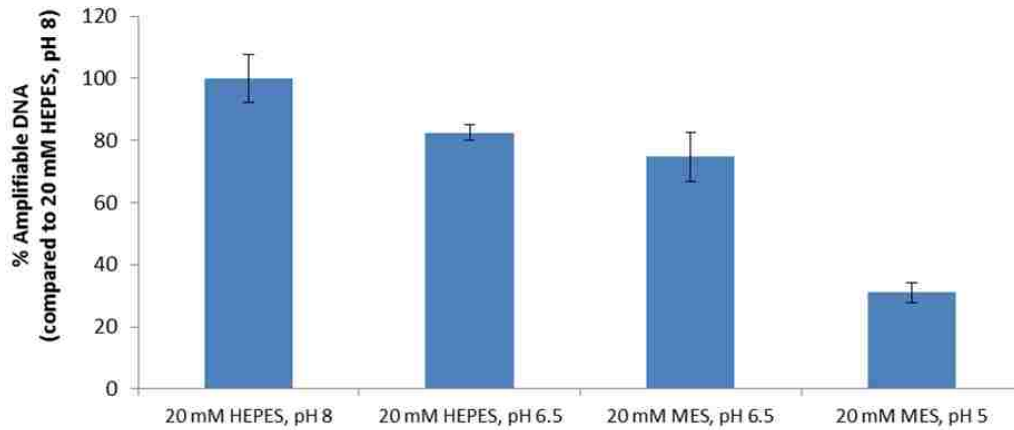


Figure 14. Effect of buffer and pH on bead beating lysis of *E. coli*. Averages of $N=3$ +/- one standard deviation is reported.

Next, the effect of temperature on thermal lysis of *E. coli* was evaluated in these buffers. Based on the results above, all recoveries were normalized to the percent of amplifiable DNA recovered from bead beating *E. coli* in 20 mM HEPES at pH 8. For all of the conditions, thermal lysis at 49°C and 55°C resulted in reduced recovery of amplifiable DNA. Lysis was also poor at 65°C in all buffers except for 20 mM MES at pH 5. These results suggest that the low pH may help increase the lysis efficiency at moderate temperatures.

Surprisingly, lysis time did not appear to be significantly correlated with recovery of amplifiable DNA for most conditions tested. The exception appears to be longer lysis times, 5 minutes, at low pH and high temperature. Similar to the bead beating conditions, this combination may cause released DNA to be degraded. Across all of the conditions, thermal lysis was able to achieve a maximum of 40–45% amplifiable DNA compared to the bead beating control. Even with this reduced recovery, thermal lysis is significantly more robust to the range of potential pH values for human urine compared to ACP-based lysis. Also, thermal lysis worked well over a wide range of temperatures. These results are summarized in **Figure 15**.

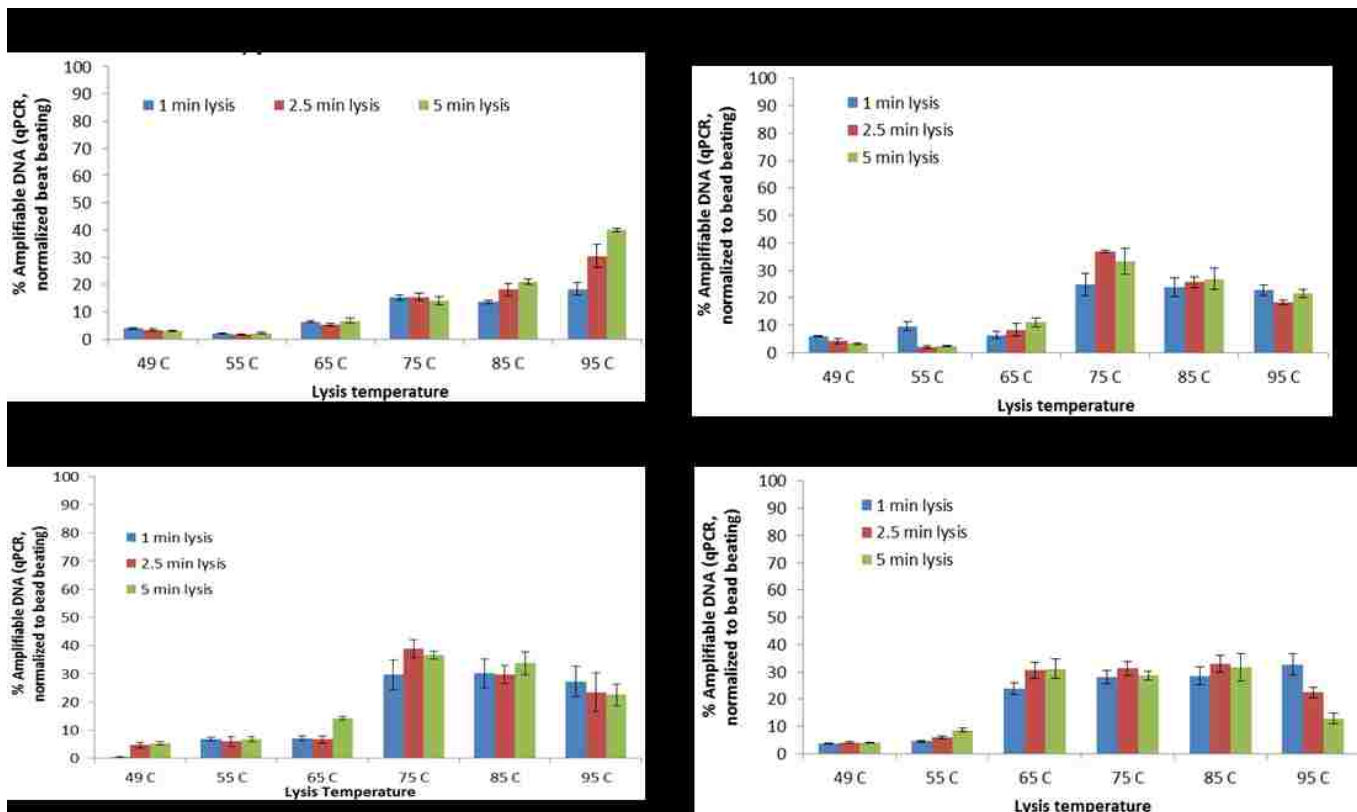


Figure 15. Comparing the effects of pH, temperature, and time on thermal lysis of *E. coli*. The average of $N=3$ \pm one standard deviation is reported for each condition. **A.** 20 mM HEPES at pH 8. **B.** 20 mM HEPES at pH 6.5. **C.** 20 mM MES at pH 6.5. **D.** 20 mM MES at pH 5.

Finally, *E. coli* lysis was tested in the urine samples provided by the Harborview STI Clinic. Each specimen was spiked with $\sim 10^5$ bacteria and lysed at 95°C for either 5 or 10 minutes. *E. coli* in 10 mM Tris (pH 8) were treated with ACP followed by 5 minutes of heating at 95°C to serve as the 100% lysis control. Lysis efficiency was quantified with qPCR. **Figure 16** shows the results of these experiments. The qPCR standards were also spiked with 1 μ L of each urine sample to verify that samples did not cause amplification inhibition (data not shown).

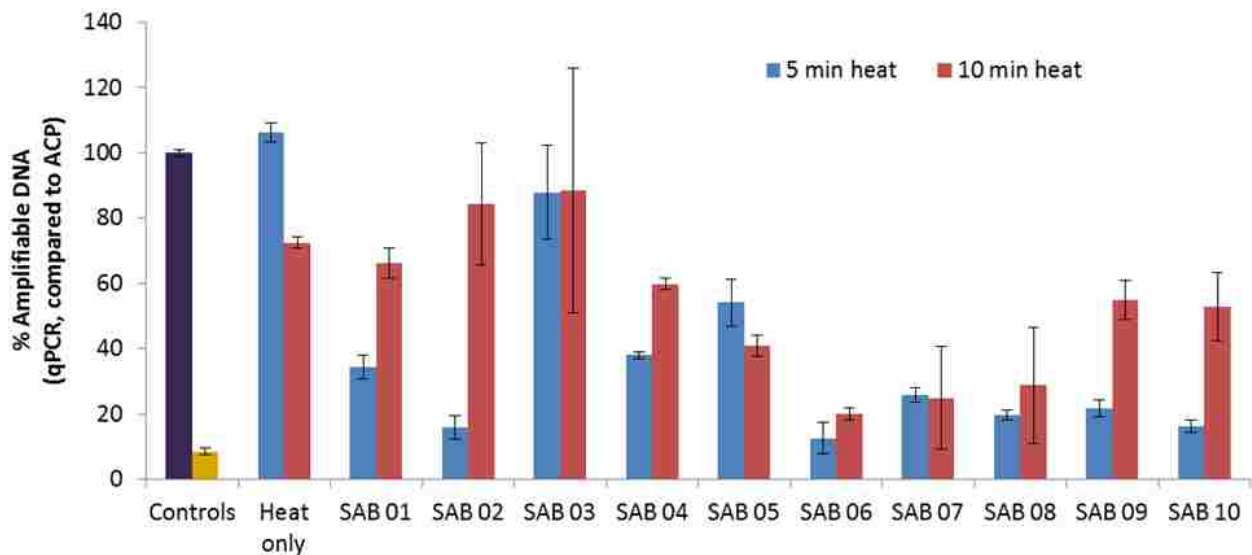


Figure 16. Thermal lysis of *E. coli* in undiluted human urine samples. Averages of $N=3$ are reported with error bars representing \pm one standard deviation. Input $\sim 10^5$ bacteria/ μL , positive control was ACP treatment in 10 mM Tris (pH 8) followed by heat deactivation at 95°C for 5 minutes, negative control was no lysis.

Each of the samples resulted in lysis and recovery of amplifiable DNA and for most samples, 10 minutes of heating at 95°C resulted in as much, or more amplifiable DNA than heating for only 5 minutes. Overall, lysis of *E. coli* in these urine samples was highly variable (19–88%), potentially due to the high variation of human cells in the system. **Table 3** summarizes the best performance for thermal lysis of *E. coli* in different conditions. These results were used as the basis for testing lysis of the pathogens of interest: *C. trachomatis* and *N. gonorrhoeae*.

Table 3. Summary of the effects of buffer, pH, and time on thermal lysis of *E. coli* in tube.

Buffer	pH	Time (min)	Temperature (°C)	Salinity (mM)
HEPES	8	2.5, 5 min	95 °C	n/a
HEPES	6.5	1–5 min	75–95 °C	n/a
MES	6.5	1–5 min	75–95 °C	n/a
MES	5	1–5 min (expect 5 min at 95°C)	65–95 °C	n/a
Human urine	5.3–7.8	5–10 min	95 °C	0–416 mM

Lysis of N. gonorrhoeae and C. trachomatis. Initially, three methods were tested for *N. gonorrhoeae* lysis: 1) thermal lysis at 95°C for 10 minutes, 2) enzymatic lysis with ACP for 2 minutes at room temperature followed by 10 minutes of heating to 95°C, and 3) mechanical lysis using the bead beater with 800 mg of 0.1 mm glass beads for three one-minute cycles with one minute of rest in between. All methods showed comparable efficiency for recovery of amplifiable DNA by qPCR.

The next set of experiments focused on evaluating the effects of varying pH and salinity on thermal lysis of *N. gonorrhoeae* because the enzymatic lysis was previously shown to be significantly inhibited by varying pH and salinity. The conditions for these tests were based on early work performed with *E. coli*. Solutions with pH values ranging from 5–8 were spiked with freshly cultured *N. gonorrhoeae* and subjected to thermal lysis at 95°C for 2-10 minutes. Bacterial cells were also spiked into human urine samples and thermally lysed for 10 minutes at 95°C. After lysis, samples were diluted in 1000 mL of 10 mM Tris, pH 8, to remove any potential interfering effects from the buffers or urine on the qPCR. Overall, there was no significant difference in lysis efficiency between the different pH values tested or times. Also, all of the urine samples resulted in high recovery of *N. gonorrhoeae* DNA, but with high variability, **Figure 17**.

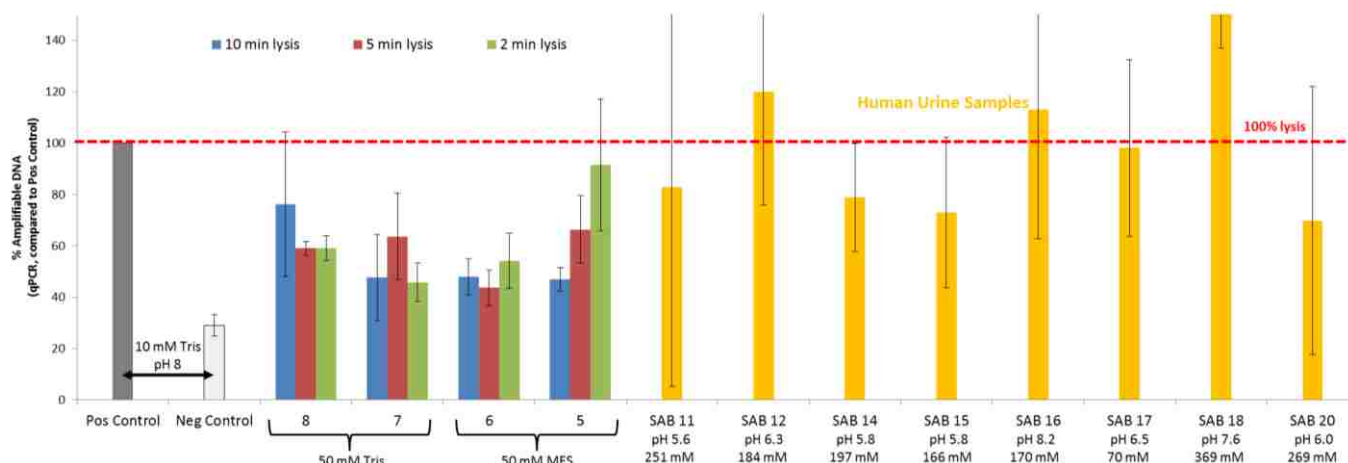


Figure 17. Comparing lysis pH values, times, and urine samples with NG direct from culture. The positive control was lysed for 10 minutes at 95°C. Overall, there was no significant difference between the different times or buffers tested. Additionally, thermal lysis for 10 minutes in human urine resulted in a high lysis efficiency of the pathogen. Averages of N=4 +/- one standard deviation are plotted.

The next set of experiments was performed with *C. trachomatis*, the second urine pathogen of interest. Unlike *N. gonorrhoeae*, which is an extra-cellular bacterium, *C. trachomatis* is an obligate intracellular pathogen, requiring a host cell to survive. This requirement complicates lysis because both the host cell and the pathogen need to be effectively broken down to access the pathogen DNA. Chlamydia infects epithelial cells lining mucus membranes in the urinary tract. The *C. trachomatis*-infected (CT+) cells were provided by either the Harborview STI Clinic or the Hybiske Lab at the University of Washington.

Lysis of the CT+ cells was performed using multiple conditions including heat only, heat+NaCl, heat+detergent (tween or SDS), and detergent only. All conditions with heat were heated to 95°C for 10 minutes and the lysis efficiency of both the host epithelial cell and the intracellular bacteria

were quantified with qPCR. Samples were compared to the 100% lysis control of ACP for 2 minutes at room temperature followed by heating to 95°C for 10 minutes. (Bead beating was also tested as a 100% lysis control and showed statistically similar results to ACP treatment, data not shown.)

A subset of the most robust lysis conditions is reported in **Figure 18**. Generally, heating for 10 minutes works well to release amplifiable *C. trachomatis* DNA while lysis and availability of epithelial cell DNA is highly variable. The high variability seen with the epithelial cell lysis may be due to the degree of cell breakdown. If the large mammalian membranes are punctured, the bacterial cells and DNA may be able to escape the epithelial cells, but the larger mammalian cell DNA is either too large to escape or still inside a potentially intact nuclear envelop. For the purpose of this work, it does not matter whether the mammalian DNA is freed during lysis; ideally, this non-target DNA would remain unavailable while the bacterial DNA is freed to reduce inhibitory effects of non-target DNA on the NAAT.

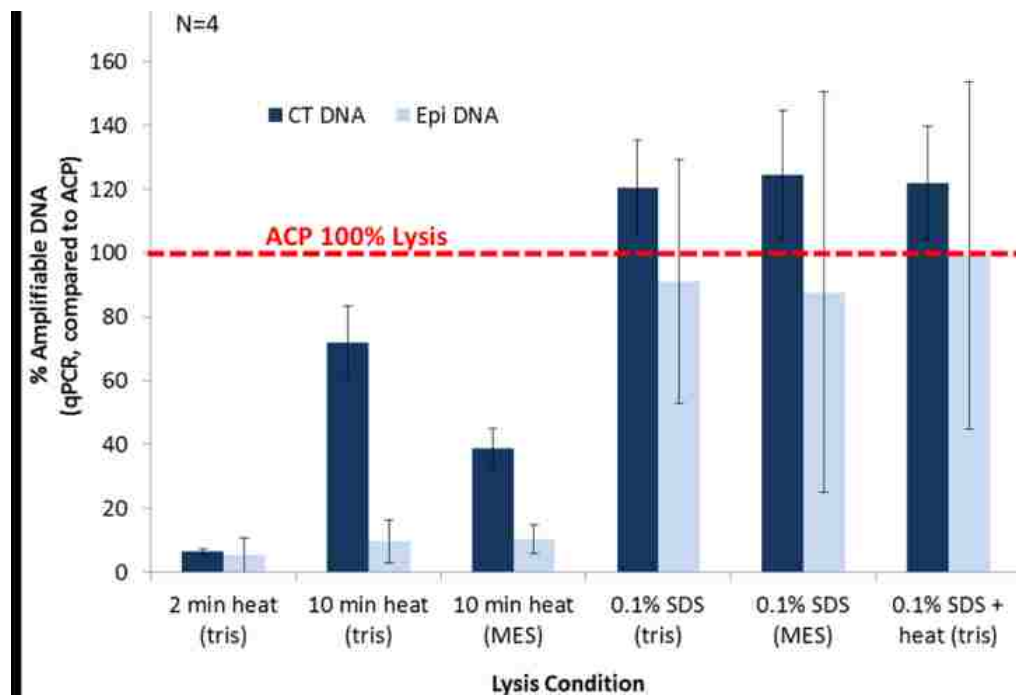


Figure 18. Comparing multiple lysis methods for CT+ cells. All samples were compared to lysis of CT+ epithelial cells in buffer with ACP for 2 minutes at room temperature followed by 10 minutes of heating to 95°C. Averages of at least N=4 are reported with error bars representing one standard deviation. Lysis of both the *C. trachomatis* and epithelial cells were quantified with separate qPCR assays. Lysis of the epithelial cells was highly variable.

Translating bacterial lysis into porous membranes. Small volume sample processing, 50–200 μ L, works well in a tube as demonstrated above, but requires multiple user steps, which is not practical

for POC use. These steps include mixing the bacterial sample with ACP, waiting 2 minutes for lysis, and moving the tube to a heating device for a set period of time. The MAD NAAT project has developed unique valving and timing components that integrate in tube sample processing with porous membrane-based amplification and detection to achieve a full sample to result device with minimal user steps^{138,139}. Although these integrated mechanisms work well, they require robust control of valve timing and some challenging fabrication steps. Additionally, the current prototype is designed to work with swab transfer of samples into ~180 μ L of buffer. To expand the capabilities of the current system to process urine samples, paper-based lysis was explored to reduce the required number of integrated parts and timing mechanisms in the final device.

Bacteria flow through paper. Membrane-based lysis requires that pathogens are able to flow through the pores to a designated lysis region. Standard 17 glass fiber was selected by the MAD NAAT project as the main porous material due to its high flow rate for rapid fluid processing and its compatibility with in-membrane NAATs. Standard 17 glass fiber has a pore size distribution of ~10–100 μ m in diameter and many bacterial cells are ~1 μ m wide indicating that they should be able to traverse through the matrix. There are, however, smaller pores in this membrane so some bacteria may get stuck. Also, bacteria may interact with the fibers of the membrane reducing their overall ability to flow.

To test these assumptions, a solution containing *E. coli* cells was introduced to a glass fiber membrane followed by a wash buffer to saturate the fluid capacity of the membrane. The distribution of cells was quantified by qPCR after liquid fractions were removed from the membrane (see methods for a detailed schematic). **Figure 19** shows that ~60% of the cells added to the membrane successfully flowed into the downstream regions of the membrane, while 25% were retained near the inlet. Over 95% of the total cells added into the membrane were recovered (data not shown) indicating that this distribution accurately represents the flow of *E. coli* pathogens through Standard 17 glass fiber.

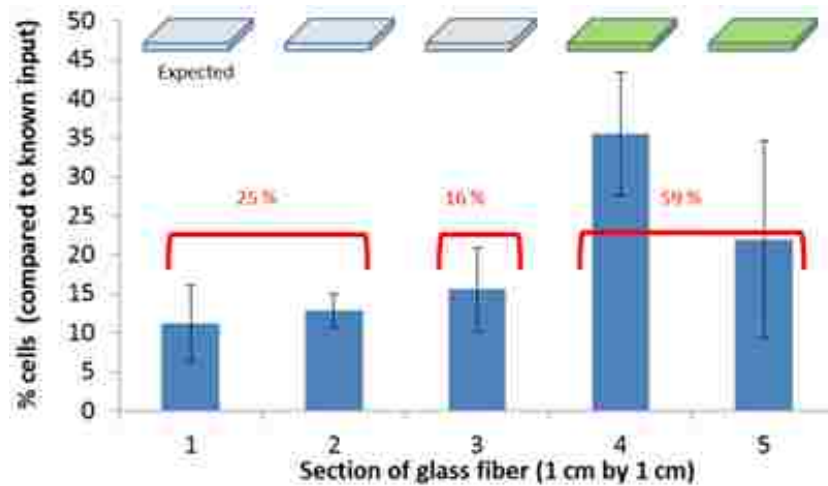


Figure 19. *E. coli* movement through a glass fiber membrane. Averages of $N=5$ +/- one standard deviation are reported.

Thermal and enzymatic lysis in porous membranes. After confirming that *E. coli* will flow through this particular glass fiber membrane, the next set of experiments compared thermal lysis at 95°C and ACP treatment with heat in-tube and in-membrane. A solution containing *E. coli* cells was added to a tube or a 1x1 cm² section of a glass fiber membrane. The reaction vessels were then subjected to one of five lysis treatments: no lysis control, 95°C for 5 minutes, ACP treatment with mixing in tube followed by addition of a membrane, ACP treatment with mixing in membrane (add cells and ACP separately to the membrane), or ACP followed by heating to 95°C for 5 minutes, **Figure 20A**. After treatment, bacterial killing was assessed through plating, **Figure 20B**, which shows that three of the treatments effectively kill bacteria. ACP with poor mixing worked well in tube, but not in membrane likely due to restricted diffusion in the complex matrix. Bacterial killing in the context of membrane-based lysis was chosen as the evaluation metric here instead of directly quantify amplifiable DNA in order to isolate the killing and lysis from gDNA fragmentation (and potential entanglement) in-membrane, discussed in detail in Aim 2.

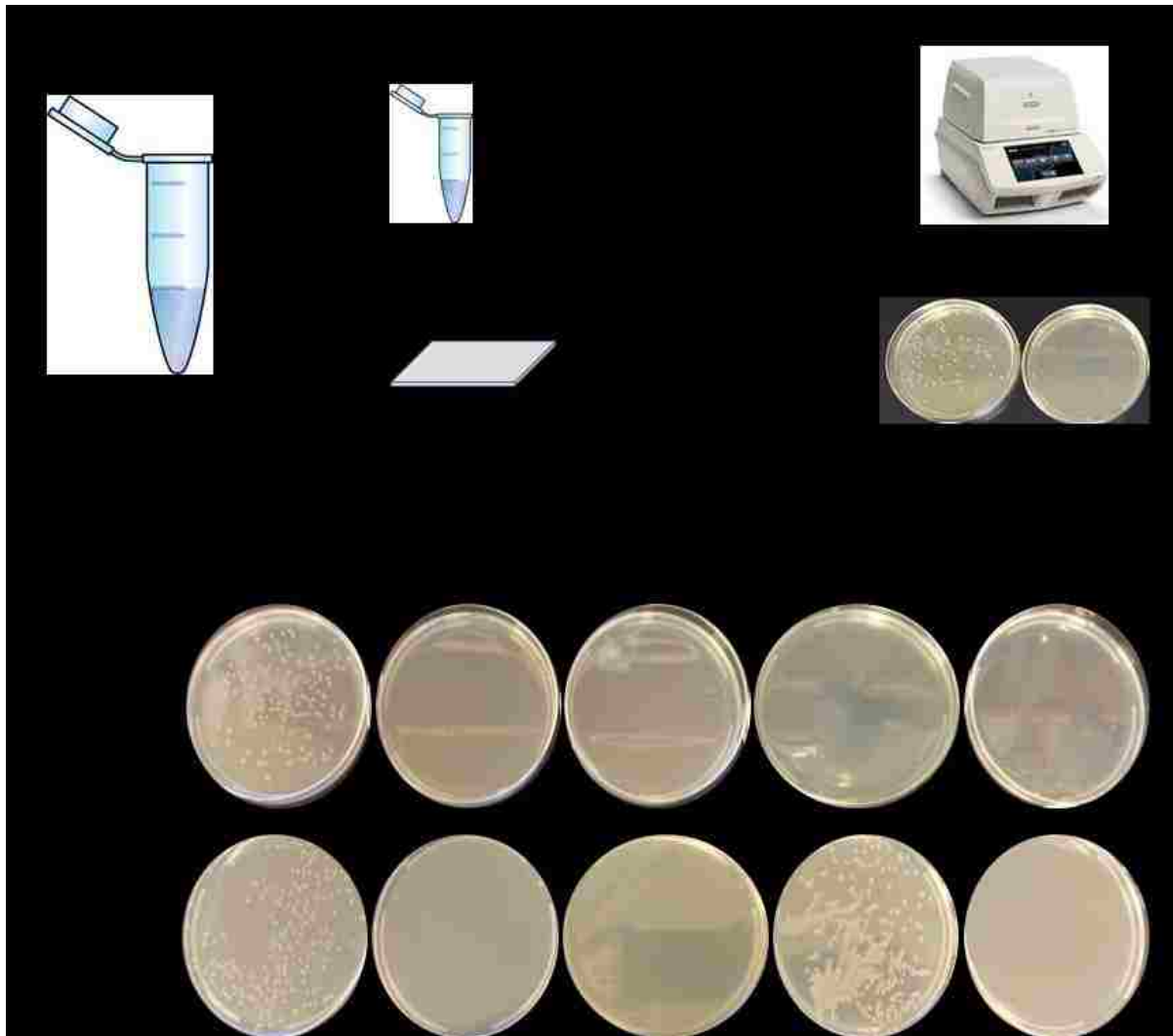


Figure 20. Translating *E. coli* lysis from tube to membrane. **A.** Schematic of experimental set-up. **B.** Plating results after lysis treatment in tube and in Standard 17 glass fiber. Each plate is a representative from a set of $N=3$. These images show that both heating and/or well mixed ACP samples effectively killed the pathogens whether they were heated in-tube or in-membrane. Samples with poor ACP mixing that were introduced to a membrane did not result in cell death, as seen by growth on the agar plate. *Well-mixed samples were mixed in tube prior to introduction to paper. **Poorly-mixed samples were not mixed in tube. The cell solution was added to the membrane followed by the ACP.

The above data show that bacterial killing is not inhibited by the porous matrix. Killing, however, is not the same as pathogen lysis, which involves breaking open the cells to expose DNA. To assess DNA availability post lysis treatment in membrane, the above samples were also quantified by qPCR. In tube, ACP treatment of *E. coli* cells with and without heat resulted in similar quantities of amplifiable DNA while thermal lysis at 95°C for 5 minutes resulted in ~40% of the DNA. In membrane, on the other hand, all four lysis methods resulted in less than 10% of DNA recovery compared to in tube ACP treatment, **Figure 21**.

There are a few potential mechanisms that may be at work. First, ACP may be inactivated when introduced to the membrane because heating the solution in tube after ACP treatment in membrane results in a similar recovery of DNA with heat only. ACP inactivation, however, is unlikely the cause of poor DNA recovery in membrane. Dr. Xiaohong Zhang from the Yager group has demonstrated that ACP stored in

Standard 17 for up to three months remains as active as fresh enzyme (unpublished data). The specifics of this experiment, however, are different than those described above. Dr. Zhang's storage experiments involved adding a small piece of membrane containing stored ACP to liquid in a tube.

ACP in a membrane added to a solution of bacteria in a tube showed high DNA recovery, **Figure 22A**, but both ACP and a solution of bacteria in a membrane showed low DNA recovery, **Figure 22B**. These results indicate two potential failure modes for membrane-based lysis. First, the complex and tortuous structure of porous membranes likely decreases diffusion of molecules therefore reducing

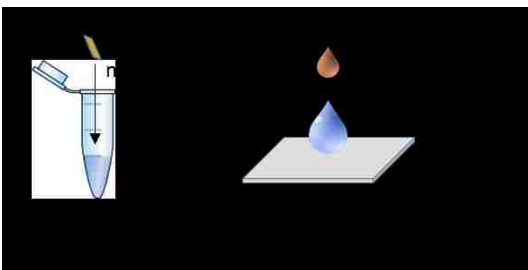


Figure 22. ACP treatment for bacterial lysis. **A.** ACP in membrane added to a bacterial solution results in high recovery of amplifiable DNA, Dr. Xiaohong Zhang. **B.** Both ACP and bacterial solution added to a membrane result in low recovery of amplifiable DNA.

the interactions between lysis enzymes and bacterial cells. This limited diffusion is further complicated by the fact that the ACP reagent is actually a combination of enzymes, many of which may be required for efficient lysis. However, thermal lysis of *E. coli* performed in a porous membrane also resulted in limited recovery of DNA. In this case, the low recovery of amplifiable DNA is potentially due to the entanglement of large gDNA fragments in the porous matrix post lysis. The plating and qPCR analyses can only quantify the available DNA after lysis, but not the size of the DNA fragments. With fragmentation data, we can determine whether lysis, fragmentation, or both are inhibited in porous membranes. These results were further explored in the following chapter.

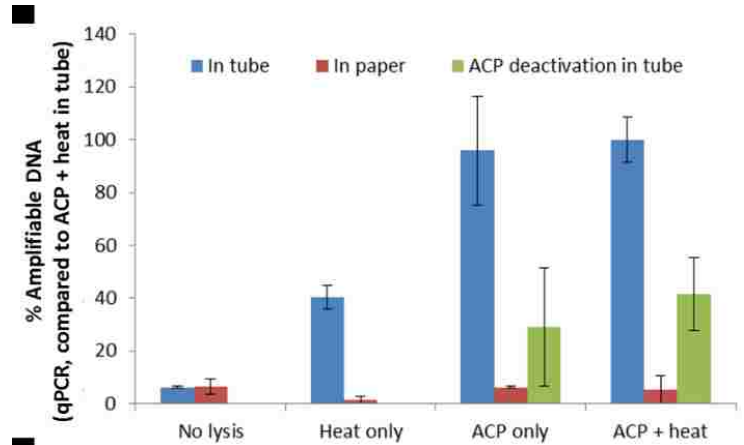


Figure 21. Comparing amplifiable DNA from in-tube and in-membrane lysis experiments. Averages of $N=3$ \pm one standard deviation are reported.

1.3.2 Characterizing the range of variability in human urine samples

Throughout this project, the Harborview STI Clinic has provided 35 de-identified, discarded human urine



Figure 23. Example of urine variability from discarded human specimens provided by the Harborview STI Clinic.

samples for characterization and testing in various experiments. This information was valuable for understanding how these variables effect assays, especially because the samples are highly variable, **Figure 23.**

The pH values and salinities of all samples were measured. The pH values ranged from 5.2–8.2 (average 6.3, SD 0.7, N=35). The salinities ranged from 11–416 mM (average 165 mM, SD 91 mM, N=35). Both of these values were consistent with previously published literature^{120,121}.

The other variables quantified from the urine samples were not available in the literature. These included the total dissolved solids, total NA, and protein content. Each of these variables may affect both the sample preparation and analysis assays, and are therefore important to assess test performance. The total dissolved solids varied between 0.8–68 $\mu\text{g}/\mu\text{L}$ (average 31 $\mu\text{g}/\mu\text{L}$, SD 20 $\mu\text{g}/\mu\text{L}$, N=10).

The amount of total NA (DNA and RNA, measured by the Nanodrop) in the urine samples ranged from 0.46–44.2 $\text{ng}/\mu\text{L}$ (average 8.0 $\text{ng}/\mu\text{L}$, SD 10.1 $\text{ng}/\mu\text{L}$, N=20). The higher end of these concentrations may inhibit NAAT, especially when processing large volumes of urine in the range of 1000–5000 μL . Pre-filtering of samples is often used to reduce non-target NA from a sample, but this is not an option because filtering would remove the CT+ epithelial cells.

The amount of protein in a subset of urine samples was also qualitatively assessed using a commercially available protein concentration kit (Vivaspin 500, as described in the methods section above. After concentration from a 500 μL aliquot of urine, proteins were visualized by gel, **Figure 24.** Pathogen lysis was also performed in many of these samples. The full details of urine sample characterization are available in **Appendix 2.**



Figure 24. Protein gel of concentrated human urine samples.

1.3.3 Development of a simple method to modulate the urine pH

The characterization described above verified the wide range of urine pH; this variation can be problematic when developing assays. To combat sample variability, the lysis method was adjusted to include pH modulation through the simple addition of dried buffer. This mechanism was selected due to its simplicity, making it compatible with POC use. The buffer of choice was MES, with the goal to reduce the pH of all samples to below ~6.5. This pH value is directly compatible with downstream DNA purification, as described in detail in Aim 3.

To test the pH modulation method, freshly cultured *N. gonorrhoeae* and *C. trachomatis* cells were spiked into human urine. A subset of these samples was then used to rehydrate dry MES buffer to reduce the pH < 6.5. Samples were then heated to 95°C for 10 minutes to compare cell lysis with and without pH modulation. **Figure 25** shows that pH modulation did not significantly reduce lysis efficiency for the tested samples. This lysis protocol was incorporated into an integrated device for purification of *C. trachomatis* and *N. gonorrhoeae* DNA from urine specimens, as described in Aim 4.

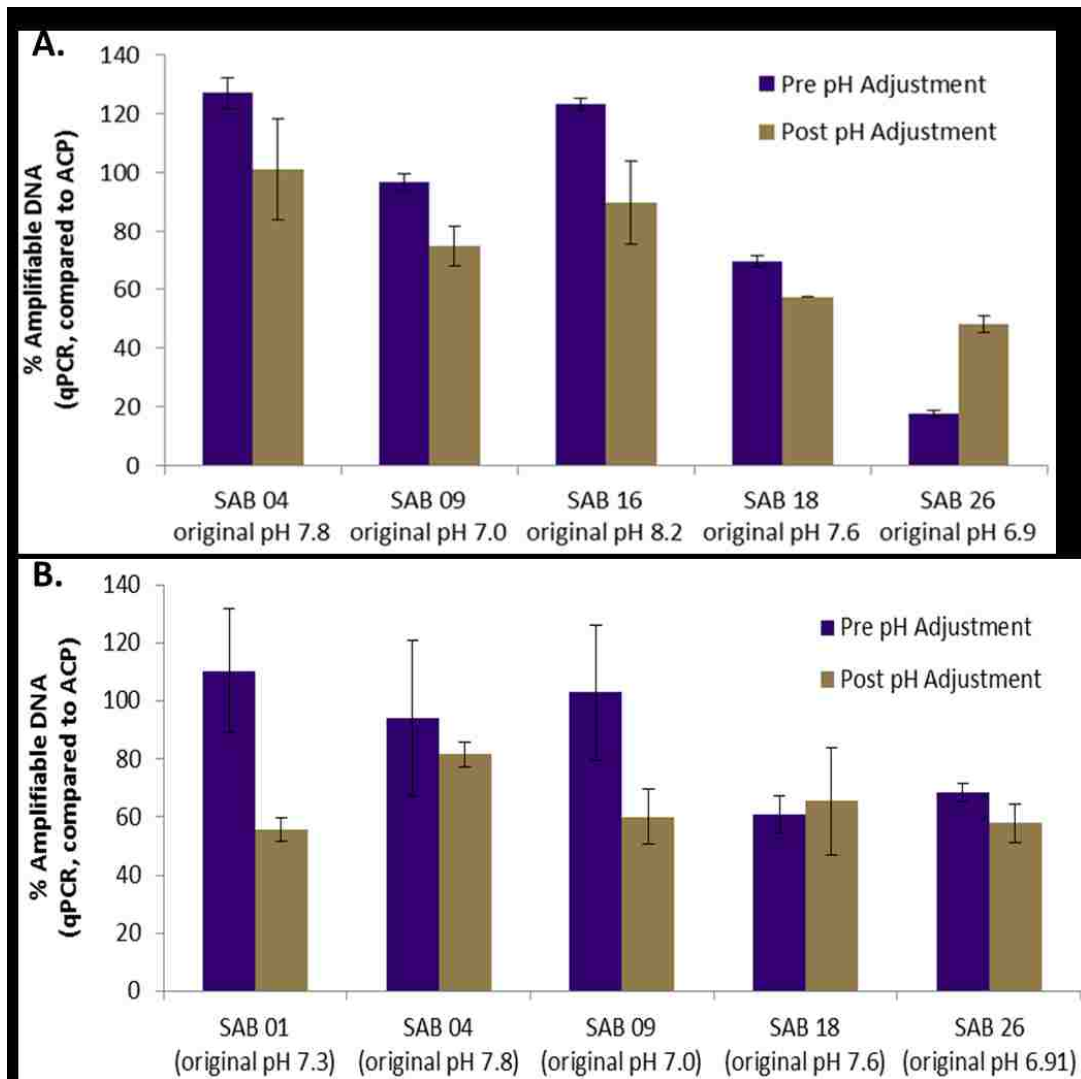


Figure 25. Lysis efficiency of *N. gonorrhoeae* and *C. trachomatis* spiked into human urine with and without pH modulation. Modulated samples were treated with dry MES buffer to a final concentration of 100 mM and a pH <6.5. All samples were compared to ACP treatment in buffer. Averages of N=3 are reported with error bars representing +/- one standard deviation. **A.** *N. gonorrhoeae* and **B.** *C. trachomatis*.

3.4. Conclusions and Future Work

This work evaluated the effectiveness of enzymatic and thermal lysis methods on bacterial samples in discarded human urine samples. Though effective in less complex mixtures like nasal swabs^{56,123}, the data above has shown that ACP treatment is highly sensitive to both pH and salinity of urine. These sensitivities indicate it may not be a practical method of bacterial lysis for raw urine samples. Thermal lysis is more effective in urine samples than enzymatic lysis and can result in equal recovery of amplifiable DNA compared to the gold standard method of bead beating. Thermal lysis is robust over a range of pH values and salinities. When these methods are translated to porous membranes, however, the effectiveness decreases. Heat can kill bacteria in porous membranes, but

releases minimal amplifiable DNA (more details on this in Aim 2). Thermal lysis was also shown to be compatible with urine samples that had modulated pH; this result allowed for integration of lysis with a wide range of downstream processes, including pH-dependent DNA purification (see Aim 3 for more details).

Finally, 35 de-identified, discarded human urine samples were characterized to allow for better understanding of the factors that may influence assay performance. Average sample pH was 6.3 (SD=0.7, N=35), average salinity was 165 mM (SD=91 mM, N=35), average total nucleic acid (DNA and RNA) content was 8.0 ng/ μ L (SD=10.0 ng/ μ L, N=20), and average total dissolved solids was 31.2 μ g/ μ L (SD=22.8 μ g/ μ L, N=10). These characteristics are summarized in **Appendix 2**.

These results were integrated with other sample preparation components to develop an automated system for processing complex samples. Specifically, thermal lysis was linked with thermal DNA scission to develop a simple POC-compatible assay that simultaneously lyses cells and fragments the nucleic acids for use with porous membrane-based systems. Future extensions of this work should evaluate the recovery of both RNA and proteins from pathogens in order to expand its usefulness to additional disease types.

4. Specific Aim 2: Develop a POC-compatible gDNA fragmentation method

Paper-based nucleic acid diagnostics have the potential to translate laboratory assays to simple-to-use, point-of-care devices, but many prototypes of these systems still lack the ability to process realistic samples due to the inability of genomic-sized DNA to move through porous membranes used in these devices. For applications involving pathogen or human gene identification, the ability to fragment and transport DNA would provide more options for device design and broaden the range of applications.

To address this challenge, this chapter describes the development and characterization of a method that combines cell lysis with DNA fragmentation to allow for lateral transport of genomic DNA through commonly-used porous membranes. This work was described in four subsections including: (i) demonstrating that varying heating times and temperatures allows for control of both lysis and fragmentation, (ii) evaluating these methods for multiple cell types and genome sizes, (iii) matching the experimental data to previously published models that describe both DNA denaturation and thermal scission, and (iv) using this method for semi-selective transport of pathogenic DNA over human DNA, which reduced the amount of interference in downstream applications. This method was easily automated and rapid, occurring in less than 10 minutes with

one user step. Initial assay validation was done with *S. aureus* and *E. coli* bacteria; studies were expanded to include mixed samples with *N. gonorrhoeae* and human epithelial cells. This assay was integrated with the other components of the dissertation to develop an automated device for multiplexed detection of chlamydia and gonorrhea from urine samples.

4.1. Background

Paper-based nucleic acid diagnostics promise to convert laboratory assays to simple-to-use, POC devices. A major challenge associated with these systems is how to control the transport of genomic DNA (gDNA) or large fragment DNA (~1 Mbp) through or along the length of a membrane in order to perform additional assay steps. Previously published work has demonstrated the ability to purify and concentrate nucleic acids from complex samples^{50,140} and to amplify and detect in paper membranes^{71,138,141}. These techniques rely on either DNA entanglement in the membrane to restrict the desired target to a specific location⁷¹ or the transport of small nucleic acid fragments such as RNA⁵⁰ or pre-processed DNA^{6,140}. Nucleic acid-based devices designed for POC use, however, must have the ability to process realistic samples, such as gDNA, directly from human or pathogenic cells.

Recent reports have relied on DNA entanglement at the device inlet to demonstrate “sample-to-result” assays that collect a sample and return a result with minimal user steps^{57,138,142}. Although these methods have been successful, there are some notable limitations. First, they often require extensive washing of the nucleic-acid-capturing region to remove amplification inhibitors, which can increase time and device complexity¹⁴³. Second, they require multiple user steps in order to properly deliver additional assay reagents or physically connect downstream detection systems, such as a lateral flow strip^{50,71}. Third, systems that rely on DNA entanglement often require high volumes or concentrations of amplification reagents, increasing both the cost and complexity of a device. As an alternative to DNA entanglement, a simple-to-use method has been developed that enables lateral transport of DNA through porous membranes by employing fragmentation that relies on the application of heat. This method was designed to be directly compatible with POC devices that use nucleic acid amplification tests. In addition to entanglement, this work evaluated the potential effects of adsorption on DNA transport through porous membranes. It was hypothesized that DNA may adsorb directly to a porous substrate, or adsorption may be mediated by DNA-associated proteins.

The major constraint of transporting gDNA through paper-based devices that rely on lateral flow is entanglement of large nucleic acid strands in the porous matrix. Bacterial pathogens have DNA

that is at least 1 Mbp (one million base pairs) in length, which, fully extended, is $\sim 330 \mu\text{m}$ end-to-end. Most bacterial cells, however, are only 1–20 μm long (*E. coli* is $\sim 2 \mu\text{m}$ long), requiring the DNA to be compacted into structures called nucleoids. In *E. coli*, for example, nucleoids can range from 4–15 μm long when extended during cell replication^{144,145} and are composed of looped regions with diameters of $\sim 2 \mu\text{m}$ ¹⁴⁶. In its most compact state, *E. coli* DNA arranged as a nucleoid is approximately $\sim 1 \mu\text{m}$ long. These studies measured nucleoid size during *E. coli* growth phases using microscope imaging. Nucleoid structure can be disrupted by cell lysis or DNA extraction which can reduce compaction and greatly increase DNA end-to-end length^{147,148}. In eukaryotic cells, DNA is compacted into chromosomes. In humans, these chromosomes are between 48–250 Mbp long; their length can range from 2–20 μm when compacted and 14,000–85,000 μm if fully extended¹⁴⁹.

Many commonly used porous membranes in lateral flow devices consist of entangled fibers that effectively form a matrix of interconnected cavities, or pores. This structure describes the membrane (Standard 17) used in the MAD NAAT device for sample processing and amplification. The pores of Standard 17 membranes have dimensions in the range of ~ 10 –100 μm ^{150,151}, but are not uniform throughout a material. Instead, membranes have a pore size distribution with some pores as small as 1 μm and some that are $>100 \mu\text{m}$. Because DNA structure is disrupted by lysis, the reduced compaction may result in limited transport of the DNA through a porous membrane. To compensate for the change in structure achieved by lysis, both bacterial and mammalian DNA require fragmentation after cell lysis to allow for lateral flow through commonly-used porous membranes such as Standard 17 or Fusion 5 (GE Healthcare Life Sciences). There are multiple theories describing the fragmentation, or scission, process of DNA. These theories are supported by different mechanisms that cause DNA fragmentation.

Extensive research on the movement of DNA through complex porous media has been conducted using electrophoresis^{152,153}. Specifically, pulsed-field gel electrophoresis (PFGE) was developed to improve the transport of large fragments of DNA (>15 –20 kbp) through porous gels for improved chromatographic sizing^{154,152,155}. The pore size of an agarose gel can range from 5x–30x smaller¹⁵⁶ than pores in Standard 17 and Fusion 5 membranes. PFGE, however, is assisted by the controlled application of electrical fields in several directions, which requires expensive equipment not easily adaptable to POC settings. Therefore, transport of DNA through porous membranes for diagnostic applications requires fragmentation that produces smaller pieces of DNA to flow through membranes driven only by passive flow.

DNA fragmentation methods. There are four main mechanisms used to fragment DNA: bond breakage through mechanical shear, enzymatic cleavage, chemical cleavage, and thermal scission^{98,157–159}. Recently, these techniques have been used to prepare DNA libraries prior to cloning, however, many of these methods cannot easily be applied to POC devices or in porous membranes.

The mechanical or physical based fragmentation methods rely on high shear to break the bonds between bases. There are multiple approaches that use mechanical-based fragmentation to control nucleic acid scission, and two of the most common are nebulization and sonication. Nebulization forces a solution containing DNA through small pores resulting in high shear stresses and aerosolization of the sample. The degree of fragmentation can be tuned through changes in the applied pressure¹⁶⁰. Although simple to perform, nebulization can result in up to 30% loss of the starting DNA concentration¹⁶¹. Sonication produces hydrodynamic shearing, which creates shear force through the motion of different layers of fluid at varying velocities. Studies have shown sonication produces DNA fragments between 1–4 kbp^{157,162}. Larginho *et al.* extensively compared the effectiveness of many of these physical fragmentation methods¹⁶³ and although they work well to fragment gDNA, these methods often require expensive equipment or multiple user steps, which renders them incompatible with many POC applications^{157,160–163}.

Enzymatic fragmentation methods target cleavage sites *via* enzymes that recognize specific sequences or general structural characteristics of DNA. The most common form of sequence-specific fragmentation is through restriction endonucleases, which are a class of enzymes, each of which recognizes a specific sequence of DNA bases as the cleavage site^{78,164}, **Figure 26A**. There are many commercially available restriction enzymes (RE) and they are most commonly used for cloning applications¹⁶⁴. For more general fragmentation, a cocktail of RE can be used to target multiple ubiquitous sequences. Enzymes that fragment NA without sequence specificity, called nucleases, target cleavage of the phosphodiester bond between bases¹⁶⁵, **Figure 26B**.

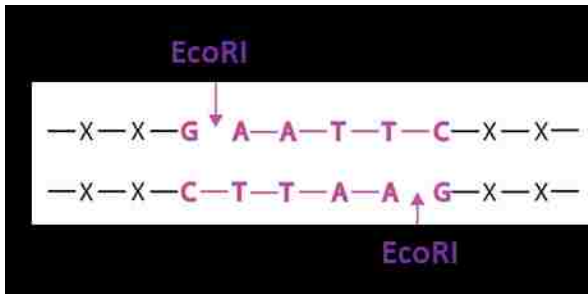
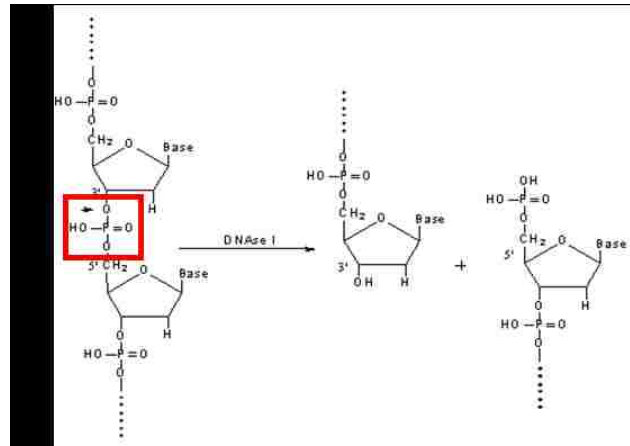


Figure 26. Enzymatic DNA fragmentation with **A.** sequence-specific restriction enzymes¹⁶⁶ and **B.** general nucleases¹⁶⁷. The phosphodiester bond is outlined in red.



Common and commercially available nucleases include DNA fragmentase and deoxyribonucleases (DNases). According to New England Biolabs, DNA fragmentase creates 100–2000 bp fragments in a time-dependent manner. DNA fragmentase combines two enzymes, one that nicks dsDNA and a second that recognizes nicked sites and cleaves the complementary strand¹⁶⁸. The recommended protocol suggests heating at 37°C for up to 30 minutes at neutral pH. Beyond these recommendations, there are few, if any, published reports detailing the sensitivity of DNA fragmentase to pH, salinity, or increased temperature. There are two main types of DNase¹⁶⁹; DNase I nucleases target the phosphodiester bond adjacent to pyrimidines (C, T, and U bases)^{170,171}, while DNase II nucleases do not preferentially cleave at specific nucleotides and are more effective at acidic pH¹⁷². It has been well demonstrated that enzymatic methods work effectively to fragment DNA, but the reagents can be expensive and, like most enzymes, require relatively narrow ranges of pH, temperature, and buffer concentration for optimal performance, making them incompatible for direct use in many realistic sample types.

Chemical fragmentation methods rely on the formation of reactive oxygen species and specific reaction conditions to achieve reliable DNA cleavage^{173–178}. These reactive oxygen species are often generated from hydrogen peroxide (H₂O₂) and are used to oxidize DNA, causing strand scission¹⁷³. Bai *et al.* demonstrated that H₂O₂ treatment effectively fragments ssDNA and the degree of fragmentation is dependent on time, temperature, and H₂O₂ concentration¹⁷⁴; they also showed, however, that hydrogen peroxide treatment alone was not sufficient to fragment dsDNA. To improve the efficiency of dsDNA fragmentation, divalent cations were added to the system because these metals have rich coordination and redox chemistry. Fenton chemistry describes the generation of hydroxide radicals from H₂O₂ in the presence

of transition metals such as Cu(I), Fe(II), Co(II), Ti(III), Cr(V), and Mg(II)^{174–176}, as in the following reaction, (Equation 2).



The metal ion, iron above, is oxidized from $Fe^{2+} \rightarrow Fe^{3+}$ in the presence of H_2O_2 , which generates a hydroxide free radical causing dsDNA fragmentation¹⁷⁵. Although effective at fragmenting gDNA into sizes of ~100s kbp and less, this reaction still requires incubation for 60 min at 37°C¹⁷⁴. To help improve the rate of free radical generation, a reducing agent, such as sodium ascorbate, can be used to reduce the oxidized metal, Fe^{3+} above, back to the reduced state, Fe^{2+} , and the cycle can begin again^{177,178}, Figure 27.

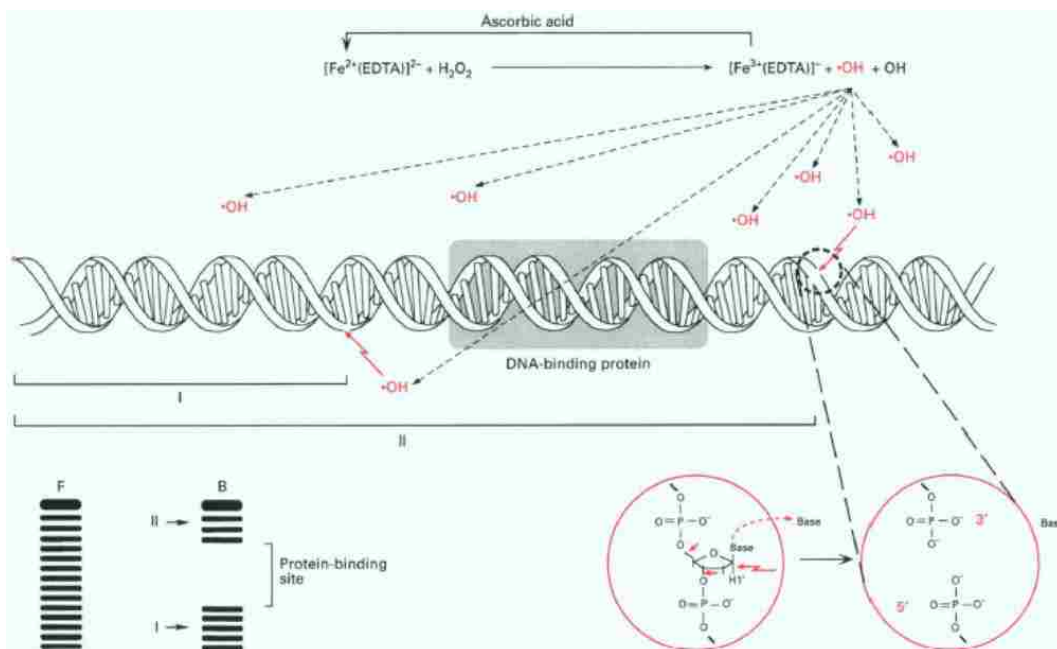


Figure 27. Fenton reaction with Fe(II)EDTA, H_2O_2 , and ascorbic acid for DNA fragmentation¹⁷⁸.

Using this reaction mixture, Hakenberg *et al.* showed simultaneous enzymatic cell lysis and fragmentation of *E. coli* gDNA in 5 minutes at 60°C in a microchip format¹⁷⁷. Although these studies are promising, there is currently limited published work detailing the effectiveness of chemical fragmentation methods in realistic samples with widely varying pH and salinities.

Thermal scission of DNA has been studied since the early 1960s and involves two main mechanisms: hydrolysis of the phosphodiester backbone and depurination, which is followed by backbone hydrolysis. Depurination is the hydrolytic cleavage of purine bases. This cleavage pathway begins with the removal of a purine at the N-C bond that connects the 5-membered backbone ring to

the base. Depurination is followed by scission at the 3' phosphodiester bond resulting in a strand break^{179,180}. Lindahl *et al.* noted that the 3' phosphodiester bond near an apurinic site is weakened, which results in a break in the backbone¹⁸¹. Hydrolysis of the phosphodiester backbone does not only occur at apurinic sites, but can also be a result of a nucleophilic attack by water on the oxygen-phosphorus bond off the 3' carbon¹⁸².

The rates of depurination and backbone hydrolysis have been studied and differ greatly between single-stranded (ss) and double-stranded (ds) DNA. Unsurprisingly, dsDNA shows improved stability and reduced rates of thermal cleavage. For ssDNA, multiple research groups have demonstrated that increasing temperature, decreasing pH, and decreasing the ionic strength of the solution leads to increases in both depurination and backbone hydrolysis^{158,159,182-184}. Additionally, the rates of these reactions have been separately quantified at elevated temperatures (79-100°C)^{158,185,186}. The majority of these studies have focused on mammalian DNA that has been denatured through high temperature (95°C) or DNA-binding proteins. A few groups have extended these studies to scission of single-stranded, heat-denatured bacterial DNA. These results are consistent with studies of thermal scission of mammalian DNA that indicate elevated temperatures (79-100°C) lead to increases in scission events^{159,187}.

The main theories of DNA scission describe two important physical steps: first the denaturation of dsDNA to ssDNA, and second the rates of depurination and backbone scission. To understand and predict DNA scission, it is imperative to consider both of these steps because scission rates are significantly faster for ssDNA compared to dsDNA. The first step in the process is DNA denaturation, defined as the transitions from ssDNA to dsDNA. The time for denaturation is inversely related to temperature and proportional to the square of DNA size^{188,189}, (Equation 3, where τ is time for full denaturation in seconds, T is temperature in Kelvin, and M is the molecular weight of a DNA strand).



(Equation 3)

This relationship predicts that increases in temperature and decreases in size will decrease the time required to denature a piece of dsDNA. The authors note that for very long pieces of DNA, human genomes for example, the predicted denaturation time by this model exceeds the expected time for replication which has led to the hypothesis that long DNA may exist in a partially denatured

state to allow for processes such as replication to occur that require the molecule be single-stranded¹⁸⁸.

The second step in the thermal DNA scission model describes the rates of depurination and backbone hydrolysis. Both Ginoza¹⁸⁵ and Hoff¹⁸⁶ have described that the number of breaks due to thermal scission of ssDNA is proportional to length, (Equation 4, where p is the number of scission events, N is the number of nucleotides in the ssDNA strand, k is the rate constant of scission, and t is time in minutes¹⁸⁶). Ginoza and Eigner have also described that the rate constant, k , is temperature dependent^{158,185}.



(Equation 4)

These two relationships show that longer DNA pieces require longer time to denature from dsDNA to ssDNA. Once denatured, the resulting breaks in ssDNA will be greater for longer fragments. Therefore, there appears to be a balance between overall heating time, heating temperature, and initial length of the DNA strand to describe the resulting size of ssDNA fragments post thermal scission. These theories also assume the DNA is purified and fully unconstrained in dilute solutions. These assumptions are not true for realistic samples, like those used in this work. Realistic samples have DNA constrained in cells, often with bound proteins, and solutions are not dilute or purified.

Methods to measure DNA fragmentation. There are multiple techniques used to measure DNA fragmentation including the COMET assay, the Tunel assay, and pulsed field gel electrophoresis (PFGE). The COMET assay, also known as single cell gel electrophoresis, utilizes a dilute solution of cells and encapsulates them in agarose followed by lysis. Various enzymatic and chemical lysis procedures are compatible with this system, which requires reagents to diffuse into the agarose plug in order to lyse the cells¹⁹⁰⁻¹⁹². Mechanical and thermal lysis methods, however, are not compatible with the COMET assay due to the high temperatures and forces that would break the agarose plugs and mix the cells, preventing single-cell identification and analysis. After lysis, the agarose plug is subjected to electrophoresis to assess DNA fragmentation. Because smaller DNA fragments

electrophoresis more quickly, more fragmentation indicates further movement of DNA through the gel^{194,195}. The resulting shape looks like a comet with the cell as the head and the electrophoresed contents as the tail, **Figure 28**¹⁹³. The ratio of head to tail size is used as a measure of DNA fragmentation.

The original application for the COMET assay was meant to identify spontaneous cell death in a single eukaryotic cell^{194,195}; clinically this assay is commonly used to determine damage to sperm DNA during fertility assessments^{196,197}. Recent research has also adapted this technique to study DNA fragmentation in bacterial cells^{198,199} by preparing small, multi-layer agarose plugs that incorporate bacteria-specific lysis reagents²⁰⁰. Many of these reports focus on *E. coli*.

Another common method used to identify DNA fragmentation is the TUNEL assay, which utilizes an enzyme to detect nicks in dsDNA. When a nick is found, it is repaired with a modified base that can be fluorescently tagged²⁰¹. This method focuses on DNA damage and fragmentation that arises from pre-apoptotic cells. The output is a semi-quantitative measurement where cells with more fluorescence have more nicked DNA. Similar to the COMET assay, the TUNEL assay is most commonly used for intact cells to assess damage to sperm, but it can also be applied to fragmentation of bacterial DNA^{202,203}.

The resulting measurement from both the COMET and TUNEL assays is the DNA fragmentation index (DFI) which quantifies the percentage of cells from a sample that have detectable fragmentation²⁰⁴. Determination of DFI requires the user to assess individual cells and although highly sensitive, does not give any indication of actual fragment size.

Pulsed field gel electrophoresis (PFGE), on the other hand, is a widely used technique for determining the range of DNA fragment sizes in a sample. This technique was originally developed to improve the resolution of fragments larger than 15–20 kbp; with traditional 1D electrophoresis these large fragments become entangled in the gel near the sample input well, and show limited separation. In 1984, Schwartz *et al.* first demonstrated PFGE by applying pulses of an alternating voltage gradient from different angles around the gel which enabled long DNA molecules to overcome entanglement in gel matrix, **Figure 29A**¹⁵⁴. This

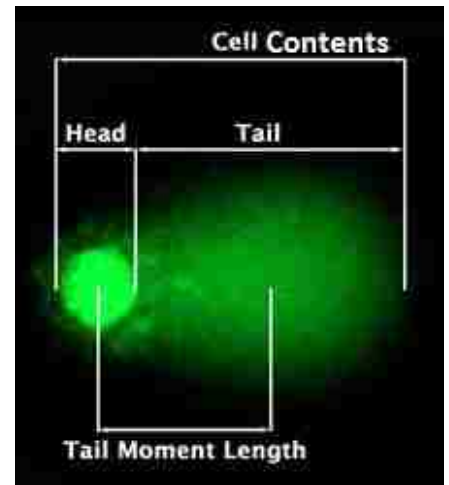


Figure 28. Example of the COMET assay for visualizing DNA fragmentation¹⁹³.

variable pulsing helps distinguish DNA in the kbp to Mbp range because fragment size is proportional to the amount of time it takes a molecule to realign to the field direction¹⁵². This method has led to greatly improved resolution of large fragment sizes, **Figure 29B**, and the evaluation of gDNA fragmentation after cell lysis¹⁵⁵.

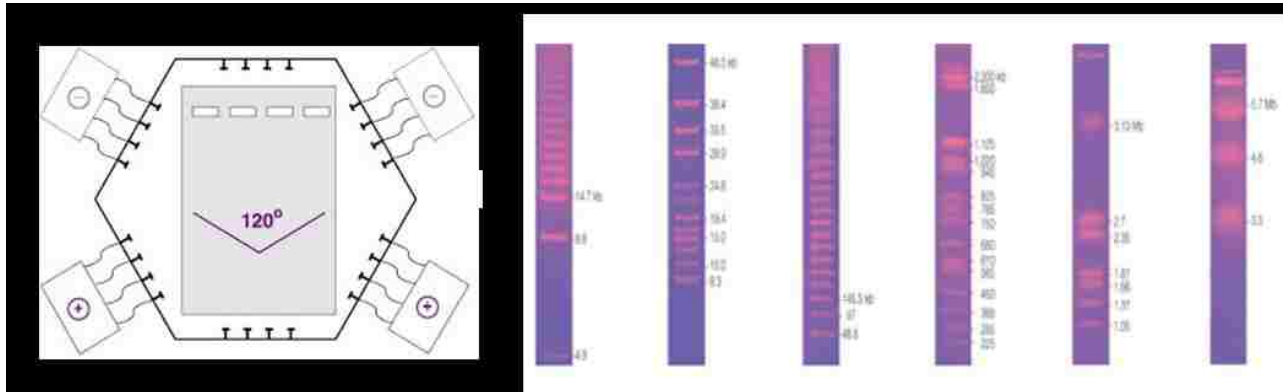


Figure 29. Pulsed field gel electrophoresis. **A.** Schematic²⁰⁵. **B.** Range of PFGE ladders²⁰⁶.

Besides the ability to detect fragment sizes, some additional benefits of PFGE are the evaluation of a variety of samples that contain large DNA fragments and compatibility with multiple lysis techniques. One important challenge to note, however, is that high concentrations of DNA (1 µg, ~10⁸ copies of gDNA) are needed for visualization. A summary comparing the COMET assay, the TUNEL assay, and PFGE is presented in **Table 4**.

Table 4. Comparison of different methods to analyze gDNA fragmentation.

Assay	Measurement	Compatible with all lysis methods	Quantification of fragment size	Min required concentration
COMET assay	Cell-specific	No	No	50–100 cells
TUNEL assay	Cell-specific	No	No	50–100 cells
Pulsed field gel electrophoresis	Total sample	Yes	Yes	> 10 ⁸ copies of gDNA

DNA movement in porous membranes. In porous membranes, such as Standard 17 and Fusion 5, pore diameter can range from less than 1 micron to 100's of microns. Genomic DNA from bacterial pathogens is often at least one million bases pairs (1 Mbp). As noted above, the length of a 1 Mbp genome is approximately 340 µm, which is too large, on average, to move through many of the pores in porous membranes. These mismatched scales require efficient fragmentation of gDNA for reliable transport through porous membranes. Fusion 5 membranes are commonly used and they have moderate pore sizes which range from ~1-11

μm (according to the manufacture²⁰⁷). Based on these size scales, the ideal fragmentation mechanism would produce transportable DNA fragments below ~ 50 kbp.

If DNA is too fragmented, however, the desired gene for amplification may be cut, preventing downstream detection. The acceptable fragmentation range of **~ 10 kbp– 50 kbp** can be calculated based on the size of the membrane pores, the length of the amplicon, and the probability (P) of fragmentation in the amplicon region. These calculations were adapted from work by Dr. Erin Heiniger and are based on a fixed genome length (G), amplicon size (A), and a variable fragment size (F).

$$\text{Maximum fragment size} = \frac{\text{average maximum pore size}}{\text{length per base pair}} = \frac{11 \mu\text{m}}{3.4 \text{ \AA}} = 2.9 \times 10^4 \text{ bp}$$

$$\text{Minimum fragment size} = P(\text{fragmentation in amplicon region}) = \frac{G}{F} \times \frac{A}{G} = \frac{A}{F}$$

$$\text{where } \frac{\# \text{ breaks}}{\text{genome}} = \frac{\text{genome length (G)}}{\text{fragment size (F)}} \text{ and } \frac{\text{amplicon size (A)}}{\text{genome size (G)}}$$

$$P(\text{failure}) \text{ if } A = 100 \text{ bp and } F = 50 \text{ kbp} \rightarrow \frac{100 \text{ bp}}{50 \text{ kbp}} = 0.2\% \text{ failure}$$

$$P(\text{failure}) \text{ if } A = 100 \text{ bp and } F = 10 \text{ kbp} \rightarrow \frac{100 \text{ bp}}{10 \text{ kbp}} = 1\% \text{ failure}$$

$$P(\text{failure}) \text{ if } A = 100 \text{ bp and } F = 1 \text{ kbp} \rightarrow \frac{100 \text{ bp}}{1 \text{ kbp}} = 10\% \text{ failure}$$

Many of the cited studies have focused on purified ss- or dsDNA as their starting material, but preparation from cell-based samples requires the addition of a lysis step to expose the internal gDNA. To address this constraint, we have designed a method to integrate DNA fragmentation with cell lysis. This work is the first demonstration of an integrated lysis/fragmentation method to facilitate lateral transport of DNA through porous membranes. The information presented below can serve as a set of design rules for the development of nucleic acid-based POC devices. First, the effects of adsorption and entanglement on lateral DNA transport through porous membranes was explored. Second, it was demonstrated that increased heating time and temperature increased DNA fragmentation and transport through porous membranes, consistent with the models detailed above. Next, fragmentation and transport through a porous substrate for genomes with varying sizes was compared. Finally, mixed samples containing multiple cell types were used to demonstrate how

varying fragmentation conditions can allow for selective transport of bacterial v. mammalian DNA. Urine is the primary sample type of interest, therefore the lysis and fragmentation methods must perform well over large pH and salinity ranges, as discussed more in Aim 4. This work is applicable beyond the demonstrations presented here. Additional sample types and pathogens could be used to expand the scope of porous membrane-based devices that target gDNA.

4.2. Methods

Materials and Reagents. All reagents were prepared with sterile, molecular biology-grade water (Thermo Fisher Scientific, Waltham, MA, USA). Tris base, MES buffer, achromopeptidase (ACP, A3547), Tris/Borate/EDTA (TBE), phosphate buffered saline (PBS), 0.25% trypsin, Trypticase Soy Broth (TSB), and Lysogeny broth (LB) were purchased from Sigma Aldrich (St. Louise, MO, USA). Pre-poured chocolate agar plates were purchased from Fisher Scientific (Waltham, MA, USA). Proteinase K, SensiFAST probe No-Rox, and SensiFAST SYBR No-Rox kits were purchased from Bioline (Taunton, MA, USA). Mung bean nuclease and DNase I were purchased from New England Biolabs (Ipswich, MA, USA). The *S. cerevisiae* DNA ladder, pulsed-field certified agarose, and DNA sample loading dye were purchased from Bio-Rad (Hercules, CA, USA). The SYBR Safe gel stain was purchased from ThermoFisher Scientific (Waltham, MA, USA). The 10 mM Tris (pH 8), 50 mM MES (pH 5), 50 mM MES (pH 6.5), and 50 mM Tris (pH 8.5) buffers were prepared in sterile water and the pH values were adjusted using solutions of NaOH or HCl. A 20 U/ μ L solution of ACP from lyophilized stock was prepared in 10 mM Tris, pH 8, immediately before each experiment.

Bacterial Cell Culture. Methicillin-resistant *Staphylococcus aureus* (*S. aureus*, strain 1770) was cultured in TSB and *Escherichia coli* (*E. coli*, strain K12) was cultured in LB. Both cultures were heated to 37°C with shaking (250 rpm). Secondary cultures were prepared from overnight cultures diluted 1:100 in fresh medium and grown to mid-log phase ($OD_{600} = \sim 2$). After three hours of secondary culture, cells were pelleted by centrifugation at 13000 $\times g$ for 3 minutes. The supernatant was decanted and the cells were resuspended in 1 \times volume of 10 mM Tris buffer, pH 8.

Neisseria gonorrhoeae (*N. gonorrhoeae*, strain 19424) was cultured directly from frozen stock on chocolate agar plates at 36°C in a 5% CO₂ environment. After 24-48 hours, colonies were collected from the plate and resuspended in 10 mM Tris buffer, pH 8.

Mammalian Cell Culture. Freshly cultured HeLa cells (ATCC CCL-2) were obtained from collaborators in the Hybiske Lab in the Department of Microbiology at the University of Washington. To prepare the cells for experiments, culture media was removed and cells were washed with an

equal volume of PBS, followed by treatment with 0.25% trypsin with shaking at 37°C for 15 minutes. Detached cells were pelleted by centrifugation at 13000 ×g for 3 minutes. The supernatant was decanted and the cells were resuspended in 1× volume of 10 mM Tris buffer, pH 8.

Cell Lysis and Fragmentation of gDNA. Aliquots of 10 μL of freshly cultured cells (bacterial or mammalian) were added to 90 μL of either buffer only (10 mM Tris buffer, pH 8) or buffer with enzyme (10 mM Tris buffer, pH 8, with ACP at a final concentration of 0.5 U/μL). Buffer with enzyme samples were incubated at room temperature for 2 minutes prior to heating. All samples were heated to either 85, 87.5, 90, 92.5, or 95°C for 0–30 minutes. After treatment, samples were allowed to flow laterally through a porous membrane. Additionally, a subset of samples was subjected to pulsed-field gel electrophoresis (PFGE), proteinase K treatment, and entanglement studies (see below).

Porous Membrane Test Card Construction. All porous membranes and test card materials were cut using a CO₂ laser (Universal Laser Systems, Scottsdale, AZ, USA). The untreated and unbacked Fusion 5 and FF80HP nitrocellulose were purchased from GE Healthcare Life Sciences (Niskayuna, NY, USA). Glass fiber 8964 was purchased from Ahlstrom (Helsinki, Finland) and CFSP223000 cellulose was purchased from EMD Millipore (Billerica, MA, USA).

Test cards were made with 0.254 mm-thick plastic backing with adhesive (10 mil Melinex with T-5501 adhesive on one side, Fralock, Valencia, CA, USA). Test cards were assembled by using the adhesive layer of the plastic backing to hold the Fusion 5 porous membrane in place. The test cards were also laser-scored with 1 cm markings for easy membrane sectioning. Control experiments were performed to ensure the adhesive layer of the plastic backing did not inhibit the qPCR.

Adsorption of DNA Fragments to Porous Membranes. A 1 cm × 1 cm section of membrane (either Fusion 5, nitrocellulose, glass fiber, or cellulose) was filled to fluid capacity with sample containing 1×10⁵ copies of fragmented DNA. This DNA was purified from *S. aureus* cells that had been treated with ACP at room temperature followed by heating to 95°C for 10 minutes. After this treatment, the concentration of DNA was quantified by qPCR. The sample was pipetted directly into the center of the membrane. After 5 minutes at room temperature, fluid was collected by placing the membrane, *along the axis parallel to flow*, in a 0.6 mL microcentrifuge tube with a hole in the bottom. The small microcentrifuge tube was then placed in a larger (1.7 mL) microcentrifuge tube; the samples were then centrifuged at 10000 ×g for 3 minutes. The collected elution volumes were measured, and the amount of DNA recovered from each elution was quantified with qPCR to determine the fraction of the DNA remaining in the membrane. Retention was tested in three different buffers across a range

of pH values: 50 mM MES at pH 5, 50 mM MES at pH 6.5, and 50 mM Tris at pH 8.5. Additionally, “blank” samples (buffer only, containing no DNA) were added to each membrane, and the fluid spun out of the membranes was tested to determine whether any chemicals from the membrane affected the qPCR assay.

Lateral Flow Through Porous Membranes. After lysis and fragmentation, 40 μL of each sample was wicked into a 1 cm \times 4 cm Fusion 5 porous membrane to characterize the effect of fragmentation on DNA transport. The samples were chased with 120 μL of a 10 mM Tris, pH 8, to saturate the fluidic capacity of the membrane.

After the Fusion 5 was fully saturated with fluid, membranes were cut into two 1 cm \times 2 cm sections: “Retained” and “Transported.” Fluid was collected from these sections as described above and in **Figure 30**. The collected elution volumes were measured and the recovery of DNA was quantified using qPCR.

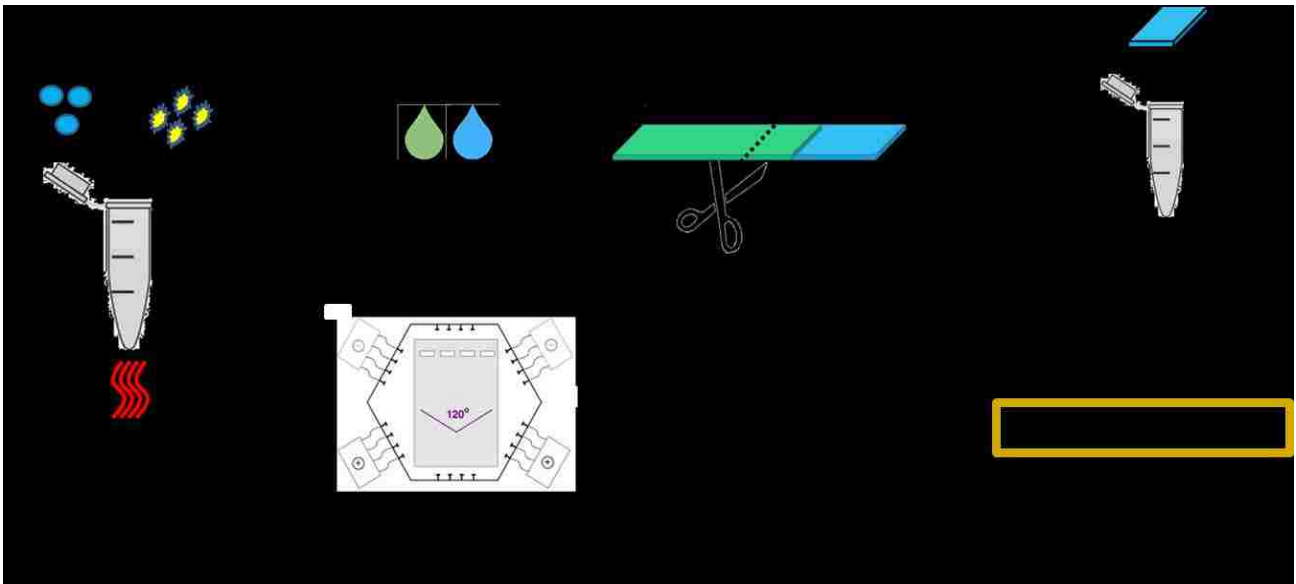


Figure 30. Experimental schematic to assess fragmentation of DNA and transport through porous membranes. After in-tube lysis and fragmentation experiments, sample and wash solutions were wicked into the membranes. Once the membranes were saturated, membrane sections were placed into a tube vertically and fluid was collected via centrifugation along the axis parallel to flow. Some samples were also qualitatively analyzed with PFGE after in-tube lysis and fragmentation to assess the distribution of DNA fragment sizes.

Enzymatic and chemical DNA fragmentation in tube. Freshly cultured bacterial cells (MSSA or *E. coli*) were diluted 10^{-1} in 1x TE buffer (10 mM Tris, 1 mM EDTA, pH 8) or water. The first set of experiments involved treating samples with ACP at room temperature for 2 minutes followed by heating to 85–95°C for 0–10 minutes. Additional samples were subjected to bead beating as described above. The second set of experiments involved treating *E. coli* gDNA with varying amounts

of DNase I, hydrogen peroxide, divalent cations, and/or ascorbic acid. The 25 μ L DNase I reactions occurred at room temperature for 5 minutes. For some samples, the treatment was stopped by adding 25 mM EDTA followed by heat deactivation at 65°C for 10 minutes; this protocol was provided by the Invitrogen DNase I kit²⁰⁸. Treatment with hydrogen peroxide, divalent cations, and/or ascorbic acid, known as the Fenton Reaction, was performed as described in the literature by Hakenberg *et al.* at 60 or 65°C for 5 minutes.¹⁷⁷ Some reactions were stopped using 100 mM urea and 20 mM EDTA. For all experiments, fragmentation was quantified using PFGE.

DNA fragmentation in porous membranes. Fragmentation was also tested in porous membranes. Freshly cultured bacterial cells (MSSA or *E. coli*) were treated with ACP in tube, **Figure 31A,B**, or in membrane, **Figure 31C,D**, at room temperature for two minutes. Some of the tube samples were added to Standard 17 glass fiber members followed by a wash buffer to fill the paper, **Figure 31E,F,G**. All samples, tube or membrane, were heated for 0 or 5 minutes at 95°C.

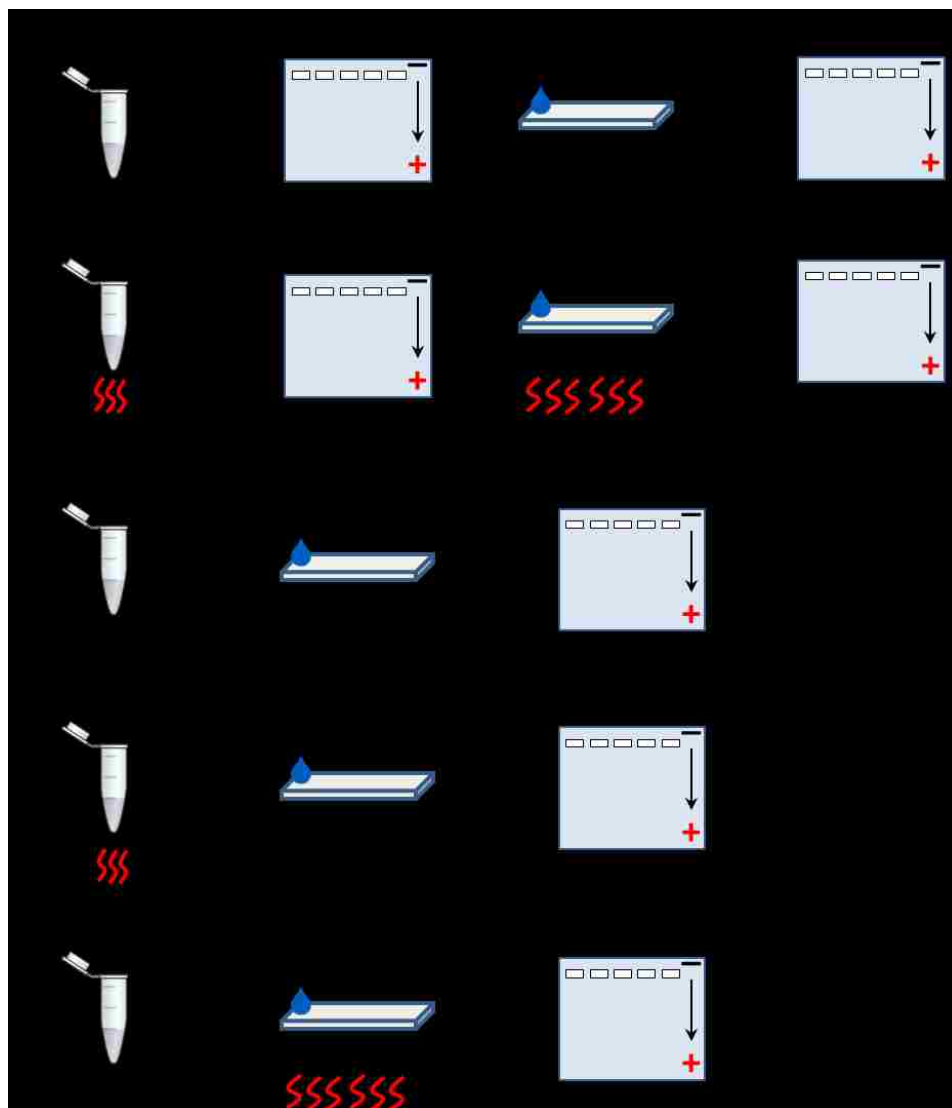


Figure 31. Schematic of DNA fragmentation experiments.

Proteinase K Treatment. A subset of samples was treated with proteinase K (PK) to digest proteins prior to flow through porous membranes. After lysis and fragmentation, these samples were placed in a refrigerator at 4°C for 10 minutes. After cooling, PK was added (final concentration of 50 µg/µL) and the samples were heated to 50°C for 10 minutes, for optimal enzyme activity, followed by heating to 75°C for 10 minutes to deactivate the enzyme. This protocol was adapted from the Bioline product manual²⁰⁹. After PK treatment, samples were wicked laterally into a porous membrane as described above.

Elution of Entangled DNA Fragments from Porous Membranes. After flow of samples through porous membranes and collection of fluid *via* centrifugation, the dried membranes were placed into 100 µL of 10 mM Tris buffer, pH 8. The solutions were heated overnight at 50°C with shaking in an attempt to elute entangled or adsorbed DNA from the membranes. Negative controls of membranes

without any DNA were also included to ensure there was no PCR inhibitor released from the membranes. Finally, samples were pulse-vortexed 10 times. After treatment, the amount of DNA in each sample was quantified by qPCR.

Nuclease Treatment to Quantify Amount of ssDNA v. dsDNA. In order to quantify the amount of ssDNA and dsDNA in a sample following lysis and thermal fragmentation, a subset of samples was treated with mung bean nuclease, which selectively digests ssDNA. After lysis and fragmentation (10 minutes heating at 95°C) of either *E. coli* or *S. aureus*, samples were slow-cooled at room temperature (slow, liquid) or fast-cooled (fast, liquid) on ice for 10 minutes. Additionally, samples were fast-cooled by immediately adding them to Fusion 5 membranes (fast, membrane) at room temperature. The membrane-cooled samples sat for 5 minutes followed by fluid collection *via* centrifugation at 10,000 ×g rpm for 3 minutes.

These samples (slow, liquid; fast, liquid; and fast, membrane) were then treated with 1 U of mung bean nuclease in 1× mung bean nuclease reaction buffer for 30 minutes at 30°C, as recommended by the manufacturer. After nuclease treatment, the remaining DNA was purified by ethanol precipitation and quantified by qPCR. These experiments also included three controls: no nuclease treatment (100% input control), no nuclease treatment and recovery from membrane (to control for potential losses due to interactions with the membrane), and DNase I control (negative control, DNase I should digest all of the DNA in a sample).

Pulsed-Field Gel Electrophoresis. PFGE was used to determine the range of fragment sizes of DNA after treatment. A 1.0 agarose gel was prepared in 0.5× TBE buffer and set overnight at 4°C. Gels were run using the BioRad CHEF Mapper XA System (Hercules, CA, USA) in a cold room (4°C) in 0.5× TBE running buffer. Agarose plugs containing the high molecular weight *S. cerevisiae* DNA ladder were loaded into the gel before submerging in running buffer. Liquid samples were added to the gel with sample loading buffer (1:5 sample:loading buffer). The “Auto-Algorithm” function was used with an input size range from 50 kbp to 1000 kbp, all other conditions were unaltered from the automatic settings. Gels ran for ~27 hours and were stained in a 1× solution of SYBR Safe in 0.5× TBE for 20 minutes with shaking. Gels were de-stained for 10–15 minutes in DI water, then imaged with the BioRad Gel Doc EZ System (Hercules, CA, USA).

qPCR. *S. aureus* DNA was quantified with a qPCR kit for the *ldh1* gene provided by the ELITech Group (ELITech Group Molecular Diagnostics, Bothell, WA, USA). The 20 µL reactions were run on a Bio-Rad CFX real-time PCR instrument (Hercules, CA, USA) using the following protocol: 50°C hold for 2 minutes, 93°C hold for 2 minutes, 45 cycles of 93°C for 10 seconds, 56°C for 30 seconds, and 72°C

for 15 seconds, ending with final elongation step at 72°C for 5 minutes. Fluorescence data were collected during the 56°C annealing step in the Texas Red channel. The qPCR results were analyzed using the automated threshold cycle (C_T) value calculation in the Bio-Rad software (Hercules, CA, USA). This assay was sensitive down to ~10 copies of the target sequence. Assay primer and probe sequences can be found in **Appendix 1**.

E. coli DNA recovery was quantified with qPCR for the *rodA* gene¹³¹ and NG DNA recovery was quantified with qPCR for the *porA* gene¹³² using the SensiFAST probe No-Rox kit from Bioline (Taunton, MA, USA). The 20 μ L reactions were run on a Bio-Rad CFX real-time PCR instrument (Hercules, CA, USA) using the following protocol: 95°C hold for 3 minutes, 40 cycles of 95°C for 10 seconds, 60°C for 30 seconds. Fluorescence data were collected during the 60°C annealing step in the FAM channel. The qPCR results were analyzed using the automated threshold cycle (C_T) value calculation in the Bio-Rad software (Hercules, CA, USA). These assays were sensitive down to ~10 copies of the target sequences. Assay primer and probe sequences can be found in **Appendix 1**.

HeLa DNA recovery was quantified with qPCR for the β -globin gene²¹⁰ using the SensiFAST SYBR No-Rox kit from Bioline (Taunton, MA, USA). The 20 μ L reactions were run on a Bio-Rad CFX real-time PCR instrument (Hercules, CA, USA) using the following protocol: 95°C hold for 5 minutes, 40 cycles of 95°C for 30 seconds, 58°C for 30 seconds and 72°C for 1 minute. Fluorescence data were collected during the 58°C annealing step in the FAM channel. The qPCR results were analyzed using the automated threshold cycle (C_T) value calculation in the Bio-Rad software (Hercules, CA, USA). This assay was sensitive down to ~10 copies of the target sequence. Assay primer and probe sequences can be found in **Appendix 1**.

4.3. Results and Discussion

The ultimate goal of this work was to design POC-compatible methods that allow reliable transport of DNA laterally through porous membranes like those used in lateral flow tests. These methods were designed to directly integrate with devices that use nucleic acid amplification tests¹³⁸. Transport was measured in two ways: 1) quantitatively measuring the amount of DNA that was transported laterally through a membrane after a thermal fragmentation treatment, by qPCR (see Figure 30); and 2) qualitatively assessing the distribution of DNA fragment sizes by PFGE.

All samples used in this work began as intact bacterial or mammalian cells to mimic real-world samples; therefore, all samples required a lysis step to access the DNA. DNA was not isolated prior to fragmentation for two reasons. First, nearly all lysis and nucleic acid (NA) purification assays

inherently fragment DNA, which would unintentionally bias the starting sample prior to testing intentional fragmentation treatments. For example, many enzymes are used to lyse cells, but lytic enzymes often require heat denaturation or NA purification prior to qPCR analysis. Second, realistic samples have intact cells, so using cells as the starting material better represents expected conditions in the application of these methods.

Two metrics were used to evaluate gDNA transport. The first metric, Percent Normalized Transport, removes potential variation in lysis between samples by normalizing transport to lysis efficiency, (Equation 5. This metric isolates the effects of fragmentation on DNA transport through membranes. Lysis efficiencies were quantified by qPCR.



(Equation 5)

The second metric, Percent Absolute Transport, does not normalize to lysis efficiencies, (Equation 6. This metric therefore combines the effect of both lysis and fragmentation when processing the DNA from a sample. This measure was especially important for samples with multiple cell types that may have very different lysis efficiencies.



(Equation 6)

For example, a sample with 100 cells and an 80% lysis efficiency would have 80 copies of the DNA available for fragmentation. If 60 of these copies transported through the membrane, then the Percent Normalized Transport would be 75% [60 copies recovered from membrane / (100 input copies × 80% lysis) = 60/80 = 75%]. The Percent Absolute Transport, however, would only be 60% [60 copies recovered from membrane / 100 input copies = 60/100 = 60%].

There are many parameters that could be varied to determine their effect on DNA fragmentation and transport through porous membranes. In this work, the three main variables that were evaluated were reaction time, reaction temperature, and cell type which relates to DNA length. These three factors were selected because the literature and published equations (Equation 3 and (Equation 4) indicate a direct effect on fragmentation. Also, reaction time and temperature are directly controllable by assay users. Cell type is not controllable, but these methods are being designed for use with real samples in order to develop bacterial diagnostic assays. Real samples

contain mixtures of both bacterial and human cells; therefore exploring fragmentation in these different cell types directly translates to useful information for the desired application.

4.3.1. *Thermal DNA fragmentation in tube.* Initial experiments began by screening multiple fragmentations methods to determine feasibility. These included enzymatic, chemical, and thermal scission. Mechanical fragmentation methods were ruled out due to the complexity and expense of required equipment such as bead beaters or sonicators.

Preliminary work by Dr. Xiaohong Zhang and Dr. Joshua Bishop involved quantifying the distribution of amplifiable DNA in a glass fiber membrane after lysis of MSSA cells (ACP treatment followed by heating at 95°C for 10 minutes). Their work demonstrated that ~65% of the input DNA was able to successfully flow through the membrane to the end of the strip. The other 35% was distributed from the inlet through the middle of the membrane. These results were quantified with qPCR which does not measure gDNA fragment sizes. Based on this preliminary work, the effect of fragmentation on DNA's ability to flow through porous membranes was investigated. This work was performed in either Standard 17 (a glass fiber membrane) or Fusion 5 (a membrane of proprietary constitution), both are commercially available. Both of these membranes have pore size distributions ranging from 1-100 microns, with Standard 17 generally having larger pores than Fusion 5.

Based on these pore size distributions, DNA fragments below ~250 kbp should flow freely through the membranes. To test this theoretical threshold, fragmented gDNA from freshly cultured MSSA cells were flowed through small pore (FF80HP nitrocellulose) and large pore (Standard 17 glass fiber) membranes. DNA length was assessed using PFGE. On average, both nitrocellulose and glass fiber membranes permitted flow of fragments below ~50 kbp, **Figure 32.**

Initial demonstration of thermal fragmentation of DNA and transport through porous membranes was performed with *E. coli* and *S. aureus*, which are Gram-negative and Gram-positive pathogens, respectively. Both types of bacteria were studied to evaluate and

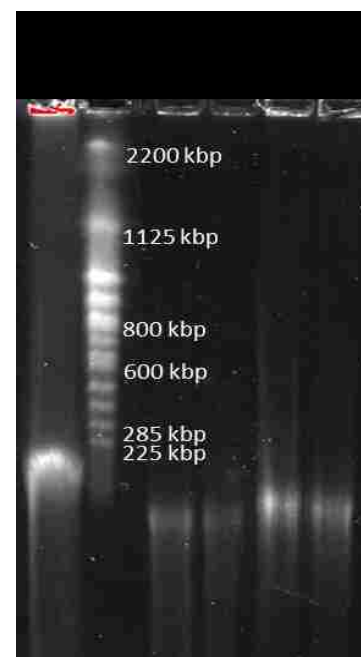


Figure 32. PFGE to determine range of fragment sizes that flowed through nitrocellulose (NC) and glass fiber (GF) membranes.

compare the effects of thermal fragmentation for pathogens with divergent biology. Samples containing one of these pathogens were treated with ACP, a mixture of lytic enzymes^{123,155}, for 2 minutes at room temperature, followed by heating to 95°C for 10 minutes. 95°C was chosen as the target temperature because boiling or near-boiling temperatures are easy to achieve with POC devices and they effectively denature ACP²¹¹. **Figure 33** shows the results from this study. For both pathogens, the Percent Normalized and Percent Absolute Transports are roughly equivalent, **Figure 33A**, because the lysis efficiencies for these conditions were ~100%. A higher percentage of fragmented DNA from *S. aureus* cells transported effectively through the membrane compared to DNA from *E. coli* cells. These differences in transport will be discussed in a later section.

The distribution of DNA fragments was also qualitatively assessed using PFGE, **Figure 33B**. This image shows two conditions for both *E. coli* and *S. aureus*. The “ACP only” condition lyses the cells, but does not significantly fragment the DNA, as observed by the high concentration of DNA in the wells compared to the rest of the lane (note that the red color of the wells are saturated pixels; saturation indicates the presence of high DNA concentrations, also data is presented in Figure 37 and Figure 38 to show effective lysis but limited transport due to limited DNA scission). The “ACP + heat” conditions were first treated with ACP at room temperature followed by heating to 95°C for 10 minutes. For both pathogens under the “ACP + heat” condition, there is significantly less DNA observed in the wells than for the “ACP only” condition.

Under these treatment conditions, the average size of *S. aureus* DNA fragments is smaller than the *E. coli* DNA fragments because some large-fragment *E. coli* DNA remained in the wells, while the *S. aureus*-containing “ACP + heat” wells had very little visible DNA. These differences will be further discussed in the following sections.

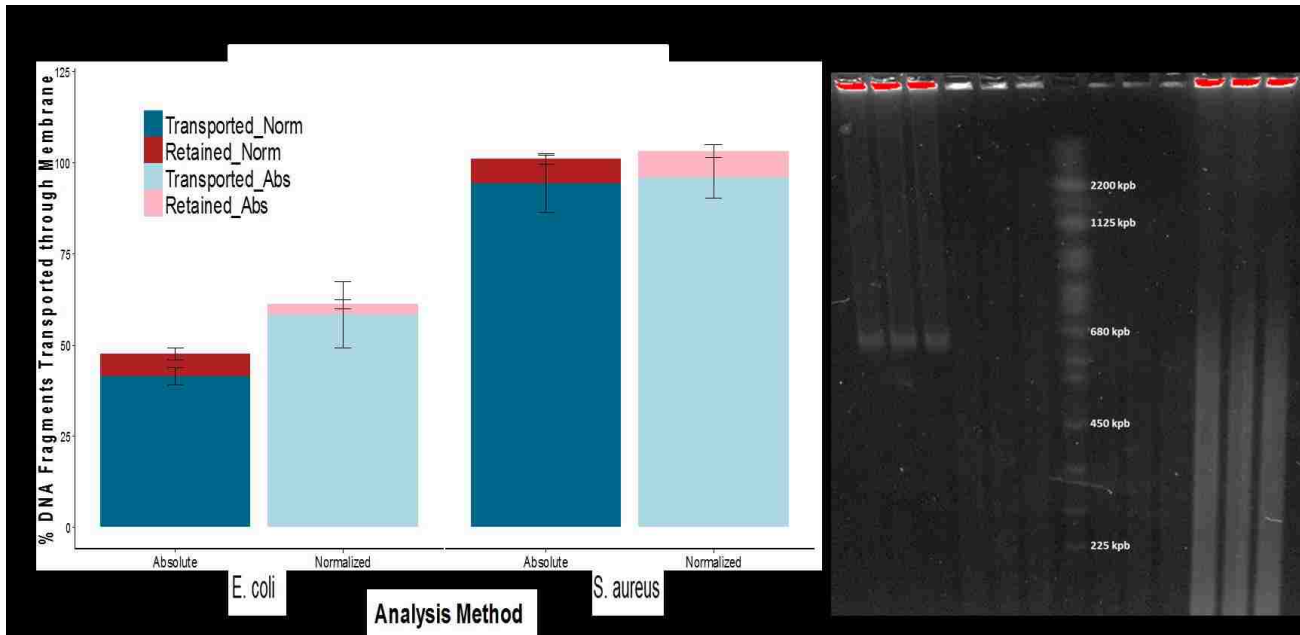


Figure 33. Methods for analyzing thermal gDNA fragmentation and transport through porous membranes using *E. coli* and *S. aureus* pathogens. **A.** Comparing two quantitative measurements of transport: Percent Absolute Transport (Absolute) and Percent Normalized Transport (Normalized). For this data, the lysis efficiencies for both pathogens were ~100% so the two transport quantification methods showed the same results. These data were collected using Fusion 5 membranes. Averages of N=6 (N=3 from two separate cultures) are reported with error bars representing standard error. **B.** PFGE comparing “ACP only” and “ACP + heat” lysis samples. Under these treatment conditions, the average size of *S. aureus* DNA fragments is smaller than the *E. coli* DNA fragments because some large fragment *E. coli* DNA remained in the wells while the *S. aureus*-containing “ACP + heat” wells had no visible DNA. Note that the red color of the wells in the upper part of the gel are saturated pixels, indicating the presence of very high concentrations of DNA.

4.3.2. *Enzymatic and chemical fragmentation in tube.* Experiments involving enzymatic and chemical fragmentation included treatment with DNase I or Fenton reagents (Fe^{2+} with H_2O_2 and ascorbic acid), respectively. The goal of these initial attempts was to reproduce previously published data that detailed fragmentation of *E. coli*¹⁷⁷. For these experiments, freshly cultured MSSA cells were treated with ACP at room temperature followed by one minute of enzyme heat-deactivation at 95°C. The short heat-deactivation was designed to help kill the enzyme without significantly fragmenting the gDNA. The samples were allowed to cool to room temperature followed by treatment with DNase I or the Fenton reaction, as described above. Resulting fragmentation was assessed through PFGE.

The first two rounds of experimentation did not produce quantifiable gel results. **Figure 34** shows the resulting gel from a Fenton fragmentation experiment. Based on published literature, the samples treated with $\text{Fe}(\text{II})\text{SO}_4$, H_2O_2 , and ascorbic acid should produce the most fragmented DNA during the 5-minute experiment. Samples without ascorbic acid should not fragment well during this short time because ascorbic acid helps increase the rate of the reaction¹⁷⁸. The ladder shows up well,

but the rest of the lanes show little product. Either the initial input concentration was too low to visualize or the treatments had no effect on the gDNA size. The intensity of bands in the wells (top of the gel with red pixels indicating image saturation) showed that there was likely a sufficient concentration of DNA, but limited fragmentation.

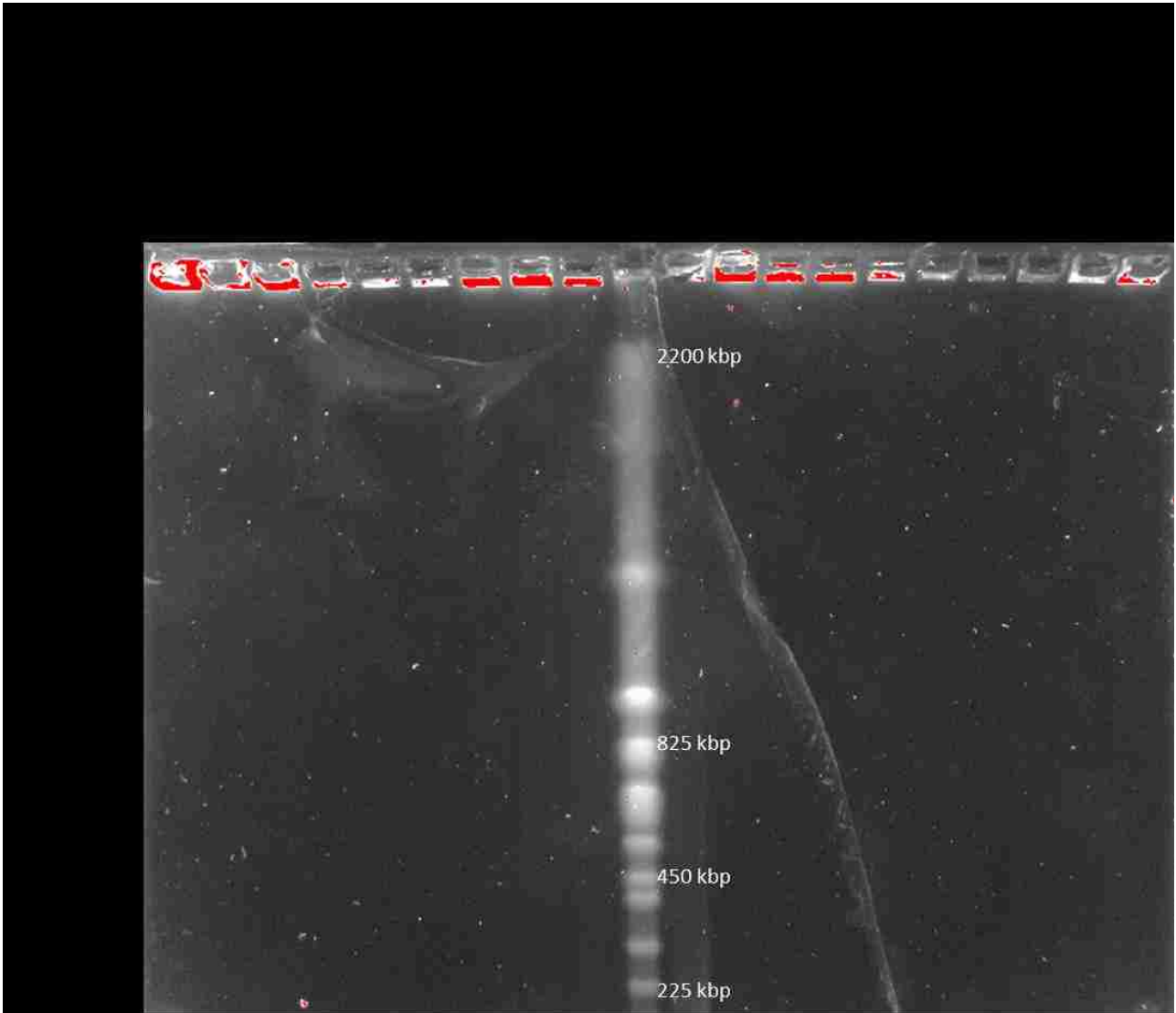


Figure 34. Fragmentation of *E. coli* gDNA in tube from the Fenton reaction. None of the treatments showed significant fragmentation.

Additional rounds of treatment with DNase I or Fenton reagents resulted in similarly poor fragmentation. Based on the initial results presented above, thermal scission was selected as the fragmentation method for this point-of-care focused application. Additionally, thermal fragmentation requires a significantly less complex heating profile than either enzymatic or chemical fragmentation. **Table 5** summarizes these results. All methods were compared to bead beating as the gold standard method.

Table 5. Summary of gDNA fragmentation in tube. *Bead beating treatment heating is a result of the violent agitation method and was not directed measured. **Gel results were not resolvable so the extent of fragmentation could not be quantified.

Treatment	Heating Time (min)	Heating Temperature (°C)	% Transportable fragments (Standard 17 glass fiber)
Bead beating	3x 1 min cycles (during agitation)	Not measured*	~60 %
ACP no heating	n/a	n/a	20–40 %
ACP with heating	5 – 10 min	95°C	50–100 %
Fenton reaction	5 min	65°C	> 10 %
DNase I	5 min	65°C	Could not quantify**

4.3.3. *Effect of adsorption versus entanglement on gDNA transport through porous membranes.* After the initial demonstrations, experiments were performed to test the hypothesis that transport of DNA through porous membranes was dependent on the extent of gDNA fragmentation. Competing hypotheses were considered that might explain a lack of transport: adsorption to the membrane matrix by DNA or DNA-associated proteins (which should not depend on the length of the DNA strands) or DNA entanglement (which should be reduced as the mean fragment size is reduced by fragmentation).

DNA adsorption was evaluated in four different membranes (FF80HP nitrocellulose from GE Healthcare Life Sciences, Fusion 5 from GE Healthcare Life Sciences, CFSP223000 cellulose from EMD Millipore, and Standard 17 glass fiber from GE Healthcare Life Sciences) using three buffers with varying pH values (5, 6.5, and 8.5) that spanned the range observed in human samples such as urine¹²⁰. The DNA used in these experiments was purified from *S. aureus* cells and fragmented by heat in order to remove the potential confounding effect of DNA entanglement.

For both the cellulose and glass fiber membranes tested, adsorption to the membrane was pH-dependent, lower pH values resulted in reduced recovery of DNA indicating higher amounts of DNA adsorption. The DNA added to both nitrocellulose and Fusion 5 was recovered at all three pH values tested indicating little-to-no adsorption, **Figure 35**.

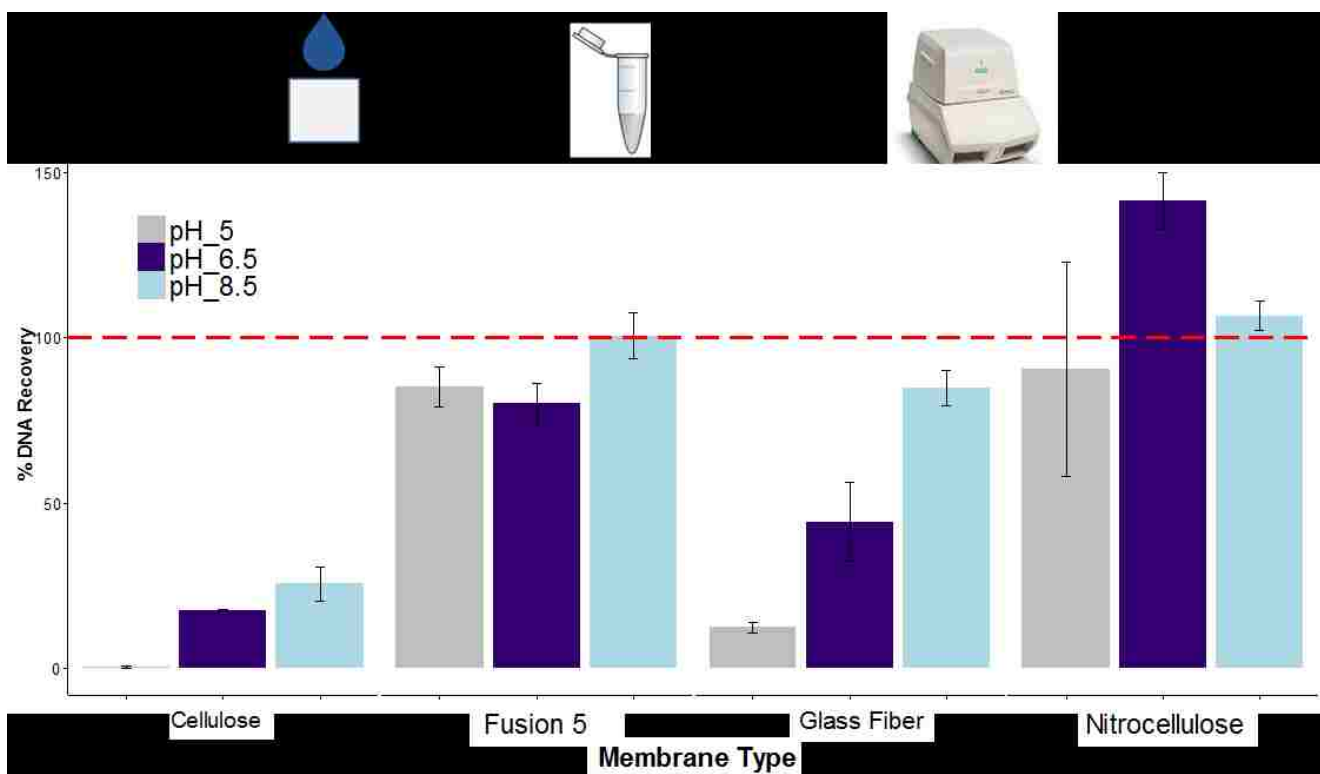


Figure 35. Adsorption of DNA in porous membranes. Heat-fragmented *S. aureus* DNA was diluted in buffer (pH 5, 6.5, or 8.5) and added directly to 1 cm × 1 cm membranes. Samples sat at room temperature for 5 minutes followed by fluid collection by centrifugation at 10,000 ×g for 3 minutes. Elution volumes were measured and the total amount of recovered DNA was quantified by qPCR. Recoveries were adjusted for elution volume: % recovery = [qPCR output (copies/μL) × elution volume (μL)] / input (copies). Averages of at least N=4 are reported with error bars representing standard error of the mean. Buffers containing no DNA (“Blank samples”) were also added to and eluted from the membranes to test for any effects on qPCR. The Blank samples eluted from the nitrocellulose membranes showed slight enhancement of qPCR signals which may explain both the variability and the observed recovery for DNA from nitrocellulose.

These results were consistent with our understand of the material properties because both nitrocellulose and Fusion 5 are negatively charged, and therefore are unlikely to adsorb DNA¹⁵¹. However, DNA recovery from nitrocellulose was variable and elutions of only buffer (no DNA added) showed slight enhancement of the qPCR signal. Based on these considerations, Fusion 5 was selected as the material for the remaining experiments detailed below.

DNA is not the only molecule that can adsorb to the membrane. It is well known that proteins can readily adsorb to porous membranes depending on the buffer conditions^{48,151,212}; because cellular gDNA is coated with proteins, a protein coating could play a role in reducing DNA transport.

To test this hypothesis, samples were treated with proteinase K (PK) after initial lysis and heat-based fragmentation. Short (2 minutes) and long (8 minutes) heating times were compared for four different cell types: *N. gonorrhoeae*, *S. aureus*, *E. coli*, and human epithelial cells. After PK treatment,

the samples were allowed to flow laterally through Fusion 5 membranes, after which DNA recovery from different membrane sections was quantified (Percent Normalized Transport). For all four cell types at both heating times, there was no observable difference between samples with or without PK treatment, **Figure 36**, indicating that presence of protein on the DNA does not significantly affect transport of DNA through Fusion 5 membranes under these assay conditions.

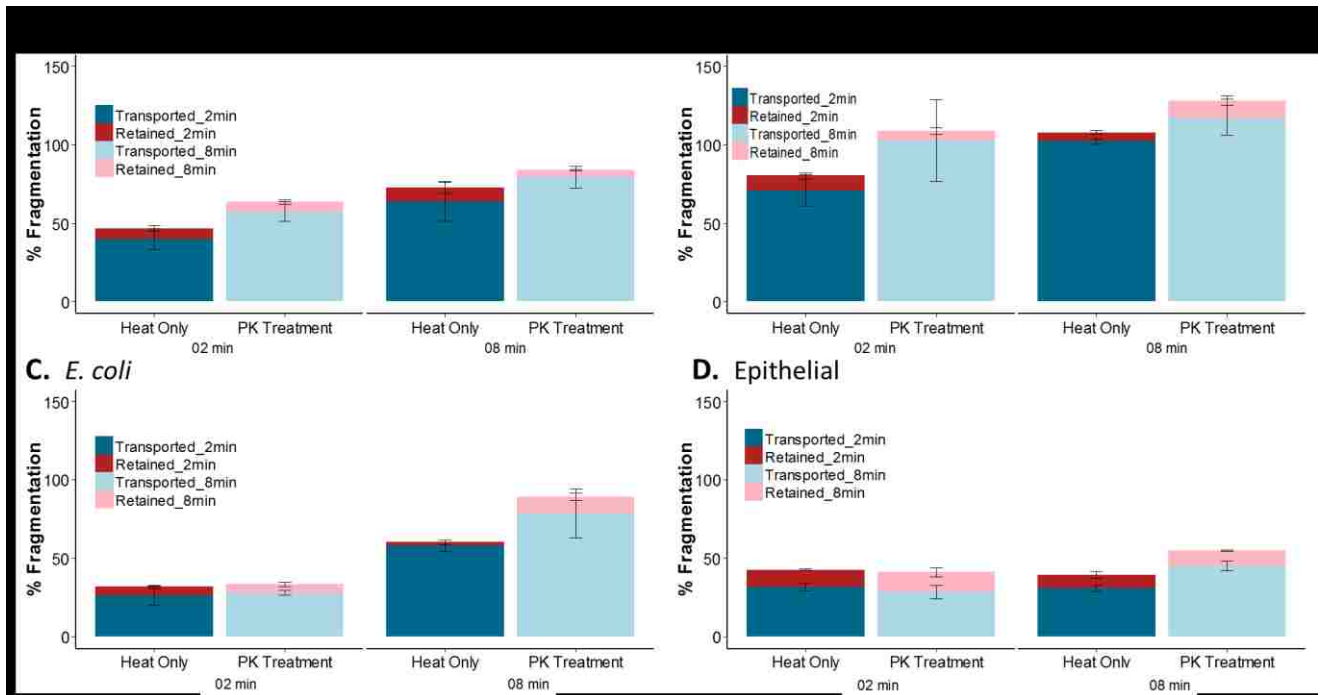


Figure 36. Effect of proteinase K (PK) treatment on samples post lysis and thermal fragmentation. All samples, except MRSA, were lysed by heating to 95°C for either 2 or 8 minutes; MRSA was treated with ACP for 2 minutes at room temperature prior to heating to 95°C. For all samples and heating times tested, treatment with PK does not improve flow through the porous membrane suggesting that proteins in the sample are not significantly contributing to DNA movement. Averages of N=3 are reported with error bars representing standard error. **A.** *N. gonorrhoeae*, **B.** MRSA, **C.** *E. coli*, and **D.** HeLa epithelial cells.

For the samples in Figure 33, less than 75% of the *E. coli* DNA was recovered from the membrane while nearly 100% of the *S. aureus* DNA was recovered. Based on the genome sizes of the bacterial strains used in this study (*E. coli* ~5 Mbps and *S. aureus* ~2.5 Mbps), the known pore size distribution of the Fusion 5 membrane, and the models that describe the length dependence of DNA denaturation and scission, it was hypothesized that the *E. coli* DNA fragments were, on average, larger than the *S. aureus* fragments. These larger *E. coli* DNA fragments were entangled in the membrane. This entanglement would prevent the large DNA fragments from transporting through the membrane and being eluted during centrifugation. To test this hypothesis, membranes were

saved after elution and placed in buffer. These samples were then heated overnight at 50°C with shaking in an attempt to elute unrecovered DNA from the membranes. The effects of the overnight treatments were then characterized *via* qPCR.

After overnight treatment, the *E. coli* samples had 25% (SE 4.6%, N=3) of the input DNA remaining entangled in the membrane after transport and collection while the *S. aureus* samples had only 2.0% (SE 0.6%, N=3). These data support the information presented in Figure 33 because nearly 100% of the *S. aureus* DNA was recovered from transport and only 2% was recovered from the overnight treatment. The results from Figure 33 also showed ~75% of the *E. coli* DNA was recovered from transport and the remaining ~25% from the overnight treatment. These data combined resulted in ~100% recovery of input DNA from both pathogens.

Finally, the amount of ssDNA vs. dsDNA in a sample after lysis and thermal scission was quantified to determine the output of those processes prior to introduction to a porous membrane. The literature indicates that the rate of thermal fragmentation of ssDNA is significantly faster than that of dsDNA^{158,185,186}. All samples in our work were heated to 95°C, suggesting that the majority of the DNA should be single-stranded.

After lysis and fragmentation at 95°C for 10 minutes, both *E. coli* and *S. aureus* DNA were treated with mung bean nuclease, which specifically degrades ssDNA. If the above hypothesis is true – that the majority of the DNA should be single-stranded – then this nuclease should digest the majority of the DNA in the sample, resulting in low yields by qPCR. For both pathogens, this was exactly what was observed; after mung bean treatment, less than 10% of *E. coli* DNA remained and less than 3% of *S. aureus* DNA remained. These results indicate that after lysis and thermal fragmentation at 95°C, followed by a period of 5 minutes or less at room temperature, over 90% of the DNA in these samples was still single-stranded.

The observed difference between *E. coli* and *S. aureus* is consistent with the denaturation model described above, which notes that time for denaturation is dependent on the square of DNA length. The *E. coli* DNA used in these studies was ~2× longer than the *S. aureus* DNA, therefore we expected more *E. coli* dsDNA than *S. aureus* dsDNA, which is what these results show.

4.3.4. *Effect of heating time on DNA fragmentation and transport through porous membranes.* After performing the experiments probing the mechanisms of effective transport discussed above, the effects of varying sample heating times at 95°C on fragmentation of DNA and transport through porous membranes was characterized. Based on previously published literature and the initial

experiments above, it was hypothesized that increasing heating times would result in increased fragmentation and transport of DNA through a membrane. Additionally, an important goal of this aim was to understand the impact of heating time on fragmentation to guide assay design.

Samples containing either *E. coli* or *S. aureus* bacteria were heated for 0–10 minutes followed by flow through Fusion 5. In order to decouple the effects of lysis and fragmentation, Percent Normalized Transport was used as described above, (Equation 5). For the conditions presented in Figure 38 below, all lysis efficiencies were >80%, **Figure 37**.

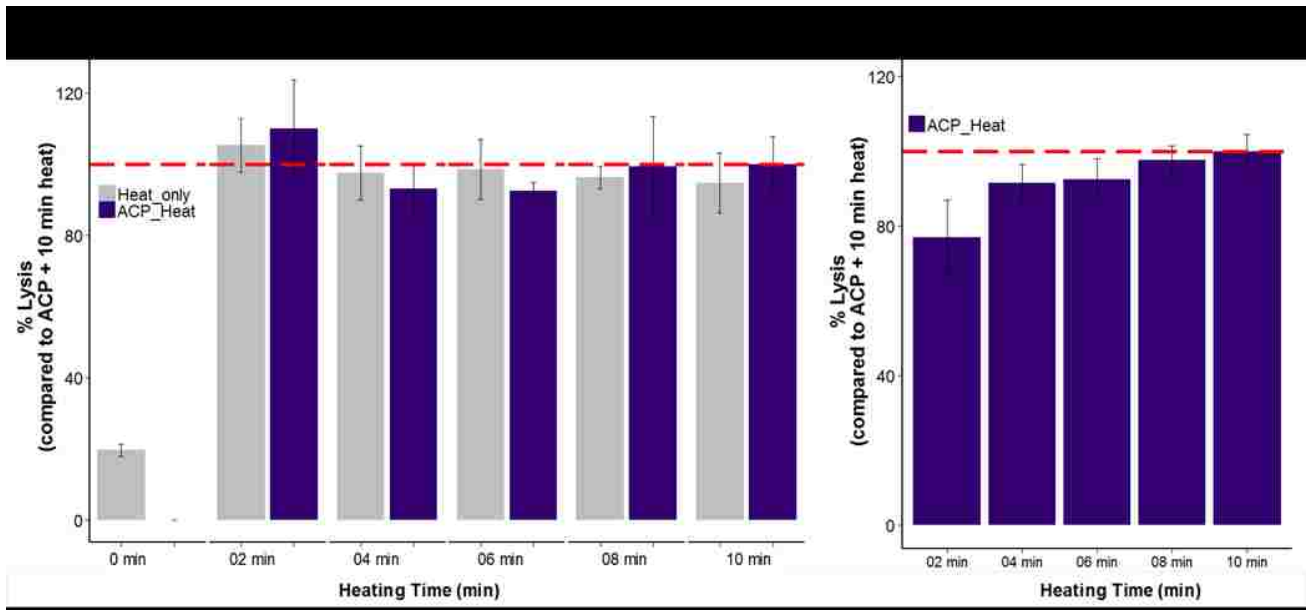


Figure 37. Lysis efficiencies for various methods and heating times at 95°C. Treatment with ACP + 10 minutes of heating was set to 100% (dashed red line) for each pathogen tested. In general, lysis efficiencies were similar for each condition. Samples treated with ACP could not have a 0 min heat condition because the non-denatured enzyme inhibits qPCR. The average of N=6 (N=3 from two independent cultures) is reported with the error bars representing standard error. **A.** *E. coli* treated with and without ACP, and **B.** MRSA treated with ACP.

For both pathogens, increased heating time resulted in a higher Percent Normalized Transport, **Figure 38**, indicating a higher degree of fragmentation. These results were also verified by PFGE, **Figure 39**. After 4 minutes, there is little additional observed fragmentation. These results are consistent with the theory described by Ginoza and Hoff that longer heating times results in more scission events which would lead to smaller DNA fragments. Smaller fragments should transport more effectively through porous membranes. Therefore, transport is directly proportional to heating time.

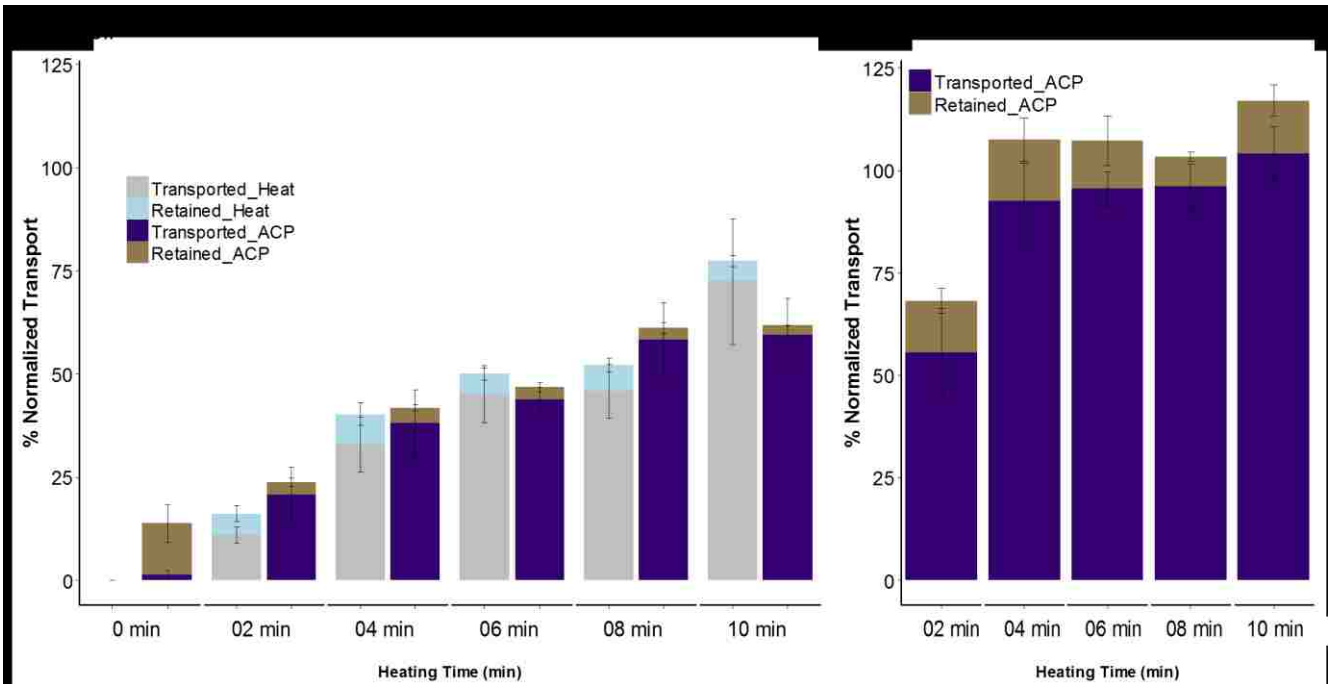


Figure 38. Effect of heating time on DNA fragmentation and transport through porous membranes. Averages of $N=6$ ($N=3$ from two independent cultures) are reported with error bars representing standard error. Samples treated with ACP and no-heat cannot be quantified because the non-denatured enzyme inhibits qPCR. **A.** *E. coli* treated with and without ACP, and **B.** *S. aureus* treated with ACP. *S. aureus* is not susceptible to thermal lysis.

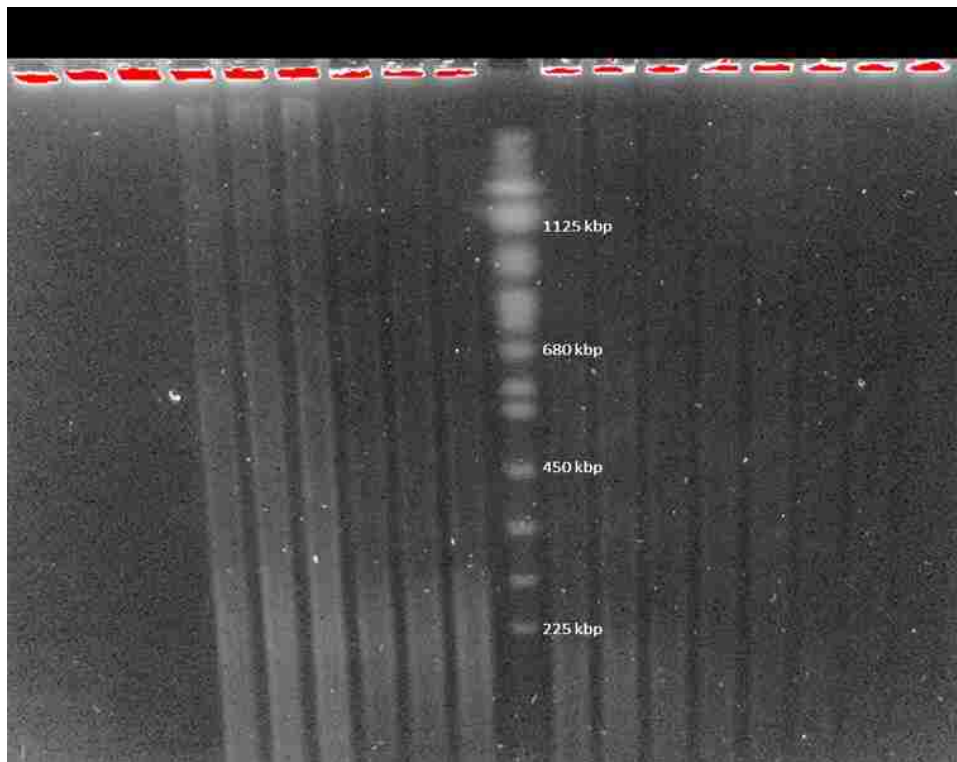


Figure 39. Example PFGE for varying *E. coli* heating time at 95°C. *E. coli* containing samples were treated with ACP at room temperature for 2 minutes followed by heating to 95°C for 0-10 minutes. A qualitative assessment of fragmentation was visualized using PFGE with $N=3$ samples per heating time. As heating time increased, the amount of DNA retained in the wells decreased.

E. coli treated with or without ACP did not show any difference in transport, indicating that the enzyme does not significantly affect DNA fragmentation in this assay. Experiments with ACP and no heat were not performed because ACP that is not heat-deactivated inhibits qPCR.

E. coli is Gram-negative, with a thin cell wall making it susceptible to thermal-based lysis without ACP. *S. aureus*, however, is Gram-positive; the thick cell wall composed of peptidoglycan is comparatively resistant to thermal lysis¹²³. ACP was used to lyse *S. aureus* and make the DNA available for thermal fragmentation^{123,211}.

There was a significant difference in transport of *E. coli* vs. *S. aureus* DNA when comparing across heating times. For example, the maximum percent transported for *E. coli* was ~75% for 10 minutes of heating at 95°C whereas *S. aureus* heated at the same temperature for the same amount of time resulted in ~100% transport.

This suggested that heating the *E. coli* sample for longer would result in more fragmentation and therefore a higher percentage that transports through the membrane. To test this hypothesis, samples were heated for up to 30 minutes at 95°C followed by immediate flow laterally through Fusion 5. Fluid was collected from the membrane as described above and transport was quantified. The results from the experiment support this hypothesis and show that the extended heating times do result in a higher percent of *E. coli* DNA (~65% for 5 minutes v. ~90% for 20 minutes) that effectively transports through Fusion 5, **Figure 40**.

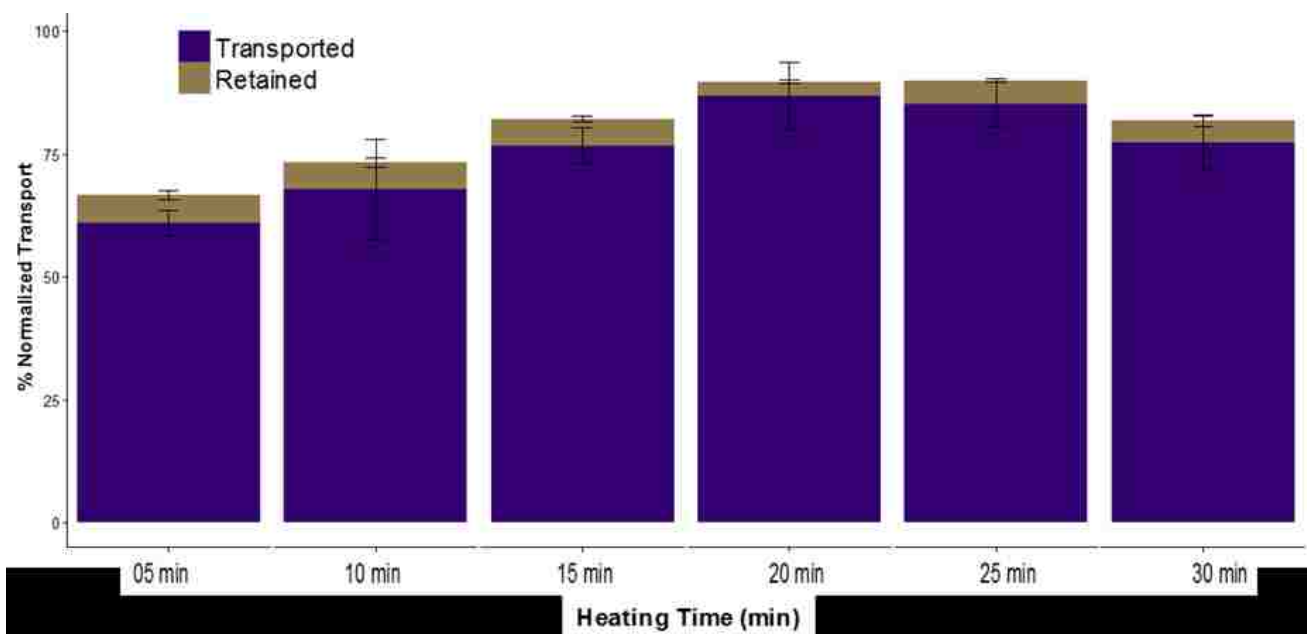


Figure 40. Extended *E. coli* heating times at 95°C. Increased heating times to 20-25 minutes results in a higher

percentage of DNA that transports through the membrane indicating a higher degree of fragmentation. The slight drop-off at 30 minutes may be caused by DNA degradation. Averages of N=3 are reported with error bars representing standard error.

These results could also be explained using the models described above. *S. aureus* DNA is only ~2× smaller than *E. coli* DNA, but the model in (Equation 3) indicates that DNA denaturation time is proportional to the square of DNA size. Therefore, *E. coli* DNA should take ~4× longer to denature than *S. aureus* DNA, which would reduce the amount of time the *E. coli* ssDNA was available for effective thermal scission. Based on the data presented above, *S. aureus* DNA was sufficiently fragmented for transport through membranes by 4-6 minutes (100% transport), while *E. coli* DNA did not show the same transport efficiency until 20 minutes, ~3-5× times longer, as suggested by the model. It is hypothesized that the reduced transport for *E. coli* DNA after 20 minutes is a result of either DNA degradation and or fragmentation in the qPCR gene of interest, therefore resulting in a loss of qPCR signal.

4.3.5. Effect of heating temperature on DNA fragmentation and transport through porous membranes.

Next, the effect of varying heating temperature on DNA fragmentation and transport through porous membranes was tested. As with heating time, another important goal of this aim was to understand the impact of heating temperature on fragmentation to guide assay design. Again, lysis and fragmentation were decoupled using Percent Normalized Transport. For the conditions presented in Figure 42, all lysis efficiencies were >80%, Figure 41.

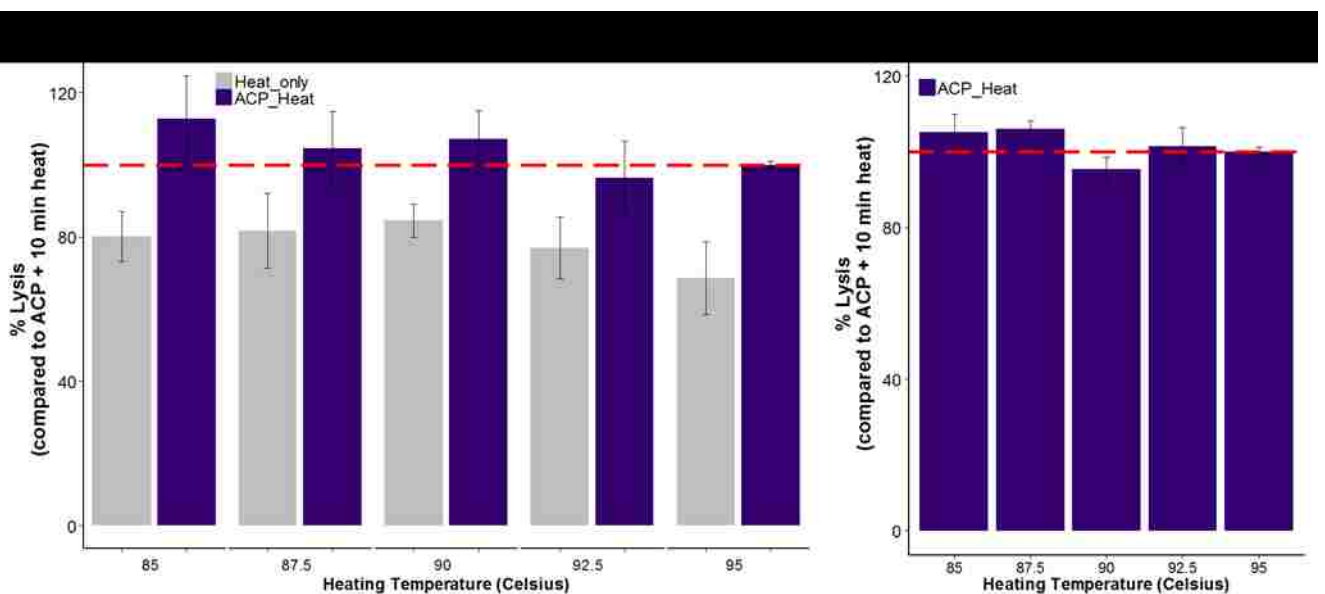


Figure 41. Lysis efficiencies for various methods and heating temperatures for 10 minutes. Treatment with ACP + 10 minutes of heating at 95°C was set to 100% (dashed red line) for each pathogen tested. In general, lysis efficiencies were similar for each condition across temperatures for each pathogen. Heat only lysis was less effective than heat + ACP for *E. coli*. The average of N=6 (N=3 from two independent cultures) is reported with the error bars representing standard error. **A.** *E. coli* treated with and without ACP, and **B.** *S. aureus* treated with ACP.

Samples containing either intact *E. coli* or *S. aureus* were heated at 85–95°C for 10 minutes followed by flow through a porous membrane. For *E. coli*, increased heating temperature, up to a point, resulted in a higher percentage of DNA that was transported through the porous membrane, **Figure 42**, indicating a higher degree of fragmentation. These results were also observed by PFGE, **Figure 43**. Temperatures at or above 92.5°C resulted in similar fragmentation and transport. As with the previous experiments, *E. coli* treated with or without ACP did not show any difference in transport. The temperature dependence of thermal scission, and therefore lateral transport through porous membranes, also aligned well with the models described in (Equation 3) and (Equation 4), which note that increasing temperatures increase the rates of scission^{158,185}.

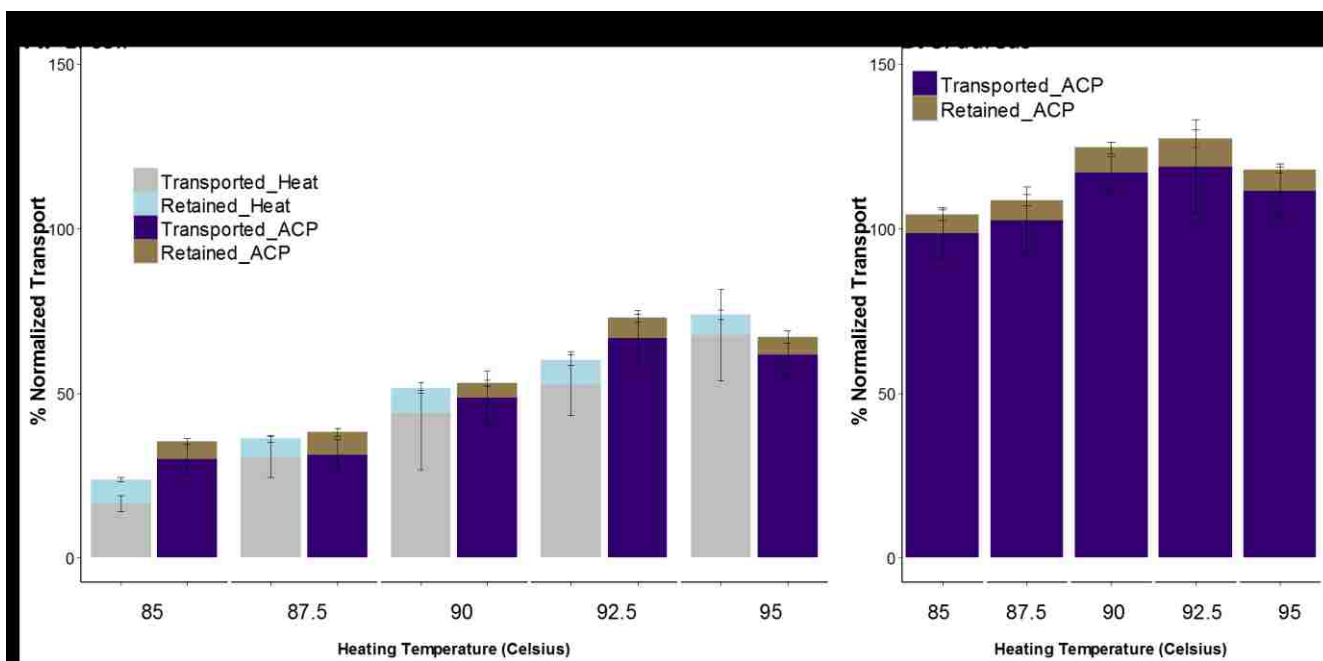


Figure 42. Effect of heating temperature on DNA fragmentation and transport through porous membranes. Averages of N=6 (N=3 from two independent cultures) are reported with error bars representing standard error. **A.** *E. coli* treated with and without ACP, and **B.** *S. aureus* treated with ACP. *S. aureus* is not susceptible to thermal lysis.

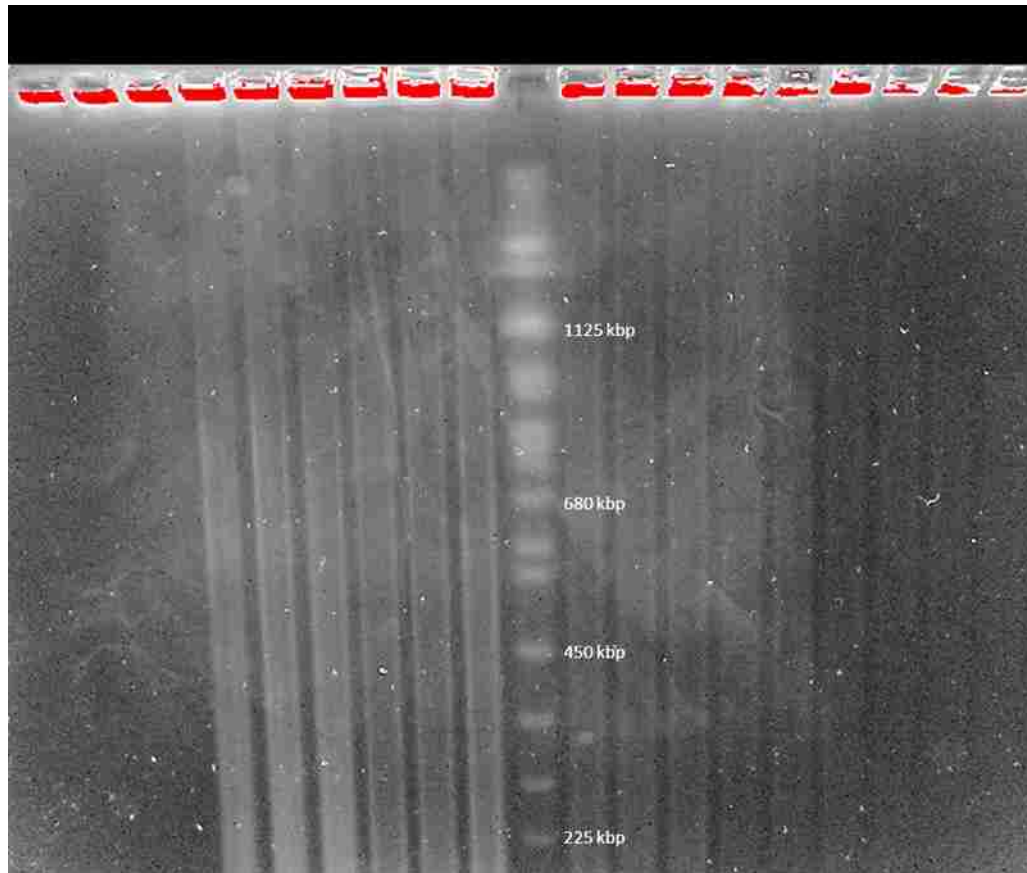


Figure 43. Example PFGE for varying *E. coli* heating temperatures for 10 minutes. *E. coli* containing samples were treated with ACP at room temperature for 2 minutes followed by heating to 85 – 95°C for 10 minutes. A qualitative assessment of fragmentation was visualized using PFGE with N=3 samples per heating time. As heating temperature increased, the amount of DNA retained in the wells decreased as did the amount of longer fragments.

There was little effect on transport of *S. aureus* DNA after heating to these varied temperatures. This outcome did not appear to be a result of lysis method, ACP, because changes in fragmentation and transport with temperature were observed for *E. coli* treated with and without ACP. This outcome may result from the smaller size of the *S. aureus* gDNA being more readily denatured at lower temperatures compared to the larger *E. coli* genome, as described in (Equation 3).

4.3.6. *Effect of genome size on transport through porous membranes.* For the samples tested above, longer heating times (4+ minutes) at higher temperatures (>92.5°C) resulted in more DNA transported through the membrane, indicating a greater degree of fragmentation. Additionally, each of these conditions resulted in high lysis efficiencies (>80%) signifying that the majority of the DNA from the cells was available for fragmentation and transport.

The next round of experiments directly compared the Percent Normalized Transport of DNA from four cell types with varying genome sizes: *N. gonorrhoeae* (2.2 Mbp), *S. aureus* (2.5 Mbp), *E. coli* (5 Mbp), and human epithelial cells (HeLa, 48–250 Mbp). Note that the human genome is composed of chromosomes, the shortest of which is #21 at ~48 Mbp and the longest of which is #1 at ~250 Mbp.

Based on the results presented above, ACP does not appear to significantly contribute to DNA fragmentation when heating to >85°C for up to 10 minutes. It can, however, play an important role in cell lysis because some cells, such as Gram-positive bacteria, are not susceptible to thermal lysis¹²³. Lysis of human epithelial cells was significantly improved when treated with ACP + heat instead of just heat (ACP + heat: 62% lysis v. heat only: 25% lysis). In order to reduce this variation in lysis, all samples for this round of experiments were treated with ACP for 2 minutes at room temperature prior to heating to 95°C for 2 or 8 minutes followed by flow through Fusion 5. After flow, DNA transport was quantified by qPCR.

As observed in previous experiments, heating of samples for only 2 minutes resulted in reduced Percent Normalized Transport compared to heating for 8 minutes. The same results are observed across all four cell types, **Figure 44**.

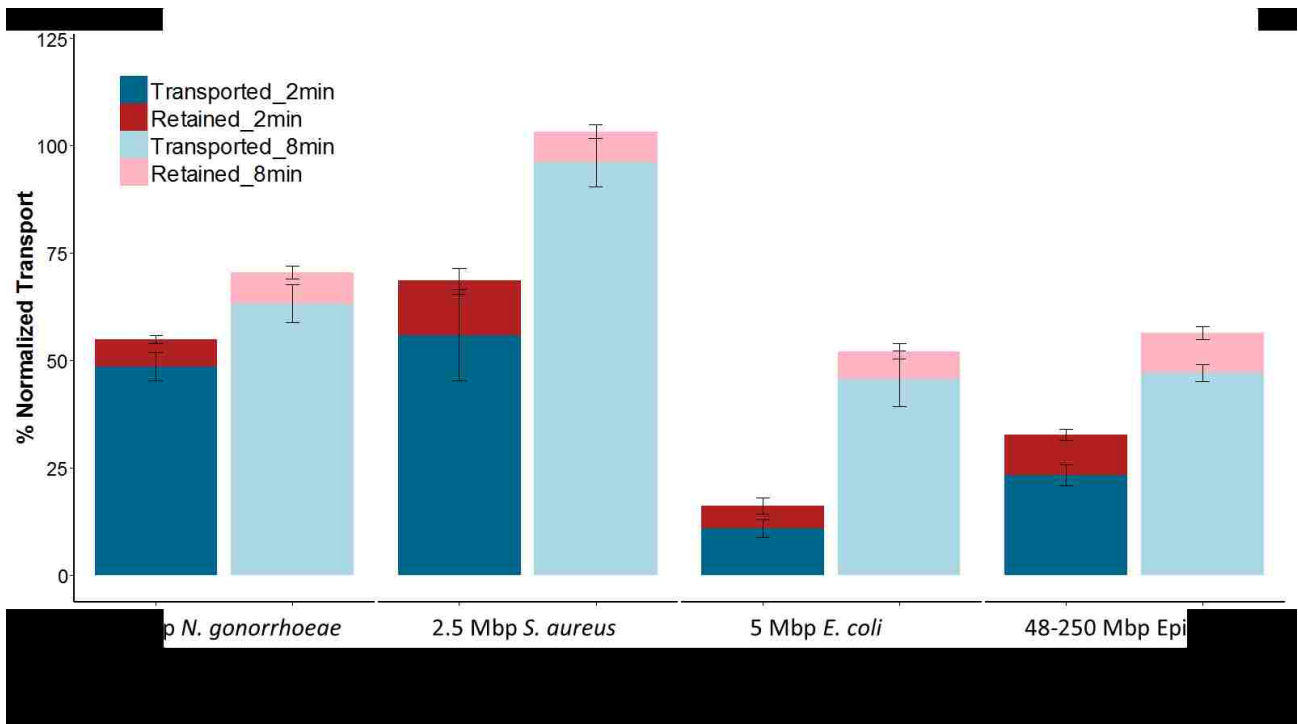


Figure 44. Effect of gDNA size on transport through porous membranes. For larger genomes, significantly less DNA was able to effectively transport through the membrane. For all genomes, heating for 8 minutes resulted in a higher percentage of DNA transported through the membrane. All samples were treated with ACP prior to heating to 95°C to reduce potential lysis variation. Averages of N=6 (N=3 from two independent cultures) are reported with error bars representing standard error.

There is a noticeable size trend in increasing the % normalized transport for each heating time. The smaller *N. gonorrhoeae* and *S. aureus* genomes (2.2 Mbp and 2.5 Mbp, respectively) show a higher percentage of transport through the Fusion 5 membrane compared to the larger *E. coli* and epithelial cell genomes (5 Mbp and 48-250 Mbp, respectively). This trend may be partially explained with the models of DNA denaturation and scission, (Equation 3 and (Equation 4. The shorter genomes denature from dsDNA to ssDNA in quadratically less time than the longer genomes. This difference results in the smaller genomes having more time as ssDNA and therefore more time to experience thermal scission compared to the larger genomes. Ultimately, more time spent as ssDNA under thermal scission conditions would result in smaller fragments and therefore higher transport efficiencies, as seen in **Figure 44**. This trend holds for bacterial DNA – *N. gonorrhoeae*, *S. aureus*, and *E. coli* – but does not appear to describe fragmentation and transport through porous membranes for the mammalian DNA. The microbiology of prokaryotic and eukaryotic cells is different, and generally eukaryotic cells are more complex. Therefore, it is hypothesized that a more complex model is needed to better describe the results for the human cells tested, which is outside the scope of this project. The goal of this work was to develop fragmentation methods for bacterial cells and diagnostic applications. Future work could compare these methods across a range of eukaryotic cells to determine if the fragmentation and DNA transport trend holds within more similar cell types.

4.3.7. *Fragmentation and transport of DNA from mixed samples.* Realistic human samples for pathogen detection contain a mix of pathogens, commensal bacteria, and human cells. For example, sampling for *N. gonorrhoeae* is typically done with a swab or urine³, both of which also contain human epithelial cells. For some applications, excess non-target DNA can reduce assay sensitivity by overloading the capacity of an assay^{140,213} or by reducing target amplicon generation through amplification reagent sequestration^{51,214}. Reducing or eliminating non-target DNA would help increase sensitivity for the target of interest. Therefore, for mixed samples, it is important to quantify the total amount of DNA (both target and non-target) that successfully transported through a porous membrane, which has been described as the Percent Absolute Transport, (Equation 6).

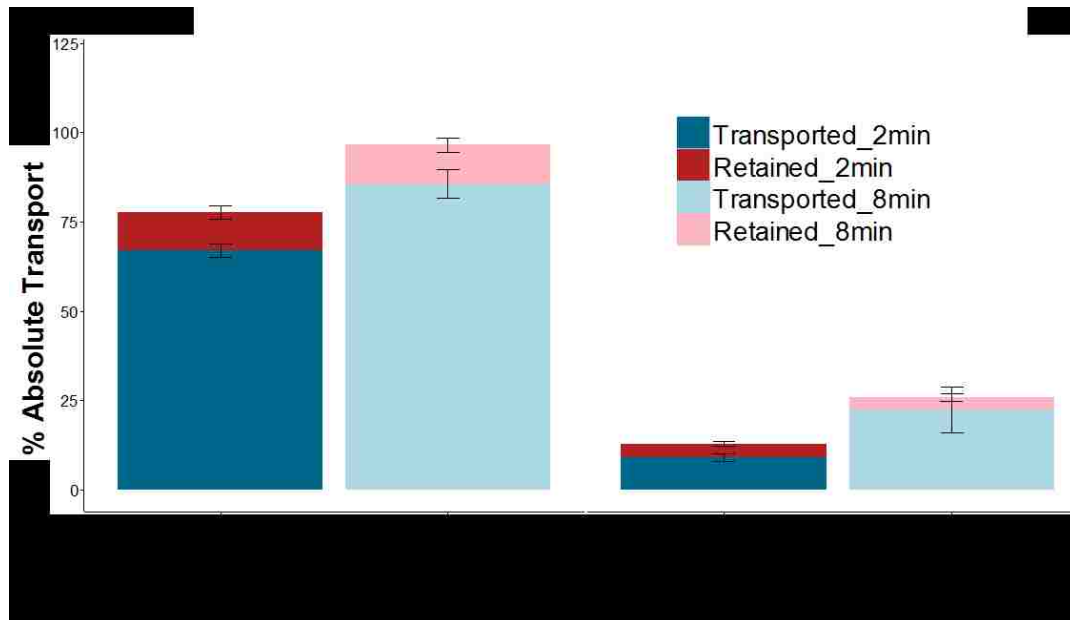


Figure 45. Fragmentation and transport of mixed samples through porous membranes: The epithelial cell does not lyse as effectively as the small bacterial cell in these conditions, therefore reducing the amount of DNA available for fragmentation. For both heating times tested, 4x more *N. gonorrhoeae* DNA successfully transported through the membrane compared to epithelial cell DNA. Averages of N=6 (N=3 from two independent cultures) are reported with error bars representing standard error. Samples were treated with ACP for 2 minutes at room temperature followed by heating to 95° for either 2 or 8 minutes.

For experiments with mixed samples containing two cell types, it is important to account for individual lysis efficiencies. Samples with both *N. gonorrhoeae* and HeLa cells were lysed with ACP at room temperature for 2 minutes followed by heating to 95°C for either 2 or 8 minutes. Samples were then allowed to flow laterally through porous membranes.

Within these mixed samples, the epithelial cells showed reduced lysis efficiency compared to the *N. gonorrhoeae* bacteria (2 min: *N. gonorrhoeae* 98% vs. epithelial cells 39% and 8 min: *N. gonorrhoeae* 95% vs. epithelial cells 62%, respectively). Using the Percent Absolute Transport and accounting for these reduced lysis efficiencies, significantly more total input DNA was recovered from *N. gonorrhoeae* compared to the human epithelial cells for both times tested, **Figure 45**. The transport data, measured by qPCR, indicate that fragments on the order of 200 kbp to 250 kbp (0.2 Mbp – 0.25 Mbp) effectively transport through Fusion 5.

Bacterial DNA is ~10–100x shorter than mammalian DNA, based on the range of chromosome sizes in human cells (48–250 Mbp). This data set suggested that the significantly larger mammalian DNA does not sufficiently fragment during the applied heating to effectively transport through the

porous membrane. The smaller bacterial DNA, however, is sufficiently fragmented and therefore transports well.

These results were consistent with the models for DNA denaturation and thermal scission described in above. Both cells experience the same temperature and time of heating. The denaturation model indicates that the significantly longer mammalian DNA could take 100× longer to fully denature from dsDNA to ssDNA because denaturation time is proportional to the square of DNA length^{188,189}. Based on this model, during the 2 or 8 minute heating steps portions of the mammalian DNA would remain double-stranded and be significantly less susceptible to thermal scission than the bacterial DNA. The sections of mammalian DNA that are single-stranded, would result in 10-100× more scission events because thermal scission is directly proportional to DNA length. Overall, this work describes a balance between multiple factors including DNA length, heating time, and heating temperature. In order to selectively fragment and transport smaller bacterial DNA while retaining larger mammalian DNA, moderate heating times of 2–8 minutes at 90–95°C should be used. These differences in length, cell type (pro v. eukaryote), and the relatively short heating times may be enough to describe the transport and recovery of DNA from various cell types in a sample.

4.3.8. *Translating DNA fragmentation into porous membranes.* After characterization of fragmentation in tube, the next step was to attempt to translate these methods into a membrane. *E. coli* cells were added to a tube or membrane and exposed to one of the following treatments: no lysis control, 95°C for 5 minutes, ACP treatment only at room temperature for 2 minutes, or ACP treatment followed by heating to 95°C for 5 minutes. The resulting fragmentation was analyzed by PFGE and the distribution of fragment sizes was quantified.

For *E. coli* samples treated in tube, heating, ACP only, or a combination of both resulted in ~50% of the total fragments being small enough to transport through a porous membrane. For samples treated in membrane, however, most of the resulting fragment sizes were too large to flow through a membrane by capillary action, **Figure 46**. These results suggest that fragmentation of gDNA is likely inhibited in porous membranes.

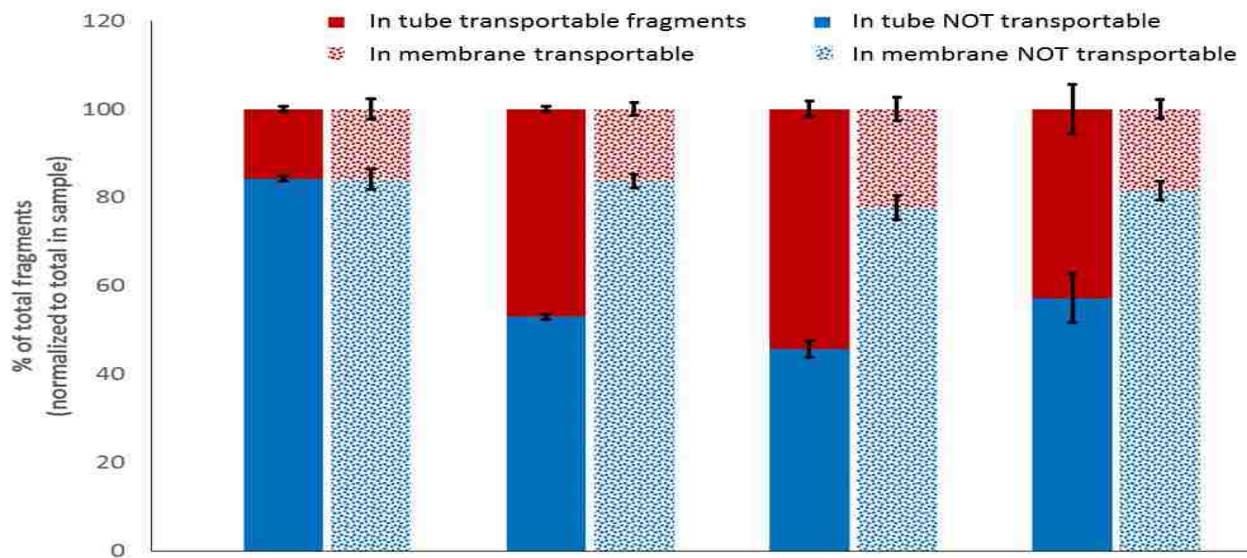


Figure 46. Comparing fragmentation methods of *E. coli* gDNA in tube and in membrane. Fragmentation is significantly reduced when cells are treated in a glass fiber membrane compared to in a tube. Averages of $N=3 \pm$ one standard deviation are presented.

These results were further verified by PFGE which show considerable DNA remaining in the wells for these treatments, **Figure 47.**



Figure 47. Gel from fragmentation experiments in tube v. in membrane.

4.4. Conclusions and Future Work

Here a novel application of thermal DNA fragmentation for preparing pathogen-containing samples for use in porous membrane devices has been demonstrated and characterized. First, mechanisms governing DNA transport through porous membranes were evaluated. Direct adsorption or protein-mediated adsorption of DNA to Fusion 5, and DNA entanglement in the membrane post scission did not significantly contribute to DNA transport in these studies. Also, varying heating time and temperature was shown to have a predictable effect on DNA transport laterally through Fusion 5 for the tested bacterial cells. For all four tested cell types lysed with ACP (*N. gonorrhoeae*, *S. aureus*, *E. coli*, and epithelial), heating to 95°C for at least 8 minutes resulted in greater than 50% of the available DNA effectively transporting through the Fusion 5 membrane. These data normalize DNA transport to cell lysis (Equation 5). Finally, this information enabled the use of controlled lysis and fragmentation to selectively move or retain DNA from samples containing multiple cell types. When smaller bacterial cells (*N. gonorrhoeae*) and larger mammalian cells (epithelial cells) were simultaneously lysed and thermally fragmented, at least 4× more of the total bacterial DNA was successfully transported through the membrane compared to the total mammalian DNA. This difference was observed for samples heated to 95°C for either 2 or 8 minutes.

The data presented in this work indicated that controlled heating times and temperatures could be applied to different samples to effectively reduce non-target human DNA in downstream applications. Conversely, assays could be designed that fragment pathogenic DNA, remove it under flow, and retain the human DNA for further processing. Future work should characterize complex samples, such as blood or urine, to elucidate the ability to do targeted fragmentation in these contexts. Future work should also include the application of these methods to complex human samples or organisms with significantly smaller or RNA-based genomes. As discussed above, the simple models describe the fragmentation and transport trend observed for bacterial DNA, but do not fully describe the results for the mammalian DNA. Future work should further explore the differences between prokaryotic and the more complex eukaryotic cells including comparison across multiple eukaryotic cells.

A final consideration that future work should address is membrane variability. This work explored the fragmentation and transport of DNA through a single membrane type: Fusion 5. While parallel

experiments in a second membrane (Standard 17 glass fiber, GE Healthcare Life Sciences) have yielded similar results (data not presented), it is important to consider that porous membranes may or may not differ in average pore size, but they almost always differ in the pore size distribution, which is based on the specifics of their manufacture. Because the failure to transport DNA through porous membranes appears to be dominated by entanglement, the pore size distribution of the membrane will play a significant role in the transport of specific distributions of DNA fragments. This work establishes some control over the fragmentation process and can help better identify desired membrane characteristics based on the need for DNA transport in a target application. Additionally, initial experiments testing thermal fragmentation in porous membranes showed poor transport of DNA.

The results contained within this work can serve as a guide for how to evaluate DNA fragmentation and as a set of design rules for assay and device development for porous membrane-based systems. In fact, the results of this work have already been applied to an integrated paper-based POC nucleic acid amplification system that requires DNA fragmentation¹³⁸. Aim 4 of this dissertation will demonstrate the integration of DNA fragmentation into a POC sample preparation device.

5. Specific Aim 3: Develop a method to purify and concentrate DNA in porous membranes

This chapter of my dissertation included three subsections: (i) investigation of polyamine interaction with common porous substrates; (ii) utilizing polyamine modified membranes to simultaneously purify and concentrate DNA from complex samples and (iii) testing the efficacy of these modified membranes after long-term storage. The combination of these capabilities was used on a wide range of sample types, which are prepared for use in downstream processes, such as NAATs, without additional purification. Further, this purification system uses a novel, one-step, sequential reagent delivery mechanism designed in the Yager and Lutz labs that directly translates to a simple, one-step user experience.

5.1. Background

Over the last 20 years, the field of microfluidics has aimed to address and overcome the gap between laboratory capabilities and POC systems through the development of single-use, plastic microfluidic chips²⁹. In the microchip format, NA purification for the POC often adapts techniques from traditional laboratory methods. For example, multiple groups have published on the use of SPE membranes in microfluidic devices^{215–218}. The Klapperich group embedded silica particles in a porous polymer monolith (PPM) within microfluidic channels to combine DNA purification from complex samples with on-chip PCR^{59,60,219}. The Bau group designed a sample-to-answer polycarbonate cassette with on-chip reagent storage for NA isolation using a silica membrane⁶¹. There has also been initial work published on the use of sequence-specific capture for isolating NA targets in microfluidic chips^{93,94}.

Another widely used technique for DNA purification in microfluidic devices exploits the negative charge of DNA molecules; DNA can associate with coated magnetic beads^{85,86}, cationic polymers^{87–89}, and can be separated through electrophoretic methods^{90–92}. The

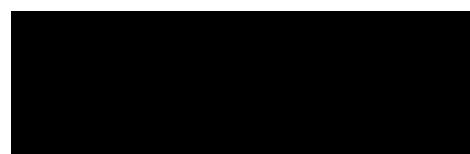


Figure 48. Chitosan structure in protonated and unprotonated forms.

Landers group utilized chitosan, a cationic polymer, to selectively isolate NAs in a microchip from complex solutions^{52,220–222}. Chitosan is a linear polymer comprised of linked sugar rings with a primary amine functional group on each monomer. Below its pK_a (6.3–6.5²²³) the amine is protonated, and the polymer becomes polycationic. In its protonated form, chitosan binds DNA and RNA *via* electrostatic interactions. When exposed to a solution above the pK_a , the primary amines are deprotonated and the electrostatic interaction is lost. This charge reversal enables a controllable electrostatic attraction between NAs and chitosan at low pH values that can be reversed through a buffer exchange, **Figure 48**. Early work with the chitosan-NA interaction focused on NA compaction and delivery for gene therapy applications^{224–226}.

Although many of the above microchip-based systems show promise for translation to realistic POC systems, there is a drawback to their implementation due to the use of potentially expensive equipment for operation (e.g. syringe pumps). Devices that require this type of equipment have limited usability in POC settings such as a patient's home or rural health clinics in the developing world. Due to these constraints, many groups have begun to focus on the use of porous membranes for diagnostic devices.

Porous membranes were first used as diagnostic platforms in the mid to late-1970s for home-based pregnancy tests⁴²⁻⁴⁴. More recently, George Whitesides' group began patterning cellulose paper to simultaneously detect glucose and proteins in urine samples⁴⁵. Work in this field has continued to expand to perform complex, sequenced assays⁴⁶⁻⁴⁸ that are compatible with various detection techniques⁴⁹. Porous-membrane-based assays do not require mechanical pumps because capillarity wicks fluids into and through the paper⁵². These devices are also inexpensive, easy to manufacture, and disposable, making them ideal candidates for POC tests. Two recent reviews detail the use of porous membrane-based microfluidics for diagnostic devices⁵³ and the translation of multi-step processes from laboratory gold-standard techniques to paper-based systems⁵⁵.

There is still a significant gap in translating NA tests to paper platforms, especially those that may require NA purification and concentration. Mariella *et al.* noted that few paper-based devices have developed reliable solutions for the use of NA in paper-based formats⁵⁸. Recent publications have detailed systems that isolate NA using commercially available extraction membranes such, as FTA or Fusion 5^{96,97}, or chromatography paper⁷¹. Although these membranes do selectively isolate NA, they have only been demonstrated in conjunction with plastic microchips or require equipment with multiple user steps.

Furthermore, sample concentration can be an additional critical step in the NA purification process, especially for environmental testing where only a few targets may be present in large volumes (mL to L) of sample. As such, an ideal porous membrane-based NA purification system should also substantially concentrate the target.

In this work, a novel DNA purification and concentration system that uses the linear polysaccharide chitosan was developed in porous membrane substrates for POC applications. It is well known that surfaces can be modified with polymers to engineer or control surface properties such as charge^{227,228}; these principles have been used to investigate chitosan's interaction with different porous membranes. On the basis of this method, a system was developed and tested using porous membranes to simultaneously purify and concentrate DNA from complex samples containing high protein content, excess non-target DNA, blood, and urine. Further, the purification system uses a novel, one-step, sequential reagent delivery mechanism developed in the Yager and Lutz labs²²⁹ that directly translates to a simple, one-step user experience; this further supports the feasibility of this system for use in POC applications.

5.2. Methods

Reagent preparation. Chitosan solutions for patterning porous membranes were prepared in 50 mM MES at pH 5. The 50 mM MES DNA capture and wash buffers were prepared in sterile water and the pH was adjusted to 5. The 50 mM Tris DNA elution buffer was prepared in sterile water with red food coloring to track fluid flow; the pH was adjusted to 9. The simulated nasal matrix (SNM) was prepared as previously described²³⁰. Defibrinated sheep's blood was purchased from Hemostat Laboratories. Buffers containing additional salts were prepared by adding known concentrations of NaCl to the 50 mM MES buffer and pH was adjusted to 5.

Device patterning and construction. All porous membranes and test card materials were cut using a CO₂ laser. Untreated, backed, ~5–10 μm pore diameter nitrocellulose membranes (FF80HP) untreated, unbacked, ~10–100 μm pore diameter Standard 17 glass fiber membranes, and Fusion 5 membranes were patterned with chitosan. Test cards were made with 0.254 mm-thick Mylar backing with adhesive and cellulose wicking pads for waste fluid uptake.

The nitrocellulose, glass fiber, and Fusion 5 membranes were patterned with a low molecular weight chitosan solution prepared in 50 mM MES at pH 5 using either a piezoelectric noncontact printer or by hand spotting. After printing, the membranes were stored in a desiccator. Membranes patterned with fluorescently tagged chitosan were also wrapped in foil to protect from light and photobleaching.

SEM of porous membranes. All images were collected using an FEI Sirion electron microscope and samples were Au/Pd sputter coated (SPI Module Control, Structure Probe, Inc., West Chester, PA, USA) with an estimated 12 nm Au/Pd. A 5 kV beam was used for imaging. Using these images, membrane surface area was estimated by representing the features as spheres and cylinders to simplify calculations. The calculated surface areas per volume of nitrocellulose and glass fiber were 2.0 μm²/μm³ and 0.19 μm²/μm³, respectively. These calculated values are consistent within an order of magnitude with other published values^{231,232}. SEM images were collected by Dr. Joshua Buser.

Fluorescent labeling of chitosan. Chitosan was fluorescently labeled using the commercially available 488 or 594 Amine-Reactive Dye Kit from Thermo Scientific. Chitosan was dissolved in 50 mM MES at pH 5 to make a 1% w/v solution. After a one-hour incubation at room temperature with the amine-reactive dye, the chitosan was purified by precipitation using 5 M NaOH followed by

centrifugation at 9400 xg for 3 minutes. The precipitated chitosan was re-dissolved in 50 mM MES and the pH was adjusted to 5 to prepare it for reagent patterning. The solution was stored in the dark at 4°C for up to one month.

Purifying and fluorescent labeling of DNA. All DNA was purified from freshly cultured methicillin-sensitive *Staphylococcus aureus* (MSSA, strain RN4220) bacterial cells. The DNA was purified using the commercially available Qiagen Genra Puregene Kit with a slightly modified protocol. During the lysis step, 50 μ L of lysostaphin (100 μ g/mL) was added with the recommended 1.5 μ L of Lytic Enzyme Solution provided by the kit. Purified DNA was resuspended in 20 μ L of sterile water and incubated for 20 minutes at 65°C to complete resuspension. The final DNA concentration was calculated by qPCR (described below).

After purification, DNA was fluorescently labeled using the Alexa Fluor 488 or 594 ARES DNA Labeling Kit with a slightly modified protocol. During the initial nick translation step, the concentration of each of the dNTPs was 0.5 mM. After labeling, the final concentration of the fluorescent DNA was determined using qPCR for the *ldh-1* gene.

Pulsed field gel electrophoresis. PFGE was used to determine the fragment size of DNA from bacterial cells. A 1.0 % agarose gel was prepared in 0.5x TBE buffer and set overnight at 4°C. Gels were run using the BioRad CHEF Mapper XA System in a cold room (4°C) in 0.5x TBE running buffer. Porous membrane samples and agarose plugs containing the high molecular weight *S. cerevisiae* DNA ladder were loaded into the gel before submerging in running buffer. Liquid samples were added to the gel with sample loading buffer. The “Auto-Algorithm” function was used with an input sizes range from 10 kbp to 2200 kbp, depending on the resolution required for different fragment sizes. Gels were stained with either 2x SYBR Gold or SYBR Safe in 0.5 x TBE for 20 minutes with shaking followed by 10 minutes of de-staining in DI water. Gels were imaged with the BioRad Gel Doc EZ System.

Porous membrane capacity for chitosan. To determine the capacity of a membrane for chitosan, small punches (radius = 2.4 mm) were taken from sheets of nitrocellulose and Standard 17 glass fiber. These punches were filled to capacity for nitrocellulose and glass fiber, 1.81 or 7.56 μ L, respectively, with varying concentrations of fluorescent chitosan in solution to produce different chitosan concentrations in the membranes. Here, chitosan concentration is defined as μ g of chitosan per μ m² of membrane surface area (μ g/ μ m²), assuming an even coating on all surfaces. The membranes were placed in clear Petri dishes

and incubated in a dark chamber at 95% relative humidity for 24 hours to allow equilibration of chitosan adsorption to the membrane.

After incubation, the membranes were imaged wet to determine a baseline fluorescence signal for the input amount of chitosan. Next, the membranes were washed with 1x volume capacity of 50 mM MES at pH 5 and fluid was wicked away using a cellulose waste pad to remove unadsorbed chitosan. The membranes were re-wet with 50 mM MES at pH 5 and imaged a second time to track the loss in fluorescent signal. The loss of chitosan was measured as the difference between the baseline fluorescence and the post-wash fluorescence of the coated membranes. All fluorescence images were captured using an Axiovert fluorescence microscope fitted with a Retiga 1300i digital CCD camera. Images were taken with MicroManager software²³³ using a 50 ms exposure and 2.5x objective.

Chitosan adsorption was calculated as the percent change in the integrated fluorescence intensity over the entire patterned region from pre- to post-wash conditions, **(Equation 7)**. These intensity values were measured using ImageJ²³⁴.



(Equation 7)

For both membranes, the chitosan concentrations tested ranged from 0 to $3.6 \times 10^{-8} \mu\text{g}/\mu\text{m}^2$. The upper limit of chitosan concentration for each membrane was bounded by the solubility of chitosan in buffer (50 mM MES, pH 5), the volume capacity of the membrane, and the pore surface area. Membrane capacity was determined by plotting the percent of chitosan adsorbed to each surface against the input chitosan concentration (in $\mu\text{g}/\mu\text{m}^2$). These capacities were further verified by theoretical calculations based on the length of the chitosan polymer and the membrane surface areas.

Chitosan retention in porous membranes during flow. To determine the retention of chitosan in each porous membrane during flow, a 2.5 mm long by 10 mm wide region of each membrane was patterned with fluorescent chitosan. Three concentrations were tested to determine if retention during flow was concentration dependent. The three tested concentrations for both membranes were based on the results of the previous adsorption studies. The concentrations in the patterned regions were 4.5×10^{-10} , 8.9×10^{-10} , and $1.3 \times 10^{-9} \mu\text{g}/\mu\text{m}^2$ for nitrocellulose and 8.9×10^{-10} , 1.8×10^{-9} , and $2.7 \times 10^{-9} \mu\text{g}/\mu\text{m}^2$ for glass fiber.

The patterned membranes were attached to 10 mil thick Mylar backing with adhesive for ease of handling. An untreated cellulose pad, cut using the CO₂ laser cutter, was used as a waste collection reservoir. Before the initiation of flow, the chitosan regions on each membrane were wetted with 50 mM MES at pH 5 and excess unadsorbed chitosan were removed *via* wicking with a cellulose waste pad through the thickness of the membrane. This step was important to decouple the loss of chitosan due to incomplete adsorption to the membrane from the loss of chitosan during lateral flow.

To test chitosan retention during flow, two solutions were sequentially wicked through the membrane. These solutions were the DNA capture and elution buffers, which were selected to mimic an actual DNA purification experiment. The volume of the solutions was set to 2x the fluid capacity of the membrane (120 µL total for nitrocellulose and 500 µL total for glass fiber).

Dimensions of the patterned region and the fluorescence intensity of the chitosan were measured in ImageJ from uncompressed, time-lapse videos acquired using HandyAVI, in a humidified, light-tight box illuminated with two blue LEDs. Videos were captured using a web camera fitted with a 550 nm high-pass filter. The fluorescence intensity of the chitosan during flow was normalized to the initial wetted intensity to determine the percent of polymer retained in the membrane during flow.

Chitosan capacity for DNA and DNA concentration factor. Chitosan's capacity for DNA in both nitrocellulose and glass fiber was determined by increasing the concentration of DNA in the input sample until a decrease in the relative amount of DNA recovered was observed by qPCR. The range of input DNA concentrations tested in both membranes was between 1×10^5 copies (0.3 ng) to 4×10^8 copies (1200 ng) of fragmented MSSA DNA purified from cells. On average, the target DNA was less than ~250 kbp long; larger DNA fragments are unable to flow through the pores of the membranes, (Figure 32).

For these experiments, DNA was spiked into 100 µL of DNA capture buffer. This solution was wicked into the membrane, followed sequentially by 100 µL of wash and elution buffers for nitrocellulose, and 250 µL of wash and elution buffers for glass fiber to accommodate for the higher fluid capacity. These experiments were run in a humidified chamber to reduce effects from evaporation.

DNA was recovered post-elution by placing the membrane in a centrifugal filter tube (0.45 µm Nylon centrifugal filters, VWR, Radnor, PA) and centrifuging for 3 minutes at 10,000

x g. The elution volumes were measured and the target DNA concentration was determined by qPCR.

Concentration effects were measured by adding 1×10^5 to 1×10^6 copies (0.3 to 3 ng) of DNA into 100, 200, 500, 1000, or 2000 μL of capture buffer. These solutions were wicked through a membrane patterned with chitosan followed sequentially by either 100 μL for nitrocellulose or 250 μL for glass fiber of DNA wash and elution buffers. Post-elution, the DNA purification efficiency (% recovery) was quantified by qPCR. The concentration factor was calculated as the initial input volume divided by the measured elution volumes times the % recovery, **(Equation 8)**.



(Equation 8)

Effect of pH on DNA purification using chitosan. The effect of solution pH on the purification of DNA was tested by varying the pH of the capture buffer between 5, 5.5, and 6 and the elution buffer between 7, 8, and 9. Using nitrocellulose patterned with chitosan, 1×10^5 to 1×10^6 copies of fluorescently tagged fragmented MSSA gDNA was spiked into one of the capture buffers. The membrane was then washed with 50 mM MES at pH 5 and eluted with one of the elution buffers. Capture and elution were visualized in a fluorescence box and tracked using a web camera. Images were analysed *via* ImageJ. All images were normalized to the fluorescent signal prior to elution.

Recovery of DNA from complex samples. To determine the ability of a porous membrane patterned with chitosan to purify DNA, approximately 1×10^5 to 1×10^6 copies of MSSA and/or *E. coli* DNA was diluted into 100 μL of DNA capture buffer. The sample was wicked into the patterned membrane followed by wash and elution buffers, as described above. In addition to purification of DNA in water, the experiment was repeated with 1 μg BSA, 0.1% w/v mucins, 1% w/v mucins, up to 1000x non-target human gDNA, 1% or 10% SNM, 15 to 50 μL of defibrinated sheep's blood, or up to 500 mM NaCl to mimic more complex solutions. 50 μL of sheep's blood was also spiked into sample volumes ranging from 100 μL to 2000 μL . The percent recovery for each sample was determined by qPCR. These experiments were run in a humidified chamber to reduce effects of evaporation.

Chitosan storage studies in porous membranes. Storage studies were designed to evaluate the feasibility of this system for use in POC devices. Porous membranes were pre-patterned with chitosan and stored in a desiccated environment at either 20°C or 40°C for up to six months. After

each week, membranes were removed from storage and a DNA purification experiment was performed as described above using 1×10^5 to 1×10^6 copies of fragmented MSSA DNA. The percent recovery for each sample was determined by qPCR. These experiments were run in a humidified chamber to reduce the effects of evaporation.

RNA purification using chitosan in porous membranes. Standard 17 glass fiber and Fusion 5 membranes patterned with chitosan were also used to purify RNA from either 100 or 500 μL of capture buffer. These samples contained 5×10^4 – 5×10^5 copies of RSV RNA. The solutions were wicked into the membranes, followed sequentially by 250 μL of wash and elution buffers. The elutions were collected and measured as described above followed by quantification by qRT-PCR. These experiments were run in a humidified chamber to reduce effects from evaporation.

qPCR. Recovery MSSA DNA was quantified with a kit for the *ldh-1* gene provided by the ELITechGroup. The 20 μL reactions included 1 μL of input sample and were run on a BioRad CFX96 real-time PCR instrument using the following protocol: 50°C hold for 2 minutes, 93°C hold for 2 minutes, 45 cycles of 93°C for 10 seconds, 56°C for 30 seconds, and 72°C for 15 seconds, ending with final elongation step at 72°C for 5 minutes. Fluorescence data were collected during the 56°C annealing step using the Texas Red channel. The results were analyzed using the automated cycle threshold (CT) value calculation in the BioRad CFX Manager software. This assay is sensitive down to $\sim 10^1$ copies of the target sequence. Assay primer and probe sequences can be found in **Appendix 1**.

qRT-PCR. Recovery of RSV RNA was quantified with a qRT-PCR for the virus polymerase gene. Reagents from the RNA Ultrasense qRT-PCR kit (Life Technologies) were spiked with 5 μL of input sample and were run on a BioRad CFX96 real-time PCR instrument using the following protocol: 50°C hold for 15 minutes, 95°C hold for 2 minutes, 40 cycles of 95°C for 15 seconds and 60°C for 55 seconds. Fluorescence data were collected during the 60°C annealing step using the FAM channel. The results were analyzed using the automated cycle threshold (CT) value calculation in the BioRad CFX Manager software. This assay is sensitive down to $\sim 10^1$ copies of the target sequence. Assay primer and probe sequences can be found in **Appendix 1**.

5.3. Results and Discussion

The goal of this work was to demonstrate a simple, porous membrane-based system that purifies and concentrates DNA from complex samples, **Figure 49**. There are multiple methods available to pattern porous membranes; this work utilized a piezoelectric noncontact printer which allows the user to highly control spatial location and concentration of the printed reagent⁴⁸.

A polymer such as chitosan can interact in multiple ways with the surface of a membrane. These interactions can be dictated by factors including solution pH, the membrane or polymer isoelectric point, solution salinity, chemical composition of the membrane and polymer, etc. These interactions are further explored in the following experiments.

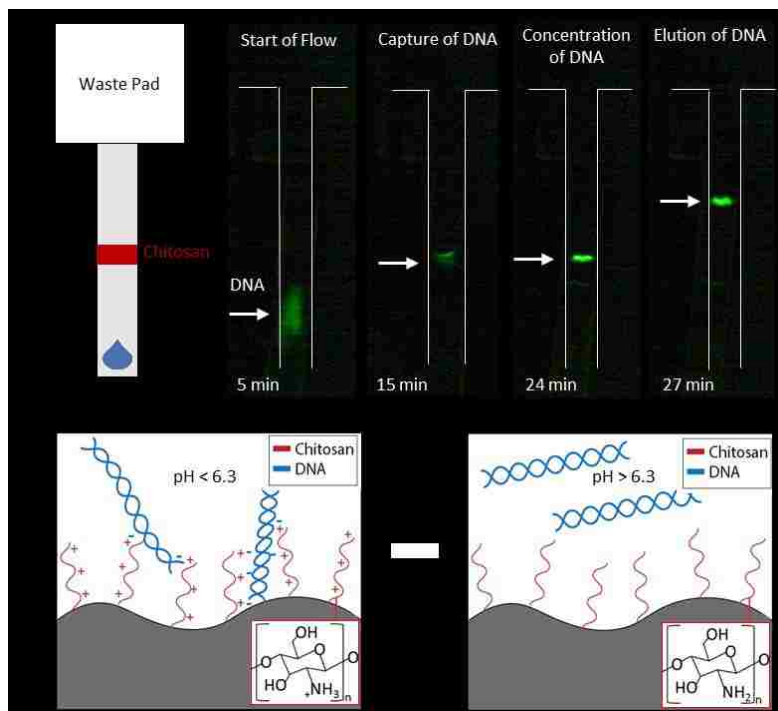


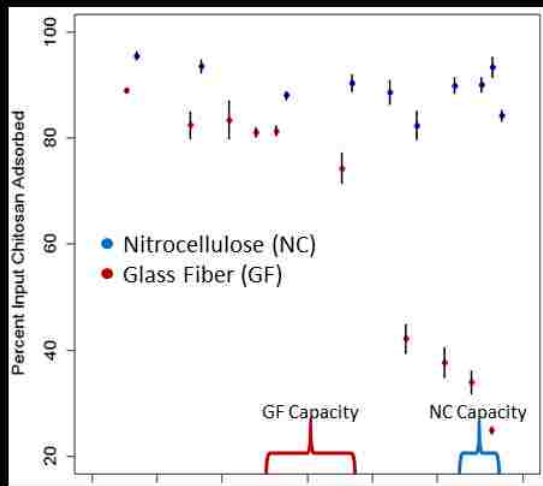
Figure 49. DNA purification in porous membranes using chitosan. **A.** Schematic and images from a purification experiment in nitrocellulose. The DNA is initially seen as a smear; as it reaches the chitosan region the DNA is captured and concentrated. Once DNA is eluted, it remains concentrated. **B.** Schematic of a membrane surface patterned with chitosan (red). In solutions with a pH below 6.3, the primary amines on each monomer become protonated and bind DNA. When the pH is increased above the amine pK_w , the charge on the polymer returns to neutral and DNA is released.

The first set of experiments determined the amount of chitosan available to bind DNA when patterned onto different porous membranes. The amount of *available* chitosan depends on its adsorption to the porous membrane.

5.3.1. *Porous membrane capacity for chitosan.* For all concentrations tested in FF80HP nitrocellulose, the amount of input chitosan that adsorbed to the membrane was above 90%, indicating that the membrane was not fully saturated with polymer. This same trend was not observed for the Standard 17 glass fiber; at concentrations at or below $3.6 \times 10^{-9} \mu\text{g}/\mu\text{m}^2$, the percent of input chitosan adsorbed remained high. At concentrations above $3.6 \times 10^{-9} \mu\text{g}/\mu\text{m}^2$, the percent adsorbed dropped, indicating that the membrane capacity had been reached,

Figure 50A. The results are consistent with our understanding of the physical properties of these porous membranes; the high surface area of the nitrocellulose, with its small pores and features, provides a higher capacity (experimentally determined capacity: $3.3 \times 10^{-8} \mu\text{g}/\mu\text{m}^2$) for polymer adsorption than the coarser glass fiber (experimentally determined capacity: $\sim 5.4 \times 10^{-9} \mu\text{g}/\mu\text{m}^2$). This difference between nitrocellulose and glass fiber may be due to the way chitosan adsorbs to different surfaces. This data suggests that only a few monomers of the chitosan chain adsorb to nitrocellulose allowing more space for additional molecules to adsorb. In glass fiber, on the other hand, a larger fraction of the total polymer might bind to the surface restricting the space available for other molecules to bind, **Figure 50B.**

These empirical capacities were further supported by theoretical calculations that predict the chitosan capacity of nitrocellulose should be between 9.7×10^{-10} and $3.3 \times 10^{-8} \mu\text{g}/\mu\text{m}^2$. An adsorption capacity was not observed for the concentrations tested, up to $\sim 3.3 \times 10^{-8} \mu\text{g}/\mu\text{m}^2$, which is at the maximum of the theoretical range. Based on the theoretical calculations and empirically determined capacities, the chitosan coverage of the nitrocellulose surface was $\sim 100\%$ of the theoretical geometric monolayer coverage, **Figure 50C.** For glass fiber, the theoretical capacity for chitosan should be between 9.5×10^{-10} and $3.2 \times 10^{-8} \mu\text{g}/\mu\text{m}^2$. The experimentally measured capacity for glass fiber falls within the lower range of the theoretical values and approximates to $\sim 15\%$ of the theoretical geometric monolayer coverage, **Figure 50C.** Using these conditions, there is a monolayer of chitosan coverage on the nitrocellulose surface and less than a monolayer on glass fiber surface. The upper limit of chitosan concentration tested for each membrane was bounded by the solubility of chitosan in buffer (50 mM MES, pH 5) and the volume capacity of the membrane.



Membrane	Experimental Capacity ($\mu\text{g}/\mu\text{m}^2$)	Theoretical Capacity ($\mu\text{g}/\mu\text{m}^2$)
----------	---	--

Glass Fiber	$3.6 \times 10^{-9} - 7.2 \times 10^{-9}$	$9.5 \times 10^{-10} - 3.2 \times 10^{-8}$
-------------	---	--

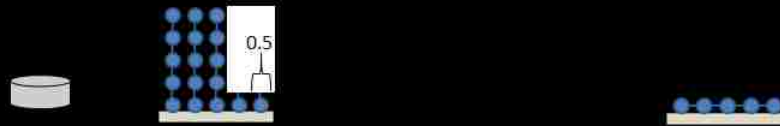




Figure 50. Membrane capacity for chitosan. **A.** Experimental data. **B.** Schematic of chitosan on membrane surfaces. **C.** Theoretical calculations.

5.3.2. *Chitosan retention in porous membranes during flow.* The total amount of chitosan available for DNA binding, **Table 6**, is determined by the amount patterned onto the membrane minus losses from incomplete adsorption, described above, and capillary flow, described below.

Table 6. Final chitosan concentration in each membrane after accounting for losses from incomplete adsorption and flow. *The “Mean final concentration” is based on the average percent adsorbed and retained. **The “Range final concentration” is based on the standard deviations for the percent retained during flow.

Input Concentration ($\mu\text{g}/\mu\text{m}^2$)	% adsorbed	% retained	Mean final concentration* ($\mu\text{g}/\mu\text{m}^2$)	Range final concentration** ($\mu\text{g}/\mu\text{m}^2$)
Nitrocellulose				
4.5×10^{-10}	89%	83%	3.3×10^{-10}	$3.3 \times 10^{-10} - 3.4 \times 10^{-10}$
8.9×10^{-10}	85%	74%	5.6×10^{-10}	$5.4 \times 10^{-10} - 5.7 \times 10^{-10}$
1.3×10^{-9}	91%	71%	8.6×10^{-10}	$8.3 \times 10^{-10} - 9.0 \times 10^{-10}$
Glass Fiber				
8.9×10^{-10}	79%	89%	6.3×10^{-10}	$5.4 \times 10^{-10} - 7.1 \times 10^{-10}$
1.8×10^{-9}	58%	71%	7.3×10^{-10}	$6.8 \times 10^{-10} - 7.8 \times 10^{-10}$
2.7×10^{-9}	40%	82%	8.7×10^{-10}	$8.1 \times 10^{-10} - 9.4 \times 10^{-10}$

After characterizing the membrane capacity for chitosan, the effects of capillary flow on chitosan retention were measured. The three tested concentrations for nitrocellulose were 4.5×10^{-10} , 8.9×10^{-10} , and 1.3×10^{-9} $\mu\text{g}/\mu\text{m}^2$ and for glass fiber were 8.9×10^{-10} , 1.8×10^{-9} , and 2.7×10^{-9} $\mu\text{g}/\mu\text{m}^2$. The concentrations vary in nitrocellulose and glass fiber due to the different surface areas of each membrane. These values were based on high, medium, and low concentrations from the adsorption studies detailed above. Retention of chitosan in nitrocellulose is slightly concentration-dependent, with larger concentrations of patterned chitosan losing a higher percentage during flow, **Figure 51A**. For glass fiber, this trend is not observed. The loss of chitosan due to flow does not appear to be concentration-dependent, **Figure 51B**.

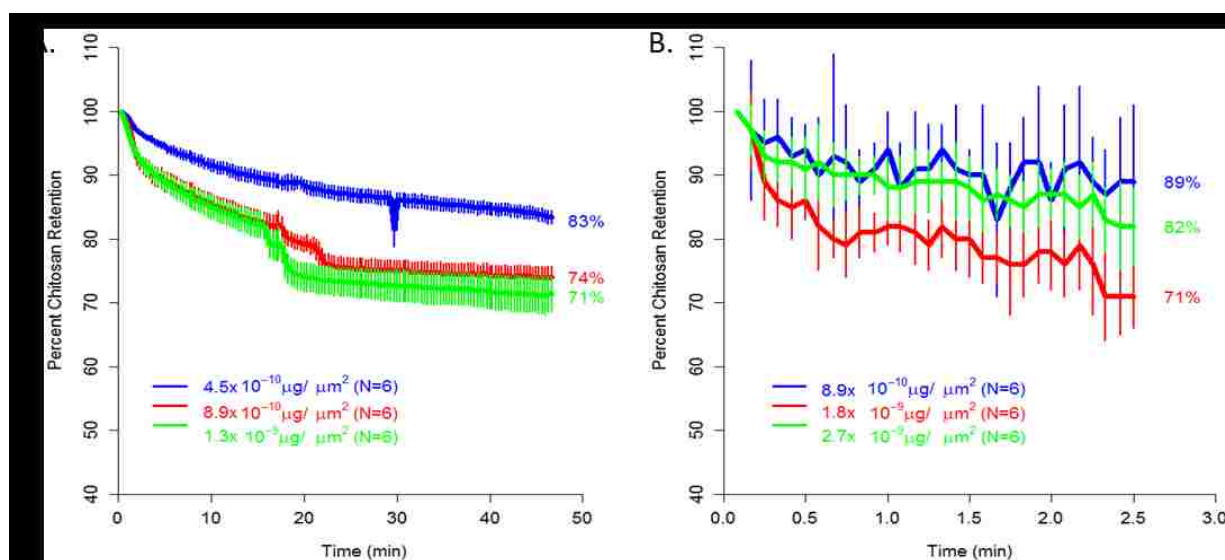


Figure 51. Chitosan retention during flow after accounting for losses due to incomplete chitosan adsorption. **A.** In nitrocellulose, retention during flow appears to be slightly concentration dependent. **B.** In glass fiber all three tested concentrations resulted in similar losses due to flow. The average retention ($N=6$) with \pm one standard deviation is plotted for each time point.

5.3.3. *Chitosan capacity for DNA and DNA concentration factor.* To evaluate the ability of chitosan to purify and concentrate DNA in paper, 60×10 mm membranes were patterned with chitosan in 50 mM MES at pH 5. The patterned region was set to an area 2.5 mm long by 10 mm wide to remain consistent with the chitosan retention experiments. Based on the capacity and retention experiments, the chitosan concentrations in nitrocellulose and glass fiber were set to 1.3×10^{-9} and 1.8×10^{-9} $\mu\text{g}/\mu\text{m}^2$ ($\pm 5\%$), respectively.

Chitosan capacity for DNA in nitrocellulose and glass fiber was evaluated after optimizing adsorption and retention. The capacity for DNA in nitrocellulose was 1.9×10^6 copies of

DNA/ μg of chitosan ($\text{c}/\mu\text{g}$) (95% CI: 2.9×10^5 to 3.5×10^6 $\text{c}/\mu\text{g}$). The capacity for DNA in glass fiber was 9.9×10^6 $\text{c}/\mu\text{g}$ (95% CI: 5.9×10^6 to 1.4×10^7 $\text{c}/\mu\text{g}$), **Figure 52**. These results are calculated using the mean final chitosan concentration from Table 6, which accounts for losses due to incomplete adsorption and retention. These data show that chitosan has a higher capacity for DNA in glass fiber than in nitrocellulose.

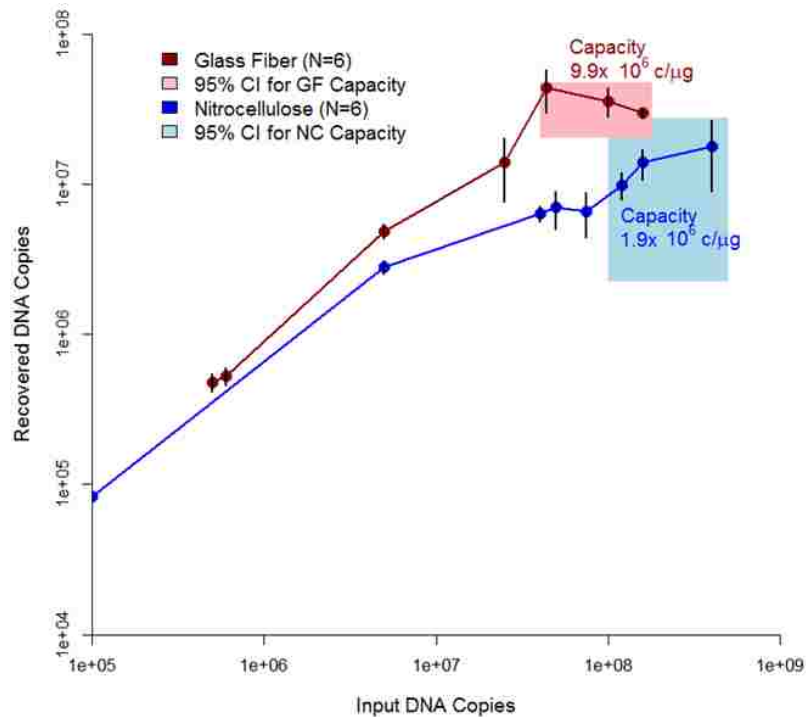


Figure 52. Capacity of chitosan for DNA in nitrocellulose and glass fiber over a range of input concentrations ($N=6$ for each point) after normalization for membrane surface area. The capacity of chitosan for DNA is 1.9×10^6 $\text{c}/\mu\text{g}$ (95% CI: 2.9×10^5 to 3.5×10^6 $\text{c}/\mu\text{g}$) in nitrocellulose and 9.9×10^6 $\text{c}/\mu\text{g}$ (95% CI: 5.9×10^6 to 1.4×10^7 $\text{c}/\mu\text{g}$) in glass fiber.

To enable broader use of these methods, the DNA capacities of each membrane have been converted to other common units, **Table 7**. Using the membrane capacity for chitosan and the chitosan capacity for DNA, this method can be adapted to capture and concentrate DNA from a variety of samples based on the expected amount of total nucleic acids.

Table 7. Chitosan capacity in nitrocellulose and glass fiber.

*Assuming average DNA fragment size of 2.0×10^5 bp.

***E. coli* O157:H7, genome length 5.4×10^6 bp.

****MSSA RN4220*, genome length 2.8×10^6 bp.

Capacity per μg chitosan	Nitrocellulose	Glass Fiber
copies DNA*	1.9×10^6	9.9×10^6
# bp*	3.8×10^{11}	2.0×10^{12}
ng DNA*	0.4	2.2
# <i>E. coli</i> bacteria**	7.0×10^4	3.7×10^5
# <i>MSSA</i> bacteria***	1.4×10^5	7.1×10^5

The smaller pores ($10 \mu\text{m}$) and higher surface area per volume ($2.0 \mu\text{m}^2/\mu\text{m}^3$) of nitrocellulose adsorbs more chitosan than glass fiber; but these results indicate that only a proportion of the chitosan is available for DNA binding in nitrocellulose. The chitosan used in this study was small, ~ 5000 MW. This size may allow polymer to integrate into the smallest pore features of nitrocellulose, some of which may be inaccessible to large DNA fragments (100s kbp), causing a high membrane capacity for the chitosan and a lower than expected binding capacity for DNA. Further, chitosan may hinder convective transport in the smaller pore features (or block flow completely) in nitrocellulose, reducing or preventing flow of DNA-containing sample through these membrane regions. On average, the pore features in Standard 17 glass fiber are larger (~ 10 - $100 \mu\text{m}$) and the material has a lower surface area per unit volume ($0.19 \mu\text{m}^2/\mu\text{m}^3$) than nitrocellulose ($2.0 \mu\text{m}^2/\mu\text{m}^3$). This reduced surface area lowers the overall chitosan capacity of the membrane, but may allow more of the chitosan to be available for DNA binding.

Using these results, the calculated ratio of positive (chitosan) to negative (DNA) charges when the system has reached its maximum capacity for DNA indicates that there is less than a monolayer of nucleic acid bound to the chitosan in both nitrocellulose and glass fiber, **Figure 53**. These calculations assume that a full monolayer of DNA would equate to an equal ratio of charges at the DNA-chitosan binding capacity. Further, these estimates and calculations assume all of the chitosan patterned in the membrane, after accounting for losses presented in Table 6, is available for DNA binding. More reasonably, only some percentage would be available because some of the polymer is interacting with the membrane surface, potentially rendering it unavailable for DNA binding. Additionally, both of these membranes have a range of pore size features and some fraction of the polymer may be trapped in the smallest of these features preventing it from interacting with DNA. Further, Strand *et al.* found that the most stable chitosan-DNA complexes were formed with

a ratio of 6–9 positive charges per one negative charge (amines:phosphates ratio)²³⁵. This evidence further supports the calculations that there is less than a monolayer of nucleic acid bound to the chitosan in each membrane.

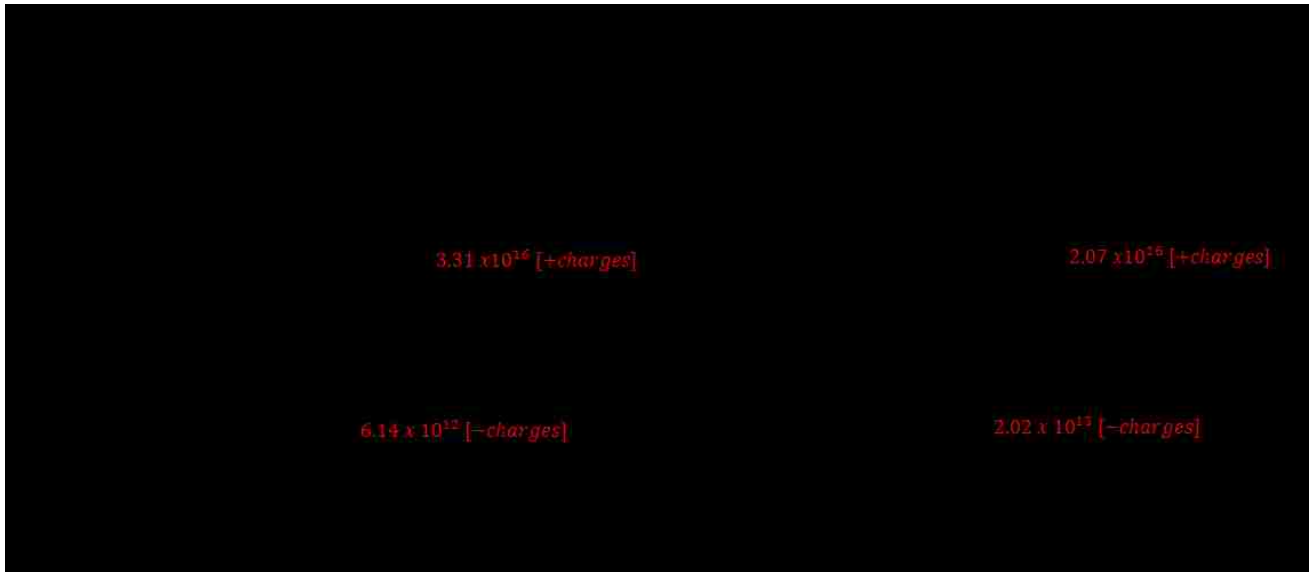


Figure 53. Calculation of less than a monolayer of DNA coverage when chitosan capacity is reached. **A.** FF80HP nitrocellulose and **B.** Standard 17 glass fiber.

In nitrocellulose, which has a relatively homogenous pore size distribution, the interface between two sequentially delivered fluids is sharply defined. In this system, the wash and elution buffers have low and high pH values, respectively; the well-defined interface between the buffers under flow in nitrocellulose produces a sharp pH change, **Figure 54A**. When the interface reaches the chitosan patterned region, the rapid change from low to high pH deprotonates the chitosan quickly, and releases purified DNA in a concentrated plug, **Figure 54B**. In glass fiber, however, which has a relatively broad pore size distribution, the interface is poorly defined, which increases mixing between the two sequentially delivered buffers and causes a more gradual pH gradient to develop. When this gradient reaches the chitosan region, the gradual change from low to high pH deprotonates the chitosan slowly, resulting in a slower release (and therefore less concentrated plug) of purified DNA, **Figure 54C**. In nitrocellulose, DNA samples eluted in $\sim 8 \mu\text{L}$ while for glass fiber, the elution volume was 100-150 μL .

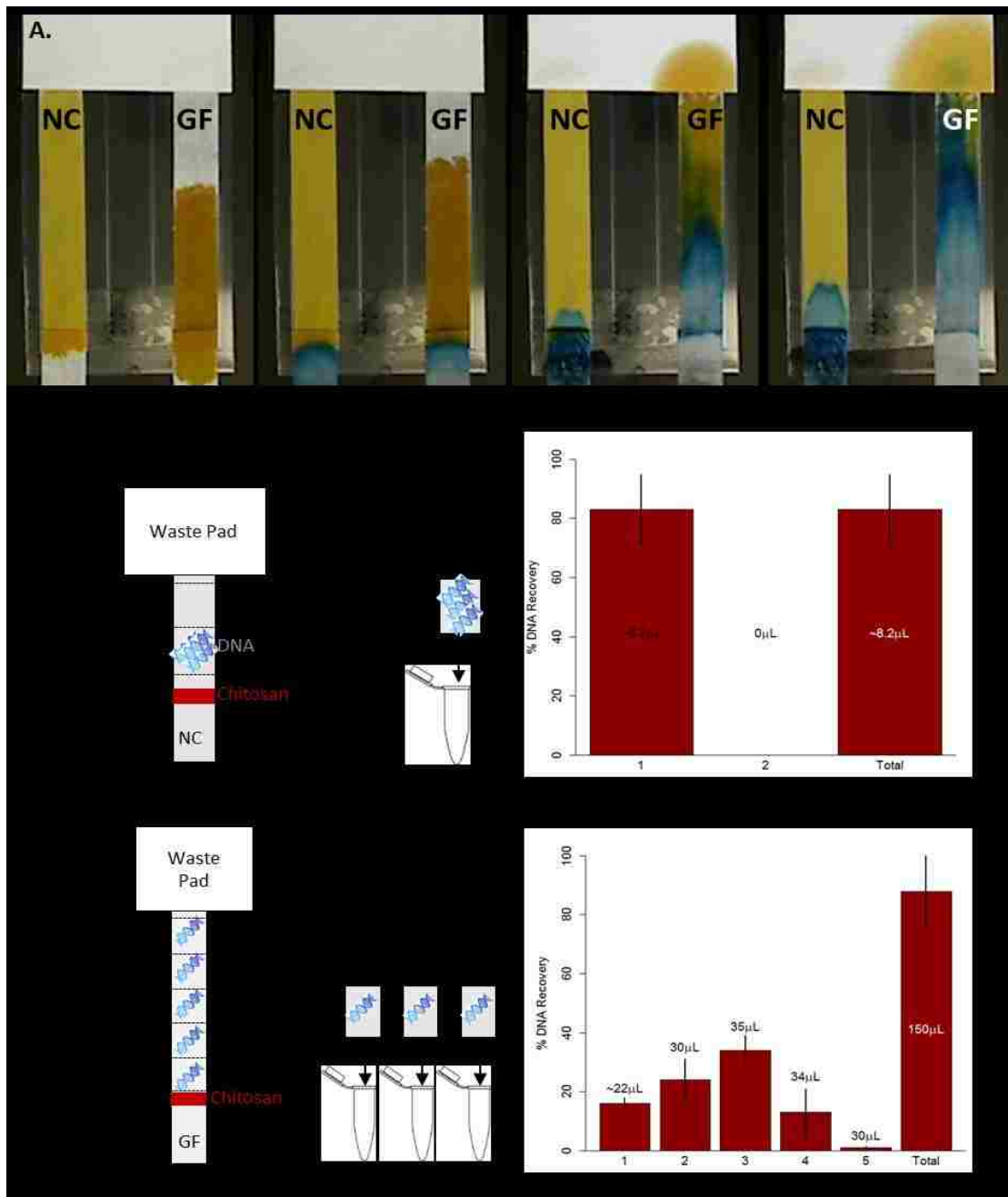


Figure 54. Dispersion of sequentially delivered fluids in nitrocellulose (NC) and glass fiber (GF). **A.** Capture buffer, 50 mM MES at pH 5, with bromothymol blue is flowed through the membranes. At pH values below 6.0, the indicator is yellow. As elution buffer, 50 mM Tris at pH 9, flows into the membranes, the interface of the buffers exchange ions. At pH values above 7.6, the indicator turns blue. In nitrocellulose, which has a relatively homogenous pore size distribution, the interface between two sequentially delivered fluids is sharply defined, which limits mixing at the interface and produces a sharp pH change. The relatively inhomogeneous pore size distribution in glass fiber, however, results in a poorly defined buffer interface. **B.** Elution profile of DNA from chitosan capture in nitrocellulose and **C.** glass fiber.

The maximum DNA concentration factors achieved with chitosan in nitrocellulose and glass fiber were 13.3x and 12.3x, respectively, **Figure 55B**. These results are based on the input sample volume and the purification efficiency of DNA since each membrane type yielded a specific elution volume.

The theoretical concentration factor assumes 100% recovery of DNA. In nitrocellulose, DNA recovery decreased as the input sample volume increased, **Figure 55C**, likely due to the time it took to flow large volumes through the membrane. Wicking a 2000 μL sample, followed by 100 μL of wash and elution buffers, through nitrocellulose took over seven hours. This reduced recovery greatly reduced the actual concentration factors achieved in nitrocellulose. The same experiment in glass fiber only took 25 minutes and DNA recovery was independent of input sample volume, **Figure 55C**. The long flow times required in nitrocellulose may exceed the chitosan/DNA off-rate which would cause bound DNA to prematurely release from chitosan and be lost to waste. The chitosan-DNA binding constant has been well studied and ranges from 10^9 to 10^{10} M^{-1} ^{236,237}, but, to our knowledge, the chitosan-DNA binding rates have not been published. There have been reported off-rates in the range of $3\text{-}5 \times 10^{-2} \text{ s}^{-1}$ ^{238,239} for similar polycation-DNA interactions.

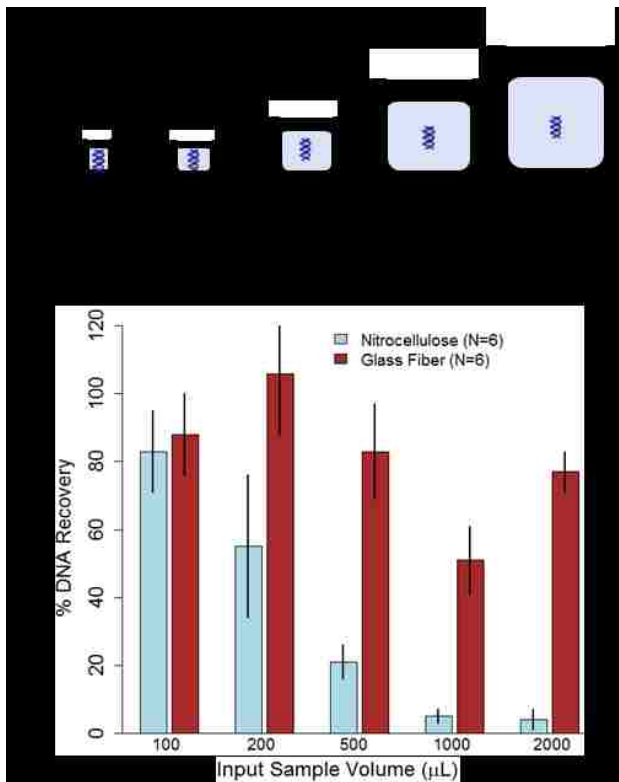
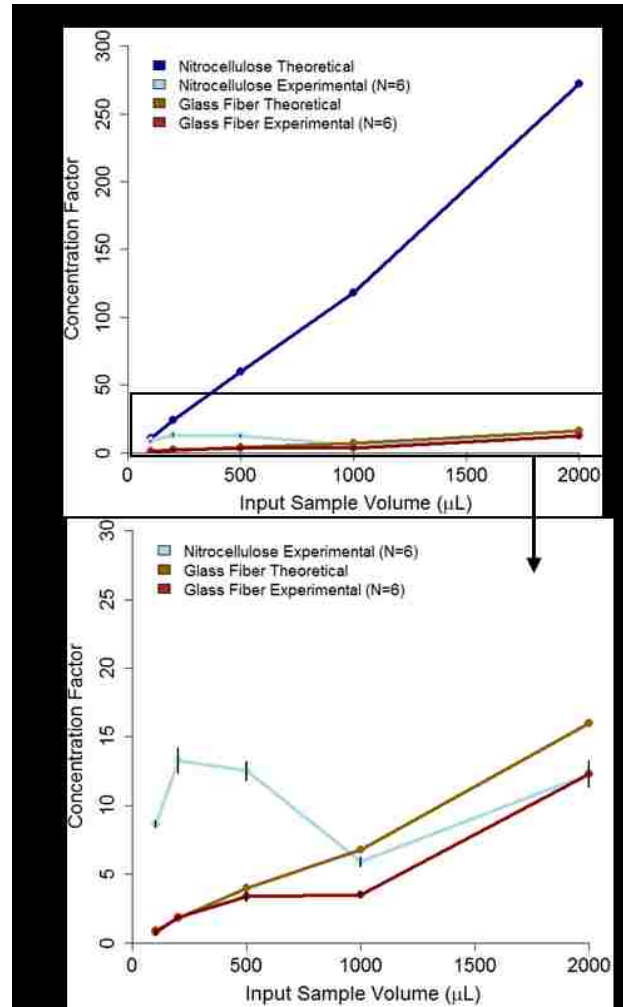


Figure 55. DNA concentration effects in nitrocellulose and glass fiber. **A.** Experimental schematic. **B.** Concentration factor from various input sample volumes. **C.** Corresponding recovery of DNA.



In this system, which involves complex surfaces in porous membranes as well as in-flow binding, both concentration factor and percent recovery were independent of the starting DNA concentration in the sample within the ranges tested. Using the data presented in Figure 52, the corresponding elution volumes, and the resulting recovery percentages, consistent concentration factors and percent recovery were measured for input DNA concentrations ranging from 1×10^3 copies of target per μL ($\text{c}/\mu\text{L}$) through 1×10^5 $\text{c}/\mu\text{L}$ where total input volume was set to $100 \mu\text{L}$, **Figure 56**. These concentrations were below the saturation limit of the modified membranes' binding capacity for DNA. Testing more dilute samples in larger input volumes indicates that this trend holds and is further detailed in Aim 4.

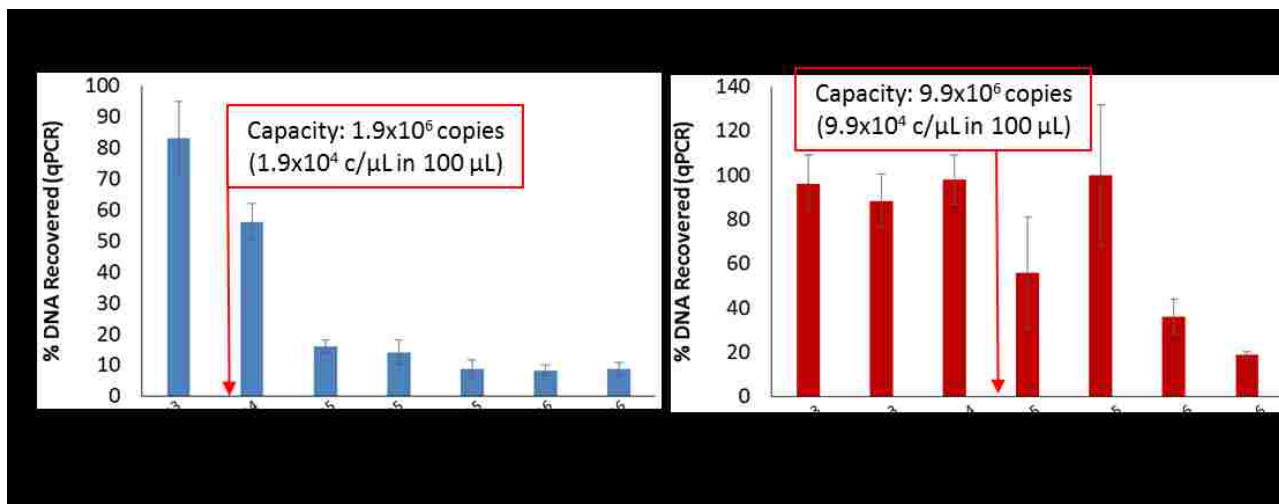


Figure 56. Recovery of DNA using chitosan-modified membranes is concentration independent, below the binding capacity in **A.** nitrocellulose and **B.** glass fiber.

There are potential applications where concentration factor would matter less than purification but not necessarily recovery. For very dilute samples, such as urine, concentration factor would play a critical role to ensure enough pathogen nucleic acid was recovered for downstream analysis. Additionally, different infections present at a highly variable pathogen loads. For example, clinical studies have quantified active chlamydia infections in urine at 10^1 – 10^5 elementary bodies/mL¹⁰⁵, Ebola in serum at 10^3 – 10^9 RNA copies/mL²⁴⁰, and influenza in nasopharyngeal wash at 10^3 – 10^7 TCID50/mL²⁴¹. Each of these infections would benefit from a combination of both target purification and concentration. Specifically, for infections that occur at low copy number or in dilute samples such as urine, concentration is especially important. Some of these samples would require the processing of larger volumes (mL instead of μ L) to ensure a sufficient number of pathogens for infection identification. The current approach, especially using nitrocellulose, is too slow to process larger volumes and may result in decreased recovery, Figure 55C. Future iterations of this work involved developing fluidic systems that can rapidly process large volumes in order to purify and concentrate targets from complex, dilute samples (see Aim 4).

Effect of pH on DNA purification using chitosan. The electrostatic interaction between chitosan and DNA is highly dependent on solution pH and the pK_a of chitosan. If the $pH < pK_a$, the primary amines will shift toward protonation and the resulting positive charge will attract the negative charge on the backbone of DNA. If the $pH > pK_a$, the primary amines will remain neutral and not interact electrostatically with DNA.

In a porous membrane, a buffer switch results in an interface between the two buffers. Depending on the membrane characteristics, this interface can be well or poorly defined,

Figure 54A. In both cases, however, small molecules such as protons are able to exchange across this interface resulting in mixing on the molecular scale. For the paper-based purification system, the two buffers at an interface have different pH values: a low pH for capture followed by a high pH for elution. Chitosan's pK_a has been reported as $\sim 6.3\text{--}6.5$ ²²³. The closer a buffer is to this pK_a , the less dramatic the effect on protonation because pK_a is a measure of equilibrium. At chitosan's pK_a , there is an approximately equal amount of protonated and unprotonated amines. To shift the equilibrium, the pH of a solution needs to be further away from the molecule's pK_a .

This effect was tested by varying the capture and elution buffer pH values for a DNA purification experiment in porous membranes. For the capture pH values tested, there was little effect on the overall purification of DNA, **Figure 57A**. For the elution, however, pH values closer to the amine pK_a resulted in delayed elution from the chitosan patterned region, **Figure 57B**. These results support the model of mixing at the buffer interface and reduced rate of de-protonation. This pH-sensitivity also allowed for temporal control over DNA elution depending on the desired downstream application. If highly concentrated DNA is required, then an elution buffer with a higher pH should be used. If a less concentrated, longer release of DNA is required, elution buffers with a pH closer to the amine pK_a should be used.

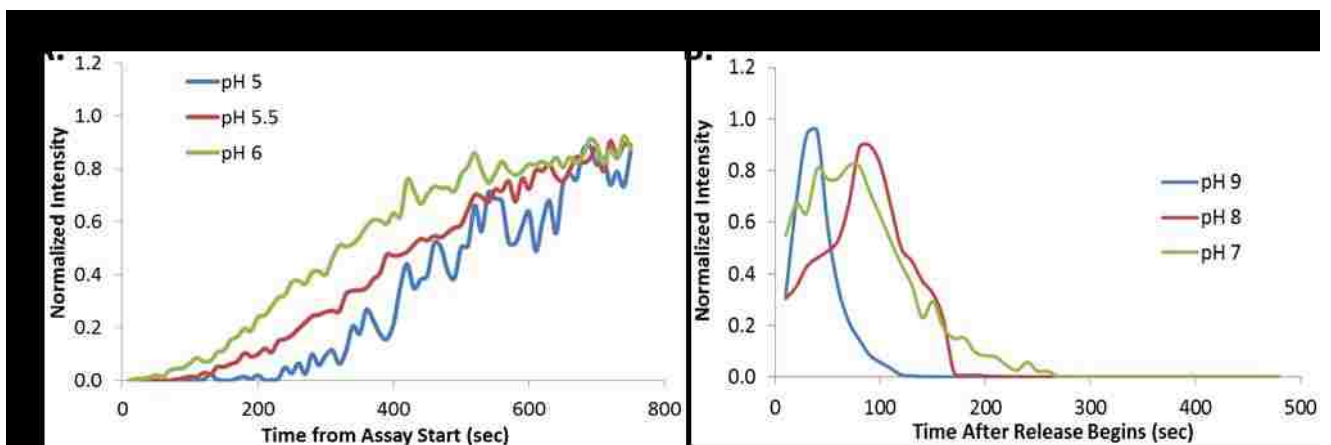


Figure 57. Effect of pH on DNA purification in nitrocellulose with chitosan. Averages of $N=3$ are reported, error bars were omitted for clarity. **A.** Capture works similarly well at the three pH values tested. **B.** Release is influenced by pH. At pH values significantly above the pK_a , release in nitrocellulose is rapid. At pH values closer to the amine pK_a , release is extended. *Note, the fluorophore used to label DNA is more efficient in higher pH values, as indicated by the manufacturer. This results in an initial spike of fluorescent signal after elution begins.

5.3.4. *Recovery of DNA from complex samples.* The system's ability to purify DNA from complex sample types was demonstrated and, overall, this method was able to recover $\sim 80\%$

of the input DNA from most of the sample types tested. In both nitrocellulose and glass fiber, the recovery of target DNA was reduced when samples contained a non-target:target ratio of greater than 100:1. These data are slightly higher than the limits dictated by the capacity data above (~10:1 for nitrocellulose and ~20:1 for glass fiber). This discrepancy is likely a result of larger DNA fragments (greater than ~250 kbp) from the non-target DNA being too large to flow through the small pore features of the membranes (see Aim 2 for more details). This size-exclusion effect is expected to be more severe in nitrocellulose than in glass fiber due to the differences in pore size distribution between the two membranes. This would suggest that some non-target DNA is essentially filtered upstream of the chitosan capture region rendering it unavailable to compete for binding (see Figure 45). The data in **Figure 58** support this explanation because at large non-target:target ratios of 200:1, there is a greater reduction in recovery for glass fiber than in nitrocellulose. At higher ratios, 500:1, the reduction in target DNA recovery is similar in both membranes. Recovery of target DNA in glass fiber with an extreme non-target:target ratio of 1000:1 was higher than expected.

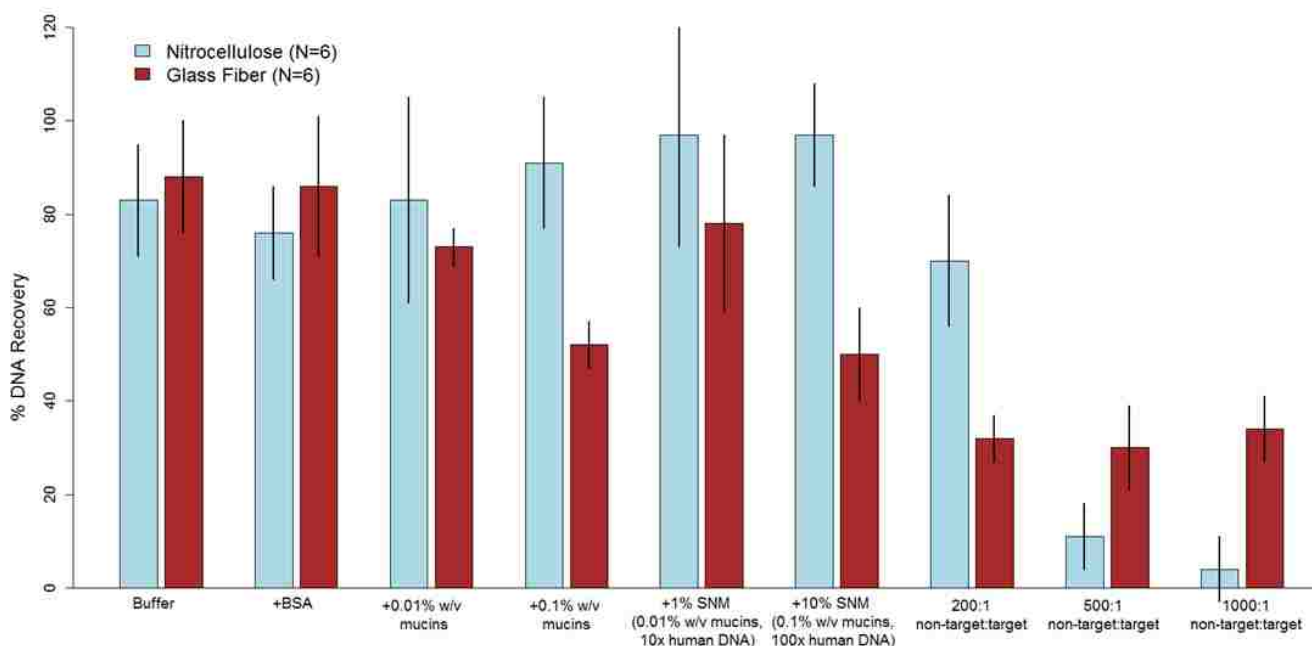


Figure 58. DNA purification in porous membranes by chitosan capture. Recovery of DNA in either nitrocellulose or glass fiber. The average of N=6 is reported with error bars representing +/- one standard deviation. Chitosan concentration at the capture line was $1.3 \times 10^{-9} \mu\text{g}/\mu\text{m}^2$ for nitrocellulose and $1.8 \times 10^{-9} \mu\text{g}/\mu\text{m}^2$ for glass fiber. Input DNA was between 1×10^5 and 1×10^6 copies of fragmented MSSA DNA. For SNM: 1% SNM contained 10:1 non-target to target DNA, 0.01% w/v mucins, 1.1 mM NaCl; 10% SNM contained 100:1 non-target to target DNA, 0.1% w/v mucins, 11 mM NaCl.

The addition of mucins, to mimic nasal swab samples, reduced recovery of target DNA in glass fiber but not in nitrocellulose. Mucins are large protein aggregates (mass $> 10^6$ Da) that

are glycosylated with oligosaccharides that commonly form negatively charged side groups²⁴². These negatively charged molecules can interact with positively charged chitosan, blocking the binding of DNA. These large aggregates may not pass through the small pores of nitrocellulose because DNA recovery is not affected by their presence in the sample. In glass fiber, however, the larger pores may allow these negatively charged aggregates to flow downstream and prevent DNA binding to chitosan, leading to reduced recovery as the concentration of mucins increases. When both mucins and non-target DNA is present in samples (from simulated nasal matrix, SNM), DNA recovery remains high in nitrocellulose and decreases in glass fiber. Once again, the magnitude of this decrease is correlated to increasing concentrations of mucins. For applications containing mucins or high concentrations of non-target DNA, the chitosan-patterned region can be extended to increase the system's overall capacity.

5.3.5. *Recovery of DNA in porous membranes from samples containing blood.* Blood preparation procedures often require many user steps to remove blood components that can inhibit downstream amplification reactions, notably heme²⁴³. The chitosan-based DNA purification system is able to rapidly purify target DNA from blood samples with only one user-step. The eluted samples were quantified by qPCR without further purification. In both membranes, samples with lower blood concentrations resulted in higher recovery of DNA, **Figure 59A**. In nitrocellulose, recovery of target DNA from blood-containing samples was significantly inhibited and the flow rate of the sample through the membrane decreased as blood concentration increased. The reduced flow rate appeared to be a result of membrane clogging. For the sample containing 50% blood in nitrocellulose, only a small volume wicked into the membrane before flow stopped completely.

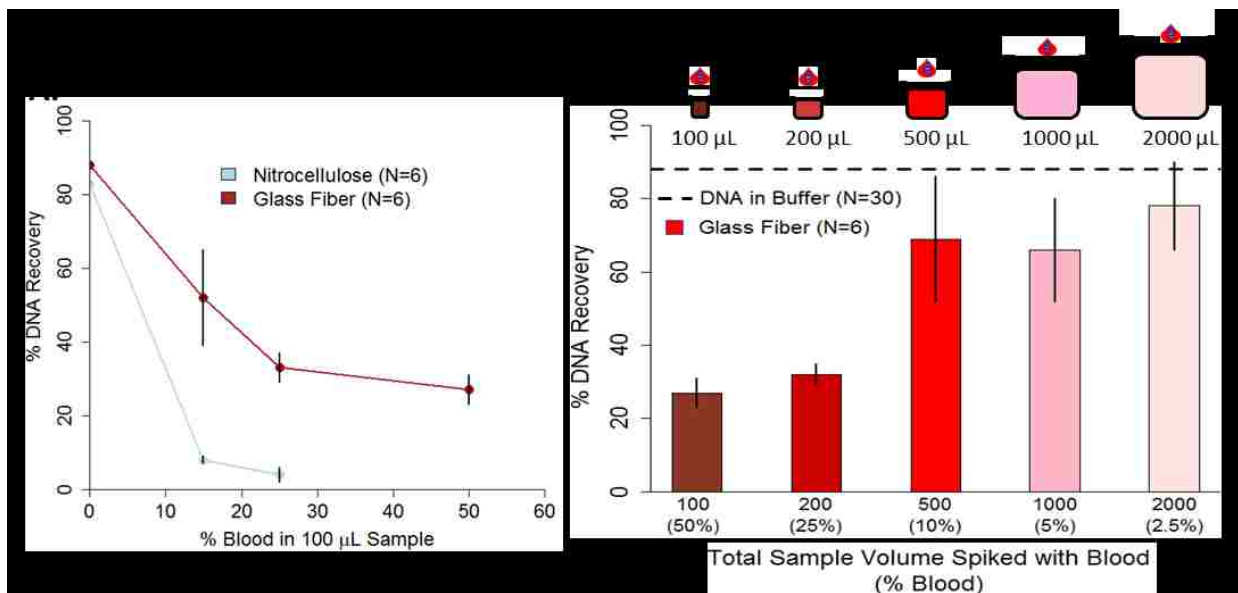


Figure 59. DNA purification in porous membranes from samples containing blood. Averages of $N=6$ \pm one standard deviation are reported. Chitosan concentration at the capture line was $1.3 \times 10^{-9} \mu\text{g}/\mu\text{m}^2$ for nitrocellulose and $1.8 \times 10^{-9} \mu\text{g}/\mu\text{m}^2$ for glass fiber. Input DNA was between 1×10^5 – 1×10^6 copies of MSSA DNA. **A.** Increasing the percent of blood in a 100 μL sample reduced recovery in both nitrocellulose and glass fiber. The 50% blood sample clogged the nitrocellulose membrane preventing any DNA recovery. **B.** Diluting 50 μL of blood into large sample volumes improved recovery in glass fiber.

In glass fiber membranes, target DNA was purified from samples containing up to 50% whole blood but, as blood concentration increased, DNA recovery decreased. To verify this result, 50 μL of whole blood plus target DNA was diluted into increasing volumes of buffer. As blood concentration decreased, DNA recovery increased, **Figure 59B**.

For samples that were less than 25% blood, DNA purification efficiency is similar to the “DNA in buffer” control. This restored recovery is likely due to increased washing of the chitosan region to remove blood components that interfere with chitosan/DNA binding and not with the qPCR analysis. Based on the dilution factor of DNA eluted from chitosan in glass fiber (Figure 54C) and the sample volume used for qPCR (1 μL of the elution), the maximum amount of blood in a qPCR reaction would be less than 0.5%. For whole blood concentrations at or below 0.5%, qPCR is not inhibited²⁴⁴.

5.3.6. *Recovery of DNA in porous membranes in high salt conditions.* In addition to nasal swabs and blood, urine is a high priority sample because it is easy to collect in LRS. The salinity of urine can vary greatly between individuals and within in the same person^{120,121}. Our membrane-based DNA purification system relies on an electrostatic interaction between the NA and our capture polymer²⁴⁴. Electrostatic interactions can be sensitive to the surrounding microenvironment,

especially those with variable salt concentrations. The addition of salt can stabilize electrostatic interactions within a given concentration range; outside of that range an electrostatic interaction can be destabilized by the surrounding ions²⁴⁵.

To determine whether physiological concentrations of urine interfered with chitosan capture of DNA in porous membranes, up to 500 mM of NaCl was added to the 100 μ L samples containing DNA used in purification experiments. For these studies, purification was tested in Standard 17 glass fiber and Fusion 5 membranes. On average, purification in Fusion 5 was very robust to salt concentrations of up to 250 mM and only showed a moderate decrease in recovery at 500 mM NaCl. Capture in Standard 17 was more sensitive; addition of 0–100 mM of NaCl resulted in high recovery of DNA. Above or below these concentrations showed a NaCl concentration dependent loss of DNA recovery, **Figure 60**.

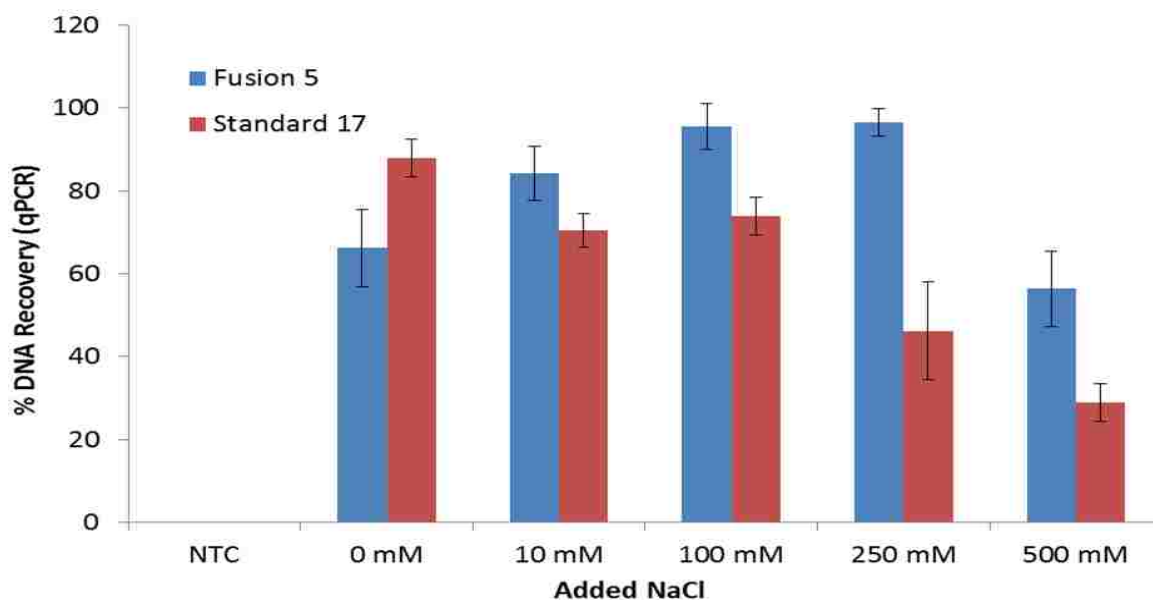


Figure 60. Effect of increasing NaCl concentration on chitosan purification of DNA in glass fiber and Fusion 5 membranes. Averages of $N=7$ +/- standard error are reported for all samples except for NTCs where averages and standard errors are from $N=3$.

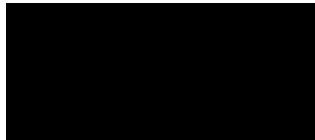
The reduced recovery from samples with higher salt concentrations is likely a result of the weakened electrostatic interactions between chitosan and DNA due to salt screening. Simple electrostatic interactions are explained by Coulomb's Law. In the presence of additional ions, the Coulomb interaction is screened because the primary species now have additional charges to interact with, (**Equation 9**)²⁴⁶. The electrostatic force of interaction, F , is proportional to a screening term, $e^{-rk^{-1}}$, which dampens the effective interaction. This screening term is dictated by the Debye length which is a measure of the size of the screening effect, (**Equation 10**)²⁴⁷. Within the Debye

length, the charged species will interact, but outside of the Debye length, the electrostatic interactions are shielded.



(Equation 9)

Where F is the electrostatic force, r is the distance between the two charges, q_1 and q_2 , k_e is Coulomb's constant, and e^{-r/λ_D} is the screening term.



(Equation 10)

Where λ_D^{-1} is the Debye length, ϵ_r is the relative permittivity of the system (material and fluid), ϵ_0 is the permittivity of free space, k_B is Boltzmann's constant, T is absolute temperature, N_A is Avogadro's number, e is the valence of the ions, and I is the ionic strength of the solution. The relative permittivity can be influenced by different components of the system,

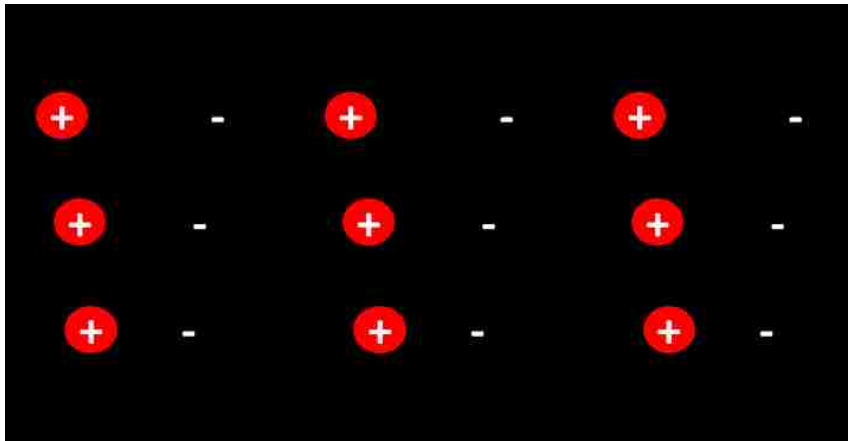


Figure 61. Effect of increasing ionic strength and ion valence on Debye length of electrostatic interactions. Charge species represented by "+" and "-" connected by arrows are successfully interacting. Increasing the quantity or valence of ions decreases the Debye length causing charged species that are further away to no longer interact as indicated by the loss of connecting arrows.

but for this application it is dominated by the buffer which is mostly water. The relative permittivity of proteins, DNA, and glass-like substances are $\sim 2-4$, $\sim 8^{248}$, and $3.7-10^{249}$, respectively. The relative permittivity of water at room temperature is $\sim 80^{250}$; this term will dominate other components of the system and therefore is essentially a constant in the calculation of the Debye length for this application.

The Debye length is inversely proportional to both ionic strength, I , and ion valence, e ; as the salt concentration and/or the valence (Na^+ v. Mg^{2+}) increase, the Debye length decreases therefore reducing the effective length of the primary electrostatic interactions, **Figure 61**.

Salt screening has been characterized for polycation-DNA interactions^{237,251–254}. Strand *et al.* found that destabilization of chitosan-DNA complexes increased linearly with increasing NaCl concentration; they also found that this destabilization was more severe with shorter chitosan molecules²³⁵. For the results presented above, the effects of salt screening were more severe in Standard 17 compared to Fusion 5.

After exploring the effects of salt concentration on chitosan purification of DNA, we began to integrate these urine-

like conditions with larger volumes. Sample volumes ranging from 0.1–2 mL were spiked with 1×10^5 to 1×10^6 copies of fragmented MSSA DNA and NaCl. The average salt concentration found in healthy human adults¹³⁴ of 130 mM was chosen for this experiment. In general, increasing the sample volume or the NaCl concentration did not reduce recovery for either membrane type tested, **Figure 62**. Even though these results were variable, they show the ability to combine DNA purification from increasingly complex samples with the rapid volume processing methods that have been developed.

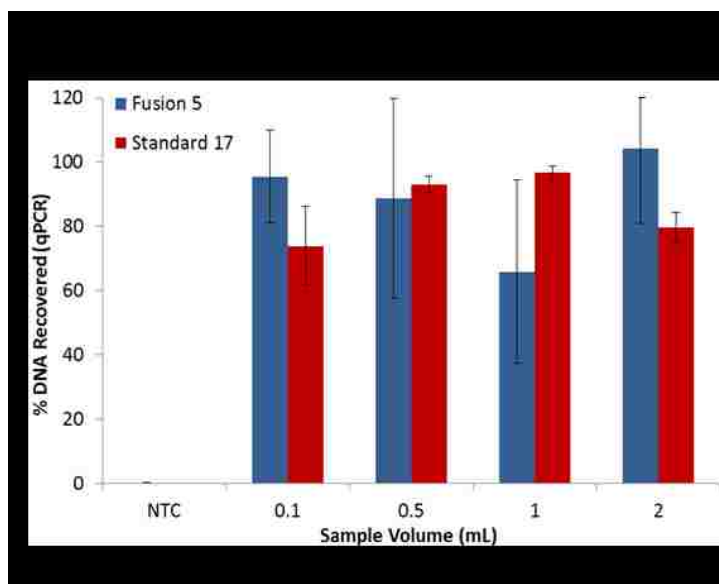


Figure 62. DNA purification from large volumes in Fusion 5 and Standard 17. Recovery of DNA from up to 2 mL samples containing 130 mM NaCl. Averages of $N = 3 \pm$ one standard deviation are reported.

5.3.7. Expanding DNA purification capabilities in porous membranes.

As shown above with the non-target DNA studies, chitosan is able to capture all DNA in a system. To further explore this opportunity for multiplexing, we tested the system's ability to purify *E. coli* and MSSA DNA from a single input sample.

Figure 63 shows the results of the bplexed purification of *E. coli* and MSSA DNA using two different chitosan-coated membranes, Standard 17 glass fiber and Fusion 5. The MSSA purification worked as expected. The *E. coli*

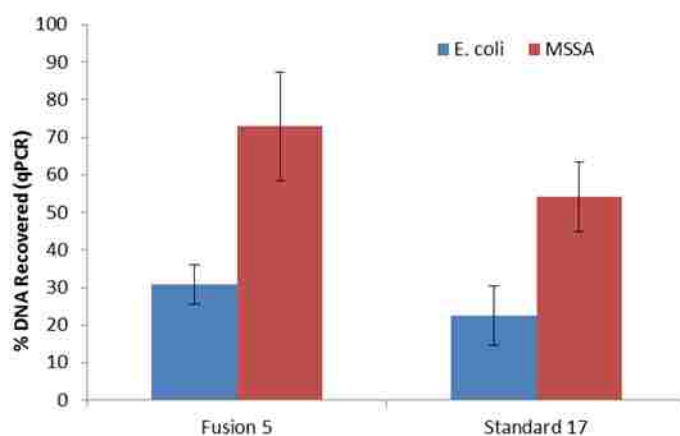


Figure 63. Simultaneous purification of *E. coli* and MSSA DNA in membranes patterned with chitosan. Averages of $N=4 \pm$ one standard deviation are reported.

The MSSA purification worked as expected. The *E. coli*

purification also worked well but with slightly lower recovery. The total concentration of DNA (*E. coli* + MSSA) added to the system was well below chitosan's binding capacity indicating that the reduced recovery of *E. coli* DNA may have been a result of insufficient fragmentation during purification from bacteria (as described in Aim 2).

Chitosan storage studies in porous membranes. The ability of chitosan-patterned membranes to retain their function during storage is an important metric to determine the usefulness of this assay for LRS. To test storage, Fusion 5 membranes were patterned with chitosan and stored in a desiccated environment for up to six months at either 20 or 40°C. These results are somewhat variable, but on average, the storage periods did not significantly reduce chitosan's ability to purify DNA in the porous membrane, **Figure 64**. These data serve as a baseline that indicates chitosan retains functionality when stored at either ambient (20°C) or elevated temperatures (40°C).

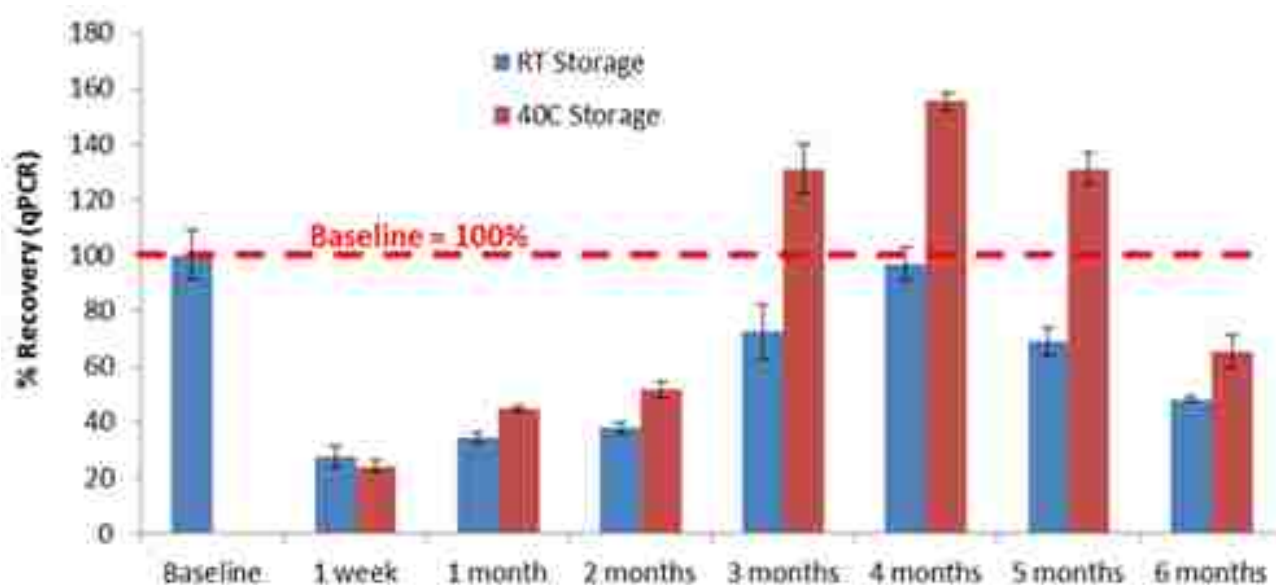


Figure 64. Chitosan storage studies in Fusion 5 compared to baseline recovery (no storage). Overall, storage for up to six months does not appear to significantly reduce chitosan's ability to purify DNA; there is also minimal differences between storage temperatures. Averages of at least N=4 +/- one standard deviation are plotted.

5.3.8. *RNA purification using chitosan in porous membranes.* In addition to DNA purification, initial experiments evaluated the feasibility of using chitosan-patterned membranes to purify RNA from samples. For this work, purified RNA was spiked into either 100 or 500 μ L of nucleic acid capture buffer (50 mM MES, pH 5) and introduced to Fusion 5 membranes patterned with chitosan. After flow of the RNA-containing solution, membranes were washed, and RNA was eluted using the same protocol as described for DNA. Although the overall recovery was ~3-4x lower than the same conditions for DNA, this proof of concept experiment shows that this assay is capable of purifying

RNA, **Figure 65**. These results are not meant to show an optimized system for RNA capture, rather, they should serve as a starting point for future projects.

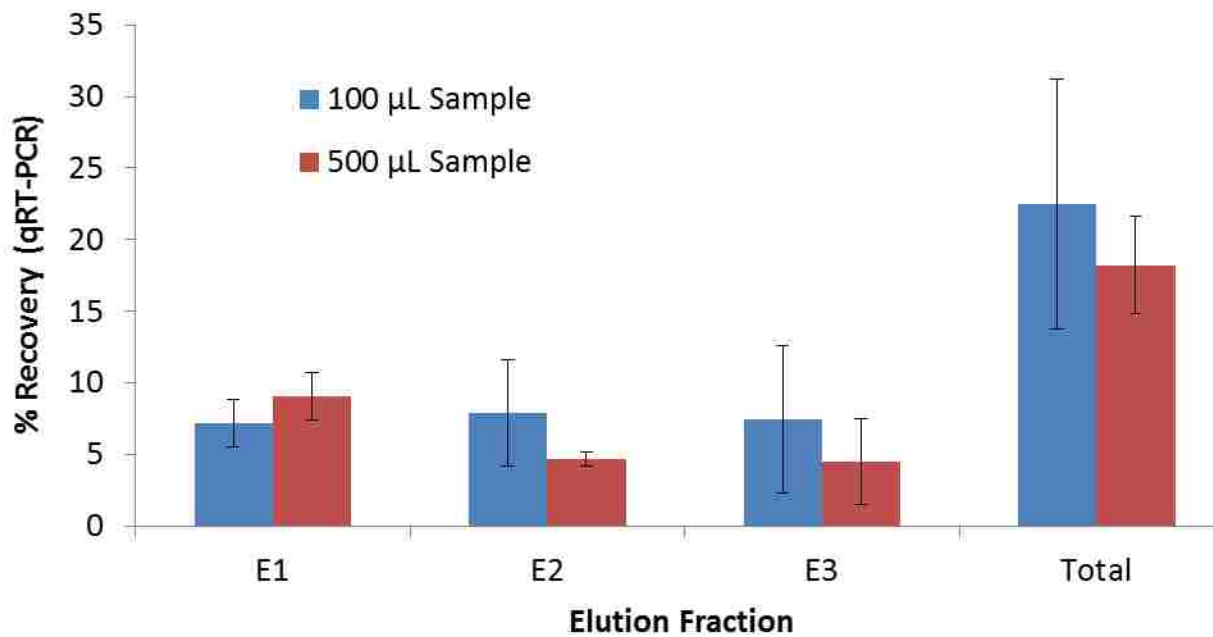


Figure 65. RNA purification in chitosan-patterned Fusion 5. Recoveries from two sample volumes (100 and 500 µL) showed no significant difference. RNA input per sample ranged from 5×10^4 – 5×10^5 copies. Averages of $N=9$ for the 100 µL volume and $N=5$ for the 500 µL volume are reported with error bars representing +/- one standard deviation.

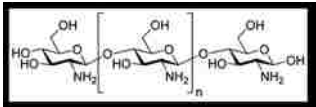
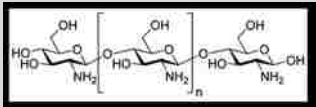
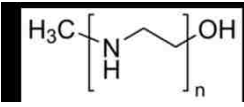
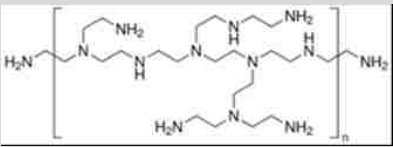
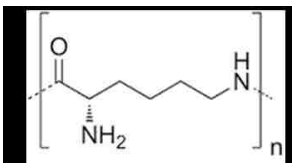
5.4. Conclusions and Future Directions

This work has demonstrated the first example of a system for the simultaneous purification and concentration of DNA from complex samples using chitosan and constructed entirely from porous membranes. First, the interaction of porous membrane substrates with chitosan was characterized and a method to determine the adsorption capacity of these membranes for polymers was described. Next, to exhibit the broad applicability of this system, it was used to purify DNA from complex samples including those with high protein content, non-target DNA, high salinity, and known amplification inhibitors such as blood. These samples are just a few examples of potential inputs that can be handled by this system. The choice of membrane and pH of assay solutions provides the ability to control the sample processing time, volume, and concentration factor. Thus, large volume samples such as urine or contaminated environmental water can be rapidly processed with this system at the POC. RNA purification using this in-membrane system was also demonstrated as initial proof of

concept data. Further, this system is already well-suited for untrained end users *via* the use of automatic sequential reagent delivery^{139,229}. Finally, the assay has shown to be stable over a six-month period at two storage temperature. This method can directly integrate with other paper-based point-of-care technologies such as in-membrane amplification¹⁴¹ and detection (see Aim 4 for more details).

The next project that builds upon this work should continue to investigate and optimize RNA purification and concentration from complex sample matrices. Ideally, a simultaneous DNA/RNA purification system would allow for expanded use. Further, this work should be tested with other polyamines. Chitosan has proven to be very effective, but it is one of many polyamines that interact strongly with nucleic acids. An interesting extension of this work could involve the investigation and comparison of other common polyamines such as: high molecular weight (Mw) chitosan, linear polyethylenimine (PEI), branched PEI, and poly-L-lysine (PLL). The variation in properties such as size and pKa may enable more effective purification and concentration for different sample types. Examples of common polyamines are summarized in **Table 8**.

Table 8. Comparison of polyamines for DNA purification in porous membranes. *Based on availability from Sigma Aldrich.

Polymer	Mw Range	Length (nm)	pK _a	Price (g)*
Low Mw chitosan 	4–6 kDa	14–20 nm	6.3–6.5 ²²³	\$18.85
High Mw chitosan 	50–190 kDa	170–646 nm	6.3–6.5 ²²³	\$1.04
Linear PEI 	2–25 kDa	18–273 nm	8.5–9 ²⁵⁵	\$53.90
Branched PEI 	~ 25 kDa	~ 138 nm	8.3–8.5 ²⁵⁵	\$0.62
Poly-L-lysine 	150–300 kDa	985–1970 nm	9.9 ²⁵⁶	\$0.10

6. Specific Aim 4: Automation of large volume sample processing through controlled fluid movement in multi-material porous networks

Laboratory assays to diagnose chlamydia and gonorrhoea from urine specimens require up to 25 mL of sample. At the point-of-care, immunoassays can call for anywhere from 0.1–15 mL, but these tests often require multiple pre-processing steps, mains electricity, and expensive equipment prior to pathogen detection²⁵⁷. Additionally, these commercially available rapid tests tend to have poor accuracy, leaving patients with ambiguous results. To broaden the effectiveness of POC STI testing, new devices are being developed that rely on detecting pathogen DNA. Many of these devices use paper-based platforms that avoid the need for expensive equipment, but still lack automation and require multiple user steps. Additionally, most POC paper-based devices are limited to processing only a few hundred microliters (μL) of sample, which is far less than is needed for clinical utility.

This work describes the development and testing of a paper-based platform to automate sample processing from large volumes of urine (1–5 mL). This system relies on updating the fundamental understanding of how membranes wet and how fluid flows through multi-material networks. This need is also driven by the high complexity of human samples that requires multiple pre-processing steps. These methods are utilized for complex sample preparation from urine samples with downstream biomolecule detection, which would not otherwise be feasible with traditional paper microfluidic approaches.

This chapter included five subsections: (i) enhancing flow through porous membranes to reduce processing time of large volume samples; (ii) controlling fluid flow direction to sequence reagent delivery; (iii) automating multiplexed purification and concentration of *C. trachomatis* (CT) and *N. gonorrhoeae* (NG) DNA directly from pathogens in human urine; (iv) demonstrating platform compatibility with in-membrane NAAT and lateral flow readout; and (v) comparing device results to a clinical system used to detect CT/NG. This work linked the sample preparation modules developed in Aims 1–3.

6.1. Background

Valving options for controlling fluid flow in porous networks. During the last decade, multiple groups have demonstrated mechanisms for controlling fluid flow in porous networks through a variety of valving options. Materials can be embedded into a membrane to slow or delay flow. Noh

et al. utilized varying concentrations of patterned wax to control fluidic timing in porous devices^{258,259}. Lutz *et al.* developed a different approach by embedding sugar barriers into porous membranes. Higher concentrations of sugars resulted in longer delays for fluid delivery²⁶⁰. The Yager, Lutz, and Fu groups have also designed methods for the sequential timed delivery of reagents through two-dimensional paper networks that rely on volume metering^{47,229,261,262}. Chen *et al.* developed a fluidic diode using a combination of hydrophobic and hydrophilic coatings to control direction and sequencing of fluid flow, **Figure 66**²⁶³.

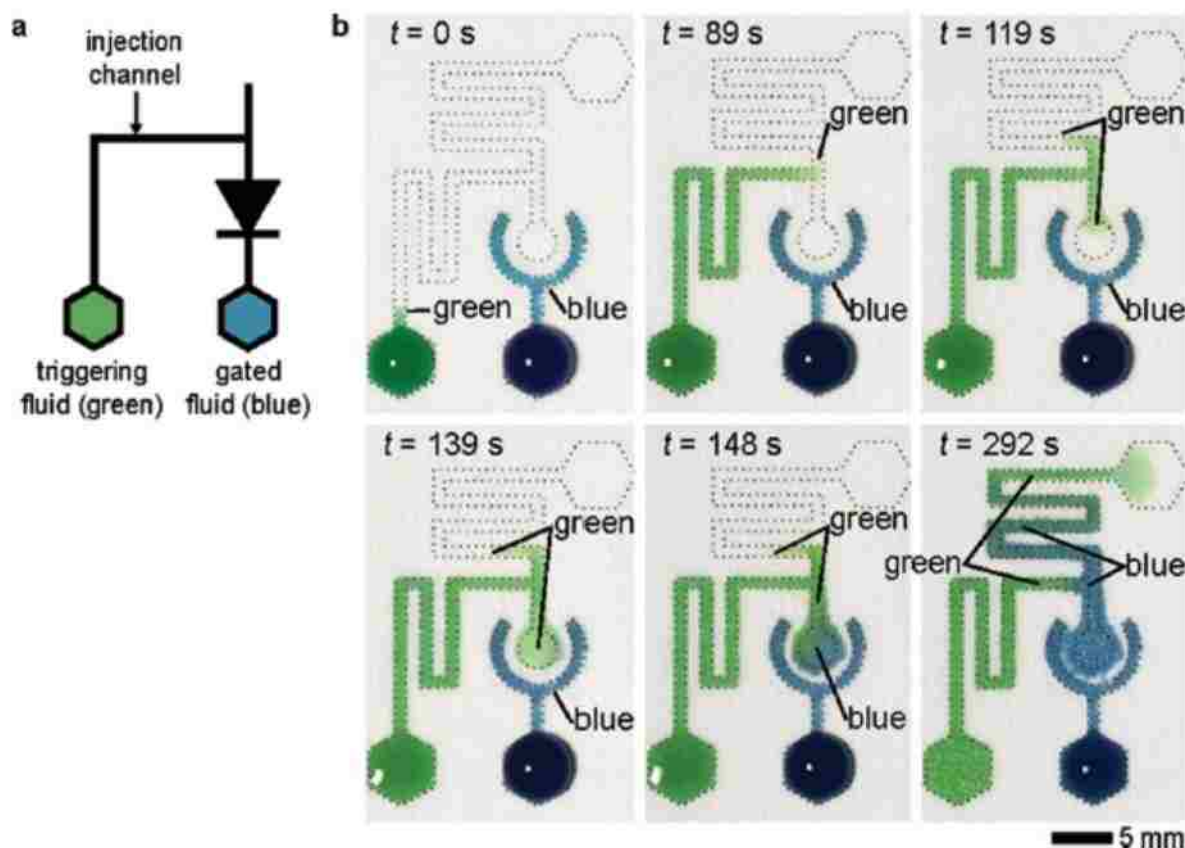


Figure 66. Paper diodes for controlling reagent flow in porous networks. **A.** Schematic of paper diode. **B.** Time series of paper diode where the triggering fluid which contains surfactant, green, wets the hydrophobic region separating the gated fluid, blue, from the main fluidic path. Once the gap has been wetted by the surfactant-containing fluid, the gated fluid can flow freely. Reproduced from Chen *et al.*²⁶³

Although many of these systems effectively control flow, they also share some limitations. For example, most of these methods are only able to turn flow on or off, but cannot do both. Many of these systems also introduce an additional reagent (wax, sugar, etc.) into the primary fluid path. These reagents may interfere or completely inhibit downstream reactions such as NAATs²⁶⁴⁻²⁶⁶.

With these concerns in mind, Toley *et al.* developed valves that utilize fluid to actuate expanding elements. These elements and fluids are isolated from the main fluid pathway and do not introduce

additional reagents. Also, these expanding valves can turn flow on or off and cause fluid diversion/redirection, **Figure 67**²⁶⁷. This system was able to achieve fluidic delays ranging from 5 seconds to 25 minutes with coefficients of variation of less than 9%.

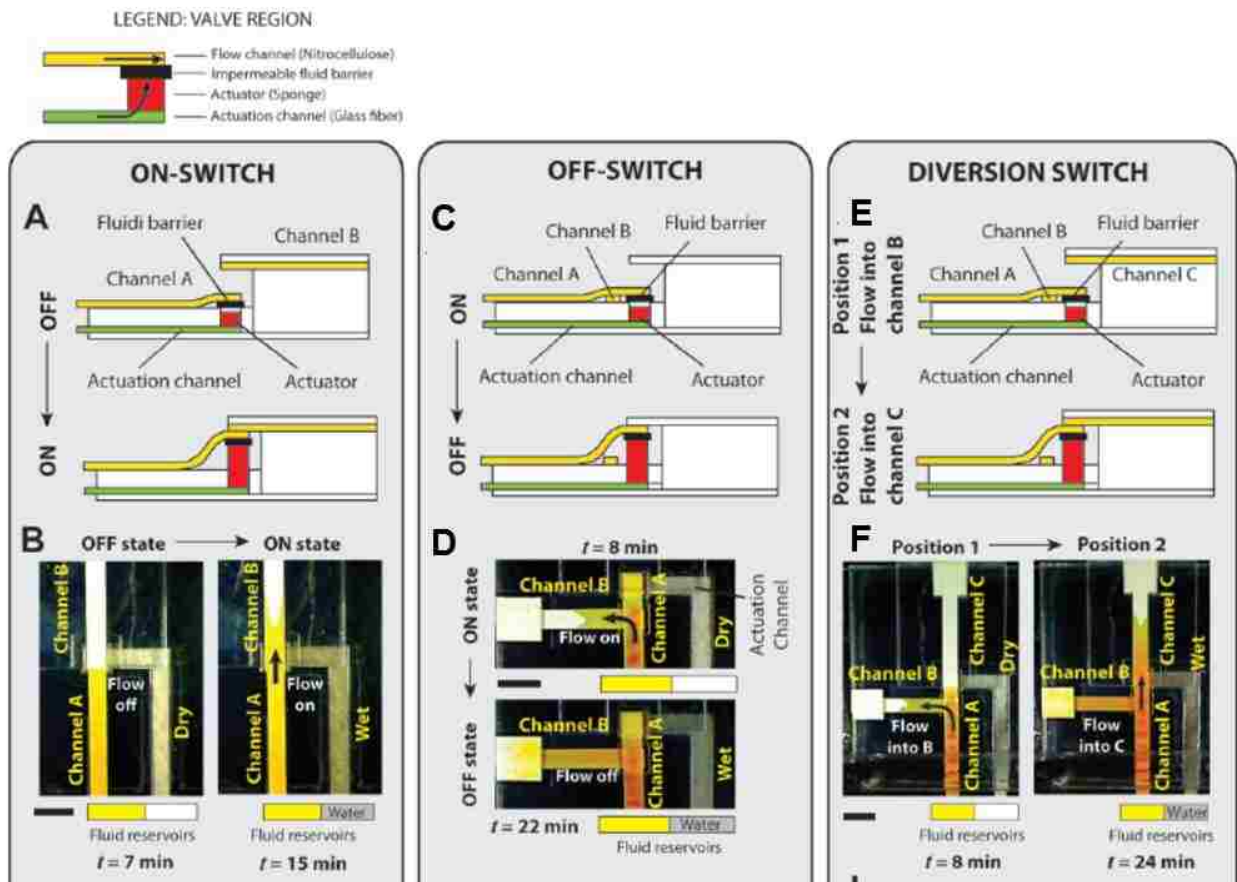


Figure 67. Controlling fluid flow through paper-actuated expanding elements. **A.** Schematic of an on-switch and **B.** experimental verification. **C.** Schematic of an off-switch and **D.** experimental verification. **E.** Schematic of a diversion or fluid re-direction switch and **F.** experimental verification. All images were modified from Toley et al.²⁶⁷

Recent publications have reviewed valves for paper microfluidics including those detailed above^{268–270}. Although effective, many these systems are limited to use with a maximum of a few hundreds of μL s of input sample. When processing large volumes such as urine or dilute blood, devices may need to manage up to 5–10 mL of fluid. In urine, for example, the first 5–10 contain the highest concentration of pathogens and biomarkers¹⁰¹.

In recent years, multiple groups have used isotachopheresis to concentrate pathogen biomarkers from complex samples^{92,95,271}, but these systems often use small sample volumes and involve multiple pre-processing steps, such as off-device centrifugation and sample dilution²⁷². Additionally, isotachopheresis can be sensitive to high salt and white blood cell concentrations found in clinical samples²⁷².

Linnes *et al.* developed an integrated method for paper-based NA extraction that relies on solid phase extraction. This method was then coupled to in-membrane isothermal amplification to detect chlamydia⁷¹. Although effective, this device required multiple user steps, utilized only a small volume of urine (between 10–100 μL), and only processed chlamydia elementary bodies instead of the biologically accurate chlamydia infected epithelial cells. Our group has previously published on an in-membrane sample processing method that concentrated DNA from up to 2 mL of sample (see Aim 3), but that system did not include any automation to enable development of an integrated device¹⁴⁰. This complexity of realistic samples requires a reimaging of device design and fluid processing.

Volumetric flow rate through fully saturated porous membranes is dictated by Darcy's law, **(Equation 11).**



(Equation 11)

Where the flow rate (Q), is proportional to the membrane permeability (κ), the cross-sectional area of flow (A), and the pressure drop from the inlet (p_a) to the wetting front (p_b). In porous membranes, the pressure at the point of measurement is equal to the membrane capillary pressure ($p_b = p_c$). The volumetric flow rate is inversely proportional to the fluid viscosity (μ), and the length of imbibition (L)^{273,274}. This equation indicates that as flow progresses further into a porous membrane, it begins to slow down due to the $1/L$ term (as described by the Lucas-Washburn equation²⁷⁵).

Mendez *et al.* reduced the slowing of flow rate during membrane wetting through optimized geometry to achieve a nearly constant flow rate in the rectangular section of the membrane, **Figure 68**. An increase in fan angle leads to an increase in cross-sectional area, decreasing the wetted length for a given fluid volume and thereby increasing the flow rate, as dictated by Darcy's Law.

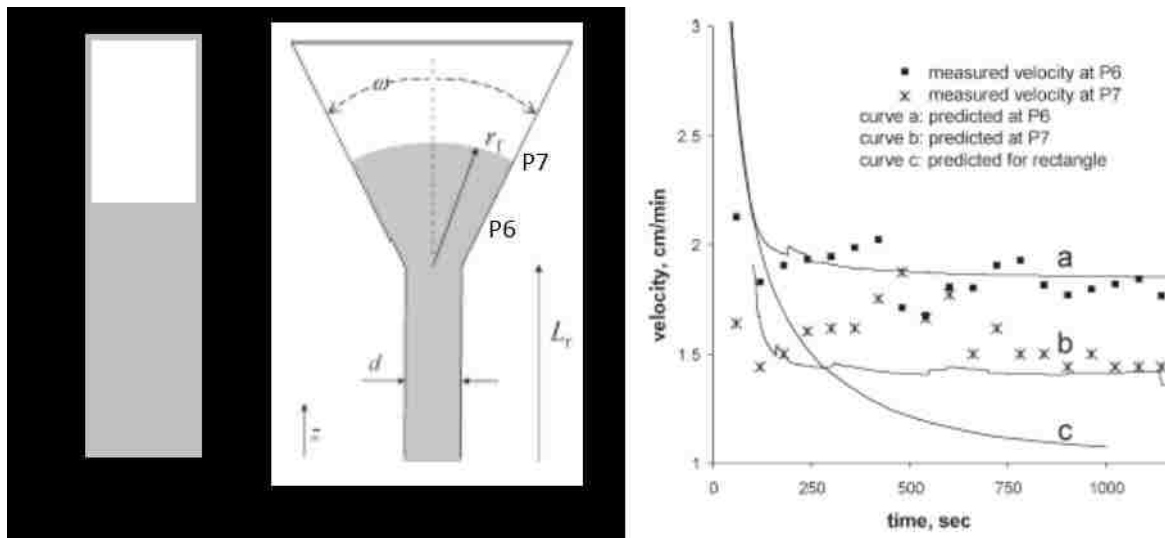


Figure 68. Models and experiments predicting flow through porous membranes. Wet-out of the standard rectangular membrane shows decreased velocity with increasing length and time. The modified geometry of the fan-shaped membrane increases the cross sectional area while decreasing the length required for fluid to travel leading to nearly constant flow rate through the rectangular section of the membrane. Modified from Mendez et al.²⁷⁶

Most of these situations still rely on two-dimensional flow in x and y through a porous network. After flow has developed in a primary membrane, the waste pad begins to wet, **Figure 69**. Flow through this multi-material network now becomes a series implementation of Darcy's Law²⁷⁷ through the two different membranes. As the fluid wicks further into a waste pad, flow velocity decreases due to increased resistance. This slowing velocity with increasing distance means that in order to accommodate large sample volumes, such as urine, the very large waste pads required can take a long time to uptake the fluid.

An alternative method for handling flow of large volumes while maintaining fast flow rates is to increase z-direction or transverse flow. By stacking multiple waste pads in the z-direction, rapid flow rates can be maintained and the overall x- and y-dimensions of a

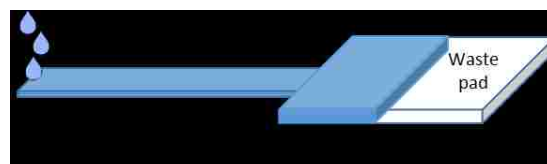


Figure 69. Multi-material porous network.

porous network device can be greatly reduced for a given fluid volume. For example, cellulose is a common waste pad material with a fluid capacity of $\sim 80 \mu\text{L}/\text{cm}^2$ of membrane area (CFSP223000 cellulose from EMD Millipore). A 1 mL sample would fill 12.5 cm^2 of membrane. Flow laterally through a membrane with dimensions of 1 cm wide by 12.5 cm long would slow significantly as it filled the entire 12.5 cm of length, according to Darcy's Law. The thickness of this membrane is ~ 0.2 cm. If transverse flow was exploited *via* stacked waste pads of dimensions 1 cm by 1 cm, a distance of only 2.4 cm in the z-direction would be required for the entire volume to flow. Darcy's Law

describes that flow rate is inversely proportional to the distance traveled by the fluid. Comparing the single waste pad and stacked waste pad configurations estimates that flow rate with the stacked waste pads is more than 5x faster than the large single waste pad.

The use of porous materials for affordable diagnostics is partially driven by their automatic wicking of fluids, removing the need for potentially expensive equipment for operation such as syringe pumps²⁶¹. This automatic wicking is driven by two principles: pressure and saturation. Fluid wicks into a membrane based on a pressure differential between a fluid source and the wetting front in the membrane. The pressure of the wetting front, called the capillary pressure, is defined by the surface tension (γ) of the imbibed fluid, the liquid/solid contact angle (θ), and the radius of the pores in the membrane (r_m)²⁷⁶, **(Equation 12).**

(Equation 12)

Capillary pressure is inversely proportional to pore radius; materials with smaller pores have higher magnitude, more negative, capillary pressures. In order for a porous material to wet, the supply fluid needs to provide a more positive pressure than the capillary pressure, resulting in flow down a pressure gradient. This is often achieved through an unrestricted fluid source such as a well, **Figure 70A**. If one porous material is acting as a source for a second material, then the capillary pressures at the junction of the materials needs to flow from more positive to more negative in order for the second material to wet, **Figure 70B**.

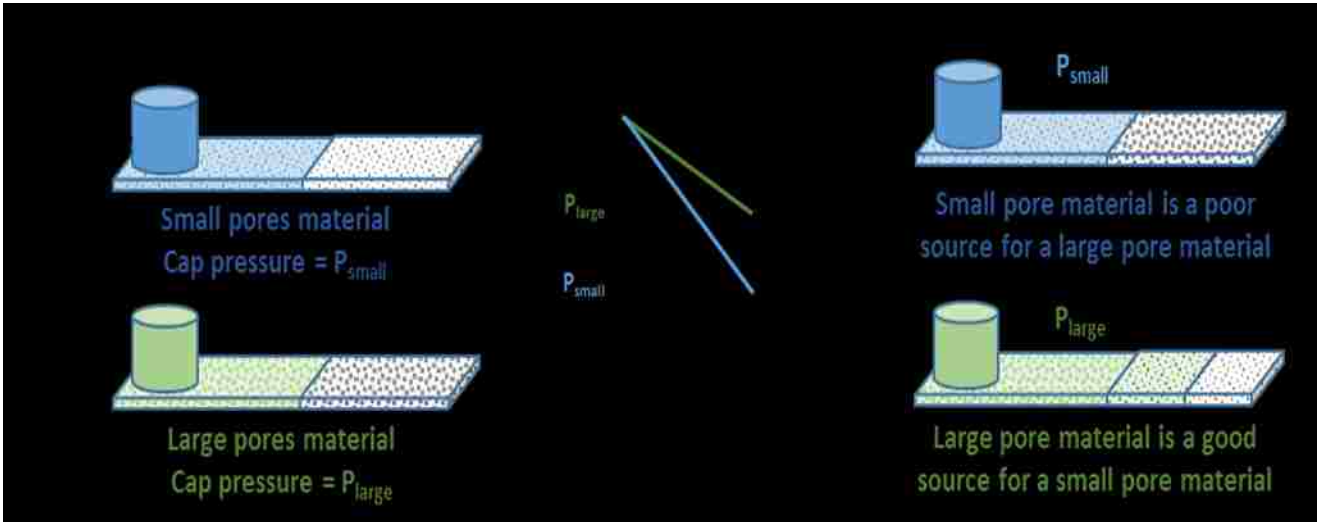


Figure 70. Wetting of porous membranes based on membrane capillary pressures (P_c). **A.** Pressure vs. position for a porous media wicking fluid from a well. The pressure at the fluid source is set to zero, and the pressure at the wetting front is the negative capillary pressure ((Equation 12). Based on Darcy's Law, this causes the wetting front to advance further into a porous membrane. Image adapted from Dr. Joshua Buser. **B.** A porous membrane can act as a source for another membrane if the capillary pressure of the primary membrane is more positive than that

of the secondary membrane at the intersection of the two materials.

Additionally, capillary pressure is a function of membrane saturation. Many previous publications use the simplified models described above for flow in paper microfluidic devices. The most commonly cited are the Washburn equation and Darcy's Law. The Washburn equation is limited to flow in one dimension while Darcy's Law can be used in multi-dimensional flows. Both of these models, however, are not fully representative of complex flow in porous media. For example, both Washburn and Darcy assume a fully saturating wetting front. In reality, the wetting front in a porous membrane is only partially-saturated and the degree of saturation depends on specific properties of the individual membranes such as the water retention curve (WRC) and the system geometry. To accurately predict wetting of multi-material systems, the effect of membrane saturation on capillary pressure needs to be incorporated.

Figure 71 shows three WRC for three hypothetical membranes (these curves are very similar to the actual curves of porous materials, but are used here as a simple demonstration). For each material, the less saturated, the more pressure is available to wet. This is partially driven by the heterogeneous pore size distribution in individual membranes. Small pores within a membrane will wet first due to

the more negative capillary pressure; smaller pores hold small volumes hence the low saturation at large pressures. Once the smaller pores have filled, the larger pores will begin to fill, taking up more volume at moderate pressures therefore leading to a rapid increase in saturation as shown by the sigmoidal shape

of the WRC. If the WRC of two connected membranes do not overlap in a given pressure range, then there will be minimal wetting of the low-pressure membrane (dashed black) if the higher-pressure membrane (solid black) starts off with the fluid. On the other hand, the medium-pressure membrane (solid green) would be predicted to partially drain the higher-pressure membrane (solid black) by the overlap of WRC. This section of work is in collaboration with Dr. Joshua Buser. A full description of the partially-saturated fluid flow model is beyond the scope of this thesis, but can be

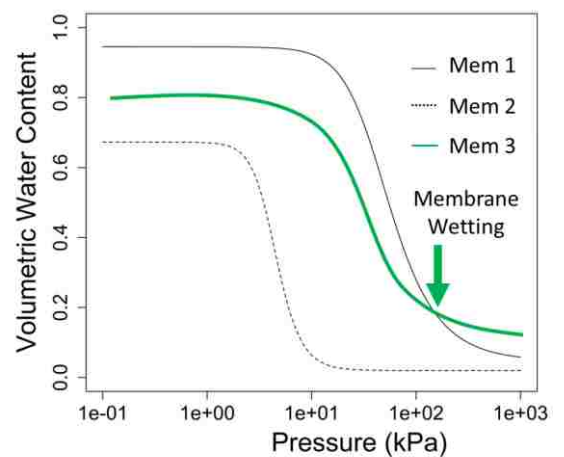


Figure 71. Example water retention curves (WRC) for three different membranes. Membrane 1 would serve as a poor source for membrane over this pressure range. Membrane 1, however, would serve as a good source for membrane 3 above the noted overlap pressure.

found in Dr. Buser's thesis (University of Washington, Department of Bioengineering, 2016) and in a separate manuscript (Buser *et al. in preparation*).

These properties and careful selection of materials and geometry were used to control flow direction in multi-material networks. **Figure 72** shows a porous network composed of multiple materials; the primary membrane is connected to a fluid source and a waste pad. This primary membrane is sandwiched between two pieces of the secondary membrane at the overlap region, **Figure 72B**. During wetting, the primary membrane will take up fluid. The secondary membrane has larger pores and a smaller magnitude pressure than the local fluid pressure at the junction, therefore it remains dry as the fluid flows through the overlapped region, **Figure 72C**. The secondary membrane will remain dry as long as the pressure magnitude in the primary membrane is greater than the capillary pressure of the secondary membrane. If an additional fluid source is connected to the secondary membrane, the pressure magnitude in the membrane decreases during wet-out and fluid can now flow through the overlap region. Because this mechanism relies on membrane pressures, we have dubbed it the pressure-switch, or p-switch for short.

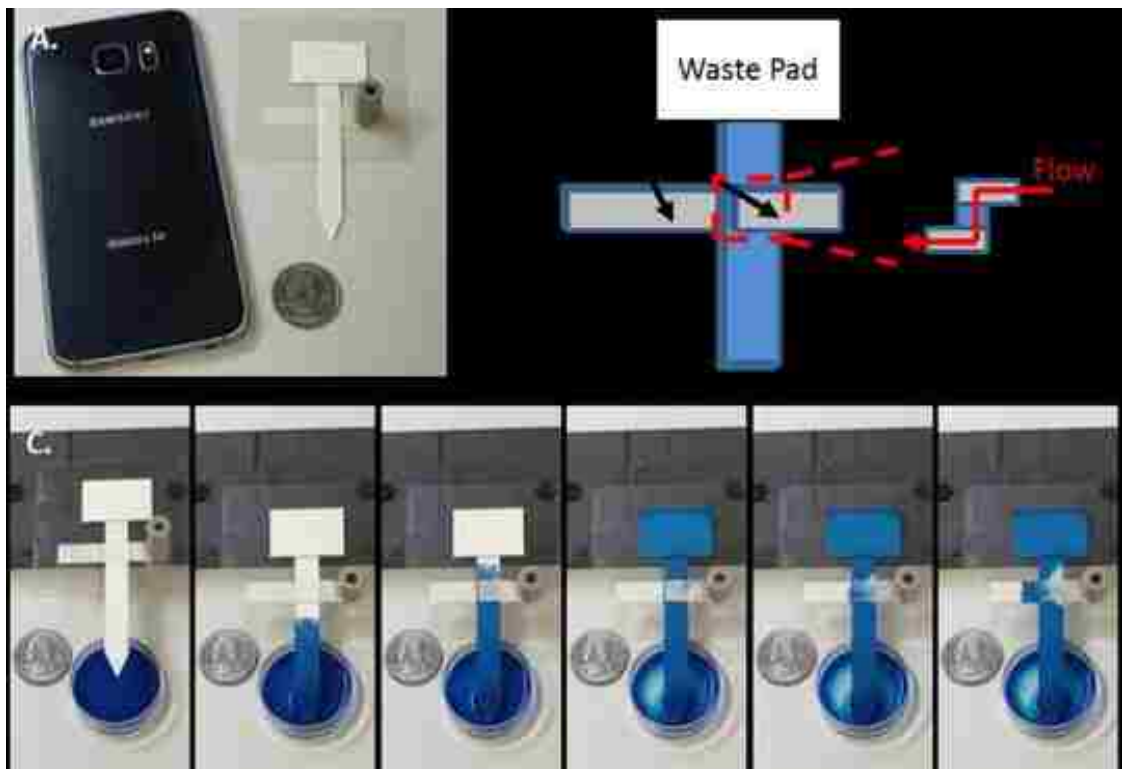


Figure 72. P-switch: pressure-controlled flow through multi-material networks. **A.** Device imaged next to a Samsung Galaxy S6 mobile phone and US quarter for scale. **B.** Schematic of the device using a multi-material network. The primary membrane is sandwiched and making contact with the two halves of the secondary membrane as shown in the cross-section. **C.**

Image from a video using colored liquids to show fluid flow in the device. Initially, flow is directed through a small-pore, higher-pressure primary membrane. The secondary membrane has larger pores and a smaller magnitude pressure; therefore it remains dry as the fluid flows through the overlapping region. Flow can be directed through the secondary membrane from an additional fluid source.

Currently available POC tests for chlamydia and gonorrhea. There are a number of rapid tests available for the diagnosis of chlamydia and gonorrhea at the POC. Many of these tests target pathogen-specific antigens in the urine. Although they are simple to use, they also have very poor predictive value^{117,118}. Causer *et al.* compared two antigen-detecting paper-based tests and the GeneXpert, an instrumented NAAT for POC tertiary clinical settings, to laboratory PCR tests for the detection of chlamydia and gonorrhea. Both of the antigen-detecting tests had poor sensitivity, 27.3 and 66.7%, while the GeneXpert performed very well, 100% sensitivity, compared to conventional laboratory PCR²⁵⁷. A major review in late 2014 also showed that most rapid immunoassays for detection of these pathogens perform very poorly, but all the tested NAATs have sensitivities of at least 86%²⁷⁸. Although systems like the GeneXpert are very sensitive, they also are very expensive²⁷⁹ and require electricity, multiple trained user steps for operation, and maintenance. The operational requirements for some of the common methods of chlamydia and gonorrhea diagnosis at the POC and in the laboratory are detailed in **Table 9**.

Table 9. Summary of the operational characteristics for common methods of chlamydia (CT) and gonorrhea (GN) diagnosis. Adapted from Causer *et al.*²⁵⁷, Gaydos *et al.*²⁸⁰, and Lowe *et al.*²⁸¹

Test	On-device sample reparation	Starting Sample Vol. (mL)	Sample prep time (min)	Time to result (min)	Number of steps	Ease of result interpretation	Required equipment	Sens & spec
Laboratory PCR (CT/GN)	No	Up to 25 mL	Varies: 5-30	90	Multiple	Easy (with computer)	Power supply, laptop, thermocycler, CT/GN assay reagents	Gold standard
GeneXpert (CT/GN)	Yes	1 mL	1	90	4	Easy (with computer)	Power supply, laptop, GeneXpert machine, CT/GN cartridges	100% 100%
Diaquick CT	No	15 mL	18	10	8	Moderate (qualitative)	Test kit, buffers, centrifuge and power supply, timer	27.3% 98.5%
Lateral flow card GN	No	15 mL	18	10	8	Moderate (qualitative)	Test kit, buffers, centrifuge and power supply, timer	66.7% 76.9%

Recently, interest has increased in the development paper-based NAATs for the detection of chlamydia and gonorrhea at the POC. Multiple groups have used isotachopheresis for the

purification of NA combined with NAAT^{92,271}. These systems are able to achieve high concentrations of the desired NA targets, but often involve multiple pre-processing steps and small volumes. Bercovici *et al.* used isotachopheresis for the purification of NA from mock urine samples, but their system involved off-device centrifugation and sample dilution²⁷². Additionally, the authors noted that this method was sensitive to the high salt and white blood cell concentrations found in clinical urine samples²⁷². Recently, Moghadam *et al.* demonstrated a system for paper-based isotachopheresis. Their system was able to achieve upwards of 1000x concentration, but they only used small volumes, 100 μ L, in simple TE buffer⁹⁵. Linnes *et al.* developed an integrated method for paper-based NA extraction system coupled to in-membrane isothermal amplification to detect chlamydia⁷¹, but again it only can handle small sample volumes and requires multiple trained user steps.

Although effective, all of these systems require multiple user steps and small volumes of urine, between 10–100 μ L. In contrast, the methods detailed in Table 9 utilize between 1 and 25 mL of urine for diagnosis. The clinical load of chlamydia and gonorrhea in the urine can vary between $2 \times 10^1 - 2 \times 10^6$ CFU/mL ($2 \times 10^{-2} - 2 \times 10^6$ CFU/ μ L)^{102–105} and $1 \times 10^2 - 1 \times 10^7$ CFU/mL ($2 \times 10^{-1} - 2 \times 10^4$ CFU/ μ L)¹⁰⁶, respectively. Based on these values, many of the current POC paper-based devices are using at least an order of magnitude too little sample to detect the clinically-relevant range of concentrations of these pathogens.

The main objective of this chapter was to develop an automated and integrated paper-based sample preparation device. This device linked cell lysis, gDNA fragmentation, and NA purification and concentration, as described in the previous aims. Additionally, this system was able to rapidly process at 1–5 mL of sample. This device serves as a demonstration of the p-switch for automated reagent sequencing. Urine was the primary sample type tested, but this work serves as a platform for large volume processing in porous membranes that can be extended to other sample types such as water or diluted blood. This system enables the integration and automation of complex, multi-step assays which would otherwise not be feasible with traditional porous membrane-based microfluidic approaches.

6.2. Methods

Cell Culture. *Neisseria gonorrhoeae* (*N. gonorrhoeae*, strain 19424) was cultured directly from frozen stock on chocolate agar plates at 36°C in a 5% CO₂ environment. After 24-48 hours, colonies were collected from the plate and resuspended in 10 mM Tris buffer, pH 8.

Mammalian Cell Culture. Freshly cultured McCoy cells (ATCC CLR-1696) infected with *C. trachomatis* serovar L2 (LGV 434) were obtained from collaborators at the Harborview STI Clinic. To prepare the cells for experiments, culture media was removed and cells were washed with an equal volume of PBS, followed by treatment with 0.25% trypsin with shaking at 37°C for 15 minutes. Detached cells were pelleted by centrifugation at 13000 ×g for 3 minutes. The supernatant was decanted and the cells were resuspended in 1× volume of 10 mM Tris buffer, pH 8.

qPCR. *S. aureus* DNA was quantified with a qPCR kit for the *ldh1* gene provided by the ELITech Group (ELITech Group Molecular Diagnostics, Bothell, WA, USA). The 20 µL reactions were run on a Bio-Rad CFX real-time PCR instrument (Hercules, CA, USA) using the following protocol: 50°C hold for 2 minutes, 93°C hold for 2 minutes, 45 cycles of 93°C for 10 seconds, 56°C for 30 seconds, and 72°C for 15 seconds, ending with final elongation step at 72°C for 5 minutes. Fluorescence data were collected during the 56°C annealing step in the Texas Red channel. The qPCR results were analyzed using the automated threshold cycle (C_T) value calculation in the Bio-Rad software. This assay was sensitive down to ~10 copies of the target sequence. Assay primer and probe sequences can be found in **Appendix 1**.

N. gonorrhoeae DNA recovery was quantified with qPCR for the *porA* gene¹³² using the SensiFAST probe No-Rox kit from Bioline (Taunton, MA, USA). The 20 µL reactions were run on a Bio-Rad CFX real-time PCR instrument (Hercules, CA, USA) using the following protocol: 95°C hold for 3 minutes, 40 cycles of 95°C for 10 seconds, 60°C for 30 seconds. Fluorescence data were collected during the 60°C annealing step in the FAM channel. The qPCR results were analyzed using the automated threshold cycle (C_T) value calculation in the Bio-Rad software (Hercules, CA, USA). These assays were sensitive down to ~10 copies of the target sequences. Assay primer and probe sequences can be found in **Appendix 1**.

C. trachomatis DNA recovery was quantified with qPCR for the *omcB* gene¹³³ using the SensiFAST Probe No-Rox kit from Bioline (Taunton, MA, USA). The 20 µL reactions were run on a Bio-Rad CFX real-time PCR instrument (Hercules, CA, USA) using the following protocol: 95°C hold for 3 minutes, 40 cycles of 95°C for 10 seconds and 60°C for 30 seconds. Fluorescence data were collected during the 60°C step in the FAM channel. The qPCR results were analyzed using the automated threshold cycle (C_T) value calculation in the Bio-Rad software (Hercules, CA, USA). This assay was sensitive down to ~10 copies of the target sequence. Assay primer and probe sequences can be found in **Appendix 1**.

Reducing timing for large volume sample processing. Flow through the transverse section of a porous membrane can greatly increase sample processing time due to shorter distances for fluid to travel and increased surface area for volumetric uptake.

Glass fiber members were used as the primary membrane type and were cut into 1 x 5 cm pieces. Cellulose membranes were selected as the waste collection reservoirs and were cut to either 2 x 3.3 cm, **Figure 73A**, or 9.5 x 6.7 cm, **Figure 73B**. Waste pads overlapped the last 2 cm of the glass fiber membrane. Up to 2 mL of 50 mM MES buffer at pH 5 was flowed through each set up and the total processing time was recorded.

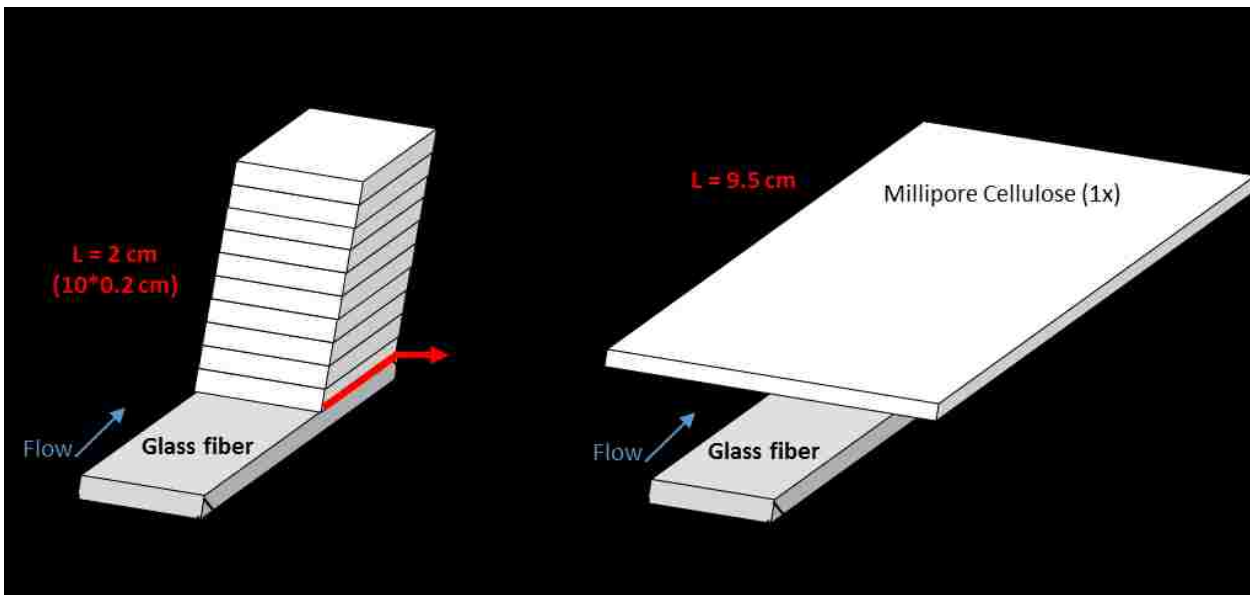


Figure 73. Schematic of waste pad configurations for large volume sample processing experiments. **A.** Stacked waste pads where $L = 2\text{ cm}$ ($10 \times 0.2\text{ cm}$, thickness of the cellulose membranes). **B.** Large single waste pad where $L = 9.5\text{ cm}$.

The p-switch: pressure-based system for controlling fluid flow in porous membranes. The novel porous membrane-based DNA purification system detailed in Aim 3 worked very well as a single unit module. Moving forward, this system was integrated with cell lysis and amplification. The first iteration of the purification module utilized only flow in one direction, **Figure 74A**. After capture and wash, the eluted DNA also flowed toward the waste pad. This linear purification was not compatible with amplification for multiple reasons: (i) the linear flow directed the purified DNA toward the waste pad, and (ii) amplification reagents could not be stored directly

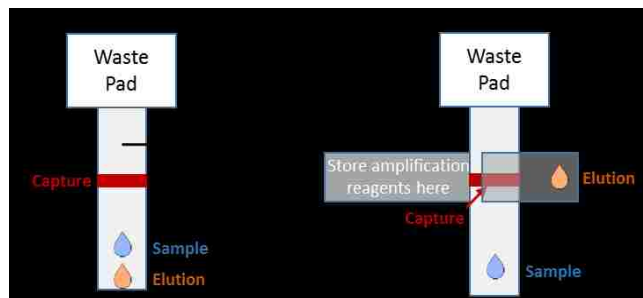


Figure 74. Schematic of **A.** linear purification and **B.** purification with controlled fluid flow.

upstream of the capture region because they would flow into waste. In order to integrate this purification module with downstream amplification, the eluted DNA was flowed into a clean membrane in a different direction than the primary linear purification, **Figure 74B**. The p-switch was used to accomplish this task.

Devices were built as shown in Figure 74B with Fusion 5 (GE Healthcare Life Sciences) as the primary membrane and 8964 glass fiber (Ahlstrom) as the secondary membrane. The waste pad was made from cellulose (CFSP223000 EMD Millipore) and the membranes were held in place by the adhesive layer of the Mylar backing.

The purification experiments were run as previously described¹⁴⁰, with the following changes. For these tests, 10 μL of fragmented MRSA gDNA ($\sim 1 \times 10^4 - 1 \times 10^5$ copies/ μL) was diluted into 990-3990 μL of either buffer or discarded urine samples (**Appendix 2**) for a resulting concentration of $\sim 1 \times 10^2 - 1 \times 10^3$ copies/mL. The full volume was then flowed through the device followed by 250 μL of wash buffer (50 mM MES, pH 5). The 250 μL of elution buffer (50 mM Tris, pH 9) was manually added to the secondary membrane.

After the secondary membrane was fully wet, the chitosan and elution sections of the device were removed and fluid was recovered by centrifugation at 10,000 $\times g$ for 3 minutes. The amount of target DNA in the fluid from each membrane region was quantified by qPCR, correcting for volume recovered from the section.

Automating the p-switch through timed release of the secondary fluid source – the pinch valve. The secondary fluid source can be activated automatically, causing elution of the nucleic acid through the secondary membrane, **Figure 75**. For this purpose, a small leg of Fusion 5 membrane extends from underneath the cellulose waste pads, which only wets once the cellulose pads reach a certain level of saturation. This leg of Fusion 5 is in contact with a section of water-soluble paper, which dissolves on contact with liquid. This paper is holding closed a pinched section of silicone tubing that prevents flow of the elution buffer. When the water-soluble paper dissolves, the pinch is released, allowing fluid to flow through the previously closed tubing and into the inlet of the secondary membrane, activating elution through the overlapped junction of the p-switch.

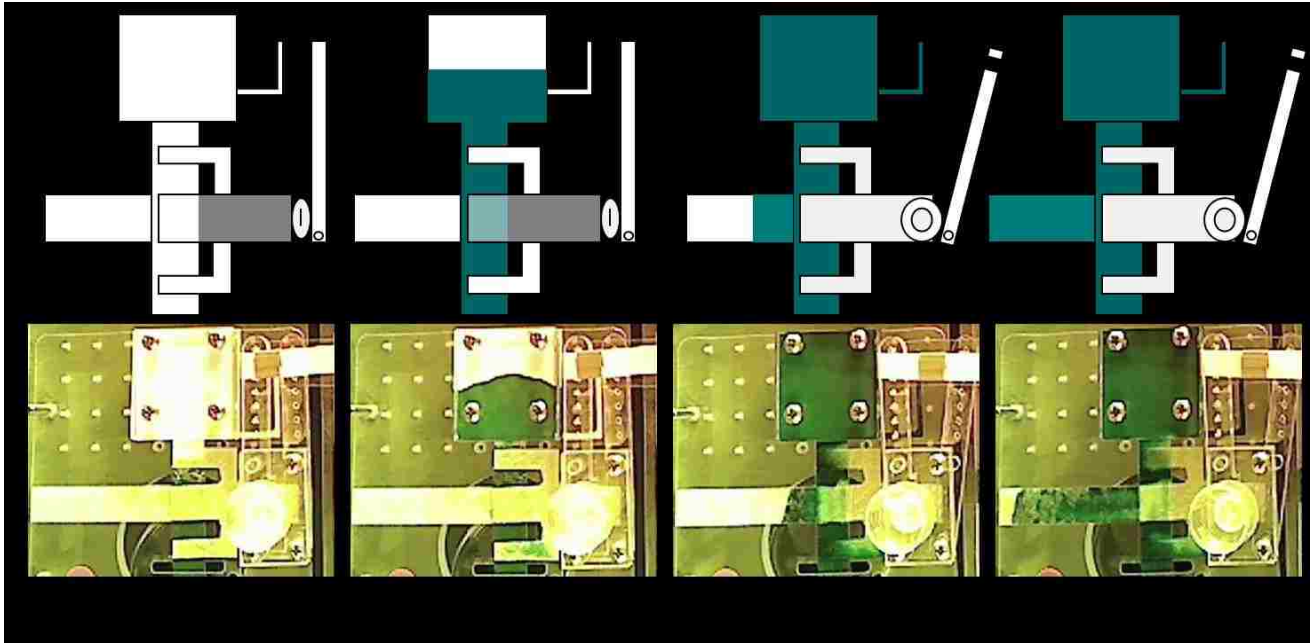


Figure 75. Automating the p-switch for the large volume sample concentration: schematic and image from a video of the device. **A.** Before sample has reached the waste pad. **B.** Initially, the elution buffer well is full, but the tubing connecting the well to the secondary network is pinched closed. The sample flows through the primary network into the waste pad. **C.** When the waste pad reaches a sufficient level of saturation, the activation leg wets a water-soluble membrane (black), which dissolves and breaks causing the pinch on the elution tube to be released. **D.** When the pinch is released, the elution buffer flows through the junction and fills the secondary network.

The geometry of the p-switch device was optimized to improve elution from the overlapping region. First, the number of legs connecting the elution fluid to the overlap region was tested, **Figure 76A**, followed by the degree of overlap at the junction, **Figure 76B**. The goal of the optimization experiments was to improve both DNA recovery and concentration factor.

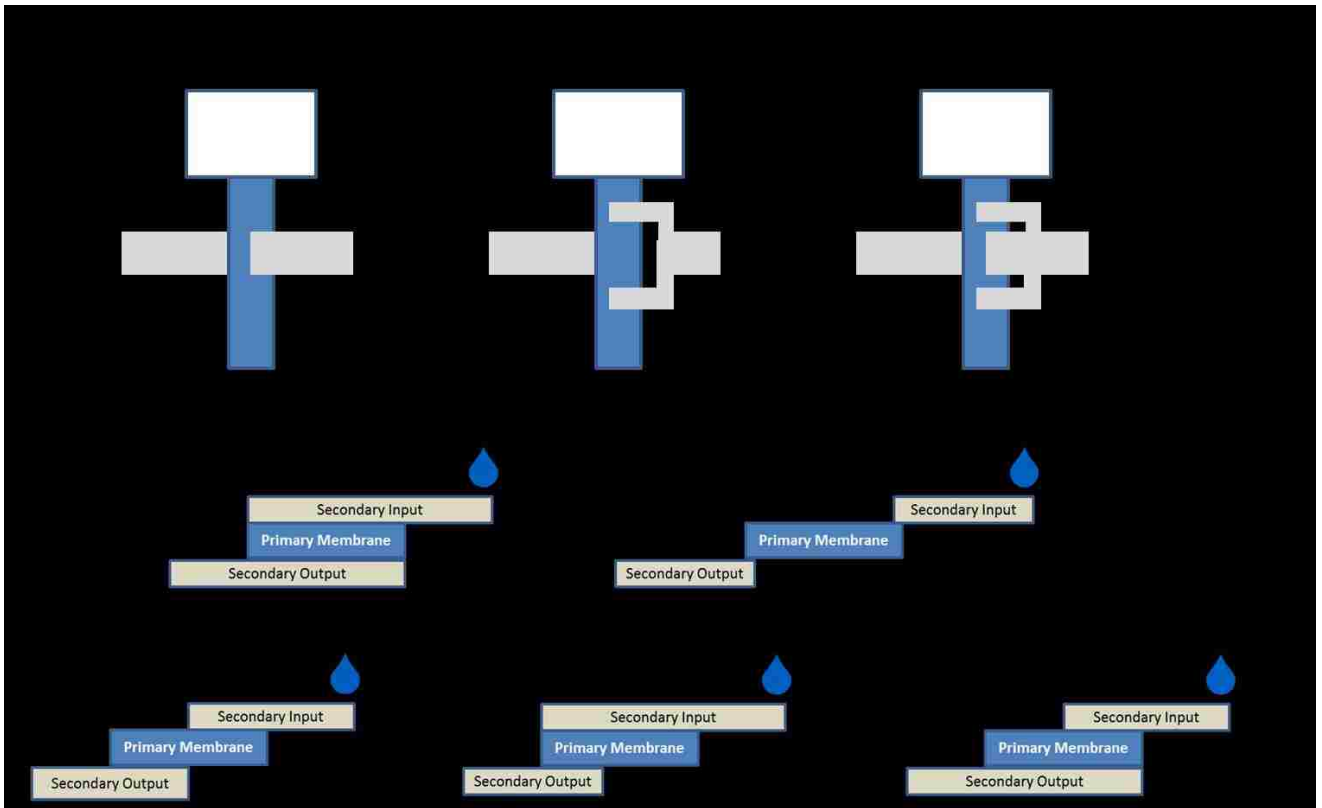


Figure 76. Optimizing p-switch geometry to improve elution of DNA from the junction. **A.** Comparing one v. two v. three leg overlaps. **B.** Comparing degree of membrane overlap.

The automated p-switch for DNA purification experiments were run as described above with fragmented MRSA gDNA ($\sim 1 \times 10^4 - 1 \times 10^5$ copies) diluted into 1–4 mL of 50 mM MES buffer, pH 5. The sample contain DNA was added to the sample collection well and flowed through the device without a wash step. After the flow of sample was complete, 750 μ L of the elution buffer (250 mM Tris, pH 9) was automatically released *via* the pinch valve to wet the secondary membrane, as described above. After the secondary membrane was saturated, fluid was recovered from the removed sections of membrane by centrifugation at 10,000 xg for 3 minutes. Recovery of target DNA was quantified by qPCR correcting for elution volume. Elution volume was measured using a Pipetman and qPCR signal was multiplied by the volume to account for total recovery of input DNA, **(Equation 13)**. Sample concentration factor was also determined as described in Aim 3.



(Equation 13)

Freshly cultured *N. gonorrhoeae* and/or *C. trachomatis* infected epithelial cells (CT+ epi cells) were spiked into 1–2 mL of de-identified, discarded human urine provided by the Harborview STI Clinic. Samples included dry MES buffer for pH modulation (see Aim 1 for details) and were heated

using a heat block for 10 or 15 minutes at 95°C to lyse cells and fragment DNA (see Aims 1 and 2). After heating, samples were added to the sample reservoir and devices were run as described above. Recovery was quantified by qPCR.

Validating individual components of the integrated p-switch device. In addition to measuring the device output (qPCR of the elution), the performance of individual device components was quantified. Lysis was quantified by taking a 10 µL aliquot of the lysate after heating and prior to introducing to the p-switch device. Lysates were diluted before qPCR to reduce potential inhibitory effects from urine. DNA fragmentation was evaluated by quantifying the amount of DNA that transported effectively through a Fusion 5 membrane. This was measured as described in Aim 2 using a 40 µL aliquot of the lysate after heating and prior to introducing to the p-switch device. These components were individually quantified to determine areas of loss or reduced device performance, **Figure 77**.

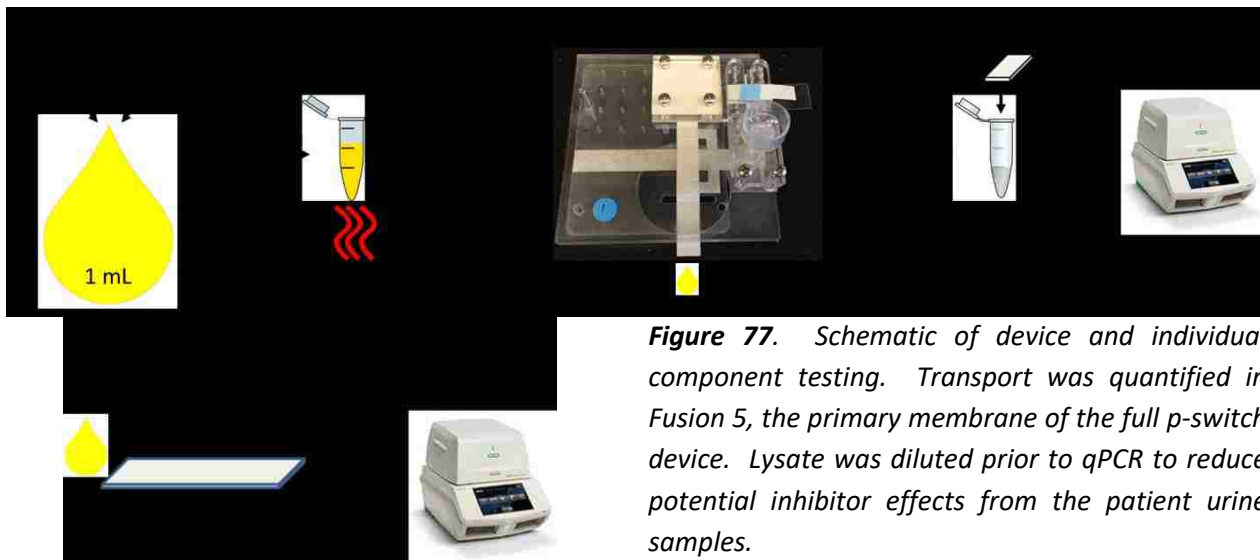


Figure 77. Schematic of device and individual component testing. Transport was quantified in Fusion 5, the primary membrane of the full p-switch device. Lysate was diluted prior to qPCR to reduce potential inhibitor effects from the patient urine samples.

Effect of non-target urine DNA on automated p-switch. The NA from 500 µL of urine specimens were purified by lysing intact cells at 95°C for 10 minutes followed by ethanol precipitation using glycogen. Purified NA were resuspended in 50 µL of sterile water and quantified using a Nanodrop. This method accounts for both DNA and RNA in a sample because actual human samples will contain both molecules. Increasing amounts of these NA (non-target NA from urine) were spiked into 1000 µL of 50 mM MES, pH 5, with 1×10^5 copies of purified *N. gonorrhoeae* DNA (0–500 ng; 0–5000x non-target DNA compared to target DNA). These samples were then processed using the automated p-switch to determine the amount of non-target urine NA that would reduce recovery of the target

DNA. *N. gonorrhoeae* DNA recovery was quantified with qPCR. Increasing amounts of purified urine NA were also spiked into the qPCR standards to account for potential amplification inhibition.

Compatibility of p-switch with in-membrane NAAT and lateral flow detection. Purified samples from p-switch devices were used to rehydrate amplification reagents stored in porous membranes. These experiments demonstrate the potential to integrate this sample processing platform with in-membrane NA detection *via* lateral flow. Either 20 μ L of lysate (urine samples spiked with pathogens post lysis and fragmentation, but prior to DNA purification) or p-switch purified samples were added to Standard 17 membranes with dried with *N. gonorrhoeae* or *C. trachomatis* isothermal Strand Displacement Assay (iSDA) reagents, **Figure 78**. The rehydrated membranes were sealed in a commercially available hybridization chamber and heated to 49°C for 30 minutes to facilitate amplification, as described previously¹³⁸.

After heating, fluid was collected from the membranes *via* centrifugation at 8000 xg for 1 minute followed by the addition of sodium chloride and PEG to aid in lateral flow⁵⁶. Pre-stripped lateral flow membranes, provided by collaborators at ELITechGroup, were placed in the post-amplification solution and signal developed as sample flowed. Results were read by eye after 15 minutes of lateral flow and imaged using a benchtop scanner.

Clinical test comparison. Results from the integrated p-switch system were compared to results from a standard clinical test to detect chlamydia and gonorrhea. Five NG/CT negative urine specimens were spiked with freshly cultured *N. gonorrhoeae* and CT+ epithelial cells, one sample was not spiked with pathogens to serve as a negative control. This sample was the same urine as one of the five spiked samples to evaluate the effects of the background matrix on the systems.

The six spiked samples (five with NG/CT and one without) were labeled HS1-6 (HS for Harborview Samples) and 2 mL aliquots given to collaborators at the Harborview STI Clinic to run blinded using the Aptima 2 Combo CT/NG test. The remainder of the samples were split into N=3 of 2 mL each, to match the volume used by the Aptima test, and processed using the automated p-switch as described above. The results from the clinical Aptima system (+/- for the pathogens) were compared to outputs from the p-switch. P-switch outputs were quantified by qPCR and tested in dry iSDA pads with lateral flow detection.

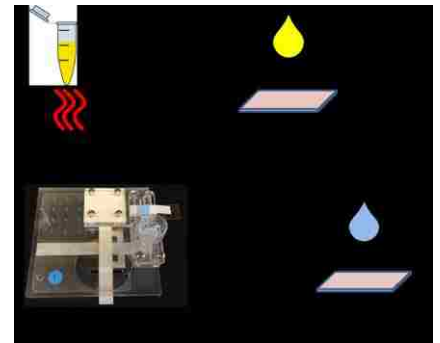


Figure 78. Schematic of in-membrane amplification tests.

6.3. Results and Discussion

The main objectives of this work were to develop methods and tools to integrate the sample preparation modules for complex samples described in Aims 1–3. These developments included ways to decrease the time to process large volume (1–5 mL) samples, controlling flow direction and reagent sequencing, and testing this integrated system with clinical samples.

6.3.1. Reducing timing for large volume sample processing.

As described above, Darcy’s Law dictates that flow rate through porous media is inversely proportional to the length traveled by the fluid. This is especially important for large volume samples. To reduce the length fluid travels through the membrane, the geometry of a porous network can be optimized by stacking the waste collection pads. **Figure 79** compares the total flow time for processing up to 2 mL of sample using stacked waste pads (stacked) v. one large pad (single) in both Fusion 5 and Standard 17 glass fiber.

For both membranes tested, the stacked waste reservoir geometry significantly reduced total flow time. Between the two membranes, Standard 17 was significantly faster than Fusion 5, which was expected because Standard 17 has a higher permeability (Buser and Byrnes *et al.* 2016, in preparation). In general, shorter assay times are desirable to reduce the overall time to diagnosis.

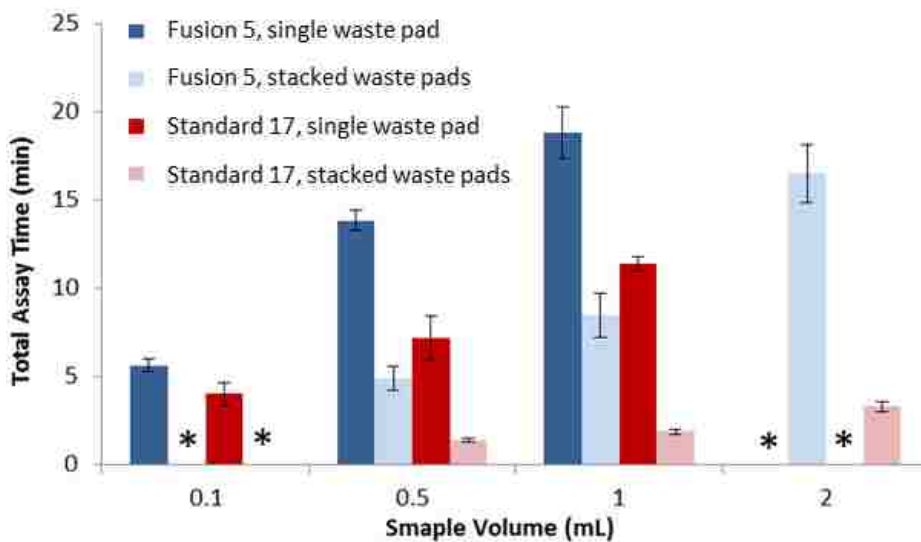


Figure 79. Comparing total flow time of stacked waste reservoirs and single large reservoirs for flow through Fusion 5 and Standard 17 (schematic in Figure 73). Averages of at least N=3 +/- one standard deviation are reported.

*These conditions were not tested.

The geometry of this system can be further optimized. Volumetric flow rate is proportional to membrane cross sectional area (A). By increasing the width and decreasing the length of the

primary membrane as well as stacking the elution pads, the total time to flow large volumes can be further decreased if required by the assay. Additionally, work detailed in Aim 3 shows that changes in assay time do not significantly effect purification of DNA from the sample. The rate of electrostatic interactions – like the interaction of protonated chitosan and DNA – is significantly faster than any flow rate that can be achieved in the membranes using this geometry.

6.3.2. The P-switch: controlling fluid flow direction to sequence reagent delivery

The images in Figure 72 show the p-switch function with colored fluids. The next step was to verify the efficacy of chitosan capture of DNA in the primary membrane followed by elution into the secondary membrane using the p-switch device to control direction of fluid flow. On average, this device worked as well as the standard linear purification and resulted in similar elution profiles, **Figure 80**. This result is ideal because the p-switch performance enables automation of multiple assay steps and redirection of purified sample to a clean membrane rather than having the upward waste. The p-switch device was more variable than the linear purification device, likely due to secondary membrane misalignment. If the chitosan region was not directly aligned with the second membrane, some of the captured DNA would remain in the primary membrane and not move into the elution membrane.

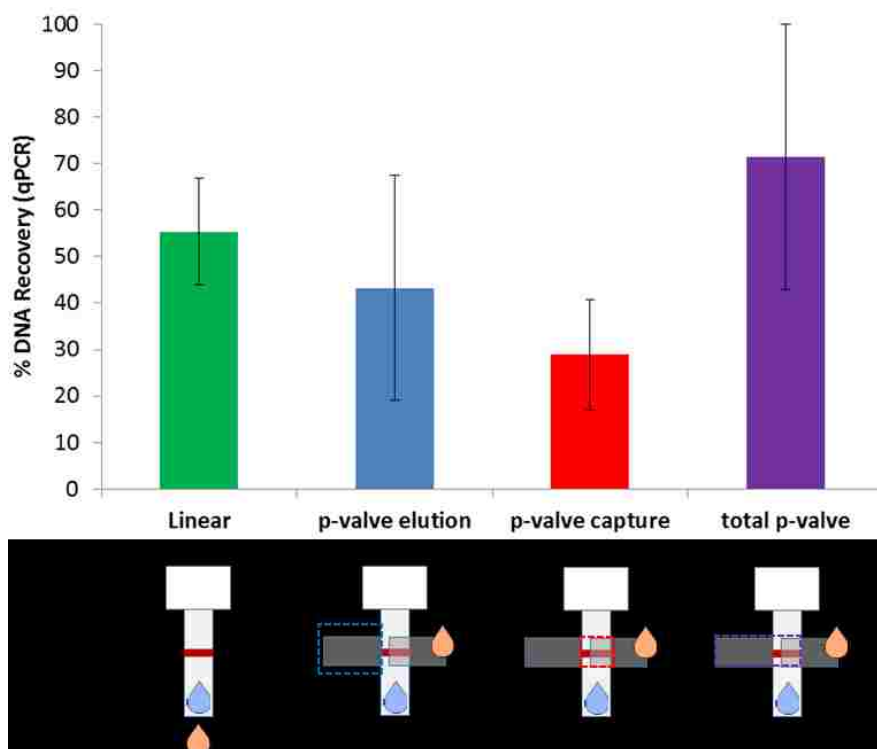


Figure 80. DNA purification comparing a p-switch device to a linear geometry in Fusion 5. Averages of at least $N=3$ \pm one standard deviation are reported.

Next, the p-switch was used as a platform for DNA purification and concentration from 1 mL samples. In this configuration, the device recovered $>80\%$ of the target DNA spiked into discarded human urine, **Figure 81**. Samples 08, 03, 02, and 05 had pH values at or below 6.8 and showed high recovery of target DNA. The samples also had widely varying salinities (11–214 mM) which may have a slight effect of PCR enhancement that would lead to slightly higher than 100% recoveries. These results were expected because chitosan, the DNA capture molecule, is positively charged below a pH of ~ 6.5 as described in Aim 3²⁴⁴. Additionally, this variation is why the pH modulation system was developed as described in Aim 1.

Unsurprisingly, urine samples with pH values above the amine pK_a (samples 09, 01, and 04) resulted in reduced DNA recovery. The exception in this dataset is sample 10, which had an appropriate pH (5.8) for DNA capture by chitosan, but showed very low DNA recovery. We hypothesize that sample 10 had reduced recovery due to an overloading of the chitosan with non-target nucleic acids that were present in the patient sample. Patient 10 had 10x more non-target nucleic acids (both DNA and RNA from the urine) compared to the rest of the samples tested. Based on previous work, this amount of non-target nucleic acid is above the capacity of the chitosan patterned in this membrane. The amount of DNA remaining in the chitosan region after elution was

less than 10% of the input for each sample and the overall device runtime was between 13-15 minutes. **Appendix 2** shows characterization of each sample.

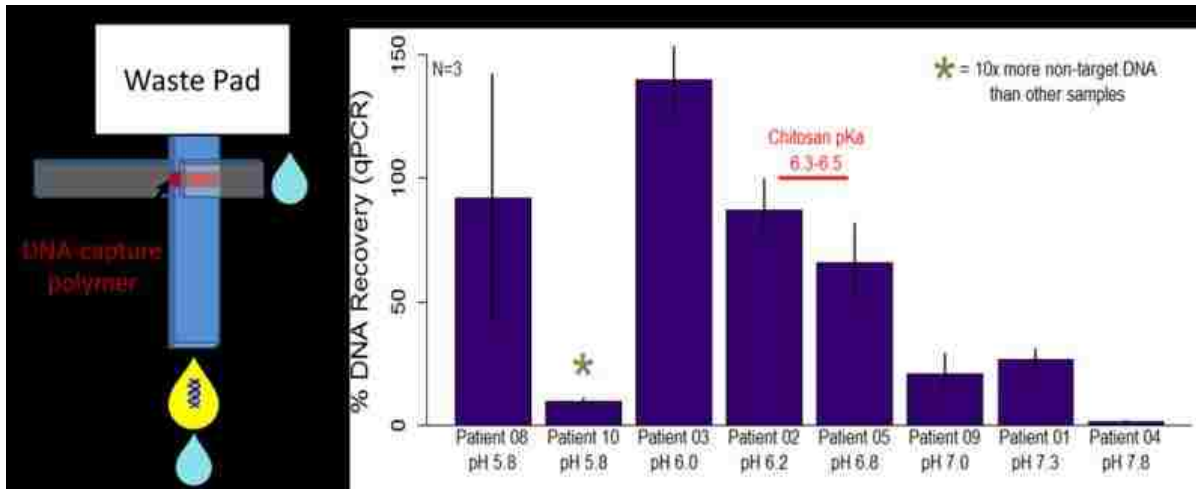


Figure 81. Application of the p-switch for in-membrane DNA purification and concentrated from 1 mL of discarded human urine samples. The primary membrane was patterned with a DNA-capture polymer. Flow of the 1 mL urine sample through primary the membrane resulted in DNA captured by the polymer in the primary membrane at the membrane junction. After a wash step through the primary membrane, an elution buffer was introduced to the secondary membrane causing the DNA to flow through the junction and into the elution region. Sample recovery was quantified with qPCR. Averages of N=3 are reported with error bars representing +/- one standard deviation. Generally, as sample pH increased, recovery of target DNA decreased.

These results were very promising, but this iteration of the p-switch device still required multiple user steps: one to add the sample and a second, timed step, to add the elution buffer. With this in mind, the next generation of the device was designed to appropriately time the automatic release of the elution buffer into the secondary membrane.

6.3.3. Automating the p-switch for multiplexed purification and concentration of *C. trachomatis* (CT) and *N. gonorrhoeae* (NG) DNA directly from pathogens in human urine

To enable device operation without user intervention, a timed release mechanism was added to the p-switch system to automatically deliver a secondary buffer after the waste pad was sufficiently saturated with sample fluid. In the automated devices, the waste pad was in contact with a connecting arm made of a Fusion 5 membrane. Fusion 5 was selected as the primary membrane because it has been successfully demonstrated with the purification chemistry and due to the required differences in membrane characteristics that drive the function of the p-switch, as described above. The connecting arm contacted a water-soluble membrane that restrained a plastic

lever arm which pinched closed the buffer tubing. This tubing connected the elution buffer to the secondary membrane, as shown in **Figure 75**.

Once the waste pad was full, the connecting arm began to fill and wet the water-soluble membrane which dissolved and released the lever arm and then the pinch on the tubing. The opened tubing then allowed elution buffer to flow into the secondary membrane, which was made of 8964 glass fiber. Flow of elution buffer through the junction eluted DNA captured on the chitosan in the overlap junction. The eluted DNA then flowed into the dry secondary membrane. The purified and concentrated sample was quantified by qPCR to determine recovery of target DNA.

The original automated p-switch devices were designed and tested with one leg of the secondary membrane overlapping the primary membrane, Figure 72, but those automated devices resulted in poor recovery of DNA in the elution region (less than 10%). Based on the videos run with colored fluids, it appeared that target was being eluted upstream and downstream in the primary membrane and therefore was lost to waste. To address this loss, the next prototype employed additional legs on the secondary membrane to help focus the flow of eluted DNA to the elution pad. The one, two, and three leg designs were compared. The two leg system showed very poor elution of the overlap region, likely due to the fluid following the path of least resistance into the elution region and bypassing the chitosan-coated area, as indicated by the arrows. Based on these results, the three leg device was selected for all remaining experiments, **Figure 82**.

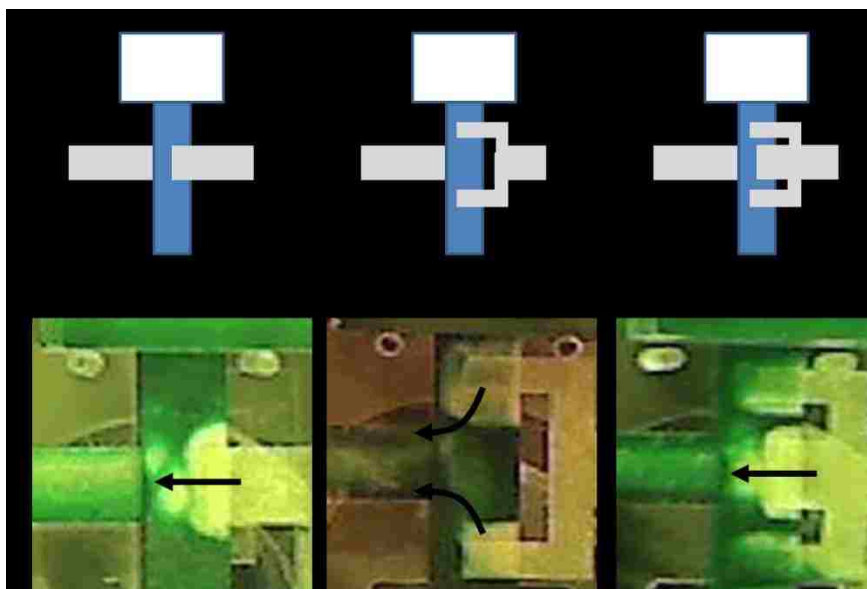


Figure 82. Improving elution from the overlap region of p-switch networks. **A.** Schematic of the geometries tested. **B.** Video images of final elution results from each design with arrows representing major flow patterns into the elution region. Based on these studies, the three

leg design was selected for further optimization.

Next, the degree of overlap at the junction of the primary and secondary membranes was varied. First, multiple geometries were tested with colored fluid to observe general flow patterns, **Figure 76B**. Based on the videos using colored fluid, three designs were compared: the “Double Partial”, “Top Full, Bottom Partial”, and “Double Full” designs. In general, greater amounts of overlap lead to a more thorough wash out of the overlap region.

Next, these three designed were tested with the DNA purification assay using DNA spiked into 1 mL of buffer. Both % recovery of input DNA and concentration factor were assessed for each of these designs. These results showed that the “Top Full, Bottom Partial” geometry resulted in the highest recovery of DNA and concentration factor with minimal DNA being retained in the chitosan region, **Figure 83**. All further experiments were performed using the geometries selected from these optimization experiments.

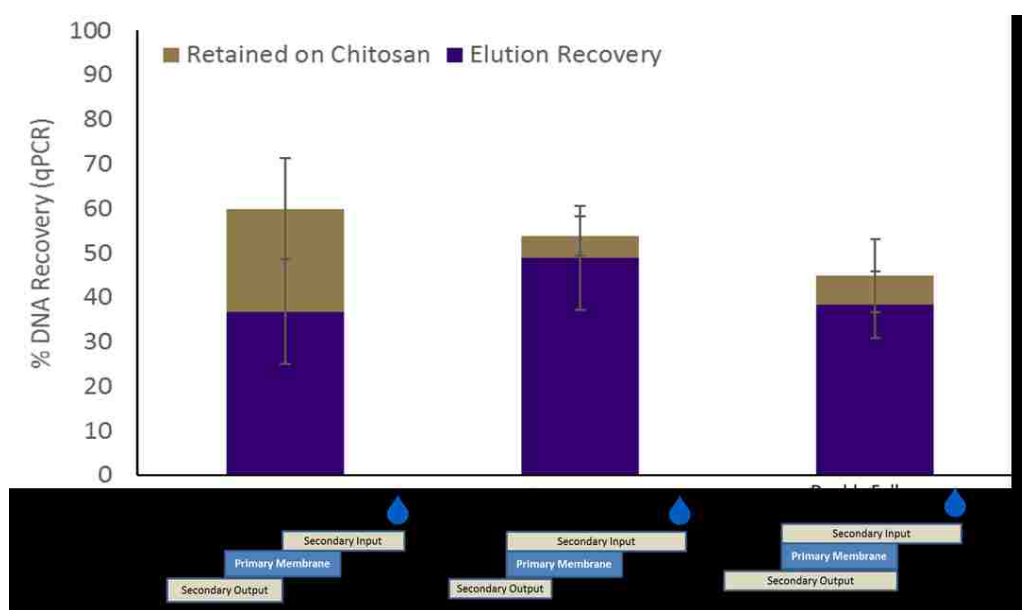


Figure 83. Comparing DNA recovery for devices with varying overlap geometries. Devices were tested with DNA spiked into 1 mL of buffer and the elution was analyzed by qPCR. The DNA remaining in the chitosan region was also quantified. Averages of $N=3$ are reported with error bars representing \pm one standard deviation.

The “optimized geometry p-switch” devices were then tested with 1 and 4 mL inputs (the device that had the 4 mL input only processed 3.25 mL before the waste pad filled). All samples were spiked with purified DNA. Multiple elutions were collected from each device to build an elution profile and track when the DNA was eluting from the capture region. With the optimized system,

the majority of the DNA was recovered in the first two elutions. This is an ideal elution profile because the purified sample could immediately flow downstream into an assay (such as a NAAT). Each elution volume was ~60 μ L. Overall, the fully automated device recovered ~40 % of the target DNA from both the 1 mL and 3.25 mL inputs, **Figure 84**. For the 1 and 3.25 mL samples, the concentration factors ranged from 1.8-2.9x and 5.2-8.3x, respectively (calculated as described in Aim 3).

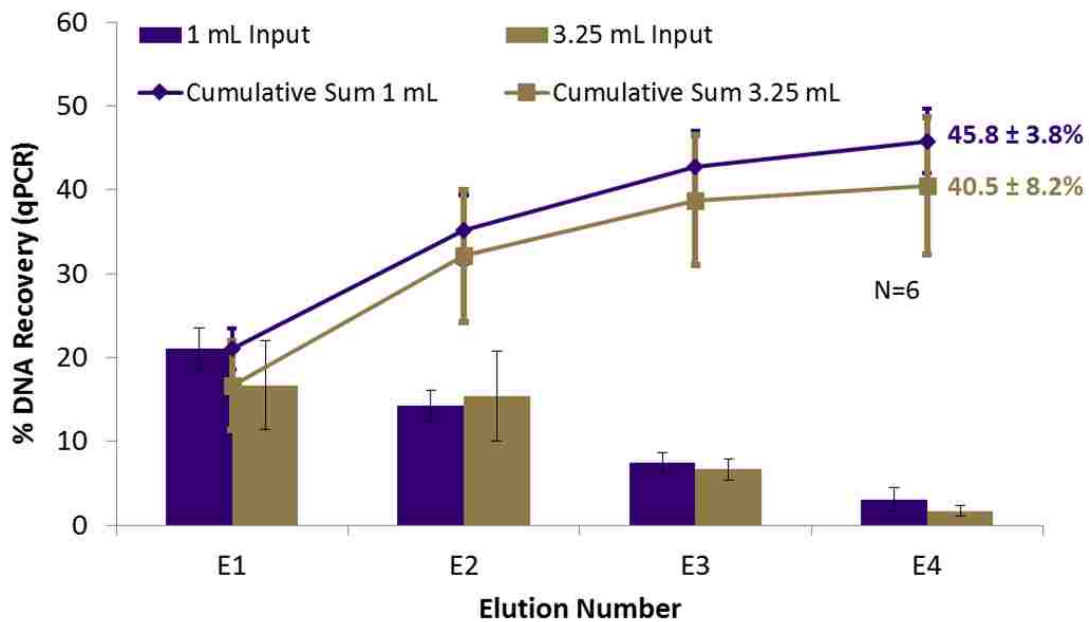


Figure 84. Automating the p-switch for the large volume sample concentration. Results from a DNA purification and concentration experiment using the three-leg automated p-switch device with “Top Full, Bottom Partial” junction overlap. Averages of N=6 are reported with error bars representing +/- standard error. The highest percentage of purified DNA was recovered in the first two elution volumes (each ~ 60 μ L). The 1 mL samples were processed in 12-13 minutes while the 3.25 mL samples were processed in 32-33 minutes.

With the optimized geometry validated, the next rounds of experiments included testing increasingly complex sample types to evaluate their effect on the device. First, increasing amounts of non-target urine NA were spiked into 1 mL samples containing purified *N. gonorrhoeae* DNA in 50 mM MES buffer, pH 5. Urine NA (both DNA and RNA) were purified from patient samples and used as the non-target NA because they closely represent what would be in an actual urine specimen processed with the p-switch device. The ratios of target:non-target NA tested ranged from 1:0x – 1:5000x (adding between 0–500 ng of urine NA). Based on the provided urine samples from the Harborview STI Clinic, 1 mL of urine could have up to ~50000x non-target NA (assuming target inputs

of $\sim 1 \times 10^5$ copies). This study only evaluated ratios up to 1:5000x because this concentration of non-target NA began to inhibit qPCR preventing accurate quantification of sample recovery, **Figure 85A**.

Overall, the concentrations tested showed similar DNA recovery to the baseline experiment (no non-target DNA). Two of the ratios (1:500x and 1:5000x) fell outside the standard deviation (SD) of the baseline recovery results. The 1:500x was not statistically different than the baseline (using the 95% confidence intervals). The 1:5000x was statistically different, but as noted above, this amount of non-target NA showed inhibitory effects on the qPCR. Therefore, the reduced recovery may actually be an artifact of the measurement method, and not the actual assay. These results indicate the current device configuration and purification assay can handle between 500x-1000x non-target urine NA before a significant loss in target recovery.

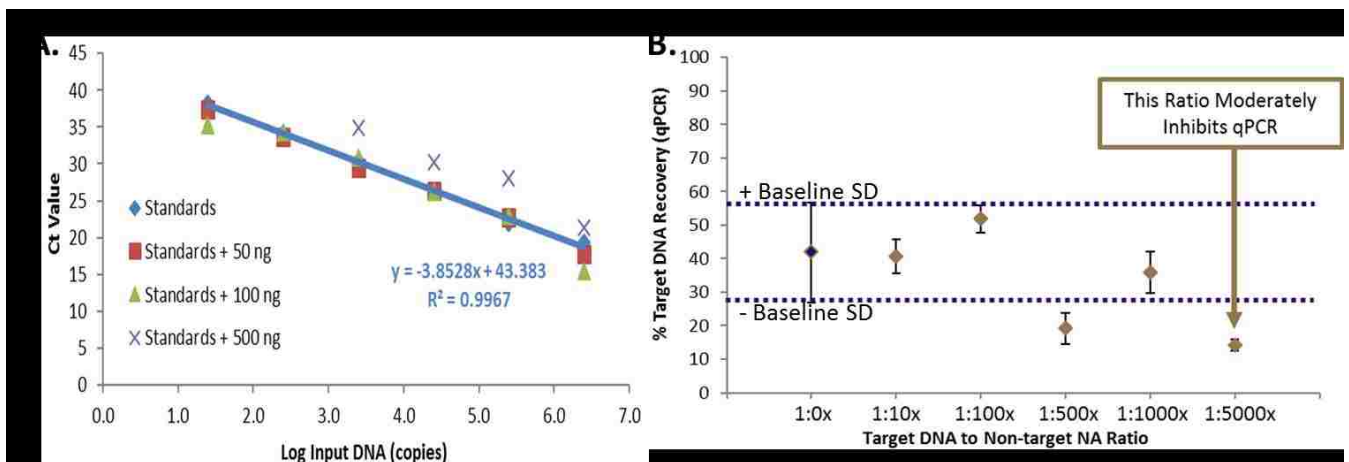


Figure 85. Testing increasing amounts of urine non-target NA in the p-switch device. The target was $\sim 1 \times 10^5$ copies of purified *N. gonorrhoeae* DNA. **A.** qPCR standard curves spiked with increasing amounts of urine non-target NA to determine effects on quantification. Standards with 500 ng of non-target NA (1:5000x target:non-target for 1×10^5 input) were moderately inhibited compared to those without any non-target NA. **B.** Recovery of DNA across the ratios tested was similar to the baseline recovery (within the standard deviation, dashed line). These results indicate the current device configuration can handle between 500x-1000x non-target urine NA before resulting a significant loss in target recovery. Averages of at least $N=3$ are reported with error bars representing \pm one standard deviation.

Next, the device was tested using discarded human urine samples. In addition to the purification assay, these experiments included the integration of lysis, pH modulation, and gDNA fragmentation. Either 1 or 2 mL of urine was spiked with freshly cultured *N. gonorrhoeae* and/or CT+ epithelial cells as well as dry MES buffer to modulate sample pH below 6. Samples were heated to 95°C using a heat block and then introduced to the automated p-switch device. Aliquots of the lysate were also characterized for lysis efficiency and DNA transport, as described above, Figure 77. After the device runs were completed, all elutions and component aliquots were analyzed by qPCR.

The first demonstration of the full system was done with urine sample 18 (pH 7.6, 369 mM salinity, 6.3 ng/μL of total nucleic acid content). For both *N. gonorrhoeae* and *C. trachomatis*, $\sim 1 \times 10^7$ copies were spiked into 1 mL of urine; these are high input copy numbers at the top of the clinical range, but were selected as a baseline for device validation. Future studies varied the input concentrations of each target. Overall recovery of purified DNA from both pathogens was low, $\sim 14\%$, which appears to be a result of poor lysis, **Table 10**.

Table 10. Summary of the integrated sample preparation device. Performance of each device component was quantified as described in Figure 77. Total Device % Recovery = (% lysis)*(% transport)*(% purification). Averages of N=3 for urine sample 18 are reported.

Assay Step	<i>N. gonorrhoeae</i>	<i>C. trachomatis</i>
Cell Lysis	19 %	48 %
DNA Transport	90 %	54 %
DNA Purification	82 %	54 %
Total Device	14 %	14 %

Even with the low recovery, this was still an exciting result because it was the first demonstration of the full system working with real samples. To address the low lysis efficiency, all future samples were heated for 15 minutes, instead of 10. In addition to urine specimen 18, twelve other urine specimens have been tested in the full device with spiked pathogens. These samples showed a wide range of both salinity and pH. Recovery and concentration factor varied across samples, **Table 11**, likely due to both matrix variation and device construction. About half of the samples were run using the original one leg elution device prior to optimization; the other half were run post redesign with the three leg device. In general, the device showed better recovery of *C. trachomatis* DNA compared to *N. gonorrhoeae* DNA likely due to the reduced effectiveness of cell lysis for NG compared to CT. The thermal lysis and release of pathogen DNA may be significantly effected by the salinities of the solutions that can stabilize membranes.

Table 11. Summary of device results for urine samples spiked with pathogens. All recoveries and concentration factors are averages of N=3 devices for the same sample.

Sample	% NG Rec	% CT Rec	Conc. Factor (NG,CT)	Original pH	Original Salinity (mM)	NG Input (c/mL)	CT Input (c/mL)
One leg elution geometry							
12	5.5 %	37.2 %	0.3, 3.4	6.3	184	10^6	10^4
18	10.3 %	10.5 %	1.2, 1.2	7.6	369	10^7	10^7
21	16.5 %	35.9 %	0.7, 0.9	7.1	137	10^5	10^4
26	1.2 %	2.6 %	0.2, 0.2	6.9	49	10^7	10^7
28	26.6 %	65.7 %	1.8, 4.3	5.6	193	10^5	10^4

35	5.8 %	1.1 %	0.7, 0.7	6.5	67	10 ⁵	10 ⁴
Three leg elution geometry							
11	15 %	n/a	1.4	5.6	251	10 ⁵	-
12	7 %	28 %	0.7, 2.5	6.3	184	10 ⁷	10 ⁶
20	16 %	n/a	0.7	6.0	269	10 ⁶	-
23	2 %	7 %	0.1, 0.6	6.7	70	10 ⁵	10 ⁴
24	10 %	45 %	0.9, 4.1	6.8	110	10 ⁵	10 ⁴
29	9 %	37 %	0.7, 3.0	5.4	199	10 ⁵	10 ⁴
31	10 %	70 %	0.9, 6.3	6.8	319	10 ⁵	10 ⁴

The recovery results in the above table vary between 1%–27% for *N. gonorrhoeae* and 1%–70% for *C. trachomatis*, but they demonstrate the feasibility of the device and full integration of multiple sample preparation assay steps. This platform is the first paper-based POC device able to automate the rapid (< 30 minutes) processing of large volumes (mL) with minimal user steps. Additionally, these samples are not compatible with downstream NAAT or pathogen identification prior to purification (see below), so even with non-ideal low recovery the device is still practical for use in many settings.

6.3.4. Demonstration platform compatibility with in-membrane NAAT and lateral flow readout

The demonstrations above all relied on a heavily instrumented qPCR system for output quantification. Although useful for development, qPCR is not compatible with many POC settings. To address this limitation, the device output was tested with in-membrane isothermal amplification followed by lateral flow detection. The ability to link sample preparation with on-device NAAT and lateral flow allows for usage in truly POC situations.

To test compatibility, iSDA reagents were dried into Standard 17 porous membranes and rehydrated with either device elution or urine lysate post lysis but prior to purification, as described in the methods section (membrane and NAAT preparation courtesy of Ryan Gallagher and Enos Kline). After isothermal amplification, pathogen (*N. gonorrhoeae* or *C. trachomatis*) detection was confirmed by lateral flow. The results from the dried iSDA pads showed that purified samples were able to be successfully amplified, but the lysates, unsurprisingly, inhibited the reactions, **Figure 86**.

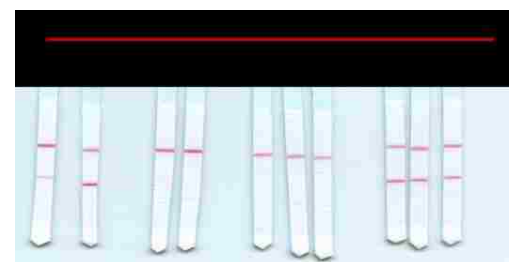
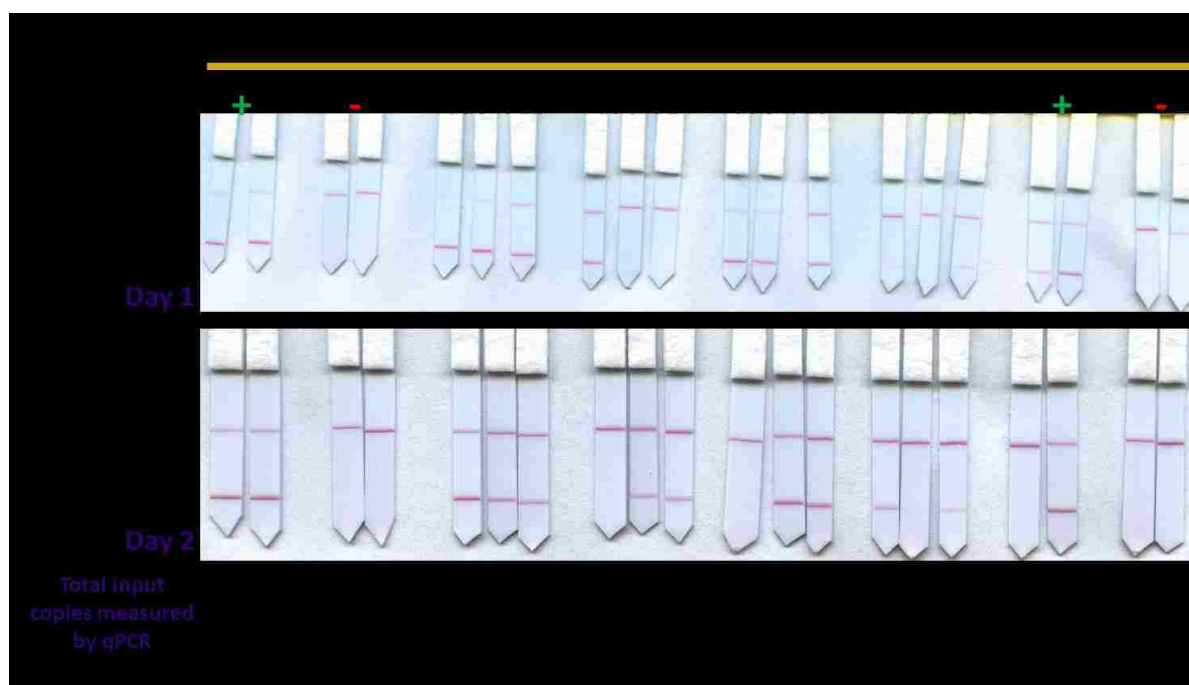


Figure 86. In-membrane NAAT comparing purified and non-purified samples. Input *C. trachomatis* concentration was $\sim 10^4$ copies per reaction.

After the initial demonstration of NAAT compatibility, six additional purified samples were used to rehydrate membranes with dried iSDA reagents, **Figure 87**. There are a few drop outs (no signal at the expected place on the lateral flow strip), likely due to limit of assay detection, and some non-specific binding with the chlamydia assay (because the NG-specific line was appearing on some strips, but there were no NG amplification reagents included in the assay), but overall these results show strong performance of in-membrane amplification with device outputs. The *N. gonorrhoeae* assay was run with the same samples on two separate days to show reproducibility of the dried iSDA pads. Patient sample 23 was separated into two aliquots, one was spiked with pathogens and the other was not to compare the effects of the sample. Both the purification and the concentration mechanisms enable detection of pathogen signal from dilute patient urine specimens.



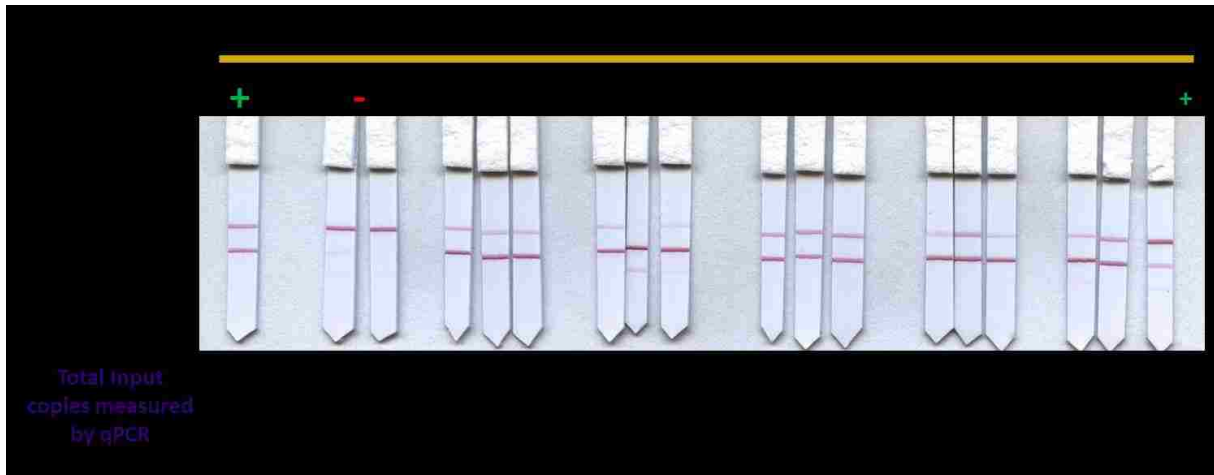


Figure 87. Lateral flow detection of in-membrane iSDA rehydrated with sample purified using the p-switch device. **A.** *N. gonorrhoeae* iSDA performed with the same samples on two separate days. **B.** *C. trachomatis* DNA.

6.3.5. Comparing p-switch device results to a clinical system used to detect CT/NG

The final experiment to demonstrate this automated sample processing device was to compare its results with a clinically relevant test. The Harborview STI Clinic uses the Aptima 2 Combo NG/CT test for diagnosing chlamydia and/or gonorrhea infection. This laboratory platform served as the clinical comparison to the automated p-switch device.

The Aptima system processes 2 mL of urine sample using multiple timed heating steps, expensive equipment, and trained personnel. The purification process is highly effective, but also takes multiple hours. After purification, the samples are detected by PCR giving a “positive” or “negative” result. In comparison, the p-switch device takes ~20-25 minutes to process 2 mL of sample and requires only two untrained user steps. To compare performance, patient specimens were spiked with pathogens and aliquots were tested in both the Aptima and p-switch platforms. Collaborators at Harborview were blinded to the contents of the samples. After device purification, outputs were tested in both qPCR and in-membrane amplification with lateral flow detection. All results were recorded as “+” or “-” to match the output from the clinical system.

Overall, the device and clinical results were nearly identical, **Table 12**. Both the device qPCR and Aptima results had one false negative (determined to be a false negative because pathogen was knowingly spiked into the sample.) When the device output was characterized by in-membrane NAAT with lateral flow readout, the false negative was restored to a true positive. This result is likely due to the amount of sample used in each detection test. Both the device and Aptima PCR only use 1 μ L of purified sample, while the in-membrane NAAT is rehydrated with 20 μ L of sample.

Table 12. Comparing the device output measured by qPCR to the clinical result (as measured by the Aptima 2 CT/NG Combo Test) and in-membrane amplification with lateral flow readout. Device results were considered positive if 3/3 replicates were positive by qPCR. In-membrane iSDA with lateral flow readout was considered positive if 2/3 replicates had signal. Patient 23 was split into two samples, one spiked with pathogens and one without pathogens to directly compare the potential effects of the patient specimen. Overall, there was strong agreement between this device and the clinical result as measured with either qPCR or NAAT+lateral flow. The in-membrane iSDA may have restored expected signal in Patient 23 (+) for NG because 20 μ L of purified sample is used to rehydrate the membrane compared to only 1 μ L of purified sample used in the qPCR or Aptima PCR.

Specimen	Spiked Pathogen	Expected Result (+/-)	Device Result (qPCR N=3)	In-membrane iSDA (N=3-6)	Clinical Result (Aptima, N=1)
Patient 12 (HS1)	CT	+	+	+	+
	NG	+	+	+	+
Patient 24 (HS2)	CT	+	+	+	+
	NG	+	+	+	+
Patient 29 (HS3)	CT	+	+	+	+
	NG	+	+	+	+
Patient 31 (HS4)	CT	+	+	+	+
	NG	+	+	+	+
Patient 23 (+) (HS5)	CT	+	+	+	+
	NG	+	-	+	-
Patient 23 (-) (HS6)	CT	-	-	n/a	-
	NG	-	-	-	-

6.4. Conclusions and Future Work

The work described above details the integration of multiple sample preparation modules into an automated device to purify nucleic acids from complex, large volume samples. Using the principles of Darcy's Law, volumetric flow rates were improved by decreasing the overall distance fluid travels through porous membranes. This enabled up to a 5x increase in total assay speed. Simultaneous in-tube lysis and DNA fragmentation are coupled with downstream DNA purification. The chitosan-based purification system proved to effectively recover DNA from human urine samples spiked with multiple pathogens. Understanding of the material properties and the effect of membrane saturation levels allowed for the development of the pressure-based fluid switch (p-switch) that controls direction of fluid flow without the complication of additional moving parts. The p-switch was coupled to chitosan purification and resulted in high recovery of DNA. Finally, the output of this device was used to rehydrate isothermal amplification reagents dried in a paper

membrane as a step toward a fully integrated device to detect both chlamydia and gonorrhea directly from 1–5 mL of urine. The results from this device aligned with the results from the gold standard Aptima system used in clinical settings.

Beyond the applications demonstrated in this work, the p-switch technology can be used for a multitude of other systems in order to automate multi-step assays. This work provides a unique opportunity to integrate sample dilution, sample concentration, and/or controlled fluid flow. Currently, a junior graduate student, Caitlin Anderson, has demonstrated that the p-switch system can be used for automating sample dilution. Additionally, undergraduates in the Yager laboratory have begun to use the integrated system described above for purifying nucleic acids from diluted blood samples. Another potentially interesting application is using this type of device for purifying and concentration other important diagnostic biomolecules – proteins, lipids, or rare cells such as circulating tumor cells – from large volume samples. This work can stand alone as a useful system for automated processing of urine samples at the point-of-care, but it also serves as a new platform for fully integrated systems that enable automatic control of multi-step assays that would not otherwise be feasible with traditional lateral flow-based devices.

7. Overall Conclusions and Future Directions

This dissertation work has developed an integrated, POC-compatible platform that combines pathogen lysis, gDNA fragmentation, DNA purification, and sample concentration using porous membrane substrates. The device has been demonstrated with 2 mL of discarded patient urine samples and performs equally-well for identification of *C. trachomatis* and *N. gonorrhoeae* from a small set of samples compared to the clinical Aptima test. More detailed summaries of the conclusions from each aim are provided below:

Aim 1: Demonstrate lysis and urine specimen characterization

- ACP treatment for pathogen lysis is inhibited by salt or buffer concentrations above 50 mM and at pH values below 6.5
- thermal lysis of gram negative pathogens is robust over a range of salt concentrations and pH values found in clinical urine samples; and was successfully demonstrated in human urine
- both thermal and enzymatic lysis show limited effectiveness in porous membranes
- verified robust thermal lysis of pathogens in urine samples that had been pH-modulated
- 35 de-identified, discarded human urine samples were characterized
 - o average pH: 6.3 (SD=0.7, N=35)

- average salinity: 165 mM (SD=91 mM, N=35)
- average total NA: 8.0 ng/μL (SD=10.0 ng/μL, N=20)
- average total dissolved solids: 31.2 μg/μL (SD=22.8 μg/μL, N=10)

Aim 2: Develop a point-of-care-compatible DNA fragmentation method

- DNA transport through Fusion 5 is not significantly affected by direct or protein-mediated adsorption; DNA entanglement, due to length, appears to be a major contributing factor to reduced DNA transport
- Increasing heating time (0–30 min) and heating temperature (85–95°C) results in increased transport of DNA and smaller average fragment size for four different cell types (*N. gonorrhoeae*, *S. aureus*, *E. coli*, and HeLa epithelial cells)
- Controlling heating time and temperature can result in selective flow of smaller DNA targets in samples with mixed cells (bacterial v. human cells)

Aim 3: Develop a method to purify and concentrate DNA in porous membranes

- quantified chitosan retention in common porous membranes
- quantified DNA binding capacity of chitosan in porous membranes
- designed an assay to purify and concentrate DNA from complex samples including simulated nasal matrix, excess non-target DNA, high salinities, blood, and large volumes
- shown efficient purification of DNA after chitosan-modified membranes were stored for up to six months
- demonstrated proof-of-concept work for using chitosan-patterned membranes to purify RNA

Aim 4: Automation of large volume sample processing through controlled fluid movement in multi-material porous networks

- optimize device geometry to rapid process large volume samples up to 2 mL
- demonstrated recovery of pathogen DNA spiked into human urine samples
- developed the p-switch to automatically control fluid flow direction and reagent delivery for large volume samples
- developed and demonstrated an integrated sample preparation system to lyse cells, fragment DNA, purify DNA, and concentrate the sample directly from human urine samples
- showed device purified samples are compatible with downstream in-membrane NAAT and lateral flow detection
- showed results from the integrated device were the same as the clinical Aptima system to successfully identify *C. trachomatis* and *N. gonorrhoeae* from urine specimens

To date, the work presented in this dissertation has been written into nine manuscripts (with four additional manuscripts from my time before graduate school and my other extra-graduate activities). Of the nine thesis-related manuscripts, five are first author publications including one review focused on the translation of laboratory-based diagnostic systems to POC applications (Byrnes *et al. Bioanalysis*, 2013) and one that is co-first authored (Buser and Byrnes, *et al.* in preparation). The three additional first author manuscripts include: (i) POC compatible lysis and gDNA fragmentation methods which is ready for submission to *Lab on a Chip*, (ii) development and testing of a POC paper-based DNA purification and concentration assay (Byrnes *et al. LOC* 2015), and (iii) design and development of a fully integrated urine processing system for the POC (manuscript in preparation for *Nature Methods*).

I have also attended multiple conferences where I have presented posters (BMES 2012 and 2013; Gordon Research Conference 2013; MicroTAS 2014, 2015, and 2016) and talks (BMES 2014, MicroTAS 2016 Workshop). At the MicroTAS conference in 2015, I won the award for best poster presentation. Beyond my work in the BioE department, I had the incredible opportunity to complete a Masters of Public Health (MPH) in Health Metrics and Evaluation at UW. My MPH thesis focused on quantifying characteristics that drive the use of POC HIV diagnostic devices (**Appendix 4**). From March 2014–December 2015, I worked on a small side project with the PATH gestational diabetes (GDM) team working on a stakeholder surveys and analysis for a new POC GDM test they are developing. I’ve had the opportunity to design and conduct surveys with GDM stakeholders in Brazil and China and wrote my first qualitative research manuscript. Since May 2015, I have been working part-time as a Virtual Research Analysis with Intellectual Ventures/Global Good to help research topics related to their global health projects. Working with Dr. Bernhard Weigl, I have begun to develop one of these assignments into a manuscript focused on biomarker selection. These experiences coupled with my work in Dr. Yager’s Lab have helped drive me toward my goal of developing and implementing interventions to improve access to healthcare around the world.

8. Abbreviations and Acronyms

2DPN	<u>t</u> wo- <u>d</u> imensional <u>p</u> aper <u>n</u> etwork
ACP	<u>a</u> chromo <u>p</u> eptidase
bp	<u>b</u> ase <u>p</u> airs
bPEI	<u>b</u> ranch <u>e</u> d <u>p</u> oly <u>e</u> thylene <u>i</u> mine
CFU	<u>c</u> olony <u>f</u> orming <u>u</u> nits

COMET assay	single cell gel electrophoresis
CT	<i>Chlamydia trachomatis</i>
CT+ epi cells	<i>Chlamydia trachomatis</i> -infected epithelial cells
Ct	cycle threshold
DFI	DNA fragmentation index
EB	elementary body
<i>E. coli</i>	<i>Escherichia coli</i>
EDTA	ethylenediaminetetraacetic acid
ELISA	enzyme-linked immunosorbent assay
FVU	first void urine
gDNA	genomic DNA
GF	glass fiber
GN	<i>Neisseria gonorrhoeae</i>
iSDA	isothermal strand displacement amplification
LAMP	loop mediated isothermal amplification
IPEI	linear polyethylenimine
LFT	lateral flow test
LRS	low resource setting
MAD NAAT	Multiplexed Automated Device for Nucleic Acid Amplification Tests
MRSA	methicillin-resistant <i>Staphylococcus aureus</i>
MSSA	methicillin-sensitive <i>Staphylococcus aureus</i>
Mw	molecular weight
NA	nucleic acid
NAAT	nucleic acid amplification test
NC	nitrocellulose
NEB	New England Biolabs
PCR	polymerase chain reaction
PFGE	pulsed field gel electrophoresis
PLL	Poly-L-lysine
POC	point-of-care
POCT	point-of-care test
PPM	porous polymer monolith
p-switch	pressure switch
RE	restriction enzymes
RFU	relative fluorescence units
SES	socio-economic status
SNM	simulated nasal matrix
SPE	solid phase extraction
STI	sexually transmitted infection
Tunel assay	terminal deoxynucleotidyl transferase dUTP nick end labeling assay
WRC	water retention curve

9. Acknowledgements

This work was supported by a grant to Paul Yager from the Defense Advanced Research Projects Agency (DARPA) “Multiplexable Autonomous Disposable for Nucleic Acid Amplification Tests for LRSs” under Grant No. HR0011-11-2-0007.

Much of this work would not have been possible without guidance from my adviser, Dr. Paul Yager, and committee members: Dr. Daniel Ratner, Dr. Kim Woodrow, and Dr. Lisa Frenkel. I would also like to express my gratitude to my many collaborators and editors including Dr. Joshua Bishop, Dr. Joshua Buser, Dr. Paula Ladd, Caitlin Anderson, Dr. Lisa Lafleur, Dr. Barry Lutz, Dr. Robert Suchland, Dr. S.O. Soge, and Meghan Zuck.

10. Literature Cited

1. Centers for Disease Control and Prevention. Sexually Transmitted Infections Among Young Americans. 2014;17(4). <http://www.cdc.gov/nchstp/newsroom/docs/Youth-STI-Infographic.pdf>.
2. US Center for Disease Control and Prevention. Combating the Threat of Antibiotic-Resistant Gonorrhea. <http://www.cdc.gov/std/gonorrhea/arg/carb.htm>.
3. Papp JR, Schachter J, Gaydos CA, Van Der Pol B. Recommendations for the Laboratory-Based Detection of Chlamydia trachomatis and Neisseria gonorrhoeae. *Centers Dis Control Prev*. 2014. <http://www.cdc.gov/mmwr/preview/mmwrhtml/rr6302a1.htm#Tab1>. Accessed January 5, 2015.
4. Rosenvinge MM, Lau R. Screening for asymptomatic chlamydia in women – how often would gonorrhoea be missed? *Int J STD AIDS*. 2009;20:571-572.
5. Watchirs Smith LA, Hillman R, Ward J, et al. Point-of-care tests for the diagnosis of Neisseria gonorrhoeae infection: a systematic review of operational and performance characteristics. *Sex Transm Infect*. 2013;89(4):320-326. doi:10.1136/sextrans-2012-050656.
6. Rohrman BA, Richards-Kortum R. A paper and plastic device for performing recombinase polymerase amplification of HIV DNA. *Lab Chip*. 2012;12(17):3082-3088. doi:10.1039/c2lc40423k.
7. Lozano R, Naghavi M, Foreman K, et al. Global and regional mortality from 235 causes of death for 20 age groups in 1990 and 2010: a systematic analysis for the Global Burden of Disease Study 2010. *Lancet*. 2012;380(9859):2095-2128. doi:10.1016/S0140-6736(12)61728-0.
8. Wang H, Dwyer-Lindgren L, Lofgren KT, et al. Age-specific and sex-specific mortality in 187 countries, 1970-2010: a systematic analysis for the Global Burden of Disease Study 2010. *Lancet*. 2012;380(9859):2071-2094. doi:10.1016/S0140-6736(12)61719-X.
9. Murray CJL, Vos T, Lozano R, et al. Disability-adjusted life years (DALYs) for 291 diseases and injuries in 21 regions, 1990-2010: a systematic analysis for the Global Burden of Disease Study 2010. *Lancet*. 2012;380(9859):2197-2223. doi:10.1016/S0140-6736(12)61689-4.
10. Lozano R, Naghavi M, Foreman K, et al. Global and regional mortality from 235 causes of death for 20 age groups in 1990 and 2010: a systematic analysis for the Global Burden of Disease Study 2010. *Lancet*. 2012;380(9859):2095-2128. doi:10.1016/S0140-6736(12)61728-0.
11. Peeling RW, Mabey D, Herring A, Hook EW. Why do we need quality-assured diagnostic tests for sexually transmitted infections? *Nat Rev Microbiol*. 2006;4(12 Suppl):S7-19. doi:10.1038/nrmicro1569.
12. Litaker D, Koroukian SM, Love TE. Looking Beyond the Individual. *Med Care*. 2005;43(6):531-540.
13. Ramani S, Kang G. Viruses causing childhood diarrhoea in the developing world. *Curr Opin Infect Dis*. 2009;22(5):477-482. doi:10.1097/QCO.0b013e328330662f.
14. Hill DR, Beeching NJ. Travelers' diarrhea. *Curr Opin Infect Dis*. 2010;23(5):481-487. doi:10.1097/QCO.0b013e32833dfca5.
15. Diarrhea Causes - Mayo Clinic. <http://www.mayoclinic.org/diseases-conditions/diarrhea/basics/causes/con-20014025?p=1>. Accessed May 12, 2015.
16. Hodges K, Gill R. Infectious diarrhea: Cellular and molecular mechanisms. 2010;1(1):4-21. <http://www.scopus.com/inward/record.url?eid=2-s2.0-77954821992&partnerID=40&md5=6cd4f3ca8d11bc10a8e0b658db33c237>
<http://pubmedcentralcanada.ca/picrender.cgi?accid=PMC3035144&blobtype=pdf>.
17. WHO. *Antimicrobial Resistance Fact Sheet*.; 2015. <http://www.who.int/mediacentre/factsheets/fs194/en/#>.

18. Drancourt M, Michel-lepage A, Boyer S. The Point-of-Care Laboratory in Clinical Microbiology. *Clin Microbiol Rev.* 2016;29(3):429-447. doi:10.1128/CMR.00090-15.Address.
19. Archibald ME, Putnam Rankin C. A spatial analysis of community disadvantage and access to healthcare services in the U.S. *Soc Sci Med.* 2013;90:11-23. doi:10.1016/j.socscimed.2013.04.023.
20. Welch TF. Equity in transport: The distribution of transit access and connectivity among affordable housing units. *Transp Policy.* 2013;30:283-293. doi:10.1016/j.tranpol.2013.09.020.
21. Wendt C. Mapping European healthcare systems: a comparative analysis of financing, service provision and access to healthcare. *J Eur Soc Policy.* 2009;19(5):432-445. doi:10.1177/0958928709344247.
22. Kirby JB. Poor People, Poor Places and Access to Health Care in the United States. *Soc Forces.* 2008;87(1):325-350. doi:10.1353/sof.0.0062.
23. Etyang AO, Munge K, Bunyasi EW, et al. Burden of disease in adults admitted to hospital in a rural region of coastal Kenya: an analysis of data from linked clinical and demographic surveillance systems. *Lancet Glob Heal.* 2014;2(4):e216-e224. doi:10.1016/S2214-109X(14)70023-3.
24. Shears P. Poverty and infection in the developing world: healthcare-related infections and infection control in the tropics. *J Hosp Infect.* 2007;67(3):217-224. doi:10.1016/j.jhin.2007.08.016.
25. Al-Taiar A, Jaffar S, Assabri A, et al. Who develops severe malaria? Impact of access to healthcare, socio-economic and environmental factors on children in Yemen: A case-control study. *Trop Med Int Heal.* 2008;13(6):762-770. doi:10.1111/j.1365-3156.2008.02066.x.
26. WHO | Procurement of HIV diagnostics. http://www.who.int/diagnostics_laboratory/procurement/hiv/en/. Accessed March 3, 2014.
27. Loubiere S, Moatti J-P. Economic evaluation of point-of-care diagnostic technologies for infectious diseases. *Clin Microbiol Infect.* 2010;16(8):1070-1076. doi:10.1111/j.1469-0691.2010.03280.x.
28. Alary M, Baganizi E, Guèdèmè A, et al. Evaluation of clinical algorithms for the diagnosis of gonococcal and chlamydial infections among men with urethral discharge or dysuria and women with vaginal discharge in Benin. *Sex Transm Infect.* 1998;74 Suppl 1:S44-9. <http://europepmc.org/abstract/med/10023353>. Accessed May 11, 2015.
29. Whitesides GM. The origins and the future of microfluidics. *Nature.* 2006;442(7101):368-373. doi:10.1038/nature05058.
30. Price CW, Leslie DC, Landers JP. Nucleic acid extraction techniques and application to the microchip. *Lab Chip.* 2009;9(17):2484-2494. doi:10.1039/b907652m.
31. Kim J, Johnson M, Hill P, Gale BK. Microfluidic sample preparation: cell lysis and nucleic acid purification. *Integr Biol (Camb).* 2009;1(10):574-586. doi:10.1039/b905844c.
32. Giordano BC, Burgi DS, Hart SJ, Terray A. On-line sample pre-concentration in microfluidic devices: a review. *Anal Chim Acta.* 2012;718:11-24. doi:10.1016/j.aca.2011.12.050.
33. Bhattacharyya a, Klapperich CM. Design and testing of a disposable microfluidic chemiluminescent immunoassay for disease biomarkers in human serum samples. *Biomed Microdevices.* 2007;9(2):245-251. doi:10.1007/s10544-006-9026-2.
34. Qiu X, Thompson J a, Chen Z, et al. Finger-actuated, self-contained immunoassay cassettes. *Biomed Microdevices.* 2009;11(6):1175-1186. doi:10.1007/s10544-009-9334-4.
35. Bange A, Halsall HB, Heineman WR. Microfluidic immunosensor systems. *Biosens Bioelectron.* 2005;20(12):2488-2503. doi:10.1016/j.bios.2004.10.016.
36. Liu C, Mauk MG, Bau HH. A disposable , integrated loop-mediated isothermal amplification cassette with thermally actuated valves. *Microfluid Nanofluidics.* 2011;11:209-220. doi:10.1007/s10404-011-0788-3.
37. White AK, VanInsberghe M, Petriv OI, et al. High-throughput microfluidic single-cell RT-qPCR. *Proc Natl Acad Sci U S A.* 2011;108(34):13999-14004. doi:10.1073/pnas.1019446108.
38. Gubala V, Harris LF, Ricco AJ, Tan MX, Williams DE. Point of care diagnostics: status and future. *Anal Chem.* 2012;84(2):487-515. doi:10.1021/ac2030199.
39. Yagoda H. Applications of Confined Spot Tests in Analytical Chemistry. *Ind Eng Chem.* 1937;9(2):79-82.
40. Muller RH, Clegg ANDDL, York N. Automatic Paper Chromatography. *Anal Chem.* 1949;21(9):1123-1125.
41. Consden R, Gordon AH, Martin JP. Qualitative Analysis of Proteins : a Partition Chromatographic. *Biochem J.* 1944;38:224-232.
42. Banik UK, Hirsch MA, Irvine DS, et al. A Simple and Sensitive Nonradioactive Method for the Detection of Urinary Human Chorionic Gonadotropin and Diagnosis of Early Human Pregnancy II Single Unit Test. *Fertil Steril.* 1979;32(4):426-432.
43. EPT Do-It-Yourself Early-Pregnancy Test. *Med Lett Drugs Ther.* 1978;20(8):30-40.
44. Arora S, Tyagl S. Detection of Early Pregnancy. *Clinician (Goa).* 1978;42(5):179-183.
45. Martinez AW, Phillips ST, Butte MJ, Whitesides GM. Patterned paper as a platform for inexpensive, low-volume, portable bioassays. *Angew Chem Int Ed Engl.* 2007;46(8):1318-1320. doi:10.1002/anie.200603817.

46. Fu E, Lutz B, Kauffman P, Yager P. Controlled reagent transport in disposable 2D paper networks. *Lab Chip*. 2010;10(7):918-920. doi:10.1039/b919614e.
47. Lutz BR, Trinh P, Ball C, Fu E, Yager P. Two-dimensional paper networks: programmable fluidic disconnects for multi-step processes in shaped paper. *Lab Chip*. 2011;11(24):4274-4278. doi:10.1039/c1lc20758j.
48. Fridley GE, Le HQ, Fu E, Yager P. Controlled release of dry reagents in porous media for tunable temporal and spatial distribution upon rehydration. *Lab Chip*. 2012;12(21):4321-4327. doi:10.1039/c2lc40785j.
49. Fu E, Kauffman P, Lutz B, Yager P. Chemical signal amplification in two-dimensional paper networks. *Sens Actuators B Chem*. 2010;149(1):325-328. doi:10.1016/j.snb.2010.06.024.
50. Rodriguez NM, Linnes JC, Fan A, Ellenson CK, Pollock NR, Klapperich CM. Paper-based RNA extraction, in situ isothermal amplification, and lateral flow detection for low-cost, rapid diagnosis of Influenza A (H1N1) from clinical specimens. *Anal Chem*. 2015;87(15):7872-7879. doi:10.1021/acs.analchem.5b01594.
51. Rohrman B, Richards-Kortum R. Inhibition of Recombinase polymerase amplification by background dna: A lateral flow-based method for enriching target DNA. *Anal Chem*. 2015;87(3):1963-1967. doi:10.1021/ac504365v.
52. Cao W, Easley CJ, Ferrance JP, Landers JP. Chitosan as a Polymer for pH-Induced DNA Capture in a Totally Aqueous System. *Anal Chem*. 2006;78(20):7222-7228.
53. Yetisen AK, Akram MS, Lowe CR. Paper-based microfluidic point-of-care diagnostic devices. *Lab Chip*. 2013;13(12):2210-2251. doi:10.1039/c3lc50169h.
54. Jeong S-G, Kim J, Jin SH, Park K-S, Lee C-S. Flow control in paper-based microfluidic device for automatic multistep assays: A focused minireview. *Korean J Chem Eng*. 2016;33(10):2761-2770.
55. Byrnes S, Thiessen G, Fu E. Progress in the development of paper-based diagnostics for low-resource point-of-care settings. *Bioanalysis*. 2013;5(22):2821-2836. doi:10.4155/bio.13.243.
56. Lafleur L, Bishop JD, Heiniger EK, et al. A rapid, instrument-free, sample-to-result nucleic acid amplification test. *Lab Chip*. 2016;16:3777-3787. doi:10.1039/C6LC00677A.
57. Connelly JT, Rolland JP, Whitesides GM. A "Paper Machine" for Molecular Diagnostics. *Anal Chem*. 2015:150623233731001. doi:10.1021/acs.analchem.5b00411.
58. Mariella R. Sample preparation: the weak link in microfluidics-based biodetection. *Biomed Microdevices*. 2008;10(6):777-784. doi:10.1007/s10544-008-9190-7.
59. Cao Q, Kim M-C, Klapperich CM. Plastic Microfluidic Chip for Continuous-Flow Polymerase Chain Reaction: Simulations and Experiments. *Biotechnol J*. 2012;6(2):177-184. doi:10.1002/biot.201000100.Plastic.
60. Cao Q, Mahalanabis M, Chang J, et al. Microfluidic chip for molecular amplification of influenza A RNA in human respiratory specimens. *PLoS One*. 2012;7(3):e33176. doi:10.1371/journal.pone.0033176.
61. Chen D, Mauk M, Qiu X, et al. An integrated, self-contained microfluidic cassette for isolation, amplification, and detection of nucleic acids. *Biomed Microdevices*. 2010;12(4):705-719. doi:10.1007/s10544-010-9423-4.
62. Lafleur L, Stevens D, McKenzie K, et al. Progress toward multiplexed sample-to-result detection in low resource settings using microfluidic immunoassay cards. *2Lab a Chip*. 2012;12(1119):1119-1127.
63. Asiello PJ, Baeumner AJ. Miniaturized isothermal nucleic acid amplification, a review. *Lab Chip*. 2011;11(8):1420-1430. doi:10.1039/c0lc00666a.
64. Notomi T, Okayama H, Masubuchi H, et al. Loop-mediated isothermal amplification of DNA. *Nucleic Acids Res*. 2000;28(12):E63.
<http://www.pubmedcentral.nih.gov/articlerender.fcgi?artid=102748&tool=pmcentrez&rendertype=abstract>.
65. Liu C, Mauk MG, Hart R, Qiu X, Bau HH. A self-heating cartridge for molecular diagnostics. *Lab Chip*. 2011;11(16):2686-2692. doi:10.1039/c1lc20345b.
66. LaBarre P, Hawkins KR, Gerlach J, et al. A Simple , Inexpensive Device for Nucleic Acid Amplification without Electricity — Toward Instrument- Free Molecular Diagnostics in Low-Resource Settings. *PLoS One*. 2011;6(5):e19738. doi:10.1371/journal.pone.0019738.
67. Singleton J, Zentner C, Buser J, Yager P, LaBarre P, Weigl BH. Instrument-free exothermic heating with phase change temperature control for paper microfluidic devices. Becker H, Gray BL, eds. *Proc SPIE*. 2013;8615:86150R. doi:10.1117/12.2005928.
68. Huang S, Do J, Mahalanabis M, et al. Low Cost Extraction and Isothermal Amplification of DNA for Infectious Diarrhea Diagnosis. *PLoS One*. 2013;8(3):e60059. doi:10.1371/journal.pone.0060059.
69. Su W, Gao X, Jiang L, Qin J. Microfluidic platform towards point-of-care diagnostics in infectious diseases. *J Chromatogr A*. 2015;1377:13-26. doi:10.1016/j.chroma.2014.12.041.
70. Rohrman B, Richards-Kortum R. Inhibition of Recombinase Polymerase Amplification by Background DNA: A Lateral Flow-Based Method for Enriching Target DNA. *Anal Chem*. 2015;87:1963-1967. doi:10.1021/ac504365v.
71. Linnes JC, Fan A, Rodriguez NM, Lemieux B, Kong H, Klapperich CM. Paper-based molecular diagnostic for Chlamydia trachomatis. *RSC Adv*. 2014;4(80):42245-42251. doi:10.1039/C4RA07911F.
72. Niemz A, Ferguson TM, Boyle DS. Point-of-care nucleic acid testing for infectious diseases. *Trends Biotechnol*.

- 2011;29(5):240-250. doi:10.1016/j.tibtech.2011.01.007.
73. Cepheid | GeneXpert IV. <http://www.cepheid.com/us/cepheid-solutions/systems/genexpert-systems/genexpert-iv>. Accessed June 22, 2015.
74. Huang Y, Mather EL, Bell JL, Madou M. MEMS-based sample preparation for molecular diagnostics. *Anal Bioanal Chem*. 2002;372:49-65. doi:10.1007/s00216-001-1191-9.
75. Brehm-Stecher B, Yong C, Jaykus L-A, Tortorello M Lou. Sample Preparation: The Forgotten Beginning. *J Food Protection*. 2009;72(8):1774-1789.
76. Berg JM, Tymoczko J., Stryer L. The Purification of Proteins Is an Essential First Step in Understanding Their Function. In: *Biochemistry*. 5th ed. New York: W. H. Freeman; 2002. <http://www.ncbi.nlm.nih.gov/books/NBK22410/>.
77. Doebler RW, Erwin B, Hickerson A, et al. Continuous-Flow, Rapid Lysis Devices for Biodefense Nucleic Acid Diagnostic Systems. *JALA - J Assoc Lab Autom*. 2009;14(3):119-125. doi:10.1016/j.jala.2009.02.010.
78. Voet D, Voet JG, Pratt CW. *Fundamentals of Biochemistry*. Third Edit. John Wiley & Sons, Inc.; 2008.
79. Sambrook J, Russell DW. *Molecular Cloning: A Laboratory Manual, Volume 1, 2, 3*. New York: Cold Spring Harbor; 2001. <http://www.gate2biotech.com/molecular-cloning-a-laboratory-manual/>. Accessed May 15, 2015.
80. Composition C, Garcia FAP. Cell wall disruption. In: Flickinger MC, ed. *Encyclopedia of Industrial Biotechnology: Bioprocess, Bioseparation, and Cell Technology*. John Wiley & Sons, Inc.; 2009:1-12.
81. Bonner OD. Denaturation of proteins by urea, substituted ureas, guanidinium salts, and alcohols. *Physiol Chem Phys*. 1978;10(5):399-404.
82. Hukari KW, Patel KD, Renzi RF, West J a a. An ultra-high temperature flow-through capillary device for bacterial spore lysis. *Electrophoresis*. 2010;31(16):2804-2812. doi:10.1002/elps.201000176.
83. Boom, R.; Sol, C.J.A.; Salimans, M.M.M.; Jansen, C.L.; Wertheim-van Dillen, P.M.E.; Noordaa J van der. Rapid and Simple Method for Purification of Nucleic Acids. *J Clin Microbiol*. 1990;28(3):495-503.
84. Chomczynski P. Single-Step Method of RNA Isolation by Acid Guanidinium Extraction. *Anal Biochem*. 1987;159(1):156-159.
85. Yeung SW, Hsing I-M. Manipulation and extraction of genomic DNA from cell lysate by functionalized magnetic particles for lab on a chip applications. *Biosens Bioelectron*. 2006;21(7):989-997. doi:10.1016/j.bios.2005.03.008.
86. den Dulk RC, Schmidt K a, Sabatté G, Liébana S, Prins MWJ. Magneto-capillary valve for integrated purification and enrichment of nucleic acids and proteins. *Lab Chip*. 2013;13(1):106-118. doi:10.1039/c2lc40929a.
87. Liu X, Erickson D, Li D, Krull UJ. Cationic polymer coatings for design of electroosmotic flow and control of DNA adsorption. *Anal Chim Acta*. 2004;507(1):55-62. doi:10.1016/j.aca.2003.10.075.
88. Nakagawa T, Hashimoto R, Maruyama K, Tanaka T. Capture and Release of DNA Using Aminosilane-Modified Bacterial Magnetic Particles for Automated Detection System of Single Nucleotide Polymorphisms. *Biotechnol Bioeng*. 2006. doi:10.1002/bit.20904.
89. Witek M a, Hupert ML, Park DS-W, Fears K, Murphy MC, Soper S a. 96-well polycarbonate-based microfluidic titer plate for high-throughput purification of DNA and RNA. *Anal Chem*. 2008;80(9):3483-3491. doi:10.1021/ac8002352.
90. Marshall L a, Wu LL, Babikian S, Bachman M, Santiago JG. Integrated printed circuit board device for cell lysis and nucleic acid extraction. *Anal Chem*. 2012;84(21):9640-9645. doi:10.1021/ac302622v.
91. Kenyon SM, Meighan MM, Hayes M a. Recent developments in electrophoretic separations on microfluidic devices. *Electrophoresis*. 2011;32(5):482-493. doi:10.1002/elps.201000469.
92. Rogacs A, Marshall L a., Santiago JG. Purification of nucleic acids using isotachopheresis. *J Chromatogr A*. 2014;1335:105-120. doi:10.1016/j.chroma.2013.12.027.
93. Wang J, Morabito K, Tang JX, Tripathi A. Microfluidic platform for isolating nucleic acid targets using sequence specific hybridization. *Biomicrofluidics*. 2013;7(4):44107. doi:10.1063/1.4816943.
94. Liu P, Li X, Greenspoon S a, Scherer JR, Mathies R a. Integrated DNA purification, PCR, sample cleanup, and capillary electrophoresis microchip for forensic human identification. *Lab Chip*. 2011;11(6):1041-1048. doi:10.1039/c0lc00533a.
95. Moghadam BY, Connelly KT, Posner JD. Isotachopheretic Preconcentration on Paper-Based Microfluidic Devices. *Anal Chem*. 2014;86:5829-5837.
96. Govindarajan a V, Ramachandran S, Vigil GD, Yager P, Böhringer KF. A low cost point-of-care viscous sample preparation device for molecular diagnosis in the developing world; an example of microfluidic origami. *Lab Chip*. 2012;12(1):174-181. doi:10.1039/c1lc20622b.
97. Jangam SR, Yamada DH, McFall SM, Kelso DM. Rapid, point-of-care extraction of human immunodeficiency virus type 1 proviral DNA from whole blood for detection by real-time PCR. *J Clin Microbiol*. 2009;47(8):2363-2368. doi:10.1128/JCM.r00092-09.
98. Knierim E, Lucke B, Schwarz JM, Schuelke M, Seelow D. Systematic comparison of three methods for fragmentation of long-range PCR products for next generation sequencing. *PLoS One*. 2011;6(11). doi:10.1371/journal.pone.0028240.
99. Sugunendran H, Birley HDL, Mallinson H, Abbott M, Tong CYW. Comparison of urine , first and second endourethral

- swabs for PCR based detection of genital Chlamydia trachomatis infection in male patients. *Sex Transm Dis.* 2001;77:423-426.
100. Cook RL, Hutchison SL, Braithwaite RS, Ness RB. Review Systematic Review : Noninvasive Testing for Chlamydia trachomatis. *Ann Intern Med.* 2005;142:914-925.
 101. Chernesky M, Jang D, Chong S, Sellors J, Mahony J. Impact of Urine Collection Order on the Ability of Assays to Identify Chlamydia trachomatis Infections in Men. *Sex Transm Dis.* 2003;30(4):345-347.
 102. Jaton K, Bille J, Greub G. A novel real-time PCR to detect Chlamydia trachomatis in first-void urine or genital swabs. *J Med Microbiol.* 2006;55(Pt 12):1667-1674. doi:10.1099/jmm.0.46675-0.
 103. Michel C-EC, Sonnex C, Carne C a, et al. Chlamydia trachomatis load at matched anatomic sites: implications for screening strategies. *J Clin Microbiol.* 2007;45(5):1395-1402. doi:10.1128/JCM.00100-07.
 104. Wisniewski C a, White J a, Michel C-EC, et al. Optimal method of collection of first-void urine for diagnosis of Chlamydia trachomatis infection in men. *J Clin Microbiol.* 2008;46(4):1466-1469. doi:10.1128/JCM.02241-07.
 105. Blocker ME, Krysiak RG, Behets F, et al. Quantification of Chlamydia trachomatis Elementary Bodies in Urine by Ligase Chain Reaction. *J Clin Microbiol.* 2002;40(10):3631-3634. doi:10.1128/JCM.40.10.3631.
 106. Isbey SF, Alcom TM, Davis RH, Haizlip J, Leone PA. Characterisation of Neisseria gonorrhoeae in semen during urethral infection in men. *Genitourin Med.* 1997;73:378-382.
 107. Owusu-Edusei K, Chesson HW, Gift TL, et al. The estimated direct medical cost of selected sexually transmitted infections in the United States, 2008. *Sex Transm Dis.* 2013;40(3):197-201. doi:10.1097/OLQ.0b013e318285c6d2.
 108. Sary A, Wilson JS, Honey E, Templeton A, Paavonen J, Ma P. A systematic review of the prevalence of Chlamydia trachomatis among European women. 2002;8(4):385-394.
 109. Lewis D, Newton DC, Guy RJ, et al. The prevalence of Chlamydia trachomatis infection in Australia: a systematic review and meta-analysis. *BMC Infect Dis.* 2012;12:113. doi:10.1186/1471-2334-12-113.
 110. Satterwhite CL, Torrone E, Meites E, et al. Sexually transmitted infections among US women and men: prevalence and incidence estimates, 2008. *Sex Transm Dis.* 2013;40(3):187-193. doi:10.1097/OLQ.0b013e318286bb53.
 111. Dielissen PW, Teunissen D a M, Lagro-Janssen ALM. Chlamydia prevalence in the general population: is there a sex difference? a systematic review. *BMC Infect Dis.* 2013;13(1):534. doi:10.1186/1471-2334-13-534.
 112. Creighton S, Tenant-Flowers M, Taylor CB, Miller R, Low N. Co-infection with gonorrhoea and chlamydia : how much is there and what does it mean ? *Int J STD AIDS.* 2003;14:109-113.
 113. Saison F, Mahilum-Tapay L, Michel C-EEE, et al. Prevalence of Chlamydia trachomatis infection among low- and high-risk Filipino women and performance of Chlamydia rapid tests in resource-limited settings. *J Clin Microbiol.* 2007;45(12):4011-4017. doi:10.1128/JCM.01343-07.
 114. Hurly DS, Buhner-Skinner M, Badman SG, et al. Field evaluation of the CRT and ACON chlamydia point-of-care tests in a tropical, low-resource setting. *Sex Transm Infect.* 2014;90(3):179-184. doi:10.1136/sextrans-2013-051246.
 115. Mullick S, Watson-Jones D, Beksinska M, Mabey D. Sexually transmitted infections in pregnancy: prevalence, impact on pregnancy outcomes, and approach to treatment in developing countries. *Sex Transm Infect.* 2005;81(4):294-302. doi:10.1136/sti.2002.004077.
 116. Smith Fawzi MC, Lambert W, Singler J, et al. Identification of chlamydia and gonorrhoea among women in rural Haiti: maximising access to treatment in a resource poor setting. *Sex Transm Infect.* 2006;82(2):175-181. doi:10.1136/sti.2005.016733.
 117. Hislop J, Quayyum Z, Flett G, Boachie C, Fraser C, Mowatt G. Systematic review of the clinical effectiveness and cost-effectiveness of rapid point-of-care tests for the detection of genital chlamydia infection in women and men. *Health Technol Assess.* 2010;14(29):1-97, iii-iv. doi:10.3310/hta14290.
 118. Howick J, Cals JWL, Jones C, et al. Current and future use of point-of-care tests in primary care: an international survey in Australia, Belgium, The Netherlands, the UK and the USA. *BMJ Open.* 2014;4(8):e005611. doi:10.1136/bmjopen-2014-005611.
 119. Moncada J, Chow JM, Schachter J. Volume Effect on Sensitivity of Nucleic Acid Amplification Tests for Detection of Chlamydia trachomatis in Urine Specimens from Females. *J Clin Microbiol.* 2003;41(10):4842-4843. doi:10.1128/JCM.41.10.4842-4843.2003.
 120. Alguacil J, Pfeiffer RM, Moore LE, et al. Measurement of urine pH for epidemiological studies on bladder cancer. *Eur J Epidemiol.* 2007;22(2):91-98. doi:10.1007/s10654-006-9101-2.
 121. Mccance RA, Young WF, Black DAK. The secretion of urine during dehydration and rehydration. *J Physiol.* 1944;102:415-428.
 122. Peeling RW, Mabey D. Point-of-care tests for diagnosing infections in the developing world. *Clin Microbiol Infect.* 2010;16(8):1062-1069. doi:10.1111/j.1469-0691.2010.03279.x.
 123. Heiniger EK, Buser JR, Mireles L, et al. Comparison of point-of-care-compatible lysis methods for bacteria and viruses. *J Microbiol Methods*2. 2016:Accepted.
 124. Kusuma CM, Kokai-kun JF, Sam S a. Comparison of Four Methods for Determining Lysostaphin Susceptibility of

- Various Strains of *Staphylococcus aureus*. *Society*. 2005;49(8):3256-3263. doi:10.1128/AAC.49.8.3256.
125. Salazar O, Asenjo J a. Enzymatic lysis of microbial cells. *Biotechnol Lett*. 2007;29(7):985-994. doi:10.1007/s10529-007-9345-2.
 126. Ota F, Kiso M, Fukui K. Lysis of *Streptococcus mutans* with achromopeptidase and release of osmotically fragile bodies. *Microbiol Immunol*. 1982;26(10):957-963.
 127. SigmaAldrich. Enzymatic Assay of Achromopeptidase. <http://www.sigmaaldrich.com/technical-documents/protocols/biology/enzymatic-assay-of-achromopeptidase.html>. Accessed May 18, 2015.
 128. Daniel RM, Dines M, Petach HH. The denaturation and degradation of stable enzymes at high temperatures. *Biochem J*. 1996;317 (Pt 1):1-11.
 129. Wang J, Yiu B, Obermeyer J, Filipe CDM, Brennan JD, Pelton R. Effects of temperature and relative humidity on the stability of paper-immobilized antibodies. *Biomacromolecules*. 2012;13(2):559-564. doi:10.1021/bm2017405.
 130. Zhu K, Jin H, Ma Y, et al. A continuous thermal lysis procedure for the large-scale preparation of plasmid DNA. *J Biotechnol*. 2005;118(3):257-264. doi:10.1016/j.jbiotec.2005.05.003.
 131. Chern EC, Siefiring S, Paar J, Doolittle M, Haugland R a. Comparison of quantitative PCR assays for *Escherichia coli* targeting ribosomal RNA and single copy genes. *Lett Appl Microbiol*. 2011;52:298-306. doi:10.1111/j.1472-765X.2010.03001.x.
 132. Hjelmevoll SO, Olsen ME, Sollid JUE, Haaheim H, Unemo M, Skogen V. A fast real-time polymerase chain reaction method for sensitive and specific detection of the *Neisseria gonorrhoeae* porA pseudogene. *J Mol Diagn*. 2006;8(5):574-581. doi:10.2353/jmoldx.2006.060024.
 133. Pickett MA, Everson JS, Pead PJ, Clarke IN. The plasmids of *Chlamydia trachomatis* and *Chlamydomydia pneumoniae* (N16): Accurate determination of copy number and the paradoxical effect of plasmid-curing agents. *Microbiology*. 2005;151(3):893-903. doi:10.1099/mic.0.27625-0.
 134. Putnam DF. *COMPOSITION AND CONCENTRATIVE ADMINISTRATION*.; 1971.
 135. SigmaAldrich. Buffer Reference Center. <http://www.sigmaaldrich.com/life-science/core-bioreagents/biological-buffers/learning-center/buffer-reference-center.html>. Accessed May 18, 2015.
 136. Good NE, Winget GD, Winter W, Connolly TN, Izawa S, Sing RMM. Hydrogen ion buffers for bifological Research. *Biochemistry*. 1966;5(2):467-477. doi:10.1021/bi00866a011.
 137. REACH Devices. "Biological buffers list with chemical structures and pKa calculator. <http://www.reachdevices.com/Protein/BiologicalBuffers.html>. Accessed June 8, 2015.
 138. Lafleur L, Bishop JD, Heiniger EK, et al. A rapid, instrument-free, sample-to-result nucleic acid amplification test. *Lab Chip*. 2016. doi:10.1039/C6LC00677A.
 139. Bishop J, Buser J, Byrnes S, et al. Sequential Delivery of Fluid Volumes and Associated Devices, Systems and Methods. 2014.
 140. Byrnes SA, Bishop JD, Lafleur L, Buser J, Lutz B, Yager P. One-step purification and concentration of DNA in porous membranes for point-of-care applications. *Lab Chip*. 2015;15(12):2647-2659. doi:10.1039/C5LC00317B.
 141. Rohrman B a, Leautaud V, Molyneux E, Richards-Kortum RR. A lateral flow assay for quantitative detection of amplified HIV-1 RNA. *PLoS One*. 2012;7(9):e45611. doi:10.1371/journal.pone.0045611.
 142. Zhang L, Zhang Y, Wang C, Feng Q, Fan F, Zhang G. An Integrated Microcapillary for Sample-to-Answer Nucleic Acid Pretreatment , Amplification and Detection An Integrated Microcapillary for Sample-to-Answer Nucleic Acid Pretreatment , Amplification and Detection. 2014. doi:10.1021/ac503072a.
 143. Gan W, Zhuang B, Zhang P, Han J, Li C, Liu P. A Filter Paper-Based Microdevice for Low-Cost, Rapid, and Automated DNA Extraction and Amplification from Diverse Sample Types. *Lab Chip*. 2014;14(19). doi:10.1039/C4LC00686K.
 144. Dame RT, Kalmykova OJ, Grainger DC. Chromosomal macrodomains and associated proteins: Implications for DNA organization and replication in gram negative bacteria. *PLoS Genet*. 2011;7(6). doi:10.1371/journal.pgen.1002123.
 145. Athale CA, Chaudhari H. Population length variability and nucleoid numbers in *Escherichia coli*. *Bioinformatics*. 2011;27(21):2944-2948. doi:10.1093/bioinformatics/btr501.
 146. Dorman CJ. Genome architecture and global gene regulation in bacteria: making progress towards a unified model? *Nat Rev Microbiol*. 2013;11(5):349-355. doi:10.1038/nrmicro3007.
 147. Zimmerman SB. Macromolecular crowding effects on macromolecular interactions: Some implications for genome structure and function. *BBA - Gene Struct Expr*. 1993;1216(2):175-185. doi:10.1016/0167-4781(93)90142-Z.
 148. Manasherob R, Zaritsky A, Metzler Y, Ben-Dov E, Itsko M, Fishov I. Compaction of the *Escherichia coli* nucleoid caused by Cyt1Aa. *Microbiology*. 2003;149(12):3553-3564. doi:10.1099/mic.0.26271-0.
 149. e!Ensembl. Human: *Homo sapiens*. http://uswest.ensembl.org/Homo_sapiens. Accessed October 17, 2016.
 150. Vashist SK, Lupp PB, Yeo LY, Ozcan A, Luong JHT. Emerging Technologies for Next-Generation Point-of-Care Testing. *Trends Biotechnol*. 2015. doi:10.1016/j.tibtech.2015.09.001.
 151. Jones K. FUSION 5: A New Platform for Lateral Flow Immunoassay Tests. In: *Lateral Flow Immunoassay*.; 2008:115-129. doi:10.1007/978-1-59745-240-3.

152. Smith SB, Aldridge PK, Callis JB. Observation of individual DNA molecules undergoing gel electrophoresis. *Science*. 1989;243(4888):203-206. <http://www.ncbi.nlm.nih.gov/pubmed/2911733>.
153. Zimm BH, San C, Jolla L. Mechanism of gel electrophoresis unexpected findings of DNA : :373-376.
154. Schwartz DC, Cantor CF. Separation of Yeast Chromosome-Sized DNAs by Pulsed Field Gradient Gel Electrophoresis. *Cell*. 1984;37:67-75.
155. Leonard RB, Carroll KC. Rapid lysis of gram-positive cocci for pulsed-field gel electrophoresis using achromopeptidase. *Diagn Mol Pathol*. 1997;6(5):288-291. doi:10.1097/00019606-199710000-00007.
156. Pernodet N, Tinland B, Sadron IC, Pasteur CL. Pore size of agarose gels by atomic force microscopy. *Electrophoresis*. 1997;18:55-58.
157. Wang X, Son A. Effects of pretreatment on the denaturation and fragmentation of genomic DNA for DNA hybridization. *Environ Sci Process Impacts*. 2013;15(12):2204-2212. doi:10.1039/c3em00457k.
158. Eigner J, Boedtke H, Michaels G. The thermal degradation of nucleic acids. *Biochim Biophys Acta*. 1961;51:165-168.
159. Doty P, Marmur J, Eigner J, Schildkraut C. Strand Separation and Specific Recombination in Deoxyribonucleic Acids : Physical Chemical Studies. *Proc Natl Acad Sci*. 1960;46(4):461-476.
160. Surzycki S. *Basic Techniques in Molecular Biology*. Springer; 2000.
161. Lentz YK, Worden LR, Anchordoquy TJ, Lengsfeld CS. Effect of jet nebulization on DNA: Identifying the dominant degradation mechanism and mitigation methods. *J Aerosol Sci*. 2005;36(8):973-990. doi:10.1016/j.jaerosci.2004.11.017.
162. Tseng Q, Lomonosov AM, Furlong EEM, Merten C a. Fragmentation of DNA in a sub-microliter microfluidic sonication device. *Lab Chip*. 2012;12(22):4677. doi:10.1039/c2lc40595d.
163. Larginho M, Santos HM, Doria G, Scholz H, Baptista P V., Capelo JL. Development of a fast and efficient ultrasonic-based strategy for DNA fragmentation. *Talanta*. 2010;81:881-886. doi:10.1016/j.talanta.2010.01.032.
164. Meyer M, Stenzel U, Hofreiter M. Parallel tagged sequencing on the 454 platform. *Nat Protoc*. 2008;3(2):267-278. doi:10.1038/nprot.2007.520.
165. Avery OT, MacLeod CM, McCarty M. Studies on the chemical nature of the substance inducing transformation of pneumococcal types. *J Exp Med*. 1944;79(6):137-158. doi:10.1084/jem.79.2.137.
166. New England Biolabs. EcoRI. <https://www.neb.com/products/r0101-ecori>. Accessed May 28, 2015.
167. SigmaAldrich. Enzyme Explorer - Learning Center: Nucleases for DNA and RNA Digestion. <http://www.sigmaaldrich.com/life-science/metabolomics/enzyme-explorer/learning-center/nucleases.html>. Accessed May 28, 2015.
168. New England Biolabs. NEBNext dsDNA Fragmentase. <https://www.neb.com/applications/library-preparation-for-next-generation-sequencing/dna-fragmentation/nebnext-dsna-fragmentase>. Accessed May 28, 2015.
169. Counis MF, Torriglia a. DNases and apoptosis. *Biochem Cell Biol*. 2000;78(4):405-414. doi:10.1139/o00-051.
170. Kunitz M. Crystalline desoxyribonuclease II. digestion of thymus nucleic acid. *J Gen Physiol*. 1950:363-377.
171. Kunitz M. Crystalline desoxyribonuclease I. Isolation and general properties. *J Gen Physiol*. 1950:349-362.
172. Evans CJ, Aguilera RJ. DNase II: Genes, enzymes and function. *Gene*. 2003;322(1-2):1-15. doi:10.1016/j.gene.2003.08.022.
173. Yang Q, Xu J, Qian X, Zhang K, Lei X. Eliminating nucleic acids contaminants by hydrogen peroxide-induced free radicals during the preparation of proteins. *Biochem Eng J*. 2006;29(1-2):23-26. doi:10.1016/j.bej.2005.02.022.
174. Bai H, Konat GW. Hydrogen peroxide mediates higher order chromatin degradation. *Neurochem Int*. 2003;42(2):123-129. doi:10.1016/S0197-0186(02)00072-4.
175. Prousek J. Fenton chemistry in biology and medicine. *Pure Appl Chem*. 2007;79(12):2325-2338. doi:10.1351/pac200779122325.
176. Goldstein S, Meyerstein D. Comments on the mechanism of the "Fenton like" reaction. *Acc Chem Res*. 1999;32(7):547-550. doi:10.1021/ar9800789.
177. Hakenberg S, Hügler M, Meyer P, Behrmann O, Dame G, Urban G a. Fenton fragmentation for faster electrophoretic on chip purification of amplifiable genomic DNA. *Biosens Bioelectron*. 2014;67:49-52. doi:10.1016/j.bios.2014.06.003.
178. Papavassiliou AG. Chemical nucleases as probes for studying DNA-protein interactions. *Biochem J*. 1995;305:345-357.
179. Suzuki T, Ohsumi S, Makino K. Mechanistic studies on depurination and apurinic site chain breakage in oligodeoxyribonucleotides. *Nucleic Acids Res*. 1994;22(23):4997-5003. doi:10.1093/nar/22.23.4997.
180. Marguet E, Forterre P. DNA stability at temperatures typical for hyperthermophiles. *Nucleic Acids Res*. 1994;22(9):1681-1686. doi:10.1093/nar/22.9.1681.
181. Lindahl T, Nyberg B. Rate of depurination of native deoxyribonucleic acid. *Biochemistry*. 1972;11(19):3610-3618. doi:10.1021/bi00769a018.
182. Gol'dshtein BI, Gerasimova V V. Denaturation and fragmentation of DNA in cells of the animal organism. *Ukrayins'kyi Biokhimichnyi Zhurnal*. 1963;35(1):T821-T826.
183. Antoku S. DNA Single-Strand Breaks of Prehated Cultured Mammalian Cells Irradiated under Nitrogen- and Nitrous

- Oxide-Saturated Conditions. *Radiat Res.* 1977;682:678-682.
184. Jorritsma JBM, Konings AWT. The Occurrence of DNA Strand Breaks after Hyperthermic Treatments of Mammalian Cells with and without Radiation. *Radiat Res.* 1984;98:198-208.
185. Ginoza W, Zimm BH. Mechanisms of inactivation of deoxyribonucleic acids by heat. *Biochemistry.* 1961;47:639-652.
186. Hoff AJ. On the degradation of DNA by Heat. *Proc K Ned Akad van Wet.* 1971;74(2):167-171.
187. Eigner J, Doty P. The native, denatured and renatured states of deoxyribonucleic acid. *J Mol Biol.* 1965;12(3):549-580. doi:10.1016/S0022-2836(65)80312-6.
188. Freese EB, Freese E. The Rate of DNA Strand Separation. *Biochemistry.* 1963;2(4):707-715.
189. Alvarez-Estrada GFC and RF. The time duration for DNA thermal denaturation. *J Phys Condens Matter.* 2008;20(3):35101. doi:10.1088/0953-8984/20/03/035101.
190. Liu Y-G, Whittier RF. Rapid preparation of megabase plant DNA from nuclei in agarose plugs and microbeads. *Nucleic Acids Res.* 1994;22(11):2168-2169.
191. Barton BM, Harding GP, Zuccarelli AJ. A General Method for Detecting and Sizing Large Plasmids. *Anal Biochem.* 1995;226:235-240.
192. Zhang H-B, Zhao X, Ding X, Paterson AH, Wing RA. Preparation of megabase-size DNA from plant nuclei. *Plant J.* 1995;7(1):175-184.
193. Cell Biolabs Inc. Comet Assay Kits. <http://www.cellbiolabs.com/comet-assay-kits-3-well>. Accessed May 27, 2015.
194. Ostling O, Johanson KJ. Microelectrophoretic study of radiation-induced DNA damages in individual mammalian cells. *Biochem Biophys Res Commun.* 1984;123(1):291-298. doi:10.1016/0006-291X(84)90411-X.
195. Singh NP, McCoy MT, Tice RR, Schneider EL. A simple technique for quantitation of low levels of DNA damage in individual cells. *Exp Cell Res.* 1988;175(1):184-191. doi:10.1016/0014-4827(88)90265-0.
196. Speyer BE, Pizzey a. R, Ranieri M, Joshi R, Delhanty JD a, Serhal P. Fall in implantation rates following ICSI with sperm with high DNA fragmentation. *Hum Reprod.* 2010;25(7):1609-1618. doi:10.1093/humrep/deq116.
197. Shamsi MB, Kumar R, Dada R. Evaluation of nuclear DNA damage in human spermatozoa in men opting for assisted reproduction. *Indian J Med Res.* 2008;127(2):115-123.
198. Bafana A, Jain M, Agrawal G, Chakrabarti T. Bacterial reduction in genotoxicity of Direct Red 28 dye. *Chemosphere.* 2009;74(10):1404-1406. doi:10.1016/j.chemosphere.2008.11.043.
199. Solanky D, Haydel SE. Adaptation of the neutral bacterial comet assay to assess antimicrobial-mediated DNA double-strand breaks in Escherichia coli. *J Microbiol Methods.* 2012;91(2):257-261. doi:10.1016/j.mimet.2012.08.009.
200. Singh NP, Stephens RE, Singh H, Lai H. Visual quantification of DNA double-strand breaks in bacteria. *Mutat Res - Fundam Mol Mech Mutagen.* 1999;429(2):159-168. doi:10.1016/S0027-5107(99)00124-4.
201. Gavrieli Y, Sherman Y, Ben-Sasson S. Identification of Programmed Cell Death In Situ via Specific Labeling of Nuclear DNA Fragmentation. *J Cell Biol.* 1992;119(3):493-501. <http://jcb.rupress.org/content/119/3/493.short>.
202. Lee W, Kim K-J, Lee DG. A novel mechanism for the antibacterial effect of silver nanoparticles on Escherichia coli. *Biometals.* 2014;1191-1201. doi:10.1007/s10534-014-9782-z.
203. Lee W, Lee DG. Magainin 2 Induces Bacterial Cell Death Showing Apoptotic Properties. *Curr Microbiol.* 2014;69(6):794-801. doi:10.1007/s00284-014-0657-x.
204. Pérez-Cerezales S, Miranda A, Gutiérrez-Adán A. Comparison of four methods to evaluate sperm DNA integrity between mouse caput and cauda epididymidis. *Asian J Androl.* 2012;14(2):335-337. doi:10.1038/aja.2011.119.
205. UVM Genetics & Genomics Wiki. Pulsed Field Gel Electrophoresis. http://uvmgg.wikia.com/wiki/Pulsed_Field_Gel_Electrophoresis. Accessed May 27, 2015.
206. BioRad. Pulsed Field Gel Electrophoresis Systems. 2015:2015. <http://www.bio-rad.com/en-us/category/pulsed-field-gel-electrophoresis-systems>.
207. Material O, Functions F. FUSION 5™ One Material , Five Functions For the first time , all the functions of a lateral. 5.
208. Life Technologies. DNase I, Amplification Grade. <https://www.lifetechnologies.com/order/catalog/product/18068015>. Accessed June 7, 2015.
209. Bioline. Proteinase K. http://www.bioline.com/us/downloads/dl/file/id/2782/proteinase_k_product_manual.pdf. Accessed June 28, 2016.
210. Steube KG, Meyer C, Uphoff CC, Drexler HG. A SIMPLE METHOD USING BETA-GLOBIN POLYMERASE CHAIN REACTION FOR THE SPECIES IDENTIFICATION OF ANIMAL CELL LINES - A PROGRESS REPORT. *Vitr Celluar Dev Biol.* 2003;(December):468-475.
211. Buser J, Zhang X, Byrnes S, et al. A disposable chemical heater and dry enzyme preparation for lysis and extraction of DNA and RNA from microorganisms. *Anal Methods.* 2016;8(14):2880-2886. doi:10.1039/C6AY00107F.
212. Kim D, Herr AE. Protein immobilization techniques for microfluidic assays Advertisement : Protein immobilization techniques for microfluidic assays. *Biomicrofluidics.* 2013;41501:1-47. doi:10.1063/1.4816934.
213. Qiagen. RNeasy Mini Handbook. 2012;(June).
214. Altshuler ML. *PCR Troubleshooting: The Essential Guide*. Caister Academic Press; 2006.

215. Breadmore MC, Wolfe K a, Arcibal IG, et al. Microchip-based purification of DNA from biological samples. *Anal Chem.* 2003;75(8):1880-1886. <http://www.ncbi.nlm.nih.gov/pubmed/12713046>.
216. Wu Q, Bienvenue JM, Hassan BJ, et al. Microchip-based macroporous silica sol-gel monolith for efficient isolation of DNA from clinical samples. *Anal Chem.* 2006;78(16):5704-5710. doi:10.1021/ac060390t.
217. Tian H, Hühmer a F, Landers JP. Evaluation of silica resins for direct and efficient extraction of DNA from complex biological matrices in a miniaturized format. *Anal Biochem.* 2000;283(2):175-191. doi:10.1006/abio.2000.4577.
218. Wen J, Guillo C, Ferrance JP, Landers JP. DNA Extraction Using a Tetramethyl Orthosilicate-Grafted Photopolymerized Monolithic Solid Phase. *Anal Chem.* 2006;78(5):1673-1681. doi:10.1021/ac051796t.
219. Bhattacharyya A, Klapperich CM. Thermoplastic microfluidic device for on-chip purification of nucleic acids for disposable diagnostics. *Anal Chem.* 2006;78(3):788-792. doi:10.1021/ac051449j.
220. Reedy CR, Hagan K a, Strachan BC, et al. Dual-domain microchip-based process for volume reduction solid phase extraction of nucleic acids from dilute, large volume biological samples. *Anal Chem.* 2010;82(13):5669-5678. doi:10.1021/ac100649b.
221. Hagan K a, Meier WL, Ferrance JP, Landers JP. Chitosan-Coated Silica as a Solid Phase for RNA Purification in a Microfluidic Device. *Anal Chem.* 2009;81(13):8453-8460. doi:10.1021/ac900820z.
222. Hagan K a, Reedy CR, Uchimoto ML, et al. An integrated , valveless system for microfluidic purification and reverse transcription-PCR amplification of RNA for detection of infectious agents †. *Lab Chip.* 2011;11(5):957-961. doi:10.1039/c0lc00136h.
223. Danielsen S, Vårum KM, Stokke BT. Structural analysis of chitosan mediated DNA condensation by AFM: influence of chitosan molecular parameters. *Biomacromolecules.* 2004;5(3):928-936. doi:10.1021/bm034502r.
224. Alatorre-meda M, Taboada P, Hartl F, Wagner T, Freis M, Rodríguez JR. Colloids and Surfaces B : Biointerfaces The influence of chitosan valence on the complexation and transfection of DNA : The weaker the DNA – chitosan binding the higher the transfection efficiency. *Colloids Surfaces B Biointerfaces.* 2011;82:54-62. doi:10.1016/j.colsurfb.2010.08.013.
225. Prevetle LE, Kodger TE, Reineke TM, Lynch ML. Deciphering the role of hydrogen bonding in enhancing pDNA-polycation interactions. *Langmuir.* 2007;23(19):9773-9784. doi:10.1021/la7009995.
226. Maurstad G, Danielsen S, Stokke BT. The influence of charge density of chitosan in the compaction of the polyanions DNA and xanthan. *Biomacromolecules.* 2007;8(4):1124-1130. doi:10.1021/bm0610119.
227. Decher G. Fuzzy Nanoassemblies: Toward Layered Polymeric Multicomposites. *Science (80-).* 1997;277(5330):1232-1237.
228. Díez-Pascual A, Shuttleworth P. Layer-by-Layer Assembly of Biopolyelectrolytes onto Thermo/pH-Responsive Micro/Nano-Gels. *Materials (Basel).* 2014;7:7472-7512. doi:10.3390/ma7117472.
229. Dharmaraja S, Lafleur L, Byrnes S, et al. Programming paper networks for point of care diagnostics. *Proc SPIE, 8615, Microfluid BioMEMS, Med Microsystems XI.* 2013. doi:10.1117/12.2006138.
230. Panpradist N, Toley BJ, Zhang X, et al. Swab sample transfer for point-of-care diagnostics: characterization of swab types and manual agitation methods. *PLoS One.* 2014;9(9):e105786. doi:10.1371/journal.pone.0105786.
231. Eckerskorn C, Lottspeich F. Structural characterization of blotting membranes and the influence of membrane parameters for electroblotting and subsequent amino acid sequence analysis of proteins. *Electrophoresis.* 1993;14:831-838.
232. Millipore. Rapid Lateral Flow Test Strips.
233. Edelstein A, Amodaj N, Hoover K, Vale R, Stuurman N. Computer control of microscopes using µManager. *Curr Protoc Mol Biol.* 2010;Chapter 14(October):Unit14.20. doi:10.1002/0471142727.mb1420s92.
234. Abràmoff MD, Hospitals I, Magalhães PJ, Abràmoff M. Image Processing with ImageJ. *Biophotonics Int.* 2004.
235. Strand SP, Danielsen S, Christensen BE, Vårum KM. Influence of Chitosan Structure on the Formation and Stability of DNA- Chitosan Polyelectrolyte Complexes. *Biomacromolecules.* 2005;6(6):3357–3366. <http://pubs.acs.org/doi/abs/10.1021/bm0503726>.
236. Ma PL, Lavertu M, Winnik FM, Buschmann MD. New insights into chitosan-DNA interactions using isothermal titration microcalorimetry. *Biomacromolecules.* 2009;10(6):1490-1499. doi:10.1021/bm900097s.
237. Buschmann MD, Merzouki A, Lavertu M, Thibault M, Jean M, Darras V. Chitosans for delivery of nucleic acids. *Adv Drug Deliv Rev.* 2013;65(9):1234-1270. doi:10.1016/j.addr.2013.07.005.
238. Moriyama R, Shimada N, Kano A, Maruyama A. DNA assembly and re-assembly activated by cationic comb-type copolymer. *Biomaterials.* 2011;32(9):2351-2358. doi:10.1016/j.biomaterials.2010.11.064.
239. Wang Y, Wang J, Yang F, Yang X. Probing biomolecular interactions with dual polarization interferometry: real-time and label-free coralyne detection by use of homo adenine DNA oligonucleotide. *Anal Chem.* 2012;84(2):924-930. doi:10.1021/ac2019443.
240. Towner JS, Rollin PE, Bausch DG, et al. Rapid Diagnosis of Ebola Hemorrhagic Fever by Reverse Transcription-PCR in an Outbreak Setting and Assessment of Patient Viral Load as a Predictor of Outcome Rapid Diagnosis of Ebola

- Hemorrhagic Fever by Reverse Transcription-PCR in an Outbreak Setting an. *J Virol.* 2004;78(8):4330-4341. doi:10.1128/JVI.78.8.4330.
241. Wright PF, Neumann G, Kawaoka Y. Orthomyxoviruses. In: *Fields Virology.*; 1985:1692-1740.
242. Hollingsworth M a, Swanson BJ. Mucins in cancer: protection and control of the cell surface. *Nat Rev Cancer.* 2004;4(1):45-60. doi:10.1038/nrc1251.
243. Akane a, Matsubara K, Nakamura H, Takahashi S, Kimura K. Identification of the heme compound copurified with deoxyribonucleic acid (DNA) from bloodstains, a major inhibitor of polymerase chain reaction (PCR) amplification. *J Forensic Sci.* 1994;39(2):362-372. <http://www.ncbi.nlm.nih.gov/pubmed/8195750>.
244. Byrnes SA, Bishop JD, Lafleur L, Buser J, Lutz B, Yager P. One-step purification and concentration of DNA in porous membranes for point-of-care applications. *Lab Chip.* 2015;15:2647-2659. doi:10.1039/C5LC00317B.
245. Lindman S, Xue W-F, Szczepankiewicz O, Bauer MC, Nilsson H, Linse S. Salting the charged surface: pH and salt dependence of protein G B1 stability. *Biophys J.* 2006;90(8):2911-2921. doi:10.1529/biophysj.105.071050.
246. Debye P. The theory of electrolytes I. The lowering of the freezing point and related occurrences. *Phys Zeitschrift.* 1923;24:185-206.
247. Ullner M, Langevin D. Debye-Huckel Theory. In: Dias R, Lindman B, eds. *DNA Interactions with Polymers and Surfactants.* Hoboken, New Jersey: John Wiley & Sons, Inc.; 2008:9-10, 266-267.
248. Cuervo a., Dans PD, Carrascosa JL, Orozco M, Gomila G, Fumagalli L. Direct measurement of the dielectric polarization properties of DNA. *Proc Natl Acad Sci.* 2014:E3624-E3630. doi:10.1073/pnas.1405702111.
249. The Engineering ToolBox. Relative Permittivity - Dielectric Constant. http://www.engineeringtoolbox.com/relative-permittivity-d_1660.html. Accessed June 18, 2015.
250. Malmberg CG, Maryott A a. Dielectric constant of water from 0 to 100 C. *J Res Natl Bur Stand (1934).* 1956;56(1):1-8. doi:10.6028/jres.056.001.
251. Kayitmazer a. B, Shaw D, Dubin PL. Role of Polyelectrolyte Persistence Length in the Binding of Oppositely Charged Micelles, Dendrimers, and Protein to Chitosan and Poly(dimethyldiallylammonium chloride). *Macromolecules.* 2005;38(12):5198-5204. doi:10.1021/ma050328i.
252. Ou Z, Muthukumar M. Entropy and enthalpy of polyelectrolyte complexation: Langevin dynamics simulations. *J Chem Phys.* 2006;124(15):154902. doi:10.1063/1.2178803.
253. Ziebarth JD, Wang Y. Understanding the protonation behavior of linear polyethylenimine in solutions through Monte Carlo simulations. *Biomacromolecules.* 2010;11(1):1-29. doi:10.1021/bm900842d.Understanding.
254. Ziebarth J, Wang Y. Molecular dynamics simulations of DNA-polycation complex formation. *Biophys J.* 2009;97(7):1971-1983. doi:10.1016/j.bpj.2009.03.069.
255. Choosakoonkriang S, Lobo B a, Koe GS, Koe JG, Middaugh CR. Biophysical Characterization of PEI / DNA Complexes. *Russell J Bertrand Russell Arch.* 2003;92(8):1710-1722. file:///C:/Users/Rachel/Documents/Minnesota Research/Literature/10437_ftp.pdf.
256. Dos A, Schimming V, Huot MC. Acid-Induced Amino Side-Chain Interactions and Secondary Structure of Solid Poly- L-lysine Probed by 15 N and 13 C Solid State NMR and ab Initio Model Calculations. *J Phys Chem B.* 2008;112:15604-15615.
257. Causer LM, Hengel B, Natoli L, et al. A field evaluation of a new molecular-based point-of-care test for chlamydia and gonorrhea in remote Aboriginal health services in Australia. *Sex Health.* 2015;12:27-33.
258. Noh H, Phillips ST. Fluidic timers for time-dependent, point-of-care assays on paper. *Anal Chem.* 2010;82(19):8071-8078. doi:10.1021/ac1005537.
259. Noh H, Phillips ST. Metering the capillary-driven flow of fluids in paper-based microfluidic devices. *Anal Chem.* 2010;82(10):4181-4187. doi:10.1021/ac100431y.
260. Lutz B, Liang T, Fu E, Ramachandran S, Kauffman P, Yager P. Dissolvable fluidic time delays for programming multi-step assays in instrument-free paper diagnostics. *Lab Chip.* 2013;13(14):2840-2847. doi:10.1039/c3lc50178g.
261. Osborn JL, Lutz B, Fu E, Kauffman P, Stevens DY, Yager P. Microfluidics without pumps: reinventing the T-sensor and H-filter in paper networks. *Lab Chip.* 2010;10(20):2659-2665. doi:10.1039/c004821f.
262. Kauffman P, Fu E, Lutz B, Yager P. Visualization and measurement of flow in two-dimensional paper networks. *Lab Chip.* 2010;10(19):2614-2617. doi:10.1039/c004766j.
263. Chen H, Cogswell J, Anagnostopoulos C, Faghri M. A fluidic diode, valves, and a sequential-loading circuit fabricated on layered paper. *Lab Chip.* 2012;12(16):2909. doi:10.1039/c2lc20970e.
264. An SF, Fleming K a. Removal of inhibitor(s) of the polymerase chain reaction from formalin fixed, paraffin wax embedded tissues. *J Clin Pathol.* 1991;44(11):924-927. doi:10.1136/jcp.44.11.924.
265. Al-soud WA, Rådström P. Purification and Characterization of PCR-Inhibitory Components in Blood Cells Purification and Characterization of PCR-Inhibitory Components in Blood Cells. *J Clin Microbiol.* 2001;39(2):485-493. doi:10.1128/JCM.39.2.485.
266. Schrader C, Schielke a., Ellerbroek L, John R. PCR inhibitors - occurrence, properties and removal. *J Appl Microbiol.*

- 2012;113:1014-1026. doi:10.1111/j.1365-2672.2012.05384.x.
267. Toley BJ, Wang J a., Gupta M, et al. A versatile valving toolkit for automating fluidic operations in paper microfluidic devices. *Lab Chip*. 2015;15:1432-1444. doi:10.1039/C4LC01155D.
268. Srinivasan B, Tung S. Development and Applications of Portable Biosensors. *J Lab Autom*. 2015;20(4):365-389. doi:10.1177/2211068215581349.
269. Ahmed S, Bui MPN, Abbas A. Paper-based chemical and biological sensors: Engineering aspects. *Biosens Bioelectron*. 2016;77:249-263. doi:10.1016/j.bios.2015.09.038.
270. He Y, Wu Y, Fu JZ, Wu WB. Fabrication of paper-based microfluidic analysis devices: a review. *Rsc Adv*. 2015;5(95):78109-78127. doi:10.1039/c5ra09188h.
271. Borysiak MD, Kimura KW, Posner JD. NAII: Nucleic Acid detection using Isotachophoresis and Loop-mediated isothermal amplification. *Lab Chip*. 2015;15:1697-1707. doi:10.1039/C4LC01479K.
272. Bercovici M, Kaigala G V, Liao JC, Santiago JG. Rapid and High Sensitivity Detection of Urinary Tract Infections Using Isotachophoresis. *Anal Chem*. 2011;83:4110-4117.
273. Darcy H. *Les Fontaines Publiques la V Dijon*. 1856.
274. Whitaker S. Flow in porous media I: A theoretical derivatio of Darcy's Law. *Transp Porous Media*. 1986;1(1):3-25.
275. Washburn E. The Dynamics of Capillary Flow. *Phys Rev*. 1921;XVII(3):273-283.
276. Mendez S, Fenton EM, Gallegos GR, et al. Imbibition in porous membranes of complex shape: quasi-stationary flow in thin rectangular segments. *Langmuir*. 2010;26(2):1380-1385. doi:10.1021/la902470b.
277. Fu E, Ramsey S a., Kauffman P, Lutz B, Yager P. Transport in two-dimensional paper networks. *Microfluid Nanofluidics*. 2010;10(1):29-35. doi:10.1007/s10404-010-0643-y.
278. Zakher B, Cantor AG, Pappas M, Daeges M, Nelson HD. Screening for Gonorrhea and Chlamydia: A Systematic Review for the U.S. Preventive Services Task Force. *Ann Intern Med*. 2014;161(6):884. doi:10.7326/M14-1022.
279. Pantoja A, Fitzpatrick C, Vassall A, Weyer K, Floyd K. Xpert MTB/RIF for diagnosis of tuberculosis and drug-resistant tuberculosis: A cost and affordability analysis. *Eur Respir J*. 2013;42(3):708-720. doi:10.1183/09031936.00147912.
280. Gaydos C a., Crotchfelt K a., Shah N, et al. Evaluation of dry and wet transported intravaginal swabs in detection of Chlamydia trachomatis and Neisseria gonorrhoeae infections in female soldiers by PCR. *J Clin Microbiol*. 2002;40(3):758-761. doi:10.1128/JCM.40.3.758-761.2002.
281. Lowe P, O''Loughlin P, Evans K, White M, Bartley PB, Vohra R. Comparison of the Gen-Probe APTIMA Combo 2 assay to the AMPLICOR CT/NG assay for detection of Chlamydia trachomatis and Neisseria gonorrhoeae in urine samples from Australian men and women. *J Clin Microbiol*. 2006;44(7):2619-2621. doi:10.1128/JCM.00476-06.
282. Storm M, Gustafsson I, Herrmann B, Engstrand L. Real-time PCR for pharmacodynamic studies of Chlamydia trachomatis. *J Microbiol Methods*. 2005;61(3):361-367. doi:10.1016/j.mimet.2004.12.015.
283. Wilson IG a NG, Wilson IG a NG. Inhibition and Facilitation of Nucleic Acid Amplification Inhibition and Facilitation of Nucleic Acid Amplification. *Appl Environ Microbiol*. 1997;63(10):3741-3751.
284. Berg ES, Ånestad G, Moi H, Størvoold G, Skaug K. False-negative results of a ligase chain reaction assay to detect Chlamydia trachomatis due to inhibitors in urine. *Eur J Clin Microbiol Infect Dis*. 1997;16(10):727-731. doi:10.1007/BF01709252.
285. Mercier B, Gaucher C, Feugeas O, Mazurier C. Direct PCR from whole blood, without DNA extraction. *Nucleic Acids Res*. 1990;18(19):5908.
286. Al-Soud WA, Jönsson LJ, Rådström P. Identification and characterization of immunoglobulin G in blood as a major inhibitor of diagnostic PCR. *J Clin Microbiol*. 2000;38(1):345-350.
287. Satsangi J, Jewell DP, Welsh K, Bunce M, Bell JI. Effect of heparin on polymerase chain reaction. *Lancet*. 1994;343:1509-1510. doi:10.1016/S0140-6736(94)92622-0.
288. Opel KL, Chung D, McCord BR. A study of PCR inhibition mechanisms using real time PCR. *J Forensic Sci*. 2010;55(1):25-33. doi:10.1111/j.1556-4029.2009.01245.x.
289. Rossen L, Nørskov P, Holmstrom K, Rasmussen OF. Inhibition of PCR by components of food samples, microbial diagnostic assays and DNA-extraction solutions. *Int J Food Microbiol*. 1992;17:37-45. doi:10.1016/0168-1605(92)90017-W.
290. Adlerova L, Bartoskova a., Faldyna M. Lactoferrin: A review. *Vet Med (Praha)*. 2008;53(7):457-468.
291. Jenssen H, Hancock REW. Antimicrobial properties of lactoferrin. *Biochimie*. 2009;91:19-29. doi:10.1016/j.biochi.2008.05.015.
292. He J, Furmanski P. Sequence specificity and transcriptional activation in the binding of lactoferrin to DNA. *Nature*. 1995;373:721-724. doi:10.1038/373721a0.
293. Khan G, Kangro HO, Coates PJ, Heath RB. Inhibitory effects of urine on the polymerase chain reaction for cytomegalovirus DNA. *J Clin Pathol*. 1991;44(Cmv):360-365. doi:10.1136/jcp.44.5.360.
294. Hu Q, Liu Y, Yi S, Huang D. A comparison of four methods for PCR inhibitor removal. *Forensic Sci Int Genet*. 2015;16:94-97. doi:10.1016/j.fsigen.2014.12.001.

295. Mahony J, Chong S, Jang D, et al. Urine specimens from pregnant and nonpregnant women inhibitory to amplification of Chlamydia trachomatis nucleic acid by PCR, ligase chain reaction, and transcription-mediated amplification: Identification of urinary substances associated with inhibition. *J Clin Microbiol.* 1998;36(11):3122-3126.
296. Zhang Z, Kermekchiev MB, Barnes WM. Direct DNA amplification from crude clinical samples using a PCR enhancer cocktail and novel mutants of Taq. *J Mol Diagn.* 2010;12(2):152-161. doi:10.2353/jmoldx.2010.090070.
297. Taylor BJ, Martin K a, Arango E, Agudelo OM, Maestre A, Yanow SK. Real-time PCR detection of Plasmodium directly from whole blood and filter paper samples. *Malar J.* 2011;10(1):244. doi:10.1186/1475-2875-10-244.
298. Tian L, Cronin T, Weizmann Y. Enhancing-Effect of Gold Nanoparticles on DNA Strand Displacement Amplifications and its Application to an Isothermal Telomerase Assay. *Chem Sci.* 2014;5(11):4153-4162. doi:10.1039/C4SC01393J.
299. Nixon G, Garson J a, Grant P, Nastouli E, Foy C a, Huggett JF. Comparative Study of Sensitivity, Linearity, and Resistance to Inhibition of Digital and Nondigital Polymerase Chain Reaction and Loop Mediated Amplification Assays for Quantification of Human Cytomegalovirus. *Anal Chem.* 2014;86:4387-4394.
300. Zhang G, Brown EW, González-Escalona N. Comparison of real-time PCR, reverse transcriptase real-time PCR, loop-mediated isothermal amplification, and the FDA conventional microbiological method for the detection of Salmonella spp. in produce. *Appl Environ Microbiol.* 2011;77(18):6495-6501. doi:10.1128/AEM.00520-11.
301. Curtis K a., Rudolph DL, Owen SM. Rapid detection of HIV-1 by reverse-transcription, loop-mediated isothermal amplification (RT-LAMP). *J Virol Methods.* 2008;151:264-270. doi:10.1016/j.jviromet.2008.04.011.
302. Curtis KA, Rudolph, Donna L, Owen SM. Sequence-Specific Detection Method for Reverse Transcription, Loop-Mediated Isothermal Amplification of HIV-1. *J Med Virol.* 2009;81:966-972. doi:10.1002/jmv.
303. Belousov YS, Alabeyev B, Scarr N. Methods for true isothermal strand displacement amplification. 2014.
304. Source BioScience. DNA Extraction. <http://www.lifesciences.sourcebioscience.com/genomic-services/faq/dna-extraction/>. Accessed June 16, 2015.
305. Dicken Weatherby, Scott Ferguson, Dicken Weatherby SF. *Blood Chemistry and CBC Analysis.*; 2004.
306. Gohda T, Walker WH, Wolkow P, et al. Elevated urinary excretion of immunoglobulins in nonproteinuric patients with type 1 diabetes. *AJP Ren Physiol.* 2012;303(1):F157-F162. doi:10.1152/ajprenal.00443.2011.
307. Pan Y, Sonn G a., Sin MLY, et al. Electrochemical immunosensor detection of urinary lactoferrin in clinical samples for urinary tract infection diagnosis. *Biosens Bioelectron.* 2010;26(2):649-654. doi:10.1016/j.bios.2010.07.002.
308. Mullo J, Raphael GD, Lundgren JD, et al. Comparison of human nasal mucosal secretion in vivo and in vitro. *J Allergy Clin Immunol.* 1992;89(2):584-592.
309. Kim C-H, Song KS, Koo JS, et al. IL-13 suppresses MUC5AC gene expression and mucin secretion in nasal epithelial cells. *Acta Otolaryngol.* 2002;122(6):638-643. doi:10.1080/000164802320396321.
310. Polymerase chain reaction. *Wikimedia Commons.* 2015:Figure 2. http://commons.wikimedia.org/wiki/File:Polymerase_chain_reaction.svg. Accessed May 16, 2015.
311. Ellis RJ. Macromolecular crowding: Obvious but underappreciated. *Trends Biochem Sci.* 2001;26(10):597-604. doi:10.1016/S0968-0004(01)01938-7.
312. Ballantyne KN, van Oorschot R a H, John Mitchell R, Koukoulas I. Molecular crowding increases the amplification success of multiple displacement amplification and short tandem repeat genotyping. *Anal Biochem.* 2006;355(2):298-303. doi:10.1016/j.ab.2006.04.039.
313. Sasaki Y, Miyoshi D, Sugimoto N. Effect of molecular crowding on DNA polymerase activity. *Biotechnol J.* 2006;1(4):440-446. doi:10.1002/biot.200500032.
314. Fei J, Ha T. Watching DNA Breathe One Molecule at a Time. *Proc Natl Acad Sci U S A.* 2013;110(43):17173-17174. doi:10.1073/pnas.1316493110.
315. Ando BT, Takagi JUN, Kosawa T. Isolation and Characterization of Enzymes with Nicking Action from Phage T4-infected Escherichia coli. *J Biochem.* 1969;66(1):1-10.
316. Odell JA, Keller A. Flow-Induced Chain Fracture of Isolated Linear Macromolecules in Solution. *J Polym Sci B Polym Phys.* 1986;24(9):1889-1916.
317. Narh KA, Odell JA, Mueller AJ, Keller A. Polymer-Solution Degradation - the Combined Effects of Flow and Temperature. *Polym Commun.* 1990;31(1):2-5.
318. Sasaki N, Maki Y, Nakata M. Elongation flow studies of DNA as a function of temperature. *J Appl Polym Sci.* 2001;83(6):1357-1365. doi:10.1002/app.10015.
319. Brockman C, Kim SJ, Schroeder CM. Direct observation of single flexible polymers using single stranded DNA. *Soft Matter.* 2011;7(18):8005. doi:10.1039/c1sm05297g.
320. Choi HJ, Lim ST, Lai P-Y, Chan CK. Turbulent drag reduction and degradation of DNA. *Phys Rev Lett.* 2002;89(8):88302. doi:10.1103/PhysRevLett.89.088302.
321. Noiphung J, Talalak K, Hongwarittorn I, Pupinyo N, Thirabowonkitphithan P, Laiwattanapaisal W. A novel paper-based assay for the simultaneous determination of Rh typing and forward and reverse ABO blood groups. *Biosens Bioelectron.* 2015;67:485-489. doi:10.1016/j.bios.2014.09.011.

322. Songjaroen T, Laiwattanapaisal W. Simultaneous forward and reverse ABO blood group typing using a paper-based device and barcode-like interpretation. *Anal Chim Acta*. 2015;921. doi:10.1016/j.aca.2016.03.047.
323. R Core Development Team. R: A language and environment for statistical computing. 2008. <http://www.r-project.org>.
324. Atkinson A.J. J, Colburn WA, DeGruttola VG, et al. Biomarkers and surrogate endpoints: Preferred definitions and conceptual framework. *Clin Pharmacol Ther*. 2001;69(3):89-95. doi:10.1067/mcp.2001.113989.
325. Zhao X, Modur V, Carayannopoulos LN, Laterza OF. Biomarkers in pharmaceutical research. *Clin Chem*. 2015;61(11):1343-1353. doi:10.1373/clinchem.2014.231712.
326. Strimbu K, Tavel J a. What are Biomarkers? *Curr Opin HIV AIDS*. 2011;5(6):463-466. doi:10.1097/COH.0b013e32833ed177.What.
327. Rauch A, Kotalik Z, Descombes P, et al. Genetic Variation in IL28B Is Associated With Chronic Hepatitis C and Treatment Failure: A Genome-Wide Association Study. *Gastroenterology*. 2010;138(4):1338-1345. doi:10.1053/j.gastro.2009.12.056.
328. Umansky SR, Tomei LD. Transrenal DNA testing: progress and perspectives. *Expert Rev Mol Diagn*. 2006;6(2):153-163. doi:10.1586/14737159.6.2.153.
329. Kim Y-H, Yan C, Lee I-S, et al. Value of urinary topoisomerase-IIA cell-free DNA for diagnosis of bladder cancer. *Investig Clin Urol*. 2016;57(2):106. doi:10.4111/icu.2016.57.2.106.
330. Sugiura K, Akiyama M. Update on autosomal recessive congenital ichthyosis: MRNA analysis using hair samples is a powerful tool for genetic diagnosis. *J Dermatol Sci*. 2015;79(1):4-9. doi:10.1016/j.jdermsci.2015.04.009.
331. Zhou Q, Hu HG, Hou L. Discover, Develop & Validate--Advance and Prospect of Tumor Biomarkers. *Clin Lab*. 2015;61(11):1589-1599. doi:10.7754/CUn.Lab.2015.150332.
332. Sun B, Rodriguez-Manzano J, Selck D a., Khorosheva E, Karymov M a., Ismagilov RF. Measuring Fate and Rate of Single-Molecule Competition of Amplification and Restriction Digestion, and Its Use for Rapid Genotyping Tested with Hepatitis C Viral RNA. *Angew Chemie Int Ed*. 2014;53(31):8088-8092. doi:10.1002/anie.201403035.
333. Natesan M, Ulrich RG. Protein microarrays and biomarkers of infectious disease. *Int J Mol Sci*. 2010;11(12):5165-5183. doi:10.3390/ijms11125165.
334. James P. Protein identification in the post-genome era : the rapid rise of proteomics. *Q Rev Biophys*. 1997;30(4):279-331.
335. Swanson PE. Immunohistochemistry as a surrogate for molecular diagnosis in hepatic tumours. *Appl Immunohistochem Mol Morphol*. 2015;23(2):81-96. doi:10.1016/j.mpdhp.2015.03.002.
336. Omenn GS. Exploring the Human Plasma Proteome. *Proteomics*. 2005;5:3223-3225. doi:10.1002/9783527609482.
337. Luna Coronell J a, Syed P, Sergelen K, Gyurján I, Weinhäusel a. The current status of cancer biomarker research using tumour-associated antigens for minimal invasive and early cancer diagnostics. *J Proteomics*. 2012;76:102-115. <http://www.embase.com/search/results?subaction=viewrecord&from=export&id=L52204506%5Cnhttp://dx.doi.org/10.1016/j.jprot.2012.07.022%5Cnhttp://sfx.library.uu.nl/utrecht?sid=EMBASE&issn=18743919&id=doi:10.1016/j.jprot.2012.07.022&atitle=The+current+status+of+ca>.
338. Ray S, Patel SK, Kumar V, Damahe J, Srivastava S. Differential expression of serum/plasma proteins in various infectious diseases: Specific or nonspecific signatures. *Proteomics - Clin Appl*. 2014;8(1-2):53-72. doi:10.1002/prca.201300074.
339. Holliger P, Hudson PJ. Engineered antibody fragments and the rise of single domains. *Nat Biotechnol*. 2005;23(9):1126-1136. doi:10.1038/nbt1142.
340. Diamandis EP. Mass spectrometry as a diagnostic and a cancer biomarker discovery tool: opportunities and potential limitations. *Mol Cell Proteomics*. 2004;3(4):367-378. doi:10.1074/mcp.R400007-MCP200.
341. Simpson RJ, Lim JWE, Moritz RL. Exosomes : proteomic insights and diagnostic potential. *Expert Rev Proteomics*. 2009;6(3):267-283.
342. Simak J, Gelderman MP. Cell membrane microparticles in blood and blood products: Potentially pathogenic agents and diagnostic markers. *Transfus Med Rev*. 2006;20(1):1-26. doi:10.1016/j.tmr.2005.08.001.
343. Taylor DD, Gercel-Taylor C. MicroRNA signatures of tumor-derived exosomes as diagnostic biomarkers of ovarian cancer. *Gynecol Oncol*. 2008;110(1):13-21. doi:10.1016/j.ygyno.2008.04.033.
344. Wenk MR. Lipidomics in drug and biomarker development. *Expert Opin Drug Discov*. 2006;1(7):723-736. doi:10.1517/17460441.1.7.723.
345. Kelly RS, Vander Heiden MG, Giovannucci E, Mucci LA. Metabolomic Biomarkers of Prostate Cancer: Prediction, Diagnosis, Progression, Prognosis, and Recurrence. *Cancer Epidemiol Biomarkers Prev*. 2016. doi:10.1158/1055-9965.EPI-15-1223.
346. Upadhyay RK. Emerging risk biomarkers in cardiovascular diseases and disorders. *J Lipids*. 2015;2015:971453. doi:10.1155/2015/971453.
347. Sakamuri RM, Capek P, Dickerson TJ, Barry CE, Mukundan H, Swanson BI. Detection of stealthy small amphiphilic biomarkers. *J Microbiol Methods*. 2014;103:112-117. doi:10.1016/j.mimet.2014.05.012.

348. Passos-castilho AM, Carvalho VM, Helena K, et al. Serum lipidomic profiling as a useful tool for screening potential biomarkers of hepatitis B-related hepatocellular carcinoma by ultraperformance liquid chromatography – mass spectrometry. *BMC Cancer*. 2015;1-9. doi:10.1186/s12885-015-1995-1.
349. Lawrence R, Brown JR, Lorey F, Dickson PI, Crawford BE, Esko JD. Glycan-based biomarkers for mucopolysaccharidoses. *Mol Genet Metab*. 2014;111(2):73-83. doi:10.1016/j.ymsgme.2013.07.016.
350. Alavi A, Axford JS. Glyco-biomarkers: potential determinants of cellular physiology and pathology. *Dis Markers*. 2008;25(4-5):193-205. <http://www.ncbi.nlm.nih.gov/pubmed/19126964>.
351. Svarovsky S a., Joshi L. Cancer glycan biomarkers and their detection – past, present and future. *Anal Methods*. 2014;6(12):3918. doi:10.1039/c3ay42243g.
352. Ueda K. Glycoproteomic strategies: From discovery to clinical application of cancer carbohydrate biomarkers. *Proteomics - Clin Appl*. 2013;7(9-10):607-617. doi:10.1002/prca.201200123.
353. Semiglazov VF, Semiglazov V V., Dashyan G a., et al. Phase 2 randomized trial of primary endocrine therapy versus chemotherapy in postmenopausal patients with estrogen receptor-positive breast cancer. *Cancer*. 2007;110(2):244-254. doi:10.1002/cncr.22789.
354. Limper M, de Kruijff MD, Duits a. J, Brandjes DPM, van Gorp ECM. The diagnostic role of Procalcitonin and other biomarkers in discriminating infectious from non-infectious fever. *J Infect*. 2010;60(6):409-416. doi:10.1016/j.jinf.2010.03.016.
355. Catanzaro a., Davidson BL, Fujiwara PI, et al. Rapid diagnostic tests for tuberculosis - What is the appropriate use? *Am J Respir Crit Care Med*. 1997;51(11):1054-1055.
356. Betanzos-Reyes AF, Rodríguez MH, Duran-Arenas LG, et al. Comparative analysis of two alternative models for epidemiological surveillance in the Mexican Malaria Control Program. *Health Policy (New York)*. 2007;80(3):465-482. doi:10.1016/j.healthpol.2006.01.013.
357. Viraka Nellore BP, Kanchanapally R, Pramanik A, et al. Aptamer-conjugated graphene oxide membranes for highly efficient capture and accurate identification of multiple types of circulating tumor cells. *Bioconjug Chem*. 2015;26(2):235-242. doi:10.1021/bc500503e.
358. Goulart LR, Vierira CU, Freschi APP, et al. Biomarkers for Serum Diagnosis of Infectious Diseases and Their Potential Application in Novel Sensor Platforms. *Crit Rev Immunol*. 2010;30(2):201-222.
359. Sunde RA. mRNA transcripts as molecular biomarkers in medicine and nutrition. *J Nutr Biochem*. 2010;21(8):665-670. doi:10.1016/j.jnutbio.2009.11.012.
360. Tarasow TM, Penny L, Patwardhan A, Hamren S, McKenna MP, Urdea MS. Microfluidic strategies applied to biomarker discovery and validation for multivariate diagnostics. *Bioanalysis*. 2011;3(19):2233-2251. doi:10.4155/bio.11.224.
361. Sherin K, Klekamp BG, Beal J, Martin N. What is new in HIV infection? *Am Fam Physician*. 2014;89(4):265-272. <http://www.ncbi.nlm.nih.gov/pubmed/24695446>.
362. Fung ET. A recipe for proteomics diagnostic test development: The OVA1 test, from biomarker discovery to FDA clearance. *Clin Chem*. 2010;56(2):327-329. doi:10.1373/clinchem.2009.140855.
363. Rutstein SE, Kamwendo D, Lugali L, et al. Measures of viral load using Abbott RealTime HIV-1 Assay on venous and fingerstick dried blood spots from provider-collected specimens in Malawian District Hospitals. *J Clin Virol*. 2014;60(4):392-398. doi:10.1016/j.jcv.2014.05.005.
364. Weigl BH, Boyle DS, de los Santos T, Peck RB, Steele MS. Simplicity of use: a critical feature for widespread adoption of diagnostic technologies in low-resource settings. *Expert Rev Med Devices*. 2009;6(5):461-464.
365. Yeat NC, Lin C, Sager M, Lin J. Cancer proteomics: developments in technology, clinical use and commercialization. *Expert Rev Proteomics*. 2015:1-15. doi:10.1586/14789450.2015.1051969.
366. Gibson DS, Rooney ME, Finnegan S, et al. Biomarkers in rheumatology, Now and in the future. *Rheumatology*. 2012;51(3):423-433. doi:10.1093/rheumatology/ker358.
367. Kumar A a., Hennek JW, Smith BS, et al. From the Bench to the Field in Low-Cost Diagnostics: Two Case Studies. *Angew Chemie Int Ed*. 2015;54(20):5836-5853. doi:10.1002/anie.201411741.
368. Ely S. Personalized Medicine: Individualized Care of Cancer Patients. *J Lab Clin Med*. 2009;154(6):303-308.
369. WHO. Diagnostic criteria and classification of hyperglycaemia first detected in pregnancy: A World Health Organization Guideline. *Diabetes Res Clin Pract*. 2014;103(3):341-363. doi:10.1016/j.diabres.2013.10.012.
370. Bellamy L, Casas J-P, Hingorani AD, Williams D. Type 2 diabetes mellitus after gestational diabetes: a systematic review and meta-analysis. *Lancet*. 2009;373(9677):1773-1779. doi:10.1016/S0140-6736(09)60731-5.
371. Kim C, Newton KM, Knopp RH. Gestational Diabetes and the Incidence of Type 2 Diabetes. *Diabetes Care*. 2002;25(10):1862-1868.
372. Quick WW, Yang W, Zhang Y, et al. Cost of Gestational Diabetes Mellitus in the United States in 2007. 2009;12(3).
373. Nielsen KK, Courten M De, Kapur A. The urgent need for universally applicable simple screening procedures and diagnostic criteria for gestational diabetes mellitus - lessons from projects funded by the World Diabetes Foundation.

Glob Health Action. 2012;5(January).

374. Hanna FWF, Peters JR. Screening for gestational diabetes; past, present and future. *Diabet Med*. 2002;19(5):351-358. doi:10.1046/j.1464-5491.2002.00684.x.
375. Lurie S, Levy R, Weiss R, Boultin G, Hagay ZJ. Low values on 50 gram glucose challenge test or oral 100 gram glucose tolerance test are associated with good perinatal outcome. 1998;18(5):451-454.
376. Perucchini D, Fischer U, Spinass G a., Huch R, Huch A, Lehmann R. Using Fasting Plasma Glucose Concentrations to Screen for Gestational Diabetes Mellitus: Prospective Population Based Study. *Obstet Gynecol Surv*. 2000;55(4):199-201. doi:10.1097/00006254-200004000-00005.
377. Ayach W, Costa RAA, Calderon I de MP, Rudge MVC. Comparison between 100-g glucose tolerance test and two other screening tests for gestational diabetes : combined fasting glucose with risk factors and 50-g glucose tolerance test. *Sao Paulo Med J*. 2006;124(1):4-9.
378. *Diagnostic Criteria and Classification of Hyperglycaemia First Detected in Pregnancy.*; 2013.
379. Metzger BE, Gabbe SG, Persson B, et al. International Association of Diabetes and Pregnancy Study Groups recommendations on the diagnosis and classification of hyperglycemia in pregnancy. *Diabetes Care*. 2010;33(3):676-682. doi:10.2337/dc09-1848.
380. *Standards of Medical Care in Diabetes--2014.*; 2014. doi:10.2337/dc14-S014.
381. Yeral MI, Ozgu-Erdinc a. S, Uygur D, Seckin KD, Karsli MF, Danisman a. N. Prediction of gestational diabetes mellitus in the first trimester, comparison of fasting plasma glucose, two-step and one-step methods: A prospective randomized controlled trial. *Endocrine*. 2014;46(3):512-518. doi:10.1007/s12020-013-0111-z.
382. Lapolla a., Dalfrà MG, Ragazzi E, De Cata a. P, Fedele D. New International Association of the Diabetes and Pregnancy Study Groups (IADPSG) recommendations for diagnosing gestational diabetes compared with former criteria. retrospective study on pregnancy outcome. *Diabet Med*. 2011;28(9):1074-1077. doi:10.1111/j.1464-5491.2011.03351.x.
383. Meltzer SJ, Snyder J, Penrod JR, Nudi M, Morin L. Gestational diabetes mellitus screening and diagnosis: A prospective randomised controlled trial comparing costs of one-step and two-step methods. *BJOG An Int J Obstet Gynaecol*. 2010;117(4):407-415. doi:10.1111/j.1471-0528.2009.02475.x.
384. Metzger BE. International Association of Diabetes and Pregnancy Study Groups recommendations on the diagnosis and classification of hyperglycemia in pregnancy. *Diabetes Care*. 2010;33(3):676-682. doi:10.2337/dc09-1848.
385. Nagalla S, Snyder C, Michaels J, et al. Maternal serum biomarkers for risk assessment in gestational diabetes. A potential universal screening test to predict GDM status. *Indian J Endocrinol Metab*. 2015;19(1):155. doi:10.4103/2230-8210.140226.
386. Bethel MA, Price HC, Sourij H, et al. Evaluation of a Self-Administered Oral Glucose Tolerance Test. *Diabetes Care*. 2013;36:1483-1488. doi:10.2337/dc12-0643.
387. Weigl BH, Zwisler G, Peck R, Abu-Haydar E. Rapid screening test for gestational diabetes: public health need, market requirement, initial product design, and experimental results. Becker H, Gray BL, eds. *Proc SPIE, 8615, Microfluid BioMEMS, Med Microsystems XI*. 2013;8615:86150L. doi:10.1117/12.2008326.
388. Jiwani A, Marseille E, Lohse N, Damm P, Hod M, Kahn JG. Gestational diabetes mellitus: results from a survey of country prevalence and practices. *J Matern Neonatal Med*. 2012;25(May 2011):600-610. doi:10.3109/14767058.2011.587921.
389. Seshiah V, Sahay B, Das A, et al. Gestational Diabetes Mellitus - Indian Guidelines. *J Indian Med Assoc*. 2009;107(11).
390. Emirates UA. National Diabetes Guidelines United Arab Emirates. 2009.
391. Schmidt MI, Matos MC, Reichelt a. J, et al. Prevalence of gestational diabetes mellitus - do the new WHO criteria make a difference? *Diabet Med*. 2000;17(5):376-380. doi:10.1046/j.1464-5491.2000.00257.x.
392. Cavassini ACM, Lima SAM, Calderon IMP, Rudge MVC. Cost-benefit of hospitalization compared with outpatient care for pregnant women with pregestational and gestational diabetes or with mild hyperglycemia , in Brazil Custo-benefício da hospitalização comparada ao atendimento ambulatorial em. *Sao Paulo Med J*. 2012;130(1):17-26.
393. McManus R, Giroux I, Zhou A, McLaren J, MacLellan J. Characteristics of women with recent gestational diabetes mellitus attending a postpartum diabetes prevention seminar. *Can J Diabetes*. 2012;36(2):68-70. doi:10.1016/j.jcjd.2012.04.002.
394. Yang X, Hsu-Hage B, Zhang H, et al. Gestational Diabetes Mellitus in Women of Single Gravidity in Tianjin City , China. *Diabetes Care*. 2002;25(5).
395. Zhang F, Dong L, Zhang CP, et al. Increasing prevalence of gestational diabetes mellitus in Chinese women from 1999 to 2008. *Diabet Med*. 2011;28(6):652-657. doi:10.1111/j.1464-5491.2010.03205.x.
396. Zhu W, Fan L, Yang H, et al. Fasting plasma glucose at 24-28 weeks to screen for gestational diabetes mellitus: new evidence from China. *Diabetes Care*. 2013;36(7):2038-2040. doi:10.2337/dc12-2465.
397. Zhang P, Zhang X, Brown J, et al. Global healthcare expenditure on diabetes for 2010 and 2030. *Diabetes Res Clin Pract*. 2010;87(3):293-301. doi:10.1016/j.diabres.2010.01.026.

398. Ritchie A V., Ushiro-Lumb I, Edemaga D, et al. SAMBA HIV semiquantitative test, a new point-of-care viral-load-monitoring assay for resource-limited settings. *J Clin Microbiol.* 2014;52(9):3377-3383. doi:10.1128/JCM.00593-14.
399. Binnicker MJ, Espy MJ, Irish CL, Vetter EA. Direct Detection of Influenza A and B Viruses in Less Than 20 Minutes Using a Commercially Available Rapid PCR Assay. *J Clin Microbiol.* 2015;53(7):2353-2354. doi:10.1128/JCM.00791-15.
400. Cohen DM, Russo ME, Jaggi P, Kline J, Gluckman W, Parekh A. Multicenter clinical evaluation of the novel Alere i Strep A isothermal nucleic acid amplification test. *J Clin Microbiol.* 2015;53(7):2258-2261. doi:10.1128/jcm.00490-15.
401. Fang R, Li X, Hu L, et al. Cross-priming amplification for rapid detection of Mycobacterium tuberculosis in sputum specimens. *J Clin Microbiol.* 2009;47(3):845-847. doi:10.1128/JCM.01528-08.
402. World Health Organization (WHO).
403. Sajid M, Kawde AN, Daud M. Designs, formats and applications of lateral flow assay: A literature review. *J Saudi Chem Soc.* 2015;19(6):689-705. doi:10.1016/j.jscs.2014.09.001.
404. Fu E, Liang T, Houghtaling J, et al. Enhanced sensitivity of lateral flow tests using a two-dimensional paper network format. *Anal Chem.* 2011;83(20):7941-7946. doi:10.1021/ac201950g.
405. Fu E, Liang T, Spicar-Mihalic P, Houghtaling J, Ramachandran S, Yager P. Two-dimensional paper network format that enables simple multistep assays for use in low-resource settings in the context of malaria antigen detection. *Anal Chem.* 2012;84(10):4574-4579. doi:10.1021/ac300689s.
406. Toley BJ, McKenzie B, Liang T, Buser JR, Yager P, Fu E. Tunable-delay shunts for paper microfluidic devices. *Anal Chem.* 2013;85(23):11545-11552. doi:10.1021/ac4030939.
407. Connelly JT, Rolland JP, Whitesides GM. "Paper Machine" for Molecular Diagnostics. *Anal Chem.* 2015;87(15):7595-7601. doi:10.1021/acs.analchem.5b00411.
408. Allen PB, Arshad S a, Li B, Chen X, Ellington AD. DNA circuits as amplifiers for the detection of nucleic acids on a paperfluidic platform. *Lab Chip.* 2012;12(16):2951-2958. doi:10.1039/c2lc40373k.
409. Pardee K, Green AA, Takahashi MK, et al. Rapid, low-cost detection of Zika virus using programmable biomolecular components. *Cell.* 2016;165(5):1-12. doi:10.1016/j.cell.2016.04.059.
410. Roskos K, Hickerson AI, Lu HW, et al. Simple System for Isothermal DNA Amplification Coupled to Lateral Flow Detection. *PLoS One.* 2013;8(7). doi:10.1371/journal.pone.0069355.
411. Song J, Mauk MG, Hackett BA, Cherry S, Bau HH, Liu C. Instrument-Free Point-of-Care Molecular Detection of Zika Virus. *Anal Chem.* 2016;acs.analchem.6b01632. doi:10.1021/acs.analchem.6b01632.
412. Sun B, Shen F, McCalla SE, Kreutz JE, Karymov MA, Ismagilov RF. Mechanistic evaluation of the pros and cons of digital RT-LAMP for HIV-1 viral load quantification on a microfluidic device and improved efficiency via a two-step digital protocol. *Anal Chem.* 2013;85(3):1540-1546. doi:10.1021/ac3037206.
413. Curtis KA, Rudolph DL, Nejad I, et al. Isothermal amplification using a chemical heating device for point-of-care detection of HIV-1. *PLoS One.* 2012;7(2):1-6. doi:10.1371/journal.pone.0031432.
414. Singleton J, Osborn JL, Lillis L, et al. Electricity-free amplification and detection for molecular point-of-care diagnosis of HIV-1. *PLoS One.* 2014;9(11):e113693. doi:10.1371/journal.pone.0113693.
415. Richardson AR, Libby SJ, Fang FC. A nitric oxide-inducible lactate dehydrogenase enables Staphylococcus aureus to resist innate immunity. *Sci (New York, NY).* 2008;319(5870):1672-1676. doi:10.1126/science.1155207.
416. EIGNER J, BOEDTKER H, MICHAELS G. The thermal degradation of nucleic acids. *Biochim Biophys Acta.* 1961;51:165-168.
417. Toley BJ, Covelli I, Belousov Y, et al. Isothermal strand displacement amplification (iSDA): a rapid and sensitive method of nucleic acid amplification for point-of-care diagnosis. *Analyst.* 2015. doi:10.1039/C5AN01632K.
418. Hoorfar J, Malorny B, Abdulmawjood a, Cook N, Fach P, Wagner M. Practical Considerations in Design of Internal Amplification Controls for Diagnostic PCR Assays MINIREVIEW Practical Considerations in Design of Internal Amplification Controls for Diagnostic PCR Assays. *J Clin Microbiol.* 2004;42(5):1863-1868. doi:10.1128/JCM.42.5.1863.
419. Ehses S, Ackermann J, McCaskill JS. Optimization and design of oligonucleotide setup for strand displacement amplification. *J Biochem Biophys Methods.* 2005;63(3):170-186. doi:10.1016/j.jbbm.2005.04.005.
420. Mermel LA, Eells SJ, Acharya MK, et al. Quantitative Analysis and Molecular Fingerprinting of Methicillin-Resistant *Staphylococcus aureus* Nasal Colonization in Different Patient Populations: A Prospective, Multicenter Study. *Infect Control Hosp Epidemiol.* 2010;31(6):592-597. doi:10.1086/652778.
421. Li S, Norioka S, Sakiyama F. Bacteriolytic activity and specificity of Achromobacter beta-lytic protease. *J Biochem.* 1998;124(2):332-339.
422. Hogg GM, McKenna JP, Ong G. Rapid detection of methicillin-susceptible and methicillin-resistant Staphylococcus aureus directly from positive BacT/Alert® blood culture bottles using real-time polymerase chain reaction: evaluation and comparison of 4 DNA extraction methods. *Diagn Microbiol Infect Dis.* 2008;61(4):446-452. doi:10.1016/j.diagmicrobio.2008.03.012.
423. Atshan SS, Shamsudin MN, Lung LTT, et al. Improved method for the isolation of RNA from bacteria refractory to disruption, including S. aureus producing biofilm. *Gene.* 2012;494(2):219-224. doi:10.1016/j.gene.2011.12.010.

424. Becker K, Pagnier I, Schuhen B, et al. Does nasal cocolonization by methicillin-resistant coagulase-negative staphylococci and methicillin-susceptible *Staphylococcus aureus* strains occur frequently enough to represent a risk of false-positive methicillin-resistant *S. aureus* determinations by molecular methods? *J Clin Microbiol.* 2006;44(1):229-231. doi:10.1128/JCM.44.1.229-231.2006.
425. Buser JR, Diesburg S, Singleton J, et al. Precision chemical heating for diagnostic devices. *Lab Chip.* 2015;15:4423-4432. doi:10.1039/C5LC01053E.
426. Lozano R, Naghavi M, Foreman K, et al. Global and regional mortality from 235 causes of death for 20 age groups in 1990 and 2010: a systematic analysis for the Global Burden of Disease Study 2010. *Lancet.* 2013;380(9859):2095-2128. doi:10.1016/S0140-6736(12)61728-0.
427. Wang H, Dwyer-Lindgren L, Lofgren KT, et al. Age-specific and sex-specific mortality in 187 countries, 1970-2010: a systematic analysis for the Global Burden of Disease Study 2010. *Lancet.* 2012;380(9859):2071-2094. doi:10.1016/S0140-6736(12)61719-X.
428. Murray CJL, Vos T, Lozano R, et al. Disability-adjusted life years (DALYs) for 291 diseases and injuries in 21 regions, 1990-2010: a systematic analysis for the Global Burden of Disease Study 2010. *Lancet.* 2012;380(9859):2197-2223. doi:10.1016/S0140-6736(12)61689-4.
429. Hodges K, Gill R. Infectious diarrhea. *Gut Microbes.* 2010;1(1):4-21. doi:10.4161/gmic.1.1.11036.
430. David MZ, Daum RS. Community-associated methicillin-resistant *Staphylococcus aureus*: epidemiology and clinical consequences of an emerging epidemic. *Clin Microbiol Rev.* 2010;23(3):616-687. doi:10.1128/CMR.00081-09.
431. Borg M a, de Kraker M, Scicluna E, et al. Prevalence of methicillin-resistant *Staphylococcus aureus* (MRSA) in invasive isolates from southern and eastern Mediterranean countries. *J Antimicrob Chemother.* 2007;60(6):1310-1315. doi:10.1093/jac/dkm365.
432. Boehme CC, Nicol MP, Nabeta P, et al. Feasibility, diagnostic accuracy, and effectiveness of decentralised use of the Xpert MTB/RIF test for diagnosis of tuberculosis and multidrug resistance: a multicentre implementation study. *Lancet.* 2011;377(9776):1495-1505. doi:10.1016/S0140-6736(11)60438-8.
433. Landscape DT. *Tuberculosis Diagnostic Technology Landscape.*; 2012.
434. Niemz A, Ferguson TM, Boyle DS. Point-of-care nucleic acid testing for infectious diseases. *Trends Biotechnol.* 2011;29(5):240-250. doi:10.1016/j.tibtech.2011.01.007.
435. Masaki T, Nakamura K. A new proteolytic enzyme from *Achromobacter lyticus* M497-1. *Agric Biol Chem.* 1978;42(7):1443-1445. doi:1961.42.1443.
436. Paule SM, Hacek DM, Kufner B, et al. Performance of the BD GeneOhm methicillin-resistant *Staphylococcus aureus* test before and during high-volume clinical use. *J Clin Microbiol.* 2007;45(9):2993-2998. doi:10.1128/JCM.00670-07.
437. Kobayashi N, Wu H, Kojima K, et al. Detection of *mecA*, *femA*, and *femB* genes in clinical strains of staphylococci using polymerase chain reaction. *Epidemiol Infect.* 2009;113(2):259. doi:10.1017/S0950268800051682.
438. Singleton J, Guelig D, Buser J, et al. Advancing electricity-free molecular diagnostics at the point-of-care: Optimizing the NINA platform for a malaria LAMP assay. In: *IEEE Global Humanitarian Technology Conference (GHTC 2014)*. IEEE; 2014:721-725. doi:10.1109/GHTC.2014.6970363.
439. Lillis L, Lehman D, Singhal MC, et al. Non-instrumented incubation of a recombinase polymerase amplification assay for the rapid and sensitive detection of proviral HIV-1 DNA. *PLoS One.* 2014;9(9):e108189. doi:10.1371/journal.pone.0108189.
440. Choi JR, Hu J, Tang R, et al. An integrated paper-based sample-to-answer biosensor for nucleic acid testing at the point of care. *Lab Chip.* 2016;16(3):611-621. doi:10.1039/C5LC01388G.
441. Buser JR, Wollen A, Heiniger EK, et al. Electromechanical cell lysis using a portable audio device: enabling challenging sample preparation at the point-of-care. *Lab Chip.* 2015;15:1994-1997. doi:10.1039/C5LC00080G.
442. Shah KG, Guelig D, Diesburg S, et al. Design of a New Type of Compact Chemical Heater for Isothermal Nucleic Acid Amplification. *PLoS One.* 2015;10(10):e0139449. doi:10.1371/journal.pone.0139449.
443. MREInfo.com - Home.
444. Kuypers J, Wright N, Morrow R. Evaluation of quantitative and type-specific real-time RT-PCR assays for detection of respiratory syncytial virus in respiratory specimens from children. *J Clin Virol.* 2004;31(2):123-129. doi:10.1016/j.jcv.2004.03.018.
445. Cowton VM, McGivern DR, Fearn R. Unravelling the complexities of respiratory syncytial virus RNA synthesis. *J Gen Virol.* 2006;87(Pt 7):1805-1821. doi:10.1099/vir.0.81786-0.
446. Casali N, Preston A. *E. Coli Plasmid Vectors: Methods and Applications.*; 2003.
447. Schüpbach J, Böni J. Quantitative and sensitive detection of immune-complexed and free HIV antigen after boiling of serum. *J Virol Methods.* 1993;43(2):247-256. doi:10.1016/0166-0934(93)90080-B.
448. Tarmann C, Jungbauer A. Adsorption of plasmid DNA on anion exchange chromatography media. *J Sep Sci.* 2008;31:2605-2618. doi:10.1002/jssc.200700654.
449. Reedy CR, Hagan K a, Strachan BC, et al. Dual-domain microchip-based process for volume reduction solid phase

- extraction of nucleic acids from dilute, large volume biological samples. *Anal Chem.* 2010;82(13):5669-5678. doi:10.1021/ac100649b.
450. R Core Team. R: A language and environment for statistical computing. 2106;5.
451. Group TL. The Value of Diagnostics Innovation, Adoption and Diffusion into Health Care. *Health Care (Don Mills)*. 2005;(July).
452. Organization WH. Global tuberculosis report 2013. 2013.
453. Weaver A a, Reiser H, Barstis T, et al. Paper analytical devices for fast field screening of beta lactam antibiotics and antituberculosis pharmaceuticals. *Anal Chem.* 2013;85(13):6453-6460. doi:10.1021/ac400989p.
454. Martinez AW, Phillips ST, Carrilho E, Thomas SW, Sindi H, Whitesides GM. Simple telemedicine for developing regions: camera phones and paper-based microfluidic devices for real-time, off-site diagnosis. *Anal Chem.* 2008;80(10):3699-3707. doi:10.1021/ac800112r.
455. Wood P, Sinton D. Portable audio electronics for impedance-based measurements in microfluidics. *J Micromechanics Microengineering.* 2010;20(8):87001. doi:10.1088/0960-1317/20/8/087001.
456. Dell N, Breit N, Chaluco T, Crawford J, Borriello G. Digitizing paper forms with mobile imaging technologies. *Proc 2nd ACM Symp Comput Dev - ACM DEV '12.* 2012;1. doi:10.1145/2160601.2160604.
457. Kaneko H, Kawana T, Fukushima E, Suzutani T. Tolerance of loop-mediated isothermal amplification to a culture medium and biological substances. *J Biochem Biophys Methods.* 2007;70:499-501. doi:10.1016/j.jbbm.2006.08.008.
458. BioSpec. BioSpec Products - Mini-beadbeater-8.
459. Hughes D. A press for disrupting bacteria and other micro-organisms. *Br J Exp Pathol.* 1951.
460. Laboratory EMB. Protein purification: Extraction and Clarification Preparation of cell lysates from E.coli.
461. Lawrence NS, French CS, Series N. Colloidal Dispersion of Chloroplast Materiall. 2015;111(2893):633-634.
462. Lange H, Taillandier P, Riba J-P. Effect of high shear stress on microbial viability. *J Chem Technol Biotechnol.* 2001;76(5):501-505. doi:10.1002/jctb.401.
463. Seltmann G, Holst O. *The Bacterial Cell Wall.*; 2002.
464. Vandeventer PE, Weigel KM, Salazar J, et al. Mechanical disruption of lysis-resistant bacterial cells by use of a miniature, low-power, disposable device. *J Clin Microbiol.* 2011;49(7):2533-2539. doi:10.1128/JCM.02171-10.
465. Jacobs J, Rhodes M, Sturgis B, Wood B. Influence of environmental gradients on the abundance and distribution of Mycobacterium spp. in a coastal lagoon estuary. *Appl Environ Microbiol.* 2009;75(23):7378-7384. doi:10.1128/AEM.01900-09.
466. Ashmore J, del Pino C, Mullin T. Cavitation in a Lubrication Flow between a Moving Sphere and a Boundary. *Phys Rev Lett.* 2005;94(12):124501. doi:10.1103/PhysRevLett.94.124501.
467. Acroname. Back-EMF Motion Feedback.
468. Sheeler RD, Houston MS, Radke S, Dale JC, Adamson SC. Accuracy of rapid strep testing in patients who have had recent streptococcal pharyngitis. *J Am Board Fam Pract.* 2001;15(4):261-265.
469. Peterson LR, Liesenfeld O, Woods CW, et al. Multicenter evaluation of the lightcycler methicillin-resistant Staphylococcus aureus (MRSA) advanced test as a rapid method for detection of MRSA in nasal surveillance swabs. *J Clin Microbiol.* 2010;48(5):1661-1666. doi:10.1128/JCM.00003-10.
470. Yam WC, Siu GKH, Ho PL, et al. Evaluation of the lightcycler methicillin-resistant Staphylococcus aureus (MRSA) advanced test for detection of MRSA nasal colonization. *J Clin Microbiol.* 2013;51(9):2869-2874. doi:10.1128/JCM.00488-13.
471. Goodell CK, Prickett J, Kittawornrat A, et al. Probability of detecting influenza A virus subtypes H1N1 and H3N2 in individual pig nasal swabs and pen-based oral fluid specimens over time. *Vet Microbiol.* 2013;166(3-4):450-460. doi:10.1016/j.vetmic.2013.06.029.
472. Wu LT, Thomas I, Curran MD, et al. Duplex molecular assay intended for point-of-care diagnosis of influenza A/B virus infection. *J Clin Microbiol.* 2013;51(9):3031-3038. doi:10.1128/JCM.00740-13.
473. Waris ME, Heikkinen T, Osterback R, Jartti T, Ruuskanen O. Nasal swabs for detection of respiratory syncytial virus RNA. *Arch Dis Child.* 2007;92(11):1046-1047. doi:10.1136/adc.2006.113514.
474. Spyridaki IS, Christodoulou I, de Beer L, et al. Comparison of four nasal sampling methods for the detection of viral pathogens by RT-PCR-A GA2LEN project. *J Virol Methods.* 2009;156(1-2):102-106. doi:10.1016/j.jviromet.2008.10.027.
475. Hassanzadeh P, Mardaneh J, Motamedifar M. Conventional Agar-Based Culture Method, and Nucleic Acid Amplification Test (NAAT) of the cppB Gene for Detection of Neisseria gonorrhoea in Pregnant Women Endocervical Swab Specimens. *Iran Red Crescent Med J.* 2013;15(3):207-211. doi:10.5812/ircmj.3726.
476. Ostergaard L, Agner T, Krarup E, Johansen UB, Weismann K, Gutschik E. PCR for detection of Chlamydia trachomatis in endocervical, urethral, rectal, and pharyngeal swab samples obtained from patients attending an STD clinic. *Genitourin Med.* 1997;73(6):493-497. doi:10.1136/sti.73.6.493.
477. Gustavsson L, Westin J, Andersson LM, Lindh M. Rectal swabs can be used for diagnosis of viral gastroenteritis with a

- multiple real-time PCR assay. *J Clin Virol.* 2011;51(4):275-278. doi:10.1016/j.jcv.2011.05.025.
478. Van Der Schee C V., Van Belkum A, Zwiijgers L, et al. Improved diagnosis of *Trichomonas vaginalis* infection by PCR using vaginal swabs and urine specimens compared to diagnosis by wet mount microscopy, culture, and fluorescent staining. *J Clin Microbiol.* 1999;37(12):4127-4130.
479. Mikalová L, Pospíšilová P, Woznicová V, Kuklová I, Zákoucká H, Smajs D. Comparison of CDC and sequence-based molecular typing of syphilis treponemes: tpr and arp loci are variable in multiple samples from the same patient. *BMC Microbiol.* 2013;13(1):178. doi:10.1186/1471-2180-13-178.
480. Jerris RC, Jarrett DK, Cherney W, Atlanta A. Comparison of StarSwab II with BD CultureSwab Max V (+) Transport Systems for Preservation of Bacterial Pathogens Important in Pediatric Medicine ; *Hemophilus influenza* , *Streptococcus pneumoniae* , and *Neisseria meningitidis*. *Clin Lab.* 2005;(June):1-4.
481. Turner J, Harry K, Lofland D, Madhusudhan K. The Characterization of the Absorption and Release Properties of Various Clinical Swabs. In: *26th Clinical Virology Symposium, Florida, USA.*; 2010.
482. Gao X, Chen XS, Yin YP, et al. Distribution study of *Chlamydia trachomatis* serovars among high-risk women in china performed using PCR-restriction fragment length polymorphism genotyping. *J Clin Microbiol.* 2007;45(4):1185-1189. doi:10.1128/JCM.02076-06.
483. Technologies I. IStrep Instruction – Clinical Diagnostic Products. 2011.
484. Scarborough A. Alere BinaxNOW RSV Card package insert. 2012.
485. Patel PA, Ledebner NA, Ginocchio CC, et al. Performance of the BD GeneOhm MRSA achromopeptidase assay for real-time PCR detection of methicillin-resistant *Staphylococcus aureus* in nasal specimens. *J Clin Microbiol.* 2011;49(6):2266-2268. doi:10.1128/JCM.02431-10.
486. Komaromy A, Boysen RI, Zhang H, Hearn MTW, Nicolau D V. Effect of various artificial surfaces on the colonization and viability of. *Proc SPIE.* 2007;6799:67990J-67990J-10. doi:10.1117/12.762416.
487. Verhoeven P, Grattard F, Carricajo A, Pozzetto B, Berthelot P. Better detection of *Staphylococcus aureus* nasal carriage by use of nylon flocculated swabs. *J Clin Microbiol.* 2010;48(11):4242-4244. doi:10.1128/JCM.01425-10.
488. Rossney AS, Herra CM, Brennan GI, Morgan PM, O'Connell B. Evaluation of the Xpert methicillin-resistant *Staphylococcus aureus* (MRSA) assay using the GeneXpert real-time PCR platform for rapid detection of MRSA from screening specimens. *J Clin Microbiol.* 2008;46(10):3285-3290. doi:10.1128/JCM.02487-07.
489. Harry KH, Turner JC, Madhusudhan KT. Comparison of physical characteristics and collection and elution performance of clinical swabs. *African J Microbiol Res.* 2013;7(31):4039-4048. doi:10.5897/AJMR12.1785.
490. Rubin LG, Rizvi A, Baer A. Effect of swab composition and use of swabs versus swab-containing skim milk-tryptone-glucose-glycerol (STGG) on culture- or PCR-based detection of *Streptococcus pneumoniae* in simulated and clinical respiratory specimens in STGG transport medium. *J Clin Microbiol.* 2008;46(8):2635-2640. doi:10.1128/JCM.01903-07.
491. Landers TF, Hoet A, Wittum TE. Swab type, moistening, and preenrichment for *Staphylococcus aureus* on environmental surfaces. *J Clin Microbiol.* 2010;48(6):2235-2236. doi:10.1128/JCM.01958-09.
492. Matheson A, Christie P, Stari T, et al. Nasal swab screening for methicillin-resistant *Staphylococcus aureus*—how well does it perform? A cross-sectional study. *Infect Control Hosp Epidemiol.* 2012;33(8):803-808.
493. Sparham PD, Lobban DI, Speller DC. Isolation of *Staphylococcus aureus* from sputum in cystic fibrosis. *J Clin Pathol.* 1978;31(10):913-918. doi:10.1136/jcp.31.10.913.
494. Freitas AI, Vasconcelos C, Vilanova M, Cerca N. Optimization of an automatic counting system for the quantification of *Staphylococcus epidermidis* cells in biofilms. *J Basic Microbiol.* 2014;54(7):750-757. doi:10.1002/jobm.201200603.
495. Jonas D, Jonas D, Speck M, et al. Rapid PCR-Based Identification of Methicillin-Resistant. *J Clin Microbiol.* 2002;40(5):1821-1823. doi:10.1128/JCM.40.5.1821.
496. Paule SM, Mehta M, Hacek DM, Gonzalzes TM, Robicsek A, Peterson LR. Chromogenic media vs real-time pcr for nasal surveillance of methicillin-resistant *staphylococcus aureus* impact on detection of mrsa-positive persons. *Am J Clin Pathol.* 2009;131(4):532-539. doi:10.1309/AJCP18ONZUTDUGAQ.
497. Ratner B, Hoffman A, Schoen F. Biomedical Engineering e-Mega Reference: Academic Press. In: ; 2009:305-347.
498. Campbell AP, Kuypers J, Englund JA, Guthrie KA, Corey L, Boeckh M. Self-collection of foam nasal swabs for respiratory virus detection by PCR among immunocompetent subjects and hematopoietic cell transplant recipients. *J Clin Microbiol.* 2013;51(1):324-327. doi:10.1128/JCM.02871-12.
499. Yager P, Edwards T, Fu E, et al. Microfluidic diagnostic technologies for global public health. *Nature.* 2006;442(7101):412-418. doi:10.1038/nature05064.
500. Martinez AW, Phillips ST, Whitesides GM, Carrilho E. Diagnostics for the developing world: microfluidic paper-based analytical devices. *Anal Chem.* 2010;82(1):3-10. doi:10.1021/ac9013989.
501. Ngom B, Guo Y, Wang X, Bi D. Development and application of lateral flow test strip technology for detection of infectious agents and chemical contaminants: A review. *Anal Bioanal Chem.* 2010;397(3):1113-1135. doi:10.1007/s00216-010-3661-4.

502. Li X, Ballerini DR, Shen W. A perspective on paper-based microfluidics: Current status and future trends. *Biomicrofluidics*. 2012;6(1):11301-1130113. doi:10.1063/1.3687398.
503. Weigl B, Domingo G, LaBarre P, Gerlach J. Towards non- and minimally instrumented, microfluidics-based diagnostic devices. *Lab Chip*. 2008;8(12):1999-2014. doi:10.1039/b811314a.Towards.
504. Ballerini DR, Li X, Shen W. Patterned paper and alternative materials as substrates for low-cost microfluidic diagnostics. *Microfluid Nanofluidics*. 2012;13(5):769-787. doi:10.1007/s10404-012-0999-2.
505. Fenton EM, Mascarenas MR, Lopez GP, Sibbett SS. Multiplex lateral-flow test strips fabricated by two-dimensional shaping. *ACS Appl Mater Interfaces*. 2009;1(1):124-129. doi:10.1021/am800043z.
506. Martinez AW, Phillips ST, Whitesides GM. Three-dimensional microfluidic devices fabricated in layered paper and tape. *Proc Natl Acad Sci U S A*. 2008;105(50):19606-19611. doi:10.1073/pnas.0810903105.
507. Gervais L, Hitzbleck M, Delamarche E. Capillary-driven multiparametric microfluidic chips for one-step immunoassays. *Biosens Bioelectron*. 2011;27(1):64-70. doi:10.1016/j.bios.2011.06.016.
508. Zimmermann M, Hunziker P, Delamarche E. Autonomous capillary system for one-step immunoassays. *Biomed Microdevices*. 2009;11(1):1-8. doi:10.1007/s10544-008-9187-2.
509. Gervais L, Delamarche E. Toward one-step point-of-care immunodiagnostics using capillary-driven microfluidics and PDMS substrates. *Lab Chip*. 2009;9(23):3330-3337. doi:10.1039/b906523g.
510. Washburn EW. The Dynamics of Capillary Flow. *Phys Rev*. 1921;17(3):273-283. doi:10.1103/PhysRev.17.273.
511. Lucas R. Rate of capillary ascension of liquids. *Kolloid Z*. 1918.

11. Appendices

11.1. Appendix 1: Amplification sequence details

qPCR

MSSA/MRSA (*ldh-1*) → waiting on details from our collaborators at EliTechGroup

- Forward primer:
- Reverse primer:
- Probe:

*E. coli (rodA)*¹³¹

- Forward primer: 5'-GCAAACCACCTTTGGTTCG-3'
- Reverse primer: 5'-CTGTGGGTGTGGATTGACAT-3'
- Probe: 5'-FAM-AACCCCTACAACCGGCAGAATACC-BHQ-1-3'

*N. gonorrhoeae (porA)*¹³²

- Forward primer: 5'-CCGGAAGTGGTTTCATCTGATT-3'
- Reverse primer: 5'-GTTTCAGCGGCAGCATTCA-3'
- Probe: 5'-FAM-CGTGAAAGTAGCAGGCGTATAGGCGGACTT-BHQ-1-3'

*C. trachomatis (omcB)*¹³³

- Forward primer: 5'-GACACCAAAGCGAAAGACAACAC-3'
- Reverse primer: 5'-ACTCATGAACCGGAGCAACCT-3'
- Probe: 5'-FAM-AAGCAAAAAGCAAGAAAAAACCACAGCAAAGAG-TAMRA-3'

HeLa epithelial cells (*β-globin*)²¹⁰

- Forward primer: 5'-CAAGACAGGTTTAAGGAGACCA-3'
- Reverse primer: 5'-GCAGAATCCAGATGCTCAAGG-3'

McCoy epithelial cells (*β-actin*)²⁸²

- Forward primer: 5'-TCACCCACACTGTGCCCATCTACGA-3'
- Reverse primer: 5'-TGGTGAAGCTGTAGCCACGCT-3'

qRT-PCR

RSV (polymerase gene)

- Forward primer: 5'-AATACAGCCAAATCTAACCAACTTTACA-3'
- Reverse primer: 5'-GCCAAGGAAGCATGCAATAAA-3'
- Probe: 5'-6FAM-TGCTATTGTGCACTAAAG-MGBNFQ-3'

iSDA

MSSA/MRSA (*ldh-1*)

- Forward primer: 5'-GCATAATACTACCAGTCTCCTCAGCCAAGCTACGCATTTTCATT-3'
- Reverse primer: 5'-TAGAATAGTCGCATACTCCTCAGCACATCTCCTCGAACTTTTT-3'
- Forward bumper primer: 5'-AGGTAATGGTGCAGTAGGT-3'
- Reverse bumper primer: 5'-CCAGCTTTCACACGAAC-3'
- Biotin probe: 5'-CTAATTCATCAACAATGC-biotin TEG-3'

N. gonorrhoeae (SSDM)

- Forward primer: 5'-CCTTCATTCTTGTCCGTCCTCAGCAAATCAGCGATAAAACAC-3'
- Reverse primer: 5'-CCGTCTCATGTATCTCACCTCAGCGGCTAATCATACCTTTCA-3'
- Forward bumper primer: 5'-ATATTCCACAAAATGCCAGT-3'
- Reverse bumper primer: 5'-CGATGCATACGACGATAAAC-3'
- Probe: 5'-CCGCGAATATCGGTAAAATTTCCACCTTCCGCGG-3'

C. trachomatis (plasmid)

- Forward primer: 5'-GCAATATAGTACCAGTCTCCTCAGCTCGTTCCGAAATAGAAAA-3'
- Reverse primer: 5'-GCAATATAGAACCAGTATCCTCAGCTCAGTAGAGTCTTCAAA-3'
- Forward bumper primer: 5'-GGATAGCACGCTCGGTA-3'
- Reverse bumper primer: 5'-AGCAAGCTGCCTCAGAAT-3'
- Biotin probe: 5'-TGTTAGGTAAAGCTCTG-biotin TEG-3'

11.2. Appendix 2: Urine characterization

Table 13. Urine characterization data for 35 de-identified, discarded human urine samples provided by the Harborview STI Clinic (all samples went through one freeze-thaw cycle). Sample pH and salinities were measured by standard laboratory pH and conductivity meters. The thermal lysis recoveries were measured by qPCR after heating cells in the urine sample for 10 minutes at 95°C. The % lysis was compared to cell lysed in 10 mM Tris, pH 8. Total NA content was measured after thermal cell lysis and ethanol precipitation. Purified NA were measured using a Nanodrop. Total dissolved solids were weighed after overnight evaporation of sample liquid at 95°C. Protein content was measured qualitatively using the commercially available Vivaspin 500 kit. Cells left blank were not measured.

Sample ID	pH	Salinity (mM)	% Thermal <i>E. coli</i> lysis	Total NA (ng/μL)	Total Dissolved Solids (μg/μL)	Protein Content
SAB 01	7.3	181	65 %	0.5	9.4	Very low
SAB 02	6.2	108	84 %	9.8	24.0	Medium
SAB 03	6.0	11	88 %	0.3	0.8	Low
SAB 04	7.8	132	58 %	1.0	22.0	Medium
SAB 05	6.8	37	40 %	3.0	15.6	Medium

SAB 06	5.3	416	19 %	15.4	68.2	Medium
SAB 07	6.0	108	24 %	9.9	45.6	
SAB 08	5.8	214	28 %	2.4	58.0	Medium
SAB 09	7.0	78	54 %	2.1	17.2	Medium-high
SAB 10	5.8	236	52 %	15.8	51.4	Very high
Sample ID	pH	Salinity (mM)	% Thermal <i>N. gon</i> lysis*	Total NA (ng/μL)	Total Dissolved Solids (μg/μL)	Protein Content
SAB 11	5.6	251	83 %	17.4		
SAB 12	6.3	184	120 %	72		
SAB 13	5.7	186		8.3		
SAB 14	5.8	197	79 %	8.0		
SAB 15	5.8	166	73 %	2.8		
SAB 16	8.2	170	113 %	1.0		
SAB 17	6.5	70	98 %	1.4		
SAB 18	7.6	369	168 %	6.3		
SAB 19	6.5	91		2.3		
SAB 20	6.0	269	70 %	44.2		
SAB 21	7.1	137	4 %			
SAB 22	6.2	170	18 %			
SAB 23	6.7	70	2 %			
SAB 24	6.8	110	19 %			
SAB 25	5.4	176	60 %			
SAB 26	6.9	49	18 %			
SAB 27	6.1	102	4 %			
SAB 28	5.6	196	92 %			
SAB 29	5.7	199	97 %			
SAB 30	6.4	62	33 %			
SAB 31	6.8	319	15 %			
SAB 32	5.8	160	0 %			
SAB 33	5.2	234	37 %			
SAB 34	5.9	169	50 %			
SAB 35	6.5	67	39 %			
Average	6.3	165	E: 51 % N: 56 %	8.0	31.2	-
SD	0.7	91	E: 24 % N: 45 %	10.1	22.8	-
N	35	35	33	20	10	10

11.3. Appendix 3: Amplification interference studies

Although NAATs are highly sensitive and specific, they often require purified NA to function properly. Common patient samples used for disease diagnosis, such as blood and urine, are very complex and contain amplification inhibiting agents. One common inhibitor found in blood is heme.

This work serves as motivation for NA purification and better understanding of the sample matrix effects on downstream NAAT. It includes three subsections: (i) quantification of qPCR inhibition from substances found in patient samples; (ii) quantification of iSDA inhibition; and (iii) comparison of methods for inhibition removal to improve NAAT performance. This study builds upon previous work by testing a large panel of inhibitors, using clinically relevant inhibitor concentrations, testing lower ranges of input nucleic acids down to 100 input copies, and by comparing the laboratory standard PCR to an isothermal NAAT. Common laboratory Inhibitor removal platforms – freeze/thaw, ethanol precipitation, and the DNeasy Qiagen kit – were compared to an alternative platform developed as part of this dissertation. The results from this study can help guide the future design of NAAT-based technology and serve as a model for future testing platforms.

Background

Reliable disease diagnosis and monitoring of treatment depends on accurate testing of patient samples. Many standard clinical assays rely on NAATs, such as quantitative polymerase chain reaction (qPCR), for pathogen identification. Although it is highly sensitive and specific, PCR is susceptible to inhibitory species found in patient samples such as urine, blood, or stool²⁸³. Inhibitors can reduce the sensitivity of an assay or lead to false-negative results^{266,284}. A recent review by Schrader *et al.* summarized many common PCR interferents and provided some mechanisms of assay inhibition²⁶⁶, **Figure 88**.

PCR is prone to inhibition when only 1–2 % (v/v) of whole blood is present in the reaction²⁸⁵. Some common components of blood that cause inhibition are heme/hemoglobin²⁶⁵, lactoferrin²⁶⁵, IgG²⁸⁶, heparin^{265,287}, and calcium ions²⁸⁸. Reagents in sample collection devices, such as EDTA, can also inhibit amplification reactions²⁸⁹. Heme/hemoglobin inhibit PCR by releasing iron ions that compete for the

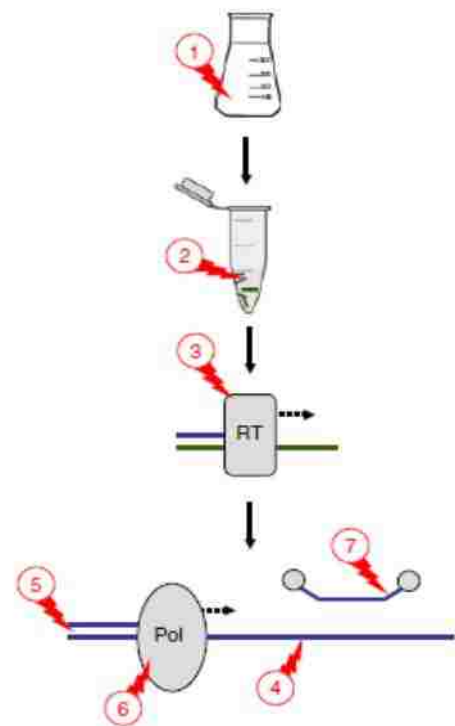


Figure 88. Methods of PCR inhibition. NA may react with the reaction vessel (1) or contaminants may be introduced during sample processing (2). Inhibitors may prevent reverse transcription (RT) for RNA-based assays (3) or degrade the NA template (4). Primer annealing (5) or polymerase (6) may be degraded or blocked. The probes for detection may also be inhibited (7)²⁶⁶.

magnesium (Mg^{2+}) binding site on polymerases. Heme/hemoglobin have also been shown to chelate Mg^{2+} , which is a required co-factor for the majority of DNA polymerases²⁶⁵. There are three proposed mechanisms by which lactoferrin can inhibit PCR: release of iron ions that then bind to the polymerase²⁹⁰, sequestering divalent cations, such as Mg^{2+} , preventing activation of the polymerase²⁹¹, and binding to DNA which can reduce the efficiency of DNA's interactions with amplification reagents²⁹². Al-soud *et al.* showed that IgG interacts with single stranded DNA, reducing its ability to interact with amplification reagents²⁸⁶ and it has been suggested that heparin competes with target DNA for binding of reaction components²⁶⁵. EDTA is a common substance that chelates important magnesium ions thereby removing them from the participating in the reaction²⁸⁹. Finally, the presence of calcium ions can inhibit DNA polymerases by competing for the co-factor binding site²⁸⁸.

In addition to inhibition from blood, PCR is also prone to reduced performance in the presence of urine. Urea is the most common interfering species found in urine samples. Khan *et al.* showed inhibition of PCR with concentrations of urea greater than 50 mM using a *Taq* polymerase²⁹³ and Hu *et al.* showed inhibition of a multiplexed system using 250 mM urea²⁹⁴. These values are similar to the average concentration of urea in urine from a healthy adult¹³⁴. To date, urea's exact PCR inhibition mechanism is unknown²⁶⁶, but it is a common agent used for denaturing proteins so at high concentrations urea may denature polymerases.

In addition to these examples of individual PCR inhibitors, studies have also tested the inhibition effects of an entire sample matrix. Mahony *et al.* evaluated the effect of patient urine on identification of chlamydia *via* PCR²⁹⁵. The authors also tested three common laboratory-based mechanisms to remove the observed inhibition. Zhang *et al.* utilized an inhibitor-resistant *Taq* polymerase and additional PCR additives to achieve successful amplification in up to 25 % whole blood²⁹⁶. Using this same amplification mixture, Taylor *et al.* achieved successful amplification of malaria infected samples in up to 5 % whole blood and calculated a PCR efficiency of 84 %²⁹⁷. As illustrated by Zhang *et al.* and Al-Soud *et al.*, the sensitivity of PCR amplification to inhibition varies based on the choice of DNA polymerase and other reaction components^{265,296}.

In recent years, there has been a focus on developing rapid diagnostic devices for POC applications^{26,38,53,55}. Many of these technologies aim to translate traditional laboratory-based tests, such as NAATs, to the POC^{59,61}. Due to the constraints imposed by many POC settings – such as limited access to laboratory equipment, potentially long time to result, and untrained users – a large field of research has focused on developing isothermal NAATs⁶³ that could help reduce the time,

cost, and equipment requirements of conventional laboratory-based tests. One of the most common isothermal NAATs is loop mediated isothermal amplification (LAMP)⁶⁴. Many of the isothermal NAATs, including LAMP, utilize some of the same reaction components as PCR, such as *Bst* polymerase. These similarities also make isothermal NAATs sensitive to inhibitory species^{51,298-300}.

To date, there has been limited research exploring the susceptibility of isothermal NAATs to inhibitory agents found in patient samples. Most of the literature in this space focuses on the inhibition of LAMP. Nixon *et al.* compared the inhibitory effects of three species – plasma, K₂EDTA, and ethanol – on PCR and LAMP. They showed inhibition of a standard LAMP reaction with 6% (v/v) ethanol, 3.5 mM K₂EDTA, and 25% (v/v) plasma²⁹⁹. However, they used relatively high copy number inputs: 10,000 copies of DNA per reaction. The inhibitory effects may have been more severe with less inhibitor at lower DNA input. Zhang *et al.* compared inhibition of qPCR, qRT-PCR, and LAMP from common produce for the detection of *Salmonella*³⁰⁰. Curtis *et al.* has demonstrated successful LAMP reactions using diluted or lysed whole blood at a moderate input copy number of 1000 cells^{301,302}.

In order for isothermal amplifications to be more widely utilized, especially for clinical applications, researchers need to duplicate the extensive work done on PCR and rigorously test isothermal NAATs against a panel of inhibitors. As such, we have conducted a study testing a range of potential assay inhibitors in two amplification systems: qPCR and a DNA-based isothermal amplification (isothermal strand displacement assay, iSDA³⁰³). We have also tested the efficacy of inhibitor removal using three common laboratory purification methods as well as one alternative platform developed in our lab.

Methods

Inhibitor selection. Common species that were shown to inhibit PCR or LAMP based on a review of the current literature were identified for this study. Additionally, we selected some of the most abundant compounds found in urine, nasal, and blood samples. Finally, we elected to test the inhibitory effects of four complete sample matrices: urine, nasal matrix, plasma, and blood. **Table 14** summarizes the selected inhibitors, the average concentration found in a healthy individual, and the concentration range tested in this study.

Table 14. Summary of the inhibiting species selected for study. The highest concentration solutes found in human samples were selected for study^{134,230,304–309} as well as reports from the literature suggesting amplification inhibition.

Inhibitory Species	Average Conc. in Health Human Sample	Concentration Range Tested in Reactions
Albumin	0.63 mM (blood) 0.61 μM (urine)	0.0063 – 0.25 mM
Creatinine	12.5 mM (urine)	0.125 – 5 mM
Glucose	23 mM (blood) 0.29 mM (urine)	0.23 – 9.2 mM
Hemin	4 mM (blood)	0.04 – 1.6 mM
Hemoglobin	0.63 mM (blood)	0.0063 – 0.25 mM
IgG	80 μM (blood) 5.9 μM (urine)	0.8 – 32 μM
Lactoferrin	40 μM (blood) 0.009 μM (nasal matrix) 0.025 μM (urine)	0.4 – 15 μM
Sodium bicarbonate	8.85 mM (blood) 4.8 mM (urine)	0.09 – 3.54 mM
Sodium chloride	600 mM (blood) 130 mM (urine)	1.5 – 60 mM
Urea	270 mM (urine)	2.7 – 108 mM

Detection of amplification inhibitors by spiking experiments. The inhibitors identified in Table 14 above were spiked into either qPCR or iSDA to achieve final assay concentrations equivalent to 1 %, 10 %, and 40 % of the average concentration observed in a healthy human individual. These levels were selected as low, medium, and high inhibitor concentrations. For example, the average active NaCl concentration in human urine is 150 mM¹³⁴ so the assays were tested with final concentrations of NaCl of 1.5 mM, 15 mM, and 60 mM. A 100 % inhibitor level was not evaluated because reactions require the addition of assay reagents which results in at least partial dilution of the sample. In addition to the individual components, the full sample matrices of urine, plasma, blood, and simulated nasal matrix (SNM) were also spiked into the amplification reactions to achieve final concentrations of 1 %, 10 %, and 40 % (v/v).

qPCR. Effect of inhibitors on qPCR was quantified with a kit for the *ldh-1* gene of methicillin resistant *Staphylococcus aureus* (MRSA) provided by the ELITechGroup. The 20 μL reactions included 1 μL of input sample and were run on a BioRad CFX96 real-time PCR instrument using the following protocol: 50°C hold for 2 minutes, 93°C hold for 2 minutes, 45 cycles of 93°C for 10 seconds, 56°C for 30 seconds, and 72°C for 15 seconds, ending with final elongation step at 72°C for

5 minutes. Fluorescence data were collected during the 56°C annealing step using the Texas Red channel. The results were analyzed using the automated cycle threshold (Ct) value calculation in the BioRad CFX Manager software. This assay is sensitive down to $\sim 10^1$ copies of the target sequence.

The effect of the inhibitor was determined by comparing the amount of DNA measured by qPCR in the presence of an inhibitor to a standard reaction with the same amount of DNA and no inhibitor. This value was labeled the % amplification activity and is a measure of qPCR performance in the presence of an inhibitor, (Equation 14).

$$\% \text{ amplification activity} = \frac{\text{amount of DNA measured}_{inhibitor}}{\text{amount of DNA measured}_{standard}} \times 100\% \quad (\text{Equation 14})$$

iSDA. Effect of inhibitors on the DNA isothermal strand displacement assay (iSDA) was quantified with a kit for the *ldh-1* gene of MRSA provided by the ELITechGroup. The 35 μL reactions included 1 μL of input sample and were run on a BioRad CFX96 real-time PCR instrument using the following protocol: 49°C hold for 30 minutes. Fluorescence data were collected every minute using the Texas Red channel. The relative fluorescent units (RFUs) of the amplification curves were extracted using the BioRad CFX Manager software. This assay is sensitive down to $\sim 10^1$ copies of the target sequence.

The effect of the inhibitor was determined by comparing the amplicon production of a reaction performed in the presence of an inhibitor to a standard reaction without any inhibitor. This value was labeled the % expected amplicons, (Equation 15). iSDA amplicons were quantified by qPCR, described below.

$$\% \text{ expected amplicons} = \frac{\# \text{ amplicons}_{inhibitor}}{\# \text{ amplicons}_{standard}} \times 100\% \quad (\text{Equation 15})$$

iSDA amplicon qPCR. This assay was developed by Dr. Erin Heiniger in the Yager lab. Post amplification, iSDA reactions were diluted between 10^{-7} to 10^{-9} because successful amplicon production results in 10^{11} to 10^{13} target sequences; qPCR, however, works best with input concentrations of 10^2 to 10^5 . The 20 μL reactions included 1 μL of the diluted iSDA result and were prepared with the Biorline SYBR Sensifast No-ROX qPCR master mix and primers that target the iSDA amplicon. Reactions were run on a BioRad CFX96 real-time PCR instrument using the following protocol: 95°C hold for 10 minutes, 40 cycles of 95°C for 15 seconds, 55°C for 15 seconds, and 72°C for 15 seconds. Fluorescence data were collected during the 72°C elongation step using the SYBR Green channel. The results were analyzed using the automated Ct value calculation in the BioRad

CFX Manager software which quantified the amount of iSDA amplicon used in equation 2 above. This assay is sensitive down to $\sim 10^1$ copies of target.

Agarose gels. All qPCR reactions were also analyzed by gel electrophoresis to determine if the inhibitor was preventing detection *via* the fluorescent probe or the actual amplification reaction. A 1% agarose gel was prepared in 0.5x TBE and 1 μL of SYBR safe gel stain per 10 mL of gel. 8 μL samples were loaded into the well with 2 μL of loading dye. The gels were run for 75 minutes at a constant voltage of 90 V. Gels were imaged using the BioRad BioDoc Gel Reader system.

Polyacrylamide gels. All iSDA reactions were also analyzed by gel electrophoresis to determine if the inhibitor was preventing detection *via* the fluorescent probe or the actual amplification reaction. All of the polyacrylamide gels for identification of iSDA products were run by Enos Kline.

Inhibitor deactivation. Deactivation of inhibitors was attempted by heat denaturation at 95 $^{\circ}\text{C}$ for 5 minutes with and without prior ACP treatment at room temperature for 2 minutes. Samples were prepared as described in the “spiking experiments” section above and the inhibition effect was determined with the defined qPCR and iSDA protocols.

Paper-based purification. A 50 mM MES solution, pH 5, containing 10^2 or 10^3 copies of purified genomic DNA per μL was spiked with an inhibitor. The sample was then introduced to a novel paper-based purification method, described in detail in Aim 3. The purified samples were analyzed by adding 1 μL to qPCR or iSDA, as described above. The efficiency of the paper-based purification system on inhibitor removal for qPCR and iSDA was determined using **Error! Reference source not found.** or **Error! Reference source not found.**, respectively.

Results and Discussion

The main objectives of this work include identifying qPCR and iSDA inhibitors and quantifying their effects at clinically relevant concentrations. After identification, multiple methods of inhibitor deactivation or removal will be compared. Finally, potential mechanisms of inhibition will be suggested and explored.

Detection of qPCR inhibitors by spiking experiments. qPCR and its mechanism is well understood. A DNA template is added to a buffered solution containing a free nucleotides, two primers that recognize a specific sequence on the template, a fluorescent probe, and a polymerase that recognizes the primers binding to template. The primers bind to the template DNA (annealing) after the two strands of the double helix are denatured into single strands. The polymerase then copies each of the two target strands (called elongation) which doubles the amount of product in the

reaction. After this elongation step, the fluorescent probe can bind to the targets, called amplicons. These steps happen at distinct temperatures: 93-95°C for denaturation, 50-65°C for primer annealing, and 72°C for elongation and probe binding (depending on the probe and target sequence elongation and probe binding may also occur at the primer annealing temperature), **Figure 89A**.

Because qPCR follows this specific mechanism during every heating cycle, the resulting number of products made can be directly calculated based on the number of input targets. Also, the number of copies made is directly linked to the resulting fluorescent signal; more amplicons equates to more probe binding and a higher fluorescent signal. Using this relationship, a standard curve can be produced by introducing known concentrations of DNA into the reaction. These known concentrations will amplify and after a certain number of cycles there will be enough amplicons that the bound fluorescent probe becomes detectable. The cycle at which the fluorescence is detectable is called the cycle threshold (Ct). A linear standard curve is then constructed using the Ct values and known input DNA concentrations, (*Equation 16*).

$$Ct = m * [\log(\text{input DNA conc})] + b \quad (\text{Equation 16})$$

Where m is the slope and b is the y-intercept of a line generated based on the log of the input DNA concentration and the output measured fluorescence signal. qPCR is an exponential amplification where a linear relationship exists between the number of input DNA molecules and the output fluorescent signal. These features enable qPCR to be highly quantitative for samples of unknown DNA concentration because a measured Ct value tracks to the original input concentration, **Figure 89B**.

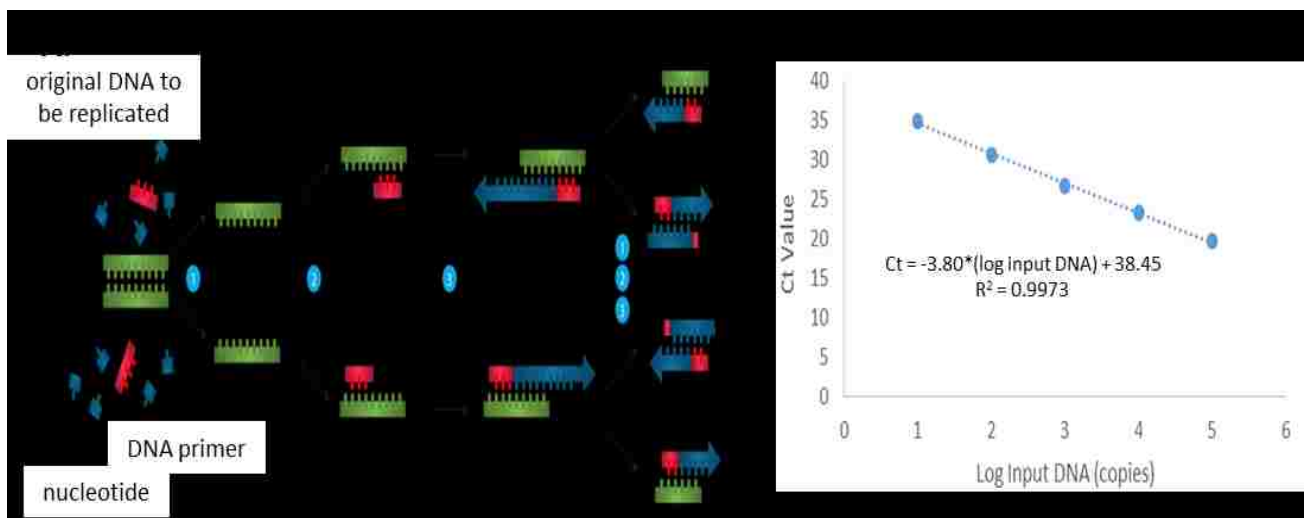


Figure 89. Summary of qPCR mechanism. **A.** Schematic with the original DNA template in green, free

nucleotides in blue, and primers in red³¹⁰. **B.** Standard curve generated from an actual experiment.

This quantitative nature of qPCR enables the measurement of assay inhibition if samples with or without inhibitor and the same amount of input DNA are compared. For example, two reactions that both have 10^3 DNA molecules as a reaction input should be quantified as 10^3 copies by qPCR. If one of the two reactions contained an inhibitor that reduced assay activity by 90 %, qPCR would only measure $\sim 10^2$ DNA molecules instead of 10^3 .

To date, 6 of the 19 selected agents have been tested for potential inhibition of qPCR. Of these six, lactoferrin and hemin show partial or total inhibition by real-time readout. Amplifications in the presence of greater than 1 % (0.0004 mM) lactoferrin are completely inhibited **Figure 3A**. The gel results show some slight amplicon production at 1 % lactoferrin but the amplification efficiency is still severely reduced, **Figure 90B**. When hemin (heme with a complexed iron molecule) is added to qPCR in concentrations above 1 % (0.04 mM), the amplification is completely inhibited by real time read out, **Figure 90C**. The gel results agree with the real time quantification showing no amplification at 10 % and 40 % hemin but moderate to strong amplification at 1 %, **Figure 90D**.

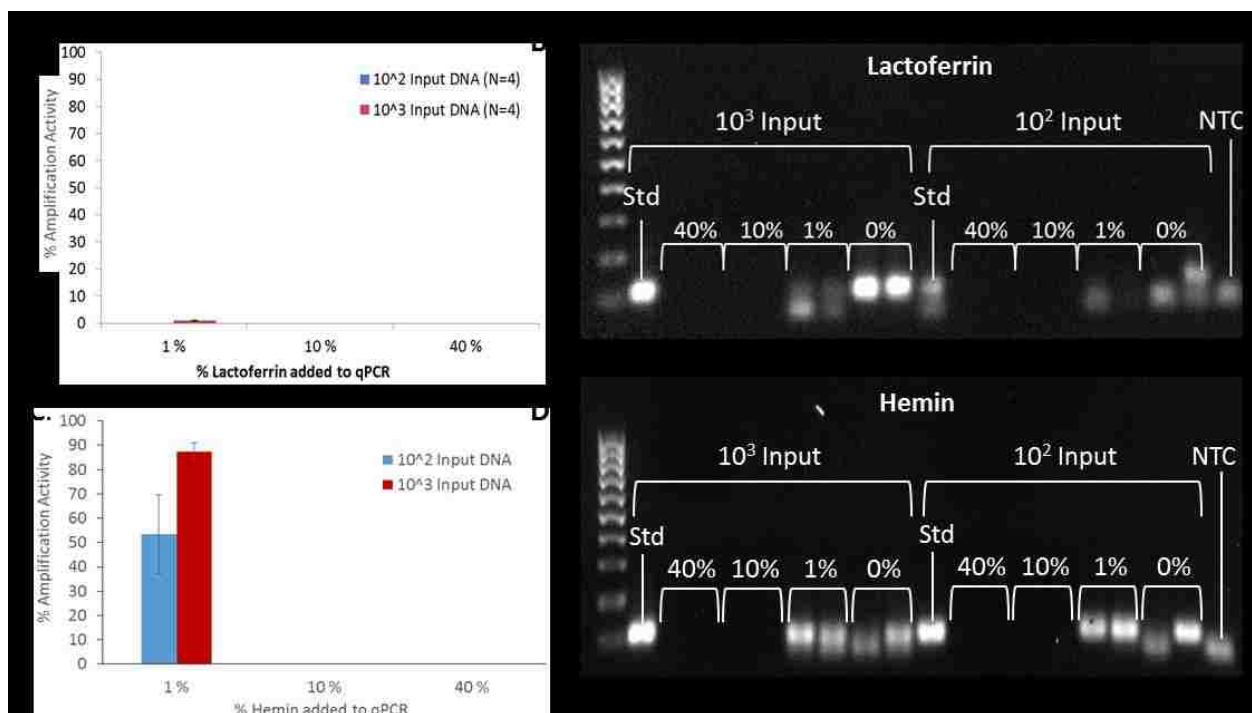


Figure 90. Example of qPCR inhibition. **A.** Real time qPCR with increasing amounts of lactoferrin. The % amplification activity is compared to a qPCR reaction with 0 % lactoferrin. The average of $N=4$ reactions \pm SE is presented. **B.** Agarose gel of lactoferrin qPCR products showing complete assay inhibition when at least 10 % (0.004 mM) of lactoferrin is added to the reaction. **C.** Real time qPCR with increasing amounts of hemin, the average of $N=4$ reactions \pm SE is presented.

D. Agarose gel of qPCR products shows complete inhibition of qPCR at 10 % and 40 % hemin.

The other four agents tested showed little inhibition of qPCR. Glucose did not reduce the activity of qPCR with 10^3 input copies of DNA. There was slight inhibition at higher glucose concentrations with the lower input copy number, 10^2 . Sodium chloride inhibited qPCR at both 10^3 and 10^2 input copy numbers when present in high concentration (40 %, 60 mM). There was little to no inhibition observed for lower NaCl concentrations.

Hemoglobin and urea seem to enhance qPCR activity in a concentration-dependent fashion. For qPCR in the presence of hemoglobin, the observed enhancement may be a result of molecular crowding which has been seen with other proteins such as albumin. Depending on the molecular structure and properties (polar v. non-polar, surface charges, etc.) additional reagents in an amplification can actually concentrate amplification components to help energetically stabilize molecular interactions. This micro-concentration is called molecular crowding³¹¹ and has been shown to enhance other amplification reactions^{312,313}. For reactions in the presence of urea, previous work has reported that 50 mM or greater concentration of urea can inhibit qPCR but this specific assay was not inhibited even at the highest concentration of urea tested (40 %, 108 mM). In fact, urea seemed to enhance qPCR activity for reactions with 10^3 input copies of DNA. Urea's structure may play a role in stabilizing molecular interactions during qPCR due to its high capacity for hydrogen bonding; this may also explain why higher concentrations seemed to enhance the activity of this qPCR more than lower urea concentrations. **Table 15** summarizes the current status of qPCR inhibition.

Table 15. Summary of qPCR inhibition results. Both qPCR and an agarose gel were performed for each inhibitor at three concentrations using either 10^3 or 10^2 input copies of DNA. The final concentration of each inhibitor in qPCR was 40, 10, or 1 % of the average concentration found in a healthy human. The % amplification activity is compared to reactions with 0 % added inhibitor. Averages \pm SE for at least N=3 is reported.

Inhibitor	Input DNA Conc.	% Amplification Activity		
		40 %	10 %	1 %
Glucose	10^3	103 \pm 5.5 %	101 \pm 2.8 %	104 \pm 5.3 %
	10^2	64 \pm 9.0 %	73 \pm 7.4 %	117 \pm 23%
Hemin	10^3	0 \pm 0 %	0 \pm 0 %	87 \pm 3.7 %
	10^2	0 \pm 0 %	0 \pm 0 %	53 \pm 16 %
Hemoglobin	10^3	72 \pm 2.2 %	114 \pm 22 %	192 \pm 25 %

	10^2	$34 \pm 12 \%$	$34 \pm 4.6 \%$	$141 \pm 33 \%$
Lactoferrin	10^3	$0 \pm 0 \%$	$0 \pm 0 \%$	$1.0 \pm 0.1 \%$
	10^2	$0 \pm 0 \%$	$0 \pm 0 \%$	$0 \pm 0 \%$
Sodium chloride	10^3	$0 \pm 0 \%$	$145 \pm 5.1 \%$	$148 \pm 3.9 \%$
	10^2	$0 \pm 0 \%$	$76 \pm 6.0 \%$	$93 \pm 10.3 \%$
Urea	10^3	$200 \pm 10.7 \%$	$152 \pm 7.5 \%$	$113 \pm 16 \%$
	10^2	$104 \pm 13 \%$	$106 \pm 31 \%$	$73 \pm 5.5 \%$

Detection of iSDA inhibitors by spiking experiments. The isothermal strand displacement assay (iSDA) utilizes some of the same reaction components and general mechanisms as qPCR such as target-specific primer recognition and elongation with a DNA polymerase. It does, however, have some notable differences. As the name implies, iSDA takes place at a single temperature. Without the initial heat denaturation step, iSDA relies on DNA breathing, the natural tendency of dsDNA to undergo random structural changes which cause base-pairs to break locally³¹⁴. There is also an additional enzyme which recognizes a specific sequence in the template DNA and creates a nick in one of the two strands³¹⁵.

iSDA also utilizes two sets of primers compared to the one set used in PCR. The first set is commonly referred to as the “bumper” primers; once they bind to the target sequence, the polymerase can then bump-off, or displace, the complementary template strand. From here, the second set of primers, called the extension primers, can bind to the DNA leading to extension. The extension primers contain a complementary sequence that binds to the target DNA, a nicking site recognized by the nicking enzyme, and a non-complementary sequence. This process is called the linear amplification stage and the intermediate product is a truncated dsDNA that contains the desired amplicon region, **Figure 91A**. The reaction, however, gets more complex because the truncated dsDNA segment becomes the template for the exponential phase of iSDA.

During the exponential phase, the truncated dsDNA is nicked at the nicking site followed by polymerization and strand displacement of the complimentary strand. Next, the displaced strand undergoes primer annealing of both the bumper and extension primers which are adjacent. The extension primer is polymerized followed by the bumper primer which then bumps the strand that was created from the adjacent extension primer. This displaced strand can then undergo primer annealing and the process is repeated, **Figure 91B**. This complex reaction generates amplicons and non-target side products.

In general, the more input template, the more amplicons that are generated resulting in higher fluorescent signals measured in relative fluorescence units (RFUs), **Figure 91C**. One down-side is that this complicated mechanism does not allow for a simple linear relationship between input template and amplicon formation. There are also no temperature cycles therefore the reactions do not have Ct values. An important benefit of this complex reaction, however, is that it greatly reduces the overall reaction time compared to qPCR which often takes 60-90 minutes. An iSDA can generate detectable product in as little as 15 minutes.

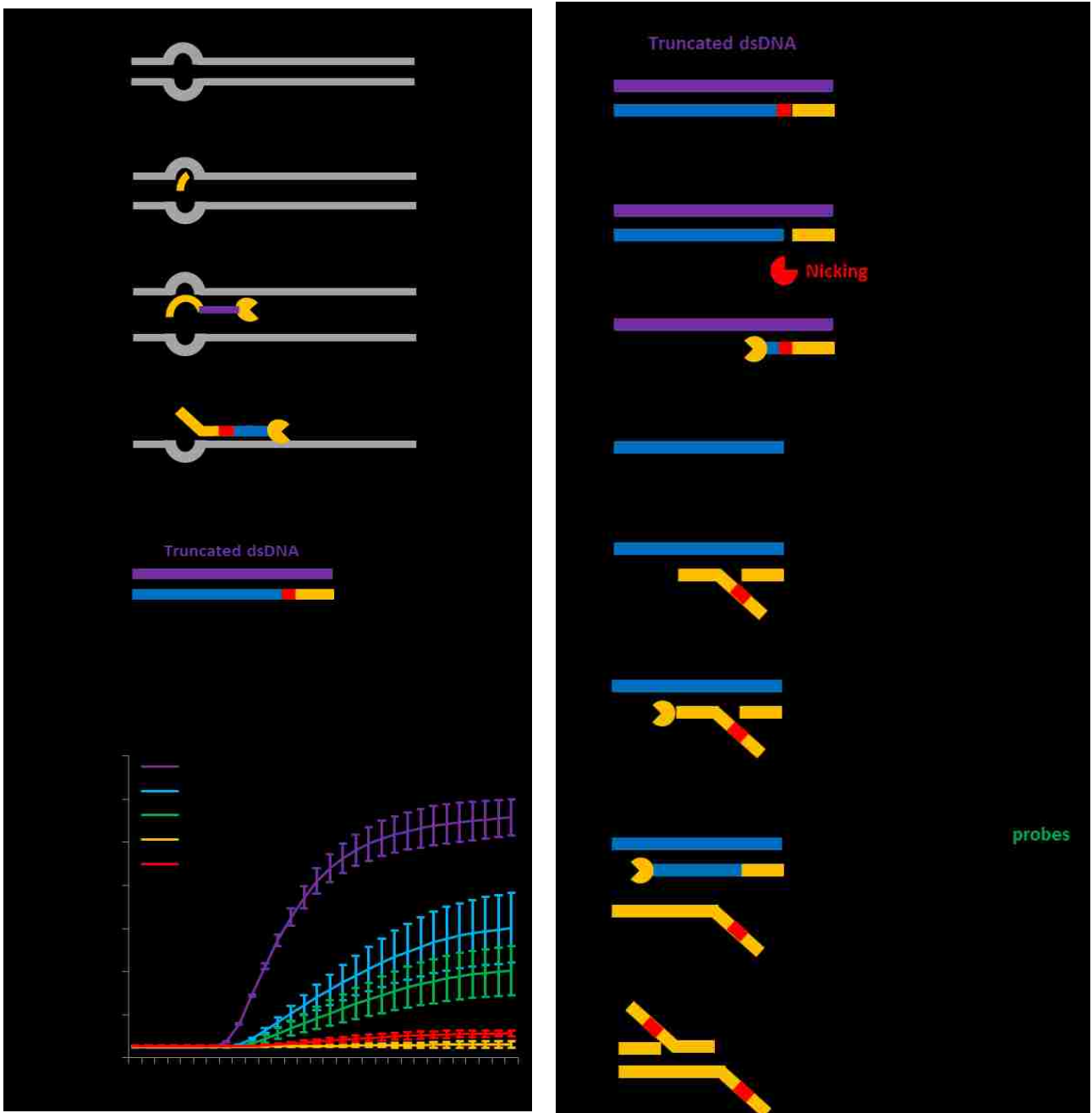


Figure 91. Summary of iSDA mechanism. **A.** Schematic of the linear phase of iSDA and the **B.** exponential phase, adapted from Dr. Joshua Bishop and Dr. Bhushan Toley. **C.** Example of real

time iSDA output with input DNA copies ranging from 10^1 to 10^4 .

Due to the lack of direct quantifiability of iSDA, Dr. Erin Heiniger in the Yager lab developed a qPCR that can measure the absolute number of iSDA amplicons produced. By comparing the number of amplicons produced from reactions with and without inhibitors, we can determine the effect of inhibitors on assay performance.

To date, 10 of the 19 selected agents have been tested for potential inhibition of iSDA. Of these ten, lactoferrin, hemin, urea, sodium chloride, and hemoglobin show partial or total inhibition by real-time readout. **Figure 92A** shows the real time results for iSDA with lactoferrin; there is significant inhibition of real time iSDA above 1 % concentration (0.0004 mM) of the inhibitor. For lactoferrin, these results were verified by both amplicon quantification, **Figure 92B**, and gel, **Figure 92C**. iSDA in the presence of 1 % lactoferrin results in 60-90 % of the expected amplicon production compared to reactions with 0 % added inhibitor. For NaCl, the real-time iSDA results show a somewhat dose-dependence on iSDA inhibition, **Figure 92D**. This result is confirmed by the amplicon quantification, **Figure 92E**. High concentrations of NaCl result in ~50 % of the expected amplicon production compared to reactions with 0 % added inhibitor. At low concentrations of NaCl, the reaction may be slightly enhanced potentially due to interaction stabilization from salt conditions. These results are further confirmed by gel, **Figure 92F**.

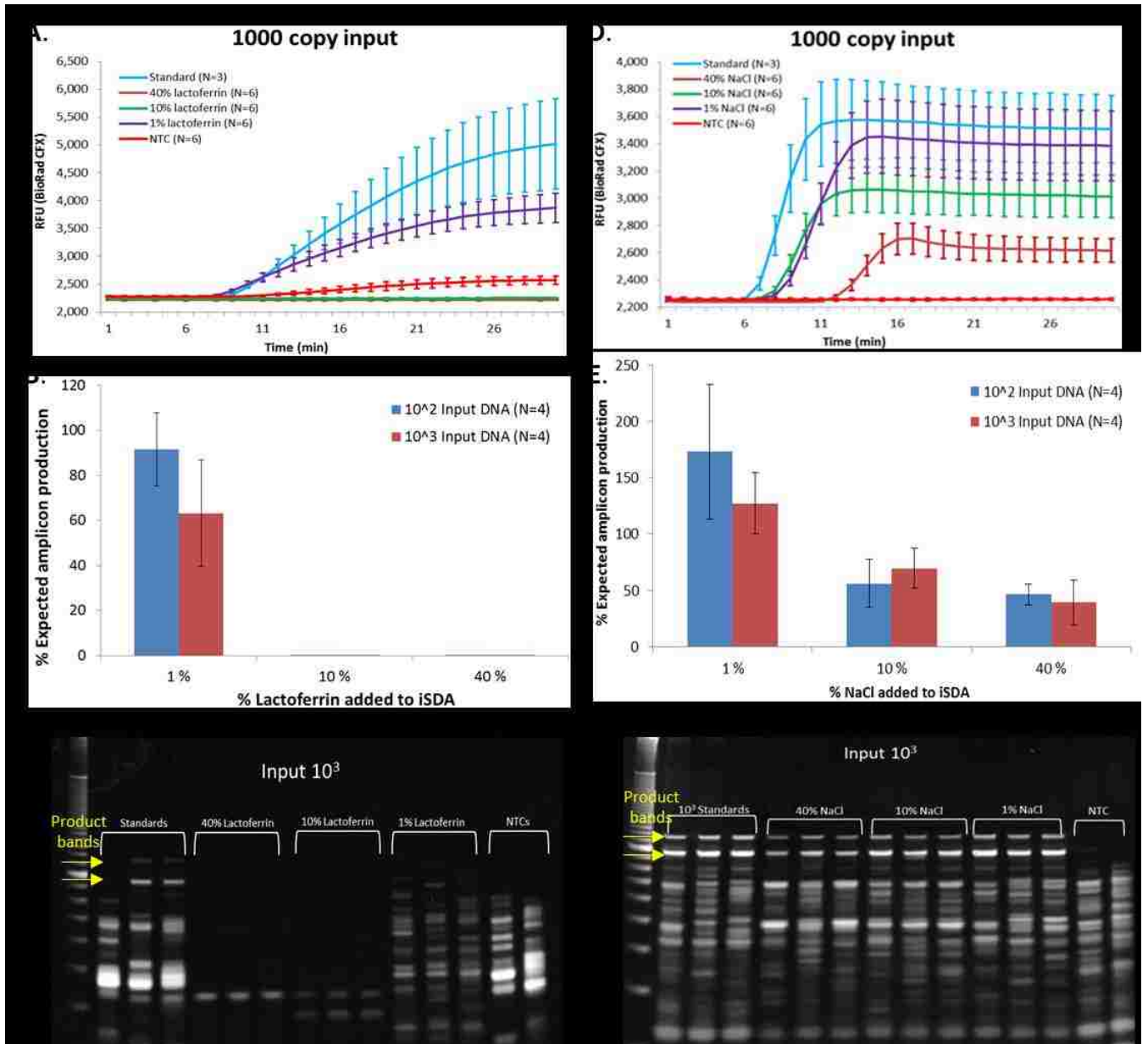


Figure 92. Example of iSDA inhibition experiments. **A.** iSDA real time results of 1000 input copies amplified with increasing amounts of lactoferrin. **B.** Quantified iSDA amplicon production with increasing amounts of lactoferrin added to the assay. The average of N=4 reactions +/- SE is presented. **C.** Polyacrylamide gel results of iSDA reactions with increasing amounts of lactoferrin. iSDA is prone to side-product formation but the addition of lactoferrin completely inhibits any reaction. **D.** iSDA real time results of 1000 input copies amplified with increasing amounts of NaCl. **E.** Quantified iSDA amplicon production with increasing amounts of NaCl added to the assay. The average of N=4 reactions +/- SE is presented. **F.** Polyacrylamide gel results of iSDA reactions with increasing amounts of NaCl.

Currently, the inhibition effects of only a few agents have quantified using the iSDA amplicon qPCR. The others have been qualitatively categorized as “None”, “Some”, or “Complete” inhibition based on iSDA real time or gel results. In general, iSDA has been robust and does not show

amplification inhibition in the presence of albumin, creatinine, glucose, IgG, or sodium bicarbonate. For most conditions tested, hemoglobin and urea did not inhibit iSDA unless at high inhibitor concentrations (40 %, 0.25 mM and 108 mM, respectively) and low input DNA copy numbers (10^2). As with qPCR, there may be some slight amplification enhancement potentially due to molecular crowding effects but these cannot be quantified until the iSDA amplicon qPCRs are performed. Based on the real time read out and amplicon quantification assays, high concentrations of sodium chloride partially inhibit iSDA at both 10^2 and 10^3 input copies.

iSDA does show significant inhibition in the presence of hemin and lactoferrin, which was also the case for qPCR. With qPCR, lactoferrin at any concentration completely inhibited the reaction but for iSDA, there is reduced but still significant amplicon production at 1 % (0.0004 mM) of lactoferrin. Based on the real time and gel results, iSDA is completely inhibited by 1 % hemin (0.04 mM). Interestingly, iSDA seems to be more robust to the addition of lactoferrin than qPCR but less robust than qPCR to the addition of hemin. Based on previously published work, both reactions are sensitive to iron which can be released by both lactoferrin and hemin. The concentration or form of iron may alter slightly between these agents which may explain the differences in assay sensitivities for iSDA and qPCR. Future work will include a quantitative analysis for each inhibitor and more exploration of the inhibition mechanisms. **Table 16** summarizes the current status of iSDA inhibition.

Table 16. Summary of iSDA inhibition results. An iSDA reaction was performed for each inhibitor at three concentrations using either 10^3 or 10^2 input copies of DNA. The final concentration of each inhibitor in iSDA was 40, 10, or 1 % of the average concentration found in a healthy human. Some of the inhibitors have been qualitatively categorized. For those with quantitative results, the % of expected amplicon production is compared to reactions with 0 % added inhibitor using the iSDA amplicon qPCR. Averages \pm SE for at least N=4 is reported.

Inhibitor	Input DNA Conc.	% Expected Amplicon Production		
		40 %	10 %	1 %
Albumin	10^3	None	None	None
	10^2	None	None	None
Creatinine	10^3	None	None	None
	10^2	None	None	None
Glucose	10^3	86 \pm 25 %	289 \pm 115 %	32+ \pm 7.9 %
	10^2	189 \pm 42 %	202 \pm 25 %	308 \pm 132 %
Hemin	10^3	Complete	Complete	Complete
	10^2	Complete	Complete	Complete

Hemoglobin	10 ³	None	None	None
	10 ²	Some	None	None
IgG	10 ³	None	None	None
	10 ²	None	None	None
Lactoferrin	10 ³	0.1 ± 0.0 %	0.1 ± 0.0 %	63.1 ± 23.6 %
	10 ²	0.1 ± 0.0 %	0.1 ± 0.0 %	91.5 ± 16.3 %
Sodium bicarbonate	10 ³	None	None	None
	10 ²	None	None	None
Sodium chloride	10 ³	39.2 ± 20 %	69.7 ± 18 %	127 ± 37 %
	10 ²	46.3 ± 9.4 %	56.0 ± 21 %	173 ± 69 %
Urea	10 ³	None	None	None
	10 ²	Some	None	None

Inhibitor deactivation and removal. After inhibitor identification, we began exploring how to reduce their effect. There are multiple laboratory methods for inhibition deactivation or removal such as sample freeze/thaw, ethanol precipitation of NAs, and Qiagen kit NA extraction. Within this dataset, lactoferrin has proven to be the most serve inhibitor of both qPCR and iSDA. As such, our initial round of inhibitor removal has focused on lactoferrin.

The first two methods tested were heat deactivation and ACP treatment. Protein structure is often disrupted by high temperatures which renders them inactivated. There are also multiple enzymes that can denature proteins, some of which may be present in ACP. Work by Dr. Xiaohong Zhang and Dr. Paula Ladd in the Yager lab has shown that the ACP reagent we use is actually a mixture of multiple agents. Unfortunately, the manufacturer does not publish the exact content of this mixture but previous work has shown it might contain protein digestive enzymes.

Samples of lactoferrin at 1, 10, and 40 % were prepared and heat-denatured with and without prior ACP treatment. These samples were then tested for inhibition of qPCR and iSDA, as described above. Even after these treatments, lactoferrin still significantly inhibited both reactions indicating that the method of inhibition was not affected by these attempts at deactivation. The literature suggests that lactoferrin has three potential amplification inhibition mechanisms: (i) release of iron ions which compete for the co-factor binding site of DNA polymerase²⁹⁰, (ii) sequestering divalent cations, such as Mg²⁺, which are a critical polymerase co-factor²⁹¹, and (iii) binding to DNA which can reduce the efficiency of DNA's interactions with amplification reagents²⁹². If heat-treatment did

deactivate lactoferrin by disrupting its structure, then it might be unable to sequester divalent cations or bind DNA. It may, however, be more likely to release iron ions which would prevent polymerase activity. Future work will aim to further verify the inhibition mechanism of lactoferrin. After heat-denaturation, higher concentrations of Mg^{2+} can be spiked into the amplification reactions. If this does not improve amplification activity, then Mg^{2+} sequestering is unlikely to be the main inhibition mechanism. We can also test the effect of adding an iron chelator to the reaction to selectively remove iron ions. If this helps restore amplification efficiency, then these results would suggest that iron ion release is the predominant mechanism by which lactoferrin inhibits amplification.

Beyond these two standard laboratory deactivation methods, we have also tested a novel DNA purification mechanism which utilizes a modified porous membrane to selectively capture NA²⁴⁴. The NAs can be eluted with a simple buffer change and are ready for amplification without further purification. Our novel DNA purification system efficiently restores both qPCR and iSDA amplification activity by removing lactoferrin from the sample before it is introduced to the amplification reaction, **Figure 93**. This system is described in detail in Aim 3.

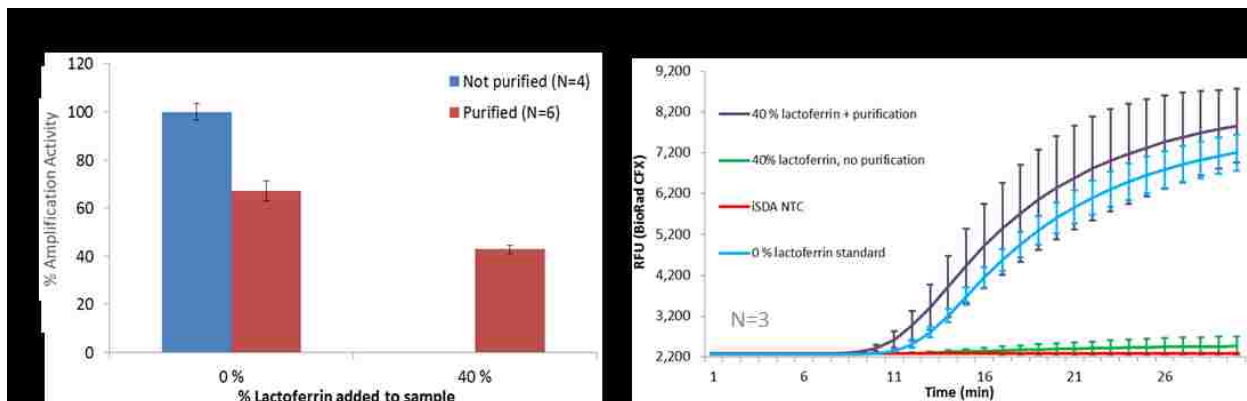


Figure 93. Porous membrane-based purification for amplification inhibitor removal. Comparison of amplification efficiency for lactoferrin spiked samples with and without purification. Averages of at least $N=3$ \pm one standard deviation is reported. **A.** qPCR. **B.** Real time iSDA.

Between the two amplification systems, there are some common inhibitors, such as lactoferrin and hemin. Each of these agents have complexed iron ions that may be released during amplification causing DNA polymerase inactivation. Our data suggest that these inhibitors might be universal to any assay that is sensitive to the presence of iron. High concentrations of NaCl (60 mM) moderately inhibit both qPCR and iSDA while lower concentrations show no effect or some slight assay enhancement. These moderate concentrations may help stabilize polymerase or primer

interactions with the target DNA strand but the higher concentrations may result in destabilization due to a change in the electrostatic micro-environment. There are, however, some differences in inhibitor effects between the two assays. For example, higher concentrations of glucose inhibits qPCR, but iSDA performance is not affected, indicating that the mechanism of inhibition may be more reaction-specific. High concentrations of urea, on the other hand, inhibit iSDA at low input copies but does not have a significant effect on qPCR.

11.4. Appendix 4: MPH summary

From 2012–2014, I completed a Masters of Public Health in Global Health Metrics. This degree included a six-week practicum in Bangladesh where I worked on developing a survey instrument to evaluate a national measles-rubella vaccination campaign. I also completed a thesis entitled ASSURED and Beyond: What characteristics drive the use of HIV rapid diagnostic tests? This work included the development of a statistical model that evaluated the relationship between test characteristics (such as cost, accuracy, and complexity) and test procurement. The experiences related to my MPH work helped shape my view of global public health and my Ph.D. dissertation. Below is the abstract from my Master's thesis.

ASSURED and Beyond: What characteristics drive the use of HIV rapid diagnostic tests?

Background: Since 1999 WHO has tracked the procurement of rapid diagnostic tests (RDT) for common infections, such as HIV, and has reported a significant increase in usage. In 1999 less than 40% of all HIV diagnoses around the world were performed with rapid tests whereas the remaining 60% were conducted with laboratory-based tests such as ELISAs. By 2009 over 80% of HIV diagnoses had transitioned to using RDTs. Many of these tests abide by the ASSURED criteria, which outline standards for the evaluation of point-of-care diagnostics. Although these criteria endorse important characteristics such as low cost and rapid time-to-results, they do not provide quantitative measures to compare similar tests or guide RDT developers. In this analysis we aim to determine how different countries select HIV RDT(s), and to parse out which characteristics are responsible for their decisions. Understanding what drives the purchase and use of current HIV RDTs can help inform future designs and specifications for test developers.

Methods: We analyzed data from The Global Fund's Price and Quality Reporting (PQR) database from January 2010 to January 2014. The sample consisted of 945 purchase records of HIV rapid

diagnostic tests, including order date, purchasing country, and the number of tests purchased per order. The main independent variable was unit cost per test (in USD). Linear regression with random effects on country was used to examine the relationship between test purchase, a proxy for test usage, and test cost. Models were adjusted for country random effects and country and test-level covariates.

Findings: This study included 945 purchase records of 38 different HIV RDTs from 93 countries. Our exploratory analysis showed that the characteristics that drive test purchase differ across a variety of settings. As cost is increased by just one \$1.00 overall purchase across all settings falls by 18.7% (95 % CI: -25.4 to -16.0 %). Other important driving characteristics were test time, maximum test storage temperature, and whether or not the test required additional equipment to run. When observations are stratified by country income level, the major driving factor is test cost and the degree of influence changes across strata. For low-income countries, every \$1.00 increase in test cost decreases test purchases by 62.1 % (95 % CI: -155 to 39.4 %). For high-income countries this decrease is only 10.4 % (95 % CI: -24.7 to 2.7 %). Stratification by country HIV prevalence, high vs. low, again showed cost was a major driving factor, while test time, maximum test storage temperature, and whether or not the test required additional equipment to run were also significant indicators. For all of the analyses, test accuracy – sensitivity and specificity – was not found to significantly influence test purchase within this dataset.

Discussion: The ASSURED criteria are a good first step toward evaluating diagnostics for a variety of settings but this work presents the first quantitative assessment of which characteristics influence the purchase and usage of HIV RDTs. Overall, cost was a major driving factor, but the degree of its influence, and whether or not other factors were also important, varies between settings. This exploratory analysis can serve as a step toward better understanding what drives HIV RDT usage and help researchers and test developers design future tests that focus on these important characteristics.

11.5. Appendix 5: Manuscripts published (or in preparation) during dissertation studies

This appendix contains reproduced copies of all of the manuscripts I've participated in preparing during my time as a graduate student. The information that is directly relevant to the main aims is included in these papers, other information or side projects were not included in the main section of the thesis but have been included below. Manuscripts marked with a ** are not in finalized form for submission.

1. **An integrated system for DNA purification from urinary pathogens: large volume sample preparation at the point of care (manuscript in preparation, outline below)

Abstract: Paper-based nucleic acid diagnostics have the potential to translate laboratory assays to simple-to-use, point-of-care devices, but many assays lack the ability to process realistic samples. Urine is an ideal sample for many applications, but can require multiple pre-processing steps, mains electricity, and expensive equipment to purify nucleic acids prior to detection. In this work, we describe the development and testing of a porous membrane-based device to automate sample processing. This simple-to-use system has been demonstrated for DNA extraction and concentration from urine samples to simultaneously detect *C. trachomatis* (CT) and *N. gonorrhoeae* (NG) via in-membrane isothermal amplification and lateral flow readout. This new platform has been compared to a clinical system used to detect CT/NG and shows promising initial results while requiring significantly less time, equipment, and user steps.

MS Outline: These are the general figures/tables that are planned for the MS. These are first drafts and will need to be beautified for the submission.

Figure 1: device schematic

- MgFe heater reference
- chitosan reference
- valving/p-switch reference

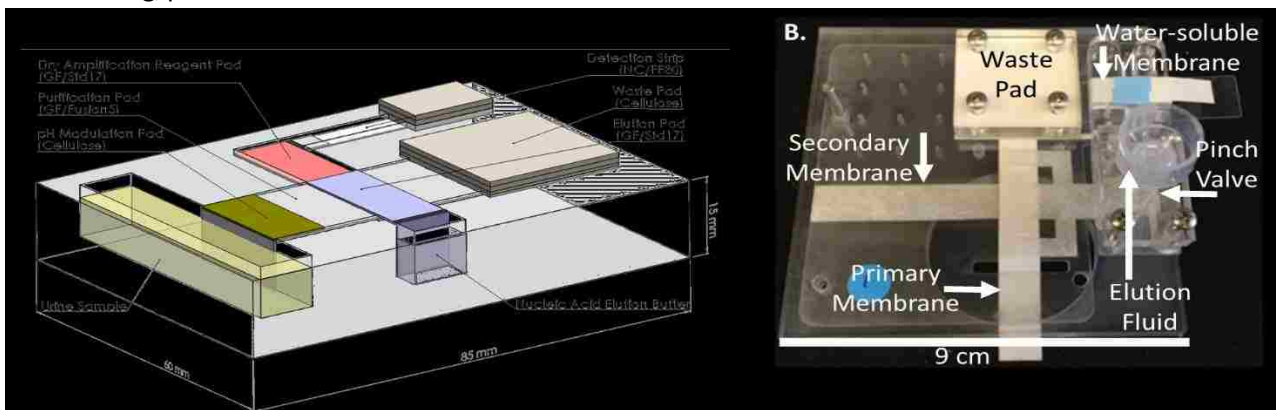


Figure 1. Integrated urine processing device. **A.** Schematic (will probably have to re-make to match current design, but this is fine as a place holder). **B.** Actual image with actual dimensions (I'd like to re-take this image with the device in someone's hand for scale or maybe with another object) but this is also fine for the current draft.

Figure 2: component validation, lysis of NG/CT in buffer and urine (may split into more than one figure)

- pH modulation studies
- chitosan sensitivity to increasing salinities
- compare MgFe heater to benchtop lysis
- supplemental: Urine characterization (pH, salinity, protein content, NA content, etc.)

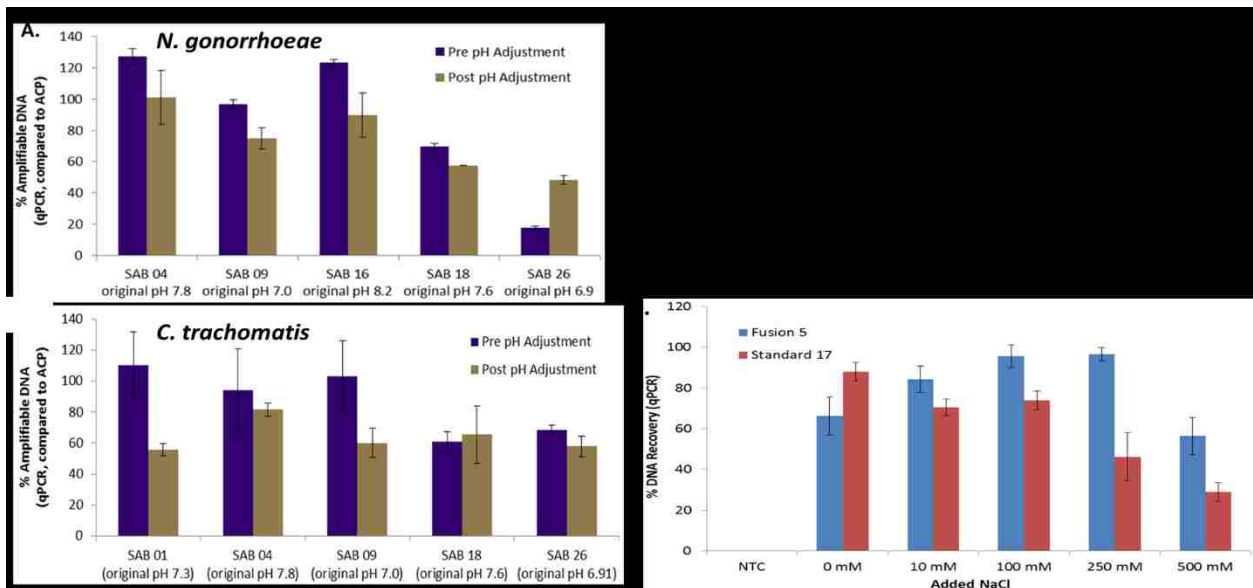
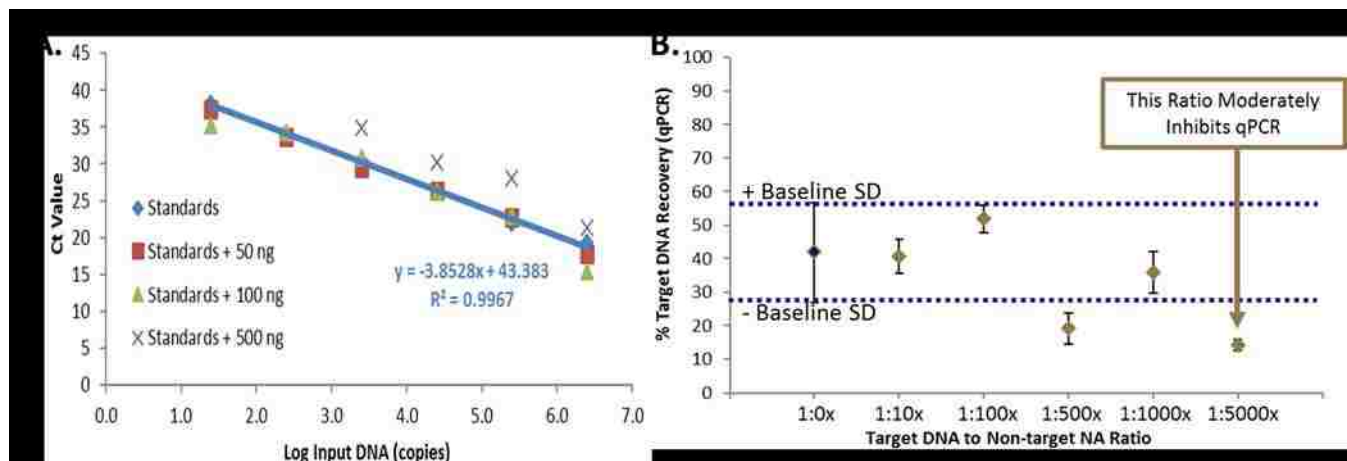


Figure 2. Device component validation. **A.** Modulation of urine pH does not significantly alter effectiveness of thermal lysis of *N. gonorrhoeae* or *C. trachomatis*. **B.** Chemical heater for large volumes (plan is to demonstrate it with *N. gonorrhoeae*). **C.** Chitosan purification of DNA performs well across a wide range of salinities expected to be seen in urine samples.

Figure 3 or Table 1: effect of non-target urine NA on system



- supplemental: figure with details of purification of NG DNA in the presence of increasing amounts of non-target urine NA

Table 2: full device with urine v. same samples tested with Aptima (clinical) system

- qPCR output
- supplemental: % rec, concentration factor, breakdown of individual processes (lysis, flow, pur?)
- supplemental: detailed experimental schematic

Table 2. Comparing the device output (as measured by qPCR) to the clinical result (as measured by the Aptima 2 CT/NG Combo Test). The device purified DNA samples were measured by qPCR and a result was considered positive if 3/3 replicates were positive by qPCR. Patient 23 was split into two samples, one spiked with pathogens and one without pathogens to directly compare the potential effects of the patient specimen. Overall, there was perfect agreement between this device and the clinical result. Both methods resulted in one false negative result.

Specimen	Spiked Pathogen	Expected Result (+/-)	Device Result (qPCR, N=3)	Clinical Result (Aptima, N=1)
Patient 12 (HS1)	CT	+	+	+
	NG	+	+	+
Patient 24 (HS2)	CT	+	+	+
	NG	+	+	+
Patient 29 (HS3)	CT	+	+	+
	NG	+	+	+
Patient 31 (HS4)	CT	+	+	+
	NG	+	+	+
Patient 23 (+) (HS5)	CT	+	+	+
	NG	+	-	-
Patient 23 (-) (HS6)	CT	-	-	-
	NG	-	-	-

Figure 4: iSDA development work from Enos

Figure 5: non-purified samples v. purified samples into dry iSDA pads

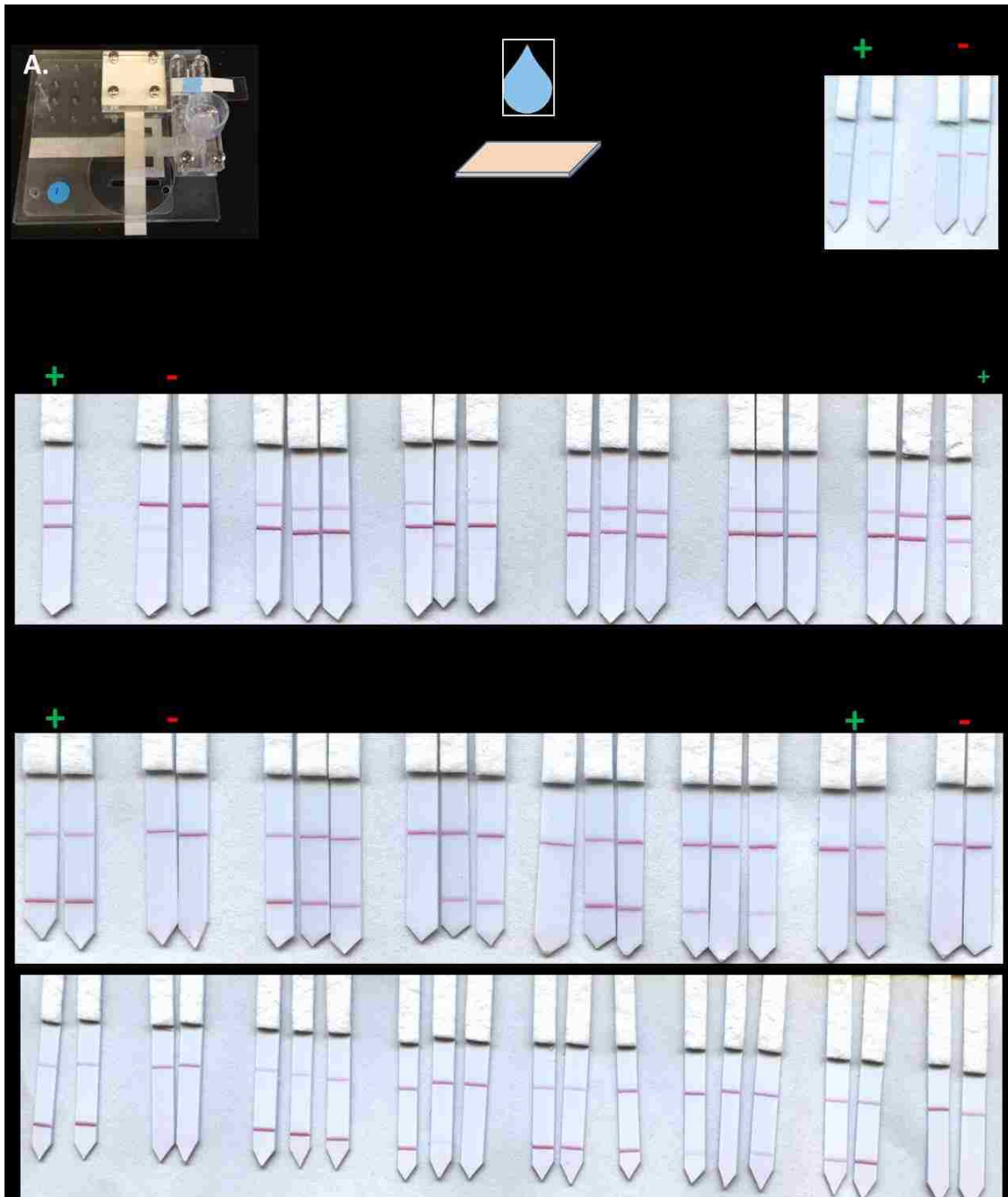


Figure 5. Device output used to rehydrate dry NAAT reagents for in-membrane amplification. **A.** Experimental schematic. Results from in-membrane iSDA were read by lateral flow. **B.** *C. trachomatis* and **C.** *N. gonorrhoeae*.

Table 3: extension of Table 2 with dry iSDA pad data added

- iSDA output

Table 3. Comparing the device output with in-membrane amplification and lateral flow readout to the clinical result (as measured by the Aptima 2 CT/NG Combo Test). Device samples were considered positive if 2/3 replicates were positive by in-membrane iSDA with lateral flow readout. Patient 23 was split into two samples, one spiked with pathogens and one without pathogens to directly compare the potential effects of the patient

specimen. Overall, there was perfect agreement between this device and the clinical result. Both methods resulted in one false negative result.

Specimen	Spiked Pathogen	Expected Result (+/-)	In-membrane iSDA (N=3)	Clinical Result (Apitma, N=1)
Patient 12 (HS1)	CT	+	+	+
	NG	+	+	+
Patient 24 (HS2)	CT	+	+	+
	NG	+	+	+
Patient 29 (HS3)	CT	+	+	+
	NG	+	+	+
Patient 31 (HS4)	CT	+	+	+
	NG	+	+	+
Patient 23 (+) (HS5)	CT	+	+	+
	NG	+	+	-
Patient 23 (-) (HS6)	CT	-	n/a	-
	NG	-	-	-

2. Transport of gDNA through porous membranes for point-of-care applications (manuscript ready to submit to *Lab on a Chip*)

S. A. Byrnes^{a*} and P. Yager^{a*}

Paper-based nucleic acid diagnostics have the potential to translate laboratory assays to simple-to-use, point-of-care devices, but many prototypes of these systems still lack the ability to process realistic samples due to the inability of genomic-sized DNA to move through porous membranes used in these devices. For applications involving pathogen or human gene identification, the ability to fragment and transport DNA would provide more options for device design and broaden the range of applications. To address this challenge, we have developed and characterized a method that combines cell lysis with DNA fragmentation to allow for lateral transport of genomic DNA through commonly-used porous membranes. Additionally, we demonstrate that varying heating time and temperatures allows for control of both lysis and fragmentation based on genome size. These data align with previously published models that describe both DNA denaturation and thermal scission. This level of control allows semi-selective transport of pathogenic DNA, which can reduce the amount of interference from non-target human DNA in downstream applications. This method can be easily automated and is rapid, occurring in less than 10 minutes with one user step.

Introduction

Paper-based nucleic acid diagnostics promise to convert laboratory assays to simple-to-use, point-of-care (POC) devices. A major challenge associated with these systems is how to control the transport of genomic DNA (gDNA) or large fragment DNA (~1 Mbp) through or along the length of a

membrane in order to perform additional assay steps. Previously published work has demonstrated the ability to purify and concentrate nucleic acids from complex samples^{50,140} and to amplify and detect in paper membranes^{71,138,141}. These techniques rely on either DNA entanglement in the membrane to restrict the desired target to a specific location⁷¹ or the transport of small nucleic acid fragments such as RNA⁵⁰ or pre-processed DNA^{6,140}. Nucleic acid-based devices designed for POC use, however, must have the ability to process realistic samples, such as gDNA, directly from human or pathogenic cells.

Recent reports have relied on DNA entanglement at the device inlet to demonstrate “sample-to-result” assays that collect a sample and return a result with minimal user steps^{57,138,142}. Although these methods have been successful, there are some notable limitations. First, they often require extensive washing of the nucleic-acid-capturing region to remove amplification inhibitors, which can increase time and device complexity¹⁴³. Second, they require multiple user steps in order to properly deliver additional assay reagents or physically connect downstream detection systems, such as a lateral flow strip^{50,71}. Third, systems that rely on DNA entanglement often require high volumes or concentrations of amplification reagents, increasing both the cost and complexity of a device. As an alternative to DNA entanglement, we have developed a simple-to-use method that enables lateral transport of DNA through porous membranes by employing fragmentation and that relies on the application of heat. This method was designed to be directly compatible with POC devices that use nucleic acid amplification tests. In addition to entanglement, adsorption may reduce or prevent DNA transport through porous membranes. DNA may adsorb directly to a porous substrate, or adsorption may be mediated by DNA-associated proteins.

The major constraint of transporting gDNA through paper-based devices that rely on lateral flow is entanglement of large nucleic acid strands in the porous matrix. Bacterial pathogens have DNA that is at least 1 Mbp (one million base pairs) in length, which, fully extended, is ~340 μm end-to-end. Most bacterial cells, however, are only 1-20 μm long requiring the DNA to be compacted into structures called nucleoids. In *E. coli*, for example, nucleoids can range from 4-15 μm long^{144,145} and are composed of looped regions with diameters of ~2 μm ¹⁴⁶. In its most compact state, *E. coli* DNA arranged as a nucleoid is approximately 1-10 μm long. Nucleoid structure can be disrupted by cell lysis or DNA extraction which can reduce compaction and greatly increase DNA length^{147,148}. In eukaryotic cells, DNA is compacted into chromosomes. In humans, these chromosomes are between 48 – 250 Mbp long; their length can range from 2–20 μm when compacted and 14,000 – 85,000 μm if fully extended¹⁴⁹.

The most commonly used porous membranes in lateral flow devices consist of entangled fibers that effectively form a matrix of interconnected cavities, or pores. These pores have dimensions in the range of 1-10 μm ^{150,151}, but are not uniform throughout a material. Instead, membranes have a pore size distribution with some pores on the order of 1 μm and some that are $>10 \mu\text{m}$. Because DNA structure is disrupted by lysis, the reduced compaction and increased size should result in limited transport of the DNA through a porous membrane. To compensate for the change in structure, both bacterial and mammalian DNA would require fragmentation after cell lysis to allow for lateral flow through commonly used porous membranes. There are multiple theories describing the fragmentation, or scission, process of DNA. These theories rely on the mechanism used to fragment DNA.

Extensive research on the movement of DNA through complex porous media has been conducted using electrophoresis. Specifically, pulsed-field gel electrophoresis (PFGE) was developed to improve the transport of large fragments of DNA ($>15\text{-}20 \text{ kbp}$) through porous gels^{154,152,155}. The pore size of an agarose gel can range from 5x–30x smaller¹⁵⁶ than pores in most porous membranes. PFGE, however, is assisted by the controlled application of electrical fields in several directions, which often requires expensive equipment not easily adaptable to POC settings. Therefore, transport of DNA through porous membranes for diagnostic applications requires fragmentation that produces smaller pieces of DNA to flow through membranes driven only by passive flow.

There are four primary mechanisms used to fragment DNA: bond breakage through mechanical stress and shear, enzymatic cleavage, chemical cleavage, and thermal scission^{98,157–159}. Recently, these techniques have been used to prepare DNA libraries prior to cloning, however, many of these methods cannot easily be applied to POC devices or in porous membranes.

Mechanical fragmentation methods rely on shear stress to break bonds between bases. There are multiple approaches that utilize mechanical-based fragmentation, but they often require expensive equipment or multiple user steps, which renders them incompatible with POC applications^{157,160–163}.

Enzymatic fragmentation methods target cleavage sites *via* enzymes that recognize specific sequences or general structural characteristics of DNA. The most common form of sequence-specific fragmentation is through restriction endonucleases^{78,164}. General enzymatic fragmentation methods typically target cleavage of the phosphodiester bond between bases¹⁶⁵. It has been well demonstrated that enzymatic methods work effectively to fragment DNA, but the reagents can be

expensive and, like most enzymes, require relatively narrow ranges of pH, temperature, and buffer concentration for optimal performance, making them incompatible with many realistic sample types.

Chemical fragmentation methods rely on the formation of reactive oxygen species and specific reaction conditions to achieve reliable DNA cleavage¹⁷³⁻¹⁷⁸. Currently, there is limited published work detailing the effectiveness of chemical fragmentation methods in realistic samples with widely varying pH and salinities.

Thermal scission of DNA has been studied since the early 1960s and involves two main mechanisms: hydrolysis of the phosphodiester backbone and depurination, which is followed by backbone hydrolysis. Depurination is the hydrolytic cleavage of purine bases. This cleavage pathway begins with the removal of a purine at the N-C bond which connects the 5-membered backbone ring to the base. Depurination is followed by scission at the 3' phosphodiester bond resulting in a strand break^{179,180}. Lindahl *et al.* noted that the 3' phosphodiester bond near an apurinic site is weakened, which results in a break in the backbone¹⁸¹. Hydrolysis of the phosphodiester backbone does not only occur at apurinic sites, but can also be a result of a nucleophilic attack by water on the oxygen-phosphorous bond off the 3' carbon¹⁸².

The rates of depurination and backbone hydrolysis have been studied and differ greatly between single-stranded (ss) and double-stranded (ds) DNA. Unsurprisingly, dsDNA shows improved stability and reduced rates of thermal cleavage. For ssDNA, multiple research groups have demonstrated that increasing temperature, decreasing pH, and decreasing the ionic strength of the solution leads to increases in both depurination and backbone hydrolysis^{158,159,182-184}. Additionally, the rates of these reactions have been separately quantified at elevated temperatures (79-100°C)^{158,185,186}. The majority of these studies have focused on mammalian DNA that has been denatured through high temperature (95°C) or DNA-binding proteins. A few groups have extended these studies to scission of single-stranded heat-denatured bacterial DNA. These results are consistent with studies of thermal scission of mammalian DNA that indicate elevated temperatures (79-100°C) lead to increases in scission events^{159,187}.

The main theories of DNA scission independently describe two important physical steps: first the denaturation of dsDNA to ssDNA, and second the rates of depurination and backbone scission. To understand and predict DNA scission, it is imperative to consider both of these steps because scission rates are significantly faster for ssDNA compared to dsDNA. The first step in the process is DNA denaturation. The time for denaturation has been shown to be inversely related to temperature and

proportional to the square of DNA size^{188,189}, *eq. 1*, where τ is time for full denaturation in seconds, T is temperature in Kelvin, and M is the molecular weight of a DNA strand.

$$\tau \propto \frac{M^2}{T} \quad (\text{eq. 1})$$

This relationship predicts that increases in temperature and decreases in size will decrease the time required to fully denature a piece of dsDNA. The authors note that for very long pieces of DNA, human genomes for example, the predicted denaturation time by this model exceed the expected time for replication which has led to the hypothesis that long DNA may partially denature allowing pieces to be effectively single stranded¹⁸⁸.

The second step in the thermal DNA scission model describes the rates of depurination and backbone hydrolysis. Both Ginoza¹⁸⁵ and Hoff¹⁸⁶ have described that the number of breaks due to thermal scission of ssDNA is proportional to length, *eq. 2*, where p is the number of scission events, N is the number of nucleotides in the ssDNA strand, k is the rate constant of scission, and t is time in minutes¹⁸⁶. Ginoza and Eigner have also described that the rate constant, k , is temperature dependent^{158,185}.

$$p \propto 2Nkt \quad (\text{eq. 2})$$

These two relationships show that longer DNA pieces require longer time to denature from dsDNA to ssDNA. Once denatured, the resulting breaks in ssDNA will be greater for longer fragments. Therefore, there appears to be a balance between overall heating time, heating temperature, and initial length of the DNA strand to describe the resulting size of ssDNA fragments post thermal scission.

Additional information about scission of DNA comes from the polymer field. The thermally activated bond scission (TABS) model describes the scission of polymers in flow fields where forces are sufficient to break covalent bonds³¹⁶. Work has also explored the combined effects of flow and temperature on polymer scission³¹⁷. As described by Sasaki *et al.*, a polymer is first stretched by a flow field aligning it with the direction of flow. Then, this extended conformation is subjected to fracture and scission at the center of the molecule, the point of highest stress^{318–320}.

These studies have focused on purified ss or dsDNA as their starting material, but preparation of DNA from cell-based samples requires the addition of a lysis step to expose the internal gDNA. To address this constraint, we have designed a method to integrate DNA fragmentation with cell lysis.

This work is the first demonstration of the integrated lysis/fragmentation method to facilitate lateral transport of DNA through porous membranes. The information presented below can serve as a set of design rules for the development of nucleic acid-based POC devices. First, the effects of adsorption and entanglement on lateral DNA transport through porous membranes was explored. Second, it was demonstrated that increased heating time and temperature increased DNA fragmentation and transport through porous membranes, consistent with the models detailed above. Next, fragmentation and transport through a porous substrate for genomes with varying sizes was compared. Finally, mixed samples containing multiple cell types were used to demonstrate how varying fragmentation conditions can allow for selective transport of bacterial v. mammalian DNA. This work is applicable beyond the demonstrations presented here and can be applied to additional sample types and pathogens to expand the scope of porous membrane-based devices that target gDNA.

Materials and Methods

Materials and Reagents

All reagents were prepared with sterile, molecular biology-grade water (Thermo Fisher Scientific, Waltham, MA, USA). Tris base, MES buffer, achromopeptidase (ACP, A3547), Tris/Borate/EDTA (TBE), phosphate buffered saline (PBS), 0.25% trypsin, Trypticase Soy Broth (TSB), and Lysogeny broth (LB) were purchased from Sigma Aldrich (St. Louise, MO, USA). Pre-poured chocolate agar plates were purchased from Fisher Scientific (Waltham, MA, USA). Proteinase K, SensiFAST probe No-Rox, and SensiFAST SYBR No-Rox kits were purchased from Bioline (Taunton, MA, USA). Mung bean nuclease and DNase I were purchased from New England Biolabs (Ipswich, MA, USA). The *S. cerevisiae* DNA ladder, pulsed-field certified agarose, and DNA sample loading dye were purchased from Bio-Rad (Hercules, CA, USA). The SYBR Safe gel stain was purchased from ThermoFisher Scientific (Waltham, MA, USA). The 10 mM Tris (pH 8), 50 mM MES (pH 5), 50 mM MES (pH 6.5), and 50 mM Tris (pH 8.5) buffers were prepared in sterile water and the pH values were adjusted. A 20 U/ μ L solution of ACP from lyophilized stock was prepared in 10 mM Tris, pH 8, immediately before each experiment.

Bacterial Cell Culture

Methicillin-resistant *Staphylococcus aureus* (*S. aureus*, strain 1770) was cultured in TSB and *Escherichia coli* (*E. coli*, strain K12) was cultured in LB. Both cultures were heated to 37°C with

shaking (250 rpm). Secondary cultures were prepared from overnight cultures diluted 1:100 in fresh medium and grown to mid-log phase ($OD_{600} = \sim 2$). After three hours of secondary culture, cells were pelleted by centrifugation at 13000 $\times g$ for 3 minutes. The supernatant was decanted and the cells were resuspended in 1 \times volume of 10 mM Tris buffer, pH 8.

Neisseria gonorrhoeae (*N. gonorrhoeae*, strain 19424) was cultured directly from frozen stock on chocolate agar plates at 36°C in a 5% CO₂ environment. After 24-48 hours, colonies were collected from the plate and resuspended in 10 mM Tris buffer, pH 8.

Mammalian Cell Culture

Freshly cultured HeLa cells (ATCC CCL-2) were obtained from collaborators in the Hybiske Lab in the Department of Microbiology at the University of Washington. To prepare the cells for experiments, culture media was removed and cells were washed with an equal volume of PBS, followed by treatment with 0.25% trypsin with shaking at 37°C for 15 minutes. Detached cells were pelleted by centrifugation at 13000 $\times g$ for 3 minutes. The supernatant was decanted and the cells were resuspended in 1 \times volume of 10 mM Tris buffer, pH 8.

Cell Lysis and Fragmentation of gDNA

Aliquots of 10 μ L of freshly cultured cells (bacterial or mammalian) were added to 90 μ L of either buffer only (10 mM Tris buffer, pH 8) or buffer with enzyme (10 mM Tris buffer, pH 8, with ACP at a final concentration of 0.5 U/ μ L). Buffer with enzyme samples were incubated at room temperature for 2 minutes prior to heating. All samples were heated to either 85, 87.5, 90, 92.5, or 95°C for 0–30 minutes. After treatment, samples were allowed to flow laterally through a porous membrane. Additionally, a subset of samples was subjected to pulsed-field gel electrophoresis (PFGE), proteinase K treatment, and entanglement studies (see below).

Porous Membrane Test Card Construction

All porous membranes and test card materials were cut using a CO₂ laser (Universal Laser Systems, Scottsdale, AZ, USA). The untreated and unbacked Fusion 5 and FF80HP nitrocellulose were purchased from GE Healthcare Life Sciences (Niskayuna, NY, USA). Glass fiber 8964 was purchased from Ahlstrom (Helsinki, Finland) and CFSP223000 cellulose was purchased from EMD Millipore (Billerica, MA, USA).

Test cards were made with 0.254 mm-thick plastic backing with adhesive (10 mil Melinex with T-5501 adhesive on one side, Fralock, Valencia, CA, USA). Test cards were assembled by using the adhesive layer of the plastic backing to hold the Fusion 5 porous membrane in place. The test cards were also laser-scored with 1 cm markings for easy membrane sectioning. Control experiments were performed to ensure the adhesive layer of the plastic backing did not inhibit the qPCR.

Adsorption of DNA Fragments to Porous Membranes

A 1 cm × 1 cm section of membrane (either Fusion 5, nitrocellulose, glass fiber, or cellulose) was filled to fluid capacity with sample containing 1×10^5 copies of fragmented DNA. This DNA was purified from *S. aureus* cells that had been treated with ACP at room temperature followed by heating to 95°C for 10 minutes. After this treatment, the concentration of DNA was quantified by qPCR. The sample was pipetted directly into the center of the membrane. After 5 minutes at room temperature, fluid was collected by placing the membrane, along the axis parallel to flow, in a 0.6 mL microcentrifuge tube with a hole in the bottom. The small microcentrifuge tube was then placed in a larger (1.7 mL) microcentrifuge tube; the samples were then centrifuged at 10,000 ×g for 3 minutes. The collected elution volumes were measured, and the amount of DNA recovered from each elution was quantified with qPCR to determine the fraction of the DNA remaining in the membrane. Retention was tested in three different buffers across a range of pH values: 50 mM MES at pH 5, 50 mM MES at pH 6.5, and 50 mM Tris at pH 8.5. Additionally, “blank” samples (buffer only, containing no DNA) were added to each membrane, and the fluid spun out of the membranes was tested to determine whether any chemicals from the membrane affected the qPCR assay.

Lateral Flow Through Porous Membranes

After lysis and fragmentation, 40 μL of each sample was wicked into a 1 cm × 4 cm Fusion 5 porous membrane to characterize the effect of fragmentation on DNA transport. The samples were chased with 120 μL of a 10 mM Tris, pH 8, to saturate the fluidic capacity of the membrane.

After the Fusion 5 was fully saturated with fluid, membranes were cut into two 1 cm × 2 cm sections: “Retained” and “Transported.” Fluid was collected from these sections as described above and in Figure 1. The collected elution volumes were measured and the recovery of DNA was quantified using qPCR.

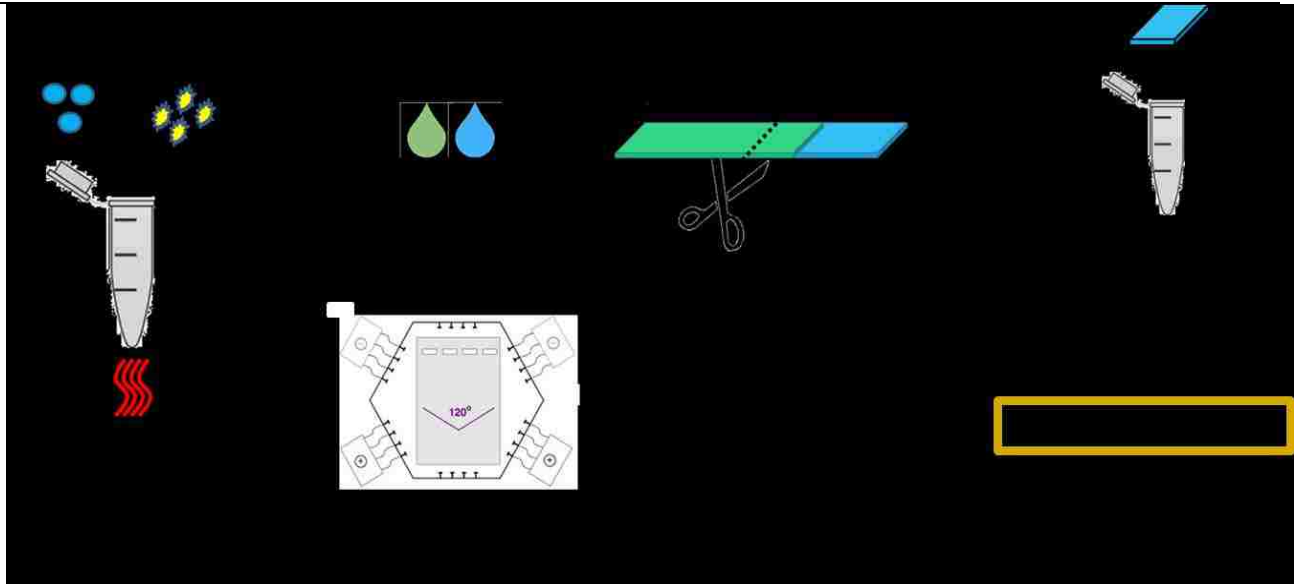


Fig 1. Experimental schematic to assess fragmentation of DNA and transport through porous membranes. After in-tube lysis and fragmentation experiments, sample and wash solutions were wicked into the membranes. Once the membranes were saturated, membrane sections were placed into a tube vertically and fluid was collected via centrifugation along the axis parallel to flow. Some samples were also qualitatively analyzed with PFGE after in-tube lysis and fragmentation to assess the distribution of DNA fragment sizes.

Proteinase K Treatment

A subset of samples was treated with proteinase K (PK) to digest proteins prior to flow through porous membranes. After lysis and fragmentation, these samples were placed in a refrigerator at 4°C for 10 minutes. After cooling, PK was added (final concentration of 50 µg/µL) and the samples were heated to 50°C for 10 minutes, for optimal enzyme activity, followed by heating to 75°C for 10 minutes to deactivate the enzyme. This protocol was adapted from the Bioline product manual²⁰⁹. After PK treatment, samples were wicked laterally into a porous membrane as described above.

Elution of Entangled DNA Fragments from Porous Membranes

After flow of samples through porous membranes and collection of fluid *via* centrifugation, the dried membranes were placed into 100 µL of 10 mM Tris buffer, pH 8. The solutions were heated overnight at 50°C with shaking in an attempt to elute entangled or adsorbed DNA from the membranes. Negative controls of membranes without any DNA were also included to ensure there was no PCR inhibitor released from the membranes. Finally, samples were pulse-vortexed 10 times. After treatment, the amount of DNA in each sample was quantified by qPCR.

Nuclease Treatment to Quantify Amount of ssDNA v. dsDNA

In order to quantify the amount of ssDNA and dsDNA in a sample following lysis and thermal fragmentation, a subset of samples was treated with mung bean nuclease, which selectively digests ssDNA. After lysis and fragmentation (10 minutes heating at 95 °C) of either *E. coli* or *S. aureus*, samples were slow-cooled at room temperature (slow, liquid) or fast-cooled (fast, liquid) on ice for 10 minutes. Additionally, samples were fast-cooled by immediately adding them to Fusion 5 membranes (fast, membrane) at room temperature. The membrane-cooled samples sat for 5 minutes followed by fluid collection *via* centrifugation at 10,000 xg rpm for 3 minutes.

These samples (slow, liquid; fast, liquid; and fast, membrane) were then treated with 1 U of mung bean nuclease in 1x mung bean nuclease reaction buffer for 30 minutes at 30 °C, as recommended by the manufacturer. After nuclease treatment, the remaining DNA was purified by ethanol precipitation and quantified by qPCR. These experiments also included three controls: no nuclease treatment (100% input control), no nuclease treatment + recovery from membrane (to control for potential losses due to interactions with the membrane), and DNase I control (negative control, DNase I should digest all of the DNA in a sample).

Pulsed-Field Gel Electrophoresis

PFGE was used to determine the range of fragment sizes of DNA after treatment. A 1.0% agarose gel was prepared in 0.5x TBE buffer and set overnight at 4°C. Gels were run using the BioRad CHEF Mapper XA System (Hercules, CA, USA) in a cold room (4°C) in 0.5x TBE running buffer. Agarose plugs containing the high molecular weight *S. cerevisiae* DNA ladder were loaded into the gel before submerging in running buffer. Liquid samples were added to the gel with sample loading buffer (1:5 sample:loading buffer). The "Auto- Algorithm" function was used with an input size range from 50 kbp to 1000 kbp, all other conditions were unaltered from the automatic settings. Gels ran for ~27 hours and were stained in a 1x solution of SYBR Safe in 0.5x TBE for 20 minutes with shaking. Gels were de-stained for 10-15 minutes in DI water, then imaged with the BioRad Gel Doc EZ System (Hercules, CA, USA).

qPCR

S. aureus DNA was quantified with a qPCR kit for the *ldh1* gene provided by the ELITech Group (ELITech Group Molecular Diagnostics, Bothell, WA, USA). The 20 µL reactions were run on a Bio-Rad

CFX real-time PCR instrument (Hercules, CA, USA) using the following protocol: 50°C hold for 2 minutes, 93°C hold for 2 minutes, 45 cycles of 93°C for 10 seconds, 56°C for 30 seconds, and 72°C for 15 seconds, ending with final elongation step at 72°C for 5 minutes. Fluorescence data were collected during the 56°C annealing step in the Texas Red channel. The qPCR results were analyzed using the automated threshold cycle (C_T) value calculation in the Bio-Rad software (Hercules, CA, USA). This assay was sensitive down to ~10 copies of the target sequence.

E. coli DNA recovery was quantified with qPCR for the *rodA* gene¹³¹ and NG DNA recovery was quantified with qPCR for the *porA* gene¹³² using the SensiFAST probe No-Rox kit from Bioline (Taunton, MA, USA). The 20 μ L reactions were run on a Bio-Rad CFX real-time PCR instrument (Hercules, CA, USA) using the following protocol: 95°C hold for 3 minutes, 40 cycles of 95°C for 10 seconds, 60°C for 30 seconds. Fluorescence data were collected during the 60°C annealing step in the FAM channel. The qPCR results were analyzed using the automated threshold cycle (C_T) value calculation in the Bio-Rad software (Hercules, CA, USA). These assays were sensitive down to ~10 copies of the target sequences.

HeLa DNA recovery was quantified with qPCR for the β -*globin* gene²¹⁰ using the SensiFAST SYBR No-Rox kit from Bioline (Taunton, MA, USA). The 20 μ L reactions were run on a Bio-Rad CFX real-time PCR instrument (Hercules, CA, USA) using the following protocol: 95°C hold for 5 minutes, 40 cycles of 95°C for 30 seconds, 58°C for 30 seconds and 72°C for 1 minute. Fluorescence data were collected during the 58°C annealing step in the FAM channel. The qPCR results were analyzed using the automated threshold cycle (C_T) value calculation in the Bio-Rad software (Hercules, CA, USA). This assay was sensitive down to ~10 copies of the target sequence.

Results and Discussion

The ultimate goal of this work was to design POC-compatible methods to reliably transport DNA laterally through porous membranes like those used in lateral flow tests. These methods have been designed to directly integrate with devices that use nucleic acid amplification tests¹³⁸. Transport was measured in two ways: 1) quantitatively measuring the amount of DNA that was transported laterally through a membrane after a thermal fragmentation treatment, by qPCR (see Figure 1); 2) qualitatively assessing the distribution of DNA fragment sizes by PFGE.

All samples used in this work began as intact bacterial or mammalian cells to mimic real-world samples; therefore, all samples required a lysis step to access the DNA. We chose not to isolate DNA prior to fragmentation for two reasons. First, nearly all lysis and nucleic acid (NA) purification assays

inherently fragment DNA, which would unintentionally bias the starting sample prior to testing intentional fragmentation treatments. For example, many enzymes are used to lyse cells, but lytic enzymes often require heat denaturation or NA purification prior to qPCR analysis. Second, realistic samples have intact cells, so using cells as the starting material better represents expected conditions in the application of our methods.

Two metrics were used to evaluate gDNA transport. The first metric, Percent Normalized Transport, removes potential variation in lysis between samples by normalizing transport to lysis efficiency, *eq. 3*. This metric isolates the effects of fragmentation on DNA transport through membranes. Lysis efficiencies were quantified by qPCR.

% Normalized Transport

$$= \frac{\text{Copies Recovered from Membrane} * \text{Elution Volume}}{\text{Input Copies} * \% \text{Lysis Efficiency}} \quad (\text{eq. 3})$$

The second metric, Percent Absolute Transport, does not normalize to lysis efficiencies, *eq. 4*. This metric therefore combines the effect of both lysis and fragmentation when processing the DNA from a sample. This measure is especially important for samples with multiple cell types that may have very different lysis efficiencies.

% Absolute Transport

$$= \frac{\text{Copies Recovered from Membrane} * \text{Elution Volume}}{\text{Input Copies}} \quad (\text{eq. 4})$$

For example, a sample with 100 cells and an 80% lysis efficiency would have 80 copies of the DNA available for fragmentation. If 60 of these copies transported through the membrane, then the Percent Normalized Transport would be 75% [60 copies recovered from membrane / (100 input copies * 80% lysis) = 60/80 = 75%]. The Percent Absolute Transport, however, would only be 60% [60 copies recovered from membrane / 100 input copies = 60/100 = 60%].

Initial demonstration of thermal fragmentation of DNA and transport through porous membranes was performed with *E. coli* and *S. aureus*, which are Gram-negative and Gram-positive pathogens, respectively. Both types of bacteria were studied to evaluate and compare the effects of thermal fragmentation across a range of potential pathogens. Samples containing one of these pathogens were treated with ACP, a mixture of lytic enzymes^{123,155}, for 2 minutes at room

temperature, followed by heating to 95°C for 10 minutes. 95°C was chosen as the target temperature because it is easy to achieve with POC devices and it effectively denatures ACP²¹¹. **Figure 2** shows the results from this study. For both pathogens, the Percent Normalized and Percent Absolute Transports are roughly equivalent, **Figure 2A**, because the lysis efficiencies for these conditions were all ~100%. A higher percentage of fragmented DNA from *S. aureus* cells transported effectively through the membrane compared to DNA from *E. coli* cells. These differences in transport will be discussed in a later section.

The distribution of DNA fragments was also qualitatively assessed using PFGE, **Figure 2B**. This image shows two conditions for both *E. coli* and *S. aureus*. The “ACP only” condition lyses the cells, but does not significantly fragment the DNA, as observed by the high concentration of DNA in the wells compared to the rest of the lane (note that the red color of the wells are saturated pixels; saturation indicate the presence of high DNA concentrations). The “ACP + heat” conditions were first treated with ACP at room temperature followed by heating to 95 °C for 10 minutes. For both pathogens under the “ACP + heat” condition, there is significantly less DNA observed in the wells than for the “ACP only” condition.

Under these treatment conditions, the average size of *S. aureus* DNA fragments is smaller than the *E. coli* DNA fragments because some large-fragment *E. coli* DNA remained in the wells, while the *S. aureus*-containing “ACP + heat” wells had very little visible DNA. These differences will be further discussed in the following sections.

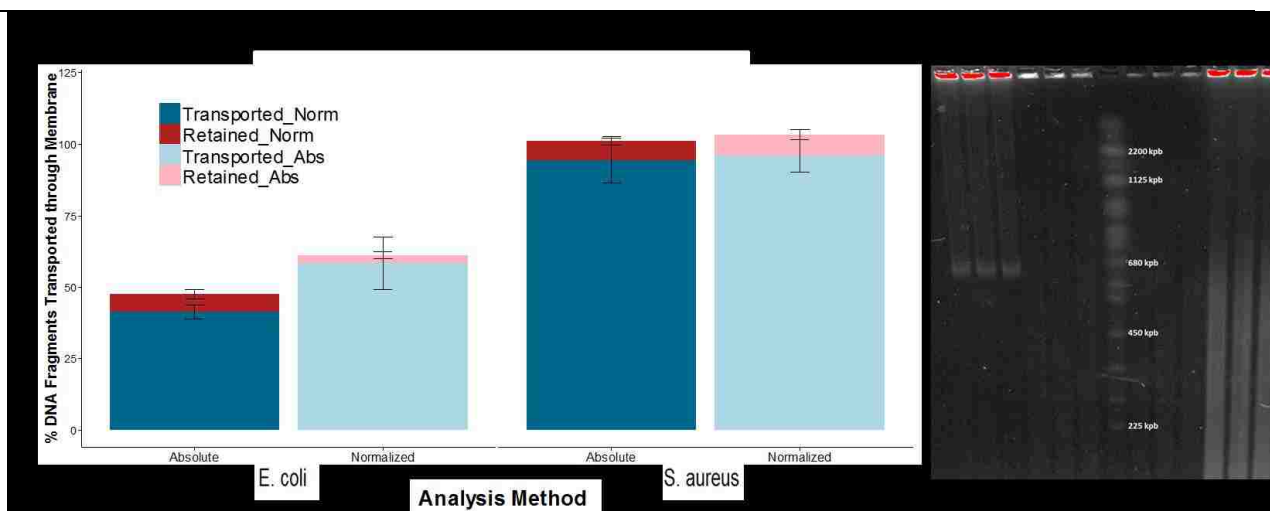


Fig. 2 Methods for analyzing gDNA fragmentation and transport through porous membranes using *E. coli* and *S. aureus* pathogens. **A.** Comparing two quantitative measurements of transport:

Percent Absolute Transport (Absolute) and Percent Normalized Transport (Normalized). For this data, the lysis efficiencies for both pathogens were ~100% so the two transport quantification methods showed the same results. These data were collected using Fusion 5 membranes. Averages of N=6 (N=3 from two separate cultures) are reported with error bars representing standard error. **B.** PFGE comparing “No lysis” and “ACP + heat” lysis samples. Under these treatment conditions, the average size of *S. aureus* DNA fragments is smaller than the *E. coli* DNA fragments because some large fragment *E. coli* DNA remained in the wells while the *S. aureus*-containing “ACP + heat” wells had no visible DNA. Note that the red color of the wells in the upper part of the gel are saturated pixels, indicating the presence of very high concentrations of DNA.

Effect of Adsorption versus Entanglement on gDNA Transport through Porous Membranes

After the initial demonstrations, experiments were performed to support the hypothesis that transport of DNA through porous membranes was dependent on the extent of gDNA fragmentation. We considered competing hypotheses that might explain a lack of transport: adsorption to the membrane matrix by DNA or DNA-associated proteins (which should not depend on the length of the DNA strands) or DNA entanglement (which should be reduced as the mean fragment size is reduced by fragmentation).

DNA adsorption was evaluated in four different membranes (nitrocellulose, Fusion 5, cellulose, and glass fiber) using three buffers with varying pH values (5, 6.5, and 8.5) that span the range observed in human samples such as urine¹²⁰. The DNA used in these experiments was purified from *S. aureus* cells and fragmented by heat in order to remove the potential confounding effect of DNA entanglement. .

For both the cellulose and glass fiber membranes tested, adsorption to the membrane was pH-dependent, lower pH values resulted in reduced recovery of DNA indicating higher amounts of DNA adsorption. The DNA added to both nitrocellulose and Fusion 5 was recovered at all three pH values tested indicating little-to-no adsorption (**Figure S1**). These results are consistent with our understanding of the material properties because both nitrocellulose and Fusion 5 are negatively charged, and therefore are unlikely to adsorb DNA¹⁵¹. However, DNA recovery from nitrocellulose was variable and elutions of only buffer (no DNA added) showed slight enhancement of the qPCR signal. Based on these considerations, Fusion 5 was selected as the material for the remaining experiments detailed below.

DNA is not the only molecule that can adsorb to the membrane. It is well known that proteins can readily adsorb to porous membranes depending on the buffer conditions^{48,151,212}; since cellular gDNA is coated with proteins, a protein coating could play a role in reducing DNA transport.

To test this hypothesis, samples were treated with proteinase K (PK) after initial lysis and heat-based fragmentation. Short (2 minutes) and long (8 minutes) heating times were compared for four different cell types: *N. gonorrhoeae*, *S. aureus*, *E. coli*, and human epithelial cells. After PK treatment, the samples were allowed to flow laterally through Fusion 5 membranes, after which DNA recovery from different membrane sections was quantified (Percent Normalized Transport). For all four cell types at both heating times, there was no observable difference between samples with or without PK treatment (**Figure S2**) indicating that presence of protein on the DNA does not significantly affect transport of DNA through Fusion 5 membranes under these assay conditions.

For the samples in Figure 2, less than 75% of the *E. coli* DNA was recovered from the membrane while nearly 100% of the *S. aureus* DNA was recovered. Based on the genome sizes of the bacterial strains used in this study (*E. coli* ~5 Mbps and *S. aureus* ~2.5 Mbps), the known pore size distribution of the porous membrane, and the models that describe the length dependence of DNA denaturation and scission, it was hypothesized that the *E. coli* DNA fragments were, on average, larger than the *S. aureus* fragments. These larger *E. coli* DNA fragments were entangled in the membrane. This entanglement could prevent the large DNA fragments from transporting through the membrane and being eluted during centrifugation. To test this hypothesis, membranes were saved after elution and placed in buffer. These samples were then heated overnight at 50°C with shaking in an attempt to elute unrecovered DNA from the membranes. The effects of the overnight treatments were then characterized *via* qPCR.

After overnight treatment, the *E. coli* samples had 25% (SE 4.6%, N=3) of the input DNA remaining entangled in the membrane after transport and collection while the *S. aureus* samples had only 2.0% (SE 0.6%, N=3). These data support the information presented in Figure 2 because nearly 100% of the *S. aureus* DNA was recovered from transport and only 2% was recovered from the overnight treatment. The results from Figure 2 also showed ~75% of the *E. coli* DNA was recovered from transport and the remaining ~25% from the overnight treatment.

Finally, the amount of ssDNA v. dsDNA in a sample after lysis and thermal scission was quantified to determine the output of the system prior to introduction to a porous membrane. The literature indicates that the rate of thermal fragmentation of ssDNA is significantly faster than that of

dsDNA^{158,185,186}. All samples in our work were heated to 95 °C, suggesting that much of the DNA should be single stranded.

After lysis and fragmentation at 95 °C for 10 minutes, both *E. coli* and *S. aureus* DNA was treated with mung bean nuclease which specifically degrades ssDNA. If the above hypothesis is true – that the majority of the DNA should be single stranded – then this nuclease should digest the majority of the DNA in the sample resulting in low yields by qPCR. For both pathogens, this is exactly what was observed; after mung bean treatment, less than 10% of *E. coli* DNA remained and less than 3% of *S. aureus* DNA remained. These results indicate that after lysis and thermal fragmentation at 95 °C, followed by a period of 5 minutes or less at room temperature, over 90% of the DNA in these samples was still single stranded.

The observed difference between *E. coli* and *S. aureus* is consistent with the denaturation model described above which notes that time for denaturation is dependent on the square of DNA length. The *E. coli* DNA used in these studies was ~2x longer than the *S. aureus* DNA, therefore, there should be more *E. coli* dsDNA than *S. aureus* dsDNA, which is what these results show.

Effect of Heating Time on DNA Fragmentation and Transport through Porous Membranes

After the experiments probing the mechanisms of effective transport discussed above, we characterized the effects of varying sample heating times at 95°C on fragmentation of DNA and transport through porous membranes. Based on previously published literature and the initial experiments above, we hypothesized that increasing heating times would result in increased fragmentation and transport of DNA through a membrane. Additionally, understanding the minimum required time for effective fragmentation can guide assay design requirements.

Samples containing either *E. coli* or *S. aureus* bacteria were heated for 0-10 minutes followed by flow through Fusion 5. In order to decouple the effects of lysis and fragmentation, Percent Normalized Transport was used as described above (eq. 3). For the conditions presented in Figure 3, all lysis efficiencies were >80% (**Figure S3**).

For both pathogens, increased heating time resulted in a higher Percent Normalized Transport, **Figure 3**, indicating a higher degree of fragmentation. These results were also verified by PFGE (**Figure S4**). After 4 minutes, there is little additional observed fragmentation. These results are consistent with the theory described by Ginoza and Hoff that longer heating times results in more scission events which would lead to smaller DNA fragments. Smaller fragments should transport

more effectively through porous membranes. Therefore, transport is directly proportional to heating time.

E. coli treated with or without ACP did not show any difference in transport, indicating that the enzyme does not significantly affect DNA fragmentation in this assay. Experiments with ACP and no heat were not performed because ACP that is not heat-deactivated inhibits qPCR.

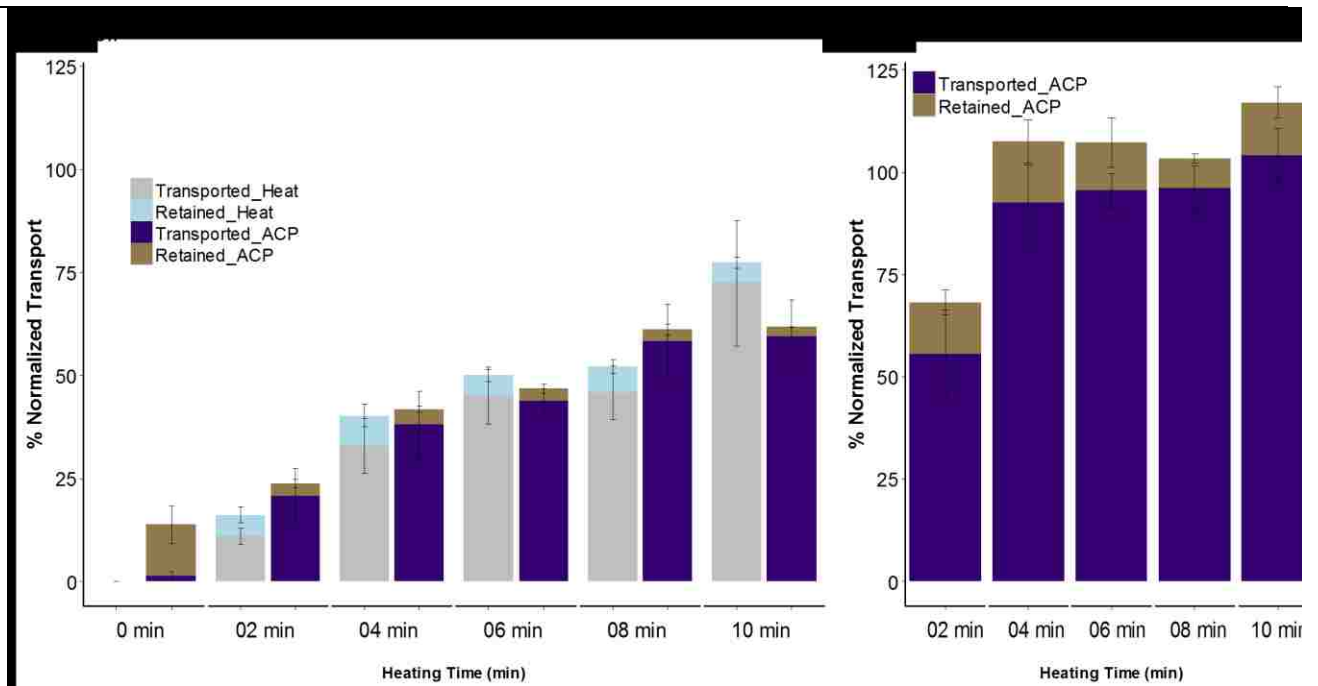


Fig. 3 Effect of heating time on DNA fragmentation and transport through porous membranes. Averages of N=6 (N=3 from two independent cultures) are reported with error bars representing standard error. Samples treated with ACP and no-heat cannot be quantified because the non-denatured enzyme inhibits qPCR. **A.** *E. coli* treated with and without ACP, and **B.** *S. aureus* treated with ACP. *S. aureus* is not susceptible to thermal lysis.

E. coli is Gram-negative with a thin cell wall making it susceptible to thermal-based lysis without ACP. *S. aureus*, however, is Gram-positive; the thick cell wall composed of peptidoglycan is comparatively resistant to thermal lysis¹²³. ACP was used to lyse *S. aureus* and make the DNA available for thermal fragmentation^{123,211}.

There was a significant difference in transport of *E. coli* v. *S. aureus* DNA when comparing across heating times. For example, the maximum percent transported for *E. coli* was ~75% for 10 minutes of heating at 95°C whereas *S. aureus* heated at the same temperature for the same amount of time resulted in ~100% transport.

This suggests that heating the *E. coli* sample for longer would result in more fragmentation and therefore a higher percentage that transports through the membrane. To test this hypothesis, samples were heated for up to 30 minutes at 95 °C followed by immediate flow laterally through Fusion 5. Fluid was collected from the membrane as described above and transport was quantified. The results from the experiment support this hypothesis and show that the extended heating times do result in a higher percent of *E. coli* DNA that effectively transports through Fusion 5 (**Figure S5**).

These results can also be explained using the models described above. *S. aureus* DNA is only ~2x smaller than *E. coli* DNA, but the model of DNA denaturation indicates that time is proportional to the square of DNA size. Therefore, *E. coli* DNA should take ~4x longer to denature than *S. aureus* DNA which would reduce the amount of time the *E. coli* ssDNA was available for effective thermal scission. Based on the data presented in Figures 3 and S5, *S. aureus* DNA is sufficiently fragmented for transport through membranes by 4-6 minutes (100% transport) while *E. coli* DNA does not show the same transport efficiency until 20 minutes, ~3-5x times longer, as suggested by the model.

Effect of Heating Temperature on DNA Fragmentation and Transport through Porous Membranes

Next, we tested the effect of varying heating temperature on DNA fragmentation and transport through porous membranes. Similar to testing heating time, understanding the minimum required temperature for effective fragmentation can guide assay design requirements. Again, lysis and fragmentation were decoupled using Percent Normalized Transport. For the conditions presented in Figure 4, all lysis efficiencies were >80% (**Figure S6**).

Samples containing either intact *E. coli* or *S. aureus* were heated at 85-95°C for 10 minutes followed by flow through a porous membrane. For *E. coli*, increased heating temperature resulted in a higher percentage of DNA that was transported through the porous membrane, **Figure 4**, indicating a higher degree of fragmentation. These results were also observed by PFGE (**Figure S7**). Temperatures at or above 92.5°C resulted in similar fragmentation and transport. As with the previous experiments, *E. coli* treated with or without ACP did not show any difference in transport. The temperature dependence of thermal scission, and therefore lateral transport through porous membranes, also aligns well with the described models which note that increasing temperatures increase the rates of scission^{158,185}.

There was little effect on transport of *S. aureus* DNA after heating to these varied temperatures. This outcome does not appear to be a result of lysis method, ACP, because changes in fragmentation and transport with temperature were observed for *E. coli* treated with and without ACP.

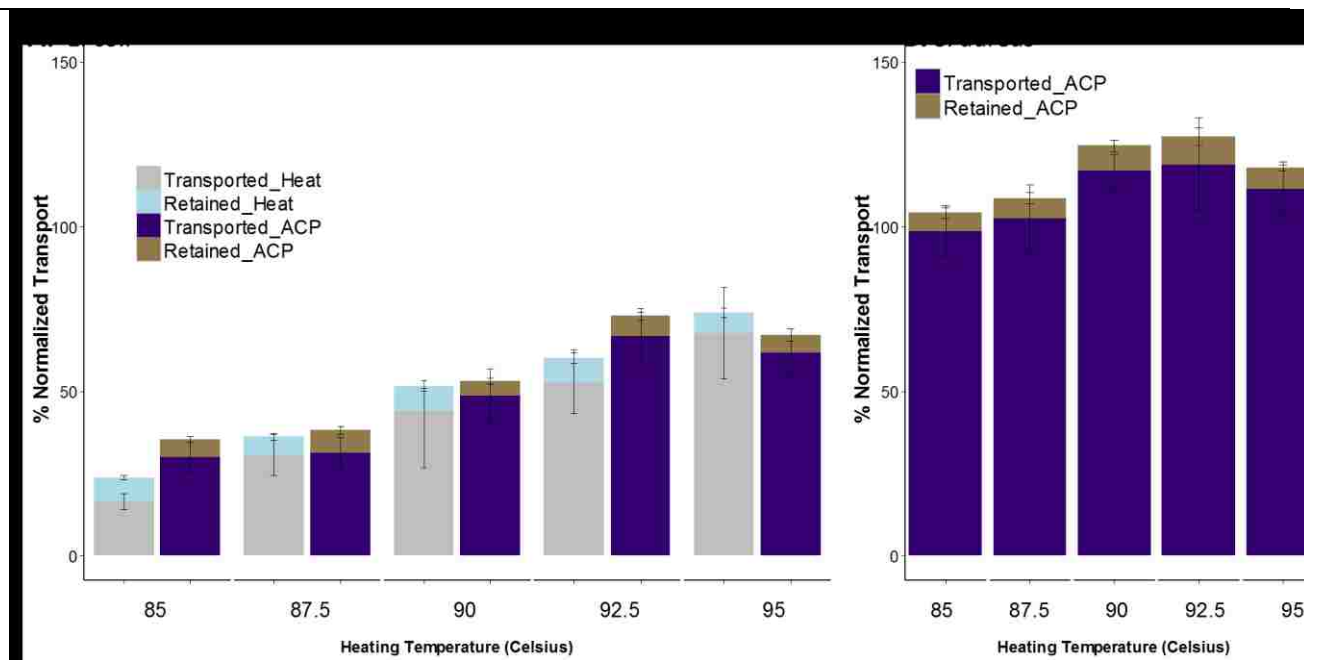


Fig. 4 Effect of heating temperature on DNA fragmentation and transport through porous membranes. Averages of N=6 (N=3 from two independent cultures) are reported with error bars representing standard error. **A.** *E. coli* treated with and without ACP, and **B.** *S. aureus* treated with ACP. *S. aureus* is not susceptible to thermal lysis.

Effect of Genome Size on Transport through Porous Membranes

For the samples tested above, longer heating times (4+ minutes) at higher temperatures (>92.5°C) resulted in more DNA transported through the membrane, indicating a greater degree of fragmentation. Additionally, each of these conditions resulted in high lysis efficiencies (>80%, see Supplemental Information) signifying that the majority of the DNA from the cells was available for fragmentation and transport.

The next round of experiments directly compared the Percent Normalized Transport of DNA from four cell types with varying genome sizes: *N. gonorrhoeae* (2.2 Mbp), *S. aureus* (2.5 Mbp), *E. coli* (5 Mbp), and human epithelial cells (HeLa, 48 – 250 Mbp). The human genome is composed of chromosomes, the shortest is #21 at ~48 Mbp and the longest is #1 at ~250 Mbp.

Based on the results presented in Figures 3 and 4, ACP does not appear to significantly contribute to DNA fragmentation when heating to >85 °C for up to 10 minutes. It can, however, play an important role in cell lysis because some cells, such as Gram-positive bacteria, are not susceptible to thermal lysis¹²³. Lysis of human epithelial cells was significantly improved when treated with ACP +

heat instead of just heat (ACP + heat: 62% lysis v. heat only: 25% lysis). In order to reduce this variation in lysis, all samples for this round of experiments were treated with ACP for 2 minutes at room temperature prior to heating to 95°C for 2 or 8 minutes followed by flow through Fusion 5. After flow, DNA transport was quantified by qPCR.

As observed in previous experiments, heating of samples for only 2 minutes resulted in reduced Percent Normalized Transport compared to heating for 8 minutes. The same results are observed across all four cell types, **Figure 5**. The time-dependence of scission and therefore transport is consistent with the scission models described above.

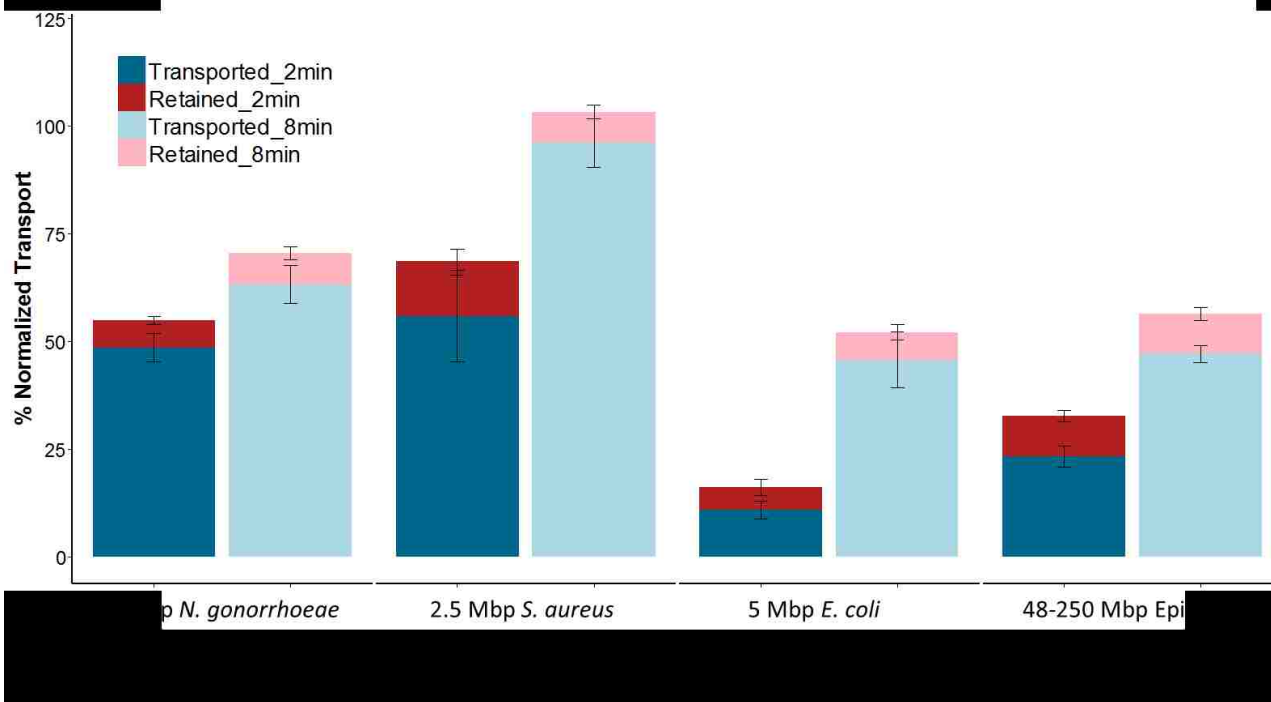


Fig. 5 Effect of gDNA size on transport through porous membranes. For larger genomes, significantly less DNA was able to effectively transport through the membrane. For all genomes, heating for 8 minutes resulted in a higher percentage of DNA transported through the membrane. All samples were treated with ACP prior to heating to 95°C to reduce potential lysis variation. Averages of N=6 (N=3 from two independent cultures) are reported with error bars representing standard error.

There is a noticeable size trend in increasing the % normalized transport for each heating time. The smaller *N. gonorrhoeae* and *S. aureus* genomes (2.2 Mbp and 2.5 Mbp, respectively) show a higher percentage of transport through the membrane compared to the larger *E. coli* and epithelial cell genomes (5 Mbp and 48-250 Mbp, respectively). This trend may be partially explained based on the two models that govern DNA scission. The shorter genomes denature from dsDNA to ssDNA in less time than the longer genomes. This difference results in the smaller genomes having more time as ssDNA and therefore more time to experience thermal scission compared to the larger genomes. Ultimately more time spent as

ssDNA under thermal scission conditions would result in smaller fragments and therefore higher transport efficiencies, as seen in Figure 5.

Fragmentation and Transport of DNA from Mixed Samples

Realistic human samples for pathogen detection contain a mix of pathogens, commensal bacteria, and human cells. For example, sampling for *N. gonorrhoeae* is typically done with a swab or urine³, both of which also contain human epithelial cells. For some applications, excess non-target DNA can reduce assay sensitivity by overloading the capacity of a system^{140,213} or by reducing target amplicon generation through amplification reagent sequestering^{51,214}. Reducing or eliminating non-target DNA would help increase sensitivity for the target of interest. Therefore, for mixed samples, it is important to quantify the total amount of DNA (both target and non-target) that successfully transported through a porous membrane, which we described as the Percent Absolute Transport, eq. 4.

For experiments with mixed samples containing two cell types, it is important to account for individual lysis efficiencies. Samples with both *N. gonorrhoeae* and HeLa cells were lysed with ACP at room temperature for 2 minutes followed by heating to 95°C for either 2 or 8 minutes. Samples were then allowed to flow laterally through porous membranes.

Within these mixed samples, the epithelial cells showed reduced lysis efficiency compared to the *N. gonorrhoeae* bacteria (2 min: *N. gonorrhoeae* 98% vs. epithelial cells 39% and 8 min: *N. gonorrhoeae* 95% vs. epithelial cells 62%, respectively). Using equation 4 and accounting for these reduced lysis efficiencies, significantly more total input DNA was recovered from *N. gonorrhoeae* compared to the human epithelial cells for both times tested, **Figure 6**.

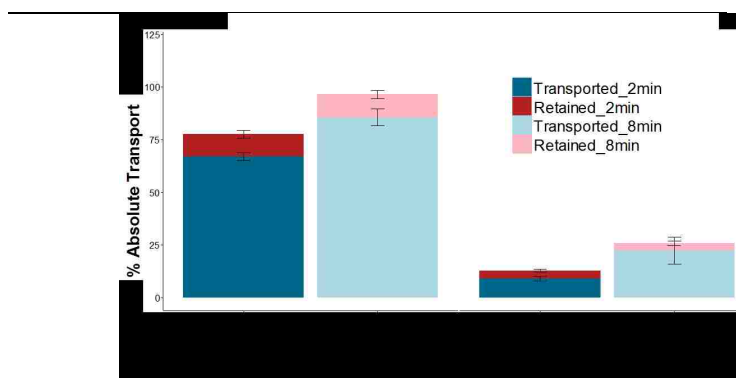


Fig. 6 Fragmentation and transport of mixed samples through porous membranes. The epithelial cell does not lyse as effectively as the small bacterial cell in these conditions, therefore reducing the amount of DNA available for fragmentation. For both heating times tested, 4x more *N. gonorrhoeae* DNA successfully transported through the membrane compared to epithelial cell DNA. Averages of N=6 (N=3 from two independent cultures) are reported with error bars representing standard error. Samples were treated with ACP for 2 minutes at room temperature followed by heating to 95°C for either 2 or 8 minutes.

The transport data, measured by qPCR, and the pulsed-field gels, provided in the supplemental information, indicate that fragments on the order of 200 kbp to 250 kbp (0.2 Mbp – 0.25 Mbp) effectively transport through Fusion 5.

Bacterial DNA is ~10-100x shorter than mammalian DNA, based on the range of chromosome sizes. This data set suggests that the significantly larger mammalian DNA (48–250 Mbp) does not sufficiently fragment during the applied heating to effectively transport through the porous membrane. The smaller bacterial DNA (Mbp), however, is sufficiently fragmented and therefore transports well.

These results are consistent with the models for DNA denaturation and thermal scission described above. Both cells experience the same temperature and time of heating. The denaturation model indicates that the significantly longer mammalian DNA could take 100x longer to fully denature from dsDNA to ssDNA because denaturation time is proportional to the square of DNA length^{188,189}. Based on this model, during the 2- or 8-minute heating steps portions of the mammalian DNA would remain double stranded and be significantly less susceptible to thermal scission than the bacterial DNA. The sections of mammalian DNA that are single stranded, would result in 10-100x more scission events because thermal

scission is directly proportional to DNA length. Overall, this work describes a balance between multiple factors including DNA length, heating time, and heating temperature. In order to selectively fragment and transport smaller bacterial DNA while retaining larger mammalian DNA, moderate heating times of 2–8 minutes at 90–95°C should be used.

These differences in length and the relatively short heating times may be enough to describe the transport and recovery of DNA from various cell types in a sample. Preliminary studies were also conducted to evaluate cell lysis and thermal fragmentation in porous membranes, instead of in solution as presented here. The results from these initial studies showed that both lysis and DNA fragmentation were greatly reduced when samples were heated in porous membranes (data not shown).

Conclusions

Here we have demonstrated and characterized a novel application of thermal DNA fragmentation for use in porous membrane devices. First, mechanisms governing DNA transport through porous membranes were evaluated. Direct adsorption or protein-mediated adsorption of DNA to Fusion 5, and DNA entanglement in the membrane post scission did not significantly contribute to DNA transport in these studies. Also, varying heating time and temperature was shown to have a predictable effect on DNA transport laterally through Fusion 5. For all four tested cell types lysed with ACP (*N. gonorrhoeae*, *S. aureus*, *E. coli*, and epithelial), heating to 95 °C for at least 8 minutes resulted in greater than 50% of the available DNA effectively transporting through the Fusion 5 membrane. These data normalize DNA transport to cell lysis (equation 3). Finally, this information enabled the use of controlled lysis and fragmentation to selectively move or retain DNA from samples with multiple cell types. When smaller bacterial cells (*N. gonorrhoeae*) and larger mammalian cells (epithelial cells) were simultaneously lysed and thermally fragmented, at least 4x more of the total bacterial DNA was successfully transported through the membrane compared to the total mammalian DNA (equation 4). This difference was observed for samples heated to 95 °C for either 2 or 8 minutes.

The data presented in this work indicate that controlled heating times and temperatures could be applied to different samples to effectively reduce human DNA in downstream applications. Conversely, assays could be designed that fragment pathogenic DNA, remove it under flow, and retain the human DNA for further processing. Future work should characterize complex samples to elucidate the ability to do targeted fragmentation.

A final consideration that future work should address is membrane variability. This work explored the fragmentation and transport of DNA through a single membrane type: Fusion 5. While parallel experiments in a second membrane (Standard 17 glass fiber, GE Healthcare Life Sciences) have yielded similar results, it is important to consider that porous membranes may or may not differ in average pore size, but they

almost always differ in the pore size distribution, which is based on the specifics of their manufacture. Because the failure to transport DNA through porous membranes appears to be dominated by entanglement, the pore size distribution of the membrane will play a large role in the transport of specific distributions of DNA fragments. The work we have done to establish some control over the fragmentation process will help to better identify desired membrane characteristics based on the need for DNA transport in a target application.

The results contained within this work can serve as a guide for evaluating DNA fragmentation and design rules for assay and device development for porous membrane-based systems. In fact, the results of this work have already been applied to an integrated paper-based POC nucleic acid amplification system that requires DNA fragmentation¹³⁸. Application of these methods to complex human samples or organisms with significantly smaller or RNA-based genomes will further expand its usefulness. Future work will therefore demonstrate the integration of DNA fragmentation into POC sample preparation devices.

Acknowledgements

This work was supported by a grant to Paul Yager from the Defense Advanced Research Projects Agency (DARPA) “Multiplexable Autonomous Disposable for Nucleic Acid Amplification Tests for LRSs” under Grant No. HR0011-11-2-0007.

We thank Meghan Zuck and Kevin Hybiske for providing fresh cultures of HeLa Cells. We also thank Joshua D. Bishop, Xiaohong Zhang, Ryan Gallagher, Paula Ladd, Erin Heiniger, Joshua R. Buser, Enos Kline, and all of our colleagues in the Yager Laboratory who provided valuable discussion and feedback on experimental design and analysis. We thank collaborators Nicolaas Vermeulen and Boris Alabyev from ELITechGroup Molecular Diagnostics (previously Epoch Biosciences) for assistance with the supply of the *ldh1* qPCR assay for *S. aureus*.

3. The p-switch: a pressure-based valving system for controlling flow and automating assays in paper microfluidics (manuscript ready to submit to *PNAS*)

J. R. Buser^{a†*}, S. A. Byrnes^{a†*}, C. Anderson^a, P. Kauffman^a, J. D. Bishop^a, M. H. Wheeler^a, and P. Yager^{a*}

Abstract

Porous membrane or paper-based assays are becoming more common due to their ease-of-use and low cost. Increasingly, these paper-based devices are translating more complex laboratory assays to point-of-care settings. However, many of the translated devices still lack automation and require multiple user steps due to the complexity of realistic sample preparation requirements. Some sample types, such as urine, require concentration for target detection; others, such as nasal swabs or blood, may require removal or dilution of species that interfere with downstream assays. Additionally, many laboratory assays utilize milliliters of sample while most point-of-care paper-based devices are limited to only a few hundred microliters. To broaden the effectiveness and availability of point-of-care testing, we have developed and characterized a technique that allows for automated sample concentration or dilution in porous membranes. This system relies on an improved fundamental understanding of how membranes wet and how fluid flows through multi-material networks. This simple-to-use system is demonstrated in two ways: (1) automated DNA extraction and concentration from mL-sized samples and (2) an automated dilution series of an immunoassay detection antibody. Our system enables the integration of complex sample preparation with downstream biomolecule detection, which would otherwise not be feasible with traditional paper microfluidic approaches.

Introduction

Fluidic controls in paper microfluidics have been demonstrated repeatedly during the last decade using a variety of valving techniques. For example, materials can be embedded into a membrane to slow or delay flow. Noh *et al.* utilized varying concentrations of patterned wax to control fluidic timing in porous devices^{258,259}. Lutz *et al.* developed a different approach by embedding sugar barriers into porous membranes. Higher concentrations of sugars resulted in longer delays for fluid delivery²⁶⁰. The Yager, Lutz, and Fu groups have also designed methods for the sequential timed delivery of reagents through two-dimensional paper networks that rely on volume metering^{47,229,261,262}. Chen *et al.* developed a fluidic diode using a combination of hydrophobic and hydrophilic coatings to control direction and sequencing of fluid flow²⁶³. Many of these systems introduce an additional reagent (wax, sugar, etc.) into the reaction, which may negatively impact sensitive reactions such as nucleic acid amplification^{264–266}.

With these concerns in mind, Toley *et al.* developed valves that utilize separated fluidic networks to actuate expanding elements. These elements are outside of the main fluid pathway and do not introduce additional reagents. These expanding valves can turn flow on or off and cause fluid diversion and redirection²⁶⁷. This system was able to achieve fluidic delays ranging from 5 seconds to 25 minutes with coefficients of variation of less than 9 %.

Recent publications have included reviews of additional valving for paper microfluidics including those detailed above^{268–270}. Although effective, many these systems are limited to use with a maximum of a few hundreds of μL s of input sample. When processing large volumes such as urine or dilute blood, devices may need to manage up to 5-10 mL of volume. In urine, for example, the first 5-10 mL contain the highest concentration of pathogen biomarkers¹⁰¹.

In recent years, multiple groups have used isotachopheresis to concentrate pathogen biomarkers from complex samples^{92,95,271}, but these systems often use small sample volumes and involve multiple pre-processing steps, such as off-device centrifugation and sample dilution²⁷². Additionally, isotachopheresis can be sensitive to high salt and white blood cell concentrations found in clinical samples²⁷². Linnes *et al.* developed an integrated method for paper-based NA extraction coupled to in-membrane isothermal amplification to detect chlamydia⁷¹. Although effective, this device required multiple user steps and utilized

only a small volume of urine, between 10 – 100 μL . We previously published on an in-membrane sample processing method that concentrated DNA from up to 2 mL of sample, but that system did not include any automation to enable development of an integrated device¹⁴⁰.

Alternatively, some samples require dilution prior to processing to reduce high concentrations of interfering species that may inhibit target detection³²¹ or restrict flow through porous membranes¹⁴⁰. Multiple groups have demonstrated paper devices that separate the input sample into multiple detection zones causing modest dilution, but there are only a few demonstrations of deliberate and automated dilution in porous-based devices. Osborn *et al* demonstrated a paper-based device capable of linear dilutions based on geometry²⁶¹ and Songjaroen *et al*. designed a system that uses a wash step to dilute a sample on-device for blood typing³²². To date, there have not been any published reports of paper devices that automate a dilution series of a sample. The complexity of realistic samples – some which need concentration and others dilution – requires a reimagining of device design and fluid processing.

Many previous publications use simplified models to describe flow in paper microfluidic devices. The most commonly cited are the Washburn equation and Darcy's Law. The Washburn equation is limited to flow in one dimension while Darcy's Law can be used in multi-dimensional flows. Both of these models, however, are not fully representative of complex flow in porous media. For example, both Washburn and Darcy assume a fully saturating wetting front. In reality, the wetting front in a porous membrane is only partially-saturated and the degree of saturation depends on specific properties of the individual membranes such as the water retention curve. To accurately model these systems, a partially-saturated modelling technique is required. The Richards equation is widely used in hydrogeology to model partially-saturated flow through soil (ref). A full description of the Richards equation for modelling flow in porous media along with characterization of commonly used membranes for paper microfluidics is covered in a separate manuscript in preparation by our group (Buser *et al*. 2016, not sure if the PNAS rules allow us to cite this but wanted to include it just in case).

Using this new insight, we have designed and developed multi-material porous networks to automate and control fluid flow in paper microfluidic devices. This simple-to-use system is demonstrated in two ways: (1) automated DNA extraction and concentration from mL-sized samples and, to our knowledge, (2) the first demonstration of automated dilution series in a paper-based device. Our system enables the integration and automation of complex, multi-step assays which would otherwise not be feasible with traditional porous membrane-based microfluidic approaches.

Results

The p-switch: pressure-based system for controlling fluid flow in porous membranes

The use of porous materials for affordable diagnostics is partially driven by their automatic transport of fluids, removing the need for expensive operational equipment such as syringe pumps²⁶¹. This fluid transport is driven by a pressure differential between a fluid source and the wetting front in the membrane, described here as the suction pressure. This simple relationship has been described previously in the literature^{47,261,262}. More complex, multi-material networks, however, have not been well described.

When one membrane serves as a fluid source for a second membrane, the pressure differential at their intersection dictates fluid flow. For example, Figure 1A shows the water retention curve (WRC) for a nitrocellulose membrane (HF135, Millipore, Billerica, MA, USA). Wetting of the nitrocellulose membrane as modeled in COMSOL (Burlington, MA, USA) is shown in Figure 1B, with the wetting front advancing into the material from a fluid source located at the lower boundary. The modelled fluid pressure at 60s is shown in Figure 1C, along with the location of an overlapping secondary membrane, Ahlstrom 8964 glass fiber. The pressure along the vertical axis of the nitrocellulose membrane is plotted in Figure 1D. It can be observed that

the fluid pressure at the junction is negative, ~ 11 kPa. A water retention curve for the 8964 membrane is shown in Figure 1E; at a suction pressure of 11 kPa, very little of the membrane is saturated. The practical implication of this is that the 8964 membrane will not pull significant fluid from the junction while the HF135 membrane is wetting, due to the pressure differential at the junction.

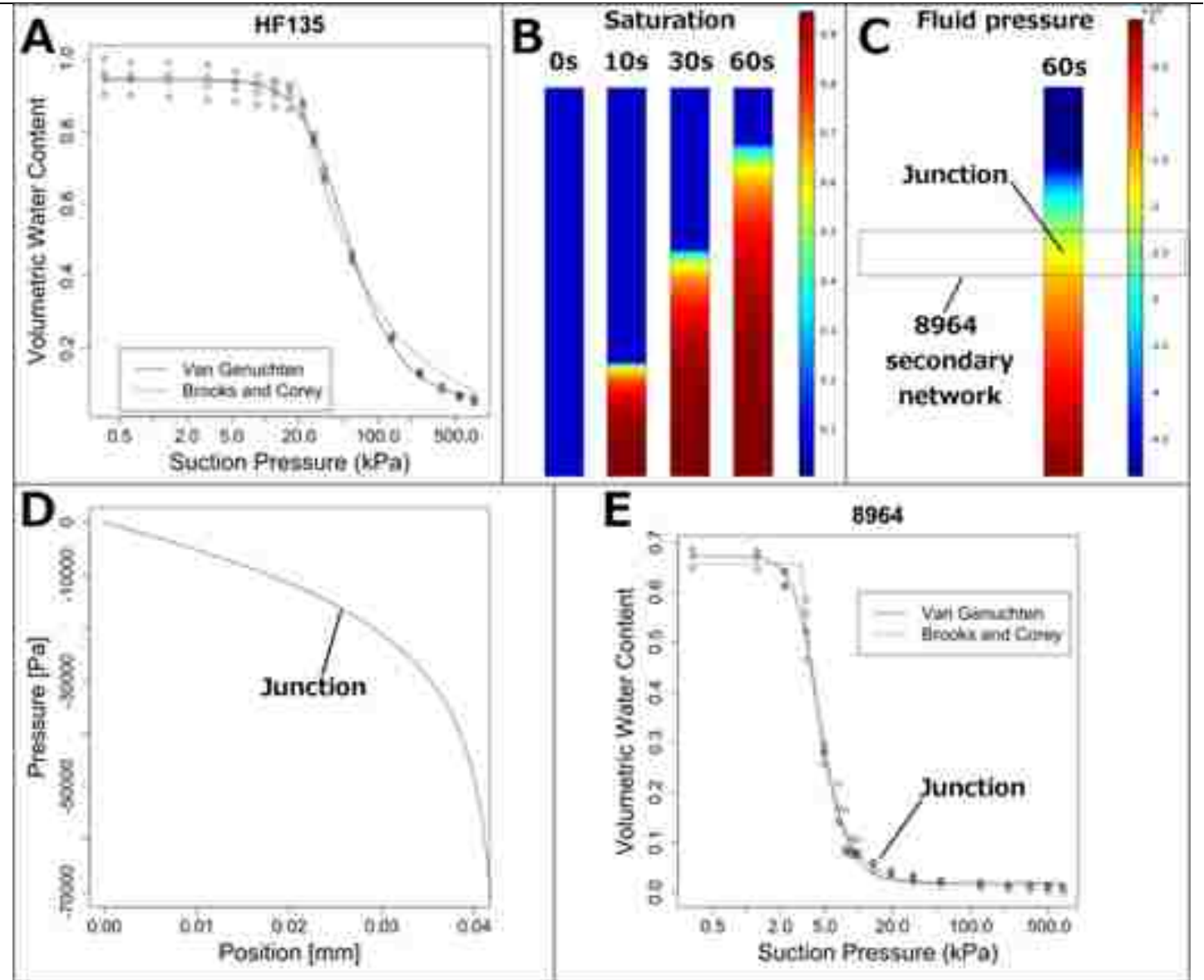


Figure 1. Theory of p-switch operation. **A.** Water retention curve (WRC) for HF135 nitrocellulose. At lower levels of saturation, a larger suction pressure is generated. **B.** The WRC data along with the measured membrane permeability can be used to model flow with the Richards equation. Here, fluid is flowing into an HF135 membrane from a fluid source located at the lower boundary of the rectangle. The fluid front advances into the membrane as time goes on. **C.** The fluid pressure is displayed at the 60 second time point. A hollow rectangle is drawn where an 8964 membrane could be located to construct a junction. **D.** Fluid pressure is plotted as a function of vertical position, with 0 mm corresponding to the lower boundary of the

rectangle. Fluid pressure starts as 0 at the fluid source, and decreases as a function of vertical position. The fluid pressure at the location of the 8964 junction is highlighted, around 11 kPa suction pressure. **E.** Water retention curve for 8964 glass fiber. At a suction pressure of 11 kPa, very little of the 8964 membrane will wet. This means that the 8964 will not pull a significant amount of fluid from the junction while the HF135 is wetting.

Careful material selection allows predictable pressure differentials at material junctions and, therefore, controllable fluid flow and material wetting. Because this controllable mechanism is driven by pressure, we've named it the p-switch.

Figure 2A shows a device composed of multiple materials; the primary membrane is connected to a fluid source and a waste pad. This primary membrane is sandwiched between two pieces of the secondary membrane at the overlap region, **Figure 2B**. During wetting, the primary membrane will take up fluid, **Figure 2C**. The secondary membrane remains dry as the fluid flows through the overlap region. If an additional fluid source is connected to the secondary membrane, fluid can now flow through the overlap region.

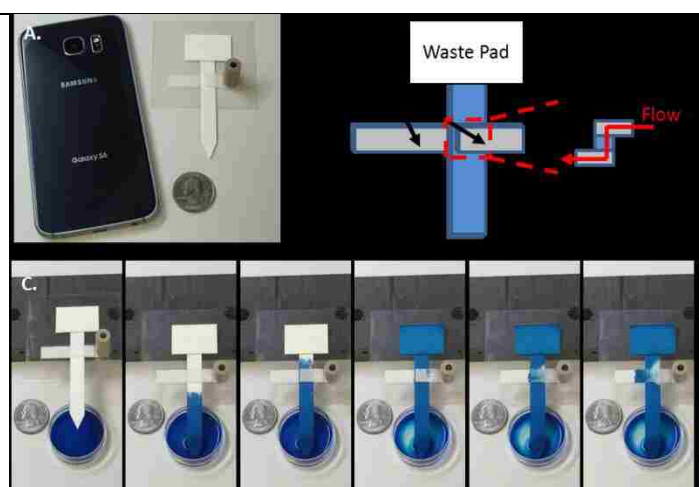


Figure 94. Demonstration of p-switch operation. **A.** Image of a p-switch device with a Galaxy S6 mobile phone and US quarter for scale. **B.** Schematic of p-switch device consisting of multiple materials and a cross-section of the overlap junction region. **C.** Images from a video showing fluid flow in a p-switch device.

Automated dilution in porous networks using the p-switch

The p-switch enables automated on-device dilution of a sample through the delivery of specific volumes of a sample across a series of test strips. **Figure 3A** shows the device designed for automated dilution, where the sample is applied to the primary membrane, named the sample pad. When the source pad is placed into a well containing running buffer, it carries varying volumes of the sample into the legs of each test strip. The decreasing widths on each subsequent test leg led to the delivery of subsequently smaller volumes of the

sample into each test strip, **Figure 3B**. The dilution factor on device was quantified using biotinylated gold nanoparticles that bind to a biotinylated oligonucleotide that is adsorbed onto a test line, **Figure 3C**. Utilizing a calibration curve (**supplemental**) the dilution factor across each test leg was calculated to be 0.8, 0.45, 0.24, and 0.1.

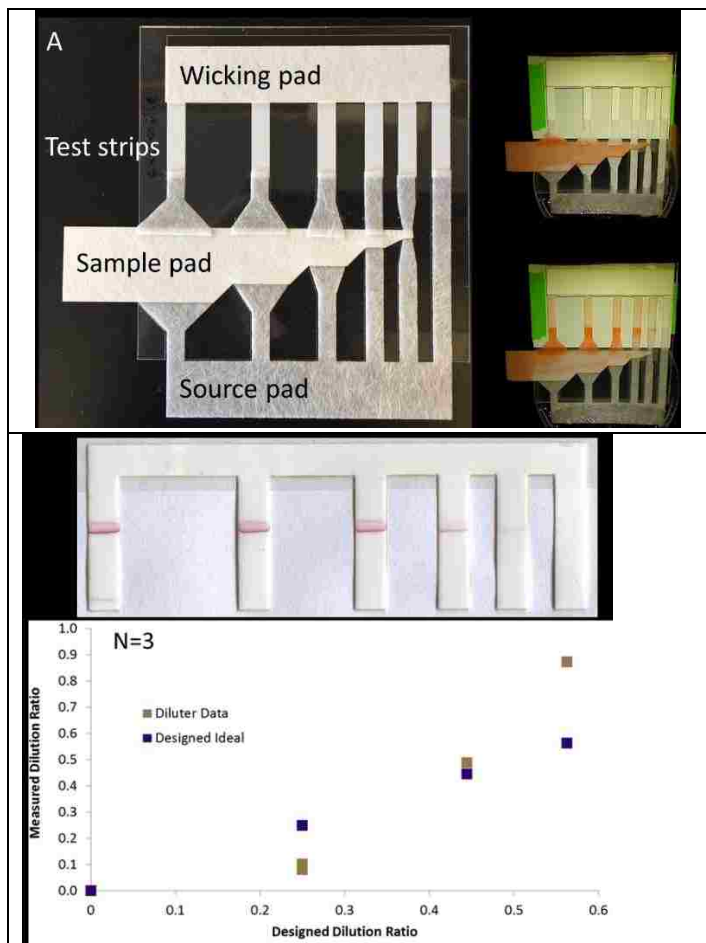


Figure 3. Paper-based automated dilution device using the p-value. **A.** Device schematic of the automation dilution device, where the primary membrane is the sample pad, and the source pad is the secondary membrane to which running buffer is applied. **B.** Video stills of the dilution device using red dye **C.** Representative test lines and the calculated dilution factor for each leg of the automated diluter. Averages of N=3 are reported with error bars representing +/- one standard deviation.

Sample concentration from mL-sized volumes using the p-switch

We demonstrated an application of the p-switch for automated DNA extraction and concentration from 1 mL samples. In this configuration, the device recovered >80% of the target DNA spiked into discarded human urine, **Figure 4**. Patient samples 08, 03, 02, and 05 had pH values at or below 6.8 and showed high recovery of target DNA. The samples also had widely varying salinities: 11–214 mM. These results were expected because the DNA capture molecule is positively charged below a pH of ~6.5. The details of this DNA purification system were previously published¹⁴⁰.

Patient samples 09, 01, and 04 had pH values above 7 resulting in poor capture and, ultimately, low recovery of target DNA. Patient sample 10 had a low pH (5.8), but did not result in a high recovery of target DNA. The amount of DNA remaining in the chitosan region after elution was less than 10% of the input for each sample. The device runtime was between 13-15 minutes.

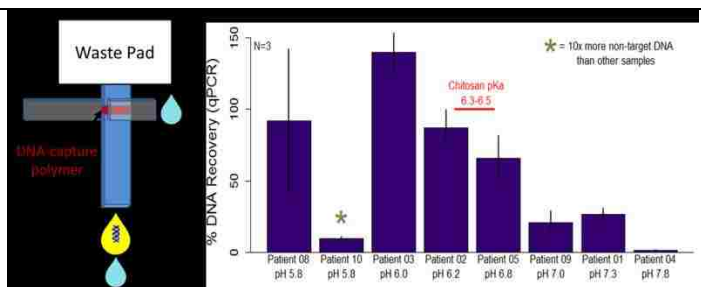


Figure 4. Application of the p-switch for in-membrane DNA purification and concentrated from 1 mL of discarded human urine samples. The primary membrane was patterned with a DNA-capture polymer. Flow of the 1 mL urine sample through primary the membrane resulted in DNA captured by the polymer in the at the membrane junction. After a wash step through the primary membrane, an elution buffer was introduced to the secondary membrane causing the DNA to flow through the junction and into the elution region. Sample recovery was quantified with qPCR. Averages of N=3 are reported with error bars representing +/- one standard deviation. Generally, as sample pH increased, recovery of target DNA decreased.

These results were very promising, but still required multiple user steps: one to add the sample and a second, timed step to add the elution buffer. With this in mind, the next generation of this device was designed to appropriately time the automatic release of the elution buffer to the secondary membrane.

Automated processing of samples with the p-switch using a pinch valve

To enable device operation without user intervention, a timed release mechanism was added to the device to automatically deliver a secondary buffer after the waste pad was sufficiently saturated with sample fluid, **Figure 5A**. This system was used to automatically concentrate DNA from 1-3.25 mL of buffer. Overall, the fully automated device recovered ~40 % of the target DNA, **Figure 5B**. For the 1 and 3.25 mL samples, the concentration factors ranged from 1.8-2.9 and 5.2-8.3, respectively (**Equation 1** in the table).

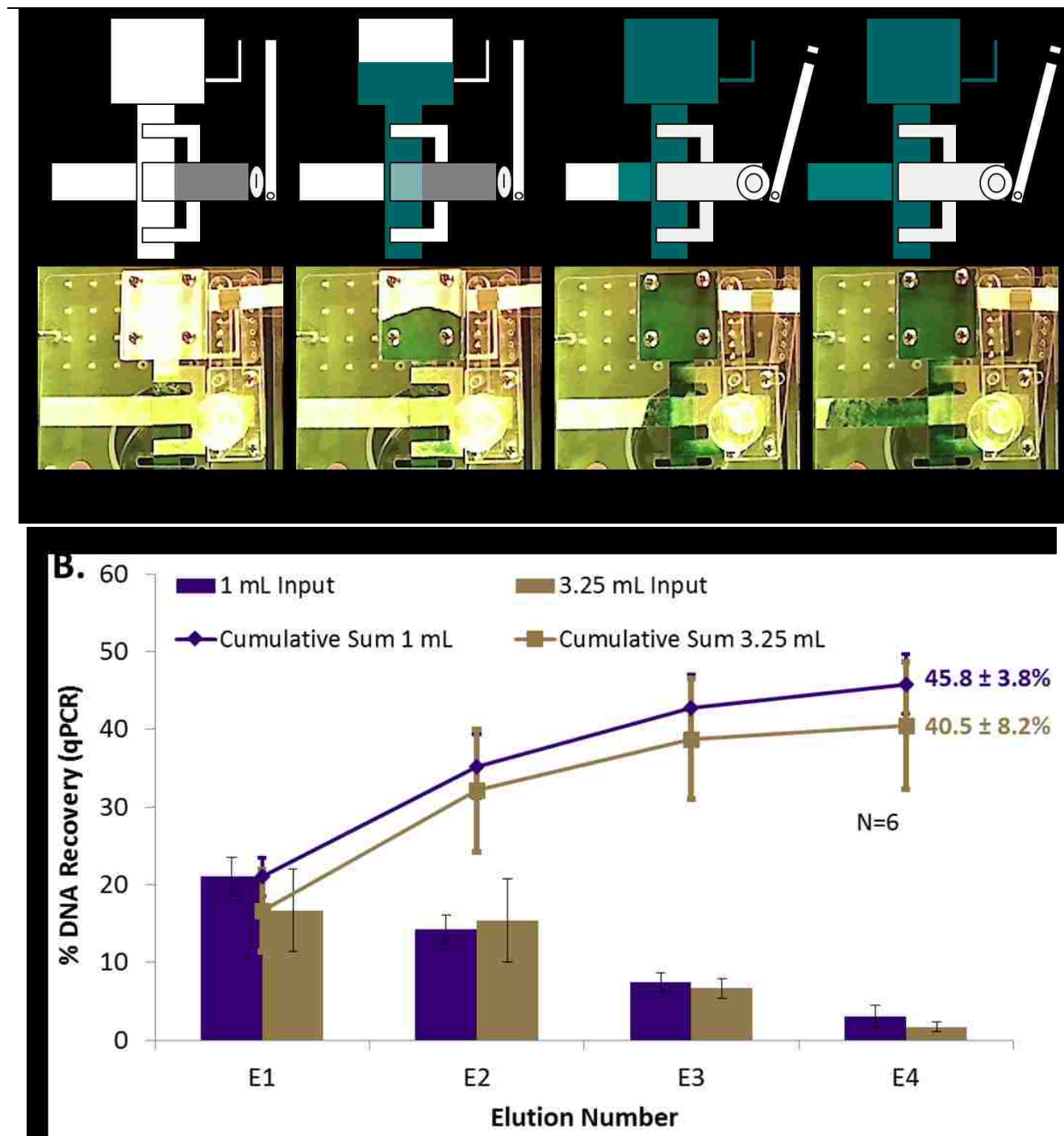


Figure 5. Automating the p-switch for the large volume sample concentration. **A.** Initially, the

elution buffer well is full, but the tubing connecting the well to the secondary network is pinched closed. The sample (red) flows through the primary network into the waste pad. When the waste pad reaches a sufficient level of saturation, the activation leg wets a water-soluble paper, which dissolves causing the pinch on the elution tube to be released. When the pinch is relieved, the elution buffer (blue) flows through the junction and fills the secondary network. **B.** Results from a DNA purification and concentration experiment using the automated p-switch device. Averages of N=6 are reported with error bars representing +/- standard error. The highest percentage of purified DNA was recovered in the first two elution volumes (each ~ 60 μ L). The 1 mL samples were processed in 12-13 minutes while the 3.25 mL samples were processed in 32-33 minutes.

Discussion

The p-switch: pressure-based system for controlling fluid flow in porous membranes

Fluid flow through complex, multi-material networks is driven by material properties and pressure differentials at the junction of overlapping materials. The negative fluid pressure a material's wetting front is developed by the contact angle at the fluid/membrane/air interface and the pore structure. The fluid pressure at various levels of membrane saturation can be characterized and modelled dynamically using previously demonstrated methods (Buser et al 2016?). Briefly, a water retention curve (WRC) is generated using a laboratory centrifuge (Fisher Scientific, Waltham, MA, USA), recording fluid recovery from a saturated membrane sample at increasing speeds. The fluid pressure at each rotational velocity is calculated (REF for how it's calculated or many an example of this calculation in the supplemental?) and the saturated fraction of the membrane pressure is plotted as a function of fluid pressure (% Water Saturation v. Suction Pressure).

This WRC data is fit using the Van Genuchten technique (REF), and parameters related to WRC data along with membrane permeability, measured using previously demonstrated techniques (REF), are used in a Richards equation model implemented in the COMSOL subsurface flow module (Burlington, MA, USA). These measurements generate the data and models shown in Figure 1 with a single fluid source connected to a primary membrane in contact with a secondary membrane at a specified junction. Due to the membrane properties and the pressure differential at this junction, there is unfavorable pressure to sufficiently wet the secondary membrane, therefore preventing flow while the primary fluid pathway is wetting.

A second fluid source connected to the network at the secondary membrane, as shown in Figure 2C, will now cause the secondary membrane to become more saturated with fluid. Higher saturation corresponds to a drop in the membrane suction pressure as described by the WRC. The change in the secondary membrane's pressure causes a more favorable differential at the junction allowing fluid to flow through the cross-section from the primary into the secondary membrane. This ability to control flow direction and timed wetting of multi-material networks enables the automation of complex assays in paper microfluidic devices.

Automated dilution in porous networks using the p-switch

Serial dilution is one of the most commonly used laboratory techniques for a variety of molecular biology applications. The applications for serial dilution in a laboratory setting range from determining the binding kinetics of a binding interaction to sample preparation methods (Paegel *et al.*, Nguyen *et al.*). Plastic microfluidic devices have been utilized for generating serial dilution series, however they require additional machinery to pump fluids throughout the entirety of the device (Kim *et al.*, Paegel *et al.*, Nguyen *et al.*). While paper based diagnostics enable the delivery of more complex chemistries at the point of care, they have not previously been utilized for on device serial dilution coupled with detection of an analyte. As paper microfluidics utilize capillary action as the primary force for fluid flow, it is possible to further simplify these designs and enable their use at the point of care. Integration of on device serial dilution into a paper microfluidic device has the potential to increase the capabilities of traditional lateral flow assays to techniques that require dilution steps.

Here, we present proof of concept for on device dilution of both dye and streptavidin coated gold nanoparticles. By varying the area of each of the glass fiber sample legs in the diluter, it is possible to control the volume of a sample that is delivered across a test line, **Figure 3**. As compared to the anticipated signal, it was discovered that there are additional factors that affect the dilution ratio besides the area of the glass fiber transfer pad. The dilution ratio for each test leg was found to be further defined by the total area in the sample pad through which the source buffer runs.

We anticipate that an automated dilution series can be integrated into a variety of devices that intend to complete complex chemistries required for laboratory based assays in an automated format.

Sample concentration from mL-sized volumes using the p-switch

As described previously, chitosan is a linear polysaccharide that electrostatically binds to DNA when the pH is below $\sim 6.3-6.5$, the pK_a of the primary amine^{223,226}. Above that pH, the amines are deprotonated and the electrostatic interaction is lost. Previously, we demonstrated chitosan's ability to capture and release DNA in porous membranes without any automation¹⁴⁰. The work presented here demonstrates an automation of this assay using realistic patient samples.

Unsurprisingly, urine samples with pH values below the amine pK_a show high recovery of target DNA while samples with higher pH values, show reduced recovery. The exception in this dataset is sample 10 which had an appropriate pH for DNA capture by chitosan, but showed very low DNA recovery. We hypothesize that sample 10 had reduced recovery due to an overloading of the chitosan with non-target nucleic acids that were present from the patient sample. Patient 10 had 10x more non-target nucleic acids compared to the rest of the samples tested. Based on previous work, this amount of non-target nucleic acid is above the capacity of the chitosan patterned in this membrane. **Table S1** shows characterization of each of the patient samples.

The geometry of these devices was designed to decrease overall processing time. One method for improving flow rate was driven by the geometry of the device waste pads. Flow through the transverse section of a porous membrane can greatly increase sample processing time due to shorter distances for fluid to travel and increased surface area for volumetric uptake. Darcy's Law dictates that flow rate through porous media is inversely proportional to the length traveled by the fluid. This is especially important for large volume samples. To reduce the fluid's path, geometry of a porous network can be

optimized by stacking the waste collection pads. The assay runtime for the stacked waste pad geometry was compared to a device with a single, large waste pad. For all sample volumes tested, the stacked waste pad configuration significantly reduced total flow time (**Figure S1**).

Automated processing of samples with the p-switch using a pinch valve

In the automated devices, the waste pad was in contact with a connecting arm made of a Fusion 5 membrane. The connecting arm contacted a water-soluble paper that restrained a plastic lever arm which was pinching closed tubing. This tubing connected the elution buffer to the secondary membrane, as shown in **Figure 5A**.

Once the waste pad was full, the connecting arm began to fill and wet the water-soluble paper which dissolved and released the lever arm and then the pinch on the tubing. The open tubing then allowed elution buffer to flow into the secondary membrane, which is made of 8964 glass fiber. Flow of elution buffer through the junction eluted DNA captured on the chitosan in the overlap junction. The eluted DNA then flowed into the dry secondary membrane. The purified and concentrated sample was quantified by qPCR to determine recovery of target DNA.

The geometry of the automated p-switch device was optimized to improve elution of the DNA from the overlapping region. First, the number of legs connecting the elution fluid to the overlap region was tested. The first generation of devices had a single leg at the junction, but they resulted in a portion of target being eluted upstream or downstream in the primary membrane and therefore lost to waste. To address this loss, two and three leg devices were tested. The additional legs upstream and downstream of the main leg at the overlap design fluidically cut-off the flow of the main overlap toward waste. After comparing these three geometries, the three leg device was selected for future tests, **Figure S2A**.

Next, the amount of overlap between the primary and secondary membranes in the junction region was optimized to improve DNA elution. In general, greater amounts of overlap lead to a more complete wash out of the overlap region, **Figure S2B**, which can improve both percent recovery and concentration factor of the DNA. After the visualization tests, DNA purification and concentration was compared in these geometries using DNA spiked into 1 mL discarded human urine sample. These results showed that the “top full, bottom partial” geometry resulted in the highest recovery of DNA and concentration factor, **Figure S2C**. All further experiments were performed using the geometries selected from these optimization experiments.

The optimized geometry p-switch devices were then tested with 1 and 4 mL inputs (the device that had the 4 mL input only processed 3.25 mL before the waste pad filled). All samples were spiked with purified DNA. Multiple elutions were collected from each device to build an elution profile and track when the DNA was eluting from the capture region. With the optimized system, the majority of the DNA was recovered in the first two elutions. This is an ideal elution profile because the purified sample could immediately flow downstream into an assay (such as an amplification assay). Each elution was ~ 60 μ L.

Beyond the applications demonstrated in this work, the p-switch technology could be used for a multitude of other systems in order to automate multi-step assays. This work provides a unique opportunity to integrate sample dilution, sample concentration, and/or controlled fluid flow. Future

iterations will show fully integrated systems that enable automatic control of multi-step assays that would not otherwise be feasible with traditional lateral flow-based devices.

Materials and Methods

Reagent preparation

All reagents were prepared with sterile molecular biology grade water (Fisher Scientific, Waltham, MA, USA). Low molecular weight chitosan oligosaccharide lactate (average MW 5000), Tris Base, MES, Achromopeptidase (ACP, A3547), 200 proof Ethanol, and Erioglaucline were purchased from Sigma Aldrich (St. Louis, MO, USA). Glycogen was purchased from Thermo Fisher Scientific (Grand Island, NY, USA). A 2 mg/mL solution of Erioglaucline was prepared in sterile water. A 20 U/ μ L solution of ACP was prepared in 10 mM Tris, pH 8. The 50 mM MES DNA wash buffer were prepared in sterile water and the pH was adjusted to 5. The 50 mM Tris DNA elution buffer was prepared in sterile water and the pH was adjusted to 9. De-identified human urine samples were provided by the Global Health STI Laboratory at the University of Washington Harborview Medical Center in Seattle, WA, USA. Urine sample pH and salinity was measured using a pH/conductivity meter (company info here). 40 nm InnovaCoat streptavidin gold conjugates were purchased from InnovaBiosciences (Cambridge, United Kingdom). Triethyl ammonium bicarbonate (TEAB) at 0.1 M and the biotinylated probe were supplied by ELITech Molecular Diagnostics (Seattle, WA, USA not sure if this is correct – Caitlin). The biotinylated probe consisted of the following sequence: 5'-TTTTTTTTTTTTTTTTTTTT-biotinTEG – 3' (T20-biotin). These reagents were diluted to 75 μ M of TEAB and 200 μ M of T20-biotin probe.

Device patterning and construction

All porous membranes and test card materials were cut using a CO₂ laser (Universal Laser Systems, Scottsdale, AZ). For the concentrator, Fusion 5 membranes (GE Healthcare Life Sciences, Niskayuna, NY) were patterned with chitosan and used as the primary network in the p-switches. The secondary network was comprised of 8964 glass fiber (Ahlstrom, Alpharetta, GA, USA). Test cards were made with 0.254 mm-thick Mylar backing with adhesive (10 mil AC Melinex, Fralock, Valencia, CA, USA) and cellulose wicking pads (CFSP223000 Millipore, Millipore, Billerica, MA, USA) for waste fluid uptake. The Fusion 5 membrane was patterned with a 1 mg/mL solution of low molecular weight chitosan solution prepared in 50 mM MES at pH 5. After patterning, the membranes were stored in a desiccator. For the diluter, nitrocellulose membranes (HF135, EMD Millipore, Billerica, MA, USA) were patterned with a T20-biotin probe at 200 μ M in 75 μ M TEAB using a piezoelectric printer (sciFLEXARRAYER S3, Scienion AG, Berlin, Germany). The solution was filtered using a 0.2- μ m nylon membrane (VWR, Radnor, PA) at 8000g for 5 minutes prior to spotting. Test lines were created by 20 spots spaced 250 μ m apart, with 30 droplets per spot. Each droplet was 450-500 μ L. After spotting, membranes were UV treated for 8 minutes with a UV transilluminator (UltraLUM Inc., Paramount, CA, USA) at wavelength 300-310 nm and stored under desiccation before use.

Automated dilution using the p-switch

The calibration curve was generated using known concentrations of streptavidin gold (InnovaCoat Gold – 40 nm streptavidin gold conjugate, InnovaBiosciences, Cambridge, United Kingdom). Dilutions between 0-0.25 OD in a final volume of 40 μ L were tested to determine the dynamic range for the system. The automated diluter was tested by applying 750 μ L of gold nanoparticles diluted to OD 0.0625 in PBST+1%(w/v) BSA to the sample application portion of the fusion 5 pad. Once the entire membrane wet, the glass fiber base was placed into a well containing 3 μ L of PBST and allowed to run until all

buffer was used. All images were immediately scanned at 600 dpi and quantitative values were analyzed using the normalized pixel intensity across the test line.

Quantifying total Nucleic Acids in patient urine samples

Nucleic acids were purified from 500 μL of discarded urine samples by first harvesting any intact cells *via* centrifugation at 13,000 $\times g$ for 3 minutes. The supernatant was saved in a separate tube and cells were resuspended in an equal volume of 10 mM tris at pH 8.

Cells were then treated with 10 μL of 20 U/ μL ACP and incubated at room temperature for 2 minutes. Then, the suspension was heated to 95 $^{\circ}\text{C}$ for 5 minutes.

Nucleic acids were purified from both the cell lysate and the supernatant by ethanol precipitation using 1/10 volume of 3 M sodium acetate (pH 5.2), 2x volumes of cold 100% ethanol, and 1/100 volume of 20 mg/mL glycogen. The solutions were mixed by inversion 10-12 times followed by incubation at -20 $^{\circ}\text{C}$ for 15 minutes. After incubation, the samples were centrifuged for 15 minutes at maximum speed: 21,000. The glycogen and nucleic acids formed a visible white pellet in the bottom of the tube. The supernatant was removed and the pellet was washed with 1 mL of 70% ethanol. The sample was mixed by inversion 10-12 times followed by centrifugation at maximum speed for 5 minutes. The supernatant was removed and the pellet air-dried for 10 minutes at room temperature. The pellet was then resuspended in 50 μL of sterile water with heating to 37 $^{\circ}\text{C}$ for 10 minutes. The concentration of nucleic acids was quantified using a Nanodrop (ThermoFisher Scientific, Grand Island, NY, USA).

qPCR for MRSA *ldh-1* gene

DNA recovery was quantified with a qPCR kit for the *ldh-1* gene provided by the ELITechGroup (ELITechGroup Molecular Diagnostics, Bothell, WA, USA). The 20 μL reactions were run on a Bio-Rad CFX real-time PCR instrument (Bio-Rad, Hercules, CA, USA) using the following protocol: 50 $^{\circ}\text{C}$ hold for 2 minutes, 93 $^{\circ}\text{C}$ hold for 2 minutes, 45 cycles of 93 $^{\circ}\text{C}$ for 10 seconds, 56 $^{\circ}\text{C}$ for 30 seconds, and 72 $^{\circ}\text{C}$ for 15 seconds, ending with final elongation step at 72 $^{\circ}\text{C}$ for 5 minutes. Fluorescence data were collected during the 56 $^{\circ}\text{C}$ annealing step in the Texas Red channel. The qPCR results were analyzed using the automated threshold cycle (CT) value calculation in the Bio-Rad software (Bio-Rad, Hercules, CA, USA). This assay is sensitive down to $\sim 10^1$ copies of the target sequence.

Automated processing of samples with the p-switch using a pinch valve

Devices were built as shown in Figure 94 with Fusion 5 glass fiber as the primary membrane and 8964 glass fiber as the secondary membrane. The waste pad was made from cellulose and the membranes were held in place by the adhesive layer of the Mylar backing.

The purification experiments were run as previously described¹⁴⁰, with the following changes. For these tests, 10 μL of fragmented MRSA gDNA ($\sim 1 \times 10^4 - 1 \times 10^5$ copies/ μL) was diluted into 990-3990 μL of either buffer or discarded urine samples (**Table S1**) for a resulting concentration of $\sim 1 \times 10^2 - 1 \times 10^3$ copies/mL. The full volume was then flowed through the device followed by 250 μL of wash buffer (50 mM MES, pH 5). 250 μL of the elution buffer (50 mM Tris, pH 9) was manually added to the secondary membrane.

After the secondary membrane was fully wet, the chitosan and elution sections of the device were removed and fluid was recovered by centrifugation at 10,000 for 3 minutes. The amount of target DNA in the fluid from each membrane region was quantified by qPCR, correcting for volume recovered from the section.

Automating the p-switch through timed release of the secondary fluid source – the pinch valve

The secondary fluid source can be activated automatically, causing elution of the nucleic acid through the secondary membrane. For this purpose, a small leg of Fusion 5 membrane extends from underneath the

cellulose waste pads, which wets once the cellulose pads reach saturation. This leg of Fusion 5 is in contact with a section of water-soluble paper (MFG), which dissolves on contact with liquid. This paper is holding closed a pinched section of silicone tubing that prevents flow of the elution buffer. When the water-soluble paper dissolves, the pinch is released, allowing fluid to flow through the previously blocked tubing and into the inlet of the secondary membrane, activating elution through the overlap junction of the p-switch.

Fully integrated system for concentrating DNA from mL-sized samples

Devices were built as shown in Figure 5A with Fusion 5 glass fiber as the primary membrane and Ahlstrom 8964 glass fiber as the secondary membrane. The waste pad stack was made from cellulose and the membranes held in place by the adhesive layer of the Mylar backing.

The fully automated purification experiments were run as described above with fragmented MRSA gDNA ($\sim 1 \times 10^4 - 1 \times 10^5$ copies) was diluted into 5 mL of buffer for a resulting concentration of $\sim 1 \times 10^1 - 1 \times 10^2$ copies/mL. The full volume was added to the sample collection well and flowed through the device without a wash step. After the flow of sample was complete, 750 μ L of the elution buffer (50 mM Tris, pH 9) was automatically released to wet the secondary membrane, as described above.

After the secondary membrane was fully wet, fluid was recovered from the device by centrifugation at 10,000 for 3 minutes. Recovery of target DNA was quantified by qPCR, correcting for elution volume.

Statistics

All statistics were run using the open-source statistical package R (64 bit, version 3.0.2)³²³.

Acknowledgments

This work was supported by a grant to Paul Yager from the Defense Advanced Research Projects Agency (DARPA) "Multiplexable Autonomous Disposable for Nucleic Acid Amplification Tests for LRSs" under Grant No. HR0011-11-2-0007.

We thank our colleagues Ryan, Gallagher, Paula Ladd, and Erin Heiniger in the Yager Laboratory who provided valuable discussion and feedback on experimental design and analysis. We thank O. Soge Olusegun from the Global Health STI Laboratory at the University of Washington Harborview Medical Center for providing deidentified human urine samples. We thank collaborators from ELITechGroup Molecular Diagnostics for assistance with the supply of the qPCR assay. SEM imaging and sputter coating work was performed at the University of Washington Nanotech User Facility (NTUF), a member of the NSF-sponsored National Nanotechnology Infrastructure Network (NNIN).

4. ****Selecting analytical biomarkers for diagnostic applications: guidelines and recommendations** (manuscript in preparation for *Clinical Chemistry and Laboratory Medicine*) → in collaboration with Dr. Bernhard Weigl from Intellectual Ventures/Global Good

Samantha A. Byrnes and Bernhard Weigl

Abstract. Biomarkers are objective indications of a medical state observed from outside the patient either, physically in vivo, or biochemically in vitro, that can be measured accurately and reproducibly. Selection of diagnostic biomarkers is an important stage in disease control efforts which often begin

with accurate disease identification. Traditional biomarkers rely on the detection of disease-specific nucleic acid or protein signatures or on distinct physiological signatures such as changes in blood pressure. Currently, the field has expanded to include a multitude of other diagnostic targets including exosomes, hormones, carbohydrates, lipids, and various forms of proteins and nucleic acids (cell free DNA, mRNA, microRNA).

This work provides an overview of biomarkers for diagnosis of both infectious and non-infection diseases. Focus was placed on markers that were amenable to analytical detection in diverse locations including both high and low resource settings. For non-communicable diseases, much of the literature supports the use of a panel of biomarkers rather than single targets to improve diagnostic accuracy. Additionally, this report details assessment criteria for successful diagnostic tests including sensitivity, specificity, time-to-result, ease-of-use, cost, and biomarker stability during storage. The goal of this work is to serve as a set of guidelines to systematically identify appropriate biomarker(s) for diagnostics devices and assay developers.

Keywords: biomarker selection; diagnostic devices; test assessment criteria

Introduction

Diagnosis of disease relies on the identification of disease-specific indicator(s) which are known as biomarkers. The Biomarker Definitions Working Group defines a biomarker as “a characteristic that is objectively measured and evaluated as an indicator of normal biological processes, pathogenic processes, or pharmacological responses to a therapeutic intervention”³²⁴. The term “biomarker” encompasses multiple categories of disease indicators including disease-specific molecules, such as proteins and nucleic acids, as well as results from imaging technologies and physiological measurements such as blood pressure³²⁵. Additionally, these indicators must be both disease-specific and generally universal in a diseased population to be measured reliably and accurately across a wide range of patients³²⁶. Biomarkers are used for diagnosis of both infectious and non-infectious diseases.

There are hundreds of cataloged biomarkers described in the literature and used in commercially available diagnostic products. But even with the range of available information, biomarker selection still remains one of the most important and challenging aspects of developing diagnostic systems (or devices instead of systems?). Test developers must assess how the choice of biomarker(s) will influence multiple aspects of a device including performance and accuracy. Often, there is more than one potential biomarker for a disease and the effectiveness of these biomarkers can vary widely. Selecting the right biomarker(s) can affect aspects of a final diagnostic test such as sensitivity and specificity. Additionally, biomarker selection may rely on availability, cost to produce, diseases prevalence, and even stage of disease detection (or time of diagnosis since disease onset). All of these considerations depend on the setting in which the test will be used; a test used in a laboratory with trained technicians *v.* in the home by untrained users, or a test performed in a hospital with constant electricity *v.* at a health outpost with no electricity will all have varying design requirements. Selecting a single or combination of targets can further complicate this choice.

In this work, we describe a wide range of biomarkers used for disease diagnosis and explore why and how to select the right biomarker(s) for an application. Using this information, we discuss the concept

of an idealized “universal biomarker”. These guidelines should be used to systematically identify appropriate biomarker(s) for diagnostic devices.

Categories of Biomarkers

As defined by The Biomarker Definitions Working Group, the term “biomarker” includes a wide range of disease indicators. In general, they can be grouped into two broad categories: Molecular Biomarkers and Non-invasive (or non-molecular??) Biomarkers. These categories also include multiple sub-classifications.

Molecular Biomarkers

Molecular biomarkers are biomolecules (proteins, nucleic acids, lipids, carbohydrates, small molecules, etc.) used to uniquely identify disease state or infection. They are often used in clinical research, and while some have been well-tested and validated, others require additional research or verification to link to disease state ³²⁶. The information below is not an exhaustive list detailing all molecular biomarkers, but rather, should serve as a review of many common and some emerging examples of molecular biomarkers. These classes (categories?) of biomarkers are summarized in **Table 1**.

Nucleic Acids: Nucleic acids have been used as biomarkers for countless diseases due to their high degree of specificity. Nucleic acids make up the unique genetic code of every organism; this characteristic allows nucleic acids to be used for highly accurate identification of disease. Additionally, variations in nucleic acid sequences can also serve as a future disease indicator. Within this category, there are two main types of nucleic acids: DNA and RNA. Both DNA and RNA can be identified by similar methods including target-specific amplification (such as PCR), next generation sequencing (NGS), and microarrays.

DNA is an extremely common molecule for disease identification and remains relatively stable over time. Unique to DNA is the identification of single nucleotide polymorphisms (SNPs) – variations in one specific nucleotide that occur in > 1% of a population. SNPs have been used to track disease progression in Hepatitis C infection and can indicate how patients will respond to different therapies ³²⁷. Also unique to DNA are epigenetic modifications, such as methylation, which have been used to track treatment of disease (ref). There are also sub-categories of DNA which include genomic DNA, cell free DNA, and DNA fragments. Cell free transrenal DNA has been used as a biomarker for identifying proviral HIV, bacteria, parasites ³²⁸, and cancer ³²⁹. A few major drawbacks to using DNA as a diagnostic biomarker are that it is often available in somewhat low abundance (only 1-2 genomic copies per cell), identification methods usually require highly purified samples, and it is not available for all diseases since some agents only have RNA.

While it shares some characteristics and detection methods with DNA, RNA has additional unique functions. Messenger RNA (mRNA) encodes all of the proteins in an organism and is often used to identify recessive genetic disorders ³³⁰. MicroRNA (miRNA) is non-protein coding RNA that can regulate gene expression and has been used as a tumor ³³¹ and infectious disease biomarker ³³². Unlike DNA, RNA can be present in very high concentrations during specific disease states and can be used to identify RNA-based organisms such as the Zika virus. Additionally, RNA may be a useful biomarker for non-

infectious diseases that can be identified through changes in miRNA and protein regulation or mRNA and protein expression levels (ref). These expression levels, however, can be a potential drawback to using RNA as a diagnostic marker if a specific disease state results in reduced instead of upregulated RNA expression.

Proteins: Proteins, along with nucleic acids, are the most commonly used biomarkers in diagnostic tests due to their potentially high abundance and specificity. Proteins are used for nearly every function in a cell. They can be found free in solution or intracellularly. When considering the use of solution proteins as diagnostic biomarkers, there are multiple design constraints that may influence biomarker selection including detection modality (labeled v. label-free detection), capture molecule option (antibodies, antigens, aptamers, affibodies, engineered protein fragments), and data analysis method, which often requires equipment or complex statistical algorithms that are not yet standardized ³³³. There are multiple methods for identifying and categorizing proteins free in solution including ELISA, microarrays, and proteomics – the study of proteins and their functions ³³⁴.

Proteins inside of in-tact cells can also be used as diagnostic biomarkers which are usually detected using immunohistochemistry (IHC) ³³⁵. Compared to other biomarkers, proteins in cells have not been readily used for diagnosis due to a few major limitations including the need for highly specific, and often costly, detection antibodies and expensive equipment for performing and analyzing IHC. A potential challenge associated with using proteins – either in solution or in cells – as biomarkers is related to protein structure and function; if protein structure is disrupted, function can be lost which often prevents proper identification.

Proteins have been used to identify both infectious and non-infectious diseases directly from samples such as serum or blood plasma. The Human Plasma Proteome Project (PPP) has created a protein database from a comprehensive analysis of the entire protein component of human plasma and serum in normal and various disease states ³³⁶. Tumor-associated antigens (TAA) have also been used as a non-invasive alternative to biopsy for diagnosis of lung, liver, breast, prostate, ovarian, and renal cancers ³³⁷. Additionally, proteins can be used individually or in groups to increase test specificity. Although proteins are common in diagnostic applications, there are also some important drawbacks to consider when selecting them as biomarkers. For instance, proteomics only provides a snap-shot in time of disease state, so it often requires comparison across multiple time-points which may lead to longer, more expensive, and more complex tests. Additionally, potential cross-reactivity between similar proteins can lead to false-positive test results (ref?). Multiple reviews of proteins used as diagnostic biomarkers have been previously published ^{338–340}.

Exosomes: Exosomes are small membrane vesicles released from many cell types and have been identified in multiple body fluids including urine, blood, amniotic fluid, synovial fluid, breast milk, and saliva ³⁴¹. Methods for identifying/detecting exosomes include Cons: concentration in body fluids??

Research has identified multiple characteristics of exosomes that makes them potentially useful biomarkers for disease. Exosomes have been found to express proteins that originated from a host cell,

contain mRNA and miRNA that could be used for disease profiling³⁴², and show increased release from tumor cells during the advanced disease stages³⁴³. Can be used for both infectious and NCDs?

Lipids: Lipids are fatty or waxy molecules that have multiple functions in cells including for cell signaling, energy storage, and structure of the cell membrane. Metabolic profiling is a common lipid identification technique³⁴⁴. Others? Pros/cons.

Lipids have been used for both infectious and non-infectious disease detection, often by measuring a panel of lipids. For example, changes in lipid metabolism can be used as a marker for prostate cancer³⁴⁵ and monitoring changes in lipid abnormalities has been linked to cardiovascular disease³⁴⁶. Lipids have also been used as biomarkers for infectious diseases such as TB³⁴⁷ and carcinoma caused by hepatitis B infection³⁴⁸.

Carbohydrates: Carbohydrates or saccharides are commonly used for energy or structure in the body. These molecules are often further separated into three main subcategories of sugars, starches, and fibers. Common methods of detection for saccharides are liquid chromatography/mass spectrometry³⁴⁹. Pros/cons as biomolecules.

The most well-known carbohydrate used as a disease biomarker is glucose, which is used to monitor diabetes. Beside glucose, other potential saccharides have been used as biomarkers for autoimmune diseases and rheumatoid arthritis³⁵⁰. Carbohydrates have also been used as cancer biomarkers^{351,352}. A recent review details the use of carbohydrates as diagnostic biomarkers for infectious disease, cancer, and cardiovascular disease (ref 42).

Hormones: Hormones are chemical messengers that can serve as diagnostic biomarkers. Hormone levels naturally fluctuate in the body, but irregular changes can arise from infection or as a response to disease treatment. Methods to identify hormone levels include... Hormones have been successfully used to track non-infectious diseases, but limited evidence is available to relate hormone levels to infectious agents. Additionally, a potential drawback to using hormones as a biomarker is the need for somewhat quantitative detection instead of simple identification of their presence because hormone levels naturally vary in an individual.

Hormone levels have been used to indicate how well a patient will respond to anti-hormone therapies for certain tumors. Breast tumor hormone receptor levels can indicate whether a patient will respond better to treatment with hormone modulators or chemotherapy³⁵³. Additionally, identification of hormone levels, such as procalcitonin, have been used to identify whether the cause of a fever is from an infectious or non-infectious agent³⁵⁴.

Cells: Analysis of a whole cell can serve as a useful diagnostic biomarker. Most commonly, target cells are identified through flow cytometry for selective cell sorting or microscopy of a tissue or fluid sample. Using cells as diagnostic biomarkers can serve as direct identification of an active infection or disease state, whereas other molecular biomarkers, such as proteins, may remain after the disease has passed. There are some notable limitations, however. Both flow cytometry and microscopy are often expensive

and require highly trained technicians to operate the necessary equipment; these requirements can limit usage to centralized laboratory settings.

Some common infectious such as, tuberculosis and malaria, are often diagnosed through microscopic observation of sputum³⁵⁵ or blood smear³⁵⁶ samples, respectively. Additionally, diseases caused by pathogens that also infect other animals, such as mosquitos, can be diagnosed by identifying the pathogen in the alternative host. For identification of non-infectious diseases, research has focused on detecting circulating tumor cells for multiple types of cancer³⁵⁷.

Table 1: Summary of major categories of molecular biomarkers for disease diagnosis.

Biomarker	Disease Type	Common Detection Methods	Potential Use Settings	Example	Noted Reference(s)
DNA: gDNA	Infectious, potentially NCDs	Amplification Microarrays Next gen sequencing	Amplification – high and low resource settings NGS – high resource settings	SNP identification in Hep C patients can predict responses to therapy	Rauch <i>et al</i> , 2010 ³²⁷ Goulart <i>et al</i> , 2010 ³⁵⁸
DNA: fragments and cell-free	Infectious and NCDs	Amplification Microarrays Next gen sequencing	Amplification – high and low resource settings NGS – high resource settings	<u>Infectious</u> : transrenal DNA in urine <u>NCD</u> : cancer detection from urine	Umansky <i>et al</i> , 2006 ³²⁸ Utting <i>et al</i> , 2002
RNA: mRNA	Infectious and NCDs	Amplification Microarrays	High and low resource settings	mRNA used for identifying recessive genetic disorders	Sunde, 2010 ³⁵⁹ Sugiura <i>et al</i> , 2015 ³³⁰
RNA: miRNA	Infectious and NCDs	Amplification Microarrays	High and low resource settings	Identification of parasitic infections Changes in concentration can serve as tumor marker	Manzano-Roman <i>et al</i> , 2012 ³³² Zhou <i>et al</i> , 2015 ³³¹
Proteins: in solution	Infectious and NCDs	Microarrays ELISA Mass spec	High and low resource settings	Proteomics for 10 common infectious diseases Tumor Associated Antigens for diagnosis of cancer	Ray <i>et al</i> , 2014 ³³⁸ Coronell <i>et al</i> , 2012 ³³⁷
Proteins: in cell	NCDs, maybe infectious	Immunohistochemistry	High resource settings	Can identify activated gene mutations	Swanson <i>et al</i> , 2015 ³³⁵
Exosomes	Infectious and NCDs	Amplification Microarrays Next gen sequencing	High and low resource settings	Express proteins from original host cell; contain mRNA and miRNA for disease profiling; show increase release during advanced stages of tumor growth	Taylor <i>et al</i> , 2008 ³⁴³ Simpson <i>et al</i> , 2009 ³⁴¹

Lipids	Infectious and NCDs	Metabolic profiling	High resource settings	Changes in metabolism can indicate prostate cancer LAM lipid as TB biomarker	Kelly <i>et al</i> , 2016 ³⁴⁵ Sakamuri <i>et al</i> , 2014 ³⁴⁷
Carbohydrates	Infectious and NCDs	Liquid chromatography/mass spectrometry	High and low resource settings	Monitoring glucose levels for diabetes Diagnosis of rheumatoid arthritis	Alavi <i>et al</i> , 2008 ³⁵⁰
Hormones	NCD, maybe infectious	Competitive binding assays ELISA	Mostly high, but some low resource	Measuring hormone levels can indicate how breast cancer patients will respond	Albain <i>et al</i> , 2005
Cells	Infectious and NCDs	Flow cytometry Microscopy	Mostly high, but some low resource settings (microscopy)	Identifying malaria parasites in blood smears CTC for cancer detection	Betanzos-Reyes <i>et al</i> 2007 ³⁵⁶ Nellore <i>et al</i> , 2015 ³⁵⁷

Physiological (Non-molecular?) Biomarkers

There are also many well-defined physiological signatures that can serve as non-molecular disease biomarkers. These signals can be used independently or in conjunction with molecular biomarkers to identify disease. Physiological biomarkers can be broadly categorized as those that rely on imaging technologies and those that rely on bodily system measurements such as blood pressure. For the purpose of this work, we will not consider physiological biomarkers that indicate non-disease states, such as broken bones.

Non-molecular or Non-invasive (?) Biomarkers

- Imaging techniques
 - o Define:
 - o Common usage/identification methods:
 - o Pros: can be used for a variety of different disease types
 - o Cons: requires trained user, may require expensive equipment but there are some examples of relatively inexpensive equipment
 - o Examples: MobiSante portable ultrasound (<http://www.mobisante.com/>)
- System measurements? (like blood pressure, breaths, or lung capacity?)
 - o Define:
 - o Common usage/identification methods:
 - o Pros:
 - o Cons:
 - o Examples:
- Others?
- Summary table here (Table 2)

Assessing Biomarker Effectiveness

There are a range of characteristics that determine effectiveness of a biomarker. Some characteristics are inherent to the disease (ex: concentration in a sample) and some depend on the measurement itself. The concentration of a biomarker in a sample can determine whether a biomarker will be useful. For example, chlamydia infections often present in urine, but concentration levels can range from $10^1 - 10^6$ copies of chlamydia gDNA per mL of urine¹⁰³. If a 100 μ L sample was collected, the amount chlamydia gDNA would be too low to detect in many samples, therefore gDNA would not serve as a good biomarker for this case. Biomarker concentration is also important to consider when diagnosing tumors using CTCs. In many cases, these cells are found in very low concentrations (look one up) so they would require larger volumes of sample for accurate diagnosis (ref). Sample volumes that match with expected biomarker concentrations need to be collected in order to properly evaluate a diagnostic test

360

Biomarker concentration is also closely linked to disease progression. Ideally, effective biomarkers would have a long half-life and concentrations that are proportional to disease severity³³¹. For example, viral RNA and an HIV specific protein – p24 antigen – can be used as HIV biomarkers. Immediately after infection during onset of disease (10-30 days), the concentrations of both HIV RNA and p24 antigen are relatively high and therefore easy to detect. After this initial state, HIV RNA remains abundant while the p24 antigen concentration is significantly decreased making it difficult to detect. Therefore, the p24 antigen would only be an effective biomarker during relatively early disease onset, whereas viral RNA is more stable over the course of the disease³⁶¹. Knowing the detection window can help identify useful biomarkers during different stages of disease progression.

A few additional considerations related to biomarker effectiveness are sample type that contains the biomarker (tissue v. fluid³³¹), stability of the biomarker, and presence of potential interferents or contaminants that may inhibit the biomarker detection assay. Stability may be important because some settings require transportation of samples prior to testing. For example, laboratory-based diagnostic systems often collect and store blood samples in a remote setting and then transport those samples back to a centralized lab. For these systems, effective biomarkers must store and travel well.

A vital characteristic for any biomarker is its specificity in determining disease state. For example, C-reactive protein does not serve as a very specific biomarker because it is often part of the general acute reaction phase when a patient has a fever³⁵⁴. Its ubiquitous presence related to multiple potential diseases makes C-reactive protein a poor individual biomarker. It may, however, still have utility as a part of a larger panel for disease detection.

Another important quality of an effective biomarker is robustness to variations in real-life use cases³⁶² such as differing patient demographics and slight variations in sample acquisition and sample handling prior to testing. For example, studies have shown that levels of malaria-specific IgG subclasses vary significantly among different genetic populations (Ref 16 from report 63). Ideally, an effective biomarker would also be able to identify asymptomatic and early disease states which would, in turn, decrease the timing between disease onset and treatment. For example, one study found that

over 80% of chlamydia infections in women are asymptomatic, and left untreated chlamydia can cause pelvic inflammatory disease and even infertility¹¹¹. Some conditions also have latent stages, such as tuberculosis, where a person is carrying the disease and not currently able to transmit (?), but may become sick in the future or serve as a vector. Biomarkers that could effectively diagnosis of asymptomatic or latent disease would help reduce adverse outcomes and disease transmission.

Table of important questions? → Table 3

Additional Factors to Consider when Selecting a Biomarker for a Diagnostic Assays (Test)

When evaluating diagnostic test performance, one of the first factors to consider is the intended end-user. Different users and settings require different test characteristics. Multiple reviews have been published that detail challenges related to biomarker identification and selection for specific settings and disease types^{358,363,364}. There are also reviews that discuss biomarker selection for NCDs such as cancer³⁶⁵, autoimmune diseases, and rheumatology³⁶⁶.

Ease-of-use for the end user includes ease of sample collection, the number of user steps, whether steps require non-automated timing, and how tests results are meant to be interpreted. Most infections can be diagnosed from multiple sample types and sampling conditions. For example, many sexually transmitted infections can be sampled from urine or swabs. For most users, urine sample collection is straight-forward while swab collection can be complex or potentially painful⁹⁹. Additionally, some NCDs require solid samples, such as a tissue biopsy, which would not be an appropriate sample for non-trained users to collect.

Other vital test performance characteristics relate to a test's including sensitivity, specificity, positive predictive value, and negative predictive value. An ideal assay would have 100% sensitivity and specificity, but in reality, trade-offs in performance exist in order to maximize test efficacy while minimizing cost³⁶⁴. For example, a diagnostic test may require high specificity if the available treatment is challenging to administer, costly, and considerably harsh on the patient, but the condition itself has low transmissibility. Cancer diagnostics would strive for a high specificity to avoid false positives and harsh chemotherapy treatment for patients. On the other hand, diagnosis of diseases that are highly infectious may prefer biomarkers with high sensitivity to avoid false negatives and prevent further disease spread. Ebola is a highly infectious disease, so a corresponding diagnostic test would want high sensitivity to ensure infected patients are treated and quarantined to avoid transmission.

Balancing test costs, accuracy, and usage are also related to disease prevalence among different affected populations. For example, research has shown that different populations develop lower titers of specific antibodies against the same infection³⁵⁸; this more systematic understand of disease presentation should be considered when selecting a biomarker. Additional criterial for evaluating a diagnostic test include test stability over time and at relevant ambient storage temperatures, test failure rate, test run time, ability to scale test manufacturing, supply chain for necessary assay reagents, and regulatory strategies for fully developed tests^{362,367} Thompson et al.

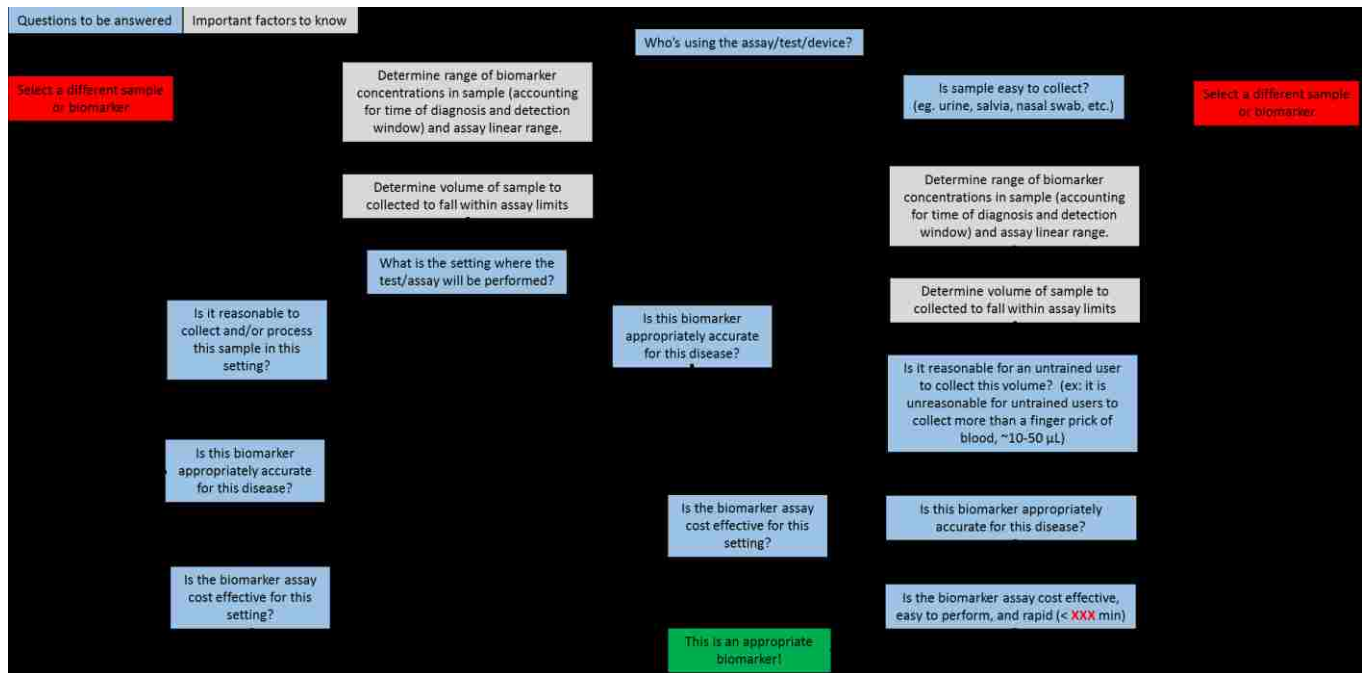


Figure 1. Guidelines for assessing biomarker effectiveness for diagnostics assays (tests?). Using these guidelines requires detailed knowledge about the entire setting surrounding this test including end-user, user setting, and clinical concentrations of selected biomarkers. (This is not the prettiest figure, but I think it's a good starting place.)

Use the flowchart for an example or two:

1. Infectious disease: HIV RNA v. p24 antigen or volume of urine for CT gDNA assay?

1.1 A p24-based HIV test from blood for low resource settings with a trained user in a health clinic (ref from literature)

- Who's using the test? → trained user in health clinic
- Range of biomarker concentrations (look this up, ref)
 - o Compare finger-stick and venipuncture samples
 - o Must be used during early infection (10-30 days post infection)
- What is the setting where the test/assay will be performed → low resource setting
- Is the biomarker appropriately accurate? → Yes, p24 is specific to HIV
- Is the biomarker assay cost effective for this setting? → yes, LFT
- Conclusion: It's a good biomarker!

1.2 A home-based dengue immunoassay from blood

- Who's using the test? → untrained user in the home
- Is the sample easy to collect? → finger stick of blood, yes
- Range of biomarker concentrations (look this up, ref)
 - o Very low concentrations if only using a finger stick (~10-50 μ L); would be better to collect venipuncture for 100s μ L to fall within clinical/detectable range
- Is it reasonable for an untrained user to collect this volume? → No
- Conclusion: Select a different biomarker or sample

2. NCD example: CTC, biopsy sample?

Bernhard Suggestion for Figure: Yes, this is a great idea. Also, a 2D graph with biomarkers listed on a chart sensitivity vs. specificity, with size or color possibly representing additional variables (one of cost, POC vs lab, invasiveness, etc.) (Figure 2)

Conclusions

- Includes discussion of “universal” biomarker?
 - o Nope! At least it doesn’t seem like it, but panels may work very well for multiple diseases
- Discussion of multiplexing diseases and current examples (most seem to be designed for HRS or with complex equipment, but still potentially useful)

Unfortunately, there are few, if any, ideal biomarkers for diagnostic testing because there are always trade-offs that must be made based on performance, cost, and usability³⁶⁰. It is also important to consider how a test will be used. For example, a different biomarker may be useful for a diagnosis v. monitoring a therapeutic treatment. The latter is referred to as a companion diagnostic which is often developed with a treatment regimen^{325,365}. Similar trade-offs must be made when a diagnostic is designed for individual v. community health surveillance. For individual diagnostics, slightly more effective and more expensive biomarkers may be appropriate, while in a community health setting, slightly less effective biomarkers that are significantly less expensive may be more acceptable. For example, the FDA-approved OraQuick Test for at-home HIV testing has lower sensitivity and specificity than many laboratory-based tests, but it’s inexpensive nature and potential to expand the number of people tested make it a useful public health intervention (FDA ref here).

Biomarkers for diagnostic tests can also be used to recommendation drug selection or dosage levels based on individual metabolism or susceptibilities³⁶⁸. Further, biomarkers may predict the course of a disease including recurrence and aggressiveness³⁶⁵. Test use-cases may require biomarkers with different characteristics including how levels change over time or the ratio between different markers. For many diseases, especially NCDs which often have complex, multi-faceted treatment programs, the choice of a “dynamic” biomarker, one that changes in response to successful intervention, with a distinct molecular signature may be desirable over tests with yes/no results³⁶⁰.

A few final considerations relate to the infrastructure supporting a selected biomarker. For example, different biomarkers require different levels of equipment and analysis methods which are not compatible with all use scenarios. Microarrays can be powerful tools for biomarker identification and disease diagnosis, but they often require expensive equipment and complex statistical analysis which may be inappropriate for settings outside of clinical laboratories³³³. Additionally, there are concerns with “time-to-impact” of new v. previously established biomarkers which require varying amounts of validation and verification³⁶⁰. While discovery of new biomarkers can result in greatly improved sensitivity and specificity, it can also be very costly and time consuming to navigate both the research and regulatory requirements.

5. Rapid, point-of-care screen test for gestational diabetes: assessing need through stakeholder surveys, with emphasis on Brazil and China (manuscript submitted to *The Journal of Maternal-Fetal and Neonatal Medicine*) → in collaboration with the PATH gestational diabetes team

Samantha A. Byrnes^{1*}, Greg Zwisler², Yonggang He³, Dunia Faulx², Bernhard H. Weigl^{2,4}

Purpose: Current practices and barriers for gestational diabetes mellitus (GDM) screening in lower-resource settings are not fully understood. Many practices suggest the need for an alternative test to replace or augment the oral glucose tolerance test (OGTT).

Materials and Methods: A series of qualitative interviews and free-form questionnaires were conducted with GDM stakeholders to identify current practices and barriers. Most participants were from Brazil or China.

Results: A total of 36 requests were made and 12 surveys were completed for a response rate of 33%. The primary barriers cited were cost, results not ready during a patient's visit, need for multiple samples, and need for fasting prior to testing. Respondents from Brazil and China advocated reducing use of the OGTT by 20–55%. Brazilian respondents also noted deviations from their current guidelines.

Conclusions: PATH and other groups are developing new low-cost, non-fasting, point-of-care GDM screening tests for use primarily in low-resource settings. These surveys identified specific assay characteristics vital for any new test. The results can guide development of technical performance goals for GDM tests to address current barriers and increase access to screening.

Keywords: GDM screening; diagnosis; point-of-care; stakeholder surveys; guidelines

Introduction

Gestational diabetes mellitus (GDM) is defined as the onset of hyperglycaemia during pregnancy. Without treatment, it can lead to life-threatening complications during pregnancy and birth³⁶⁹. Studies have linked GDM to significantly increased risks of type 2 diabetes for mother and child³⁷⁰. The International Diabetes Federation reported that more than 50% of mothers with GDM develop type 2 diabetes within 10 years after delivery. Studies also show the global rise in GDM prevalence is proportional to the rise in type 2 diabetes and obesity³⁷¹.

GDM is also extremely costly. In the United States from 2007-2012, costs associated with GDM increased from ~\$636 million to more than \$1 billion³⁷². As GDM prevalence grows, so will the economic burden, especially in low-resource settings (LRS) where prevalence ranges from 10% to 20%³⁷³. Prevalence rates depend on the availability of effective screening tests, especially in LRS.

Although multiple GDM tests are available, the most common is the oral glucose tolerance test (OGTT)³⁷⁴. The OGTT uses a 50-g, 75-g, or 100-g glucose drink followed by a blood draw every hour for up to three hours³⁷⁴. Other, less common, GDM tests include the oral glucose challenge³⁷⁵ and fasting glucose (FG) tests³⁷⁶. To decrease the cost of screening, some national guidelines combine the FG test with a risk factor assessment³⁷⁷.

There are three primary sets of GDM diagnosis guidelines. The 2006 World Health Organization³⁷⁸ and the International Association of Diabetes and Pregnancy Study Groups³⁷⁹ recommend universal screening with a 2-hour, 75-g OGTT. Some countries follow the 2014 American Diabetes Association guidelines which recommend a two-step procedure for diagnosis to reduce the number of high-cost OGTTs³⁸⁰. **Table S1** outlines the diagnostic criteria endorsed by these groups. Studies have compared

the efficacy and costs of various tests and found mixed results^{381–384}. The 75-g OGTT is often the most predictive, but can be costly when used for all pregnant women.

Recently, researchers have identified new GDM biomarkers. DiabetOmics has published data using a multi-analyte panel to diagnose GDM³⁸⁵. SmartSensor has developed an at-home electronic OGTT³⁸⁶. PATH is currently developing a lateral flow test that uses a finger stick of blood to screen for GDM. This test is inexpensive, rapid, and does not require a laboratory for analysis³⁸⁷.

To better understand usage scenarios and potential impact of any new GDM test, we surveyed GDM stakeholders. Jiwani *et al.* published a large-scale, survey-based study to assess GDM prevalence and practices across 47 countries³⁸⁸. The work presented here adds to existing data by probing deeper into the GDM guidelines and practices of two countries – Brazil and China – which represent potential early-adopter markets for new GDM screening tests. Further, results from these surveys will help guide technical performance goals for GDM tests to address current barriers and increase access to screening.

Materials and Methods

Stakeholder selection

Survey participants were selected through referrals from PATH staff and in-country experts or through international diabetes and GDM networks. Respondents were contacted *via* email and given the option of completing the survey through an in-depth, semi-structured, in-person interview (China only, conducted in Mandarin Chinese by Yonggang He), Skype, or using Microsoft Word, conducted in English. When respondents agreed to participate, they were informed that their response was part of a research project and that consent was implied by participation. Approval by an institutional review board (IRB) was waived after review by PATH's Research Determination Committee (RDC; Ref: PATH RDC–0699), see *Appendix A7* for the full report.

Survey design

Five qualitative, free-form-answer survey instruments were developed to gather information from stakeholders. Development of the survey questions drew on PATH's institutional expertise with diagnostics for LRS³⁶⁴. While a formal round of pretesting was not conducted, some minor adjustments were made after the first interviews. Survey focus was to identify key features and technical performance goals for new GDM tests and to learn about guidelines verses actual practices for GDM screening, diagnosis, and treatment in Brazil and China. Four surveys were designed for specific groups: diabetes experts, GDM researchers, maternal and child health (MCH) experts, and frontline healthcare workers (such as nurses) who are involved in GDM care and management. A fifth survey was designed for global GDM experts (see Appendices A2-A6 for surveys).

Data collection

Each survey contained questions from several research themes, including policy and guidelines surrounding GDM and antenatal care, current implementation of GDM screening/diagnosis, potential barriers to screening/diagnosis, and other available technologies. Participants were asked to rate each barrier as “high, medium, or low”.

MCH, GDM, and diabetes experts were also asked to recommend minimum performance thresholds for new tests. Questions focused on test performance metrics such as sensitivity and specificity, as well as test implementation in high- or low-resource settings.

Data analysis

Upon completion, responses were compiled into MS Excel for review and analysis. Barrier rankings were counted and recommended performance thresholds were tabulated and compared. Sample size was not pre-selected prior to the study, see Limitations for further discussion.

Results

A total of 36 survey requests were made and 12 completed surveys were received for a response rate of 33%. The majority of requests were unanswered; 4 respondents declined due to lack of time or interest, 5 declined and provided other recommendations, and 2 agreed to participate, but never returned surveys. Four respondents were from Brazil, five were from China, and three were global experts from the United Arab Emirates, India, and Pakistan. Table S2 shows a complete list of respondents, who gave their permission to be identified. Surveys were completed between May 2014 and March 2015. Using the information gathered from the surveys along with published literature, we compared in-country practices with GDM screening and treatment guidelines.

Policy, guidelines, and current implementation of GDM screening and diagnosis

Brazil

Brazilian GDM guidelines call for universal screening of pregnant women at 24 to 28 weeks of gestation using a combination of a FG test and risk-factor analysis. All respondents in Brazil stated that GDM is not currently identified as a high priority in their country, and that costs and lack of access to health services are major concerns in low-resource regions. After each test, samples are sent to a lab for analysis, and patients must return at a later date to receive results. According to survey responses, 90% to 100% of women return for their follow-up appointments.

Two participants from Brazil mentioned deviations from national guidelines. These deviations were from repeat testing for both the FG screening test and diagnosis with the OGTT due to unreliable patient fasting. Figure S1 summarizes Brazil's current guidelines and in-country practices.

China

Chinese GDM guidelines call for diagnosis using a 3-hour, 75-g OGTT for women in high-resource regions; these settings tend to be in larger cities. Low-resource regions are often more rural with limited access to larger hospitals. Women in low-resource regions undergo universal screening using a fasting plasma glucose test at 24 to 28 weeks of gestation. After each test, samples are sent to a lab for analysis, and patients must return at a later date to receive results. None of the respondents from China indicated how many women returned for their follow-up visits.

Chinese respondents stated that GDM should be a high priority in their country and mentioned cost and lack of access to health services in low-resource regions as major concerns. China's health care system is unique because diabetes-related care is organized separately from other routine antenatal care. Additionally, Chinese guidelines indicate separate GDM screening and diagnosis paradigms for high- and low-resource settings. Figure S2A summarizes China's current guidelines for low-resource regions and Figure S2B for high-resource regions.

Global

All three global experts agreed that GDM should be a high public health priority, and two of the three countries represented have nationally published guidelines^{389,390}. All three respondents indicated that de facto deviations in practice occur throughout their countries based on available resources and capabilities of health workers. These deviations occur most often in lower-resource regions. Respondents also noted that incomplete fasting prior to testing was rare. Two of three noted that loss to follow-up for receiving test results was an important concern with respect to GDM care.

Barriers to GDM screening and diagnosis

Twelve respondents answered questions about barriers to GDM screening and diagnosis, and 11 identified “results not ready during the patient’s visit” as a major barrier. Overall, there was mixed reaction about “glucose drink required” as an important barrier.

In Brazil, all participants identified both “laboratory required” and “venous blood required” as major obstacles. “Fasting required” and “multiple samples required” were also concerns, but of secondary importance. In China, all respondents noted that “multiple samples required” was a challenging barrier, but indicated that requirements for a laboratory, fasting, or use of venous blood were less important. Table 1 provides the full list of identified barriers and responses.

Table 1. Summary of GDM screening and diagnosis barriers based on survey responses, separated by location. The barriers highlighted in red were deemed the most important for each setting.

*One global interviewee did not respond to these questions.

Barrier	Glucose drink required	Fasting required	Laboratory required	Multiple samples required	Venous blood required	Results not read at patient’s visit
Brazil	High (1/4)	High (2/4)	High (4/4)	High (1/4)	High (4/4)	High (4/4)
	Med (3/4)	Med (2/4)	Med (0/4)	Med (2/4)	Med (0/4)	Med (0/4)
	Low (0/4)	Low (0/4)	Low (0/4)	Low (1/4)	Low (0/4)	Low (0/4)
China	High (2/6)	High (0/6)	High (1/6)	High (6/6)	High (1/6)	High (3/6)
	Med (3/6)	Med (2/6)	Med (1/6)	Med (0/6)	Med (4/6)	Med (3/6)
	Low (1/6)	Low (4/6)	Low (4/6)	Low (0/6)	Low (1/6)	Low (0/6)
Global*	High (1/2)	High (1/2)	High (0/2)	High (1/2)	High (0/2)	High (1/2)
	Med (0/2)	Med (1/2)	Med (0/2)	Med (1/2)	Med (1/2)	Med (0/2)
	Low (1/2)	Low (0/2)	Low (2/2)	Low (0/2)	Low (1/2)	Low (1/2)
Total	High (4/12)	High (3/12)	High (5/12)	High (8/12)	High (5/12)	High (8/12)
	Med (6/12)	Med (5/12)	Med (1/12)	Med (3/12)	Med (5/12)	Med (3/12)
	Low (2/12)	Low (4/12)	Low (6/12)	Low (1/12)	Low (2/12)	Low (1/12)

Implications for GDM screening test design

All respondents suggested that new GDM screening tests should have high sensitivity and specificity (>80%) and should reduce usage of the OGTT by at least 20%. Brazilian respondents noted identical needs for high- and low-resource regions, Chinese participants focused on potential new tests suitable for low-resource regions. Two global respondents indicated a need for differences in testing between high- and low-resource regions. These results are summarized in Table 2.

Table 2. Summary of minimum performance thresholds for GDM tests from survey respondents.

Metric	Sensitivity (%)	Specificity (%)	True to false positive ratio*	Reduction in required OGTT** (%)	Use in high v. low settings
Brazil	80-90%	70-90%	5:1 if treatment is nutritional counselling 4-10:1 if treatment is oral drugs	30-55% reduction	Identical needs for high v. low resource settings
China	70-90%	80-90%	Does not support nutritional counselling 8-10:1 if treatment is oral drugs	20-50% reduction	Only for low resource settings
Global	80%	80-90%	20:1 if treatment is oral drugs	50-80% reduction	Split –depends on country

Discussion

Our country-specific findings on GDM practices and barriers to screening revealed important common concerns as well as location-specific needs influenced by availability of resources. Brazil and China were selected for this study because they represent two distinct points along the GDM screening and diagnosis spectrum. Each country has well-defined guidelines and are potential early-adopter markets for new GDM tests.

Policy, guidelines, and current implementation of GDM screening and diagnosis

Brazil

GDM prevalence in Brazil increased from 5.5%–7.6% between 1998 and 2012³⁹¹. Because of increasing prevalence and costs associated with performing OGTTs, the government enacted a universal screening mechanism. This practice has helped reduce adverse GDM-related outcomes and associated medical costs³⁹².

Brazilian stakeholders identified multiple barriers associated with GDM screening including the inability to have results ready during a patient's initial visit and the need for a laboratory. Respondents also voiced concerns about problems with fasting that can lead to test repeats and increased costs and time burden for patients and care providers.

Many barriers could be overcome with the introduction and widespread use of a new point-of-care (POC) screening test. Figure 1A shows how a POC GDM screening test could be integrated into the current workflow in Brazil.

Compared to the current situation (see Figure S1A), the scenario shown in Figure 1A is more simple and direct. Patients would receive a screening decision at their initial visit. In many LRS, loss to follow-up is a major roadblock in medical care. A study in Canada reported at least 50% loss to follow-up for a type 2 diabetes intervention among women previously diagnosed with GDM³⁹³, and loss to follow-up will likely be worse in developing countries. A new rapid, POC screening test would eliminate the need to follow-up for results. Additionally, the proposed test is inexpensive and does not require fasting. In the Brazilian context, this could reduce or even eliminate current deviations from national guidelines with regard to retesting.

China

In China, GDM prevalence increased from 2.4%–6.8% between 1999 and 2008^{394,395}. With increasing prevalence and high health disparities, the Chinese government has developed different guidelines for high v. low-resource settings. Studies within the Chinese population have shown that this two-tiered approach reduced adverse pregnancy outcomes related to GDM and OGTTs usage by 50%³⁹⁶.

In China, the two main barriers to GDM screening were the inability to get results during a patient's visit and the need for multiple samples. Both of these barriers relate to potentially high costs and time commitments. Figure 1B shows how a new POC screening test could be integrated into the current workflow in China.

Compared to the current situation (see Figure S1B), the scenario shown in Figure 2B for low-resource regions in China is more simple and direct. Patients would receive a screening decision at their first visit. Also, a new rapid, POC screening test could greatly reduce the current costs associated with GDM screening and eliminate the need for laboratory-based analysis. In low-resource regions where costs can heavily influence decisions, less expensive alternatives help increase health care utilization³⁹⁷.

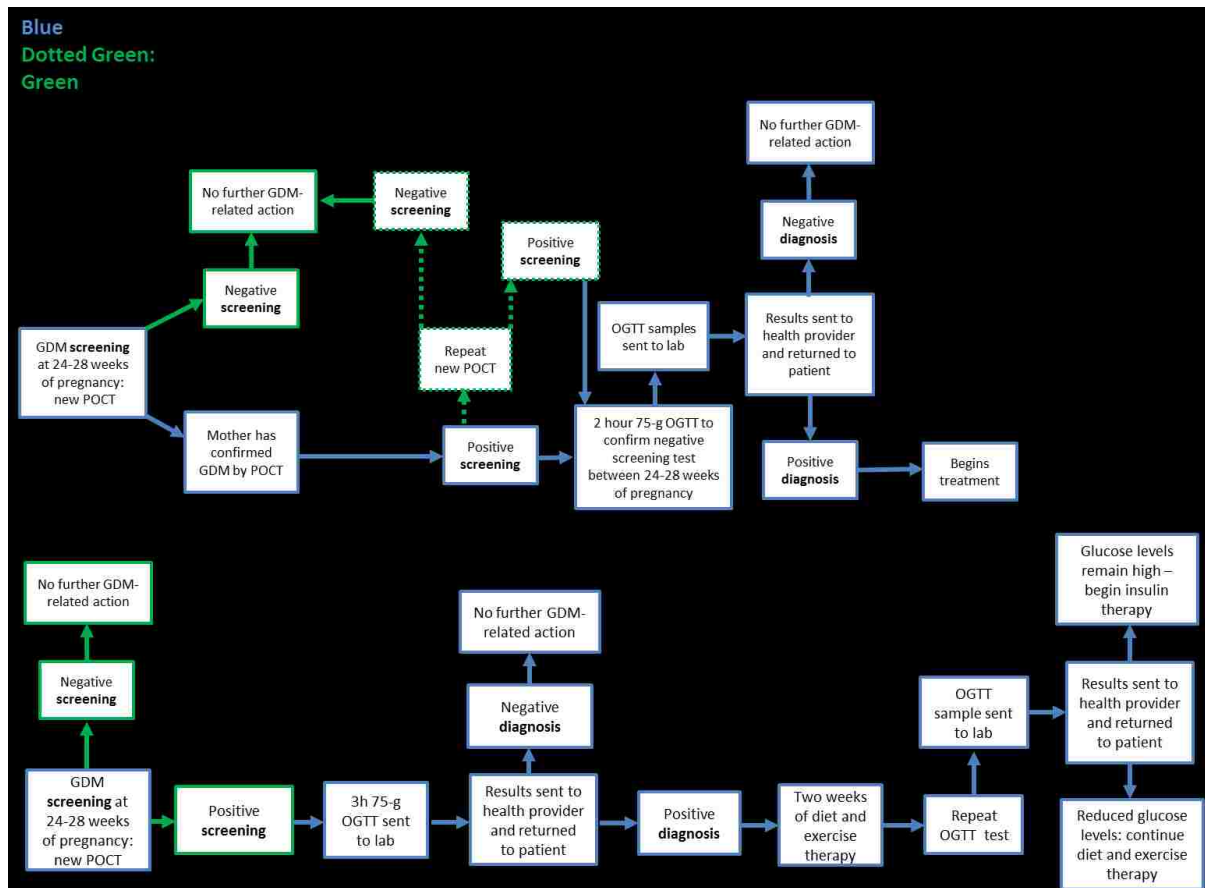


Figure 1. Potential workflow for GDM screening and diagnosis with a new POC screening test that provides results during a patient’s initial visit and does not require fasting or a laboratory for analysis. The solid blue boxes and connections represent current national guidelines, and the green boxes and connections are noted differences from the current in-country situation using a new POC test. POCT = point-of-care test; OGTT=oral glucose tolerance test. **A.** Brazil, and **B.** China.

Global

Our global respondents broaden the scope of this study by providing context for GDM screening outside of Brazil and China. Many countries do not have GDM screening guidelines³⁸⁸, but the availability of an accurate, inexpensive, and rapid test could help motivate their introduction. Countries without guidelines still perform GDM screening, but the processes vary greatly. One respondent noted: “Guidelines are followed on an ‘ad hoc’ basis irrespective of resources. Generally, the decision makers are the heads of departments of Obstetrics and Gynaecology of the hospital, and they are biased by their country of training and own understanding of the literature.” Another participant said: “Every rural setting in the world is different with a different set of problems. It is hard to generalize. One has to improvise as one goes along: it depends on local resources.” This insight shows that current limitations to policy are difficult to tackle, and any new technology needs to directly address resource limitations and implementation challenges.

Barriers to GDM screening and diagnosis

Overall, responses from Brazil noted more barriers than those from China. All respondents indicated that “results not ready during a patient’s visit” was the most prominent barrier. This finding may result from a desire to immediately begin treatment if GDM is diagnosed and to reduce loss to follow-up. When asked about different screening and diagnosis workflows in high- vs. low-resource regions, all respondents answered based on the current situation in their country. Respondents from Brazil

supported a universal GDM screening and diagnosis pathway, whereas those from China supported separate guidelines for different resource settings. The global respondents were split on the question. Both Brazilian and Chinese respondents advocated for a new test that would result in a reduction in OGTT usage of up to 50% to reduce costs. The global respondents recommended 50% to 80% reduction in OGTT usage.

Implications for GDM screening test design

One respondent noted that “The yardstick for comparison is the 50-g glucose challenge test; its sensitivity is 80%, and specificity is 80%”. Knowing the right comparisons and meaningful performance goals can set minimum clinical benchmarks for new tests.

The responses also illuminated the complexity behind these numbers. For example, many respondents mentioned different true-to-false positive ratios for different treatments (oral drugs vs. nutritional counselling). Chinese respondents did not advocate for nutritional counselling in low-resource regions due to a lack of trained nutritionists. In Brazil, by contrast, respondents advocated for nutritional changes, as well as exercise therapy, before prescribing oral medications to lower blood glucose. These data further indicate that GDM is not amenable to a one-size-fits-all solution and tools must be tailored a target population.

Survey results also guide technical performance goals for the development of new GDM tests to address barriers and improve accessibility. For example, tests being developed by both DiabetOmics and SmartSensor may not be suitable for these settings. In China, the SmartSensor test might be challenging to implement because it requires multiple user samples. In Brazil, the DiabetOmics test may not be the best option because a laboratory is needed to analyse the multi-analyte panel. By contrast, a test being developed by PATH offers a truly POC system for low-resource settings that addresses all of the barriers mentioned by the survey respondents.

Limitations

This study presents important information about actual practices and barriers to GDM screening and diagnosis in Brazil and China, but there are a few noted limitations. The first relates to the limited sample size. We conducted a series of 12 interviews, four from Brazil, five from China, and three from global experts. The response rate is equal or larger than other similar studies³⁸⁸, and our study also provides more in-depth and detailed knowledge than previous reports.

The responses from these surveys are not meant to represent the entire, complex system in either country, but instead provide insight into common themes surrounding practices and barriers. An additional limitation is the unknown accuracy of the quantitative measures such as required sensitivity and specificity of a POC GDM screening test. To confirm the usefulness of any test, validation with real samples must be performed.

Conclusions

PATH and other groups are in the advanced stages of developing new low-cost, non-fasting, POC GDM tests for use primarily in low-resource settings. Our stakeholder surveys identified specific assay characteristics vital for any new GDM test. In addition, the findings provide insight into the current state of screening and diagnosis in Brazil and China, which are potential early-adopter markets. Although there is variation in health care needs between different settings, a rapid GDM test that provides results during a patient’s initial visit is widely desired.

Acknowledgements

This work was supported by an internal grant from PATH's Health Innovations Portfolio (HIP). We thank PATH colleagues Becky Barney and Heather White, who are developing the POC GDM screening test. We also thank our survey respondents for their time and valuable insight.

Declaration of Interest

The authors report no conflicts of interest.

6. A rapid, instrument-free, sample-to-result nucleic acid amplification test (Lafleur *et al.* *LOC*, 2016)

Lisa K Lafleur,^{‡a} Joshua D Bishop,^{‡*a} Erin K Heiniger,^a Ryan P Gallagher,^a Maxwell D Wheeler,^a Peter Kauffman,^a Xiaohong H Zhang,^a Enos C Kline,^a Joshua R Buser,^a Sujatha Kumar,^a Samantha A Byrnes,^a Nicolaas MJ Vermeulen,^b Noah K Scarr,^b Yevgeniy Belousov,^b Walt Mahoney,^b Bhushan J Toley,^a Paula D Ladd,^a Barry R Lutz^a and Paul Yager^a

The prototype demonstrated here is the first fully integrated sample-to-result diagnostic platform for performing nucleic acid amplification tests that requires no permanent instrument or manual sample processing. The multiplexable autonomous disposable nucleic acid amplification test (MAD NAAT) is based on two-dimensional paper networks, which enable sensitive chemical detection normally reserved for laboratories to be carried out anywhere by untrained users. All reagents are stored dry in the disposable, and are rehydrated by stored buffer. The paper network is physically multiplexed to allow independent isothermal amplification of multiple targets; each amplification reaction is also chemically multiplexed with an internal amplification control. Total test time is less than one hour. The MAD NAAT prototype was used to characterize a set of human nasal swab specimens pre-screened for methicillin-resistant *Staphylococcus aureus* (MRSA) bacteria. With qPCR as the quantitative reference method, the lowest input copy number in the range where the MAD NAAT prototype consistently detected MRSA in these specimens was $\sim 5 \times 10^3$ genomic copies (~ 600 genomic copies per biplexed amplification reaction).

Introduction

The Yager laboratory and partners have engaged in multiple efforts to demonstrate that pathogen diagnosis can be moved out of centralized laboratories and into homes, primary care sites, and pharmacy clinics where the patients are actually located, both in the developed and the developing world. These efforts aim to reduce the cost of diagnostic tests and the time between sample collection and diagnosis, incentivizing healthcare systems to adopt a new technological platform. For large-scale adoption, however, clinical sensitivity and specificity standards must match those held by centralized laboratory evaluation. Nucleic acid amplification tests (NAATs) are the most sensitive approach to rapid pathogen detection, capable of finding just a few copies of a defined sequence of DNA or RNA in an appropriately treated biological sample. We report here on preliminary results of a collaboration aimed at making rapid NAAT diagnostics simple and accessible anywhere.

A low resource setting (LRS) can be considered any place where the tools commonly available in a sophisticated laboratory are not available to the end-user. However, diagnostic tests face similar challenges when used in health outposts in sub-Saharan Africa, clinics in rural Asia, or apartments in Seattle. Current instrumented systems are typically ill-suited to such settings because they can require laboratory training (e.g. for manual sample preparation and other steps), capital investment (e.g. up-

front equipment and on-going maintenance costs), and specific infrastructure (e.g. cold storage, sterile conditions, clean running water, and electricity).

Some integrated NAAT platforms have reached the market recently (or will soon be on the market) that are specifically designed for use in venues that may be closer to LRSs^{398–400}. These systems rely on instruments to make tests simple, and are therefore only appropriate for settings where the initial cost of instruments and continued upkeep are acceptable. NAAT kits that do not rely on instruments are commercially available, but are not fully integrated systems and therefore require many user steps⁴⁰¹. A practical diagnostic solution for the user who lacks training, infrastructure, or both does not currently exist.

The ideal diagnostic would improve the sensitivity, but mimic the simplicity, of the most successful LRS platform: the lateral flow (LF) test or “rapid diagnostic test”. The LF test eliminated the need for an instrument to carry out chemical detection, and the number of LF tests for detection of pathogens has grown continuously⁴⁰². However, most LF tests are a linear arrangement of 4-5 paper components, and the only fluids are typically the sample and a flow buffer⁴⁰³. A major weakness of this format is that they only automate a limited number of assay operations.

It has been repeatedly demonstrated that the ability of porous materials to move fluids by capillary flow is a powerful diagnostic tool, beginning with glucose detection in the 1950s⁵³. Since 2008, the Yager laboratory has been developing tools for designing, implementing, and characterizing automated microfluidic systems with porous materials. These two-dimensional paper networks (2DPNs) use geometry and porous material connectivity to automate complex fluidic operations, which minimizes the number of associated user operations^{46,48,49,96,261,262,277,404–406}. The goal is to allow an end user to introduce a sample (e.g., a nasal swab, urine, or blood) to a portable, autonomous diagnostic device. No instrument should be necessary, with the possible exception of a cell phone camera to capture an image of the result for quantification or off-site transmission to a third party.

Other research is aimed at developing non-instrumented, point-of-care, autonomous NAAT systems for LRS applications. Various paper-based microfluidic formats have integrated some NAAT operations, but still use separate instrumentation for remaining operations (e.g. sample processing, heating, or reading the result) and none are autonomous sample-to-result systems^{6,50,407–411}. Other point-of-care NAAT technologies have demonstrated useful features like digital NAAT⁴¹² and chemical heating⁶⁶, but without integrated sample preparation.

The multiplexable autonomous disposable nucleic acid amplification test (MAD NAAT) is a platform that builds on existing research and other early demonstrations of useful approaches to a non-instrumented, point-of-care, integrated NAAT system^{65,413,414}. The prototype reported here is the first demonstration of this platform. The disease target was methicillin-resistant *Staphylococcus aureus* (MRSA) and the molecular targets were two gene sequences. The first gene target, *ldh1*, is found in all *S. aureus* strains⁴¹⁵. To discriminate methicillin-susceptible from methicillin-resistant *Staph* species, we targeted a second gene, *mecA*, which confers methicillin resistance and is found in *S. aureus* and other bacteria. In less than 60 min, the prototype performed sample processing, bplexed isothermal nucleic acid amplification, and LF detection of these targets without external instrument or user intervention.

Experimental

Patient specimens

Patient specimens were discarded and de-identified (human subjects protocol not needed) nasal swab specimens from adult patients who underwent MRSA screening at the Harborview Medical Center (Seattle, WA). Swab collection was performed with BD Liquid Amies Elution Swab sampling kit (Becton, Dickinson & Company, Franklin Lakes, NJ). Per hospital policy, screening is performed on adult intensive care unit and elective surgery patients. To reduce the concentration of salt in the Amies buffer and other nasal specimen interferents, samples were diluted to 1:100 for prototype tests, manual assays, and qPCR.

Freshly prepared reagents

Achromopeptidase (ACP) lysis

ACP (A3547, Sigma-Aldrich, St. Louis, MO) was used at a final concentration of 0.5 U μL^{-1} in 10 mM Tris-HCl (pH 8.0). In manual assays and qPCR, patient specimens were diluted from Amies buffer 1:10 into 10 mM Tris-HCl (pH 8.0) then further diluted 1:10 into 10 mM Tris-HCl with ACP (a final dilution of 1:100). After two minutes of room-temperature incubation, lysates were heated to 95°C for five minutes to deactivate the ACP and fragment the DNA⁴¹⁶ (S.A.B. manuscript in preparation).

Isothermal strand displacement amplification (iSDA)

The iSDA master mix was prepared in a reaction buffer (pH 7.6) consisting of 42.5 mM potassium phosphate, dibasic (P8584, Sigma), 7.5 mM potassium phosphate, monobasic (8709, Sigma), 3.75 mM magnesium sulfate (New England Biolabs, Ipswich, MA), 250 μM of each dNTP (New England Biolabs), 0.2 U μL^{-1} Bst 2.0 WarmStart DNA Polymerase (NEB), 1.6% v/v nicking endonuclease Nt.BbvCI (mutant strain, New England Biolabs), and target-specific primers: 500 nM forward, 250 nM reverse, 50 nM each bumper (Integrated DNA Technologies, Coralville, IA)⁴¹⁷.

Internal amplification controls (IAC)

An IAC was chemically multiplexed with each gene target. IAC templates for all assays used the same interior-sequence-matching probes for IAC detection (same for both assays) flanked by primer binding sites that matched the target sequence. This approach enabled co-amplification of the IAC using the target primers, eliminating the need to add extra primer sets for the IAC⁴¹⁸. The IAC template used was a synthetic double-stranded DNA (Integrated DNA Technologies) to more closely mimic initiation from a double-stranded target. For each assay, the IAC template concentration was titrated to the lowest level that provided consistent IAC amplification in the absence of the target: 10^6 genomic copies for *ldh1* and 10^5 genomic copies for *mecA*. Sequences for iSDA primers, probes, and IAC templates for all assays are provided in Table 17.

Table 17: Isothermal strand displacement assay (iSDA) nucleic acid sequence designs for primers, probes, and internal amplification control templates.

	<i>ldh1</i>	<i>mecA</i>
Forward amplification primer (F)	5'-TAG AAT AGT CGC	5'-CCA TTA TAC TAC
(<u>CCTCAGC</u> = nicking site)	ATA CTT <u>CCTCAGC</u>	CTG TCT <u>CCTCAGC</u>
	ACA TCT CCT CGA	GGC AAA GAT ATT

	ACT TTT T-3'	CAA CTA AC-3'
Reverse amplification primer (R) (<u>CCTCAGC</u> = nicking site)	5'-GCA TAA TAC TAC CAG TCT <u>CCTCAGC</u> CAA GCT ACG CAT TTT CAT T-3'	5'-TAG AAT AGT CAC TTA CTT <u>CCTCAGC</u> GCC ATA ATC ATT TTT CAT GTT-3'
Forward bumper primer (FB)	5'-AGG TAA TGG TGC AGT AGG T-3'	5'-GAT AAT AGC AAT ACA ATC GCA CA-3'
Reverse bumper primer (RB)	5'-CCA GCT TTC ACA CGA AC-3'	5'-GTG CTA ATA ATT CAC CTG TTT GA-3'
Capture probe (<i>pDNA</i> [...] = pyranosyl DNA)	4'- <i>pDNA</i> [TTTTTTTTTC]- 2'-HEG-5'-CAG TGT CTA AAT CAA TGA TG-hexanol-3'	4'- <i>pDNA</i> [CAAGAATC]- 2'-HEG-5'-CTT TAG CAT CAA TAG TTA G- hexanol-3'
Biotin probe (A* = Super A®, ElitechGroup)	5'-CTA ATT CAT CAA CAA TGC-biotin TEG-3'	5'-GTT A*TA AAT A*CT CTT TTG A- biotin TEG-3'
Internal amplification control (IAC) (dsDNA template)	5'-AGG TAA TGG TGC AGT AGG TTC AAG CTA CGC ATT TTC ATT GAC CAG TTA CTT TAC GGA CCA CGT ACC GCA TTG GTA CAA GAT CTC AAA AAG TTC GAG GAG ATG TTG TTC GTG TGA AAG CTG G-3'	5'-GAT AAT AGC AAT ACA ATC GCA CAT GGC AAA GAT ATT CAA CTA ACG ACC AGT TAC TTT ACG GAC CAC GTA CCG CAT TGG TAC AAG ATC TCC AAC ATG AAA AAT GAT TAT GGC TTC AAA CAG GTG AAT TAT TAG CAC-3'

Lateral flow (LF) detection

Detection reagents were contained in all iSDA reactions in the following concentrations: 10 nM biotin probe, 20 nM DNA-pDNA (pyranosyl DNA) capture probe per target (*ldh1* or *mecA*), and 1.25 µL of 10 OD streptavidin-coated 40 nM gold nanoparticles (Innova Biosciences, Cambridge, UK). In manual assays, 8 µL of LF solution, comprising 1.875 M NaCl and 3.125% PEG 8000 (Hampton Research, Aliso Viejo, CA) in PBS, was added to 17 µL of iSDA amplicon product and mixed to yield final concentrations of 0.6 M NaCl and 1% PEG 8000. This solution was then allowed to flow up the LF strips.

Materials fabrication

Materials were fabricated on a CO₂ laser (VLS3.60, Universal Laser Systems, Scottsdale, AZ) or a 3D printer (Objet30 Scholar, Stratasys, Eden Prairie, MN), with exceptions noted below.

Porous materials

Standard 17 sheets (GE Healthcare Life Sciences, Pittsburgh, PA) were laser-cut into 'Y'-shaped sample delivery pads and 2.5-mm by 20-mm amplification and detection reagent pads. Standard 17 was also razor-cut into 2.5-mm by 10-mm amplification valve pads from stock that had been striped with a 1.5-mm thick beeswax (Knorr Beeswax Products, Del Mar, CA) stripe 3 mm from the upstream end. Wax striping was done on a custom motorized stage with wax heated to 74°C. Cellulose sheets (C083, EMD Millipore, Billerica, MA) were laser-cut into 2-mm by 2.5-mm salt pads and 5-mm by 12-mm waste pads. Cardboard-backed nitrocellulose sheets (FF80HP, GE Healthcare Life Sciences, Pittsburgh, PA) were striped with test lines (see below), laser-scored, then scissor-cut from the downstream end of the sheet into 2.5-mm x 23-mm LF strips.

Plastic materials

Several types of plastic were used in prototype fabrication. DuraWhitePlus (Stratasys) was 3D-printed to form the three housing pieces and the body of the lysis valve. Polymethyl methacrylate (PMMA; U.S. Plastic Corp, Lima, OH) was laser-cut to form the 0.06-in thick stages for heaters, "trays" to contain the 2DPN, elements for the lysis valve, and swab ports; and 0.098-in thick port blocks. Channels were created in the 2DPN trays by selectively ablating material with the laser. Prior to assembly, the PMMA pieces were power-washed with water (WaterJet, Stratasys) then dried in an incubator at 40°C for >1 hour. Mylar-backed, silicone adhesive tape (ARclad 7876, Valley Industrial Products, Huntington, NY) was laser-cut into pieces for lining the channels of, and adhering the port blocks to, the 2DPN trays. All silicone tape pieces were dried overnight in an incubator at 40°C before use. Polypropylene, 1-mL, Luer-Slip syringes (Henke-Sass Wolfe, Tuttlingen, Germany) were razor-cut to make the fluid introduction storage chamber and the sample chamber. Tygon E-3603 (1/32-in OD, Saint-Gobain, Paris, France) and platinum-cured silicone rubber (5/32-in OD, Saint-Gobain, Paris, France) tubing were razor-cut to 11 cm for fluid introduction and to 1.5 cm for the lysis valve, respectively.

Other materials

Wax blocks for lysis valves were fabricated from a mix of PureTemp 53 PCM (PT53, Entropy Solutions, Plymouth, MN) and 20% graphene nanoplatelet powder (N008-100-P-10, Angstrom Materials, Dayton, OH) cast in silicone rubber molds, cured under a hot air gun, then allowed to cool to room temperature. Insulating foam inserts were razor-cut from discarded polystyrene packaging to fill the negative space in the prototype housing when all components were assembled.

Dry reagent preparations

ACP dry reagent tubing

In prototypes, lysis reagents were stored dry in the fluid introduction tubing. A total of 80 U of ACP at a stock concentration of 20 U μL⁻¹ in 10 mM Tris-HCl (pH 8.0) was mixed with 1 M trehalose (TS1M-100, Life Sciences Advanced Technologies) to a final concentration of 5% trehalose. The mixture was pipetted

into the upstream end of the tubing allowed to dry for >16 hours in a desiccating environment. During prototype tests, the dried ACP was rehydrated with 160 μL of 10 mM Tris-HCl (pH 8.0) to a final ACP concentration of 0.5 U μL^{-1} .

Combined amplification and detection dry reagent pads

In prototypes and manual assays, the amplification “master mix” and detection reagents for each target and IAC were stored together dry in amplification pads. The iSDA master mix and LF detection reagents were combined with 10% (w/v) trehalose (Life Sciences Advanced Technologies, St. Petersburg, FL) and 1% (w/v) PEG 8K (Hampton Research), which were added for stabilization during dry storage. The amplification pads were pre-blocked by soaking in 1% BSA and 0.1% Tween-20 for 1 hour, blotted dry, and dried in an incubator at 45°C overnight. The reagent mix (20 μL) was added to amplification and detection reagent pads. The pads were flash frozen in liquid nitrogen and dried for 2 h using a lyophilizer (FreeZone 4.5, Labconco, Kansas City, MO).

Internal amplification control dry reagent pads

In prototypes, IAC templates were stored dry in the sample delivery pads. The IAC templates for each target were combined with 10 mM Tris-HCl with and 5% (w/v) trehalose and 10 μL was dried in pads for >16 hours in a desiccating environment.

NaCl pads

In prototypes, salt for detection was stored dry in salt pads. A volume of 10 μL of 2.5 M NaCl was added to each salt pad, which were then flash-frozen in liquid nitrogen, and dried for 2h using a lyophilizer.

LF strips

In prototypes and manual assays, detection was performed on LF strips. The LF strips were striped (XYZ3050, BioDot, Irvine, CA) in ambient conditions (20-23°C, 40-60% RH is typical). The test lines were pDNA-T20 oligos striped at 400 μM in 50 mM TEAB at 0.3 $\mu\text{L}/\text{cm}$. The process control lines were T20-biotin oligos striped at 200 μM in 50 mM TEAB at 0.3 $\mu\text{L}/\text{cm}$. Striped LF strips were exposed to UV (~310 nm; TM-36 transilluminator, UVP, Upland, CA) for 7-8 min to cross-link the T20 to the LF strips.

MAD NAAT prototype assembly

Fluid introduction sub-assembly The fluid introduction sub-assembly was constructed from a syringe, with the barrel razor-cut to the 0.45-mL mark and the plunger razor-cut to be 2 mm longer; a female Luer-Slip to 1/32-in barb connector (Qosina, Ronkonkoma, NY); and Tygon tubing. The syringe was filled by pipette with 260 μL of 10 mM Tris-HCl (pH 8.0), with 100 μL dead volume. The syringe was then inserted into a connector with tubing attached.

Sample chamber sub-assembly

A sample chamber was fabricated from a syringe, which was razor-cut at both the 0.25 mL mark and halfway through the Luer-Slip fitting, then drilled with a 3/32-in hole at the 0.23-mL mark to accommodate the fluid introduction tubing. The sample chamber was mated to a silicone rubber tubing

section using the modified Luer-Slip fitting. The tubing section was drawn through the lysis valve body and the valve was set with a graphene-wax block.

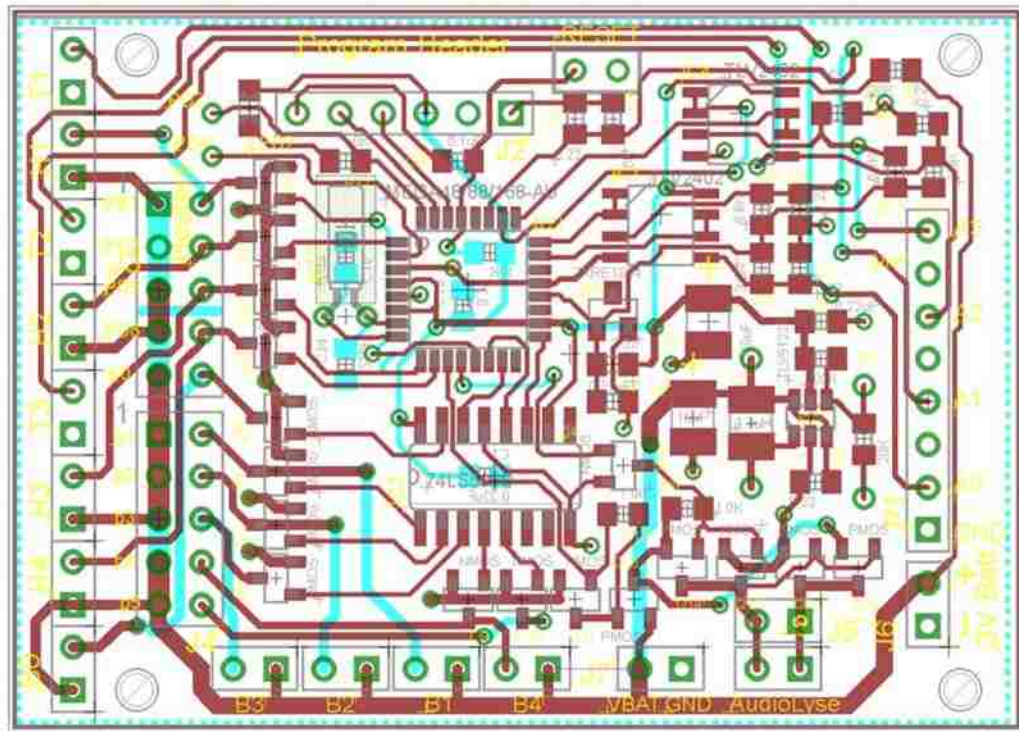
2DPN sub-assembly

The bottom of the 2DPN channels in the tray were lined with the aforementioned silicone adhesive inlays, onto which the porous material components were laid in order: amplification and detection dry reagent pads for each target, dry IAC sample delivery pad, dry salt pads, LF strips, amplification valve pads, and waste pads. After placement of these components, silicone adhesive overlay was used to seal the materials inside the tray. The wax valve was then pressed to make a full seal; pin-prick vent holes were created just upstream of the wax valve. A port block was bonded to the tray with silicone adhesive.

Housing and electronics sub-assembly

The housing of the device comprised three components: base, lid, and slide. A custom PCB control board was mounted to the housing base. The control board (Figure 95) contained an integrated microcontroller (ATmega328, Atmel, San Jose, CA) and wiring adapters for the lysis heater, lysis valve heater, amplification heater, and amplification valve heaters. The lysis heater was constructed from 9/32-in x 0.014-in aluminum tube stock (#8107, K & S Precision Metals, Chicago, IL) cut to a 12-mm length, wrapped in aluminum tape, instrumented with three thick film resistors (PWC2512-10RJI, Mouser Electronics, Mansfield, TX) and a thermistor (NB21N50104JBB, Mouser Electronics), and wrapped again in electrical tape. The lysis valve heater was made from a thick film resistor (PWC2512-10RJI, Mouser Electronics) wrapped in Kapton tape (DuPont, Wilmington, DE) and was glued into the body of the lysis valve under the wax block zone.

a



b

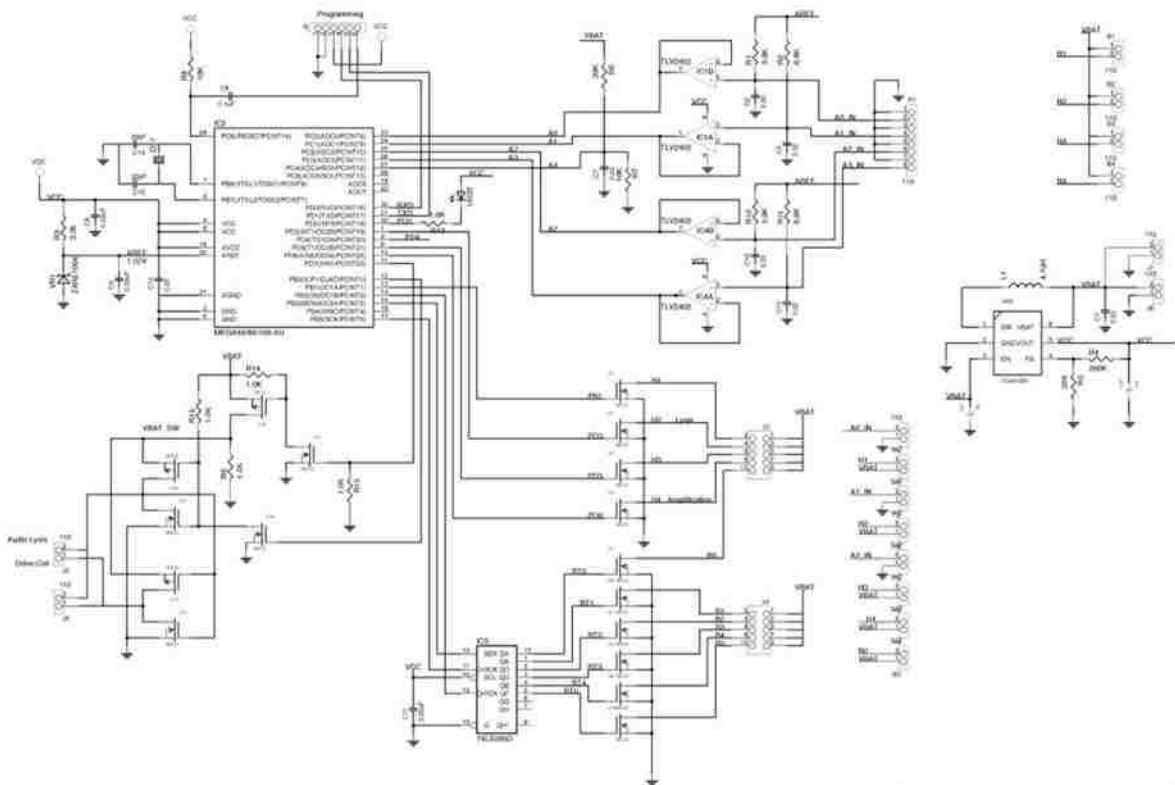
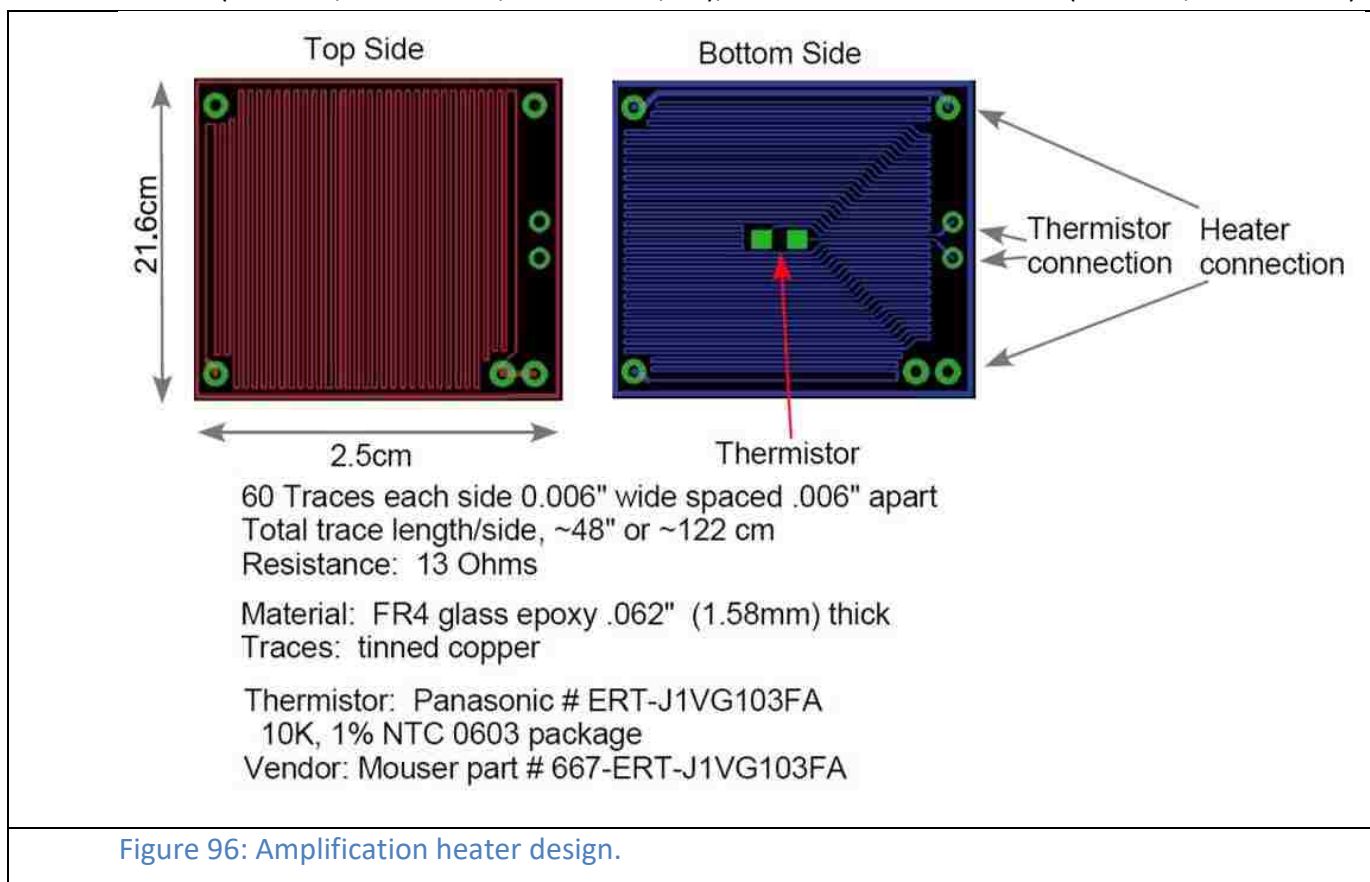


Figure 95: Control board design. (a) Layout for custom PCB. (b) Electronics schematic.

The amplification heater and amplification valve heaters were constructed from a custom PCB (Figure 96) and two more thick film resistors, respectively, aligned in the heater stage, all of which was wrapped in Kapton tape and mounted in the housing base. Two AA battery holders (BCAAPC-ND, Digikey, Thief River Falls, MN) were mounted in the housing base and connected in series to the control board, a contact switch (275-008, RadioShack, Fort Worth, TX), and a master slide switch (275-006, RadioShack).



Prototype device assembly

The fluid introduction sub-assembly and a swab port were clipped into the housing lid. The sample chamber was fitted with a lysis heater and the lysis sub-assembly was mated to the 2DPN sub-assembly by press-fitting the silicone rubber tubing below the lysis valve into the port block above the 2DPN. These two mated sub-assemblies were then snapped as one into the reusable device sub-assembly. A polystyrene foam insulating insert was placed above the 2DPN and around the lysis heater before snapping the housing lid to the housing base. The housing slide was then mounted to the prototype to complete assembly.

Patient specimen tests

MAD NAAT prototype tests

For this version of our device, the volume of the sample chamber was fixed before the dilution factor from Amies buffer was determined. Therefore, patient specimens were diluted twice to achieve the target dilution of 1:100. First, a specimen was diluted from Amies buffer 1:8.6 by 10 mM Tris-HCl (pH 8.0). A polyurethane foam swab (Foamtec International, 19304613, Oceanside, CA) was immersed in the diluted specimen, rotated three times, and removed. The prototype was slid open to expose the swab

port, with ~160 μL of 10 mM Tris-HCl (pH 8.0) forced into the sample chamber. The swab was inserted into the prototype, rotated ten times, and removed. These swabs transferred ~15 μL of sample when used as described²³⁰, resulting in a sample input to the prototype with a total dilution of ~1:100. The prototype was closed to activate the test. Prototypes were run to completion (1 h), then disassembled and the 2DPN removed for imaging by scanner, which was used only as an assay development tool. An end-user would simply read the results at test completion, without disassembly.

Manual assays

ACP lysate was mixed with both IAC templates and allowed to flow into combined amplification and detection dry reagent pads placed in hybridization chambers (Electron Microscopy Sciences, Hatfield, PA). The chambers were sealed and incubated at ~50°C for 20 min. Following incubation, the reaction products were centrifuged at 2000 $\times g$ for 1 min in a centrifugal filter tube (0.22 μm Nylon centrifugal filters, VWR, Radnor, PA) and the resultant fluid was assessed via LF detection.

qPCR

Quantitative PCR (qPCR) for the *ldh1* and *mecA* genes was used as the reference method for estimating copy number from patient specimen samples. ACP lysate (1 μL) was quantified using the MRSA/SA ELITE MGB duplexed *ldh1* and *mecA* qPCR assay. The input copy number estimate was calculated using the MAD NAAT prototype input volume (175 μL).

Image capture

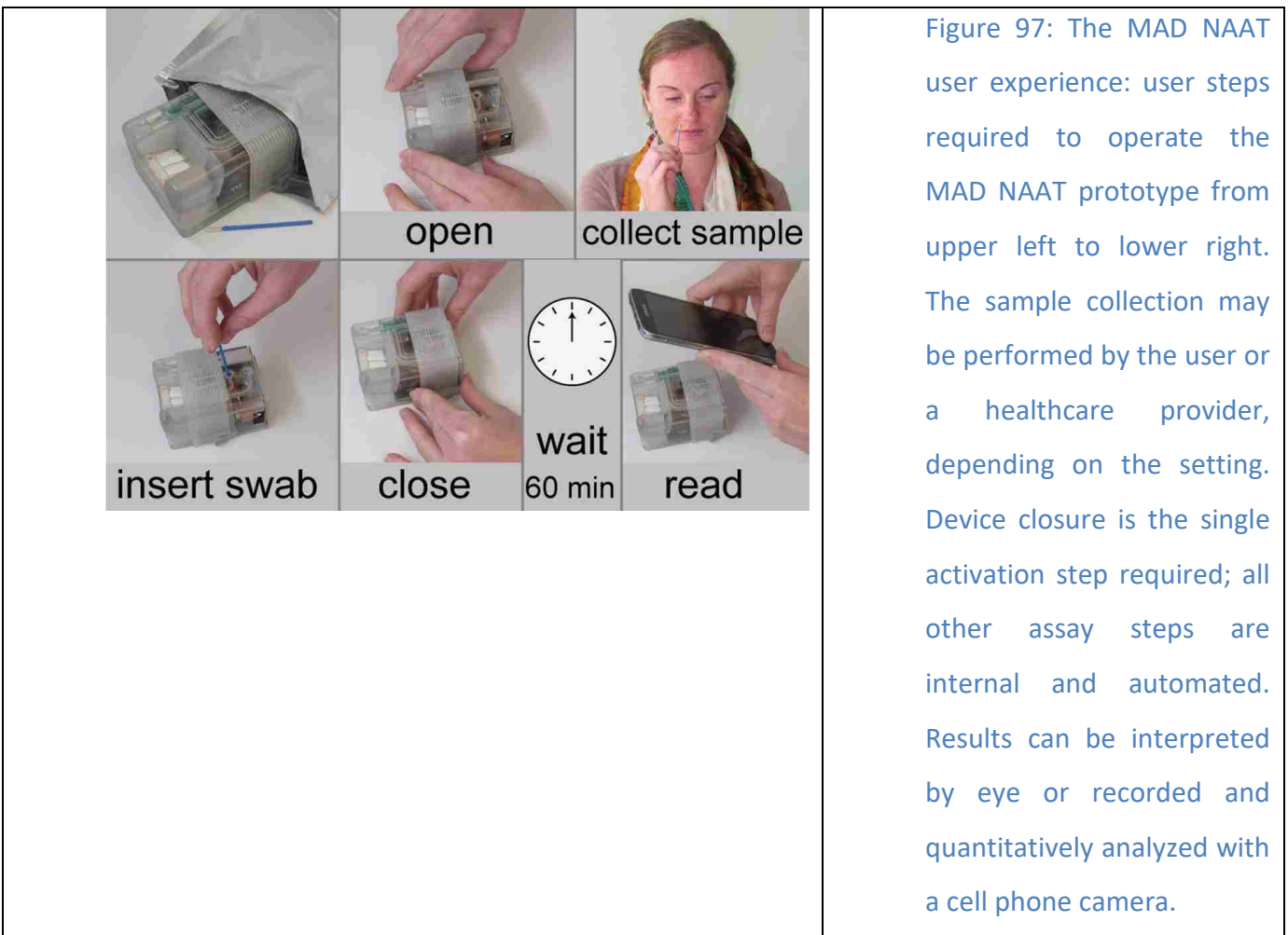
All image capture was performed using a flatbed scanner (ScanMaker i900, MicroTek International, Cerritos, CA) in 48-bit-depth RGB mode at 600 dpi. Intensity profiles were generated for LF strips in both channels in each test using ImageJ 1.50g (NIH, Bethesda, MD). The green channel of each image was isolated, inverted, cropped to the detection zone, and straightened to the edges of the LF strips. Regions 50-pixels wide and 300-pixels long were overlaid at the longitudinal upstream end and lateral center of each LF strip in these transformed images, where the width dimension was chosen to eliminate edge effects and imperfect alignment and the length dimension was chosen to capture all four test lines and surrounding background. The average intensities across the width of each region were analyzed algorithmically using Mathematica 10.4 (Wolfram, Champaign, IL). Test lines were identified as local maxima in each intensity profile that survived a Gaussian blurring up to scale 6, had minimum sharpness 6, and had an intensity greater than 28% of the maximum. The background of each intensity profile was then estimated with a sixth-order polynomial fit to five background regions, the locations of which were fixed across all intensity profiles, and subtracted away. Background-subtracted intensity profiles were integrated within fixed-size regions, centered on the local maxima, with values indicating the estimated relative intensity of the associated test line. The presence or absence of identified test lines within four signal regions, the location of which were fixed across all intensity profiles, indicated the results and the validity of each test. Occasional poor flow, depressions in the nitrocellulose that were introduced during their manufacture, and debris confounded this algorithm in eight cases. Occasional poor flow also contributed to a poor polynomial fit to the background, which resulted in some negative estimated intensity values.

Results

Our goal was to develop a rapid and accurate integrated diagnostic technology with a user experience that was as simple as a pregnancy test; the MAD NAAT prototype required only a single activation step. Results were reported as visible test and control lines that could be read by eye, or imaged with a cell phone camera for local processing or transmission to a remote location. The following results describe prototype development and subsequent repeated testing of four identical prototypes with samples from human nasal swab specimens.

Extremely simple user experience

The complete user experience for the MAD NAAT prototype comprised sample collection and introduction, test activation, and reading the result. Activation of the MAD NAAT prototype was a single, simple user step: sliding the housing closed (Figure 97). All other assay operations were automated.



Assay operations

NAATs contain three fundamental assay operations: 1) sample processing, 2) amplification, and 3) detection, all of which were automated in the MAD NAAT prototype (Figure 98). Reagents for these operations were stored dry and ready to use inside the device.

This first MAD NAAT prototype demonstration was performed on samples from human nasal swab specimens. A sample was collected with a swab and introduced to an open device by inserting the swab into a sample chamber containing buffer. Sample introduction was over 80% efficient (percentage of bacteria transferred from swab to sample chamber) for the swabs used, as measured using prepared samples in buffer and in simulated nasal matrix²³⁰. Sample processing was performed by incubating with an achromopeptidase (ACP) enzyme mixture for bacterial lysis, followed by heating for deactivation of enzymes incompatible with amplification (e.g. proteinases) and for bacterial gDNA fragmentation. ACP lysis followed by heating was previously found as effective as bead beating for release of amplifiable DNA from *S. aureus*²¹¹ and other bacteria¹²³. In addition, there was no statistical difference between the lysis performance of freshly prepared and dried ACP after 11 months of storage at ~23°C and ambient humidity (106 ± 1.6% recovery of amplifiable DNA compared to freshly prepared, p = 0.26¹²³).

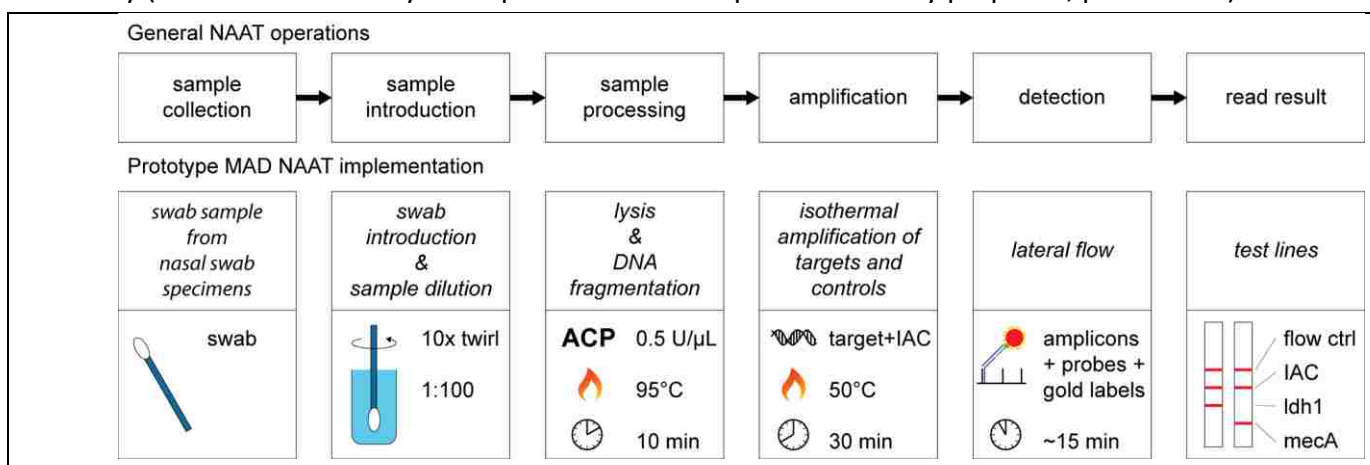


Figure 98: General NAAT operations and the implementation of each in the MAD NAAT. Swabs were used as the sample input for this prototype, which was tested with samples of human nasal swab specimens. The timing (and temperature where required) of each operation was chosen to maximize unit operation efficiency. Sample processing time (10 min) included heater warm-up and >5 min at 95°C for enzyme deactivation and DNA fragmentation. Amplification time (30 min) also included heater warm-up. Detection time was as fast as five minutes, but test line images were always captured after a total test time of 60 minutes.

We chose to develop MAD NAAT around isothermal strand displacement amplification (iSDA), a truly-isothermal method (no initial denaturation step) and one of the fastest isothermal amplification methods available (~10¹⁰⁻¹² fold from 10 target copies in ~10-30 minutes). In iSDA, amplification initiates by primer insertion during DNA “breathing,” then proceeds to exponential amplification by repeated nicking, extension, and displacement of single strands⁴¹⁷. The rules governing design and optimization of new iSDA assays is similar to that for strand displacement amplification (SDA), which is well-described in the literature⁴¹⁹. The sequences for the *Idh1* and *mecA* primers and probes are provided in Table 17. We have found that combining iSDA with LF detection under ideal conditions can lead to sensitivity of <10 copies of target (Figure 99) and specificity against similar organisms (Figure 100).

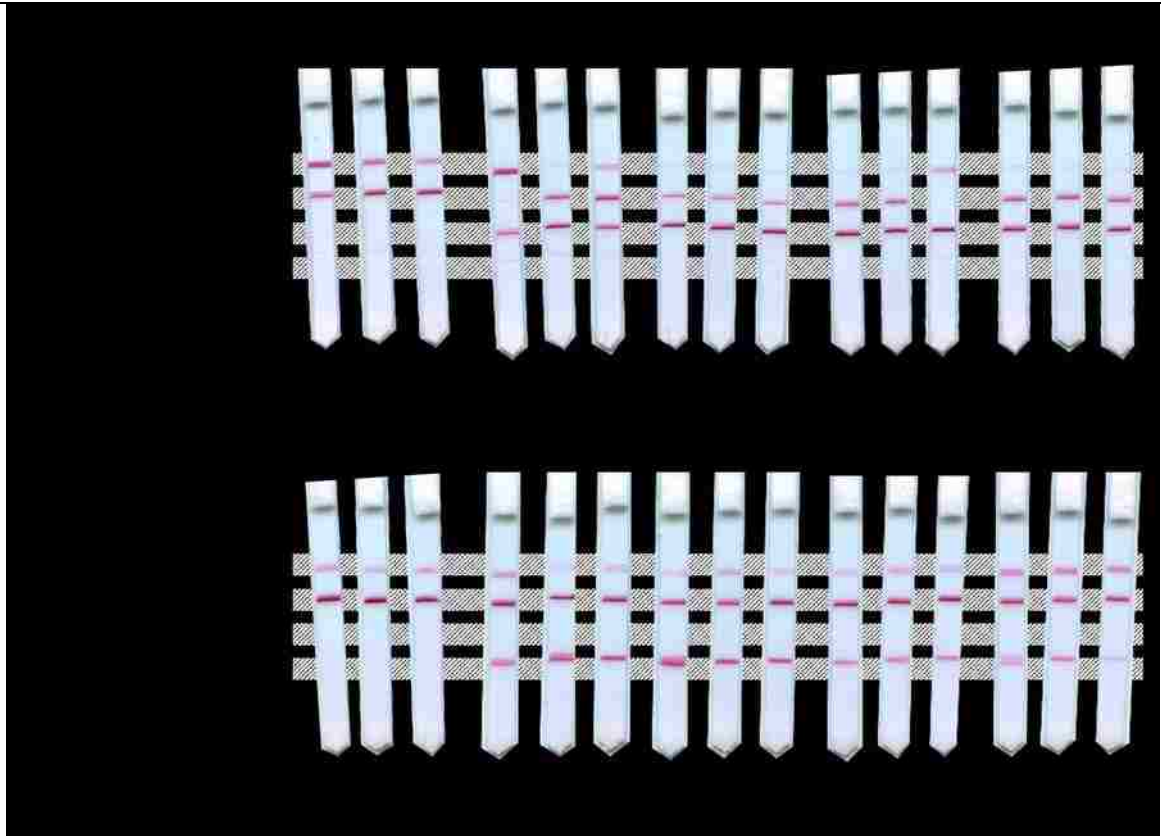


Figure 99: Manual iSDA and LF detection result for (a) *Idh1* and (b) *mecA* assays at low copy numbers of MRSA genomic DNA (gDNA) template. Amplifications were performed in tubes. The results were mixed to salt and Tween-20 to final concentrations of 600 mM and 1% w/v, respectively, then allowed to flow on LF strips. The assay showed robust detection down to at least five copies.

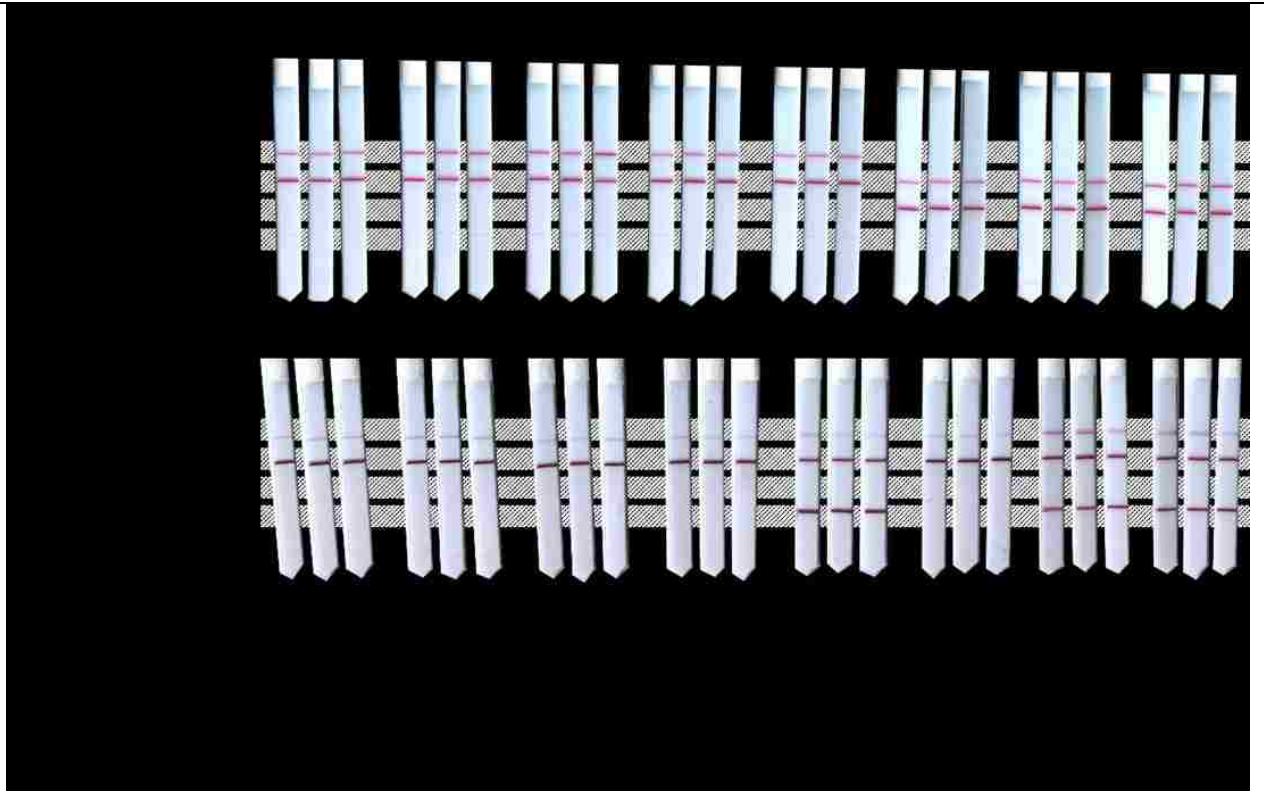


Figure 100: Manual iSDA and LF detection result for (a) *ldh1* and (b) *mecA* assays using no template (NTC); and 104 copies of human, *S. pyogenes*, methicillin-sensitive *S. epidermidis* (MSSE), methicillin-resistant *S. epidermidis* (MRSE), methicillin-sensitive *S. aureus* (MSSA), and methicillin-resistant *S. aureus* (MRSA) gDNA templates (left-to-right). Amplifications were performed in tubes. The results were mixed with salt and Tween-20 in PBS to final concentrations of 600 mM and 1% w/v, respectively, then allowed to flow on LF strips. The strips shown are the last each of a set of two *ldh1* and six *mecA* experiments. The previous experiments showed low-level signal on all nominally negative test lines, including in the NTC condition, and occasional IAC drop-outs in negative tests, which indicated invalid results. These errors were eliminated through use of new stocks of gold nanoparticles and IAC template, respectively. Across the 120 nominally negative conditions tested in the entire set of eight experiments, one NTC and one *S. pyogenes* template yielded a strong false positive, which may be indicative of contamination from five years of running these amplification assays in a single laboratory and open handling of amplicons for lateral flow detection and gel analysis.

LF detection used two probes as shown in Toley et al.⁴¹⁷: one DNA probe with a triethyleneglycol linker and terminal biotin group to allow labeling by streptavidin-conjugated gold nanoparticles, and one chimeric DNA-pDNA probe to allow binding to complementary pDNA immobilized on the detection strip. The lyophilized, combined reagents for amplification and detection were shown to be stable for at least

six weeks at $\sim 23^{\circ}\text{C}$, and at least 15 days at 40°C , at 2-3% relative humidity (Figure 101).³⁷ We have since demonstrated stability for longer times at elevated temperatures with similar stabilizers (S.K. manuscript in preparation). However, hybridization between complementary pDNAs required additional salt relative to iSDA to maintain test sensitivity over a range of ambient temperatures (Figure 102).



Figure 101: Detection results excerpted from dry storage study. (a) Prototype iSDA and LF detection on MRSA genomic DNA input using pads stored for six weeks at laboratory ambient temperature in desiccated conditions. Duplicate tests confirm dry reagent viability in these conditions through *Idh1* amplification and detection functionality. (b) Manual assay tests on low input copy number MRSA genomic DNA using pads stored for 15 days at 40°C in desiccated conditions. Triplicate tests confirm dry reagent viability in these conditions through *Idh1* amplification and detection functionality. Associated negative control indicates no contamination.

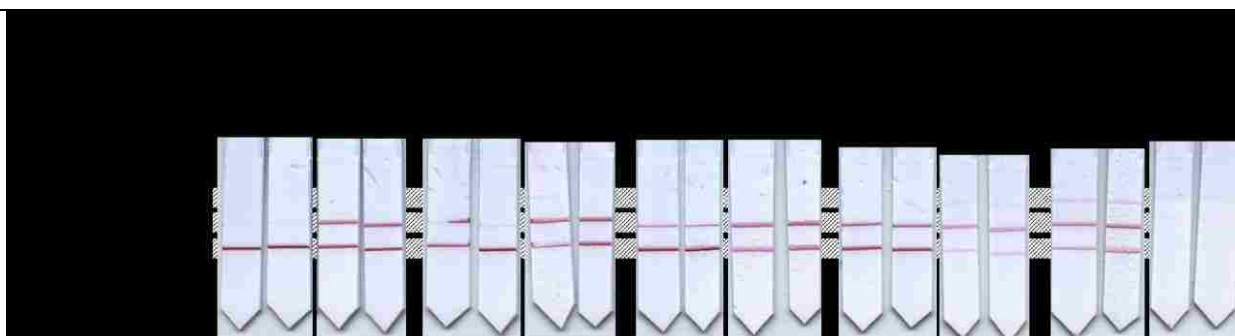


Figure 102: Detection results showing impact of salt condition on pDNA binding at $\sim 20^{\circ}\text{C}$. A synthetic truncated amplicon (STamp), which replicated the binding region of the amplicon output by the *Idh1* iSDA reaction, was mixed with detection reagents with and without 600 mM

NaCl, and allowed to flow on LF strips. Limit of detection was worse in the no-salt condition.

Internal fluid path

System operations were automated by creating a fluid path that managed sample introduction, sample processing, dry reagent reconstitution, multiplexing by routing to multiple isothermal amplification zones, amplification itself, and LF detection (Figure 104). Sample introduction and processing occurred in a sample chamber, which output lysate to a 2DPN after a valve operation. The 2DPN split the lysate and sequentially reconstituted internal amplification control (IAC) templates and dry master mixes (including primers, probes, and detection labels) into the lysate during flow into physically biplexed amplification zones. While chemical multiplexing (amplifying multiple targets in a single reaction) increases the complexity of assay development and typically decreases sensitivity of each target, physical multiplexing avoids these problems and allows for the amplification of both DNA and RNA targets on a single device (ESI† Fig. S7). After amplification, a second valve operation released both amplified lysate solutions, and the 2DPN reconstituted salt into them during flow into the detection zones.

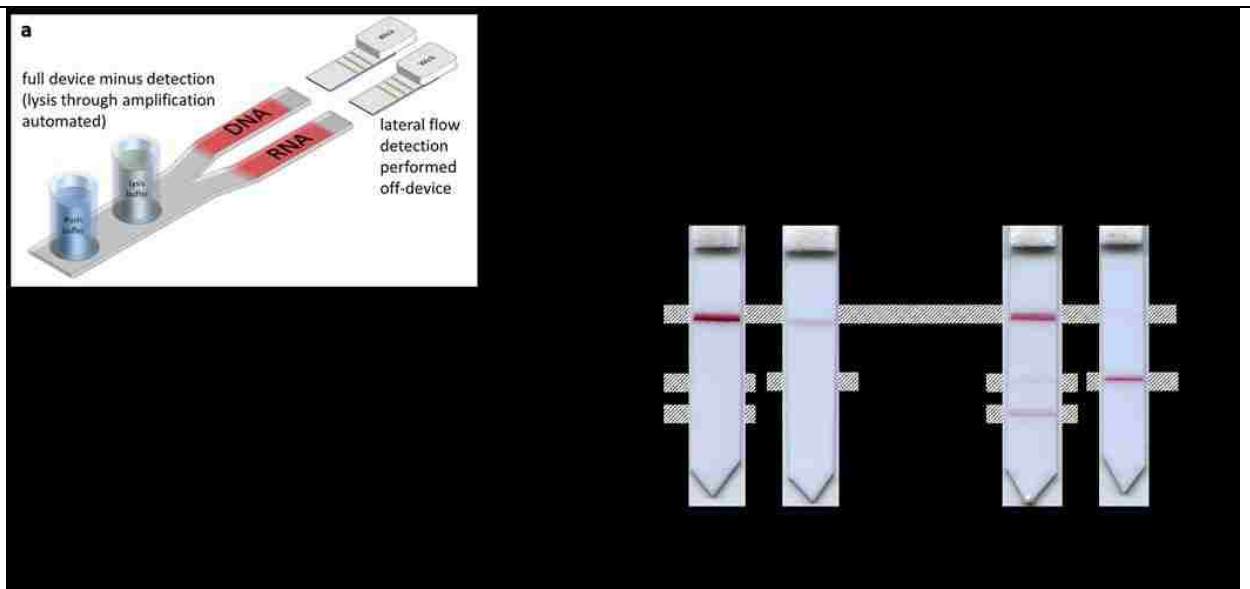


Figure 103: DNA and RNA detection in partial prototype test. (a) Cartoon of experimental setup. Sample introduction and processing, and amplification were performed on a prototype device. Amplification pads were then removed from the 2DPN and centrifuged at $10,000 \times g$ for 3 minutes. The resulting fluid was mixed to salt and Tween-20 to final concentrations of 600 mM and 1% w/v, respectively, then allowed to flow on LF strips. (b) Results show clean negatives, and positive amplification.

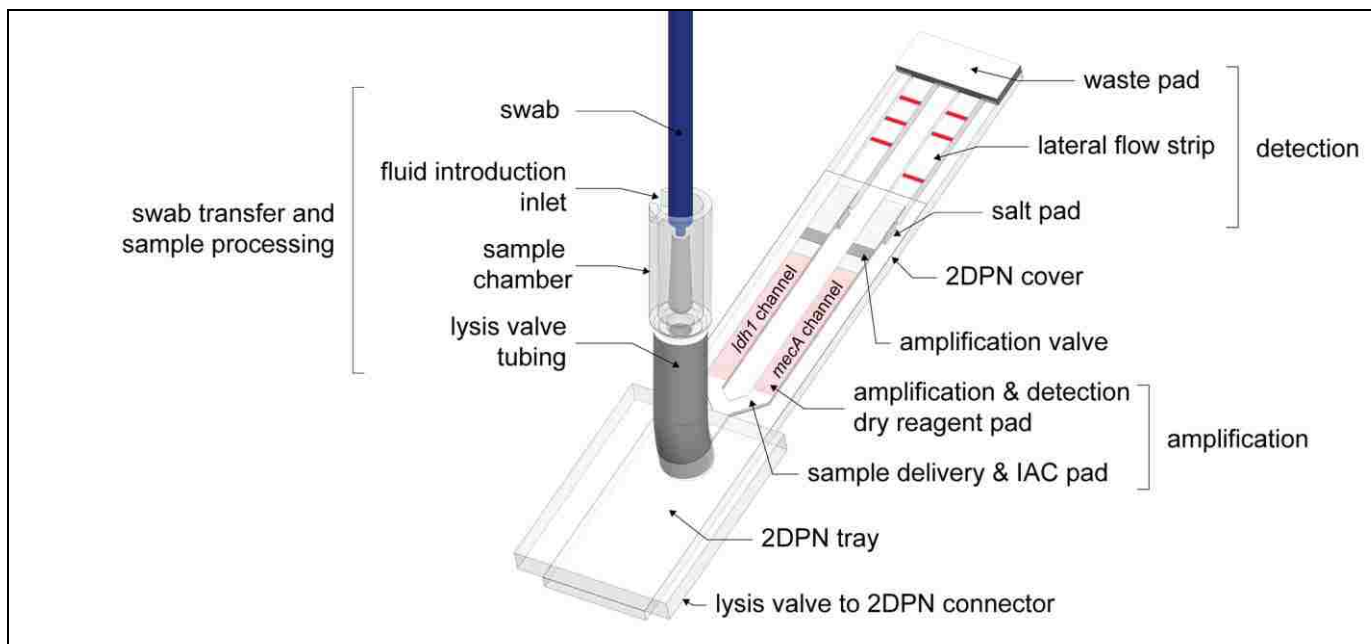


Figure 104: Fluid flow path of prototype. Sample introduction and processing are performed in a sample chamber. Processed sample is delivered by an automated valve (not shown) to a two-dimensional paper network (2DPN), where it is split into two physical channels (more channels are possible). Isothermal amplification and lateral flow (LF) detection with gold nanoparticles are also performed in the 2DPN. The LF strips are left uncovered to facilitate flash photography.

Each LF strip was striped with four capture lines. The target lines, one each for *ldh1* and *mecA*, confirmed the presence in a sample of their respective targets and at sufficient concentrations. The IAC line confirmed that amplification of nucleic acids did occur in each channel and that the detection reagents rehydrated and flowed through the LF strip (independent of the presence of target lines). The process control line, which bound gold nanoparticles, confirmed that reagents were rehydrated and flowed to the end of the 2DPN. Note that a valid test result requires proof of amplification, i.e. either a test line, IAC line, or both in each LF strip.

Complete MAD NAAT prototype

The MAD NAAT system will ultimately be produced in the form of single-use disposables, but for prototype development we integrated single-use and reusable components. Using 3D-printed materials and inexpensive, microcontroller-based electronics enabled rapid prototyping of device components and programmable control over assay timing and temperatures. The prototype used feedback-controlled heaters at 95°C for sample processing and at 50°C for amplification, and open-loop heaters for valve actuation. While future prototypes will use lower cost components, such as an injection-molded housing, and will be fully disposable, in the current prototype any components that were single-use or could not be safely re-used (due to contamination from the sample or amplification products), such as fluid introduction parts, sample chamber, and 2DPN, were used once, then disposed (Figure 105A). All other supporting components, including the housing (Figure 105B) and electronics, heaters, and mechanical valve parts (Figure 105C) were reused. Two AA batteries powered the prototype.

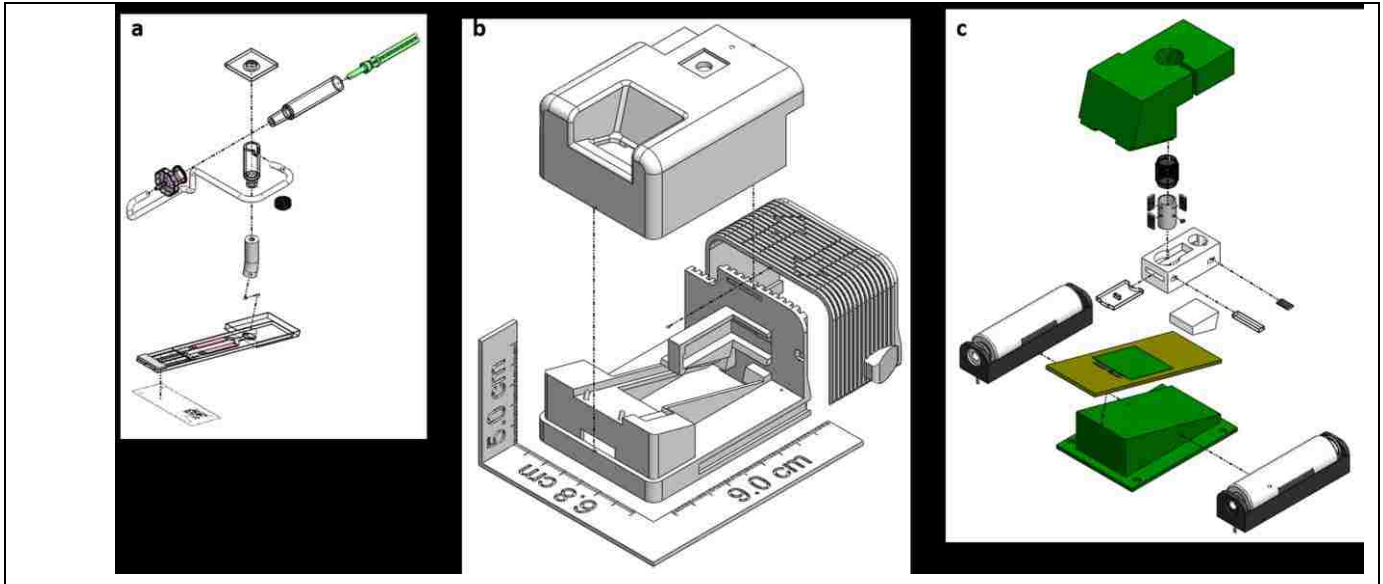


Figure 105: Exploded view of one of four identical MAD NAAT prototypes. (a) Fluid path components, including fluid storage and introduction syringe, sample chamber, and 2DPN. (b) Housing components: base, lid, and slider. (c) Supporting components, including electronics, valves, batteries, and insulation.

Autonomous operation required, in addition to dry reagents, on-device storage of a buffer, which was implemented with a syringe-based system. Opening the housing slider (Figure 105B) drove the plunger of the syringe, which delivered stored buffer through tubing containing dry lysis reagents into the sample chamber (Figure 105A). Closing the slider triggered a switch that activated the automated assay steps, after which no further user input was required.

Two styles of valves were developed for this system: a lysis valve that controlled flow from the sample chamber into the 2DPN and amplification valves that controlled flow from the amplification zones into the detection zones. Both valves used wax to create seals, and melting of that wax to release the seal. The sample chamber was connected to the 2DPN with flexible tubing pinched closed by a wax block. After the timed lysis step, a heater melted the wax, which released the pinch on the tube and delivered lysate to the 2DPN. The amplification valves were wax plugs pressed directly into the fluid pathway. After the timed amplification step, heaters melted the wax, allowing fluid to advance to the detection zone.

Sample-to-result demonstration with human nasal swab specimens

Prototype devices were tested using samples of discarded human nasal swab specimens from pre-surgical patients screened for MRSA colonization. Three types of tests were run to detect the presence of *ldh1* or *mecA* gene targets in patient specimens (PS1, 2, etc.): the MAD NAAT prototype (e.g. Figure 107A), a manual analogue of the automated assay (e.g. Figure 107B), and qPCR. LF strips were used from the prototype and the manual assay, while the qPCR results were used to generate input copy number estimates based on a standard curve of gDNA from MRSA (**Error! Reference source not found.**, Figure 106).

Table 1: Testing of nasal swab specimens from 11 de-identified patients. Samples from nasal specimens were used as inputs to prototype devices, manual assays from the same dry amplification and detection reagents, and qPCR assays. The qPCR assays were used to estimate the copy number input to the MAD NAAT prototype in each sample. ND denotes a target was not detected by qPCR. Boxes with multiple results indicate replicates. Green and red boxes show agreement and disagreement, respectively, between iSDA results and qPCR. Positive detection of a gene target in any qPCR replicate meant all corresponding iSDA results needed to be positive for agreement. The lowest input level detected by the MAD NAAT system was $\sim 3 \times 10^3$ (*mecA* from PS 4).

Patient / Sample #	iSDA		qPCR		MAD NAAT		iSDA	qPCR	MAD NAAT
	MAD NAAT iSDA	qPCR	MAD NAAT iSDA	qPCR	MAD NAAT iSDA	qPCR			
PS 1	-	-	ND	ND	-	-	ND	ND	ND
PS 2	-/-	-/-/+	ND / 1.0×10^5 / 2×10^5	ND / 1.0×10^5 / 2×10^5	-/-	-/+ / +	ND / 1.0×10^5 / 2×10^5	ND / 1.0×10^5 / 2×10^5	ND
PS 3	+/-	-/-	ND / ND	ND / ND	+/+	+/+	1×10^5 / 1×10^5	1×10^5 / 1×10^5	ND
PS 4	+	+ / + / -	1×10^5 / ND / 1×10^5	1×10^5 / ND / 1×10^5	-	+ / + / +	1×10^5 / ND / ND	1×10^5 / ND / ND	1×10^5
PS 5	-/-	-	ND	ND	+/+	+	1×10^5	1×10^5	1×10^5
PS 6	-	-	2×10^5	2×10^5	+	+	1×10^5	1×10^5	1×10^5
PS 7	+	+	1×10^5	1×10^5	+	+	1×10^5	1×10^5	1×10^5
PS 8	+/+	+	1×10^5	1×10^5	+/+	+	1×10^5	1×10^5	1×10^5
PS 9	+	+	1×10^5	1×10^5	+	+	1×10^5	1×10^5	1×10^5
PS 10	+ / + / + / +	+	2×10^5	2×10^5	+ / + / + / +	+	1×10^5	1×10^5	1×10^5
PS 11	+	+	2×10^5	2×10^5	+	+	2×10^5	2×10^5	2×10^5

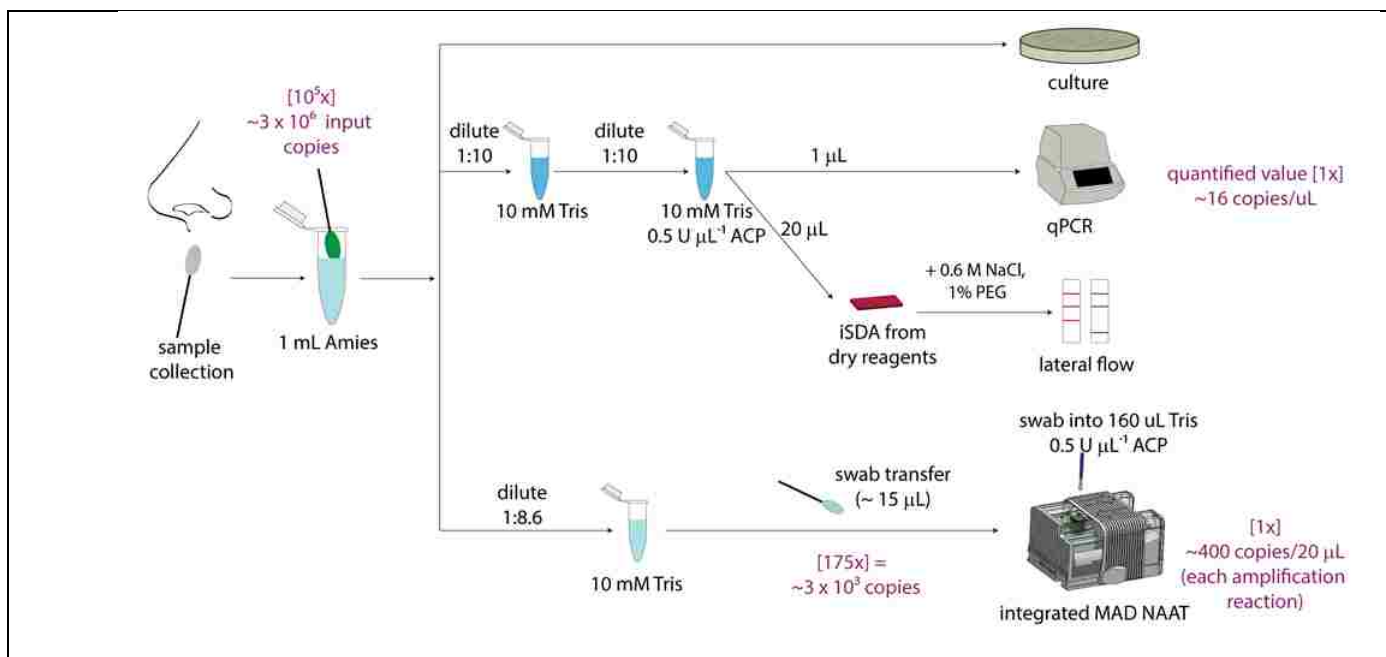


Figure 106: Illustration of methods for each patient specimen test. Green text tracks the calculations of estimated copy sensitivity. The ~ 16 copies uL^{-1} was quantified by qPCR for the lowest input where qPCR found target (PS4, *mecA*) and MAD NAAT showed this sample positive by LF detection. The MAD NAAT prototype held an input volume of 160 μL on-device buffer plus ~ 15 μL sample, and an amplification zone volume of 20 μL . That corresponded to a minimum detected value of $\sim 3 \times 10^3$ input copies in the MAD NAAT prototype.

During testing, manual assays were performed with freshly prepared ACP, IAC template, and salt, but dry amplification and detection reagents, while prototypes contained all dry reagents. Although the prototype detected as few as 3×10^3 input genomic copies (PS4), complete agreement between data occurred for patient specimens with 7×10^5 genomic copies of *ldh1* (PS8) or above and with 5×10^3 genomic copies of *mecA* (PS17) or above. We therefore estimated the sensitivity of the MAD NAAT prototype to be about 5×10^3 input genomic copies, which corresponded to detection from ~ 600 genomic copies in each amplification reaction.

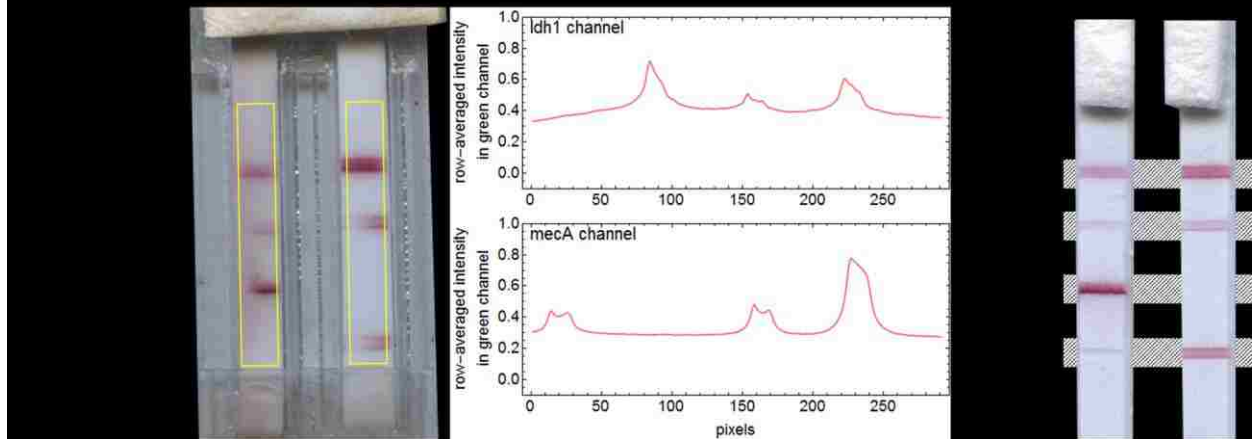


Figure 107: LF strip data for tests on a sample from PS 15, which was positive for MRSA. LF strips were 2.5 mm wide with four test lines spaced 3 mm apart. (a) MAD NAAT prototype test. Two channels amplified and detected *Idh1* with IAC (left) and *mecA* with IAC (right). Image analysis was conducted using regions of fixed size (yellow rectangles) to generate plot profiles for each channel. Non-uniform test lines and higher background in the prototype results are an artifact of valve operation, but they do not interfere with interpretation by eye or image analysis. (b) Manual assay test, which confirms results of MAD NAAT prototype test. Note that the left LF strip in the manual assay results shows a grey coloration, distinct from the red color of bound gold nanoparticles. It is a physical depression left during the striping process, not non-specific binding, and is not present in most of the strips.

In total, 33 integrated test runs were performed. Four tests did not run completely due to hardware failures unrelated to the chemical functions of the device operation (e.g. hand-soldered wire connections breaking due to wear from repeated use). Eleven other tests ran completely, but did not yield valid results due to under heating or overheating (e.g. lysis or amplification was hindered, lysis or amplification valves did not operate properly), or poor flow conditions (e.g. evaporation from uncovered LF strips at a wetting front with high concentration of solute). These tests were ruled invalid due to missing both target and IAC lines on at least one LF strip. The ratio of valid to total completed (no hardware failure) tests yielded a success rate of 62%.

Discussion

We have demonstrated the first autonomous integrated sample-to-result NAAT system for the detection of bacteria from nasal swab samples designed to be fabricated as a complete disposable. While the prototype was not yet ready for full clinical trials, these initial results suggest that, with manufacturing refinement, MAD NAAT could be of great clinical value. The one-step activation of the autonomous MAD NAAT system combines the ease-of-use of many widely available point-of-care tests with the increased sensitivity and specificity of nucleic acid amplification. The dry reagents storage

supports elimination of cold chain requirements during shipping or storage. Furthermore, the use of non-toxic materials and chemistries ensure user safety in a variety of conditions. These features make the MAD NAAT system well-suited for use in developed world settings as well as developing world LRS. Other features of MAD NAAT demonstrate its utility as a diagnostic platform. For example, higher-order multiplexing could be implemented through additional amplification channels. Splitting the sample into more channels reduces the copy number of targets in each amplification reaction, but even a 10-fold split would still leave the copy number of targets far above the LOD of the system for many clinical targets. Additionally, the ACP lysis method is broadly applicable to many pathogen types and it works directly with iSDA.

The MAD NAAT prototype consistently detected bacterial inputs at a minimum of $\sim 5 \times 10^3$ genomic copies and above, and the majority of the samples tested showed strong agreement between the MAD NAAT prototype and qPCR. Each of the bplexed amplification zones had an estimated sensitivity of ~ 600 genomic copies, and the estimated copy sensitivity from the original patient specimens was $\sim 5 \times 10^6$ MRSA genomic copies. A wide clinical range for MRSA has been reported, with one study of 444 swab specimens yielding $3\text{--}1.5 \times 10^7$ CFU per swab with a geometric mean of 794 CFU per swab⁴²⁰. The estimated device sensitivity of $\sim 5 \times 10^6$ genomic copies per swab do fall at the high end of that range, but the estimated amplification sensitivity of ~ 600 genomic copies falls below the clinically found geometric mean.

The human nasal swab specimens used for testing were all discarded clinical specimens that were stored in a high-salt buffer that inhibits ACP lysis⁴²¹, iSDA, and PCR. This collection artifact made the specimens incompatible with the MAD NAAT prototype, which was designed as a direct, sample-in device. Additional dilution was required to create a sample compatible with ACP lysis and iSDA, and to mitigate the effects of interferents from the human nasal specimens on amplification; this forced dilution step negatively impacted the sensitivity of our tests. However, our tests were largely successful anyway due to the abundance of MRSA in our positive specimens, for which our qPCR results indicate there were at least 10^6 genomic copies per original swab (prior to dilution).

Nonetheless, we are also developing new interferent depletion and target concentration mechanisms²⁴⁴, anticipating their utility for other targets. Future patient specimen characterization on direct patient-to-device samples is expected to yield a better system sensitivity.

MRSA was a challenging first clinical target for demonstrating MAD NAAT, although it is a critically important target, particularly at the point-of-care. We chose MRSA because it posed two challenges: processing of a difficult-to-lyse, Gram-positive bacterium^{422,423} and incorporating detection of multiple targets. Although most commercial NAATs use a single target—the *SCCmec-orfX* junction—their specificity is decreased by *SCCmec* variants (false-negatives) and strains that have lost *mecA* but retain the *SCC-mec* flanking sequences (false-positives). The MAD NAAT prototype mirrored the approach of a commercial NAAT (MRSA/SA Elite MGB® Kit; ELITech Molecular Diagnostics, Puteaux, France) that instead measures the ratiometric quantity of *ldh1* to *mecA* gene targets. This approach has two advantages: high sensitivity due to the highly conserved sequence of *ldh1*, which is specific for clinical *S. aureus* isolates, and high specificity for MRSA over other *mecA*-containing species, due to the ability to measure equal quantities (within tolerance) of *ldh1* and *mecA*, indicating both genes were found in a single organism. The MAD NAAT prototype did not measure the ratiometric quantity of *ldh1* to *mecA*,

which reduced test specificity but not sensitivity. The false-positive rate can be estimated by the co-colonization rate of methicillin-susceptible *S. aureus* (*ldh1* positive, *mecA* negative) with methicillin-resistant coagulase-negative *staphylococci* (*ldh1* negative, *mecA* positive), which has been measured in nasal specimens at 3.4%⁴²⁴.

This manuscript reports an important milestone in LRS NAAT technology: the first demonstration of a fully integrated, simple-to-use NAAT device, which detected two MRSA-related gene targets directly from samples of human patient swab specimens after a single activation step. Nonetheless, the MAD NAAT system is capable of more. Ongoing design improvements aim to 1) enhance reliability, sensitivity, and multiplexing; 2) reduce the time from sample introduction to results to ~30 minutes by amplification reaction optimization, dry reagent reformulation, detection improvements, valve simplifications, and shorter heat-up times; 3) improve reproducibility of signal generation by reducing evaporation from LF strips; and 4) reduce part count and cost-per-device with a focus on manufacturability and marketability. In collaboration with Seattle-based non-profit PATH, we are also developing an electronics-free version of MAD NAAT with paper timing, fluidic valve actuation, and demonstrated chemical heaters⁴²⁵, which combine to result in a device that is easily disposed, including through burning.

Acknowledgements

This work was supported by a generous grant from DARPA DSO/BTO--HR0011-11-2-0007, awarded to Dr. Paul Yager at the University of Washington. Subcontracts were awarded to Dr. Barry Lutz of UW Bioengineering, Dr. Janet Englund at Seattle Children's, Dr. Ferric Fang at UW Laboratory Medicine, Dr. David Moore at GE Global Research Center, Dr. Walt Mahoney at ELITechGroup, and Dr. Bernhard Weigl at PATH. All teams contributed materially to the concepts behind the design presented. Particular thanks are owed to Joel Atwood for manufacture of many parts, Mike Purfield for test and manufacture support, Lillian Mireles for patient sample test support, Dr. Fang for discarded nasal swab specimens from MRSA-screened patients, and to PATH for development of the graphene-impregnated wax.

7. A disposable chemical heater and dry enzyme preparation for lysis and extraction of DNA and RNA from microorganisms (Buser *et al.* *Analytical Methods*, 2016)

The work presented in this sub-aim is adapted from:

J.R. Buser, X. Zhang, S.A. Byrnes, P. D. Ladd, E. K. Heiniger, M. D. Wheeler, J. D. Bishop, J. A. Englund, B. R. Lutz, B. H. Weigl, and P. Yager, Anal. Methods, 2016, 8, 2880–2886.

Introduction

According to the 2010 Global Burden of Disease study, four of the top ten causes of death world-wide are attributed to communicable diseases, which disproportionately affect low resource settings (LRS)^{426–428}. Number four on the list is lower respiratory infections and number seven is diarrhea⁴²⁶. These infections have known and available treatments but often lack accurate diagnosis, especially in LRS where there is severely reduced availability of healthcare^{11,12}. In many settings, including the US and other developed countries, symptomatic diagnosis is commonly used by healthcare providers. Although symptoms are important, they can vary between individuals and are often shared by multiple infections. Diarrhea, for example, can be caused by viruses, bacteria, or parasites^{13–15,429}. Each of these classes of

pathogens require different treatments and within classes, treatments can vary due to different susceptibility to common drugs.

Antimicrobial resistance has been increasing around the world¹⁷; one method for curbing this trend is accurate molecular diagnosis which can lead to identification of specific pathogens and potential drug resistances. Methicillin-resistant *Staphylococcus aureus* (MRSA) is a significant pathogen causing hospital- and community-acquired infections in developing and developed regions^{430,431}; further advancement in diagnostics which can quickly identify methicillin resistance could aide in slowing the spread of this pathogen. Nucleic acid amplification tests (NAATs), which utilize a pathogen's DNA or RNA, are commonly used in pathogen identification: polymerase chain reaction (PCR) is a widely used example. The use of NAATs for disease diagnosis offers multiple advantages including increased sensitivity, the ability to multiplex, and epidemiological tracking of disease transmission and drift via nucleic acid (NA) sequencing. These approaches, however, often require expensive equipment and highly trained personnel.

Integrated microfluidic systems, such as the Cepheid GeneXpert, provide sample-to-result diagnostics using disposable cartridges that contains the assay reagents. These cartridges are coupled with automated instrumentation to process the sample and perform the bioassay, and have been shown to expedite treatment for pathogens including *Mycobacterium tuberculosis*⁴³². These systems, however, have significant cost, infrastructure, and maintenance commitments associated with them²⁷⁹ and are most appropriate for use in well-equipped laboratories with reliable electricity. Significant advances in NAATs are still required for lower-resource settings⁴³³.

Microfluidic bioassays have the potential to expand the reach of NAATs, but sample preparation, including pathogen lysis and nucleic acid extraction, remains an underdeveloped aspect of microfluidics-based bioassays, especially those designed for point-of-care use⁵⁸. Many commercially available systems that are marketed for the point-of-care are often missing sample preparation components. In 2011, Niemz *et al.* evaluated 13 commercially available point-of-care NAAT-based systems. All of these systems include an expensive, non-disposable component that requires mains electricity and, likely, a service contract. Additionally, less than half of these include on-device sample preparation thereby increasing the overall time and costs required for operation and limiting their usability as truly point-of-care systems⁴³⁴.

Enzymatic lysis has been shown to be effective in bacterial sample preparation. Some lytic enzymes are highly specialized for a specific cell type, such as lysostaphin which targets *staphylococcus* bacteria¹²⁴, while others are more generally applied. Lysozyme is a commonly used and well understood lytic enzyme which cleaves the peptide-disaccharide linkage of peptidoglycans in bacterial cell walls causing them to denature⁷⁸. Many gram-negative bacteria are insensitive to lysozyme because their thick outer membrane prevents the enzyme from interacting with the inner cell wall; additionally, some gram-positive bacteria, such as *S. aureus*, are also resistant to lysozyme treatment¹²⁵. Achromopeptidase (ACP), purified from *Achromobacter*, was found to have bacteriolytic activity as early as the early 1970s⁴³⁵. Since then, it has been widely used for the lysis of lysozyme-resistant gram-positive bacteria such as *S. aureus*. Some MRSA diagnostic assays on the market use ACP for lysis and downstream real-time PCR for pathogen identification (e.g., the BD Gene Ohm MRSA test). Most of the assays employ

ACP lysis at 37°C for 10-20 minutes, followed either by heat deactivation at a controlled temperature⁴³⁶ or KOH deactivation⁴³⁷.

Isothermal NAATs, such as loop-mediated isothermal amplification (LAMP)^{66,438} and recombinase-polymerase amplification (RPA)⁴³⁹ have received much attention recently due to their simple heating requirements. In addition, isothermal NAATs have been demonstrated on paper microfluidic platforms^{6,50,71}. Furthermore, paper microfluidics have been proven capable of automating multistep assays without external equipment⁴⁰⁵. Precise electricity-free heaters have been developed for these applications⁶⁶: these are powered by exothermic chemical reactions and use phase change to regulate temperature. Our group has demonstrated the heating of flat-profile paper microfluidic networks using this technique^{67,425}.

These technologies suggest GeneXpert-like molecular diagnostics are possible in low-cost, disposable devices^{6,71}, though many existing isothermal NAAT-based diagnostics still rely on off-device sample processing steps that will not be available in all settings. Fortunately, technologies are beginning to emerge that enable the operation of molecular diagnostics without the need for laboratory infrastructure^{50,440}. The multiplexable, autonomous, disposable nucleic acid amplification test (MAD NAAT) project^{67,229,230,244,267,406,425,441} aims to create a comprehensive isothermal NAAT platform that takes a biological sample as input, lyses cells, amplifies nucleic acid sequences from the lysate, and provides visual readout of the assay results. Non-electric heating options allow for regulated, elevated temperatures optimal for bioassays in environments without the need for external electrical power or batteries^{65,67,425,438,442}. A rapid, low-cost NAAT amenable to point-of-care diagnostics in lower-resource settings could significantly expedite identification of pathogens in people, food, and drinking water.

Here we demonstrate rapid lysis of a suspension of *S. aureus* using dry-stored ACP, followed by a rapid (<5 minutes) electricity-free heat deactivation step, the output of which can be tested directly using quantitative PCR (qPCR). In addition to lysis of *S. aureus* suspended in Tris buffer, we also demonstrate direct qPCR amplification of lysed *S. aureus* suspended in a human nasal sample. Further, human respiratory syncytial virus (RSV) virions suspended in human nasal sample are heat-treated without ACP and direct reverse transcriptase PCR (RT-PCR) used to quantify released RNA. In addition to the applications demonstrated, this methodology is easily adaptable to any assay that requires a temperature step at ~100°C.

The chemical heaters described here were produced from common laboratory supplies with minimal tooling and production steps and could be incorporated into more complex multi-step devices for sample pretreatment prior to a bioassay. This approach, when combined with advances in point-of-care nucleic acid amplification assays, could enable sample-to-result nucleic acid detection in lower-resource settings.

Materials and methods

Bacterial Culture

Staphylococcus aureus (strain RN4220 obtained from the Ferric Fang laboratory at the University of Washington) was cultured in Tryptic Soy Broth (BD Bacto, Sparks, MD, USA) at 37°C, shaking at 250 rpm. Overnight cultures were diluted 1:100 in fresh Tryptic Soy Broth and grown to mid-log phase (OD₆₀₀ = ~2). Cells were spun down at 10,000 g for 3 minutes at 20°C after growth and resuspended in the same

volume of Tris buffer (10 mM Tris, pH 8.0) or Tris-EDTA (TE: 10 mM Tris-HCl, 1 mM EDTA, pH 8.0) buffer. Cells dilutions used the same buffer.

Virus source and preparation

Human respiratory syncytial virus (RSV, laboratory strain obtained from the University of Washington Clinical Virology Laboratory) was cultured by the UW clinical virology laboratory. Virions were aliquoted at 10^6 RSV copies per microliter and stored at -80°C .

ACP lysis

S. aureus cell suspensions ($\text{OD}_{600}=2$) were diluted in Tris or TE 1:1000 to $\sim 10^6$ cfu/mL. The cell suspension was added to tubes pre-loaded with ACP (20 U/ μL stock, Sigma A3547) to a 3 U/ μL (Lot 041M1380V) or 0.5 U/ μL (Lot 031M1468V) final ACP concentration and mixed by gently pipetting up and down. Due to lot-to-lot variation of the ACP, 3 U/ μL or 0.5 U/ μL concentrations were used. The reaction was incubated at room temperature (20°C) or 37°C . ACP was deactivated by placing the tubes in a heating block (for experiments varying the heat deactivation time and temperature) or in the chemical heater (thermal profiles shown in Figure 110). Lysate tubes were briefly spun at 3000 g to pull condensation down from the tube walls before conducting qPCR.

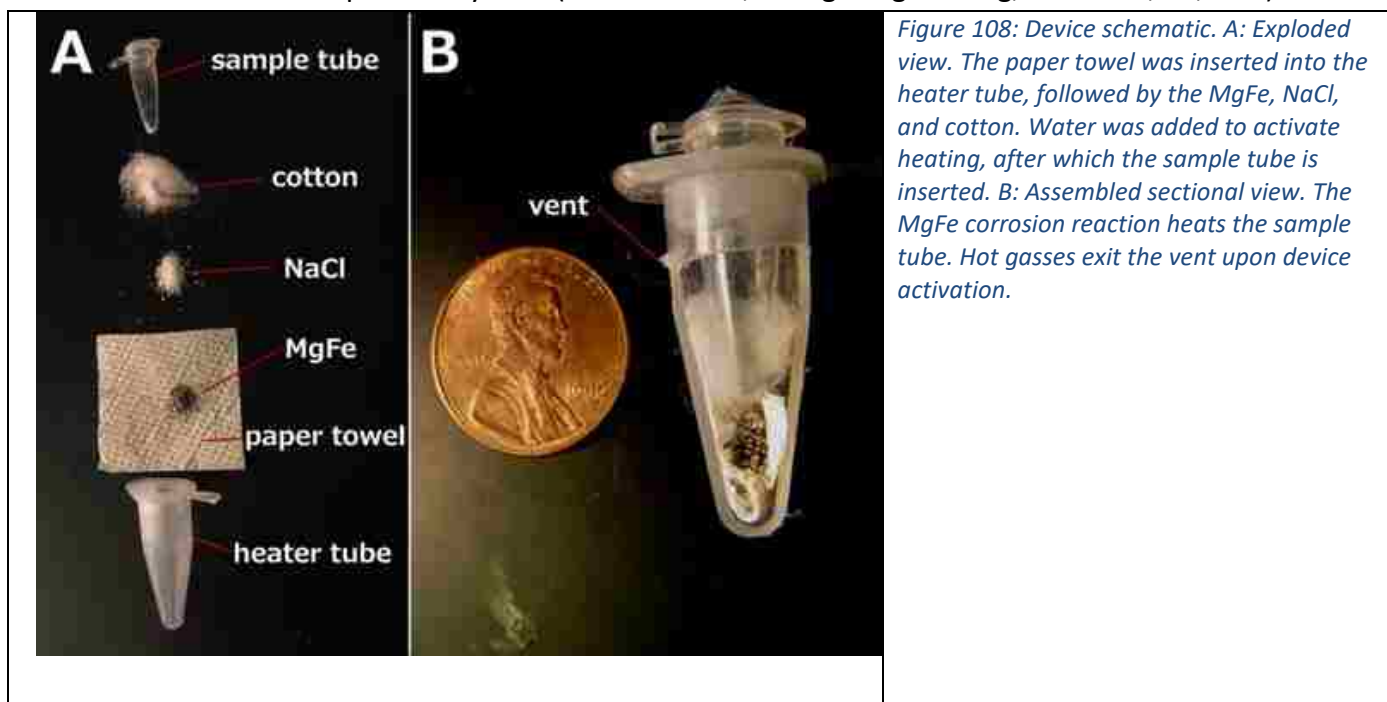
ACP mixture dehydration

In a 0.2 ml PCR tube, 37% trehalose (TS1M-100, Life Sciences Advanced Technologies, St Petersburg, FL, USA) and 20 U/ μL ACP were mixed together for a final trehalose concentration of 5% in the mixture and a final ACP concentration of 3 U/ μL or 0.5 U/ μL in the lysate (depending on the lot of ACP). The tubes were dried in a vacuum concentrator (miVac DNA, GeneVac, Stone Ridge, NY, USA) at 20°C for 1.5 hours, and then stored in a desiccator at 20°C . For cell lysis, the dried ACP was rehydrated with cell suspension following the protocol for 'ACP lysis'.

Chemical heaters

This type of heater is based on the exothermic reaction of a magnesium-iron alloy (MgFe) with a solution containing sodium chloride (NaCl). This approach is widely used to warm up portable meals⁴⁴³ and is capable of releasing heat very quickly. The chemical heaters feature a tube-in-tube design: the outer heater tube contains the elements necessary for the exothermic reaction; the inner tube contains the dried ACP and sample. The outer heater tube consists of a modified 1.5 mL snap-cap tube (89000-028, VWR, Radnor, PA, USA), separated from the cap, cut to 26 mm height as measured from the conical end, and with a 0.5 mm hole drilled in the side to serve as a vent. The separated cap was drilled with a $\frac{1}{4}$ " hole for insertion of the sample tube. A 3 cm x 3 cm square of paper towel (Kleenex C-fold towels, Kimberly Clark Professional, Roswell, GA) was inserted into the heater tube, followed by 120 mg of the solid MgFe fuel (Luxfer Magtech, Cincinnati, OH, USA), 70 mg of NaCl, and a portion of cotton ball (100% cotton, Kroger, Cincinnati, OH, USA). The modified heater tube was then fitted with the modified cap and pressed into a salvaged section of a Styrofoam shipping container. The heater was activated by adding 300 μL of deionized water through the $\frac{1}{4}$ " hole, into which the sample tube (981005, Qiagen, Hilden, Germany) was then inserted. Caution should be observed: the MgFe reaction reaches 100°C

quickly and produces hydrogen and steam, which should vent from the vent hole. Venting is critical to prevent pressure build-up and sample tube ejection. Sample temperature was measured with a type T needle thermocouple inserted into a hole drilled in the sample tube cap, recording temperature data over time with a data acquisition system (OMB-DAQ-54, Omega Engineering, Stamford, CT, USA).



Bead Beater

Samples of *S. aureus* cell suspension (800 μ L) were added to 2 mL O-ring screw top tubes (02-682-558, Thermo Fisher Scientific, Waltham, MA, USA) with 800 mg beads (9830, Research Products International Corp., Mt. Prospect, IL, USA). Tubes were loaded into the bead beater (Mini-Beadbeater-8, Biospec Products, Inc., Bartlesville, OK, USA), set to “homogenize”, and run for three 1-minute cycles with a 1 minute pause between cycles.

qPCR

For quantification of *S. aureus* DNA, a commercially available qPCR kit (ELITech Group, Bothell, WA, USA) was used. Samples (2 μ L) from the bead beater or ACP lysate were used in 20 μ L qPCR reactions (Rotor-Gene Q, Qiagen, Valencia, CA, USA or CFX96 Touch, Bio-Rad, Hercules, CA, USA) using: 50°C hold for 2 minutes, 93°C hold for 2 minutes, 45 cycles of 93°C for 10 seconds, 56°C for 30 seconds, and 72°C for 15 seconds, ending with a final elongation step at 72°C for 5 minutes. Fluorescence data were collected during the 56°C step using the orange channel. Genomic DNA copy numbers were determined relative to standard curve analysis using purified DNA of known copy number using the qPCR device software. The assay was sensitive down to \sim 10 copies of the target sequence.

qRT-PCR

For quantification of RSV RNA, UltraSense quantitative RT-PCR assay mix (Life Technologies, Carlsbad, CA, USA) was used with primer and probe sequences published previously⁴⁴⁴. The thermal protocol used was: 50°C hold for 15 minutes, 95°C hold for 2 minutes, 40 cycles of 95°C for 15 seconds and 60°C for 55

seconds using 20 μ l reactions on a CFX96 Touch (Bio-Rad). Genomic RNA copy numbers were determined relative to standard curve analysis using control RSV RNA (American Type Culture Collection (ATCC), Manassas, VA, USA) of known copy number.

Clinical sample collection

Clinical samples were collected from patients following signed parental informed consent from January to March 2015 from pediatric patients with suspected influenza infection. Nylon flocked mid-nasal swabs were collected in the hospital or emergency department for influenza and RSV testing. Each swab was placed into 750 μ l of phosphate buffered saline, 0.05% Tween-20, and 0.01% sodium azide. The diluted nasal swab sample was used for RT-PCR detection of influenza or RSV. Samples that were negative for either influenza or RSV were spiked with laboratory strains of RSV and MSSA to determine the impact of the sample composition on direct amplification assays. Seattle Children's Hospital Institutional Review Board approved the sample collection and analysis of specimens. Written consent was obtained from a parent or legal guardian, as approved by the Seattle Children's Institutional Review Board, with paper copies given to parent and also maintained under secure storage by the research team.

Statistics

A Student's t-test was performed comparing 5- and 15-minute ACP data for 20 and 37°C (Figure 109A) in Excel (Microsoft, Redmond, WA, USA), comparing temperatures $\leq 70^\circ\text{C}$ to 80-99°C (Figure 109B), comparing fresh and dried ACP results with 10^5 *S. aureus* cells, comparing performance of the thermal cycler and chemical heater for Tris buffer samples (Figure 111B), and comparing chemical heater and thermal cycler results for RNA recovery in Tris Buffer and human nasal sample matrix (Figure 112). Two-tailed comparisons were used, assuming the data were homoscedastic.

Results and discussion

As previously mentioned, NAATs that employ ACP lysis operated at 37°C for 10-20 minutes, followed by heat deactivation at a controlled temperature, have been demonstrated previously. Here, we compare ACP lysis at 20 and 37°C, for 5 and 15 minute incubations, followed by heat deactivation at 99°C. As shown in Figure 109A, the amount of recoverable DNA from *S. aureus* cells was similar for all conditions tested ($p > 0.05$). No DNA was detected for either the fresh or dried ACP no-cell control. Figure 109B shows performance is dependent on the heat deactivation temperature, with temperatures less than 80°C performing less well ($p < 0.0001$). Lot 031M1468v ACP only recovered 57% of the amplifiable DNA compared to lot 041M1380v at 3 U/ μ L (activity units were reported by the manufacturer, $p = 0.005$.) When lot 031M1468v was used at 0.5 U/ μ L, the resulting lysis performance was similar to 041M1380v at 3 U/ μ L ($p = 0.10$). No difference in lysis efficiency was observed lysing cells in Tris or TE buffer ($p = 0.45$). Heat deactivation of ACP was also found to be robust, with times from one to ten minutes leading to similar performance.

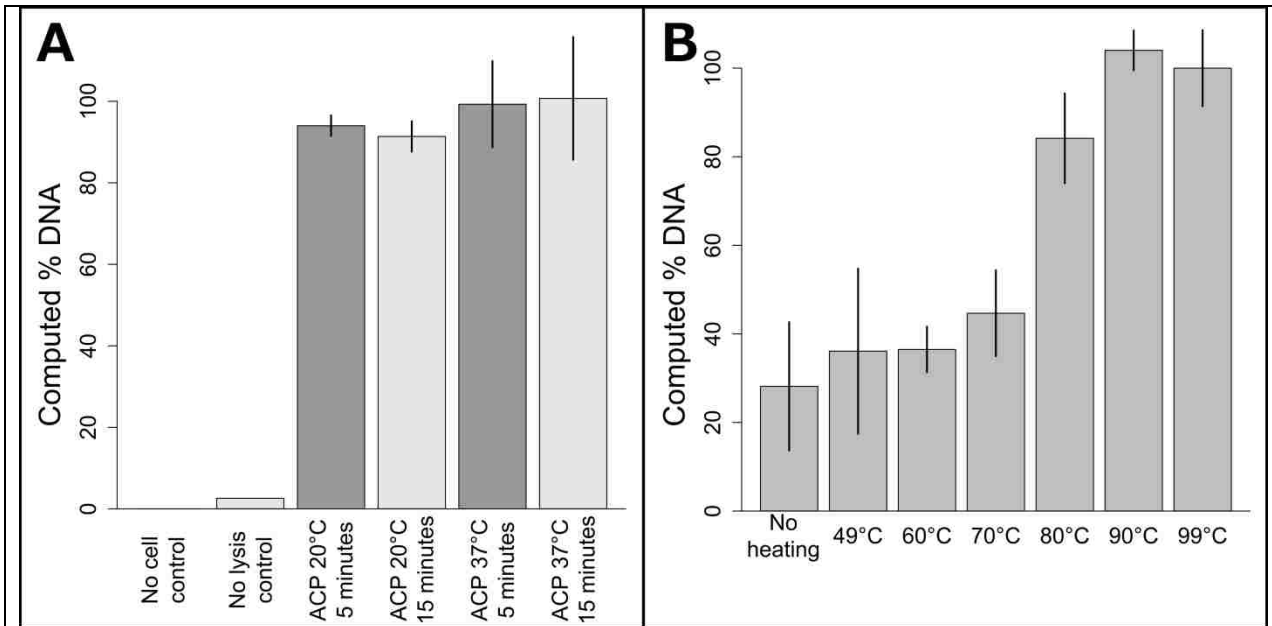


Figure 109: Optimization of ACP enzymatic lysis and heat-deactivation. A: Influence of varying ACP lysis time and temperature on DNA recovery. All ACP lysis conditions resulted in similar DNA recovery ($p > 0.05$). The plotted data is the mean \pm one standard deviation, with 37°C ACP 15 minute lysis set to 100%, $n=3$ for ACP lysis conditions, $n=2$ for no cell and no lysis controls. B: Comparison of heat deactivation temperatures for two minute ACP lysis at room temperature. Deactivation temperatures below 80°C reduced performance ($p < 0.0001$). Data points are mean \pm one standard deviation, $n=3$. Data was normalized to the 99°C data, which was set to 100%.

Based on these data, a chemical heater was designed to heat the sample to over 80°C for over one minute from a range of initial ambient temperatures. Shown in Figure 110 are temperatures measured in the lysis tube for a heater run either in our laboratory or cold room, with time-temperature profiles adequate for ACP deactivation in both cases. The chemical heater reliably exceeds 80°C, and thereby deactivates the ACP enzymes in preparation for nucleic acid amplification, even in cold ambient conditions. The heater can be expected to reliably heat the samples in warmer ambient conditions due to the nature of the exothermic reaction.

Next, the enzymatic mixture was dried down into a form that can be stored easily and that can be rehydrated by the addition of the cell suspension. Fresh and dry ACP performs similarly at room temperature with a 5 minute 95°C deactivation step for 10^5 *S. aureus* cells ($p=0.16$.) No DNA was detected for either the fresh or dried ACP no-cell control. This dried ACP does not lose activity when stored for 4 months compared to fresh ACP ($p=0.23$).

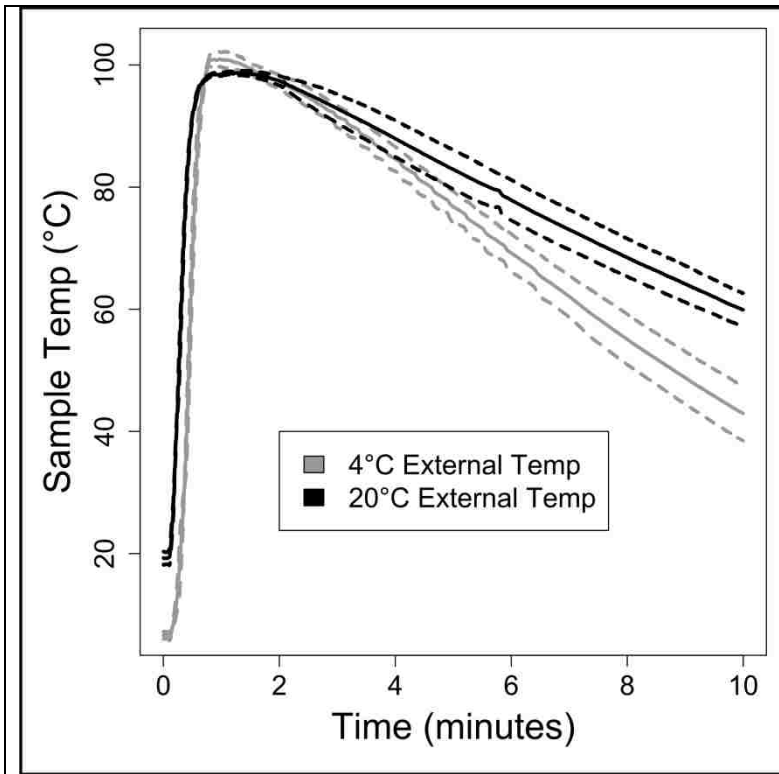


Figure 110: Chemical heater performance in varied ambient conditions. The chemical heater was run either in laboratory conditions (20°C) or in a cold room (4°C). The chemical heater was designed with enough MgFe fuel and NaCl to perform well even in cold ambient conditions. Solid lines are means, dotted lines are \pm one standard deviation, n=3.

For lysis with dried ACP and the chemical heater, the device shown in Figure 108 was constructed by combining the separately-characterized chemical heater and dry ACP tube. *S. aureus* cells were lysed in the integrated device and the lysate was directly added to a PCR reaction for quantification of the *ldh1* gene. Mechanical cell disruption is effective for difficult-to-lyse microorganisms⁴³⁴, bead beating was therefore chosen as a technique for comparison with the prototype devices. Figure 111A shows similar performance of the bead beater and the integrated device for each cell concentration tested. Figure 111B reports the amount of amplifiable DNA recovered using ACP lysis with Methicillin susceptible *S. aureus* (MSSA) in Tris buffer with chemical heat deactivation or thermal cycler, and also chemical heat deactivation for MSSA spiked into a patient nasal sample. Here, chemical-heater-powered deactivation of ACP performs similarly to deactivation using the thermal cycler (p=0.16). The negative control shows very little target DNA is recovered when no MSSA is spiked into the patient sample. 1.5 U/ μ L ACP concentration was tested in addition to 0.5 U/ μ L, to check whether higher concentrations of ACP would be beneficial to account for the additional complexity of the human nasal sample matrix.

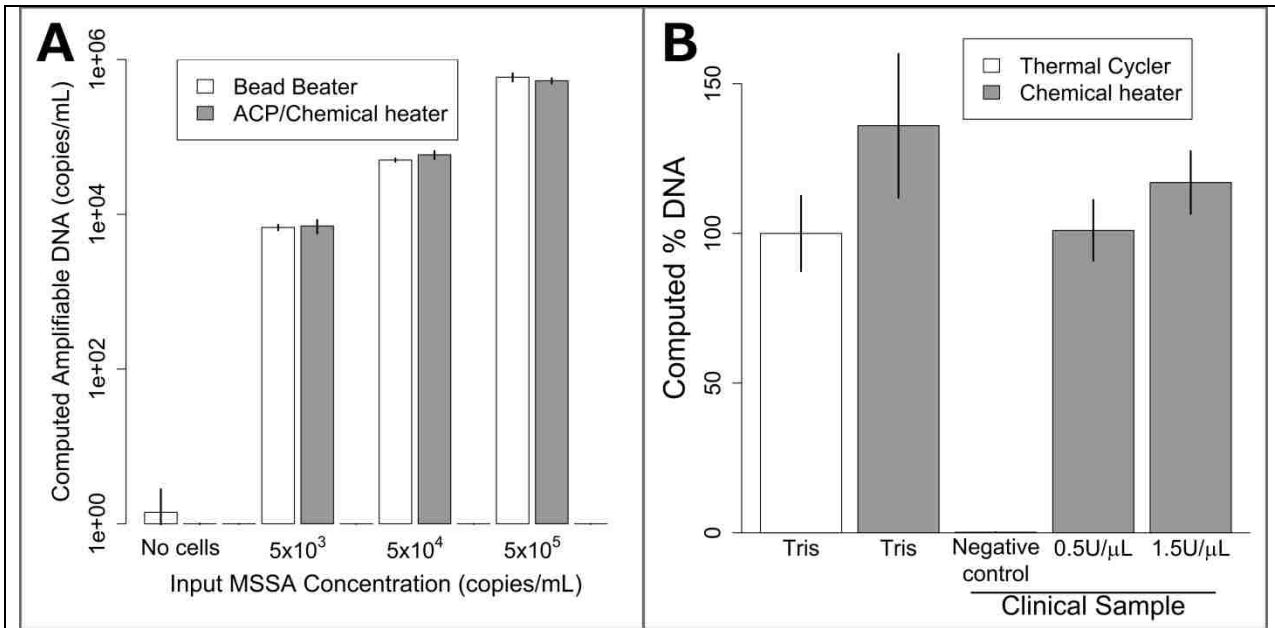


Figure 111: Lysis of MSSA with dry ACP and chemical heat deactivation in the device of Figure 108. A: Lysis of various concentrations of MSSA in Tris buffer. Bead beater DNA recovery is compared to dried ACP lysis at room temperature using a chemical heater for enzyme deactivation. The chemically-heated devices perform just as well as the bead beater for all concentrations tested. Data is mean \pm one standard deviation, n=3. B: MSSA lysis using a conventional heater (thermal cyclers) and chemical heat deactivation for samples in buffer and in human nasal sample matrix. Chemical heaters perform similarly (p=0.08) to thermal cyclers for Tris samples. MSSA added to human nasal sample matrix was also successfully amplified, with no significant difference compared to the Tris buffer thermal cyclers. The negative control shows DNA recovery when no MSSA is spiked in the clinical sample. The data were normalized to the Tris thermal cyclers, which was set to 100%. Plotted is the mean \pm one standard deviation, n=3.

With the chemical heater performing well for ACP lysis of bacteria, we wondered if it could also lyse RNA viruses. We selected RSV, an enveloped virus that contains a single segmented 15 kb genomic RNA fragment per virion⁴⁴⁵. We compared lysis of RSV virions in Tris buffer or in an RSV-negative human nasal sample matrix by a thermal cyclers to chemical heaters. The thermal cyclers and chemical heaters performed nearly identically when RSV was in Tris buffer (p=0.94, Figure 112). When RSV was spiked at a known concentration into a clinical sample that previously tested negative, the thermal cyclers and chemical heaters performed similarly as well (p=0.62, Figure 112). Overall, we conclude that the chemical heater is also an effective tool for RSV lysis.

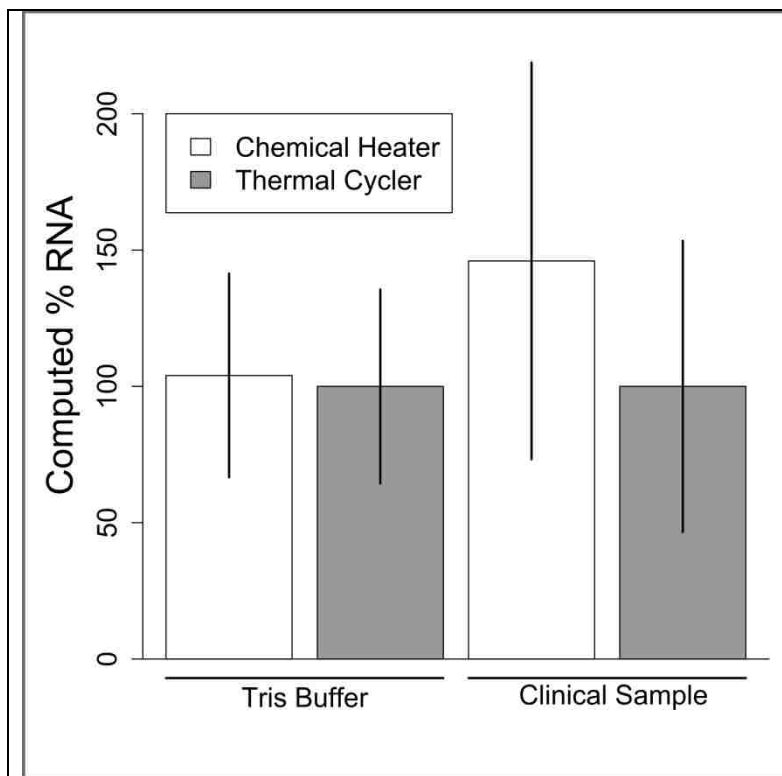


Figure 112: Lysis of RSV in Tris and human nasal sample matrix with thermal cycler and chemical heater heat deactivation. Equal concentrations of RSV in Tris buffer or human nasal sample matrix were lysed for 5 minutes then analyzed by qRT-PCR. Output is reported by percent amplifiable RNA, with thermal cycler data set to 100%. Data is mean \pm one standard deviation, n=6 for Tris Buffer, n=5 for clinical sample.

Conclusions

Here we have demonstrated effective, rapid nucleic acid extraction from *S. aureus* and RSV. The method works in the presence of a clinically-obtained human nasal sample. *S. aureus* is a relatively hard-to-lyse gram-positive pathogen, so these results highlight the robustness of the lysis method. RSV is a common childhood RNA virus, showing one potential application of the lysis method to a clinically-relevant diagnostic application. This method uses dried reagents compatible with non-refrigerated storage and a disposable chemical heat source for enzyme deactivation. No additional infrastructure or external processing was required before nucleic acid amplification. The total list price for the consumables (Eppendorf tubes, paper towel, cotton balls, NaCl, MgFe) used to construct the prototype heaters is less than \$0.41. Purchasing these items at larger quantities will likely reduce the cost. The only tools used to build the prototype heater were a razor blade, a drill press, drill bits, a ruler, and a scale to weigh the components. In addition to being a laboratory tool that many could build themselves, it would be straightforward for a manufacturer to make modified tubes for this type of application.

This work was performed with low-resource clinical settings in mind; however, this method is a generic tool compatible with any process (lysis or not) that requires heat. Such processes include the use of proteinase K or NaOH for relatively quick cell lysis in limited-resource laboratory settings, animal facilities, or for environmental sample analysis. Heat alone is sufficient to lyse many organisms⁴⁴⁶, to perform heat-shock antigen-antibody dissociation⁴⁴⁷, or to denature nucleic acid complexes or proteins. This method is ideal for thermal lysis³¹ of *E. coli* or other organisms that lyse at elevated temperature, which could enable quick screening of plasmid cultures.

We expect that this method and other sample preparation techniques in development by our group^{230,244,441} will help enable the expansion of the next generation of point-of-care diagnostics assays to areas without access to traditional diagnostic infrastructure.

Acknowledgements

Buser, Zhang, Byrnes, Heiniger, Wheeler, Bishop, Lutz, Weigl, and Yager were supported by DARPA DSO/BTO HR0011-11-2-0007, awarded to Yager. Ladd was supported by NIH 1 R01 AI 096184-01 awarded to Yager. We would like to acknowledge Anne Cent of the molecular virology laboratory for providing a laboratory RSV virus strain for experimentation, along with the team at Seattle Children's who collected the patient nasal samples, including Kirsten Lacombe, Bonnie Strelitz, Alastair Murray, and Catherine Bull, as well as all of the patients and their families who participated in the study. We would also like to acknowledge Traci Kinkel from the Ferric Fang lab at the University of Washington for providing a laboratory strain of *Staphylococcus aureus*. We wish to thank Shichu Huang, Tinny Liang, both of the University of Washington and Elain Fu, now at Oregon State University, for their help in obtaining patient samples. We would also like to thank Sujatha Ramachandran for the helpful guidance regarding ACP dry storage. We thank everyone in the Yager and Lutz labs, and collaborators at UW, PATH, GE Global Research, and the ELITech Group for the support and feedback.

8. One-step purification and concentration of DNA in porous membranes for point-of-care applications (Byrnes *et al.* *LOC*, 2015)

S. A. Byrnes, J. D. Bishop, L. Lafleur, J. R. Buser, B. Lutz, and P. Yager

Abstract

The emergence of rapid, user-friendly, point-of-care (POC) diagnostic systems is paving the way for better disease diagnosis and control. Lately, there has been a strong emphasis on developing molecular-based diagnostics due to their potential for greatly increased sensitivity and specificity. One of the most critical steps in developing practical diagnostic systems is the ability to perform sample preparation, especially the purification of nucleic acids (NA), at the POC. As such, we have developed a simple-to-use, inexpensive, and disposable sample preparation system for in-membrane purification and concentration of NAs. This system couples lateral flow in a porous membrane with chitosan, a linear polysaccharide that captures NAs via anion exchange chromatography. The system can also substantially concentrate the NAs. The combination of these capabilities can be used on a wide range of sample types, which are prepared for use in downstream processes, such as qPCR, without further purification.

Introduction

According to the WHO, the types of diagnostics used around the world have been shifting from traditional laboratory-based tests, such as ELISA and qPCR, to rapid test formats; the aim is to deliver diagnosis at the point-of-care (POC). From 1999 to 2009, the proportion of HIV rapid tests procured globally increased from ~35% to over 80%²⁶. This trend reached a peak in 2007 with over 95% of procurements being of the rapid test variety²⁶. Although this trend is encouraging, there is still a gap in the availability of accurate diagnostics for the POC.

According to the 2010 Global Burden of Disease study, four of the top ten causes of death worldwide are attributed to communicable diseases, which disproportionately affect low resource

settings (LRS)^{426–428}. Of these top ten, number four is lower respiratory infections and seven is diarrhea^{426–428}. Each of these conditions can be caused by multiple pathogens; without a proper diagnosis, accurate treatment cannot be provided. In developed settings, these diagnoses are often performed through nucleic acid (NA) detection. The use of NA for disease diagnosis offers multiple advantages including increased sensitivity, the ability to multiplex, and epidemiological tracking of disease transmission and drift via NA sequencing. These approaches, however, are not available at the POC because they often rely on sample pre-treatment techniques that require expensive equipment and highly trained personnel.

Common methods of DNA purification used in both laboratory settings and tests designed for the POC often rely on one of three general mechanisms: solid-phase extraction, electrostatic interactions, or sequence-specific capture. One of the most widely used techniques is solid-phase extraction (SPE) with silica particles. Pioneering work by Boom *et al.* demonstrated a “rapid and simple” method for nucleic acid purification using chaotropic agents, ethanol, and an acidic silica slurry. Their method cited a total assay time of less than one hour for greater than 50% recovery of DNA⁸³. The current gold standard Qiagen kit utilizes a similar technique with silica particles embedded in a centrifugal filter for NA isolation from complex samples. Other common laboratory techniques rely on NA precipitation in the presence of solutions with high alcohol content⁸⁴. Although these traditional methods are well characterized and reliable, they often require expensive laboratory equipment and highly trained laboratory technicians, limiting their availability in the developed and developing world to centralized facilities and hospitals.

Over the last 20 years, the field of microfluidics has aimed to address and overcome the gap between laboratory capabilities and POC systems through the development of single-use, plastic microfluidic chips²⁹. There have been numerous publications about the wide range of applications for these chips including cell lysis and NA purification^{30,31}, sample concentration³², immunoassays^{33–35}, and NA amplification^{36,37}. Gubala *et al.* extensively reviewed many of these pioneering applications³⁸.

In the microchip format, NA purification for the POC often adapts techniques from traditional laboratory methods. For example, multiple groups have published on the use of SPE membranes in microfluidic devices^{215–218}. The Klapperich group embedded silica particles in a porous polymer monolith (PPM) within microfluidic channels to combine DNA purification from complex samples with on-chip PCR^{59,60,219}. The Bau group designed a sample-to-answer polycarbonate cassette with on-chip reagent storage for NA isolation using a silica membrane⁶¹. There has also been initial work published on the use of sequence-specific capture for isolating NA targets in microfluidic chips^{93,94}.

Another widely used technique for DNA purification in microfluidic devices exploits the negative charge of DNA molecules; DNA can associate with coated magnetic beads^{85,86}, cationic polymers^{87–89} or resins⁴⁴⁸, and can be separated through electrophoretic methods^{90–92}. The Landers group utilized chitosan, a cationic polymer, to selectively isolate NAs in a microchip from complex solutions^{52,221,222,449}. Chitosan is a linear polymer comprised of linked sugar rings with a primary amine functional group on each monomer. Below its pK_a (6.3–6.5²²³) the amine is protonated, and the polymer becomes polycationic. At higher pH values, the amine is

deprotonated and returns to an uncharged state. This charge reversal enables a controllable electrostatic attraction between NAs and chitosan at low pH values that can be reversed through a buffer exchange. Early work with the chitosan-NA interaction focused on NA compaction and delivery for gene therapy applications^{224–226}. Although many of the above microchip-based systems show promise for translation to realistic POC systems, there is a drawback to their implementation due to the use of potentially expensive equipment for operation (e.g.: syringe pumps). Devices that require this type of equipment have limited usability in POC settings such as a patient's home or rural health clinics in the developing world. Due to these constraints, many groups have begun to focus on an alternative platform for diagnostics: porous membranes.

The use of porous membranes, or paper-based substrates, as a platform for bioassays dates back to the 1930s with the development of paper chromatography^{39–41}. In the mid to late-1970s the home-based pregnancy test brought paper-based diagnostics to the POC^{42–44}. More recently, George Whitesides' group began patterning cellulose paper to simultaneously detect glucose and proteins in urine samples⁴⁵. The field has also evolved beyond one-dimensional lateral flow systems to include two-dimensional paper networks (2DPN)⁴⁶, which offer advantages such as the ability to perform complex, multi-step processes⁴⁷, the sequential timed delivery of reagents^{46,48}, and compatibility with various detection techniques⁴⁹. Porous-membrane-based assays do not require mechanical pumps because capillarity wicks fluids into and through the paper⁵². These devices are also inexpensive, easy to manufacture, and disposable, making them ideal candidates for POC tests. Two recent reviews detail the use of porous membrane-based microfluidics for diagnostic devices⁵³ and the translation of multi-step processes from laboratory gold-standard techniques to paper-based systems⁵⁵.

There is still a significant gap in translating NA tests to paper platforms, especially those that may require NA purification and concentration. Mariella *et al.* noted that few paper-based devices have developed reliable solutions for the use of NA in paper-based formats⁵⁸. Recent publications have detailed systems that isolate NAs using commercially available extraction membranes such, as FTA or Fusion 5^{96,97}, or chromatography paper⁷¹. Although these membranes do selectively isolate NAs, they have only been demonstrated in conjunction with plastic microchips or require minimal equipment with multiple user steps.

Furthermore, sample concentration can be an additional critical step in the NA purification process, especially for environmental testing where only a few targets may be present in large volumes (mL to L) of sample. As such, an ideal porous membrane-based NA purification system should also substantially concentrate the target.

In this work, a novel DNA purification and concentration system that uses the linear polysaccharide chitosan was developed in porous membrane substrates for POC applications. It is well known that surfaces can be modified with polymers to engineer or control surface properties such as charge^{227,228}; we've used these principles to investigate chitosan's interaction with two different porous membranes. Second, the capacity of different membranes for the polymer and polymer retention during lateral flow were measured. These steps provide a quantitative method for determining the capacity for DNA binding of chitosan-coated

membranes. Finally, on the basis of this method, a system was developed and tested using porous membranes to simultaneously purify and concentrate DNA from complex samples containing high protein content, excess non-target DNA, and blood. Further, the purification system uses a novel, one-step, sequential reagent delivery mechanism developed in the Yager and Lutz labs^{139,229} that directly translates to a simple, one-step user experience; this further supports the feasibility of this system for use in POC applications.

Materials and Methods

Reagent preparation

All reagents were prepared with sterile molecular biology grade water (Thermo Fisher Scientific, Waltham, MA). Low molecular weight chitosan oligosaccharide lactate (average MW 5000), mucin from porcine stomach Type III, sodium chloride, Tris-HCl, and MES were purchased from Sigma Aldrich (St. Louis, MO). Pulse-field-certified agarose, sample loading dye, SYBR Gold gel stain, and DNA ladders were purchased from BioRad (Hercules, CA). A 10x stock of TBE buffer was purchased from Thermo Fisher Scientific (Waltham, MA). Human genomic DNA (gDNA) was purchased from Promega (Madison, WI). The 50 mM MES DNA capture and wash buffers were prepared in sterile water and the pH was adjusted to 5. The 50 mM Tris DNA elution buffer was prepared in sterile water with red food coloring (Safeway, Pleasanton, CA) to track fluid flow; the pH was adjusted to 9. The simulated nasal matrix (SNM) was prepared as previously described²³⁰. Defibrinated sheep's blood was purchased from Hemostat Laboratories (Dixon, CA).

Device patterning and construction

All porous membranes and test card materials were cut using a CO₂ laser (Universal Laser Systems, Scottsdale, AZ). Untreated, backed, 5-10 μm pore diameter nitrocellulose (NC) membranes (FF80HP, GE Healthcare Life Sciences, Niskayuna, NY) and untreated, unbacked, 10-100 μm pore diameter glass fiber (GF) membranes (Standard 17, GE Healthcare Life Sciences, Niskayuna, NY) were patterned with chitosan. Test cards were made with 0.254 mm-thick Mylar backing with adhesive (10 mil AC Melinex, Fralock, Valencia, CA) and cellulose wicking pads (CFSP223000 Millipore, Millipore, Billerica, MA) for waste fluid uptake.

The nitrocellulose and glass fiber membranes were patterned with a low molecular weight chitosan solution prepared in 50 mM MES at pH 5 using a piezoelectric noncontact printer (SciFLEXARRAYER S3, Scienion AG, Berlin, Germany). After printing, the membranes were stored in a desiccator. Membranes patterned with fluorescently tagged chitosan were also wrapped in foil to protect them from light and photobleaching.

SEM of porous membranes

All images were collected using an FEI Sirion electron microscope and samples were Au/Pd sputter coated (SPI Module Control, Structure Probe, Inc., West Chester, PA, USA) with an estimated 12 nm Au/Pd. A 5 kV beam was used for imaging (Fig. S1). Using these images, membrane surface area was estimated by representing the features as spheres and cylinders to simplify calculations. The calculated surface areas per volume of nitrocellulose and glass fiber were 2.0 μm²/μm³ and 0.19 μm²/μm³,

respectively. These calculated values are consistent within an order of magnitude with other published values^{231,232}.

Fluorescent labeling of chitosan

Chitosan was fluorescently labeled using the commercially available 488 or 594 Amine-Reactive Dye Kit from Thermo Scientific (Logan, UT). Chitosan was dissolved in 50 mM MES at pH 5 to make a 1% w/v solution. After a one-hour incubation at room temperature with the amine-reactive dye, the chitosan was purified by precipitation using 5 M NaOH followed by centrifugation at 9400g for 3 minutes. The precipitated chitosan was re-dissolved in 50 mM MES and the pH was adjusted to 5 to prepare it for reagent patterning. The solution was stored in the dark at 4°C for up to one month.

Purifying and fluorescent labeling of DNA

All DNA was purified from freshly cultured methicillin-sensitive *Staphylococcus aureus* (MSSA, strain RN4220) bacterial cells. The DNA was purified using the commercially available Qiagen Genra Puregene Kit (Qiagen, Valencia, CA) with a slightly modified protocol. During the lysis step, 50 µL of lysostaphin (100 µg/mL) was added with the recommended 1.5 µL of Lytic Enzyme Solution provided by the kit. Purified DNA was resuspended in 20 µL of sterile water and incubated for 20 minutes at 65°C to complete resuspension. The final DNA concentration was calculated by qPCR (described below).

After purification, DNA was fluorescently labeled using the Alexa Fluor 488 or 594 ARES DNA Labeling Kit (Life Technologies, Carlsbad, CA) with a slightly modified protocol. During the initial nick translation step, the concentration of each of the dNTPs was 0.5 mM. After labeling, the final concentration of the fluorescent DNA was determined using qPCR for the *ldh-1* gene.

Pulse field gel electrophoresis for DNA fragment size

Pulse field gel electrophoresis (PFGE, Fig. S2) was used to determine the fragment size of DNA both before and after purification with chitosan in-membrane. A 1.0% agarose gel was prepared in 0.5x TBE buffer and set overnight at 4°C. Gels were run using the BioRad CHEF Mapper XA System (BioRad, Hercules, CA) in a cold room (4°C) in 0.5x TBE running buffer. Agarose plugs containing the high molecular weight *S. cerevisiae* DNA ladder were loaded into the gel before submerging in running buffer. Liquid samples were added to the gel with sample loading buffer. The “Auto-Algorithm” function was used with an input size range of 100 kbp to 2200 kbp. Gels were stained with 2x SYBR Gold in running buffer (limit of detection $\sim 10^8$ copies) for 20 minutes with shaking followed by 10 minutes of de-staining in DI water. Gels were imaged with the BioRad Gel Doc EZ System (BioRad, Hercules, CA).

qPCR for MSSA *ldh-1* gene

DNA recovery was quantified with a qPCR kit for the *ldh-1* gene provided by the ELITechGroup (ELITechGroup Molecular Diagnostics, Bothell, WA). The 20 µL reactions were run on a Rotorgene real-time PCR instrument (Qiagen, Valencia, CA) using the following protocol: 50°C hold for 2 minutes, 93°C hold for 2 minutes, 45 cycles of 93°C for 10 seconds, 56°C for 30 seconds, and 72°C for 15 seconds, ending with final elongation step at 72°C for 5 minutes. Fluorescence data were collected during the 56°C annealing step in the orange channel. The qPCR results were analyzed using the automated

threshold cycle (CT) value calculation in the Rotorgene software (Qiagen, Valencia, CA). This assay is sensitive down to $\sim 10^1$ copies of the target sequence. The red dye or up to 0.5% blood in the elution buffer do not significantly interfere with the qPCR signal (Fig. S3).

Chitosan interactions with porous membranes

Porous membrane capacity for chitosan

To determine the capacity of each membrane for chitosan, small punches (radius = 2.4 mm) were taken from sheets of nitrocellulose and glass fiber. These punches were filled to capacity for nitrocellulose and glass fiber, 1.81 or 7.56 μL , respectively, with varying concentrations of fluorescent chitosan in solution to produce different chitosan concentrations in the membranes. Here, chitosan concentration is defined as μg of chitosan per μm^2 of membrane surface area ($\mu\text{g}/\mu\text{m}^2$), assuming even coating on all surfaces. The membranes were placed in clear Petri dishes and incubated in a dark chamber at 95% relative humidity for 24 hours to allow equilibration of chitosan adsorption to the membrane.

After incubation, the membranes were imaged wet to determine a baseline fluorescence signal for the input amount of chitosan. Next, the membranes were washed with 1x volume capacity of 50 mM MES at pH 5 and fluid was wicked away via a cellulose waste pad to remove unadsorbed chitosan. The membranes were re-wet with 50 mM MES at pH 5 and imaged a second time to track the loss in fluorescent signal. The loss of chitosan was measured as the difference between the baseline fluorescence and the post-wash fluorescence of the coated membranes. All fluorescence images were captured using an Axiovert fluorescence microscope (Zeiss, Thornwood, NY) fitted with a Retiga 1300i digital CCD camera (Quantitative Imaging Corporation, Surrey, BC, Canada). Images were taken with MicroManager software²³³ using a 50 ms exposure and 2.5x objective. Chitosan adsorption was calculated as the percent change in the integrated fluorescence intensity over the entire patterned region from pre- to post-wash conditions (1). These intensity values were measured using ImageJ²³⁴.

$$\% \text{ adsorbed} = \frac{\text{fluorescence}_{\text{post-wash}}}{\text{fluorescence}_{\text{pre-wash}}} \times 100\% \quad (1)$$

For both membranes, the chitosan concentrations tested ranged from 0 to $3.6 \times 10^{-8} \mu\text{g}/\mu\text{m}^2$. The upper limit of chitosan concentration for each membrane was bounded by the solubility of chitosan in buffer (50 mM MES, pH 5), the volume capacity, and the pore surface area of the membrane. Membrane capacity was determined by plotting the percent of chitosan adsorbed to each surface against the input chitosan concentration (in $\mu\text{g}/\mu\text{m}^2$) (Fig. S4C). These capacities were further verified by theoretical calculations based on the length of the chitosan polymer and the membrane surface areas; see the *Supplementary Information* (Fig. S4A and Fig. S4B) for the full calculations.

Chitosan retention in porous membranes during flow

To determine the retention of chitosan in each porous membrane during flow, a 2.5 mm long by 10 mm wide region of each membrane was patterned with fluorescent chitosan. Three concentrations were

tested to determine if retention during flow was concentration dependent. The three tested concentrations for both membranes were based on the results of the previous adsorption studies. The concentrations in the patterned regions were 4.5×10^{-10} , 8.9×10^{-10} , and 1.3×10^{-9} $\mu\text{g}/\mu\text{m}^2$ for nitrocellulose and 8.9×10^{-10} , 1.8×10^{-9} , and 2.7×10^{-9} $\mu\text{g}/\mu\text{m}^2$ for glass fiber.

The patterned membranes were attached to 10 mil thick Mylar backing with adhesive (10 mil AC Melinex, Fralock, Valencia, CA) for ease of handling. An untreated cellulose pad (CFSP223000 Millipore, Billerica, MA), cut using the CO₂ laser cutter, was used as a waste collection reservoir. Before the initiation of flow, the chitosan regions on each membrane were wetted with 50 mM MES at pH 5 and excess unadsorbed chitosan were removed *via* wicking with a cellulose waste pad through the thickness of the membrane. This step was important to decouple the loss of chitosan due to incomplete adsorption to the membrane from the loss of chitosan during lateral flow.

To test chitosan retention during flow, two solutions were sequentially wicked through the membrane. These solutions were the DNA capture and elution buffers, which were selected to mimic an actual DNA purification experiment. The volume of the solutions was set to 2x the fluid capacity of the membrane (120 μL total for nitrocellulose and 500 μL total for glass fiber).

Dimensions of the patterned region and the fluorescence intensity of the chitosan were measured in ImageJ from uncompressed, time-lapse videos acquired using HandyAVI (AZcendant, Tempe, AZ, USA) in a humidified, light-tight box illuminated with two blue LEDs. Videos were captured using a web camera (Logitech, Fremont, CA) fitted with a 550 nm high-pass filter (FEL0550, Thor labs, Newton, NJ). The fluorescence intensity of the chitosan during flow was normalized to the initial wetted intensity to determine the percent of polymer retained in the membrane during flow.

DNA purification and concentration in porous membranes using chitosan

Chitosan is a linear polysaccharide with a primary amine functional group on every monomer. In solutions buffered below the polymer's pK_a , 6.3-6.5²²³, the primary amine is protonated, resulting in a multivalent cationic polymer. In its protonated form, chitosan binds DNA and RNA *via* electrostatic interactions. When exposed to a solution above the pK_a , the primary amines are deprotonated and this electrostatic attraction is lost, resulting in release of nucleic acids (**Fig. 1**)

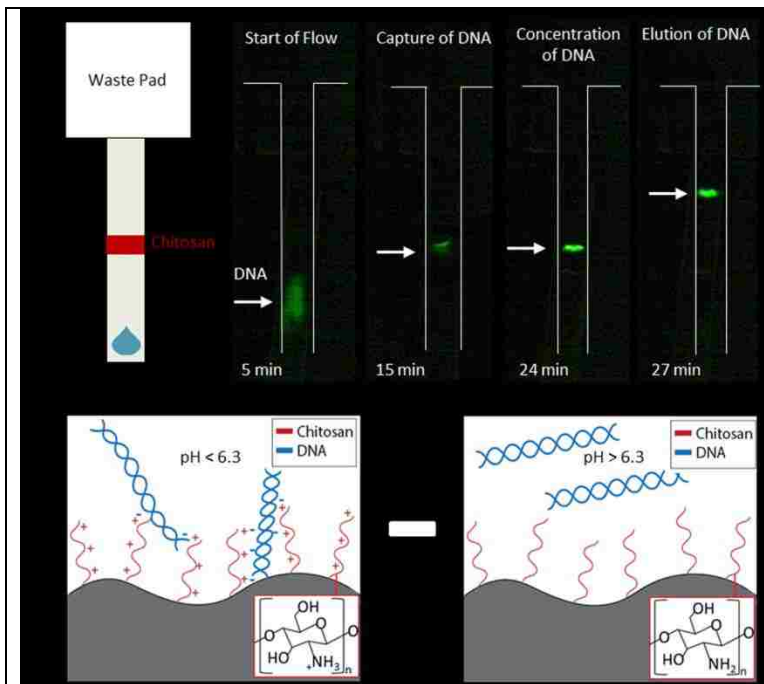


Figure 113: DNA purification in porous membranes using chitosan. A) Schematic and images from a purification experiment in nitrocellulose. The DNA (green) is initially seen as a smear. As it reaches the chitosan region, DNA stops flowing and becomes concentrated. Once DNA is eluted, it remains concentrated. B) Schematic of a membrane surface patterned with chitosan (red). In solutions with a pH below 6.3, the primary amines on each monomer become protonated and can bind DNA. When the pH is increased above the amine pK_a , the charge on the polymer returns to neutral and DNA is released. Note that the quantum efficiency of the label changes with pH and immobilization.

To evaluate the ability of chitosan to purify and concentrate DNA in paper, 60 x 10 mm membranes were patterned with chitosan in 50 mM MES at pH 5. The patterned region was set to an area 2.5 mm long by 10 mm wide to remain consistent with the chitosan retention experiments. Based on the capacity and retention experiments, the chitosan concentrations in nitrocellulose and glass fiber were set to 1.3×10^{-9} and $1.8 \times 10^{-9} \mu\text{g}/\mu\text{m}^2$ ($\pm 5\%$), respectively.

Chitosan capacity for DNA and DNA concentration factor

Chitosan's capacity for DNA in both nitrocellulose and glass fiber was determined by increasing the concentration of DNA in the input sample until a decrease in the relative amount of DNA recovered was observed by qPCR. The range of input DNA concentrations tested in both membranes was between 1×10^5 copies (0.3 ng) to 4×10^8 copies (1200 ng) of fragmented MSSA DNA purified from cells. On average, the target DNA was less than 250-300 kbp long; larger DNA fragments are unable to flow through the pores of the membranes (Fig. S2).

For these experiments, DNA was spiked into 100 μL of DNA capture buffer. This solution was wicked into the membrane, followed sequentially by 100 μL of wash and elution buffers for NC, and 250 μL of wash and elution buffers for GF to accommodate for the higher fluid capacity. These experiments were run in a humidified chamber to reduce effects from evaporation.

DNA was recovered post-elution by placing the membrane in a centrifugal filter tube (0.45 μm Nylon centrifugal filters, VWR, Radnor, PA) and centrifuging for 3 minutes at 10,000g (Fig. S6). These elution volumes were measured and the target DNA concentration was determined by qPCR.

Concentration effects were measured by adding 1×10^5 to 1×10^6 copies (0.3 to 3 ng) of DNA into 100, 200, 500, 1000, or 2000 μL of capture buffer. These solutions were wicked through a membrane patterned with chitosan followed sequentially by either 100 μL for NC or 250 μL for GF of DNA wash and elution buffers. Post-elution, the DNA purification efficiency (% recovery) was quantified by qPCR. The

concentration factor was calculated as the initial input volume divided by the measured elution volumes times the % recovery (2).

$$\text{Concentration Factor} = \frac{\text{Input volume}}{\text{Elution volume}} \times 100\% \quad (2)$$

Recovery of DNA from complex samples

To determine the ability of a porous membrane pre-loaded with chitosan to purify DNA, approximately 1×10^5 to 1×10^6 copies of MSSA DNA was diluted into 100 μL of DNA capture buffer. The sample was wicked into the patterned membrane followed by wash and elution buffers, as described above. In addition to purification of DNA in water, the experiment was repeated with 1 μg BSA, 0.1% w/v mucins, 1% w/v mucins, up to 1000x non-target human gDNA, and 1% or 10% SNM to mimic more complex solutions. The percent recovery for each sample was determined by qPCR. These experiments were run in a humidified chamber to reduce effects of evaporation.

DNA purification from blood samples

Nucleic acid purification using chitosan patterned in porous membranes was also used to purify and concentrate DNA from blood samples. Often, blood preparation procedures require multiple user steps and removal of blood components that can inhibit downstream amplification reactions, notably heme²⁴³. From 15 to 50 μL of defibrinated sheep's blood was spiked into sample volumes ranging from 100 μL to 2000 μL . These samples were wicked into porous membranes patterned with chitosan followed by sequential delivery of wash and elution buffers, as described above. The purified DNA was analyzed by qPCR. These experiments were run in a humidified chamber to reduce effects of evaporation.

Statistics

All statistics were run using the open-source statistical package R (64 bit, version 3.0.2)⁴⁵⁰.

Results and Discussion

Chitosan interaction with porous membranes

Porous membrane capacity for chitosan

In this work, we aimed to demonstrate a simple, porous membrane-based device that purifies and concentrates DNA from complex samples. We started with determining the amount of chitosan available to bind DNA when patterned onto different porous membranes. The amount of *available* chitosan should depend on its adsorption to the porous membrane.

For all concentrations tested in nitrocellulose, the amount of input chitosan that adsorbed to the membrane was above 90%, indicating that the membrane was not fully saturated with polymer. This same trend was not observed for glass fiber; at concentrations at or below 3.6×10^{-9} $\mu\text{g}/\mu\text{m}^2$, the percent of input chitosan adsorbed remained high. At concentrations above 3.6×10^{-9} $\mu\text{g}/\mu\text{m}^2$, the percent adsorbed dropped, indicating that the membrane capacity had been reached (Fig. S4C). These results are consistent with our understanding of the physical properties of these porous membranes; the high surface area of the nitrocellulose, with its small pores and features, provides a higher capacity (experimentally determined capacity: 3.3×10^{-8}

$\mu\text{g}/\mu\text{m}^2$) for polymer adsorption than the coarser glass fiber (experimentally determined capacity: $\sim 5.4 \times 10^{-9} \mu\text{g}/\mu\text{m}^2$). This difference between nitrocellulose and glass fiber may be due to the way chitosan adsorbs to different surfaces. This data suggests that only a few monomers of the chitosan chain adsorb to nitrocellulose allowing more space for additional molecules to adsorb. In glass fiber, on the other hand, a larger fraction of the total polymer might bind to the surface restricting the space available for other molecules to bind (Fig. S4A).

These empirical capacities were further supported by theoretical calculations that predict the chitosan capacity of nitrocellulose should be between 9.7×10^{-10} and $3.3 \times 10^{-8} \mu\text{g}/\mu\text{m}^2$. An adsorption capacity was not observed for the concentrations tested, up to $\sim 3.3 \times 10^{-8} \mu\text{g}/\mu\text{m}^2$, which is at the maximum of the theoretical range. Based on the theoretical calculations and empirically determined capacities, the chitosan coverage of the nitrocellulose surface was $\sim 100\%$ of the theoretical geometric monolayer coverage (Fig. S4B). For glass fiber, the theoretical capacity for chitosan should be between 9.5×10^{-10} and $3.2 \times 10^{-8} \mu\text{g}/\mu\text{m}^2$. The experimentally measured capacity for glass fiber falls within the lower range of the theoretical values and approximates to $\sim 15\%$ of the theoretical geometric monolayer coverage (Fig. S4B). Using these conditions, there is a monolayer of chitosan coverage on the nitrocellulose surface and less than a monolayer on glass fiber surface. The upper limit of chitosan concentration tested for each membrane was bounded by the solubility of chitosan in buffer (50 mM MES, pH 5) and the volume capacity of the membrane.

Chitosan retention in porous membranes during flow

The total amount of chitosan available for DNA binding (**Table 1**) is determined by the amount patterned onto the membrane minus losses from incomplete adsorption, described above, and capillary flow, described below.

Table 18: Final chitosan concentration in each membrane after accounting for losses from incomplete adsorption and flow. *The “mean final concentration” is based on the average percent adsorbed and retained. **The “Range final concentration” is based on the standard deviations for the percent retained during flow.

Input Concentration ($\mu\text{g}/\mu\text{m}^2$)	% adsorbed	% retained	Mean final concentration* ($\mu\text{g}/\mu\text{m}^2$)	Range final concentration** ($\mu\text{g}/\mu\text{m}^2$)
Nitrocellulose				
4.5×10^{-10}	89 %	83 %	3.3×10^{-10}	$3.3 \times 10^{-10} - 3.4 \times 10^{-10}$
8.9×10^{-10}	85 %	74 %	5.6×10^{-10}	$5.4 \times 10^{-10} - 5.7 \times 10^{-10}$
1.3×10^{-9}	91 %	71 %	8.6×10^{-10}	$8.3 \times 10^{-10} - 9.0 \times 10^{-10}$
Glass Fiber				
8.9×10^{-10}	79 %	89 %	6.3×10^{-10}	$5.4 \times 10^{-10} - 7.1 \times 10^{-10}$
1.8×10^{-9}	58 %	71 %	7.3×10^{-10}	$6.8 \times 10^{-10} - 7.8 \times 10^{-10}$
2.7×10^{-9}	40 %	82 %	8.7×10^{-10}	$8.1 \times 10^{-10} - 9.4 \times 10^{-10}$

After characterizing the membrane capacity for chitosan, the effects of capillary flow on chitosan retention were measured. The three tested concentrations for nitrocellulose were 4.5×10^{-10} , 8.9×10^{-10} , and $1.3 \times 10^{-9} \mu\text{g}/\mu\text{m}^2$ and for glass fiber were 8.9×10^{-10} , 1.8×10^{-9} , and $2.7 \times 10^{-9} \mu\text{g}/\mu\text{m}^2$. The concentrations vary in nitrocellulose and glass fiber due to the different surface areas of each membrane. These values were based on high, medium, and low concentrations from the adsorption studies detailed above. Retention of chitosan in nitrocellulose is slightly concentration-dependent, with larger concentrations of patterned chitosan losing a higher percentage during flow (**Fig. 2A**). For glass fiber, this trend is not observed. The loss of chitosan due to flow does not appear to be concentration-dependent (**Fig. 2B**).

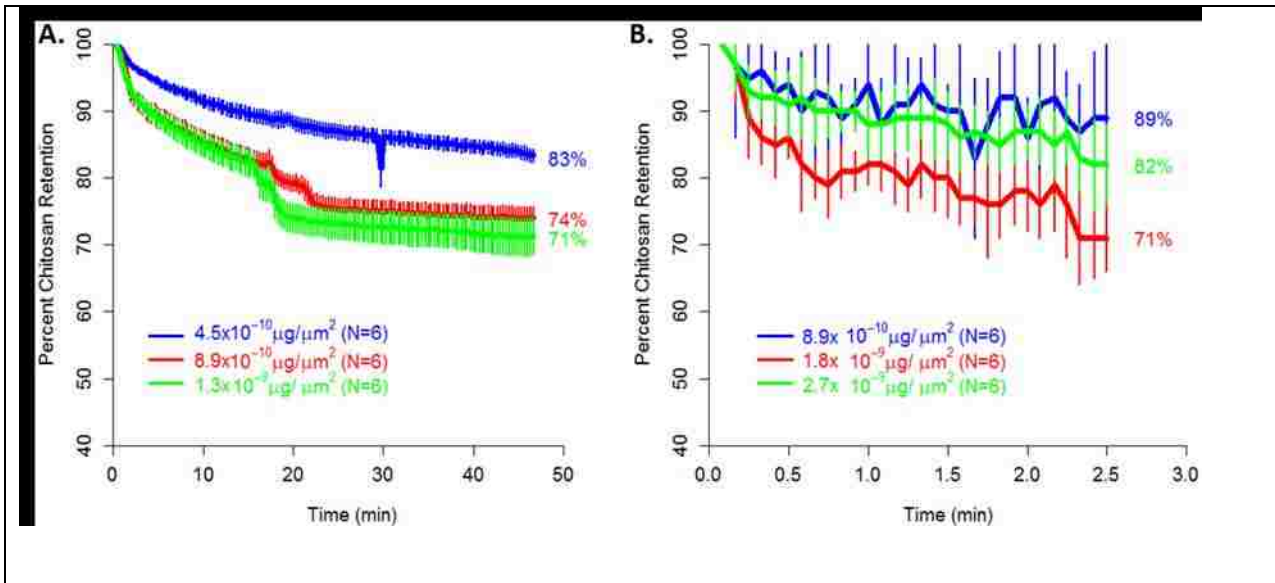


Figure 114: Chitosan retention during flow after accounting for losses due to incomplete chitosan adsorption. A) In nitrocellulose, retention during flow appears to be slightly concentration dependent. B) In glass fiber all three tested concentrations resulted in similar losses due to flow. The average retention (N=6) with +/- one standard deviation is plotted for each time point.

DNA purification and concentration in porous membranes using chitosan

Chitosan capacity for DNA and DNA concentration factor

Chitosan capacity for DNA in nitrocellulose and glass fiber was evaluated after optimizing adsorption and retention. The capacity for DNA in nitrocellulose was 1.9×10^6 copies of DNA/ μg of chitosan ($c/\mu\text{g}$) (95% CI: 2.9×10^5 to 3.5×10^6 $c/\mu\text{g}$). The capacity for DNA in glass fiber was 9.9×10^6 $c/\mu\text{g}$ (95% CI: 5.9×10^6 to 1.4×10^7 $c/\mu\text{g}$) (**Fig. 3**). These results are calculated using the mean final chitosan concentration from Table 1, which accounts for losses due to incomplete adsorption and retention. These data show that chitosan has a higher capacity for DNA in glass fiber than in nitrocellulose.

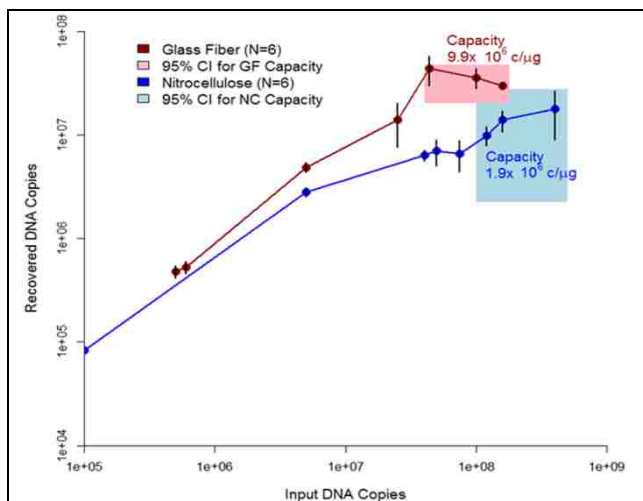


Figure 115: Capacity of chitosan for DNA in nitrocellulose (blue) and glass fiber (red) over a range of input concentrations (N=6 for each point) after normalization for membrane surface area. The capacity of chitosan for DNA is 1.9×10^6 c/ μg (95% CI: 2.9×10^5 to 3.5×10^6 c/ μg) in nitrocellulose and 9.9×10^6 c/ μg (95% CI: 5.9×10^6 to 1.4×10^7 c/ μg) in glass fiber.

The smaller pores (10 μm) and higher surface area per volume ($2.0 \mu\text{m}^2/\mu\text{m}^3$) of nitrocellulose adsorbs more chitosan than glass fiber; but these results indicate that only a proportion of the chitosan is available for DNA binding in nitrocellulose. The chitosan used in this study was small, ~ 5000 MW. This size may allow polymer to integrate into the smallest pore features of nitrocellulose, some of which may be inaccessible to large DNA fragments (100s kbp), causing a high membrane capacity for the chitosan and a lower than expected binding capacity for DNA. Further, chitosan may hinder convective transport in the smaller pore features (or block flow completely) in nitrocellulose, reducing or preventing flow of DNA-containing sample through these membrane regions. On average, the pore features in glass fiber are larger (10-100 μm) and the material has a lower surface area per unit volume ($0.19 \mu\text{m}^2/\mu\text{m}^3$) than nitrocellulose ($2.0 \mu\text{m}^2/\mu\text{m}^3$). This reduced surface area lowers the overall chitosan capacity of the membrane, but may allow more of the chitosan to be available for DNA binding.

Using these results, the calculated ratio of positive (chitosan) to negative (DNA) charges when the system has reached its maximum capacity for DNA indicates that there is less than a monolayer of nucleic acid bound to the chitosan in both nitrocellulose and glass fiber (Fig. S5). These calculations assume that a full monolayer of DNA would equate to an equal ratio of charges at the DNA-chitosan binding capacity; see the *Supplementary Information* for the full calculations. Further, these estimates and calculations assume all of the chitosan patterned in the membrane, after accounting for losses presented in Table 1, is available for DNA binding. More reasonably, only some percentage would be available because some of the polymer is interacting with the membrane surface, potentially rendering it unavailable for DNA binding. Additionally, both of these membranes have a range of pore size features and some fraction of the polymer may be trapped in the smallest of these features preventing it from interacting with DNA. Both of these scenarios further support the calculations that there is less than a monolayer of nucleic acid bound to the chitosan in each membrane.

To enable broader use of these methods, the DNA capacities of each membrane have been converted to other common units (**Table 2**). Using the membrane capacity for chitosan and the chitosan capacity for DNA, this method can be adapted to capture and concentrate DNA from a variety of samples based on the expected amount of total nucleic acids.

Table 19: Chitosan capacity in nitrocellulose and glass fiber.

*Assuming average DNA fragment size of 2.0×10^5 bp.

***E. coli* O157:H7, genome length 5.4×10^6 bp.

***MSSA RN4220, genome length 2.8×10^6 bp.

Capacity per μg chitosan	Nitrocellulose	Glass Fiber
copies DNA*	1.9×10^6	9.9×10^6
# bp*	3.8×10^{11}	2.0×10^{12}
ng DNA*	0.4	2.2
# <i>E. coli</i> bacteria**	7.0×10^4	3.7×10^5
# MSSA bacteria***	1.4×10^5	7.1×10^5

The maximum DNA concentration factors achieved with chitosan in nitrocellulose and glass fiber were 13.3x and 12.3x, respectively (Fig. 4B). These results are based on the input sample volume and the purification efficiency of DNA since each membrane type yielded a specific elution volume.

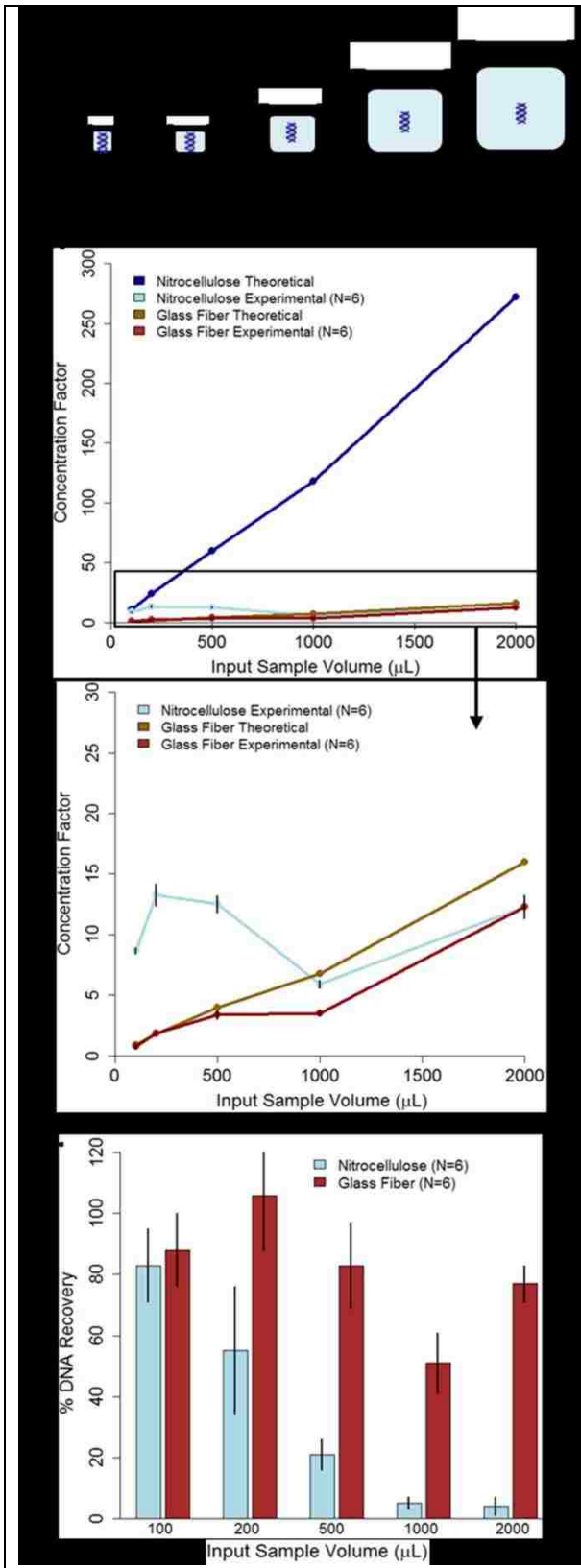


Figure 116: DNA concentration effects in nitrocellulose and glass fiber. A) Experimental schematic. B) Concentration factor from various input sample volumes. C) Corresponding recovery of DNA from various input sample volumes.

In nitrocellulose, which has a relatively homogenous pore size distribution, the interface between two sequentially delivered fluids is sharply defined. In this system, the wash and elution buffers have low and high pH values, respectively; the well-defined interface between the buffers under flow in nitrocellulose produces a sharp pH change (Fig. S6A). When the interface reaches the chitosan

patterned region, the rapid change from low to high pH deprotonates the chitosan quickly, and releases purified DNA in a concentrated plug (Fig. S6B). In glass fiber, however, which has a relatively broad pore size distribution, the interface is poorly defined, which increases mixing between the two sequentially delivered buffers and causes a more gradual pH gradient to develop. When this gradient reaches the chitosan region, the gradual change from low to high pH deprotonates the chitosan slowly, resulting in a slower release (and therefore less concentrated plug) of purified DNA (Fig. S6C). In nitrocellulose, DNA samples always eluted in 8 μL while for glass fiber, the elution volume was 100-150 μL .

In this system, which involves complex surfaces in porous membranes as well as in-flow binding, both concentration factor and percent recovery were independent of the starting DNA concentration in the sample within the ranges tested. Using the data presented in Figure 3, the corresponding elution volumes, and the resulting recovery percentages (data not reported here), we measured consistent concentration factors and percent recovery for input DNA concentrations ranging from 1×10^3 copies of target per μL ($\text{c}/\mu\text{L}$) through 1×10^5 $\text{c}/\mu\text{L}$ where total input volume was set to 100 μL . These concentrations were below the saturation limit of the modified membranes' binding capacity for DNA (measured in Fig. 3 and presented in Table 2). We have begun testing more dilute samples in larger input volumes and have preliminary data indicating this trend holds. That data will be included in a future publication.

The theoretical concentration factor assumes 100% recovery of DNA. In nitrocellulose, DNA recovery decreased as the input sample volume increased (**Fig. 4C**), likely due to the time it took to flow large volumes through the membrane. Wicking a 2000 μL sample, followed by 100 μL of wash and elution buffers, through nitrocellulose took over seven hours. This reduced recovery greatly reduced the actual concentration factors achieved in nitrocellulose. The same experiment in glass fiber only took 25 minutes and DNA recovery was independent of input sample volume in (**Fig. 4C**). The long flow times required in nitrocellulose may exceed the chitosan/DNA off-rate which would cause bound DNA to prematurely release from chitosan and be lost to waste. The chitosan-DNA binding constant has been well studied and ranges from 10^9 to 10^{10} M^{-1} ^{236,237}, but, to our knowledge, the chitosan-DNA binding rates have not been published. There have been reported off-rates in the range of $3\text{-}5 \times 10^{-2} \text{ s}^{-1}$ ^{238,239} for similar polycation-DNA interactions.

There are potential applications where concentration factor would matter less than purification but not necessarily recovery. For very dilute samples, such as urine, concentration factor would play a critical role to ensure enough pathogen nucleic acid is recovered for downstream analysis. Additionally, different infections present at a highly variable pathogen loads. For example, clinical studies have quantified active chlamydia infections in urine at $10^1\text{-}10^5$ elementary bodies/mL¹⁰⁵, Ebola in serum at $10^3\text{-}10^9$ RNA copies/mL²⁴⁰, and influenza in nasopharyngeal wash at $10^3\text{-}10^7$ TCID50/mL²⁴¹. Each of these infections would benefit from a combination of both target purification and concentration. Specifically, for infections that occur at low copy number or in dilute samples such as urine, concentration is especially important. Some of these samples would require the processing of larger volumes (mL instead of μL) to ensure a sufficient number of pathogens for infection identification. The current approach, especially using nitrocellulose, is somewhat slow to process larger volumes and may result in decreased recovery (Fig. 4C). The next iteration of this work will involve developing fluidic

systems that can rapidly process large volumes in order to purify and concentrate targets from complex, dilute samples.

DNA purification from complex samples

We demonstrated the system's ability to purify DNA from complex sample types. Overall, this method was able to recover ~80% of the input DNA from most of the sample types tested (Fig. 5).

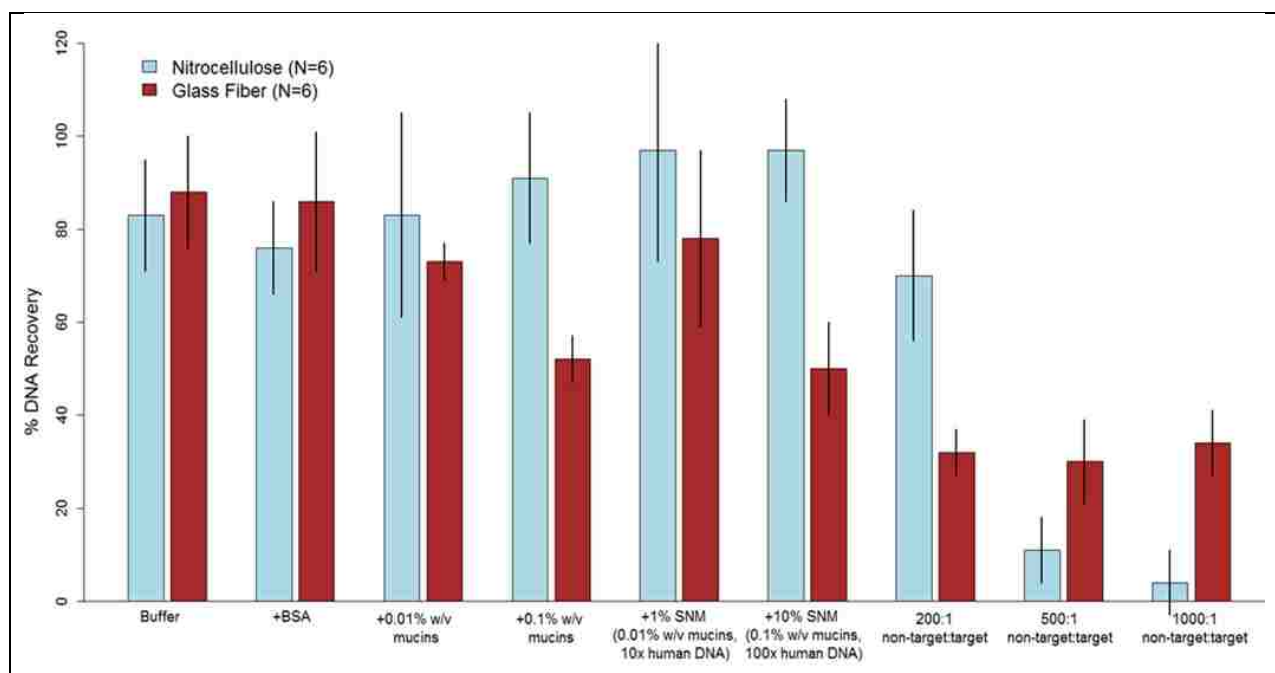


Figure 117: DNA purification in porous membranes by chitosan capture. Recovery of DNA in either nitrocellulose (blue) or glass fiber (red). The average of N=6 is reported with error bars representing +/- one standard deviation. Chitosan concentration at the capture line was $1.3 \times 10^{-9} \mu\text{g}/\mu\text{m}^2$ for nitrocellulose and $1.8 \times 10^{-9} \mu\text{g}/\mu\text{m}^2$ for glass fiber. Input DNA was between 1×10^5 and 1×10^6 copies of fragmented MSSA DNA. For SNM: 1% SNM contained 10:1 non-target to target DNA, 0.01% w/v mucins, 1.1 mM NaCl; 10% SNM contained 100:1 non-target to target DNA, 0.1% w/v mucins, 11 mM NaCl.

In both nitrocellulose and glass fiber, the recovery of target DNA was reduced when samples contained a non-target:target ratio of greater than 100:1. These data are slightly higher than the limits dictated by the capacity data above (~10:1 for nitrocellulose and ~20:1 for glass fiber). This discrepancy is likely a result of larger DNA fragments (greater than ~250 kbp) from the non-target DNA being too large to flow through the small pore features of the membranes. This size-exclusion effect is expected to be more severe in nitrocellulose than in glass fiber due to the differences in pore size distribution between the two membranes. This would suggest that some non-target DNA is essentially filtered upstream of the chitosan capture region rendering it unavailable to compete for binding. The data in Figure 5 support this assumption because at large non-target:target ratios of 200:1, there is a greater reduction in recovery for glass fiber than in nitrocellulose. At higher ratios, 500:1, the reduction in target DNA recovery is similar in both membranes. Recovery of target DNA in glass fiber with an extreme non-target:target ratio of 1000:1 was higher than expected.

The addition of mucins, to mimic nasal swab samples, reduced recovery of target DNA in glass fiber but not in nitrocellulose. Mucins are large protein aggregates (mass > 10⁶ Da) that are glycosylated with oligosaccharides that commonly form negatively charged side groups²⁴². These negatively charged molecules can interact with positively charged chitosan, blocking the binding of DNA. These large aggregates may not pass through the small pores of nitrocellulose because DNA recovery is not affected by their presence in the sample. In glass fiber, however, the larger pores may allow these negatively charged aggregates to flow downstream and prevent DNA binding to chitosan, leading to reduced recovery as the concentration of mucins increases. When both mucins and non-target DNA is present in samples (from simulated nasal matrix, SNM), DNA recovery remains high in nitrocellulose and decreases in glass fiber. Once again, the magnitude of this decrease is correlated to increasing concentrations of mucins. For applications containing mucins or high concentrations of non-target DNA, the chitosan-patterned region can be extended to increase the system's overall capacity.

DNA purification from blood samples

Blood preparation procedures often require many user steps to remove blood components that can inhibit downstream amplification reactions, notably heme²⁴³. The chitosan-based DNA purification system is able to rapidly purify target DNA from blood samples with only one user-step (Fig. S7). The eluted samples were quantified by qPCR without further purification.

In both membranes, samples with lower blood concentrations resulted in higher recovery of DNA (**Fig. 6A**). In nitrocellulose, recovery of target DNA from blood-containing samples was significantly inhibited and the flow rate of the sample through the membrane decreased as blood concentration increased. The reduced flow rate appeared to be a result of membrane clogging. For the sample containing 50% blood in nitrocellulose, only a small volume wicked into the membrane before flow stopped completely.

In glass fiber membranes, target DNA was purified from samples containing up to 50% whole blood but, as blood concentration increased, DNA recovery decreased. To verify this result, 50 μ L of whole blood plus target DNA was diluted into increasing volumes of buffer. As blood concentration decreased, DNA recovery increased (**Fig. 6B**).

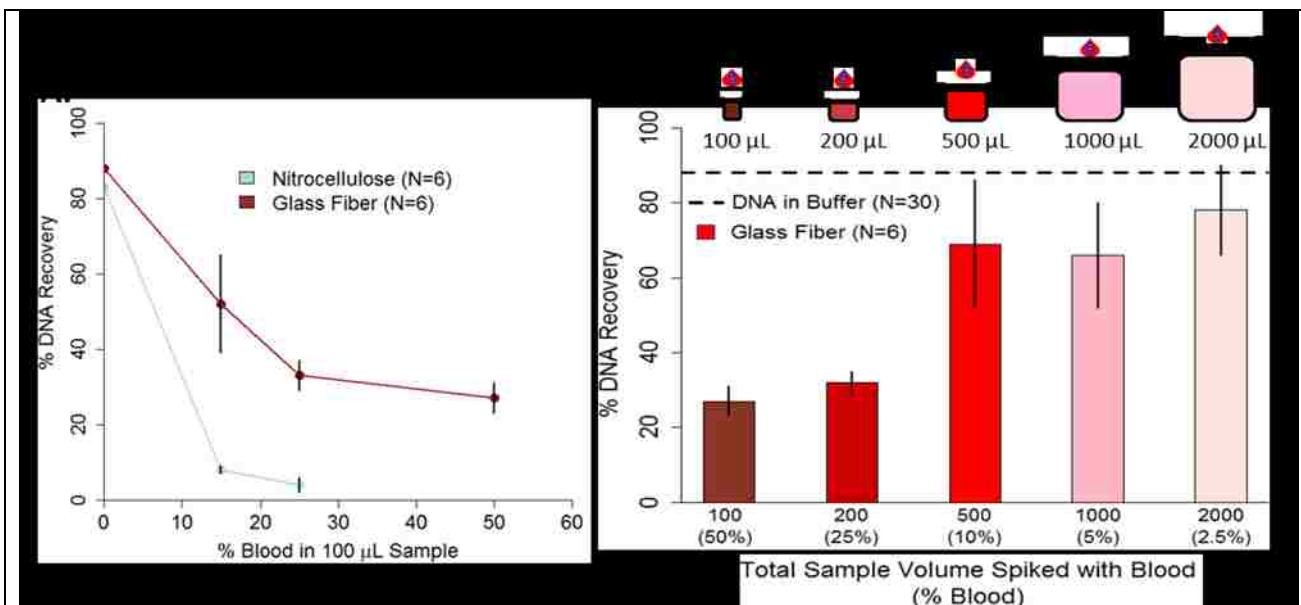


Figure 118: DNA purification in porous membranes from samples containing blood. The average of N=6 is reported with error bars representing +/- one standard deviation. Chitosan concentration at the capture line was $1.3 \times 10^{-9} \mu\text{g}/\mu\text{m}^2$ for nitrocellulose and $1.8 \times 10^{-9} \mu\text{g}/\mu\text{m}^2$ for glass fiber. Input DNA was between 1×10^5 and 1×10^6 copies of MSSA DNA. A) Increasing the percent of blood in a 100 μL sample reduced recovery in both nitrocellulose and glass fiber. The 50% blood sample in NC clogged the membrane preventing flow and therefore DNA purification. B) Diluting 50 μL of blood into increasingly large sample volumes improved recovery in glass fiber. For volumes larger than 200 μL , the recovery was similar to the “DNA in buffer” control.

For samples that were less than 25% blood, DNA purification efficiency is similar to the “DNA in buffer” control. This restored recovery is likely due to increased washing of the chitosan region to remove blood components that interfere with chitosan/DNA binding and not with the qPCR analysis. Based on the dilution factor of DNA eluted from chitosan in glass fiber (Fig. S5C) and the sample volume used for qPCR (1 μL of the elution), the maximum amount of blood in a qPCR reaction would be less than 0.5%. For whole blood concentrations at or below 0.5%, qPCR is not inhibited (Fig S3B).

Conclusions

Here we have demonstrated the first example of a system for the simultaneous purification and concentration of DNA from complex samples using chitosan and constructed entirely from porous membranes. First, the interaction of two porous membrane substrates with chitosan was characterized and a method to determine the adsorption capacity of these membranes for polymers was described. Next, to exhibit the broad applicability of this system, it was used to purify DNA from complex samples including those with high protein content, non-target DNA, and known amplification inhibitors such as blood. These samples are just a few examples of potential inputs that can be handled by this system. The choice of membrane provides the ability to control the sample processing time, volume, and concentration factor. Thus, large volume samples such as urine or contaminated environmental water could be rapidly processed with this system at the POC. This method can directly integrate with other paper-based point-of-care technologies such as in-membrane amplification¹⁴¹ and detection. Further, this system is

already well-suited for untrained end users via the use of automatic sequential reagent delivery^{139,229}. Future work will therefore demonstrate sample-to-result integrated systems that can rapidly and automatically process high input sample volumes in porous membranes.

Acknowledgements

This work was supported by a grant to Paul Yager from the Defense Advanced Research Projects Agency (DARPA) “Multiplexable Autonomous Disposable for Nucleic Acid Amplification Tests for LRSs” under Grant No. HR0011-11-2-0007.

We thank our colleagues Paula Ladd, Ryan Gallagher, and Erin Heiniger in the Yager Laboratory who provided valuable discussion and feedback on experimental design and analysis. We thank collaborators Barry Lutz and Nuttada Panpradist in the Lutz Laboratory at the University of Washington for providing useful discussions and materials for simulated nasal matrix. We thank collaborators Nicolaas Vermeulen and Boris Alabyev from ELITechGroup Molecular Diagnostics (previously Epoch Biosciences) for assistance with the supply of the qPCR assay and simulated nasal matrix. We thank collaborators David Moore, Cathryn Olsen, and Bing Li from GE Global Research for providing the porous materials and support on membrane selection. We thank our colleagues and members of the Yager Lab and Lutz Lab at the University of Washington. SEM imaging and sputter coating work was performed at the University of Washington Nanotech User Facility (NTUF), a member of the NSF-sponsored National Nanotechnology Infrastructure Network (NNIN).

9. Electrochemical cell lysis using a portable audio device: enabling challenging sample preparation at the point of care (Buser *et al.* *LOC*, 2015)

J. R. Buser, A. Wollen, E. K. Heiniger, S. Byrnes, P. C. Kauffman, P. D. Ladd, and P. Yager, *Lab Chip*, 2015, **15**, 1994–97.

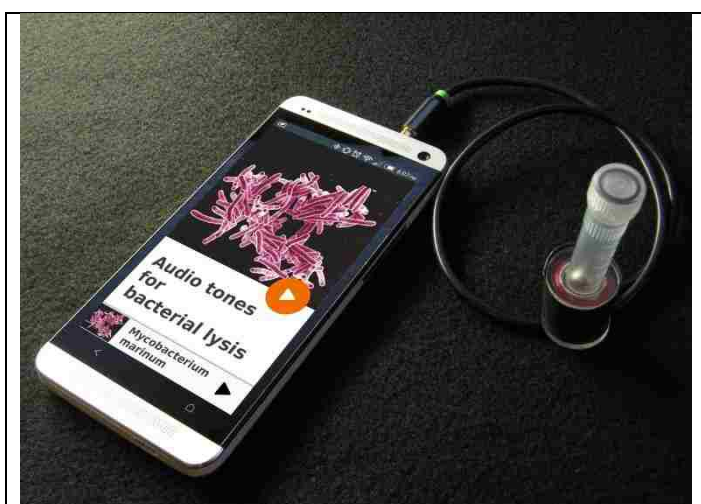


Figure 119: AudioLyse device. The headphone jack of a portable audio device (e.g. cell phone) excites an electromagnetic coil, spinning a magnet inside of a tube

containing sample to be lysed. This spinning magnet causes pathogen cell rupture and consequent nucleic acid release.

Audio sources are ubiquitously available on portable electronic devices, including cell phones.

Here we demonstrate lysis of *Mycobacterium marinum* and *Staphylococcus epidermidis* bacteria utilizing a portable audio device coupled with a simple and inexpensive electromagnetic coil. The resulting alternating magnetic field rotates a magnet in a tube with the sample and glass beads, lysing the cells and enabling sample preparation for these bacteria anywhere there is a cell phone, mp3 player, laptop, or other device with a headphone jack.

Background

Diagnosis is the first hurdle in disease management, expediting appropriate treatment in developed settings where sophisticated equipment and trained personnel are available. For example, in the US *in-vitro* diagnostic procedures represent about 1.6% of Medicare spending, yet influence 60-70% of medical decisions⁴⁵¹. Nucleic acid amplification tests (NAATs) performed in the laboratory represent the pinnacle of sensitive and specific pathogen detection. Unfortunately, this state of the art is also expensive and complex, requiring infrastructure and instrumentation not available in all settings.

The lack of adequate diagnostics is especially troublesome in the case of tuberculosis (TB), which infects 1/3 of the world's population according to the WHO⁴⁵². Sixty percent of TB patients only have access to the peripheral level of the health system, where no suitable TB diagnostics exist⁴³³. Conventional TB diagnostics in lower-resource settings, mainly sputum smear microscopy and cell culture, lack the ideal specificity and timeliness. Also, required equipment isn't always available⁴³³. Microfluidic platforms have shown promise to enable the type of point-of-care devices that could bring NAATs directly to patients in lower resource settings, but sample preparation remains the weak link in microfluidics-based bioassays⁵⁸.

Existing microfluidic systems such as the Cepheid GeneXpert, consisting of sophisticated instrumentation into which a disposable cartridge containing the assay reagents is inserted, are capable of sample-to-result nucleic acid testing within two hours. While the GeneXpert has been shown to expedite TB treatment⁴³², due to cost and infrastructure requirements it remains primarily a solution for centralized laboratories. Therefore, further advances are needed in point-of-care sample preparation compatible with low resource settings and downstream NAATs.

Cell phones have provided a new tool used to interpret and communicate health data. In addition to telemedicine applications, cell phones have shown utility for applications including interpretation of diagnostic tests^{453,454}, impedance measurements in microfluidic devices⁴⁵⁵, and digitizing information originally recorded on paper forms⁴⁵⁶. If cell phones could also assist in sample preparation, NAATs may become more feasible to perform completely free of laboratory equipment.

If a low-cost point-of-care NAAT were available, not only could disease diagnostics be performed more rapidly, but also water and food safety could be evaluated quickly and inexpensively. The development of isothermal NAATs, such as loop-mediated amplification (LAMP) and recombinase polymerase amplification, is a large step towards enabling simpler devices. These isothermal assays do not require precision thermal cycling, can be more robust against inhibitors than polymerase chain reaction (PCR)⁴⁵⁷, and are compatible with paper-based microfluidics⁶. Low-cost precision isothermal heaters have been demonstrated that could enable point-of-care application of this type of assay⁶⁵⁻⁶⁷.

Unfortunately, many low-cost point-of-care NAAT devices still rely on off-chip, instrumented sample preparation steps⁵⁸. Mechanical lysis methods, such as bead beating, are desirable in that one can avoid the need to purify the sample from a chemical lytic agent before the downstream bioassay, but these methods traditionally suffer from relatively complex, user- and power-intensive instruments and protocols⁴⁵⁸.

Many mechanical means of cell rupture have been demonstrated in the literature. Reports exist back to at least the 1960s of bacterial rupture due to compressive forces, Hughes *et al.* describe a press which crushes *Mycobacterium* with repeated hammer blows⁴⁵⁹. Cavitation, often induced *via* sonication, can also cause bacterial rupture⁴⁶⁰. In addition, other literature has demonstrated methodologies which rely on fluid shear to disrupt samples⁴⁶¹. Lange *et al.*⁴⁶² showed a lower threshold of 1,800 Pa fluid shear for *Escherichia coli* cell disruption. According to Seltmann⁴⁶³, the intact cell wall of gram-negative bacteria ruptures at ~5 atm compression, whereas gram-positive bacteria require up to 50 atm compression. The difference in mechanical thresholds of cell rupture between gram-positive and gram-negative bacteria can be explained by differences in the peptidoglycan layer of the cell wall.

A three-dimensional peptidoglycan network encapsulates the cell, and is largely accountable for the strength and rigidity of bacterial cell walls. The gram-positive cell wall is 15-30 nm thick, with the major component being highly-cross-linked peptidoglycan, which accounts for over 50% of the dry weight of the membrane. Gram-negative bacteria have an approximate monomolecular layer of peptidoglycan, whereas gram-positive bacteria have peptidoglycan which is several layers thick. In addition to thickness differences between gram-negative and -positive bacteria, differences in the degree of crosslinking can also have mechanical consequences. In *E. coli*, about 50% of the peptidoglycan is crosslinked, which is considered relatively uncrosslinked. In some bacteria, up to 90% of the peptidoglycan is crosslinked. Crosslinking in gram-negative bacteria is usually non-covalent. Covalent crosslinking is usually observed for gram-positive. These differences in peptidoglycan layer, shown in Figure 120 below, result in gram-negative bacteria usually rupturing easier than gram-positive bacteria.

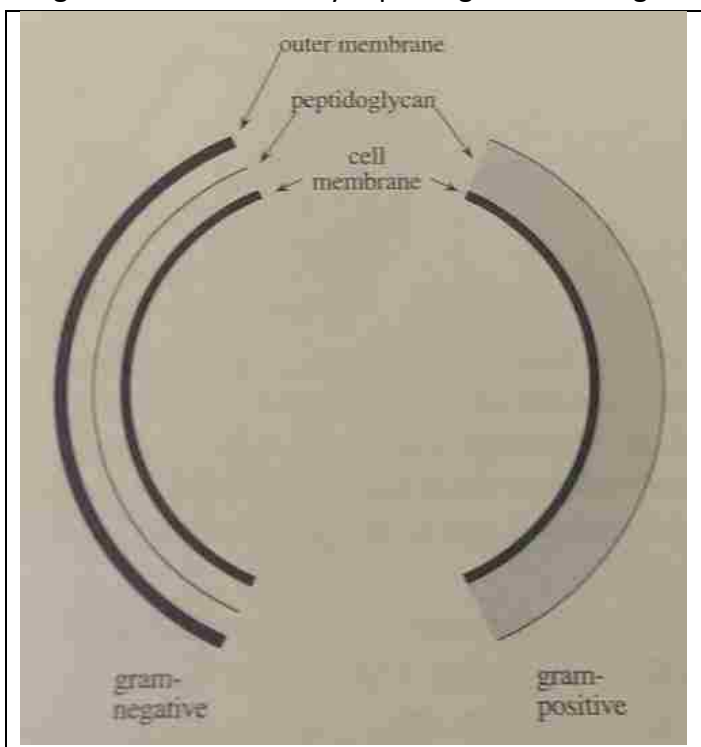


Figure 120: Gram negative and gram-positive cell walls. Gram-positive cells have a much thicker peptidoglycan layer, resulting in greater mechanical resilience.

Here we demonstrate lysis of two gram-positive bacteria—*Staphylococcus epidermidis* and a more difficult target *Mycobacterium marinum*—using a new form of highly portable, low-power, mechanical cell lysis. The choice of these bacteria

is intentional, as analogues for important clinical targets: methicillin-resistant *Staphylococcus aureus* (MRSA) and *Mycobacterium tuberculosis*, respectively. Like other mechanical approaches, it does not introduce reagents incompatible with nucleic acid amplification. We believe this new apparatus could enable point-of-care NAATs for a wide range of organisms. At least one other group has demonstrated a low-cost mechanical lysis method amenable to POC diagnostics⁴⁶⁴. What sets our device apart is that it is free from a device-specific power source: adequate power can be provided by the readily-available portable audio device signal. If one is already using a smartphone to quantify assay readout, the headphone jack of this same phone could power the sample preparation step. With the recent increase in the use of diagnostic interpretation aided by cell phones³⁸, which are fairly ubiquitous worldwide⁴⁵⁴, this type of device may help close the loop in sensitive and specific pathogen detection in low resource settings. Here we show that the headphone jack of a low-cost mp3 player provides adequate power for this lysis methodology. The resulting DNA accessible for amplification after audio-powered lysis is compared to bead beating as a gold standard.

Material and methods

Bacterial culture

Staphylococcus epidermidis (strain Fussel ATCC 14990) was cultured in Tryptic Soy Broth (BD Bacto, Sparks, MD, USA) at 37°C, shaking (250 rpm). Overnight cultures were diluted 1:100 in fresh medium and grown to mid-log phase ($OD_{600} = \sim 2$). *Mycobacterium marinum* (Aronson ATCC 927) was cultured in Middlebrook 7H9 broth with ADC enrichment (BD Difco, Sparks, MD, USA) at 30°C, shaking (250 rpm) for 4-7 days. Cultures were diluted 1:100 in fresh medium and grown for 48 hours to mid-log phase ($OD_{600} = \sim 1$). After growth, cells were pelleted and resuspended in 1 volume Tris-EDTA (TE: 10 mM Tris-HCl, 1 mM EDTA, pH 8.0:Sigma-Aldrich, St Louis, MO, USA) buffer. Cells dilutions were also done in TE.

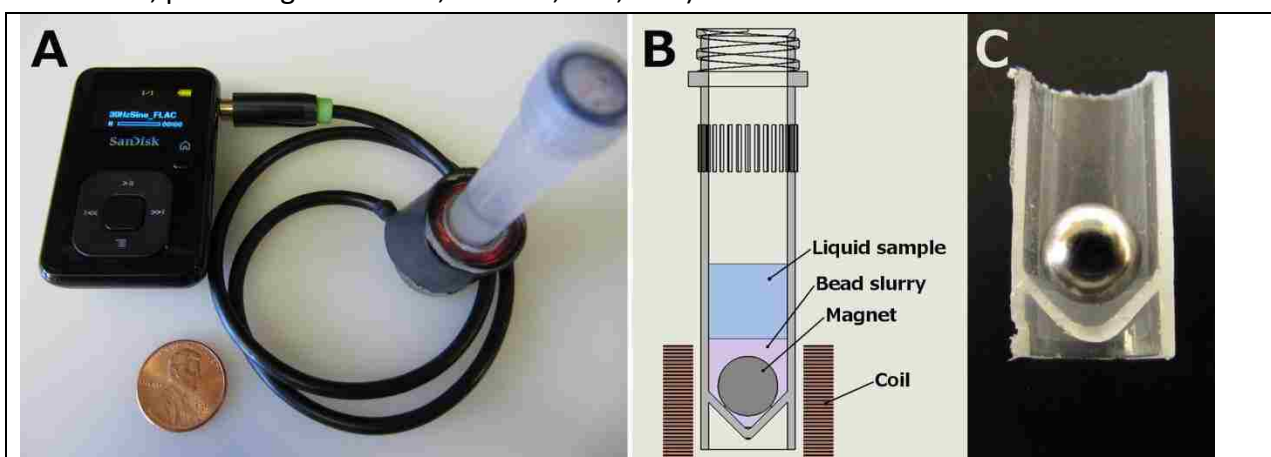


Figure 121: Overview of portable audio-powered electromagnetic cell lysis device. A: Sansa Clip mp3 player provides a 30 Hz sine wave signal to the coil using the headphone jack, US penny for scale. B: Schematic of tube showing user-added sample along with pre-loaded magnet and

beads. C: Sectioned tube with magnet. The spherical magnet rides on the lower angled tube walls when the tube is vertically oriented. When provided an alternating magnetic field by the coil, the magnet rotates against the beads and the tube walls.

Audio-powered lysis

Device layout is highlighted in Figure 121. Coil bobbins were constructed from a hacksaw-excised well from a 24-well plate adhered to laser-cut acrylic upper and lower disks. The bobbin was wound with 490 turns of 32 AWG magnet wire, for a DC resistance of 11.4 ohms. The wound coil was soldered to a 1/8" stereo cable combining the left and right channels. The assembly was then wrapped with two turns of electrical tape around the circumference. Screw-top 2 mL O-ring tubes (02-682-558, Thermo Fisher Scientific, Waltham, MA, USA) were loaded with 100 μ m glass beads (9830, Research Products International Corp., Mt. Prospect, IL, USA) and a ¼ inch NdFeB magnet (S4, K&J Magnetics, Inc., Pipersville, PA, USA). Sample was then added to the tubes, and the tubes loaded into the coils. The sample volumes tested were 800 μ L, to match the bead beater protocol, along with 500 and 300 μ L. A 30 Hz sine wave FLAC audio file was generated using Audacity 2.0.5[†], and was played on the mp3 player (Sansa Clip+ 4 GB, SanDisk, Milpitas, CA, USA) at full volume with the equalizer set to maximize bass frequency response.

Bead Beater

800 μ L samples were added to 2 mL O-ring screw top tubes (Fisher 02-682-558) with 800 mg of the 100 μ m glass beads (9830, Research Products International Corp., Mt. Prospect, IL, USA). Tubes were loaded into the bead beater (Mini-Beadbeater-8, Biospec Products, Inc., Bartlesville, OK, USA), set to "homogenize", and run for (3) 1-minute cycles with a 1 minute pause between cycles.

qPCR

To quantify DNA recovery for *S. epidermidis*, qPCR was performed using primers designed against the *htrA* gene (FWD: 5'-GAG CGC ATA AGA CGT GAG AA-3', REV: 5'-TCT TCT TGT GTC AGC TTC TCT ATT-3'), and using Bioline SensiFAST SYBR No-ROX qPCR kit (Bioline USA Inc., Taunton, MA, USA). Samples (1 μ L) from the bead beater or audio-powered lysis were used in 20 μ L qPCR reactions run on a real-time PCR instrument (Rotor-Gene Q, Qiagen, Valencia, CA, USA) using: 95°C (3 min), 40 cycles of 95°C (5 sec), 54°C (10 sec), and 72°C (15 sec). Fluorescence data were collected during the 72°C step using the green channel. To quantify DNA recovery for *M. marinum*, qPCR was performed using the assay described by Jacobs et al., substituting the SensiFAST Probe No-ROX qPCR kit (Bioline USA Inc., Taunton, MA, USA) for the master mix used previously⁴⁶⁵. Samples were amplified as follows on a real-time PCR instrument (CFX96 Touch, Bio-Rad, Hercules, CA, USA): 95°C (5 min), followed by 40 cycles of 90°C (10 sec) and 60°C (20 sec). Fluorescence data were collected during the 60°C step using the green channel. Genomic DNA copy numbers were determined relative to standard curve analysis using purified DNA of known copy number using either the Rotor-Gene or Bio-Rad CFX software. Both assays are sensitive down to ~10 copies of the target sequence.

Statistics

A student t-test was performed on bead mass data (Figure 126A) and *M. marinum* data (Figure 127) in Excel (Microsoft, Redmond, WA, USA) for a single-tailed comparison assuming the data is homoscedastic. The 200 & 400 mg bead masses were grouped and compared separately to the 0 & 100 mg and 800 mg groups for both the 300 and 800 μL sample sizes.

Exploration of AudioLyse cell disruption mechanism

As mentioned earlier in this section, multiple types of mechanical perturbations have been shown to rupture bacterial cells. To explore the mechanism of cell rupture in the AudioLyse, calculations and experiments were performed to examine the effects of fluid shear, fluid pressure, and fluid mixing.

Fluid shear-driven rupture

Lange *et al.*⁴⁶² showed a lower threshold of 1,800 Pa fluid shear for *Escherichia coli* cell disruption. *E. coli* is a comparatively fragile gram-negative bacterium, gram-positive bacteria may need higher shear for cell disruption and nucleic acid release. To estimate the fluid shear present in the AudioLyse, some simplifying assumptions will be made: 1) a minimum gap of 100 μm (one bead diameter) between moving surfaces, 2) magnet rotation of 30 Hz, with no x-y translation, 3) no slip at contacting surfaces. The beads translate in the direction of magnet rotation at half of the surface velocity of the magnet, assuming no slip at the magnet/bead and bead/tube wall interfaces. The fluid shear stress is calculated for the region between the magnet surface and the tube wall, near the glass beads separating the magnet from the tube wall. This region is approximated as Couette flow, with the fluid thickness approximated as the bead diameter. A schematic showing the simplified geometry is shown in Figure 122.

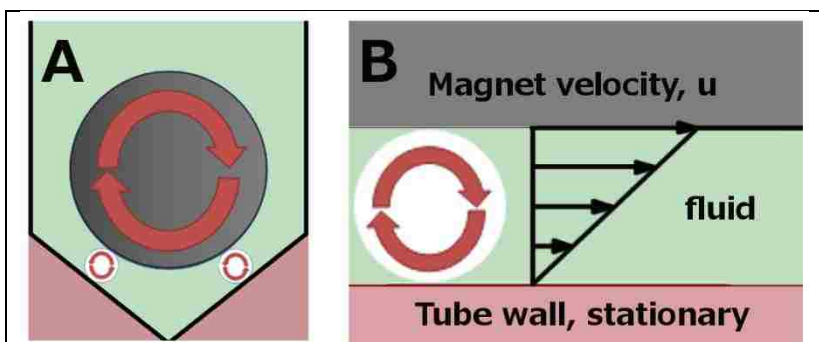


Figure 122: Schematic of geometry used for simplified fluid shear calculation, which is a 2D cross section through the center of the tube. A: The magnet (gray circle) is spaced from the angled tube walls by a 100 μm glass bead (white circles). The beads translate in the direction of rotation at half the surface velocity of the magnet assuming the magnet does not slip against the beads, and the beads do not slip against the tube wall. B: Couette flow, approximating bead and tube wall surface as parallel plates. In a Newtonian fluid, a linear velocity profile will be observed.

Calculating magnet surface velocity in this simplified system:

Magnet surface velocity (u):

$$u = \text{Magnet circumference} \times \text{frequency} = \pi \times 0.25 \text{ [in]} \times 25.4 \left[\frac{\text{mm}}{\text{in}} \right] \times 30 \text{ [Hz]} = 598 \left[\frac{\text{mm}}{\text{s}} \right]$$

Fluid shear rate (γ):

$$\text{Fluid shear rate } \gamma = \frac{u}{h} = \frac{0.6 \left[\frac{\text{m}}{\text{s}} \right]}{1E-4 \text{ [m]}} = 6000 \left[\frac{1}{\text{s}} \right]$$

Fluid shear stress (τ):

$$\tau = \text{Shear rate} \times \text{viscosity} = \gamma \mu = 6000 \left[\frac{1}{\text{s}} \right] \times 1E-3 \text{ [Pa s]} = 6 \text{ [Pa]}$$

By these assumptions and calculations, fluid shear rate is over two orders of magnitude lower than the reported 1,800 Pa necessary to rupture gram-negative *E. coli* cells. Hardier bacteria such as gram-positive *Staphylococcus aureus* and *Mycobacterium marinum*, successfully disrupted in our experiments by the AudioLyse, will likely require higher shear stress than *E. coli* for disruption, and seem unlikely to be disrupted *via* this mechanism.

Pressure-driven rupture

According to Seltmann⁴⁶³, the intact cell wall of gram-negative bacteria ruptures at ~5 atm compression, whereas gram-positive bacteria require up to 50 atm compression. To estimate the compressive pressure exerted on bacteria in the AudioLyse device, a simplified system is described. First, the downward force of the magnet (F_{magnet}) is estimated by subtracting the buoyant force (F_{buoyancy}) from the gravitational force (F_{gravity}). For the purposes of this estimation, the density of the glass bead/water slurry displaced by the magnet will be estimated as 1,800 kg/m³ (common glass is 2,400-2,800 kg/m³, water is 998 kg/m³ @ 20°C). The magnet volume is $\frac{4}{3}\pi r^3 = 1.3 \times 10^{-7} \text{ m}^3$. The buoyant force exerted on the magnet is then:

$$F_{\text{buoyancy}} = \rho_f V_{\text{disp}} g = 1,800 \left[\frac{\text{kg}}{\text{m}^3} \right] 1.3E-7 \text{ [m}^3\text{]} 9.81 \left[\frac{\text{m}}{\text{s}^2} \right] = 0.0024 \text{ [N]}$$

And the downward force of the magnet is:

$$F_{\text{magnet}} = F_{\text{gravity}} - F_{\text{buoyancy}} = 9.8 \left[\frac{\text{m}}{\text{s}^2} \right] 0.001 \text{ [kg]} - 0.0024 \text{ [N]} = 0.0074 \text{ [N]}$$

Assuming a packing density of 90% of beads (hexagonal packing) on the lower half of the magnet, ~6,500 beads would cover the bottom half of the magnet. For simplification, the projected area of the sphere will be used to estimate the amount of compressive pressure applied to the bacteria. Each bacterium is estimated to be 1 x 2 μm , with a cross sectional area of $2 \times 10^{-12} \text{ m}^2$. If each of the 6,500 beads were resting on a $2 \times 10^{-12} \text{ m}^2$ bacterium, this would result in a compressive pressure of:

$$\frac{0.0074 \text{ [N]}}{6,500 \times 2E-12 \text{ [m}^2\text{]}} = 0.6 \text{ [MPa]}$$

Based on the 5 and 50 atm (0.5 and 5 MPa) rupture pressures for gram negative and positive bacteria reported by Seltmann, this estimation predicts that the static weight of the magnet alone is enough to rupture gram-negative bacteria. Given the conservative nature of the estimation of packing density, and load-bearing contact area, and zero x-y translation, it would not be surprising if the compressive forces present in the actual device were sufficient to rupture gram-positive bacteria.

Based on the fluid shear and compression estimations, crushing of the bacteria seems more likely in the AudioLyse than shear-driven rupture. This hypothesis will be tested *via* experiments where shear effects and compression effects are somewhat isolated.

Hydrodynamic pressure

Sonication techniques cause cavitation, and consequently cell rupture⁴⁶⁰. Other studies have shown that a system with similarities to the AudioLyse can achieve negative pressure-induced cavitation near a rolling sphere submerged in a viscous liquid⁴⁶⁶. If cavitation were present in the AudioLyse, it could be an additional cell rupture mechanism. For a first-pass exploration of the pressures present within the AudioLyse tube during operation, a two-dimensional cross section (similar to a journal bearing, Figure 123 below) will be used. For now, any bouncing of the magnet will be ignored. Journal bearings are used to support rotating radial loads, usually consisting of two cylinders. The outer cylinder, called the bearing, is the negative space into which the inner cylinder, called the journal, is inserted. There is some clearance between the journal and bearing, which normally contains a liquid such as oil.

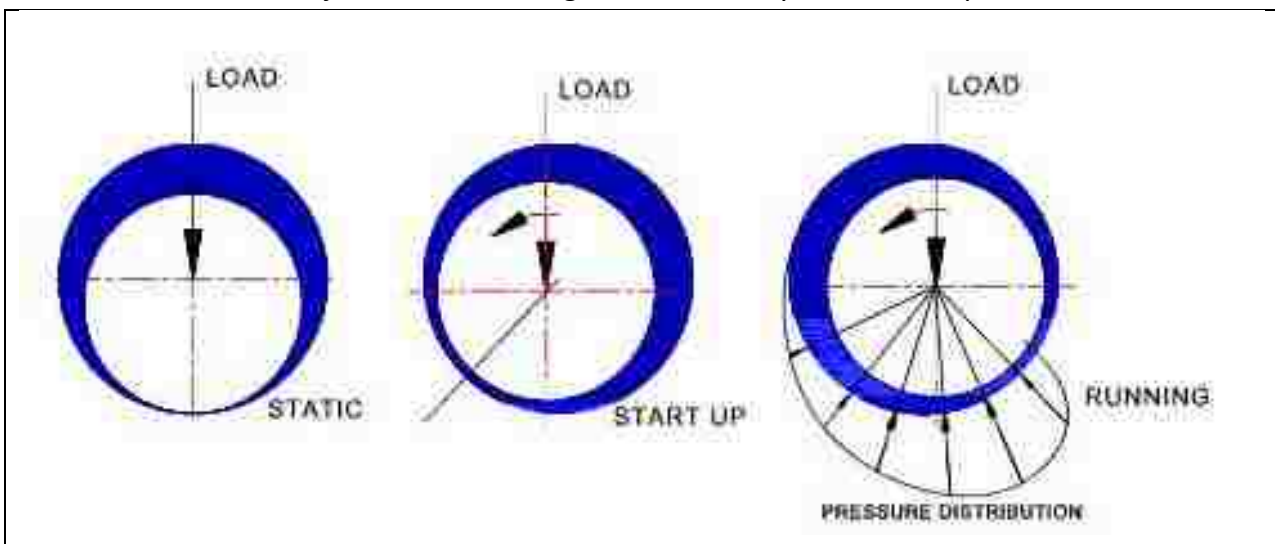
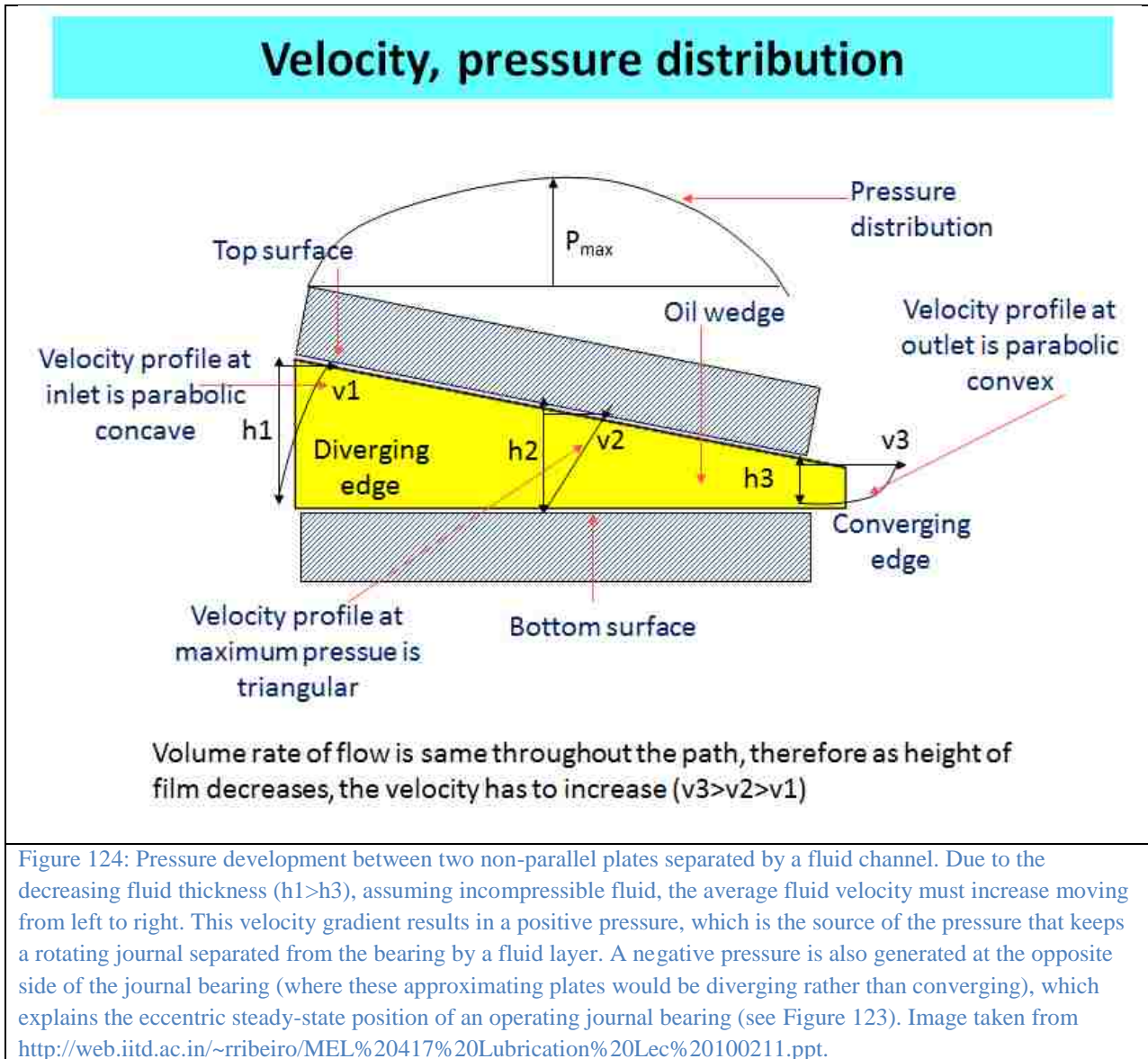


Figure 123: Journal bearing operational modes. Left: Static condition, journal is not rotating. Here, the surfaces of the journal and bearing are in contact. Center: Start up condition, boundary lubrication. Here, the fluid conditions may not allow for fluid pressures sufficient to separate the surfaces of the journal and bearing. Right: Running condition. Journal is supported by hydrodynamic fluid pressure, friction is reduced, and there is no surface-to-surface contact between the journal and the bearing. Figure from <http://www.brighthubengineering.com/manufacturing-technology/73568-hydrostatic-lubrication>

Similar generic operational modes to those shown in Figure 123 above are observed with the AudioLyse: the magnet at rest is centered at bottom of the tube. When an alternating magnetic field is applied, the static friction must be overcome to begin rotation. Once the magnet begins rotation it rotates at a constant velocity corresponding to the excitation frequency of the coil, confirmed using the back EMF of the coil generated due to the magnet rotating in the stationary coil⁴⁶⁷. To estimate the hydrodynamic pressure distribution in the AudioLyse, the mechanism of pressure generation in a journal bearing will be explored.

The journal and bearing are two solid surfaces separated by a fluid layer. To understand how this fluid layer opposes a radial load, Couette flow between two plates will be considered first (see Figure 122B). Here, the top plate is moving to the left, and the bottom plate is stationary. If a vertical load were

applied to the moving top plate, while the stationary bottom plate was held fixed, the top plate would move down, as no force opposes the downward force for parallel plates. If the plates are not parallel, however, fluid velocity gradients will cause pressure to be developed, shown in Figure 124 below.



Testing compression vs shear rupture via experimentation

To test the hypothesis that compressive forces are the primary mechanism of bacterial cell disruption, an experiment was designed to compare fluid shear effects and compressive force effects. The two experimental conditions are outlined below.

Isolated fluid shear effects: AudioLyse standard conditions with the magnet but minus beads. The hypothesized bacterial crushing zones at the bead/wall and magnet/bead interfaces have been removed in this experiment.

Isolated compressive force effects: AudioLyse conditions (including beads and magnet) attached horizontally to a rocking plate. The hypothesized high shear zone between the magnet and tube wall has been removed in this experiment.

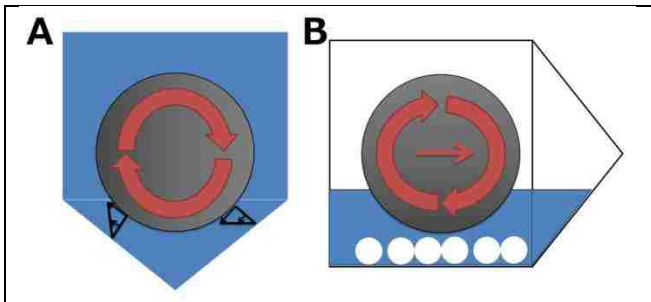


Figure 125: Comparing cell disruption due to fluid shear and compressive force. A: Schematic for experimental condition with exaggerated fluid shear effects. Without the beads, the magnet is expected to ride at the same level or lower in the tube, resulting in similar or higher fluid shear stress between the magnet and tube wall. B: Schematic for experimental condition with exaggerated compressive force. Tube is mounted horizontally on a rocking plate, which causes the magnet to roll back and forth. The fluid level is lower in the tube, resulting in less buoyant force on the magnet and higher magnet/bead, bead/wall, or magnet/wall compressive forces. The magnet rolls back and forth on the lower wall of the tube, with reduced fluid shear compared to standard AudioLyse conditions.

Results and Discussion

Figure 126 shows the dependence of lysis of *S. epidermidis* cells by the portable audio-powered device on bead mass, sample size, and processing time. The majority of amplifiable DNA is released in less than 10 minutes. Both bead and sample volumes were varied as a first-pass optimization for DNA recovery. A mass of 200-400 mg of glass beads achieves higher efficiency than the other bead volume groups ($p < 0.05$) for both 300 and 800 μL samples. Higher viscosities are interesting due to the potential of clinical applications with more viscous sample types, and for exploration of the underlying mechanism of cell rupture. A 30 Hz excitation frequency was found to produce reliable magnet rotation (starting from rest) even in samples as viscous as 50% glycerol (6 centipoise at 20°C, which was the highest viscosity tested).

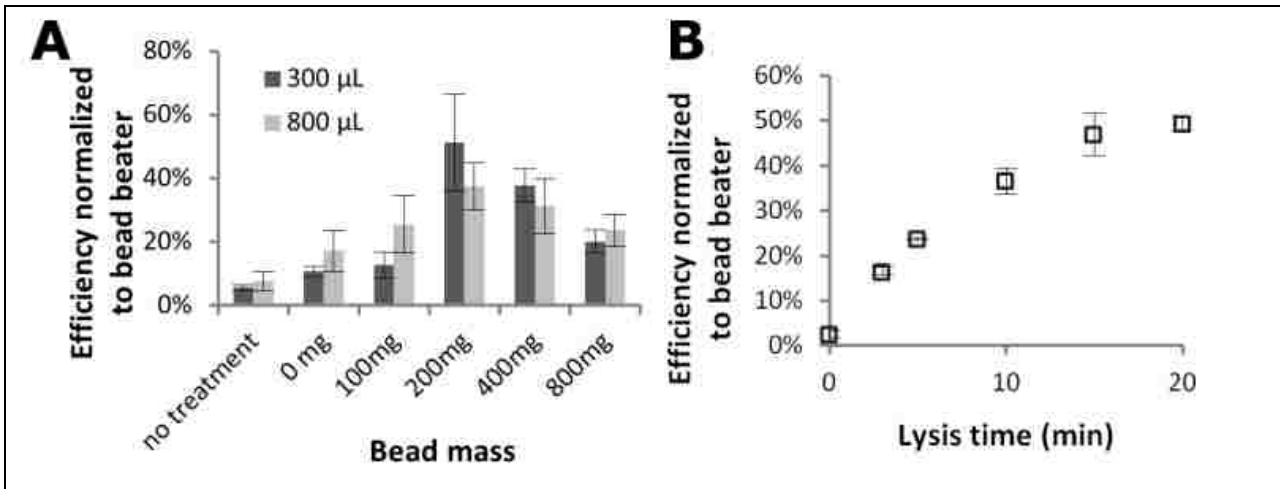


Figure 126: AudioLyse optimization for *Staphylococcus epidermidis*. A: Dependence of lysis efficiency on bead mass for 300 and 800 µL sample sizes. Amplifiable DNA quantified by qPCR, normalized to the bead beater computed copy number (7.1×10^4 copies/mL, 71 copies per PCR). Sample sizes of both 300 and 800 µL perform best with 200-400 mg beads. Data is mean \pm 1 standard deviation, n=3. B: Dependence of audio-powered lysis efficiency for *S. epidermidis* on total lysis time. Amplifiable DNA quantified by qPCR, normalized to the bead beater computed copy number (3.6×10^4 copies/mL, 36 copies per PCR) using a 800 µL sample size and 300 mg beads in the audio-powered device. Efficiency (as compared to bead-beater efficiency) plateaus near 50% at just over 10 minutes for the audio-powered device under these conditions. Data points are mean \pm 1 standard deviation, n=3.

Mycobacterium marinum, a more difficult target to lyse, was chosen for study due to its similarity to the major pathogen *Mycobacterium tuberculosis*. The performance of the audio-powered technique is compared to that of a bench-top bead beater for a range of *M. marinum* concentrations in Figure 127. The audio-powered technique achieves appreciable lysis of *M. marinum* for all concentrations tested, with 10^4 cells/mL corresponding to an estimated maximum of 10 cells being transferred in the 1 µL sample used in the PCR. All non-zero input copy concentrations were significantly higher than the 0 copy experiment ($p < 0.02$), including the 10^4 copy/mL input experiments. Thus, we have demonstrated that the portable audio-powered technique can be used as a sample preparation tool for DNA amplification for both *S. epidermidis* and *M. marinum*.

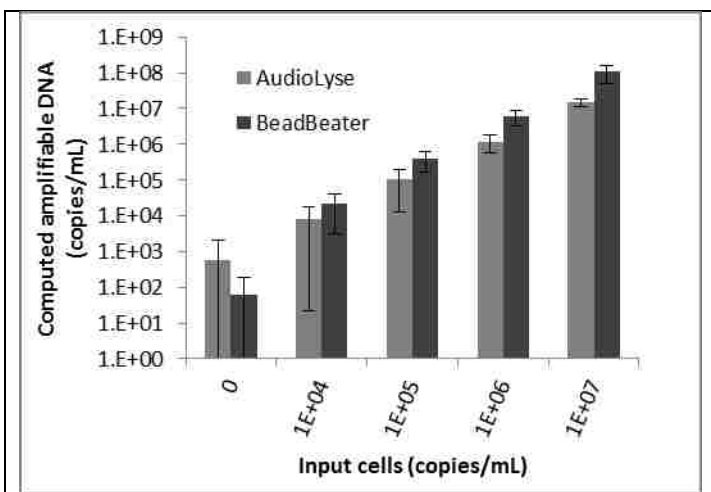


Figure 127: Amplifiable DNA quantified by PCR for varying input concentration of *M. marinum* cells. 500 µL sample size. 10^4 copies/mL corresponds to 10 copies per PCR

quantification. Data points represent mean +/- 1 standard deviation. Minimum n=9 total spread across 3 different days.

Next, the mechanism of cell rupture was explored using the isolated fluid shear and isolated compressive force experiments described above, with results shown in Figure 128. The rolling plate with magnet (exaggerated compressive force, “RP”) condition recovers more DNA than the AudioLyse without beads (exaggerated shear, “ALNM”) condition, suggesting that the compressive forces may be more important than fluid shear for cell disruption in the AudioLyse. The rolling plate without magnet (“RPMN”) condition confirms the magnet is necessary for improved DNA recovery, and the no lysis control (“NL”, stationary tube with no additives) confirms DNA is not made available without processing of some sort.

Cell rupture is necessary for the recovery of DNA. However, it is important that how the lysis technique affects the DNA is understood. Next, we explore at what efficiency DNA injected directly into either the bead beater or AudioLyse can be recovered. For this, *S. aureus* genomic DNA was spiked into a mixture with *M. marinum* cells in the AudioLyse device, bead beater, or rocking plate, and recovery of the *S. aureus* DNA was quantified after processing in the AudioLyse device, with results in Figure 129.

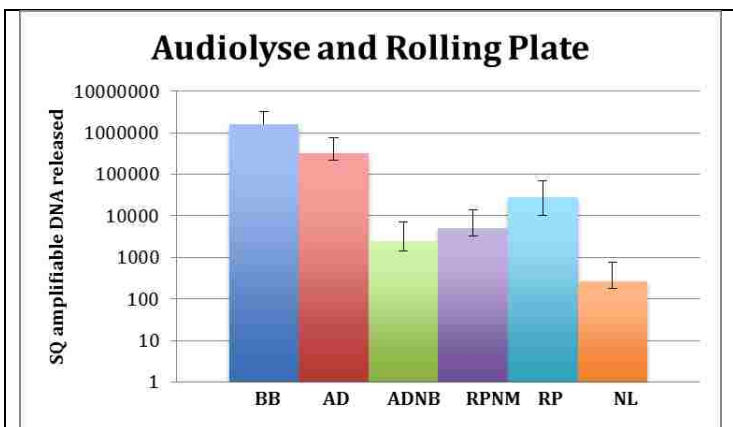


Figure 128: Exploration of lysis mechanism for AudioLyse. DNA recovery efficiency for bead beater (BB), AudioLyse (AD), AudioLyse without beads (ADNBN), rolling plate without magnet (RPNM), rolling plate with magnet (RP), and no lysis (NL). The rolling plate with magnet (RP) outperforms the AudioLyse with no beads (ALNB), suggesting that fluid shear is less important for cell rupture than compressive forces.

Next, the mechanism of cell rupture was explored using the isolated fluid shear and isolated compressive force experiments described above, with results shown in Figure 128.

The rolling plate with magnet (exaggerated compressive force, “RP”) condition recovers more DNA than the AudioLyse without beads (exaggerated shear, “ALNM”) condition, suggesting that the compressive forces may be more important than fluid shear for cell disruption in the AudioLyse. The rolling plate without magnet (“RPMN”) condition confirms the magnet is necessary for improved DNA recovery, and the no lysis control (“NL”, stationary tube with no additives) confirms DNA is not made available without processing of some sort.

Cell rupture is necessary for the recovery of DNA. However, it is important that how the lysis technique affects the DNA is understood. Next, we explore at what efficiency DNA injected directly into either the bead beater or AudioLyse can be recovered. For this, *S. aureus* genomic DNA was spiked into a mixture with *M. marinum* cells in the AudioLyse device, bead beater, or rocking plate, and recovery of the *S. aureus* DNA was quantified after processing in the AudioLyse device, with results in Figure 129.

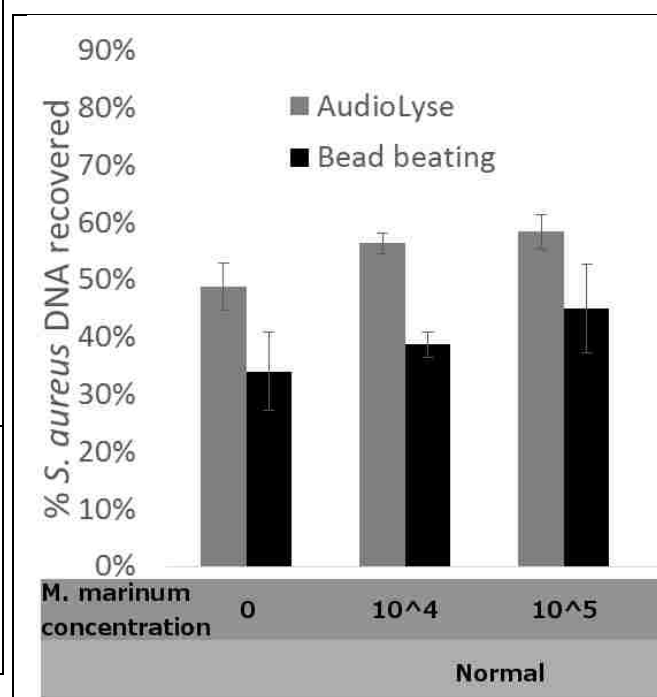


Figure 129: Potential DNA damage in bead beater and AudioLyse. Spiked *S. aureus* DNA recovery in the presence of *M. marinum* cells using AudioLyse, bead beater, and rocking plate techniques. Samples were run under normal AudioLyse and bead beater conditions,

along with rocking plate versions of both. Between 50 and 60% of *S. aureus* genomic DNA was recovered using the AudioLyse across all *M. marinum* cell concentrations, similar to the “AudioLyse” rocking plate experiment (with beads and magnet). Less *S. aureus* genomic DNA was recovered using the normal bead beater conditions, suggesting that the cell rupture mechanism also could hinder the recovery of DNA. Interestingly, more DNA was recovered in the “bead beater” rocking plate experiment (with beads, no magnet), which supports that it is indeed the cell lysis mechanism, not DNA sticking to either the beads or tube walls, that yields reduced DNA recovery.

In Figure 129, it can be seen that higher amounts of *S. aureus* DNA are recovered in normal AudioLyse operating conditions than normal bead beating conditions. The “AudioLyse” rocking plate experiments (with beads and magnet) recover a similar amount of DNA compared to the AudioLyse normal operating conditions. The “bead beater” rocking plate experiments (with beads, without magnet) recover more *S. aureus* DNA than the bead beater normal operating conditions, suggesting that no more than ~20% of the DNA loss is due to DNA sticking to either the glass beads or tube. Additional experiments will be performed which either increase (using centrifugal force) or decrease (by preventing magnet movement in the rocking plate experiments) the compressive effects of the magnet.

Viscosity and fluid density effects on cell rupture/DNA recovery

Using more complex solutions than TE buffer is important for both clinical relevance of a sample preparation technique, and could yield valuable insight into the mechanism of cell disruption. Experiments have shown decreased DNA recovery using the AudioLyse in solutions containing glycerol. Glycerol solutions are both more viscous and more dense (6 cP, 1.13 g/cc for 50% glycerol at 20°C) than water (1 cP, 1 g/cc at 20°C). Figure 130 shows that addition of glycerol differentially affects the AudioLyse method.

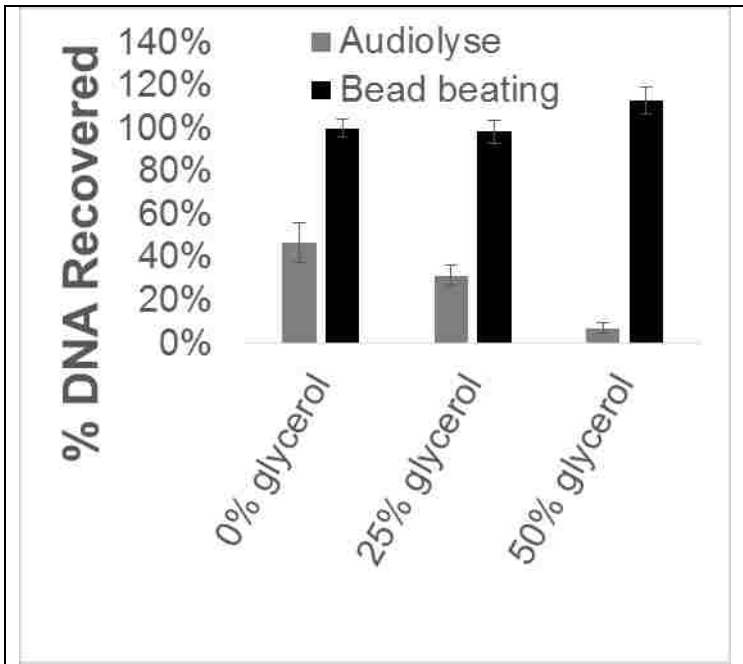


Figure 130: Glycerol affects DNA recovery from MSSA in AudioLyse. Increasing the glycerol concentration results in decreased DNA recovery. The bead beater does not appear to be affected by the higher viscosity and density glycerol solutions. The AudioLyse, on the other hand, shows reduced performance with increasing % glycerol. Results normalized to the bead beater with 0% glycerol.

The glycerol hindering the AudioLyse performance, but not the bead beater performance, suggests that the mechanisms of cell rupture may be different in these techniques. Increases in viscosity could cause the shear stress to vary, while density differences could result in differences in magnet or bead buoyancy. In addition to viscosity and density cell rupture effects, a more viscous fluid could result in different convective flow patterns in the sample tube. This could affect convective mixing, and consequently cell rupture kinetics.

Exploration of convective patterns in AudioLyse

Convective mixing in the AudioLyse is expected to affect opportunities for any given bacterium in the sample to be ruptured. Changes in viscosity and fluid density were found to affect DNA recovery (Figure 130).

This motivates a study in what convective patterns are present in the AudioLyse, and how changes in viscosity and density change the convective patterns.

To visualize fluid convection, glitter (“black licorice”, Martha Stewart Crafts, New York, NY, USA) was added to the sample. When glitter is added to the water/bead solution, it aggregates and sticks to the walls of the tube. In order to use glitter to visualize fluid movement, 0.1% micro90 detergent was used to keep the glitter mobile. An initial experiment, shown in Figure 131 below, examines whether the micro90 affects the superficial movement of the beads, etc. in the operating AudioLyse. It should be noted that the glitter is much larger than bacteria, and may not necessarily move in the same as bacteria in the sample. Glitter was chosen simply as a particle to visualize fluid movement. The glitter used is denser than water, and consequently settles, which may make it non-ideal for fluid movement visualization. Nevertheless, this glitter was used for a first-pass visualization of convective patterns present in the AudioLyse.



Figure 131: Comparing AudioLyse bead slurry movement with (right) and without (left) micro90 surfactant. The only superficial difference apparent in the videos was the presence of the bubbles at the top of the tube with the micro90, present due to vibration while the magnet, beads, micro90 and water were added.

Superficially, the only difference appears to be the formation of bubbles at the top of the solution, and it is not expected that the convective patterns in the fluid will be affected. The following experiments will use micro90 to keep the glitter mobile in the sample for flow visualization.

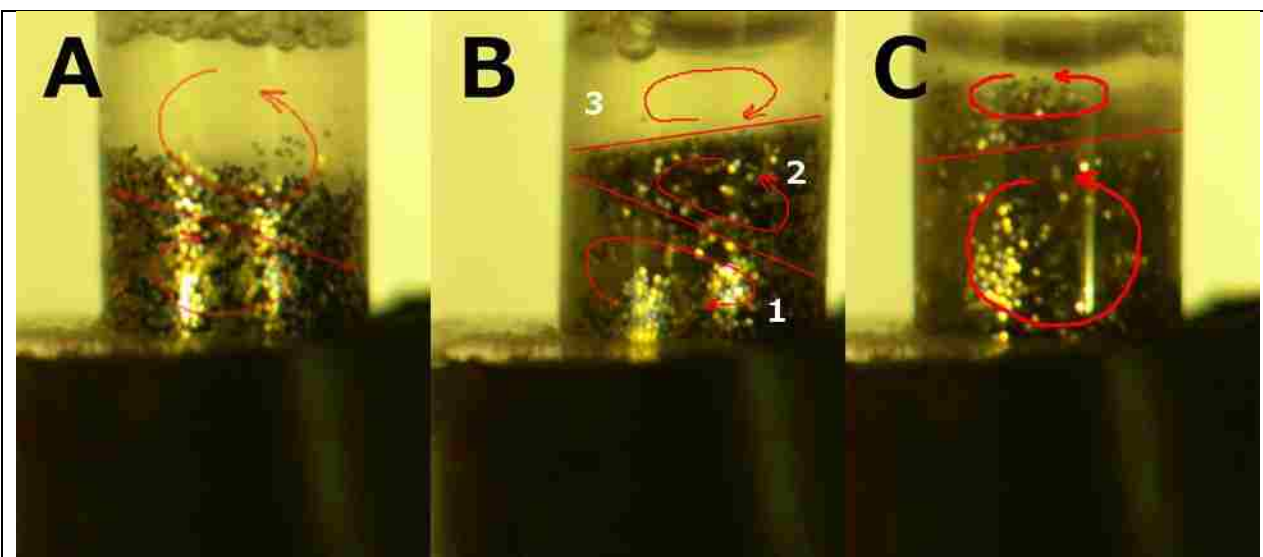


Figure 132: Comparing flow regimes with varied percent glycerol. Tube contains ¼" magnet, 250 mg of 0.1 mm glass beads, deionized H₂O, 0.1% micro 90, glitter, and a variable amount of glycerol. Glitter allows visualization of movement in the largely bead-free upper fluid zone. A: 0% glycerol. Bead slurry geometry and vortex regime in

active device looks similar to without glitter. B: 25% glycerol. An additional fluid compartment seems to appear when glycerol is added: 1) beads+liquid+glitter, 2) liquid+glitter, and 3) liquid. Each fluid compartment appears to have counter-rotating vortices. The bead slurry (compartment 1) seems to ride up higher in the tube compared to 0% glycerol, potentially due to the increased fluid density. C: 50% glycerol. The bead slurry rides even higher in the tube. It is difficult to tell if the liquid-only portion of the fluid volume has a counter-rotating vortex or not, but it appeared in the video to be a part of the glitter+liquid vortex

Modeling hydrodynamic pressure distribution in the AudioLyse

Literature describes⁴⁶⁶ cavitation in a lubrication flow separating a rolling sphere and a boundary. To examine whether the negative pressures necessary for cavitation are present in the AudioLyse, COMSOL is used to create a laminar flow model with a stationary, rotating magnet. For now, the assumption is made that the magnet is separated from the tube wall a distance of 100 μm , the bead diameter. This model was run for 10 seconds to allow the flow to fully develop. No slip conditions were assumed at the side and bottom tube walls. The top fluid/air boundary layer was set to pressure = 0, with no viscous stress. The circular magnet surface was set to 0.589 m/s tangential velocity, corresponding to the 30 Hz $\frac{1}{4}$ " magnet rotation. Fluid properties were set to 8.9×10^{-4} or 3.56×10^{-3} Pa-s viscosity, 1000 kg/m^3 density.

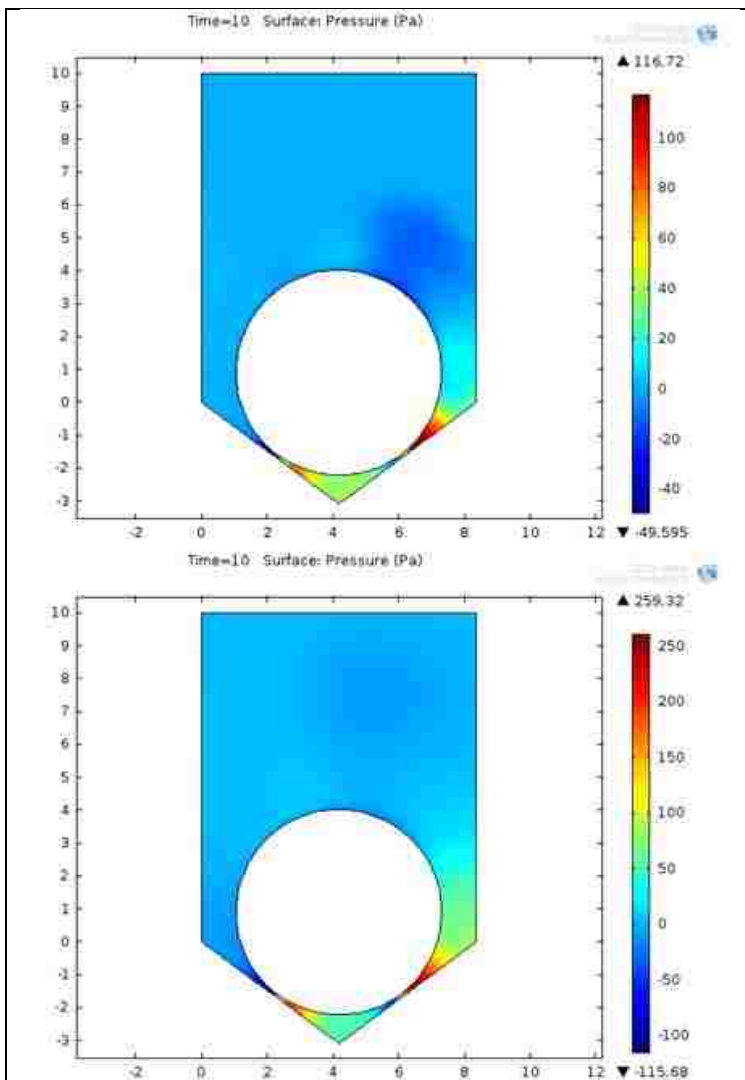


Figure 133: Modeled pressure distribution for top: water and bottom: 4x viscosity. The higher viscosity

fluid has a larger predicted pressure variation, with a maximum of 250 Pa and minimum -100 Pa. The water model predicts ~110 Pa and -45 Pa.

For cavitation resulting from negative hydrostatic pressures to occur, the pressure must drop below the vapor pressure of water. This would require a pressure of 0.1 MPa

below atmospheric pressure⁴⁶⁶. Looking at the pressure maps above, the predicted pressure is three orders of magnitude too small to achieve cavitation due to negative hydrodynamic pressure, assuming a stationary rotating magnet separated 100 μm from the tube wall. This analysis does not predict cavitation due to negative pressures developed by a rotating magnet not traveling in the x- or y-direction, assuming the fluid film thickness is the same as the bead diameter. Further analysis will be required to account for x/y translation of the magnet and impacts with the tube wall and/or beads.

Conclusions

The portable audio-powered device achieves 20-60% of the efficiency of the bench-top bead beater for various concentrations of *M. marinum* and *S. epidermidis*, while costing far less, consuming just a small fraction of the electrical power, emitting far less audible noise, and being highly portable. This decreased lysis efficiency, compared to the bead beater, is balanced by the expansion in applicable settings. Whether this level of performance is sufficient depends on infection levels, sampling technique, and the associated assay sensitivity. Cell phones have expanded communication and medical capabilities in remote settings⁵³. Additionally, portable audio devices have been shown capable of performing impedance measurements in microfluidic devices⁴⁵⁵. Now, in addition to using photo, voice, and text communication to transmit and interpret assay results, audio signals from a headphone jack can be used to power a device capable of retrieval of amplifiable DNA from some of the hardest-to-lyse bacteria in virtually any setting. The power requirements of this method are quite low. The mp3 player output of 1.6 V peak-to-peak when powering a coil with a 12 ohm impedance (11.4 ohms DC, 0.6 ohms inductive at 30 Hz) results in a power draw of 107 mW; ten minutes of lysis with this coil would account for just 0.18% of the capacity of a 2,700 mWh cell phone battery.

We expect further optimization of the sample volume and complexity, coil excitation frequency and duration, bead quantity and diameter, and other factors to lead to higher performance. Both *S. epidermidis* and *M. marinum* are difficult bacteria to lyse; performance with easier to lyse bacteria such as *E. coli* will likely be higher and testing is currently under way. Portable sample preparation could allow next generation point-of-care NAATs for bacteria such as *Mycobacterium marinum* and *Staphylococcus epidermidis* free from bench-top laboratory equipment.

What sets this device apart from other lysis techniques compatible with the point-of-care is freedom from additional power supplies (battery packs, etc.) and the potential of using the same peripheral equipment (cell phones) for sample preparation along with interpreting test results. Academic medical laboratories can implement the methodology for very little cost. As shown here, less than \$38 was spent for the mp3 player, magnet wire, cable, and bobbin materials per device, and less than \$1 per assay for the screw-top tube, magnet, and beads. Further reductions in cost would be realized if quantities were scaled up or the device were optimized to reduce magnet size, bead volume, tube cost, etc. While clinical laboratories may find the noise of bench top bead beaters acceptable, a quieter technique such

as demonstrated here may be more amenable to the point-of-care. Also, the inexpensive nature of the hardware makes it nearly disposable.

We are currently broadening the sample types tested using this technique, along with other lysis methods, for a wide range of bacteria and clinical sample types including blood, sputum, and nasal matrix. It is our expectation that this work will contribute to the next generation of portable nucleic acid amplification tests, including the multiplexable, autonomous, disposable nucleic acid amplification test (MAD NAAT) project^{67,230,406}, a collaborative effort including the Yager group at the University of Washington, PATH, the ELITech Group, and GE Global Research.

Acknowledgements

Major parts of this section of my thesis were taken from a recent publication from our group⁴⁴¹. I would like to acknowledge and thank collaborators Alec Wollen, Dr. Erin Heiniger, Samantha Byrnes, Peter Kauffman, Lily Mireles, Dr. Paula Ladd, and Dr. Paul Yager for their contributions to the AudioLyse work.

10. Swab transfer for point-of-care diagnostics: characterization of swab types and manual agitation methods (Panpradist *et al.* *PLoS One*, 2014)

Nuttada Panpradist, Bhushan J. Toley, Xiaohong Zhang, Samantha Byrnes, Joshua R. Buser, Janet A. Englund, Barry R. Lutz

Abstract

Background: The global need for disease detection and control has increased effort to engineer point-of-care (POC) tests that are simple, robust, affordable, and non-instrumented. In many POC tests, sample collection involves swabbing the site (*e.g.*, nose, skin), agitating the swab in a fluid to release the sample, and transferring the fluid to a device for analysis. Poor performance in sample transfer can reduce sensitivity and reproducibility.

Methods: In this study, we compared bacterial release efficiency of seven swab types using manual-agitation methods typical of POC devices. Transfer efficiency was measured using quantitative PCR (qPCR) for *Staphylococcus aureus* under conditions representing a range of sampling scenarios: 1) spiking low-volume samples onto the swab, 2) submerging the swab in excess-volume samples, and 3) swabbing dried sample from a surface.

Results: Excess-volume samples gave the expected recovery for most swabs (based on tip fluid capacity); a polyurethane swab showed enhanced recovery, suggesting an ability to accumulate organisms during sampling. Dry samples led to recovery of ~20–30% for all swabs tested, suggesting that swab structure and volume is less important when organisms are applied to the outer swab surface. Low-volume samples led to the widest range of transfer efficiencies between swab types. Rayon swabs (63 μ L capacity) performed well for excess-volume samples, but showed poor recovery for low-volume samples. Nylon (100 μ L) and polyester swabs (27 μ L) showed intermediate recovery for low-volume and excess-volume samples. Polyurethane swabs (16 μ L) showed excellent recovery for all sample types. This work demonstrates that swab transfer efficiency can be affected by swab material, structure, and

fluid capacity and details of the sample. Results and quantitative analysis methods from this study will assist POC assay developers in selecting appropriate swab types and transfer methods.

Introduction

Diagnostics for non-blood-associated pathogens often use swabs as a specimen-collecting tool. For example, swabs are used to collect throat specimens for Group A *Streptococcus*⁴⁶⁸; nasal and nasopharyngeal specimens for *Staphylococcus aureus*^{469,470}, *Bordetella pertussis*, influenza virus^{471,472}, and respiratory syncytial virus (RSV)^{473,474}; female endocervical or male urethral specimens for *Neisseria gonorrhoea*⁴⁷⁵ and *Chlamydia trachomatis*⁴⁷⁶; and fecal swabs for viral gastroenteritis⁴⁷⁷. Depending on the source of collection, swabs should have shaft properties (flexibility, length) and tip size/shape appropriate for the sampling site, and the swab tip material and microstructure should provide efficient sample capture and target release in the presence of sample matrix components (e.g., human cells, body fluids, and other contaminants). Commercially available swabs are currently utilized with a variety of swab tip materials (e.g., nylon, rayon, cotton, polyester, polyurethane, and alginate polymer) and microstructures (e.g., tightly wound, knitted, flocked fiber, and reticulated). In laboratory settings, swabs are typically agitated by vortex mixing to release organisms into a transfer fluid^{478–482} that is analyzed by culture, immunoassays (ELISA), or nucleic acid tests (PCR).

Swab sampling and fluid transfer are also used in lateral flow tests (LFTs) intended for point-of-care (POC) testing in non-laboratory settings. Commercial LFTs that are being used with swabs worldwide include rapid streptococcal antigen assays, respiratory syncytial virus (RSV) assays: BinaxNOW RSV Lateral Flow (Alere Inc., Waltham, MA), RSV Respi-Strip (Coris Bioconcept, Namur, Belgium); and influenza detection tests: BinaxNOW Influenza A&B Card (Alere Inc., Waltham, MA), QuickVue Influenza Test (Quidel Corp., San Diego, CA). Typical instructions require the user to dip the swab into transfer fluid (.0.7 mL to 1 mL), manually agitate the swab for a specified time⁴⁸³, and transfer a fraction of the fluid (~100 μ L) to the device⁴⁸⁴. The low fluid capacity of LFTs results in most of the sample being discarded, and manual agitation may be less effective than vigorous vortex mixing used in laboratory settings. Since the sensitivity of LFTs is typically lower than laboratory-based tests, there is a need to maximize transfer of sample from the swab to the device. Studies evaluating swab transfer use widely varied definitions of transfer efficiency, often focus on a specific clinical application, and typically rely on qualitative analysis techniques. Thus, we built on previous work to develop quantitative analysis methods and definitions for swab transfer efficiency that can be applied to a variety of swab types, sampling applications, and transfer methods. We present methods to quantify swab transfer efficiency, discuss potential pitfalls that could bias quantitative analysis, and evaluate transfer efficiency for a range of swab types, sample properties, and manual agitation methods that meet the unique needs for POC applications. The results and discussion can aid researchers or test developers in rational selection of swabs and transfer methods for diagnostics development in both POC and laboratory settings.

Materials and Methods

Model organism (*Staphylococcus aureus*)

A single colony of *S. aureus* (ATCC 25923) was inoculated in tryptic soy broth (TSB) (Fisher B11768) and shaken overnight (250 rpm, 37°C). The overnight culture was further diluted 1:100 in TSB and incubated

(250 , 37°C) for 3 hours until the OD600 reached 260.2, corresponding to a concentration of ,10⁹ CFU/ mL. *S. aureus* bacteria were then harvested and resuspended in one of two buffers: 1X Tris-EDTA buffer at pH 8.0 (TE: 10 mM Tris-HCl +1 mM EDTA) or TE buffer with in-house human simulated nasal matrix (SNM: 110 mM NaCl, 1% w/v mucin from porcine stomach Type III (Sigma, M1778-10G) and 10 µg/ mL w/v human genomic DNA (Promega G3041)) at 90% v/v of TE/SNM.

Swabs and agitation methods

Seven different commercially-available swabs were tested: rayon (Copan Diagnostics Inc., 170KS0, Murrieta, CA), cotton (Puritan Medical Products Co., LLC, 25–806, Guilford, ME), midturbinate (MT) flocked nylon (Copan Diagnostics Inc., 56380CS01, Murrieta, CA), regular-tip flocked nylon (Copan Diagnostics Inc., 502CS01, Murrieta, CA), polyester (PES) (Contec Inc., 19059209, Spartanburg, SC), polyurethane (PUR) (Foamtec International, 19304613, Oceanside, CA), and calcium alginate (Puritan Medical Products Co., LLC, 25-806-2PA, Guilford, ME).

Vortexing is commonly used in the laboratory to maximize release of organisms from swabs, but it is likely not available in low resource settings. Agitation methods for POC tests are normally specified in units of time, without definition of the method. For consistency across experiments, we defined a base case method for translating the submerged swab along a circular path against the side of the tube at a rate of 1 cycle per second (1 Hz) for a specified time (*e.g.*, “10 second 1 Hz side twirl”). The swab agitation was done by hand but using the timer as a reference for manual control of the twirling rate. The potential errors introduced by the users were not excluded in the data. The impact of these variations was tested (below in the section titled “Robustness to user variations in manual agitation”). After the sample was applied to swabs, swabs were agitated in 128 µL of transfer fluid. This volume was chosen to be compatible with the fluid capacity of typical POC devices (~100 µL for LFT) to enable complete utilization of the sample fluid.

Volume recovery experiments

To quantify fluid release volume, 15 µL TE buffer was pipetted onto the tip of a dry swab. The swab was then dipped into pre-weighed 128 µL TE buffer (or 1% w/v sodium citrate solution for calcium alginate swab) and agitated (10 second 1 Hz side twirl). The swab was removed, and the fluid left in the tube was weighed. The volume left in tube was calculated (Equation 17) and compared to a control (Equation 18). As the control, 15 µL TE buffer was pipetted into 128 µL of pre-weighed TE buffer, and the fluid in the tube was weighed. The % Volume Recovery was calculated using Equation 19.

$Vol\ avail.\ for\ analysis\ (test) = V_{initial} - V_{lost\ to\ swab}$ $= V_{initial} - \frac{(W_{1, test} - W_{2 test})}{density\ of\ fluid}$	Equation 17
---	-------------

$Vol.\ avail.\ for\ analysis\ (control) = V_{initial} - V_{added}$	Equation 18
--	-------------

%Vol. avail. for analysis (% Vol. Recovery)

$$= \frac{\text{Vol. avail. for analysis (test)}}{\text{Vol. avail. for analysis (control)}}$$

Equation 19

where $W_{1, \text{test}}$ = initial weight of test tube containing 128 μL TE buffer

$W_{2, \text{test}}$ = weight of test tube after swab transfer and removal

$W_{1, \text{control}}$ = initial weight of control tube containing 128 μL TE buffer

$W_{2, \text{control}}$ = weight of control tube after 15 μL TE buffer was added

V_{added} = added volume of TE (either onto swab or onto control tube), 15 μL

V_{initial} = initial volume of TE in test or control tube, 128 μL

$\frac{W_{2, \text{control}} - W_{1, \text{control}}}{V_{\text{added}}} = \text{density of fluid}$, used to convert weight change of fluid in the test tube ($W_{2, \text{test}} - W_{1, \text{test}}$)

into volume change. ($W_{2, \text{test}} - W_{1, \text{test}}$) is negative when the swab absorbed more fluid from the tube than it released. Adding

$$\frac{(W_{2, \text{test}} - W_{1, \text{test}}) \times V_{\text{added}}}{(W_{2, \text{control}} - W_{1, \text{control}})}$$

to V_{initial} would provide the recovered volume in the test tube (Volume available for analysis (test)). A transfer volume of 128 μL was selected because this volume allowed at least 20 μL to be recovered after the swab transfer step for all swab types for further testing by qPCR (as described in the next section); it also represents an appropriate volume for LFTs.

Organism recovery experiments.

Bacteria from swabs and control samples were lysed using a method modified from Patel *et al*⁴⁸⁵, and lysed samples were analyzed by quantitative PCR (qPCR). Regular-tip nylon, MT nylon, and rayon swabs were obtained in sterile packaging, and PES and PUR swabs and other materials were autoclaved prior to use. All swabs and materials were tested for bacteria and DNA bacteria contamination. In all experiments, bacteria were transferred from the swab to 128 μL of 3 U/ μL achromopeptidase (ACP) (Sigma #A3547) in TE to lyse the bacteria. Lysis continued for 2 minutes at room temperature. Following lysis, ACP was deactivated by heating (10 minutes, 95°C), and the sample tube was placed in ice immediately. Bacterial lysate was filtered through a centrifuge tube filter (0.2 mm pore size) to remove debris. 9 μL of the filtered lysate was analyzed by a MRSA/SA ELITE MGB qPCR assay (Elitech Group Molecular Diagnostics, formerly Epoch Biosciences, #M800346). This assay detects a single open reading frame encoding *S. aureus* specific lactate-dehydrogenase-1 (*ldh1*). The concentration of *ldh1* copies in each sample (copies/ μL) was estimated based on a standard curve (80 to 8×10^8 *ldh1* copies). To verify that swabs were not contaminated during experiments, negative control samples (15 μL of TE buffer (N = 3) and swabs with no added bacteria (N = 3)) were transferred to 128 μL of lysis buffer and analyzed by the same procedures as other samples.

S. aureus was applied to swab tips using one of the three methods described in the following sections and eluted into 128 μL of pre-weighed lysis buffer. In the control case, *S. aureus* was introduced directly to 128 μL of pre-weighed lysis buffer. Both test and control tubes were weighed and set aside to allow for the lysis to complete. Filtered lysate then underwent qPCR for quantitation of *ldh1* concentration (copies/ μL). The limit of detection (LoD) of qPCR was less than 5 *ldh1* copies per reaction, corresponding to about 1 CFU per reaction (Fig. S1²³⁰). Weights of test and control tubes were used to calculate

volumes left in the tubes (Equation 17 and Equation 18, respectively). The number of *ldh1* copies left in tube in each case was calculated using Equation 20, and the % Organism Recovery was calculated using Equation 21.

$ldh1 \text{ copies (control or test)}$ $= ldh1 \text{ concentration } \left(\frac{\text{copies}}{\mu L} \right) \times Volume (\mu L) (\text{control or test})$	Equation 20
---	-------------

$\%Organism \text{ Recovery} = \frac{ldh1 \text{ copies (test)}}{ldh1 \text{ copies (control)}} \times 100$	Equation 21
---	-------------

Further details on how *S. aureus* was introduced to swabs in each method are described below.

Low-volume fluid sample (less than swab saturation)

15 μ L *S. aureus*/TE (100, 10⁴, and 10⁶ CFU) was pipetted onto a swab tip. The amount of bacteria input exceeded the LoD of the qPCR assay (Fig. S1²³⁰). The swab was then dipped into lysis buffer, manually agitated (as described above or 10 second 1 Hz side twirl), and removed. The number of *ldh1* copies was measured and compared to a control case in which *S. aureus*/TE solution was directly pipetted into pre-weighed lysis buffer (with no submergence of pipette tip to avoid introducing bacteria from the outside surface of the tip). A fresh pipette tip was then used for mixing.

Excess-volume fluid sample (beyond swab saturation)

A dry or a pre-wet (by dipping into TE) swab was dipped into 1 mL of *S. aureus*/TE solution (10⁶ CFU/mL) and manually agitated (10 second 1 Hz side twirl) to load sample into the swab. Swabs were transferred into pre-weighed lysis buffer, manually agitated, and removed. The number of *ldh1* copies in the lysis tube was measured and reported.

Sample dried on a surface

Dried bacterial samples were prepared by pipetting 15 μ L of *S. aureus*/TSB (10⁴ CFU) onto sterilized 25/46-inch diameter polydimethylsiloxane (PDMS) punches and left in a desiccator for 30 minutes. PDMS was chosen as the surface since it is known to not adhere to *S. aureus* organisms⁴⁸⁶, and we attempted to remove effects of collection efficiency by using a very vigorous swabbing procedure (goal of 100% collection). A dry or a pre-wet swab was rubbed across the PDMS surface 10 times to pick up organisms (Fig. S2²³⁰), transferred into the pre-weighed lysis buffer (128 μ l), manually agitated, and removed. The number of *ldh1* copies in the lysis tube was measured and compared to a control. In the control, the eluate was derived from placing the PDMS punch with dried bacteria directly in lysis buffer and vortexing for 10 seconds.

Robustness to user variations in manual agitation

15 μ L of *S. aureus*/TE solution (10⁴ CFU) was pipetted onto a dry swab, and the swab was dipped into lysis buffer. Different manual-twirling methods were used to release bacteria. "Side twirl" refers moving

the swab tip around the interior side of the tube in a circular motion. “Bottom twirl” refers to placing the swab tip at the bottom of the tube and rotating the shaft.

Engineering for improved recovery

A forced-flow method using a syringe was developed as an alternative to manual agitation to improve organism recovery. In the test case, 15 μL of *S. aureus*/TE (10^4 CFU) was introduced onto a dry swab, and the swab was dipped into the lysis buffer tube, the bottom of which was connected to a syringe. The plunger of the syringe was then pushed and pulled 5 times. At the end, the swab remained in the tube whereas the eluate was contained within the syringe piston and could be purged through an opening in the side of the syringe.

Bench-top gold standard method

Swabs (N =5) were tested for organism recovery using a laboratory protocol: vortexing for 10 seconds at the maximum speed. In the test case, 15 μL of *S. aureus*/TE (10^4 CFU) was introduced onto a dry swab, and the swab was dipped into lysis buffer prior to vortexing.

Data Analysis

Statistical analysis was performed using MATLAB (MathWorks, Natick, MA). Analysis of variance (ANOVA) was used to test for significant differences among means. In the case that ANOVA indicated significant differences ($p < 0.05$), post-hoc comparisons (Tukey-Kramer procedure, adjusted for multiple comparisons) were used to determine which means were significantly different from one another. The data and analysis underlying the findings are fully available on request.

Results

A variety of swab types were evaluated under different conditions, as illustrated in Figure 135. We selected a set of commercially-available swabs representing a range of materials, microstructure, and size: low absorbent foam (reticulated polyurethane swab – PUR and knitted-pattern PES swabs – PES), low absorbent fiber (MT nylon flocked swabs – MT nylon, and regular-tip nylon flocked swabs), high absorbent fiber (tightly wound cotton and rayon swabs), and dissolvable swabs (calcium alginate swabs). Figure 134 shows scanning electron microscopy images of the nylon (flocked), PUR (reticulated), PES (knitted), and rayon (wound) swab tips; this set exhibits a wide variety of material structures and pore sizes.

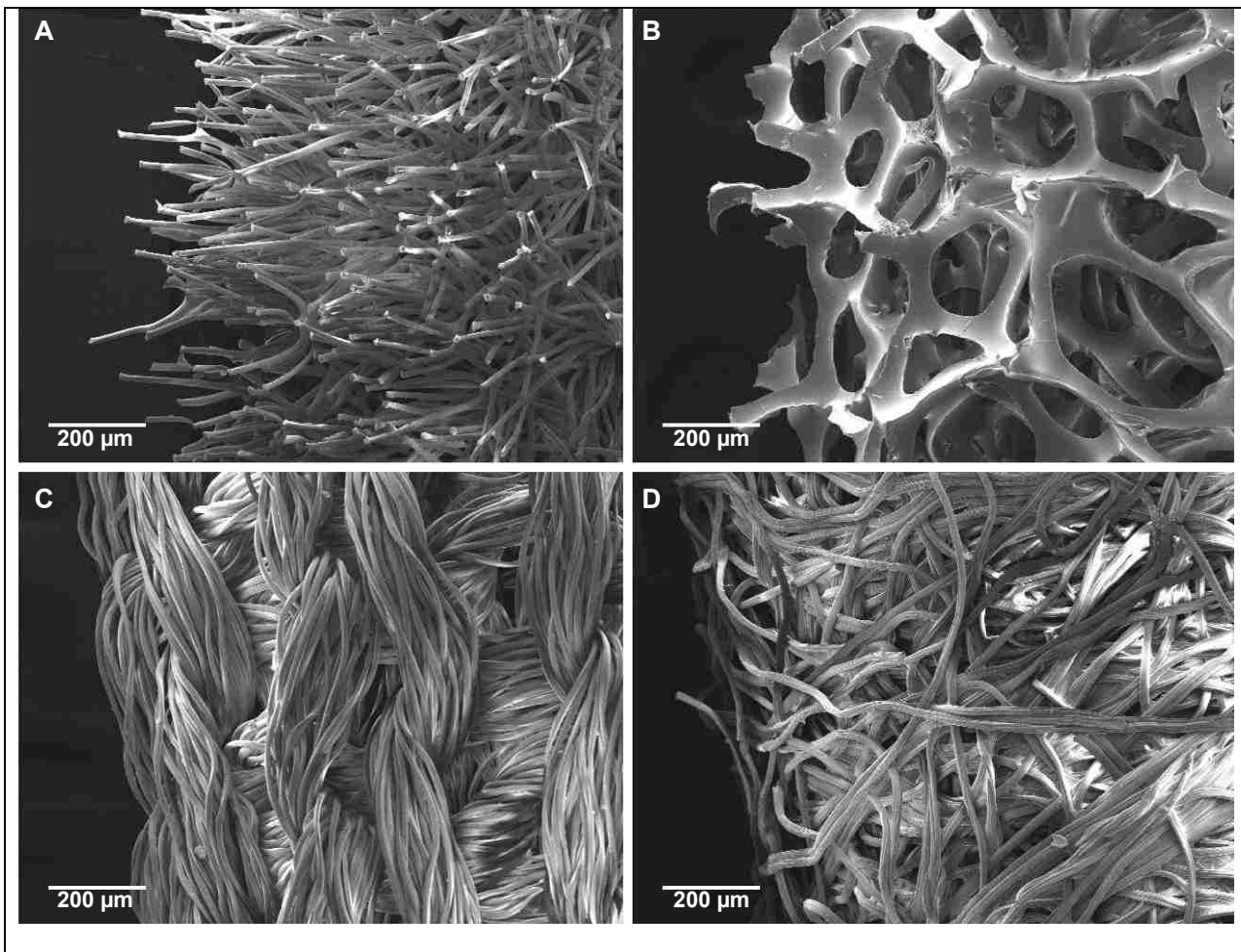


Figure 134: Scanning electron micrographs of swab tips: (A) mid-turbinate Nylon (B) polyurethane (C) polyester (D) Rayon. Scanning electron micrographs were obtained using an FEI Sirion scanning electron microscope. Samples were sputtered with an 11 nm Au/Pd coating prior to imaging (SPI Module Control, Structure Probe, Inc., West Chester, PA, USA.) SEM imaging and sputter coating work was performed at the University of Washington Nanotech User Facility (NTUF), a member of the NSF-sponsored National Nanotechnology Infrastructure Network (NNIN).

We focused on the manual “insert and twirl” agitation method common for LFTs and used a reduced fluid transfer volume (~100 μ L) appropriate for typical LFTs. Swabs were evaluated in a series of tests, with subsets of swabs chosen for each test to illustrate key differences and analysis methods. Swabs were first tested for fluid retention (loss of fluid sample to the swab), and swabs with low retention volume were carried forward to test organism recovery. We used *Staphylococcus aureus* as a model system, with recovery quantified by quantitative polymerase chain reaction (qPCR). Organisms were applied to swabs under various conditions to represent a range of sampling conditions from dry to wet: a) low-volume fluid sample (less than swab saturation), b) high-volume fluid sample (beyond swab saturation), and c) sample dried on a surface. For the low-volume sample condition, recovery was tested for a wide range of concentrations (100 to 10^6 organisms)⁴⁸⁷, and a simulated human nasal matrix was used as an example of a complex sample. Pre-wet swabs were compared to dry swabs for the cases of excess sample volume and dry sample collection. We also tested variations on manual agitation to identify sensitivity to user operation, and demonstrated an engineered manual agitation method to

improve recovery for swab-sample combinations that performed poorly. The data from all experiments are summarized in Tables S1 and S2²³⁰.

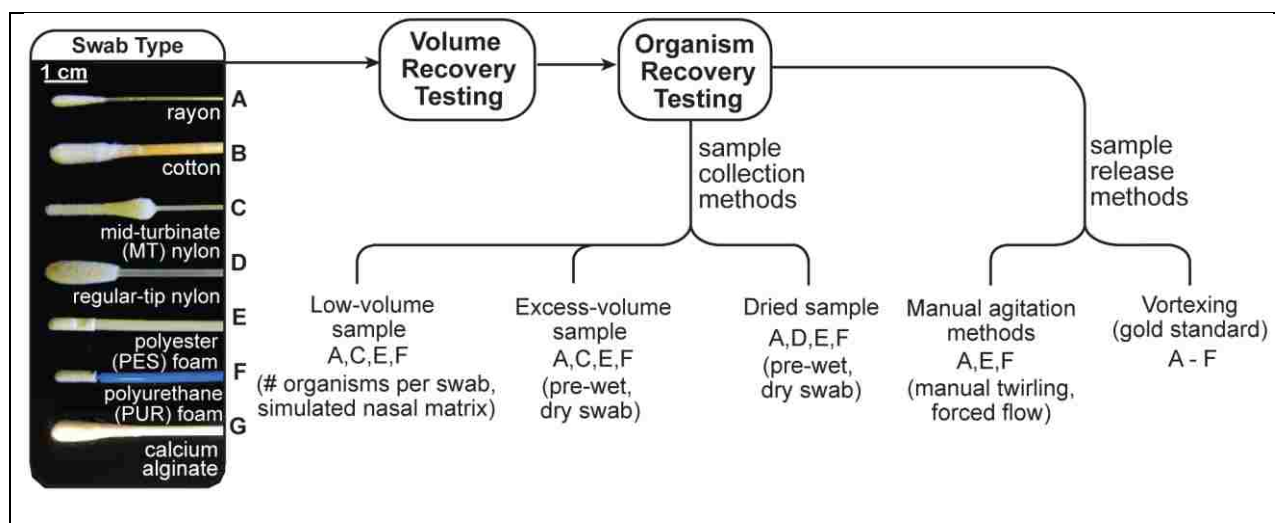


Figure 135: Schematic of swab transfer experiments. Seven commercially-available clinical swabs (labeled A, B, C, D, E, F, and G) were tested for volume recovery and organism recovery. Organisms were applied to swabs in three ways: pipetting a low-volume sample onto the swab, dipping the swab into excess-volume sample, or rubbing the swab across dried sample on a surface. Selected cases included variation in sample concentration, addition of simulated nasal matrix, and comparison of dry and pre-wet swabs. Different manual swab agitation methods, manual twirling and forced flow, were tested for their effects on swab transfer efficiency compared to vortexing (gold standard method). doi:10.1371/journal.pone.0105786.g001

Volume recovery

Fluid volume retention for seven commercially-available swabs is shown in Figure 136. Swabs with 15 μL of added fluid were inserted into tubes containing 128 μL of fluid and removed, and the fluid remaining in the tube was used to calculate fluid volume lost to the swab (Figure 136A). Figure 136B shows the fluid volume lost to each swab, and Figure 136C shows the percent volume available for analysis (% volume recovery) for a starting volume of 128 μL . PUR and PES yielded the highest volume recovery (PUR: mean \pm SE = 89 \pm 0.4%; PES: 81 \pm 0.3%). Conversely, cotton and regular-tip nylon swabs retained more fluid resulting in the poorest volume recovery (cotton: 8 \pm 0.6%; regular-tip nylon: 30 \pm 3.4%). The remaining swabs, rayon and MT nylon, had intermediate volume recovery (rayon: 56 \pm 2.5%; MT nylon: 70 \pm 0.8%). All data points in Figure 136B and C have 5 replicates. A one-way ANOVA indicated that volume recovery differed significantly across swab types ($p < 0.0001$). Post-hoc comparisons indicated that PUR had a significantly higher volume recovery than other swab types ($p < 0.05$). Additionally, we tested dissolvable calcium alginate swabs in the recommended dissolution buffer (sodium citrate). The recommended procedure uses a buffer volume that is too large for LFTs (15 mL), and using the small volume (128 μL) resulted in a glue-like gel that would not flow through an LFT (Fig. S4²³⁰).

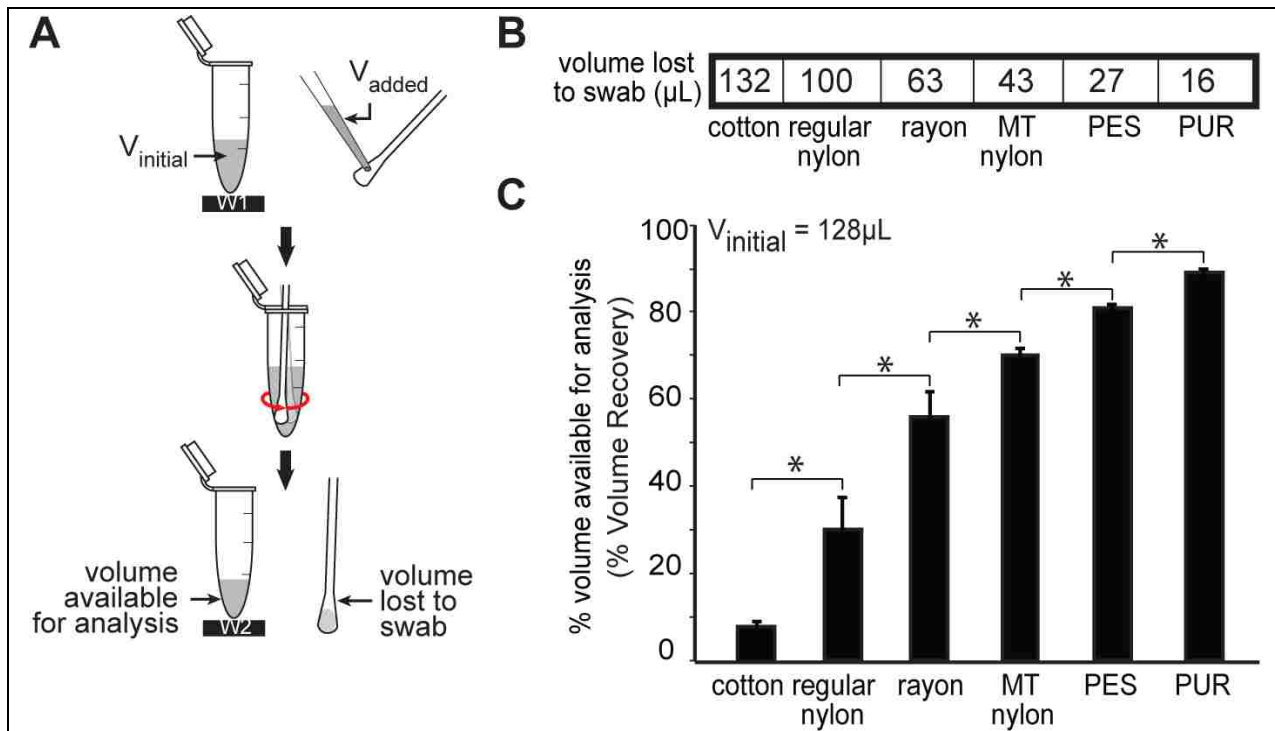


Figure 136: Volume recovery testing. (A) Schematic of the experimental setup. The tube containing 128 μL TE was weighed (W1), and 15 μL TE was pipetted onto the swab, which was then transferred into the tube using 10 second 1 Hz side twirl, and removed. The tube containing the leftover buffer (eluate) was weighed (W2). The % volume available for analysis (% Volume Recovery) was calculated using Equation 19 in the text. (B) Mean TE volume (μL) absorbed by each type of swab (N = 5). (C) Comparison of the % Volume Recovery (mean \pm SE; N = 5) from each swab. Calcium alginate swabs were resuspended in 1% w/v sodium citrate buffer to dissolve fibrous tip materials, the % Volume Recovery was not reported here due to density change of the buffer during (A). * indicates significant differences (Tukey-Kramer, $\alpha = 0.05$). doi:10.1371/journal.pone.0105786.g002

Organism recovery

We determined that our modified ACP lysis method gave the same amount of amplifiable DNA as the original method by Patel *et al*⁴⁸⁵ (Fig. S5²³⁰). Eluate recovered from swabs was devoid of bacteria or bacterial DNA (Fig. S6²³⁰) and did not interfere with qPCR or ACP lysis (Fig. S7²³⁰). The qPCR assay reported 3–6 genomic copies per CFU across all experiments; along with each experiment result we report the sample CFU for reference, but recovery values reported in this paper are based on copies measured by qPCR. Results are reported as absolute organisms recovered (Equation 20) or as % organism recovery based on a control sample analyzed by the same method (Equation 21).

Low-volume fluid samples

Swabs were tested with a sample volume that was less than the fluid capacity for all swabs (15 μL). Four dry swab types (PUR foam, knitted PES, rayon, and MT flocked nylon swabs (N = 5)) were tested for organism recovery using low-volume samples (Figure 137A). When bacterial solution was pipetted onto the swab tip, fluid absorption behaved differently among swab types. For PUR swabs, the fluid beaded up on the surface without absorbing. For PES and nylon swabs, the bacterial fluid formed a thin film

around swab tip but did not bead up. For rayon swabs, fluid was completely absorbed into swab tips.

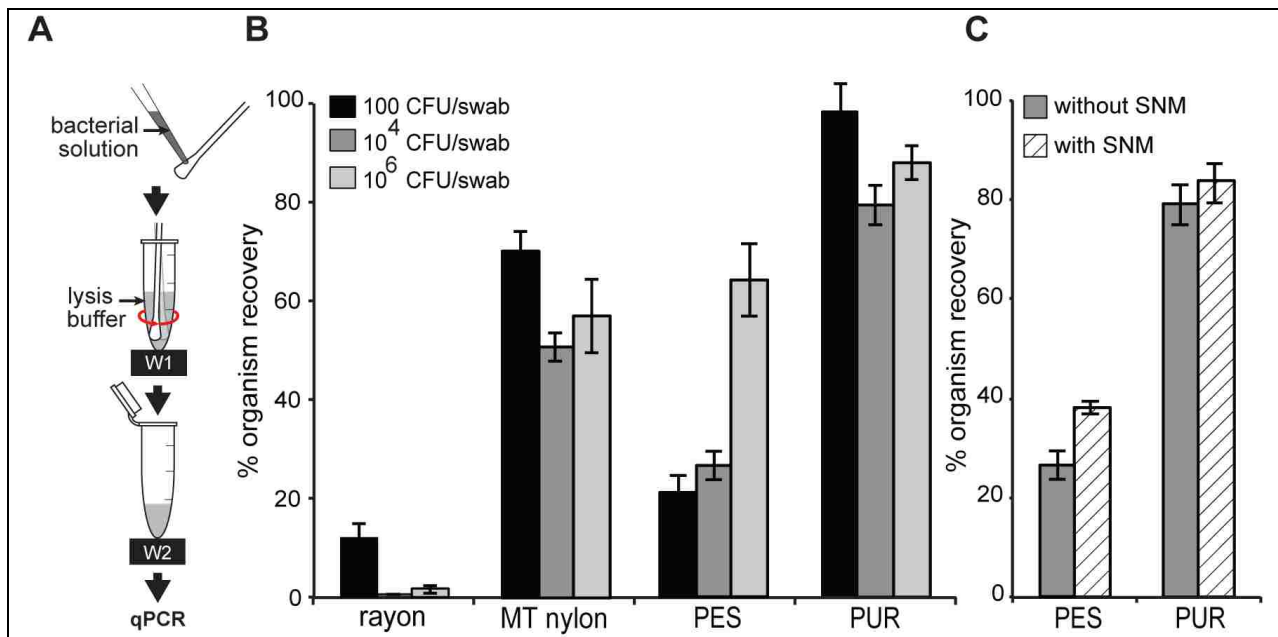


Figure 137: Organism recovery for low-volume samples. (A) Schematic of the experimental set up. 15 μL *S. aureus*/TE (~ 100 , $\sim 10^4$, or $\sim 10^6$ CFU, equivalent to 500, 6×10^4 , or 4×10^6 *ldh1* copies, respectively, as measured by qPCR) was spiked onto the swab, which was then agitated in 128 μL lysis buffer using 10 second 1 Hz side twirl, and removed. (B) Comparison of the % Organism Recovery in four swabs at three different organism input numbers (mean \pm SE, N = 5), which was calculated using Equation 21 in the text. (C) Comparison of the % Organism Recovery (mean \pm SE; N = 5) using $\sim 10^4$ CFU/swab of *S. aureus* in the presence and absence of simulated nasal matrix (SNM). doi:10.1371/journal.pone.0105786.g003

The percent organism recovery of each swab using low-volume samples is shown in Figure 137B. Regardless of the number of organisms added, PUR foam yielded the highest organism recovery of 79%–98%. MT nylon and PES had intermediate organism recovery of 51–70% and 21–65%, respectively. Rayon provided the lowest organism recovery of 1–12%. A two-way ANOVA indicated significant effects of swab type and numbers of organisms applied to swab, and a significant interaction (every $p < 0.05$). Post-hoc comparisons showed that organism recovery of PUR was significantly higher than other swabs (followed by MT nylon, PES, and rayon).

Figure 137C compares % organism recovery of PES (N = 5) and PUR (N = 5) for bacterial samples in the presence and absence of simulated nasal matrix (SNM). We verified that SNM did not interfere with qPCR and ACP lysis (Fig. S8²³⁰). Despite the presence of SNM, PUR swabs still yielded significantly higher organism recovery than PES swabs; mean \pm SE was $84 \pm 4\%$ for PUR and $38 \pm 2\%$ for PES (two-way ANOVA, effect of swab type, $p < 0.0001$). SNM significantly increased % organism recovery ($p = 0.03$).

Excess-volume fluid sample (beyond swab saturation)

Four swabs (rayon, PES, PUR, and MT nylon (N = 5)) were tested using excess-volume samples (1 mL). As the swab was submerged into 1 mL bacterial solution and twirled (Figure 138A), dry rayon, PUR and PES swabs released air bubbles and allowed solution to flow into the interior of the swab tip. Figure 138B reports the number of organisms released from the swab into lysis buffer. A two-way ANOVA showed a significant effect of swab type on the number of organisms recovered ($p = 0.0001$) and prewetting the

swab ($p = 0.001$). No significant interaction was found ($p = 0.63$). Post-hoc analysis indicated that PES swabs yielded significantly fewer organisms recovered than rayon, MT nylon and PUR. Wetting the swab reduced number of organisms recovered. The number of organisms recovered from each swab was then normalized by the product of its volume capacity and the concentration of organisms in the bacterial sample solution (Figure 138C). Two-way ANOVA indicated significant effect of swab type ($p < 0.0001$) and pre-wetting the swab ($p = 0.009$). Post-hoc analysis reported that PUR swabs had significantly higher normalized organism recovery than other swabs.

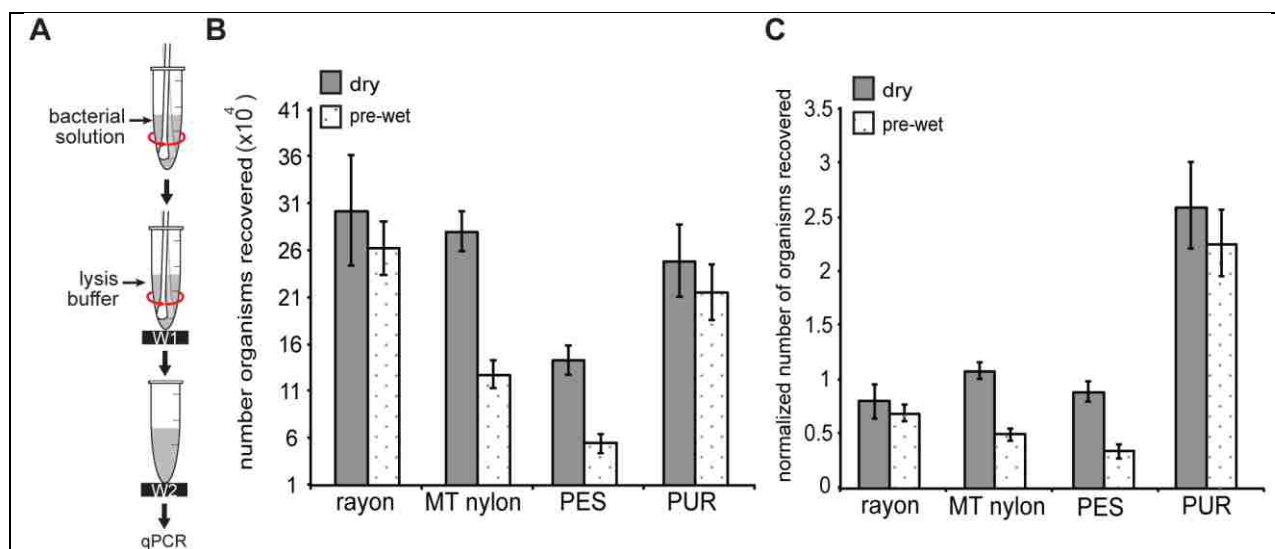
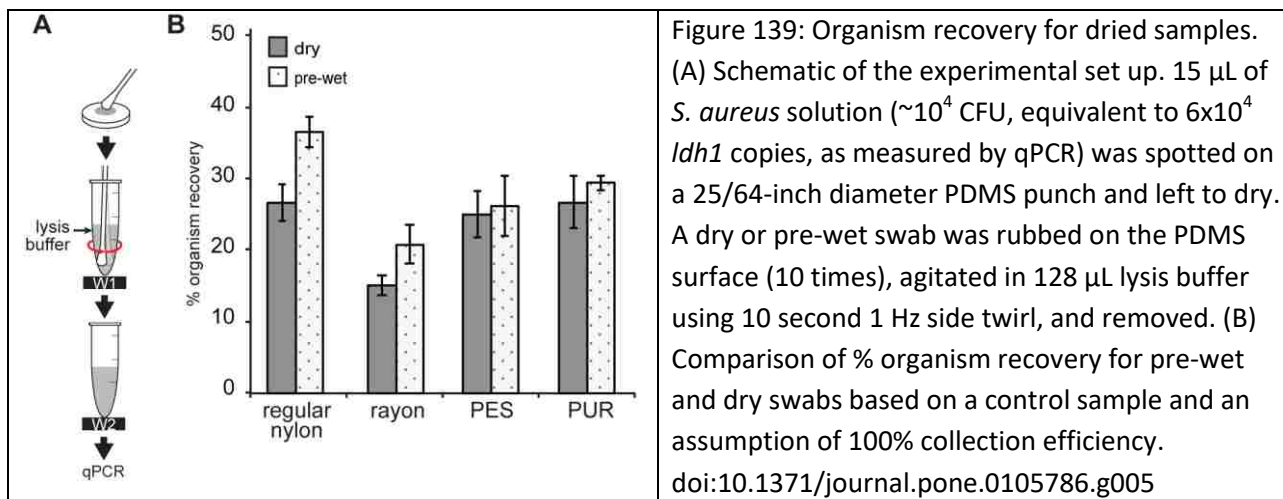


Figure 138: Organism recovery for high-volume samples. (A) Schematic of the experimental set up. Either a dry or pre-wet swab was dipped into 1 mL 10^6 CFU/mL *S. aureus* solution (equivalent to 6×10^6 *ldh1* copies/mL, as measured by qPCR) and agitated by 10 second 1 Hz side twirl. The swab was then inserted into 128 μ L lysis buffer, agitated by 10 second 1 Hz side twirl, and removed. (B) Comparison of the absolute number of organisms recovered for dry and pre-wet swabs. Absolute organism recovery was reported (rather than %) since the uptake of sample volume was different for each swab; absolute recovery was calculated using Equation 20 in the text. In all cases, recovery was larger than would be expected based on swab volume and sample concentration by colony counts due to presence of multiple target copies per CFU. (C) The number of organisms recovered from each swab from panel (B) normalized by the number of organisms expected based solely on the sample concentration and volume capacity of the swab (estimated number of organisms collected by the swab = swab volume capacity (μ L) \times bacterial stock concentration (copies/ μ L from qPCR)). doi:10.1371/journal.pone.0105786.g004

Sample dried on a surface

Four swabs (PUR, PES, rayon, and regular-tip flocked nylon swabs ($N = 5$)) were tested for organism recovery using a dried bacterial sample (Figure 139A). Swabs were dry or pre-wet (by dipping into TE buffer). To ensure that a swab was able to pick up the dried sample effectively, the swab was rubbed vigorously on the surface of PDMS (Fig. S2²³⁰). Figure 139B shows % organism recovery for dried samples. A two-way ANOVA indicated % organism recovery was affected by swab type ($p = 0.0004$) and wet/dry swab pre-conditions ($p = 0.02$) with no significant interaction ($p = 0.4$). Post-hoc comparisons showed rayon had significantly lower % organism recovery than other swabs.



Robustness to user variations in manual agitation.

Three dry swab types (PUR, PES, and rayon (N = 5)) were tested for variations in manual agitation to release organisms into the lysis buffer (Figure 140A). All manual twirl methods yielded comparable % organism recovery from PUR swabs (Figure 140B); the low variation in PUR swabs was likely due to lack of sample absorption into the hydrophobic swab tip, which allowed sample release without agitation. Greater variation was observed in PES and rayon swabs (Figure 140D), which represented more realistic sampling conditions. Coefficients of variation of organism recovery of all manual twirling methods were 7% for PUR, 23% for PES and 40% for rayon swabs.

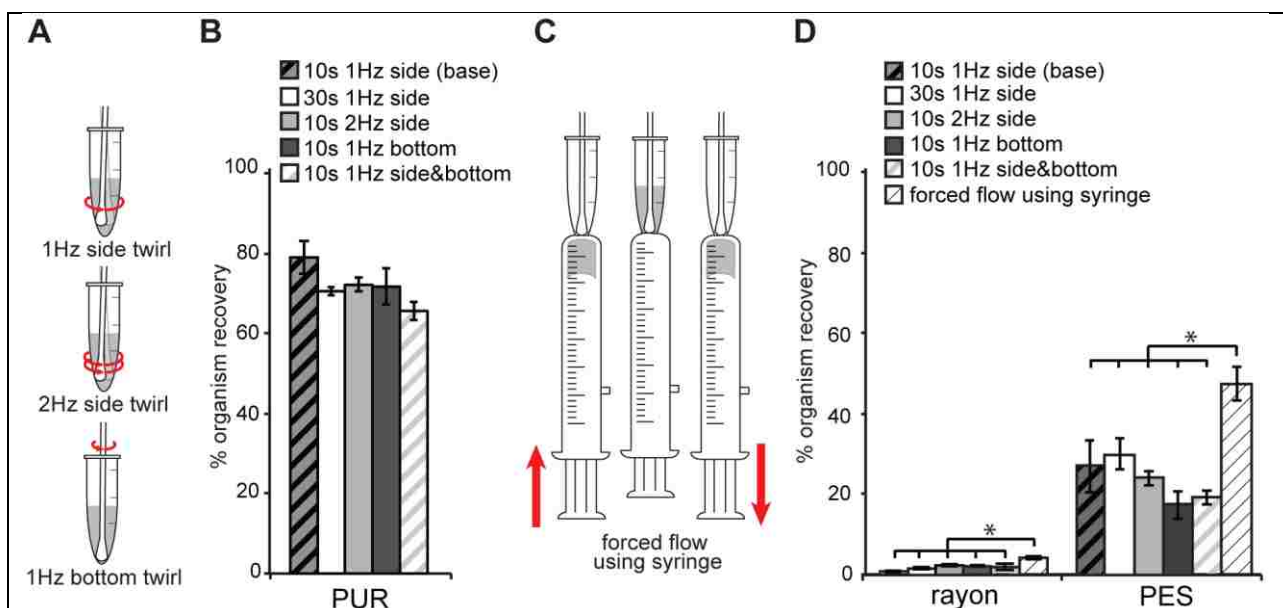


Figure 140: Comparison of manual agitation methods for swab transfer. (A) Schematic of action performed over a period of 1 second for different manual twirling methods. (B) Comparison of % organism recovery of PUR swabs using different twirling methods, which was calculated using Equation 21 in the text. (C) Schematic of the new forced flow syringe method. (D) Comparison of % organism recovery for PES and rayon swabs, using different twirling methods and the forced flow syringe method. * indicates statistically significant differences (Tukey-Kramer, $\alpha = 0.05$).

doi:10.1371/journal.pone.0105786.g006

Engineering for improved recovery.

A new manual agitation method, forced fluid flow using a syringe, was developed to increase organism recovery (Figure 140C). In order to test effectiveness of this method in improving organism recovery, intermediate-performing swabs (rayon and PES; Figure 137D) were selected. We compared % organism recovery derived from the forced-flow using the syringe method to other agitation methods (Figure 140D). A one-way ANOVA rejected the hypothesis that there was no difference among the six agitation methods. Post-hoc comparison (Tukey-Kramer, $\alpha = 0.05$) indicated that the forced flow using the syringe method yielded significantly higher organism recovery than the other five methods. This was true for both swab types.

Bench-top gold standard method.

Six swabs (PUR, PES, MT nylon, regular-tip nylon, cotton, and rayon) were tested for their organism recovery when 10 seconds of vortexing was applied. Organism recovery of cotton swabs could not be reported, since they absorbed all of the sample fluid. For the rest of swab types, a one-way ANOVA rejected the hypothesis that there was no difference among swab types. Post-hoc comparison (Tukey-Kramer, $\alpha = 0.05$) indicated that PUR, PES, and MT nylon yielded significantly higher organism recovery than rayon and regular-tip nylon (Fig. S9²³⁰). In comparing the efficiency of vortexing and 1 Hz side twirl, vortexing offered a significant improvement over 1 Hz side twirl methods for PES, MT nylon, and rayon ($p < 0.001$ in all cases). However, vortexing did not significantly increase organism recovery in PUR ($p > 0.05$). Additionally, vortexing yielded a significantly higher organism recovery for PES and rayon compared to forced flow using syringe method ($p < 0.001$ in both cases).

Discussion

In this study, we characterized several important properties of swabs currently utilized world-wide in many POC diagnostic tests. The experimental design had three overall aims: 1) to provide quantitative analysis and definitions of swab transfer efficiency that can be used to evaluate swabs and transfer methods, 2) to identify differences in swab transfer efficiency for a selection of common swabs and sample conditions, and 3) to identify commercially available swabs that perform well for sample conditions and manual agitation methods typical of POC testing. The results demonstrate that the choice of swab type for POC testing may be critical to achieving a sensitive and reliable test. We built on previous work to develop analysis methods and definitions for quantitative evaluation of swab transfer efficiency. Some studies have assumed that the volume absorbed is an accurate representation of organisms picked up by the swab^{481,488,489}. This assumption applies only when organism densities are the same inside and outside the swab; it will be inaccurate if organisms accumulate in the swab during agitation or if organisms do not flow freely into the swab. Our results show that swab transfer efficiency cannot be predicted based on fluid volume recovery alone, rather it requires analysis of organism recovery. The method for measuring the number of organisms in a sample also varies across studies. For bacteria, common measures include optical density at 600 nm (OD600), colony counts (as colony forming units, CFU)^{481,490-492}, and quantitative polymerase chain reaction (qPCR). However, OD is only applicable to high organism density. In colony counting, the transfer procedure itself can affect organism vitality (*e.g.*, due to fluid composition, physical damage by

vortexing or agitation)⁴⁹³. For clustering or biofilm forming organisms⁴⁹⁴, such as *S. aureus*, fragmentation during the transfer procedure can artificially increase the apparent recovery⁴⁹³. Thus, colony counting can bias results when comparing transfer methods or using a control to calculate percent organism recovery since each sample experiences different conditions. In contrast, qPCR provides consistent results independent of cell viability or clustering^{495,496}, and it allows calculation of transfer efficiency by normalizing organism recovery to an input control sample analyzed by the same method. Our results demonstrate that qPCR and input controls allow quantitative measurement of swab transfer efficiency that can be applied across studies.

The scenario of low-volume samples showed the largest difference between swab types. For example, the sample beaded on the hydrophobic tip of the PUR foam swab and was promptly released into the lysis buffer; this scenario is not a realistic sampling case since the swab resists collection of the small fluid volume, and the high recovery should be interpreted with caution (although we note that PUR swabs also gave high recovery for high-volume samples and dry samples). In less hydrophobic materials such as PES and MT nylon, a thin film coating of bacterial solution was created surrounding the swab tip resulting in intermediate recovery. The hydrophilic tip of the rayon swab⁴⁸¹ fully absorbed the small sample solution, and absorption of transfer fluid may have further driven sample into the swab interior resulting in poor recovery during agitation. Thus, the wettability of the swab itself may impact specimen recovery.

Intuitively, swabs with larger volume capacity will collect more organisms when excess fluid sample is available. We hypothesized that, in addition to the swab volume capacity, swab chemical composition and structure can impact organism pick up and release. To investigate this, we normalized the number of organisms recovered by the estimated number of organisms that would have been picked up if there were no impact of material composition and structure. The nylon, PES, and rayon swabs all transferred near the expected number of organisms based on their volume capacity, but the normalized organism recovery for the PUR swab was more than 2.5 fold higher than the other swabs (Figure 138C). This result suggests that swabs may accumulate organisms during agitation. Surprisingly, the PUR and rayon swabs maintained their recovery under pre-wet conditions. For the PUR swab, the large open pore structure may have allowed effective exchange of pre-wetting fluid with sample during collection. For the rayon swab, the large tip and dense structure may have prevented access to sample in the swab interior (as in Figure 137) for both dry and pre-wet conditions; the good recovery would then imply that rayon also accumulated organisms on its outer surfaces during collection. The results suggest that swab composition and structure can have a significant impact on collection and release efficiency and should be evaluated for the specific organism and sample type.

Swabs can be used to collect samples from dry surfaces, such as for environmental testing and sampling from skin or dry nasal passages, and pre-wet swabs are sometimes used to increase collection efficiency for dry samples⁴⁹¹. The improved performance of rayon swabs with dry samples (Figure 139B) compared to the low-volume case (Figure 137B) suggests that organisms collected from a dry surface were more accessible to manual agitation. This would be expected since dry collection deposits sample on the exterior surface of the swab, whereas liquid samples wick into the swab interior where they may be inaccessible by manual agitation. Similarly, the effect of pre-wetting was more pronounced for rayon and regular nylon (Figure 139B), which have relatively high volume absorption compared to PES and

PUR (Figure 136B). The pre-wetting step filled the interior volume of swabs prior to sampling, and presumably this allowed dried sample to remain on the exterior surface of swabs where they were more effectively released during manual agitation.

Biological fluids found in clinical specimens can affect organism recovery. Complex matrices can affect physical properties (*e.g.*, viscosity) or chemical properties (*e.g.*, binding to swab materials or passivating swab surfaces). For example, mucin has been found to reduce non-specific binding of protein and has been used to coat biomaterials to create non-fouling surfaces⁴⁹⁷ and repel other negatively charged molecules²⁴² (*e.g.*, DNA). However, the increased viscosity of complex matrices may reduce the effectiveness of agitation. As an example of a sample matrix, we measured recovery in the presence of simulated nasal matrix (SNM) and found that it had little effect on organism recovery (Figure 137C). The effect of sample matrix will be highly dependent on the sample type and should be evaluated for each application; the experimental design used here for SNM can be applied to quantitatively measure the effects of sample matrix on swab transfer efficiency.

User variations in swab transfer procedure could affect test sensitivity and reproducibility. Commercial LFTs typically include instructions to agitate the swab for a given time but do not specify the method. Our results with selected swabs showed that variations in agitation method and time had modest impact on organism recovery for the case of low-volume samples. Robustness to user variation will be especially important to maintain sensitivity and reproducibility for POC tests performed by untrained users and should be tested for all applications.

We demonstrated that an engineered swab transfer method can increase recovery from poorly performing swabs. However, the improved organism recovery was still significantly lower compared to vortexing (gold standard). Other engineered methods could include buffer-filled swab shafts that push fluid from the swab interior or methods that compress the swab to remove absorbed fluid. This finding has direct application to future developments in POC testing.

The PUR swab was the best performing swab across all sample conditions. This may be of clinical interest as similar PUR swabs have been found to be sensitive for the detection of respiratory viruses in immunocompetent and immunocompromised human subjects⁴⁹⁸. In addition, smaller swab size may be applicable to clinical use in subjects of diverse size and in sampling of diverse structure. The small volume of the PUR swab and reproducible recovery for variations in agitation methods also make it well suited for application in POC devices.

Limitations of this work included the use of analytical samples instead of clinical samples, and the use of a single organism, *Staphylococcus aureus*, as a model due to its relevance as a human pathogen. However, these choices allowed us to create replicable cultured samples with known numbers of organisms and to create various sample types representative of swab collection sites (from dry to wet samples, in the presence or absence of other biological components). Other limitations of this work include the evaluation of a limited number of swab types, although they represent some of the most common commercially-available swab types used in clinical testing today. Finally, although the number of organisms transferred from swabs involves both collection and release, swab collection efficiency is highly dependent on the target pathogen and details of the sampling site; our work only focused on swab transfer release efficiency.

Conclusions

We have built on previous work to develop a quantitative method to evaluate and compare swab transfer performance. We evaluated a variety of swabs under manual agitation conditions appropriate for POC testing. By selecting a set of commercially available swabs representing a variety of tip sizes, shapes, and materials, and utilizing qPCR as a direct measure of target quantity, we were able to quantitatively measure the transfer efficiency of a model organism. Our data show that swab size, structure, or composition affects swab release performance under different sampling conditions (low-volume, excess volume, or dry samples). Variations in manual agitation method and time had modest impact on swab transfer efficiency for three swabs tested, which is encouraging considering the likelihood of user variation in POC tests. For cases when a test is constrained to a swab with poor transfer efficiency, we demonstrated how forced-flow transfer methods could be used to improve transfer efficiency. The results and discussion presented here highlight key factors that should be considered in selecting swabs for POC applications. The quantitative evaluation methods developed here can be applied to other swab types in the future, both for POC applications or laboratory tests.

Acknowledgments

We thank our colleagues Paula Ladd and Erin Heiniger at the University of Washington, who provided useful discussions on experimental design and analytical methods. We thank collaborators Nic Vermeulen, Boris Alabyev and Karina Stepaniants from ElitechGroup North America Inc. Molecular Diagnostics (previously Epoch Biosciences) for input on swab selection, simulated nasal matrix, and experimental design and for supply of the qPCR assay; and David Moore, Erik Kvam, Andrew Burns, Bing Li, Frank Mondello, Scott Duthie and Matt Misner from GE Global Research for discussions on swab materials and experimental design. We thank our colleagues Paul Yager and Elain Fu and members of the Yager Lab, Fu Lab, and Lutz Lab at the University of Washington. SEM imaging and sputter coating work was performed at the University of Washington Nanotech User Facility (NTUF), a member of the NSF-sponsored National Nanotechnology Infrastructure Network (NNIN).

[Programming paper networks for point of care diagnostics](#) (Dharmaraja *et al*, *Proceedings of SPIE* Vol 8615, 2013)

Shivani Dharmaraja, Lisa Lafleur, Samantha Byrnes, Peter Kauffman, Josh Buser, Bhushan Toley, Elain Fu, Paul Yager, Barry Lutz*

Abstract

Lateral flow tests (LFTs) are well-suited for rapid point-of-care testing in low resource settings. The wicking action of the paper strip moves the sample and reagents through the device without a need for pumps, but LFTs are typically limited to tests that can be carried out in a single fluidic step. The materials from LFTs can be reconfigured to create paper networks that automatically carry out multi-step fluidic operations, while retaining the same easy-to-use format as a conventional LFT. Here, we describe basic principles of wicking and system-level behavior of paper networks by analogy to electrical circuits. We describe key design principles for a previously-developed 2D paper network (2DPN) and introduce an

alternative linear paper network (Pseudo-1DPN) that takes advantage of system-level behavior to perform clean sequential fluid delivery while reducing device running time.

Introduction

Lateral flow strip tests have been identified as a diagnostic technology well suited for point-of-care (POC) use in low resource settings^{499,500}. With fluid transport occurring due to the capillary pressure of the strip material (rather than through the use of pumps), lateral flow strip tests are entirely disposable, rapid, user-friendly, and affordable⁵⁰¹⁻⁵⁰³ (Figure 141). Numerous lateral flow strip tests have already been developed and successfully used in limited-resource settings, with applications including pregnancy testing and disease diagnosis. The basic function of a lateral flow device is to mix sample with a visible label (*e.g.*, antibody conjugated to gold nanoparticles) and capture the analyte-label complex at a detection line via an immobilized capture molecule (*e.g.*, antibody). While the simplicity of these strip tests makes them ideal for use as a POC tool, it has generally limited them to performing tests that can be carried out in a single chemical step. Using lateral flow tests (LFTs) as clinically relevant diagnostic tools is sometimes limited to targets with high(er) concentrations because of the limited analytical sensitivity of the LFT format. Recently, many research groups have been rethinking the advantages and limitations of LFTs and creating new devices with similar simplicity but added features, such as multiple assays in a single device^{45,258,259,500,502,504-506}.

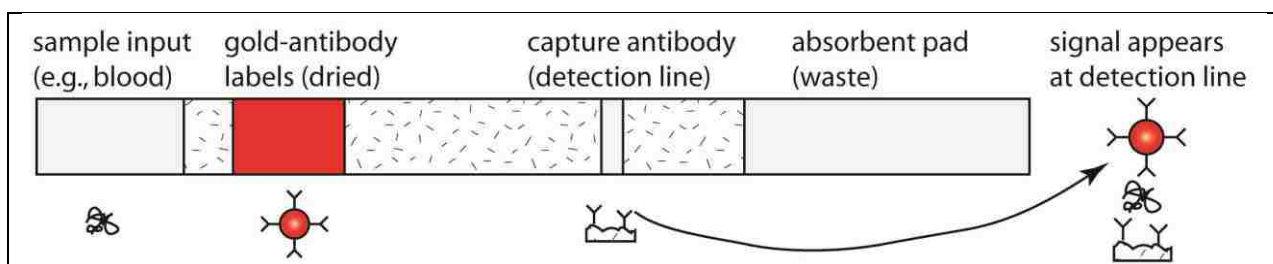


Figure 141: A common format for lateral flow tests. Fluid movement is driven by wicking, and chemical reagents are stored on the device. Most LFTs perform single-step sandwich immunoassays by binding a label to the analyte, then capturing the analyte-label complex at a detection line. In a LFT, these two reactions are carried out in a single fluidic step. LFTs typically cannot perform chemistries that require multiple steps (*e.g.*, amplification, sample preparation).

In recent years, the Fu/Lutz/Yager group at UW has worked to increase the functionality of disposable tests by patterning the membrane into two-dimensional paper networks (2DPNs)^{46-49,261,277,404,405}. Utilizing non-linear geometries of a wicking membrane makes it possible to perform automated multi-step assays without greatly increasing the device complexity from a user standpoint. Figure 142 shows an early demonstration of a 2DPN designed to deliver three fluids to a detection zone in a timed sequence. The three-legged device was contacted with three fluid droplets to initiate flow. The fluids initially wicked into the strip and met at the midway point between legs (Figure 142A), followed by wicking of fluids toward the detection region on the right of the strip (Figure 142B). Delivery from each leg stopped when its source fluid became depleted. The result was treatment of the detection zone with three fluids in a timed sequence (Figure 142C). The preliminary design, in this case, led to the undesired

co-arrival of two fluids at the detection zone (most evident in the parallel yellow and clear fluids at 9 minutes); prevention of this type of problem will be addressed in this paper.

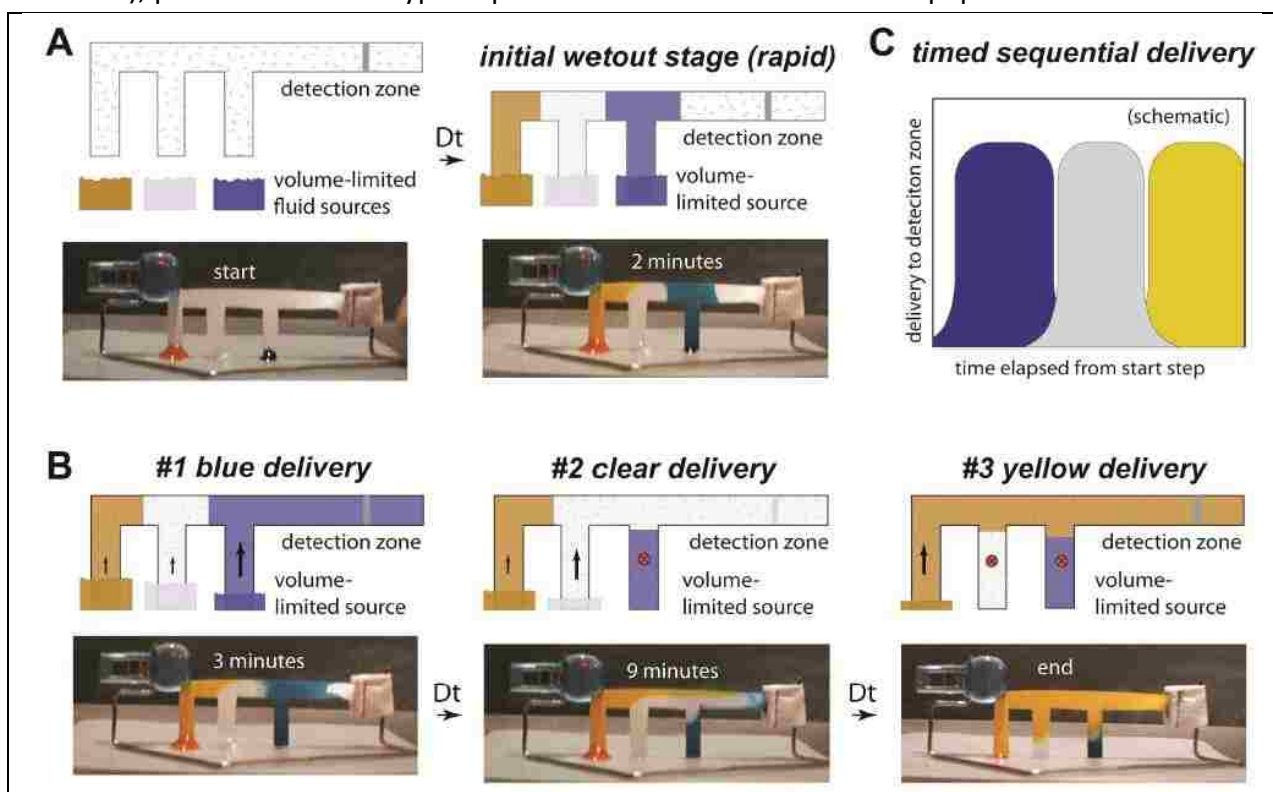


Figure 142: Early concept and demonstration of a 2-dimensional paper network (2DPN) for automated sequential fluid delivery. The device was fabricated from a porous nylon membrane cut by scissors, an absorbent pad (paper towel stapled to the membrane), and support stand (bent paper clip). Three drops of source fluid (water with food coloring) were pipetted onto a table, and flow was initiated by contacting the legs with droplets. Imperfections in sequential delivery (parallel flows of yellow and colorless fluids) can be seen in the images. The width of the main channel in the device was approximately 6 mm, and total time was about 9 minutes.

Sequential delivery in 2DPNs is controlled by two principles: 1) arrival time of each fluid at a detection zone is controlled by the length of the path followed by that fluid, and 2) fluid sources of finite volume are “shut off” by their depletion. Thus, 2DPNs represent a form of fluidic programming that depends on wicking properties of the materials and the system-level behavior of paper networks.

Since the initial concept demonstration (*circa* 2008), we have developed devices that automatically perform multi-step immunoassays using enzyme-based signal amplification (ELISA chemistry) and electroless gold deposition onto gold detection labels for signal enhancement^{49,404,405}. Design variations have included card-like formats that used porous pads as fluid sources^{49,404,405} and a cartridge format that used a single fluid well as the source for all legs⁴⁷. Figure 143 shows a previous example of a 2DPN that used porous (glass fiber) pads as the fluid sources⁴⁹. The image sequences at left show delivery of colored fluids, and those at right show the same device performing a multi-step signal enhancement. Glass fiber pads were chosen because they release nearly all fluid, but as we find in this paper, what appeared to be an ideal source actually is not. Successful fluidic sequencing depends not only on the paper network design but also on the release properties of the fluid sources.

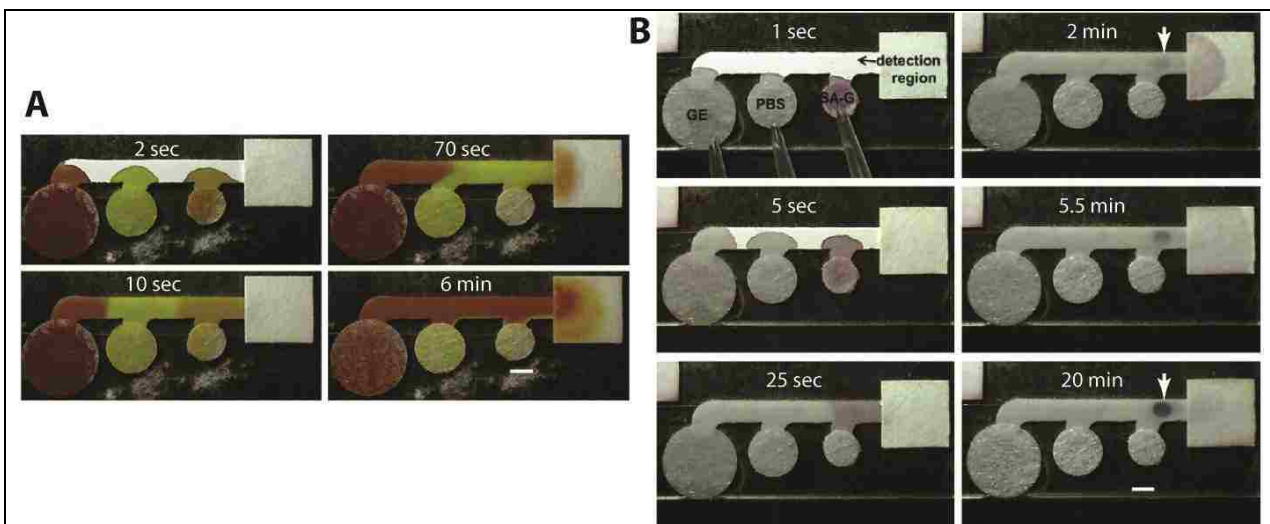


Figure 143: A 2DPN designed to automate a multi-step signal amplification [figure source: Fu, Kauffman, Lutz, Yager, "Chemical signal amplification in two-dimensional paper networks," *Sensors & Actuators B* 149 (2010) 325–328]. Porous (glass fiber) pads were used to hold finite volumes of source fluids. A) Image sequence of delivery of three fluids to a common leg in a timed sequence (orange, yellow, red). B) Image sequence for a sandwich immunoassay using a multi-step signal amplification process (SA-G: streptavidin-gold; PBS: phosphate-buffered saline; GE: gold enhancement reagent). The upper right image shows a faint gold spot (end point of a typical LFT), and the lower right image shows the darkened spot after enhancement. The device carried out all delivery steps without intervention. The width of the main channel was 3 mm.

It is possible to develop a functional 2DPN by an "estimate and check" method. However, this method generally requires multiple iterations to achieve sequential delivery with minimal overlap in the delivery of fluids. Our goal is efficient, rational design of 2DPN devices. This requires an understanding of the physical properties, namely the capillary pressure and the fluid resistances, of the multiple materials within the paper network. For example, even the simple lateral flow strip contains at least four connected materials whose physical properties affect fluid flow in the device. We note that Mendez, *et al* provided an excellent description of wicking principles and manipulated material shape to control fluid flow rates in strips²⁷⁶. In addition, the Delamarche group has done excellent work on capillary-driven flow control in microfluidic channels^{507–509}, and the channel-based format shares many principles with the porous material system discussed here.

In this manuscript, we apply simple electrical circuit models to paper networks to identify design principles for capillary driven sequential fluid delivery in paper networks. We introduce basic concepts of wicking and how electrical models can be constructed for simple cases, and we show how fluid sources can affect the extent and speed of fluid delivery into a strip. Finally, we use electrical models to identify design principles in paper networks and show that a linear paper network (Pseudo-1DPN) provides clean sequential delivery in a simple format.

Experimental

Characterization of alternative fluidic sources

Tested materials included thick glass fiber (8964; Millipore, Billerica, MA), cellulose (CFSP223; Millipore, Billerica, MA), and nitrocellulose (HF135; Millipore, Billerica, MA). A nitrocellulose (HF135) wicking membrane was used for each case. Materials were housed on adhesive Mylar (10 mil T- 5501 Mylar core with 1 mil adhesive on each side; Fraylock, San Carlos, CA) cards. All materials were cut using a CO₂ laser cutting system (Universal Laser Systems, Scottsdale, AZ).

Fabrication of sequential delivery devices

All sequential delivery devices were fabricated from nitrocellulose and adhesive Mylar. Fluid sources used were either wells (CV2024; VitroCom, Mountain Lakes, NJ) or thick glass fiber pads. Wells were held in place using a stand fabricated from thick cellulose (Grade 320; Ahlstrom, Helsinki, Finland).

General experimental protocols

Fluids used in any experiments were either deionized water or commercially available food dyes diluted in deionized water. Sequential delivery using well sources was performed in the ambient environment. All other experiments were conducted in a humidity-controlled environment (70% - 80% humidity). A web camera was used to perform all imaging (Logitech, Fremont, CA).

Computational modeling

All computational simulations were performed using MATLAB R2012a. Equations for the flow rates through each leg of a device (later denoted as Q1, Q2) were derived using mesh and nodal analysis of the analogous electrical circuit. Models were implemented only after initial wet-out occurred; initial conditions were defined by setting the position of the fluid fronts (known to be mid-way between spacer regions) and appropriately depleting the sources (based on membrane capacity). A time step of 0.2 seconds was used to track source depletion/saturation, source backpressures, the position of each fluid front, and fluid flow rates. As a note, this model has not yet been thoroughly validated and will only be used for qualitative purposes in this manuscript.

Physical principles and modeling approach

Electrical circuit analogues

Capillary-driven flow in porous media can be described conceptually by analogy to simple electrical circuits (Table 20). Pressure (P) created by capillary force or gravity is represented as voltage (V), fluid flow rate (Q) is represented as current (I), and viscous resistance ($R = \mu L / \kappa W H$) is related to properties of the fluid (fluid dynamic viscosity μ) and the permeability (κ) and dimensions of the porous material (cross-sectional area $W * H$, wetted length L). Atmospheric pressure acts on fluid-air interfaces and is represented as electrical ground at inlets and outlets. The 1D form of Darcy's Law relates the fluid flow rate to the driving pressure and viscous resistance; it is the equivalent of Ohm's Law in electrical circuits^{261,276,277}.

Table 20: Electrical analogy for capillary-driven flow in porous media

Electrical	Fluidic
Voltage, V	Pressure, P (capillary, gravity)
Current, I	Fluid Flow Rate, Q

Resistance, R	Resistance, $R = \mu L / \kappa W H$
Ground ($V=0$)	Atmospheric Pressure ($P=0$)
Ohm's Law, $V = IR$	Darcy's Law, $P = QR$

Figure 144A illustrates a simple case of fluid wicking from a finite fluid source into a straight, initially dry strip. The rate at which fluid wicks through a porous membrane is affected by two opposing forces: 1) the capillary pressure of the material (P_p) that pulls fluid into the strip, and 2) the viscous resistance (R) that opposes fluid flow through the pores. As more fluid is taken up by the material, the length of the fluid column increases as a function of time ($L(t)$), and the viscous resistance increases ($R = \mu L(t) / \kappa W H$). Figure 144B shows the electrical circuit model describing this time-dependent wicking, where an ideal fluid source is represented as ground ($P_s = 0$). Evaluating this circuit, we find that:

$Q(t) = \varepsilon W H \frac{dL(t)}{dt} = \frac{P_p}{R} = \frac{\kappa W H P_p}{\mu L(t)}$	Equation 22
---	-------------

and

$L^2 = \frac{2 P_p \kappa}{\mu \varepsilon} t$	Equation 23
--	-------------

where ε is the void volume of the porous material. Figure 144C illustrates Equation 23 for wicking of fluid into a strip from a finite fluid source. The combination of a constant capillary pressure and the rising resistance during wet out causes the fluid front to slow down over time (following $L^2 \sim t$) until the fluid source is depleted. The scaling found in Equation 23 ($L^2 \sim t$) matches exactly with the classic Lucas-Washburn expression describing 1D capillary-driven wet-out^{510,511}. Thus, electrical analogies can be useful for understanding basic concepts of capillary-driven flow in porous materials^{261,277}.

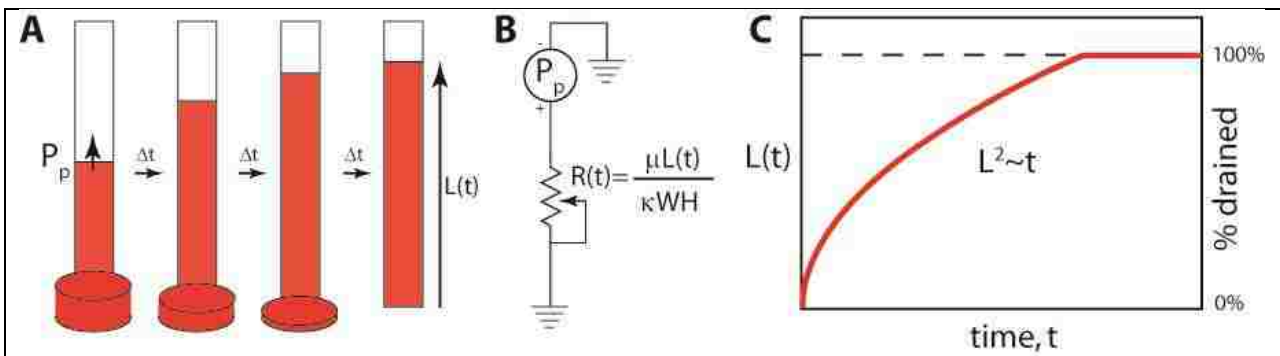


Figure 144: Principles of wicking into simple strips. A) Schematic of wicking into a straight, initially dry strip. Wicking is driven by capillary pressure (P_p) and opposed by viscous resistance to flow through pores that increases as wicking proceeds; the result is a slowing of wicking rate over time. B) An electrical circuit model for wicking into a strip. C) Illustration of migration of the fluid front as a function of time following Equation 23 for a finite fluid source.

Non-ideal fluid sources: backpressure effects

The previous derivations assumed ideal fluid sources that apply negligible backpressure on the strip during release (a condition inherently achieved using well sources). While this simplification offered by wells makes them a well-characterized fluid delivery system, alternative fluid source materials may be

better suited for POC settings. For example, LFTs commonly use a sample pad as a fluid source, and we have used glass fiber pads in 2DPNs to hold defined volumes of each source fluid (*e.g.*, Figure 143). Figure 145A shows the result of wicking fluid into strips from different source materials; images were taken after wicking had ceased. Each source material was sized to hold the same volume of fluid, and nitrocellulose was used as the wicking strip in all cases. The well case represents perfect delivery; the length of wicking into the strip is a measure of the volume released. Glass fiber completely released its fluidic content, while both cellulose and nitrocellulose source pads retained a large percentage of the fluid.

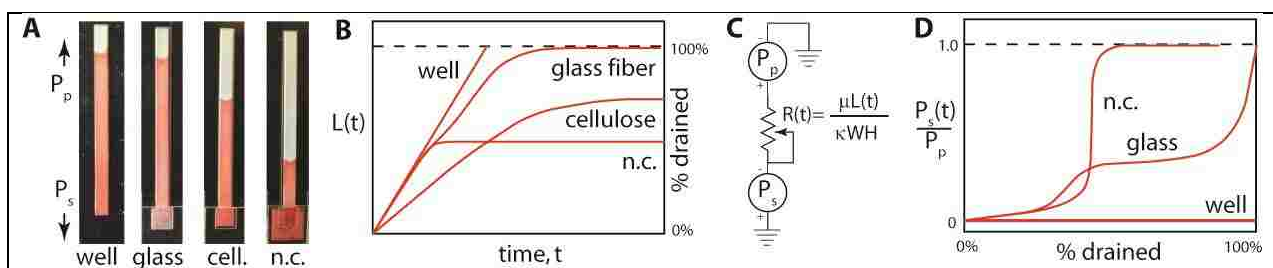


Figure 145: Effects of fluid source materials on capillary-driven fluid delivery into strips. A) Wicking of fluid from different source materials into nitrocellulose strips. Each source was sized to hold the same fluid volume, and images were taken after wicking ceased. The well source can provide complete delivery (100% drained); some materials did not deliver all fluid. B) Migration of the fluid front during wicking from different source materials as illustrations derived from experiments. The well case followed the L^2 versus t scaling from Equation 23, while other sources deviated to varying degrees. The % drained was calculated from $L(t)$ based on the fluid capacity of the nitrocellulose. C) Circuit model for wicking into a strip from a non-ideal fluid source. D) Backpressure profiles during release for different source materials. Profiles were determined from plots in C based on Equation 26 and presented here as illustrations. The backpressure applied by the source ($P_s(t)$) was normalized to the capillary pressure of the nitrocellulose strip (P_p), such that capillary flow stops when this ratio is one.

Figure 145B shows wicking profiles derived from data (not shown) for different fluid source materials. The source material affects not only the total amount of fluid released into the membrane, but also the rate at which fluid is released. While glass fiber fully drained, the release rate was slowed in comparison to the ideal case (well). When nitrocellulose was used as both a fluid source and wicking membrane, well-like delivery occurred until the source became $\sim 50\%$ depleted, at which point delivery quickly halted. In contrast to both materials, cellulose delivered an intermediate amount but showed a much slower release. The release profiles shown in Figure 145B suggest that the pressure applied on the membrane by the source pad can change as fluid is drained.

Following the electrical analogy, these fluid sources will function as a voltage source (rather than the previously used 'ground') that opposes the capillary pressure of the wicking membrane (Figure 145C). The circuit models for ideal and non-ideal sources can be used to derive the time-dependent pressure applied by a given material based on experimentally obtainable values.

$$\text{Well source: } Q^{\text{well}} = \epsilon WH \frac{dL^{\text{well}}}{dt} = \frac{P_p}{R} = \frac{\kappa W H P_p}{\mu L_{\text{well}}}$$

Equation 24

$\text{Nonideal source: } Q^{pad} = \varepsilon WH \frac{dL^{pad}}{dt} = \frac{P_p - P_s(t)}{R} = \frac{\kappa WH [P_p - P_s(t)]}{\mu L^{pad}}$	Equation 25
---	-------------

Taking the ratio of these two equations gives the time dependent applied pressure of a non-ideal fluid source ($P_s(t)$):

$\frac{P_s(t)}{P_p} = 1 - \frac{L(t)^{pad} \frac{dL(t)^{pad}}{dt}}{L(t)^{well} \frac{dL(t)^{well}}{dt}}$	Equation 26
--	-------------

As suggested by the experiments, we again see that the capillary pressure of the nitrocellulose and the backpressure exerted by the source material affect both the distance and rate at which fluid travels through the membrane ($L(t)$ and $dL(t)/dt$, respectively).

Figure 145D plots the backpressure profile during release for selected materials (curve derived from experimental data, not shown); it shows how drastically the pressure applied by a non-ideal source may deviate from the ideal case. In contrast to the constant, negligible backpressure exerted by a well, glass fiber and nitrocellulose sources had complex pressure functions that varied as they were drained. In the initial stages of delivery, the glass fiber pad behaved similar to an ideal well source and applied a very low backpressure. However, this pressure drastically increased as more fluid was released. This matches the wicking behavior observed in Figure 145B where release from glass fiber pad increasingly deviated from the well case over time. Release from nitrocellulose initially occurred with little backpressure until reaching a critical depletion level (~50%), at which point the capillary pressure of the membrane and the backpressure applied by the source equalized. This pressure equilibration eliminated the driving force for flow and as a result, the nitrocellulose pad retained the remainder of its fluid (as seen in Figure 145B).

Since many potential source materials have a non-uniform pore distribution, it is not surprising that the backpressure applied by the source changes during drainage. For example, a material composed of small and large pores may apply a bimodal backpressure. The pressure may first be low as the large pores drain but then increase when only the small pores remain filled. Glass fiber, cellulose, and nitrocellulose (all common lateral flow materials) all have non-uniform pore distributions. In the following sections, we describe the impact of ideal and non-ideal fluid sources on paper network behavior. In some cases, backpressure profiles from Figure 145D data were used in calculations.

Basic principles in 2D paper network (2DPN) design

Figure 146 illustrates the network behavior for sequential fluid delivery in a 2DPN. For simplicity, we show a device with two legs of equal length and ideal fluid sources of finite volume. Figure 146A (left) shows the state after an initial wet-out period in which the two fluids meet in the spacer region mid-way between the two legs. After this point, both sources continue to deliver fluid, but at different rates. A “leakage” flow (Q_2) causes migration of the blue fluid front, and successful sequential delivery requires that the first fluid (red) is completely drained before arrival of the blue-red fluid front. Unsuccessful design results in both fluids flowing into the detection leg in parallel (e.g., yellow and clear fluids in Figure 142). Figure 146A (right) shows the state after complete drainage of the first (red) fluid for a condition of successful delivery.

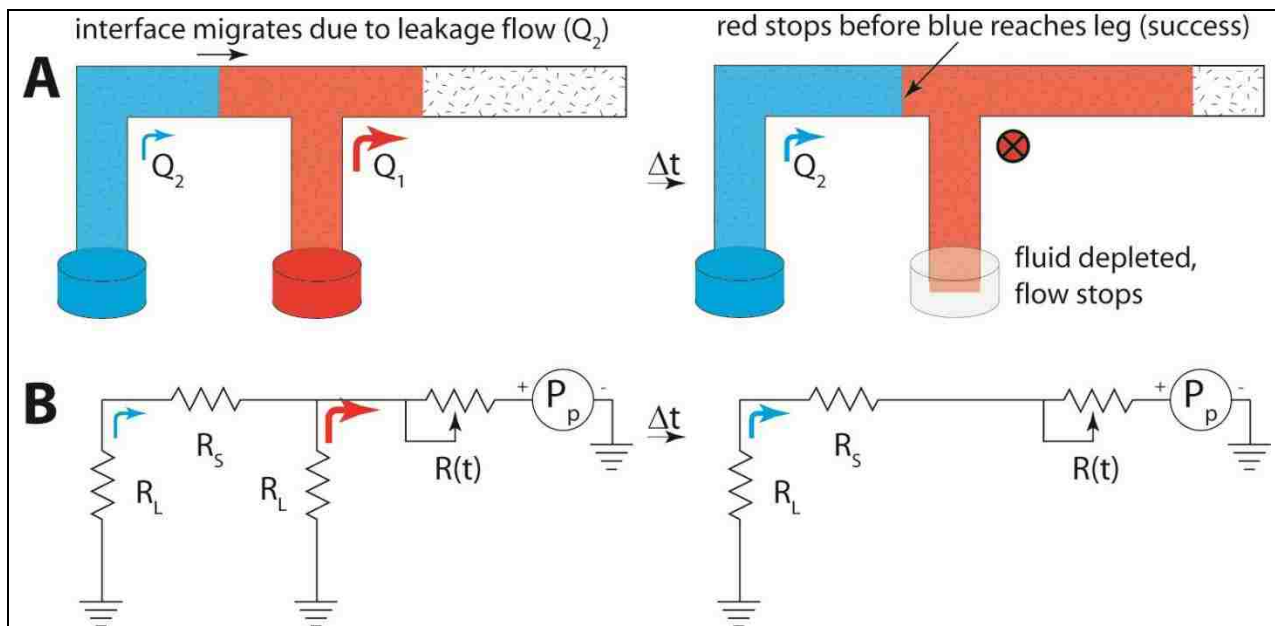


Figure 146: Network behavior for sequential delivery in a 2DPN. A) After initial wet-out occurs, fluid will continue to flow through both legs, which causes the fluid interface to migrate. Successful sequential delivery occurs if the red fluid drains completely before the blue fluid reaches its leg. B) Circuit model for the two stages of delivery in the 2DPN.

Figure 146B shows circuit diagrams for the two stages of sequential delivery in the 2DPN. The ratio of flow rates delivered by each leg is a critical parameter in achieving device success; we find that it can be determined solely by the resistances in the network:

$\frac{Q_2}{Q_1} = \frac{1}{1 + R_s/R_L}$	Equation 27
---	-------------

Ideally, this flow ratio would be zero in the first stage of delivery, with no fluid release occurring from the left source (blue, Q_2) as the right source (red, Q_1) drains. Conceptually, delivery is clean if the time for depletion of the first fluid (T_{drain}) is shorter than the time for migration of the leakage front (T_{mig}). A quantitative criterion for success must also consider the volumetric capacity of the spacer region (*i.e.*, the region that can be filled by the flow Q_2 before failure, not shown). While the 2DPN is incapable of eliminating leakage flow, the leakage flow can be mitigated by increasing the spacer resistance (R_s , *e.g.*, by increasing length or decreasing width) or by decreasing the leg resistance (R_L , *e.g.*, by decreasing length or increasing width). Non-ideal sources further increase the leakage flow (equations not shown). The simple analysis shows the most critical concept – eliminating legs should improve sequential delivery.

A linear paper network (Pseudo-1DPN): basic principles

Prior to developing the network models presented here, some of our authors (Lafleur, Kauffman, Byrnes) created a linear strip using wells as fluid sources. Their design provided clean sequential delivery for three fluids (shown later). Here, we develop the circuit model that explains this behavior and describe the effects when non-ideal fluid sources are used. Figure 147 illustrates sequential delivery in a linear paper network (Pseudo-1DPN) with ideal and non-ideal fluid sources.

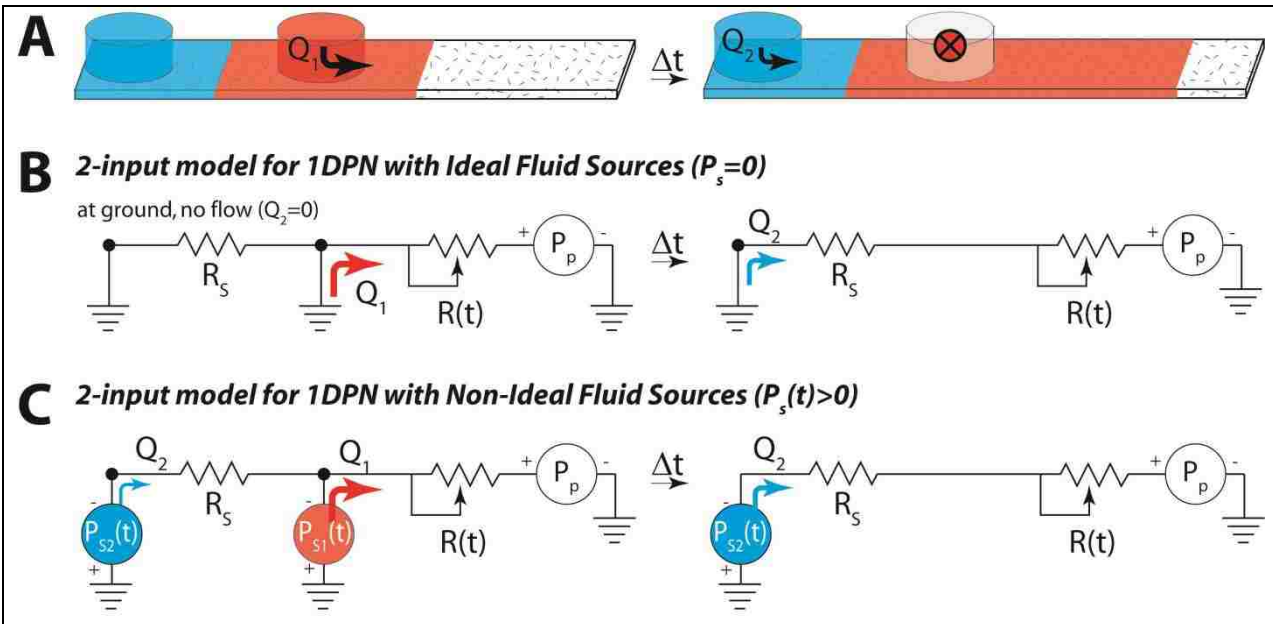


Figure 147: Network behavior of sequential delivery in a Pseudo-1DPN using ideal and non-ideal fluid sources. A) If ideal sources are used, the fluid front of the left fluid (blue) will remain stationary until the right source (red) is completely drained. Only then will the left source (blue) release its contents. B) A circuit model for sequential delivery in a Pseudo-1DPN that uses ideal fluid sources. C) A circuit model for sequential delivery in a Pseudo-1DPN that uses non-ideal fluid sources. Fluid will be released from both sources simultaneously, allowing a potential for leakage to occur (similar to the 2DPN device).

For the initial stage of sequential delivery, the case of non-ideal fluid sources is described by:

$Q_2 = \frac{P_{S1} - P_{S2}}{R_s}; \quad Q_1 = \frac{P_p - P_{S1}}{R(t)}; \quad \frac{Q_2}{Q_1} = \frac{R(t)[P_{S1} - P_{S2}]}{R_s[P_p - P_{S1}]}$	Equation 28
---	-------------

From these equations, we see that initially, the flow rate of fluid from the left source is not necessarily zero, but a function of the pressure differential between the two sources (Figure 147C) and the spacer resistance (R_s). Thus, the potential for leakage to occur will depend on the backpressure applied by the source material and how it changes as fluid is drained (see Figure 145). As with the 2DPN above, leakage caused by non-ideal fluid sources can be mitigated by increasing the spacing resistance (R_s).

For the case of ideal sources ($P_{S1}=P_{S2}=0$), the leakage flow is zero, by definition, since there is no pressure difference acting between the fluid sources (if we ignore the force of gravity acting on the fluid columns, both are at “ground”, Figure 147B). Thus, ideal sources are expected to give clean sequential delivery even for small spacing between fluid sources. Below, we explore the behavior of both cases in more complex 3-source devices.

Sequential delivery in Pseudo-1DPNs with ideal fluid sources

Figure 148 describes sequential delivery in a Pseudo-1DPN with ideal fluid sources. Figure 148A shows a mathematical simulation of a well-based device case using the previously defined circuit equations. The ideal sources provide perfect sequential delivery since there is no driving pressure for the leakage flow (as shown for the two-leg model in Figure 147B).

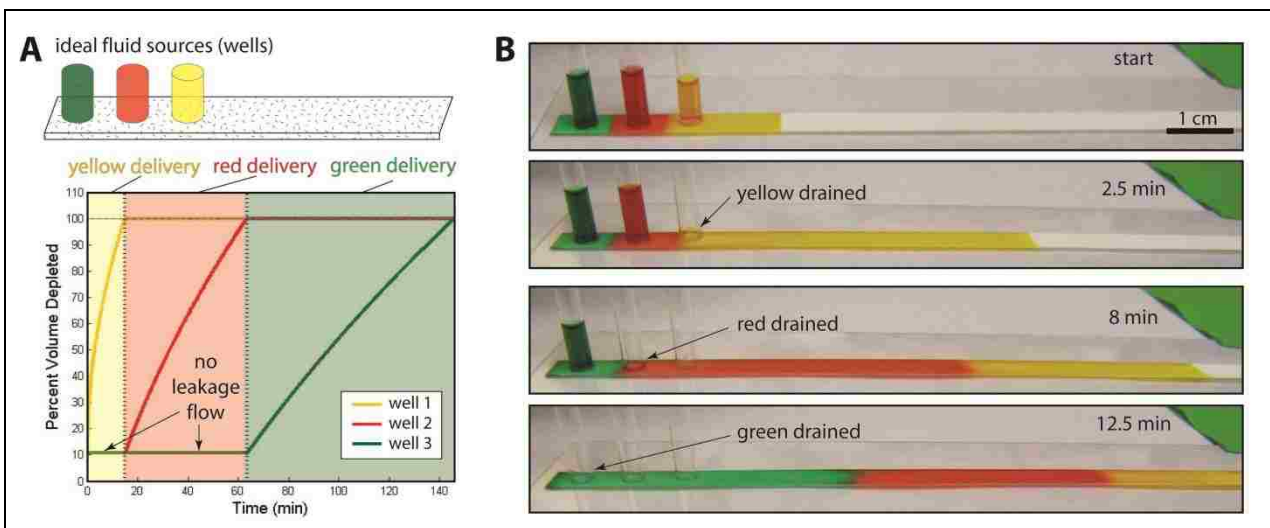


Figure 148: Model behavior and experiments for a Pseudo-1DPN with ideal fluid sources (wells, but in this case sitting above the nitrocellulose membrane). A) Schematic of the Pseudo-1DPN with ideal fluid sources, and model results showing sequential delivery of three fluids. Unlike the 2DPN, wells drain in a perfect sequence with no leakage flow. B) Experimental results for Pseudo-1DPN with ideal sources. Large diameter tubes (wells) serve as ideal sources – they apply a negligible backpressure compared to nitrocellulose capillary pressure ($P_s=0.13$ kPa, $P_p=12$ kPa); similarly, the height of fluid in the well is small, so pressure due to gravity is also negligible ($P=0.065$ kPa). After tubes were contacted with the strips, fluid from each source was delivered in a timed sequence through the strip. Images show the device a few seconds after contact ('start') and at the moments when each tube became depleted (yellow: 2.5 min, red: 8 min, green: 12.5 min). Each well delivered 20 microliters (60 microliters total for three wells).

Experiments confirm that clean sequential delivery can be achieved using a well-based Pseudo-1DPN. Time-lapse images of fluid delivery show that the fluid from one source of the device is released only after the previous source has been completely drained (Figure 148B). The position of the green and red fluid fronts and the levels of fluid in the wells did not significantly change until the fluid in the well to its right was completely drained. As a note, the discrepancy in the time scale of fluid delivery between our model predictions (~140 minutes) and our experimental results (~12.5 minutes) may be due to inaccurate membrane parameter values used in the model (*e.g.*, permeability, void volume). Using well sources in our Pseudo-1DPN allows us to achieve ideal flow behavior – fluids are released sequentially (and with no leakage) over a time scale appropriate for a potential POC device. Also, the model suggests that a Pseudo-1DPN with ideal fluid sources should provide perfect sequential delivery even when fluid volumes are changed, without the need to alter design. By contrast, the 2DPN format must be redesigned to accommodate any volume changes. Further, the model suggests that fluid sources can be placed close together without impacting behavior; this reduces the total time for delivery since the device can be short. Incorporating these sources into a usable POC test, however, may be a challenge, since they require a user to fill them with the correct volume and they may not be suitable as a storage medium for dried assay reagents.

Sequential delivery in Pseudo-1DPNs with non-ideal sources

Though glass fiber is a widely used source material in LFTs, the changing backpressure it applies on the nitrocellulose membrane during drainage has the potential to cause issues of premature flow and leakage in this Pseudo-1DPN. Figure 149 describes sequential delivery in a Pseudo-1DPN with non-ideal, glass fiber pad fluid sources (Figure 149A). Initial simulations involving three-step sequential delivery matched our expectation that premature flow will occur between the pads (Figure 149B). While fluid from the right-most pad (clear) was being released, fluid drained from all other sources. The left-most pad (red) released nearly all of its fluid (~90%) before the yellow pad was drained, demonstrating that this leakage flow may not be trivial.

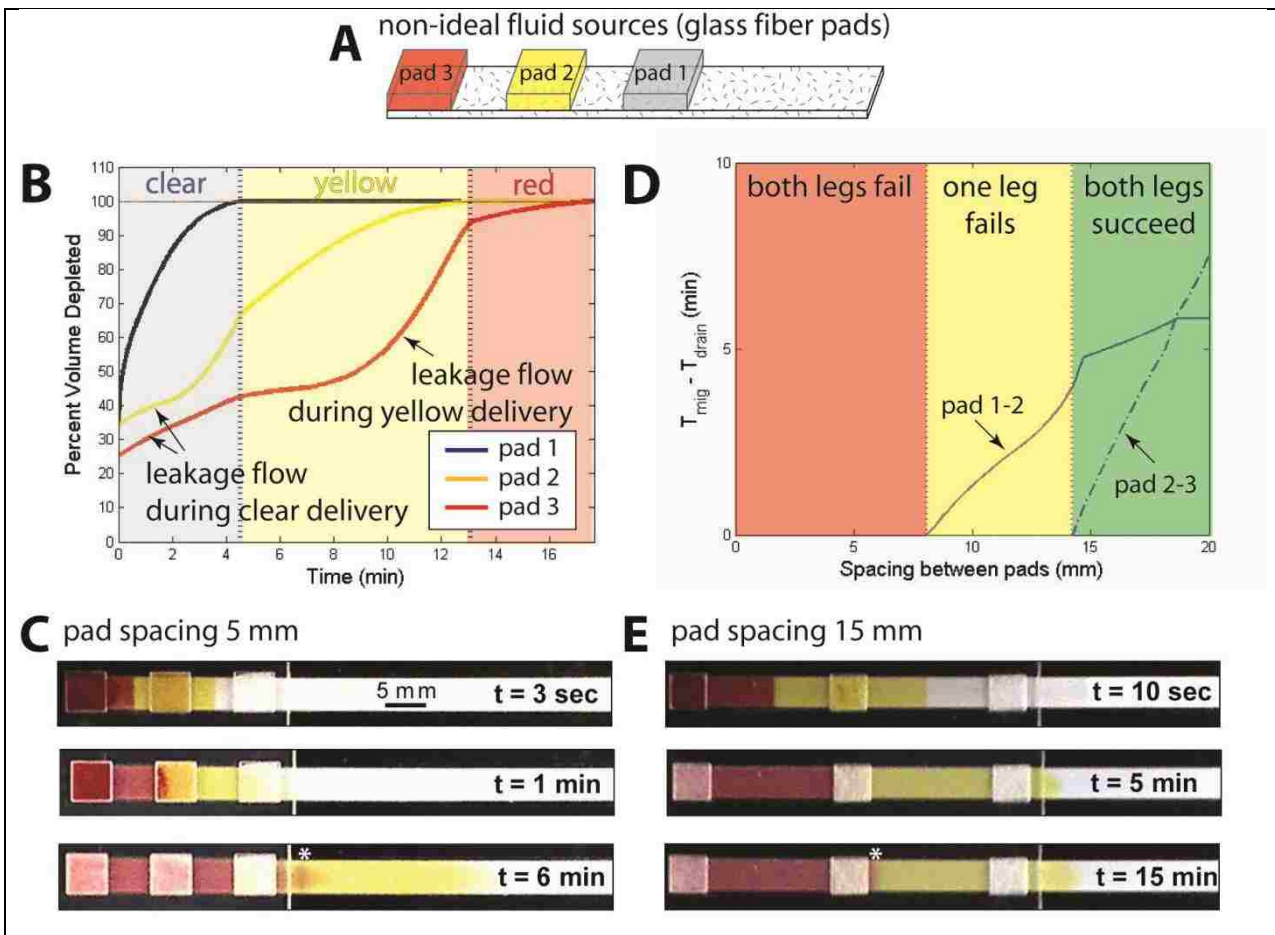


Figure 149: Model behavior and results for devices with imperfect sources (glass fiber pads). A) Schematic of a 3-source Pseudo-1DPN that uses glass fiber pads to deliver clear, yellow, and red fluids. B) A computational model of this scenario predicts that both the yellow and red fluids will be prematurely released. C) Time-lapse images of failed sequential delivery. High leakage flow (due to small spacer resistances ($L=5$ mm)) resulted in mixing and non-uniform fluid interfaces. D) A computational model was used to illustrate the effect of spacer resistance on failure and success. E) Time-lapse images of successful sequential delivery. Increased spacer resistances ($L=15$ mm) accommodate fluid leakage so that clean delivery is still achieved. No mixing occurs in the glass fiber pads and similar to the ideal Pseudo-1DPN case, there is a distinct interface between the different fluids. Each pad delivered 10 microliters (30 microliters total for three wells).

Figure 149C shows time-lapse images of a failed device, with pads spaced 5 mm apart. Initial wet-out occurred soon after device activation. However, after wet-out, fluids from the yellow and red pads continued to migrate, reaching the next pad before it was completely drained. This caused unwanted mixing to occur in both the glass fiber pad (noticeably seen at $t = 1$ min) and the nitrocellulose membrane (exhibited by the long red fluid front seen at $t = 6$ min, marked by *).

As was the case of the 2DPN, issues caused by this leakage flow can be avoided with appropriate device design. Figure 149D shows a computational model that predicts device behavior given a specific spacing distance/resistance. The times T_{mig} and T_{drain} are used to determine device success. In the model, T_{mig} is the time it takes for fluid from one pad to migrate from the middle of the spacer region (where initial wet-out has terminated) to the left boundary of the subsequent pad. T_{drain} corresponds to the time required for this 'subsequent pad' to release all of its fluid. A successful device will have non-negative $T_{\text{mig}} - T_{\text{drain}}$ values for all pairs of pads. For example, relating this to Figure 149A, $T_{\text{mig}}(\text{yellow}) - T_{\text{drain}}(\text{clear})$ and $T_{\text{mig}}(\text{red}) - T_{\text{drain}}(\text{yellow})$ must both be greater than or equal to zero for the device to be successful. The plot generated by our model is broken into three distinct regions: red (no clean delivery), yellow (clean delivery between the first and second pad), and green (clean delivery between all pads). As predicted by the circuit model, increasing spacer resistance decreases the flow ratio between sources and improves the likelihood of device success.

Figure 149E shows time-lapse images of a Pseudo-1DPN predicted to achieve clean delivery (with a pad spacing distance of 15 mm). No obvious mixing of fluids occurred in either the pads or at the fluid boundaries. While the fluid front of the red fluid stopped somewhat beneath Pad 2, there still appeared to be a relatively clear distinction between the red and yellow fluids (marked by *).

In previous work, we chose to use glass fiber pads as fluid sources (*e.g.*, Figure 143) based on their use as dry reagent storage media in lateral flow tests, their ability to self-fill to a fixed volume by wicking (potentially eliminating the need for pipetting steps), and our observation that they release nearly all fluid into a nitrocellulose strip. However, here we found that changes in backpressure during release from glass fiber pads required compensation by increasing the spacer length between fluid sources (and thus increasing total device run time). In contrast, experiments with ideal fluid sources (wells, Figure 148) showed that the Pseudo-1DPN can provide clean sequential delivery even with closely-spaced fluid sources. Our overall goal of a simple user interface (no pipetting), on-device reagent storage, and clean sequential delivery with short total run times is highly-dependent on proper selection of fluid source materials. The analysis here provides a framework to guide that selection.

Conclusions

The lateral flow test is an ingenious device that performs basic immunoassays in a rapid and easy-to-use format. Paper networks use the same set of materials but reconfigure them to automatically carry out timing for multi-step processes. The behavior of both devices depends on the connectivity of multiple materials and their wicking properties. Here, we explored basic principles of wicking in simple devices and paper networks through use of electrical circuit models. We identified key design principles in a previously-developed sequential delivery device (2DPN) and described an alternative linear paper network (Pseudo-1DPN) that can provide remarkably clean sequential delivery in a very simple device. We showed that materials used as fluid sources can affect both the rate of fluid delivery into a strip and the fraction of fluid volume released, and these fluid release properties are especially important for

programming sequential delivery in paper networks. The analysis provides a framework for more rational design and material selection for paper networks and other capillary-driven diagnostic devices.

Acknowledgements

The work presented in this paper was carried out in part with support from DARPA DSO under a grant to the University of Washington (grant number HR0011-11-2-0007) with collaborators at PATH, GE Global Research, and Epoch Biosciences.

Progress in the development of paper-based diagnostics for low-resource point-of-care settings (Byrnes *et al. Bioanalysis*, 2013)

Samantha Byrnes¹, Gregory Thiessen¹, and Elain Fu*

¹Authors contributed equally to this manuscript

*Corresponding author

Abstract

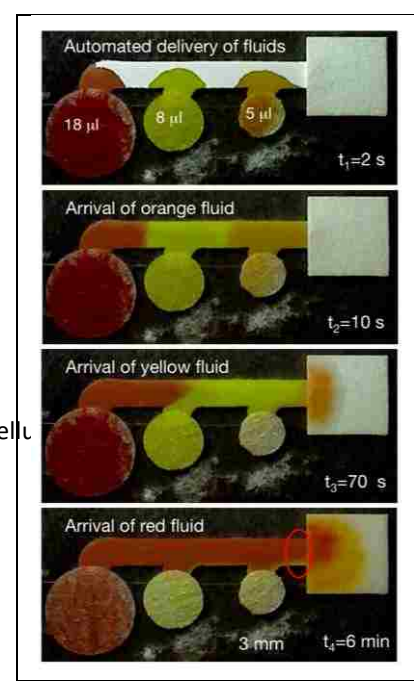
This review focuses on recent work in the field of paper microfluidics that specifically addresses the goal of translating the multi-step processes that are characteristic of gold-standard laboratory tests to low-resource point-of-care settings. A major challenge is to implement multi-step processes with the robust fluid control required to achieve the necessary sensitivity and specificity of a given application in a user-friendly package that minimizes equipment. We review key work in the areas of fluidic controls for automation in paper-based devices, readout methods that minimize dedicated equipment, and power and heating methods that are compatible with low-resource point-of-care settings. We also highlight a focused set of recent applications and discuss future challenges.

Introduction

For accurate and reliable disease detection, many gold-standard diagnostic methods rely on multi-step sample preparation and analysis techniques that require expensive laboratory equipment and trained technicians. Thus, these tests are not appropriate for point-of-care (POC) use, especially in low-resource settings, and are not available to populations who need them most. Over the last two decades, research and development in the field of microfluidics has made advances in the miniaturization, automation, and cost-reduction of gold-standard laboratory-based sample processes, in order to make them appropriate for POC applications [1]. Traditionally POC diagnostic tests were designed as single-use chips [2] composed of plastics, PDMS, or silicon, that utilized the many advantages of microfluidics, including requiring only small sample and reagent volumes and having a rapid time to result. In recent years, there has been an explosion of interest in the use of porous materials in POC diagnostic devices. The George Whitesides group is responsible for generating much of this interest, starting with their demonstration in 2007 of patterned cellulose to simultaneously detect glucose and protein in urine samples [3] (much of their early work is reviewed in [4]). Since then, there have been many advances in the still growing subfield of “porous network microfluidics” or “paper microfluidics”. Specifically, we

define a “paper”¹ or “porous” network as a device that exclusively uses capillary pressure to drive flow in the porous matrix of which it is composed, for the automatic pumping of fluid within the device. These networks are most often composed of the porous materials used in the conventional lateral flow industry: cellulose [5] and nitrocellulose [6]. These porous network devices share other attributes of the conventional lateral flow test (LFT); namely they are disposable, have a rapid time to result, are composed of inexpensive materials, and can be cost-effective to manufacture.

In recent years there have been multiple reviews focused on work in paper microfluidics. Ballerini *et al.* reviewed the increased functionality and variety of paper-based materials for the development of POC diagnostics [7]. Li *et al.* have described the various fabrication techniques and some applications for paper-based technologies [8], while other reviews have focused specifically on paper-based device fabrication via ink-jet printing or toner transfer methods [9]. Nie *et al.* [10] and Maxwell *et al.* [11] separately described electrochemical sensing techniques in paper-based devices, while Liana *et al.* took a broader perspective focusing on recent advances in all paper-based sensing technologies and the need to increase device sensitivity [12]. There have also been recent reviews on the challenges of transferring traditional plastic-based electronics to paper-based formats [13], as well as the development of LFTs for the detection of contaminated food [14]. Shah *et al.* reviewed the development of an entire paper-based analytical kit for biomarker and bacterial detection at the POC [15]. Kuo *et al.* described the emerging trend of hybrid devices that utilize the advantages of different substrates in one combined, effective device [16]. Most recently, Yetisen *et al.* have reviewed multiple areas in the field of paper microfluidics including device fabrication, device capabilities, detection techniques on paper, and quantitative handheld readout systems [17]. Although this is not a comprehensive list of porous membrane-based devices reviews, it is highly representative of the breadth of literature surrounding paper microfluidics and indicates the rapid growing interest in the field.



¹ The term “paper” is defined broadly here to include porous membranes such as nitrocellulose.

In this review, we focus on recent work in the field that specifically addresses the goal of translating the multi-step processes that are characteristic of gold-standard laboratory tests to low-resource POC settings. There are specific constraints that must be addressed when designing tests that are appropriate for use in these settings. For example, the often lengthy time to result of many laboratory-based diagnostic tests can be inappropriate in low-resource settings where requiring patients to make at least two visits before getting diagnosed may be impractical [18]. These tests need to be affordable, specific, sensitive, user-friendly, rapid and robust, equipment-free, and deliverable, or ASSURED [19]. Thus, a major challenge is to implement multi-step processes with the robust fluid control required to achieve the necessary sensitivity and specificity of a given application in a user-friendly package that minimizes equipment. We review key work in the areas of (i) fluidic controls for automation in paper-based devices, (ii) readout methods, and (iii) power and heating methods which are compatible with low-resource POC settings. Finally, we highlight a focused set of recent applications and discuss future challenges.

Figure 1. Two-dimensional paper networks with multiple inlets per detection region for automated multi-step sample processing. The sequential delivery of multiple fluid volumes has been pre-programmed into the configuration of the network [21].

Fluidic controls for automation in paper-based devices

A major challenge in creating POC diagnostic tests that are appropriate for applications in low-resource settings is to achieve precise and robust automated fluidic control of the multiple fluid sources in an assay. As in conventional lateral flow assays, properties of the porous materials, including pore size, pore structure, and surface treatments, affect the delivery of reagents in an assay. These considerations have been discussed previously in the context of conventional lateral flow tests and will not be discussed here [20]. Recently, a number of tools have been developed to control fluid flow in porous network devices. These tools serve to replace the costly and often complicated valves and pump controls in conventional microfluidics. This section will discuss fluidic controls for automation in porous network devices including network topology, channel geometry for changing flow rates, on-switches or delays for flow, off-switches for flow, and spatial and temporal controls for manipulating rehydrated reagents.

Network topology for the sequential delivery of multiple fluids. Networks with multiple inlets for each outlet have been developed to perform the automatic sequential delivery of multiple fluids to a detection region [21, 22]. **Figure 1** shows a simple 3-inlet two-dimensional paper network (2DPN). Fluids are applied simultaneously to the inlets, staged in the main horizontal leg of the device, and then delivered sequentially to the detection region. The dimensions of the network can be used to accommodate different volumes of fluids and the number of inlets increased to accommodate a greater number of reagents. Fu *et al.* have used this format to sequentially deliver sample plus label, rinse, and amplification reagent to create an amplified immunoassay [23].

More recently, Dharmaraja *et al.* demonstrated that sequential delivery can be achieved through the use of a Pseudo-1DPN [24]. This format consists of a linear strip composed of a porous material and multiple fluid-filled wells as sources. As in the case of the 2DPN above, the contents of the sources will be delivered sequentially to the detection region in order of distance from the detection region. The authors presented an electrical circuit model for explaining the sequential delivery of the multiple fluids in the strip as a balance of the capillary pressures and fluidic resistances in the system. An alternative source used in conventional LFTs that may be more appropriate than fluid filled wells for the lowest-resource settings are porous pads. Pad sources could also be used to produce clean sequential delivery when the fluidic resistances between the pads were made sufficiently large by increasing the interpad spacing.

Channel geometry to control flow rates. A key method for controlling the flow rate in porous channels is to vary the geometry of the channel. Flow in one-dimensional lateral flow strips is well characterized. The one-dimensional transport of the fluid front in a porous matrix during wet-out is characterized by the Lucas-Washburn equation, $L^2 = \frac{\gamma D t}{4\mu} \cos \theta$, where L is the distance moved

by the fluid front, t is time, D is the average pore diameter, γ is the effective surface tension, $\cos \theta$ is the contact angle dependence, and μ is viscosity [25-27] (for a review on the physics of paper see Alava and Niskanen [28]). Therefore, in a constant width strip, $L \sim \sqrt{t}$, and the length of the strip can be used to control the interaction time between reagents in an assay. Additionally, the volumetric flow rate can be adjusted by varying the width of the strip [29]. In an extension to two-dimensional structures, Medina *et al.* investigated imbibition in triangular shapes of blotting paper and characterized the deviation from Washburn flow [30]. Recently, Fu *et al.* have described the use of simple two-dimensional geometries to control the flow rates of fluids and presented some basic design rules for transport in paper networks [29]. For example, in the case of an expansion in geometry, a transition to a greater width results in an increase in the transport time of the fluid front relative to that in a constant width strip. The complementary result for the case of a contraction, a transition to a smaller width, is that the transport time of the fluid front is decreased relative to that in a constant-width strip. Thus, a simple control parameter for regulating the transport time of the fluid front is the downstream location of the expansion or contraction. In addition, the width of the expansion or contraction can be used to further adjust the transport time.

In the case of “fully-wetted” flow, when the fluid front has reached a wicking pad, an absorbent pad used to wick additional fluid through the substrate, the velocity is approximately steady and is described by Darcy’s Law. In one dimension, Darcy’s Law [31] reduces to $Q = \frac{-\kappa A}{\mu L} \Delta P$, where Q is

the volumetric flow rate, κ is the permeability of the material to the fluid, A is the area of the channel perpendicular to flow, μ is the viscosity of the fluid, and ΔP is the pressure difference along the direction of flow over the length L . An analogy to electrical circuits can be useful, where pressure difference is analogous to electrical potential difference, the volumetric flow rate is analogous to current, and the fluidic resistance depends on physical parameters of the system including geometric factors in the paper circuit. Extension to simple two-dimensional geometries is straightforward; fluidic resistances in series are summed, while fluidic resistances in parallel can be added in reciprocals. Fu *et al.*, have presented a description of how one can predict and control flow rates for simple changes in geometry, such as those shown in **Figure 2** [29]. A time series comparison of experimental and simulation results for flow in the strips of different geometries indicates good quantitative agreement [29]. Further, simple manipulation of inlet leg length and width were used to control the time of reagent delivery in a 2DPN [29].

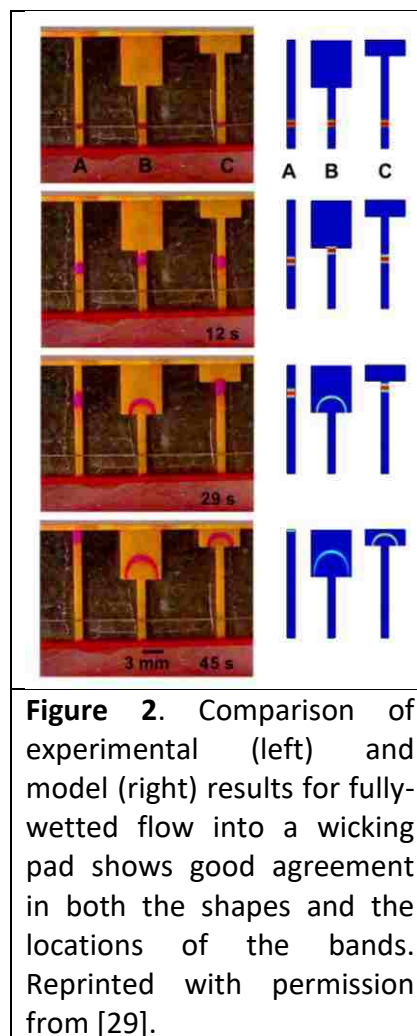


Figure 2. Comparison of experimental (left) and model (right) results for fully-wetted flow into a wicking pad shows good agreement in both the shapes and the locations of the bands. Reprinted with permission from [29].

Mendez *et al.* employed complex paper shaping to adjust the flow rate in their devices [32]. Specifically, they used fan-shapes located downstream of a rectangular strip, as shown in **Figure 3**, to achieve the quasi-stationary flow of conventional lateral flow strips that use cellulose wicking pads. Once fluid reaches the fan-shaped section, there is a sudden increase in the volume of available dry porous media, similar to the situation in a wicking pad, and the transport of the fluid front within the rectangular stem transitions from Lucas-Washburn to quasi-stationary. A significant advantage of this method is potential simplification to device fabrication and manufacturing by requiring only a single material. Additionally, quasi-stationary flow can enable approximately constant reaction time within porous membrane-based assays.

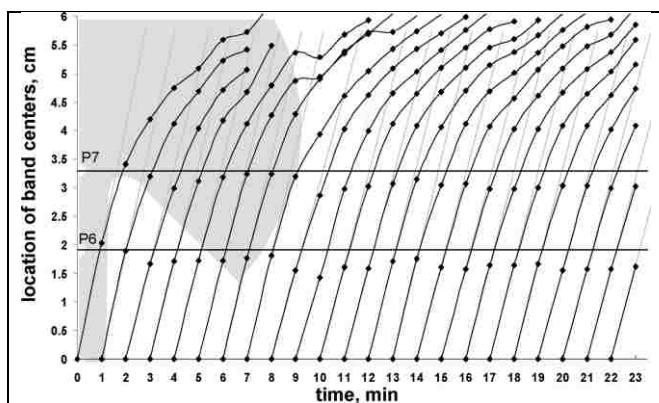


Figure 3. Velocity data from a complex shape used by Mendez *et al.* to adjust the flow rate in their nitrocellulose devices. Reprinted with permission from [32]. Copyright 2010 American Chemical Society.

On-switches/delays to control the arrival time of fluids. Another key fluidic control is the ability to delay the downstream arrival of a given fluid for a specific amount of time. As described above, the use of network topology and channel geometry can be used to achieve sequential delivery, but for the case of larger reagent volumes, these methods can significantly increase the footprint of the device. Thus, alternative paper fluidic tools that act as an on-switch, or a timed fluid flow delay are critical. Several methods have been developed and will be discussed in this section. These include methods that do not require any user intervention, such as dissolvable barriers and hydrophobic surface treatments, as well as user-activated methods, including folding tabs and push buttons.

One type of on-switch or delay for fluid flow uses dissolvable barriers. Lutz *et al.* have demonstrated that a dissolvable sugar barrier will produce a delay in the transport time of fluid relative to if the barrier were not present [34]. Both the extent of the sugar barrier and the concentration of the sugar solution used to form the barrier within the porous material were used to control the delay time. Delays from seconds to almost an hour were achieved with measured variability in arrival times between 9 and 19% [34]. One potential issue with this method is the effect of the barrier components on downstream processes. For example, low concentrations of sugar, e.g. trehalose, are used for the preservation of dry reagents and are generally compatible with common signal generation schemes for

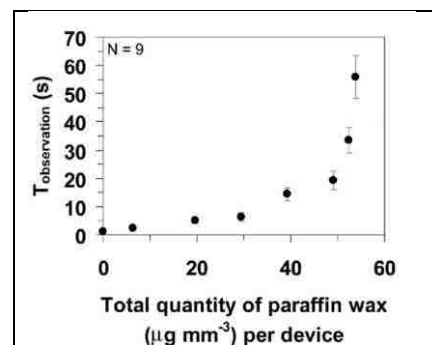


Figure 4. Plot demonstrates the ability to vary the delay time through the amount of wax deposited onto the substrate by Noh *et al.* Reprinted with permission from [33]. Copyright 2010 American Chemical Society.

LFTs. However, the impact of higher concentrations of sugar, as employed by the barrier for longer delay times, on signal generation must be considered. Another potential issue for the use of higher sugar concentration barriers is the effect on sample and reagent fluid flow downstream of the barrier due to increased fluid viscosity. A second type of on-switch for flow is based on the use of hydrophobic and hydrophilic coatings to control the wetting properties of the substrate. Noh *et al.* [33] controlled flow rate by using a hydrophobic wax coating on the cellulose substrate to affect the wettability of the cellulose and reduce the flow rate in a wax-treated region. A wide range of delays were demonstrated, from 30 seconds to over an hour, with increasing time delays achieved by depositing increasing quantities of wax [33] as shown in **Figure 4**. The use of multiple wax-treated regions in series provided fine-level control of flow rate within a device. Chen *et al.* employed hydrophobic and hydrophilic coatings to develop a single-use fluidic diode [35]. In their diode design, a hydrophobic barrier separates two channels with surfactant deposited on only one side of the barrier. Thus, fluid flow can be switched on in the direction in which surfactant is rehydrated before reaching the hydrophobic barrier; the rehydrated surfactant enables the fluid to cross the previously hydrophobic barrier. No flow is allowed in the other direction unless triggered, as shown in **Figure 5**. As in the case of the dissolvable barriers, the effect of the released chemical, i.e. the bolus of surfactant, on downstream processes must be considered. A third method for creating a delay of fluid flow was demonstrated by Toley *et al.* [36]. They demonstrated delays of fluid flow in nitrocellulose channels by using a parallel piece of cellulose to wick fluid from the nitrocellulose channel. The delay time could be varied by manipulating the length and thickness of the cellulose piece. Delays up to approximately 18 minutes were demonstrated with coefficients of variation in delay times of less than 10% [36].

In addition to the automated methods for turning on fluid flows described above, simple and user-friendly methods of turning on flows based on a mechanical step have been developed. Fu *et al.* have demonstrated a card format for simple device activation that is appropriate for use in POC settings [23]. In this method, reagents are loaded onto source pads located on one side of a folding card, while the network is located on the opposite side of the folding card, as shown in **Figure 6**. Folding then creates contact between the source pads and network, initiating fluid flow from all sources into the network simultaneously. Reagents can be stored dry in the source pads, so the user only adds sample and water, further simplifying user operation. While this technique requires a mechanical step, it is not a time-critical step. Use of the method does require careful design of the card such that folding produces a reproducible and reliable contact between the source pads and the network.

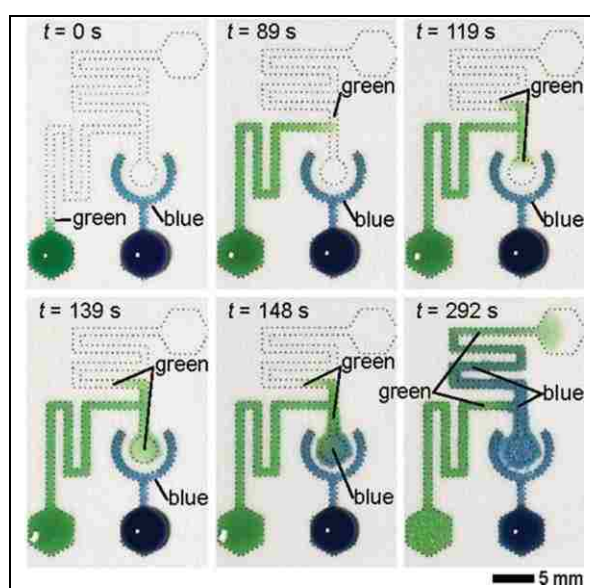


Figure 5. Images showing the use of a diode valve to program timed release of the blue fluid by the green fluid from Chen *et al.* [35]. Reproduced with permission of the Royal Society of Chemistry.

Another type of mechanically activated valve has been demonstrated by Li *et al.* in a paper device [38]. A foldable paper tab-based switch was designed such that the fluidic channel upstream of a reaction site

is discontinuous while the tab is folded. Once the tab is unfolded, fluid can then progress to the reaction site. In this manner, multiple valves can be employed to deliver multiple reagents in a desired sequence. Similarly, Martinez *et al.* designed user-activated single-use buttons in their three-dimensional microfluidic paper-based analytical devices (3D μ PADs) [37]. The 3D μ PADs were fabricated such that a gap exists between two adjacent layers of paper and fluid cannot wick between the paper layers without intervention. In order to connect the paper channels, mechanical force is applied by pressing the button with a stylus to bring the layers into contact. The authors demonstrated this valving method in the contexts of a user (i) initiating one or more assays

from a panel of assays and (ii) running a fluidic de-multiplexer. Though simple in design, a disadvantage of mechanically activated valves when used for a time-critical operator step, is the possibility of significant errors that could produce downstream variability in signal generation.

Off-switches for volume metering. A complementary fluidic control to the on-switch is a fluid flow off-switch. A critical use of an off-switch is to automatically meter multiple fluid volumes, enabling easy-to-use devices that do not require the user to make any precise measurements of fluid volumes. One automated method to control the shut-off of multiple flows independently is the use of inlet legs that are submerged by varying distances into a common well as demonstrated by Lutz *et al.* [39]. The level of the fluid in the well drops as fluid wicks into the paper inlets. Fluid shuts off from the inlets at different times, in order of shortest to longest submerged lengths as shown schematically in **Figure 7**. Additional parameters that can be used to control the shut-off volume for an inlet include the geometry of the fluid well, the geometry and composition of an inlet leg, and the use of a regulator wick (as shown in Figure 7). This method has been characterized for reproducibility with coefficient of variation in shut-off times between 5 and 20% [39]. Automated sequential reagent delivery from a single user activation step has been demonstrated using this method in a simple 2DPN [39]. A disadvantage of this method is the requirement for the device to rest on a level surface in a particular orientation. An alternative method to turn off flow from multiple inlets independently, is the use of pads of varying fluid capacity that are pre-filled to saturation [40]. Contact between the pads and inlets activates the multiple flows. Fu *et al.* have demonstrated that volume metering using source pads provides reproducible fluid release profiles, with coefficient of variation of less than 10% in the volumes delivered [23]. The properties of the pad, most

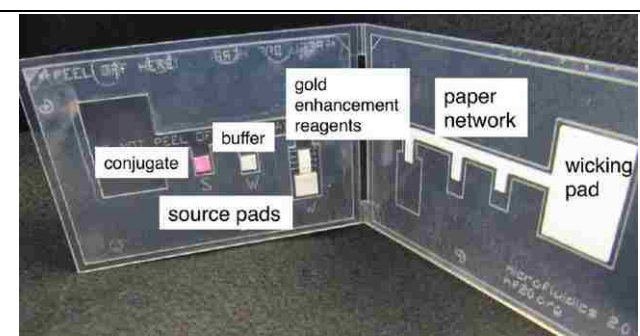


Figure 6. Automated amplified two-dimensional paper network assay developed by Fu *et al.* Reprinted with permission from [23]. Copyright 2012 American Chemical Society.

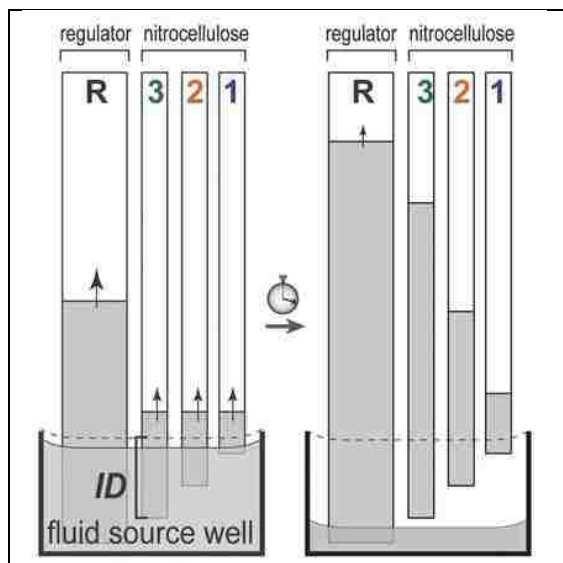


Figure 7. Schematic of a volume metering method in which fluid flows shut off from the inlets in the order of shortest to longest submerged length (i.e. ID = immersion depth) by Lutz *et al.* [39]. Reproduced with permission of the Royal Society of Chemistry.

importantly the bed volume and the surface treatment, determine the release profile of fluid from the pad to the inlet. Further, the rate of fluid volume released into the paper network can be adjusted by varying the cross-sectional area of the inlet.

Temporal and spatial control of rehydrated reagents. Complementary to the control of fluid transport using the tools described above is the ability to manipulate the spatial and temporal concentration profiles of rehydrated reagents within the porous channels. For example, Fridley *et al.* have demonstrated that the amount of reagent delivered in a pulse can be tuned by varying the amount of reagent printed in each spot and the number of spots arrayed across the channel [41]. Further, the duration of the reagent pulse can be adjusted by varying the amount of sugar patterned with the reagent. Patterning is a serial process, so the time for patterning reagents onto substrates must be factored into the time for device fabrication. However, a significant advantage of patterning directly onto the substrate is that a complete assay can be fabricated using a single material; this can translate to a reduced number of pieces that must be assembled to create the final device and lower manufacturing costs.

We have examined a variety of tools for the control of fluid flow and reagent delivery in porous materials. These constitute a set of fluidic tools that can be used alone or in combination to create automated integrated paper microfluidic assays. Examples are included in the applications section below.

Readout methods compatible with low-resource POC settings

It is important that the users of POC diagnostic devices in low-resource settings are able to easily read and interpret assay results with minimal instrumentation. High performance tests often rely on methods that require expensive dedicated instrumentation for data acquisition, analysis, and interpretation. However, the added cost and requirement for maintenance then make these tests unsuitable for many POC settings [19]. LFTs are a longstanding example of a POC immunoassay that produces a visible signal that can be simply read by eye [20]. For example, the pregnancy dipstick is a well-known example of a LFT, which detects human chorionic gonadotropin (hCG). Current disadvantages of many commercially available instrument-free LFTs are that the signal is restricted to being qualitative and that sensitivity is too low to have clinical significance for a number of analytes of interest [42]. Introduction of a dedicated reader to enable more sensitive or quantitative readout of LFTs has been a successful approach for higher resource POC settings [20] (commercially available dedicated readers including smart-phone based readers have been reviewed by Yetisen *et al.* [17]). However, this approach leads to a greater cost of the final device and a requirement for maintenance that may not be appropriate for lower resource settings. Here we focus on several promising methods that have been developed to enable quantitative or higher-sensitivity readout that are easy to use, low cost, and have minimal dedicated instrumentation. These include methods for instrument-free semi-quantitative visual readout and adapters for use with non-dedicated smart phones for extended assay readout capabilities.

Semi-quantitative visual readout. A non-instrumented approach has been developed to provide semi-quantitative readout of LFTs called a ladder-bar assay [43-46]. The ladder-bar assay is based on the stepwise capture of analyte by immobilized antibody to produce a readout in which the number of colored lines is an indication of analyte concentration. Fung *et al.* adapted the ladder-bar method to demonstrate an enzyme-based assay for the quantification of hydrogen peroxide, the product of glucose and glucose oxidase [43], as shown in **Figure 8**. The assay response can be tuned through the manipulation of the number and spacing of capture stripes, the density of capture molecules, and the

velocity of fluid flow through the detection region. According to the Lucas-Washburn relationship, the fluid front velocity decreases with the distance traveled. Therefore, the time of interaction between analyte and surface-bound antibodies increases at each subsequent test line. This complication should be taken into consideration during the development of a ladder-bar assay. More recently, a similar readout strategy was demonstrated by Lewis *et al* [47], using a device to quantify the level of hydrogen



Figure 8. Ladder-bar readout for a glucose assay demonstrated by Fung *et al.* [43]. A sample consisting of 0, 1, 5, 25, 50, 100, and 200 μm glucose was added to the strip, from left to right, respectively.

peroxide in a sample. In this method, oxidative cleavage of a hydrophobic compound by hydrogen peroxide yields hydrophilic compounds, which modify the wettability of the channel and the rate at which the sample containing hydrogen peroxide wicks through the membrane. The number of colored radial bars, read at a specific time point, determine the sample concentration. Semi-quantitative readout is achieved without instrumentation through this method; however, the requirement for readout at a specific time limits the user friendliness of the device and could lead to signal variation due to user error.

Non-dedicated smart phone reader model for expanded assay readout capabilities. The non-dedicated smart phone reader model

is promising for applications in low-resource POC settings that require an expanded assay readout, e.g. fully quantitative output, over what is possible with simple visible readout by the user. In recent years, multiple reports have testified that mobile phones hold the power to transform global health and diagnostic technologies [48, 49]. This is due to their ease of use and highly ubiquitous dissemination, with recent estimates of at least 5 billion devices worldwide [50]. Camera-equipped mobile phones have permeated throughout even the least developed countries. They are lightweight, portable, increasingly affordable, and can provide high resolution images (≥ 2 megapixels) [51].

Martinez *et al.* first outlined a process for the quantification of diagnostic assays by remote analysis of image data taken by a mobile phone camera [51]. In their demonstration, the camera on a mobile phone was used to image the colorimetric results of a bplexed glucose and protein assay. The image was then sent to a remote computer through a wireless communication system, and there the image was processed to output analyte concentration. In their use scenario, the quantitative results could then be reported back to the user's mobile phone along with a prescribed treatment. A complementary approach to extract quantitative kinetic data using smart phones was presented by Stevens and Yager [52]. They demonstrated that the rate of intensity generation extracted from smart phone-acquired image data could be correlated with the concentration of the target analyte in a flow-through membrane-based immunoassay. Potential advantages they cite are a shorter time to result and a larger dynamic range compared to end-point measurements. In an extension of this work, Dell *et al.* demonstrated the ability to process the kinetic data in real time using an Android mobile phone [53].

Further utilizing the ubiquity of camera-equipped mobile phones, the Ozcan lab has developed adapters that physically attach to the mobile phone for use in multiple contexts. Zhu *et al.* have demonstrated wide-

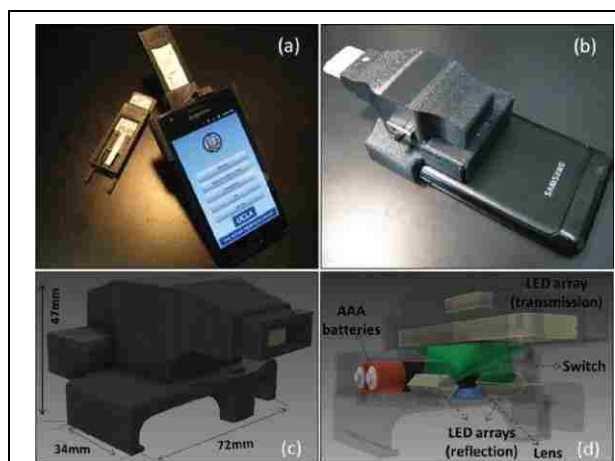


Figure 9. Adapter that interfaces with an Android phone to perform imaging and analysis of commercially-available LFTs in reflection and transmission mode by Mudanyali *et al.* [55]. Reproduced with permission of the Royal Society of Chemistry.

field fluorescent and darkfield imaging using an adapter composed of compact, light-weight, and cost-effective optical components, including a simple lens, a plastic color filter, LEDs, and a battery [54]. A spatial resolution of 10 μm was achieved with a field of view of 81 mm^2 , allowing for the possibility of a high level of multiplexing [54]. Considering the high-sensitivity of fluorescence detection, this approach is especially promising for applications that require a very low limit of detection. More recently, Mudanyali *et al.* extended this work to perform imaging and analysis of commercially-available LFTs in reflection and transmission mode using the smart phone plus adapter system shown in **Figure 9**. In this demonstration, raw images were acquired and digitally processed by an application on the smart phone, increasing robustness of the results, especially at lower concentrations that approached the limit of detection [55]. As a further extension of this work, a personalized food allergen test was demonstrated [56]. Compared to visual inspection, the optical readout was rapid (image was processed within 1 s) and allowed for a more sensitive quantitative result (between 1 and 25 ppm). The smart phone plus adapter approach is promising, directly addressing issues such as variability of ambient lighting conditions and variability of user positioning of the smart phone.

Power and heating compatible with low-resource POC settings

Many laboratory-based assays utilize mains electricity for operation. For example, power is required to generate the excitation source for fluorescence-based assays. Examples of the requirement for heating are in high-sensitivity nucleic acid amplification reactions or in cell lysis protocols. However, the requirement for mains electricity is not compatible with low-resource POC settings in which electricity is either unreliable or unavailable. Recently, several groups have developed novel techniques to deliver consistent power or heat to assays without this requirement.

Fluidic batteries. Various groups have developed fluidic or paper-based batteries in order to avoid the expense and hazardous waste associated with traditional lithium ion batteries. These fluidic batteries can be powered by electrochemical reactions and are fully disposable. Hilder *et al.* have characterized the open-circuit voltage and discharge current – up to 1.2 V and 500 μA , respectively – of screen-printing zinc/carbon-PEDOT/air batteries on various paper substrates [58]. Liu *et al.* further developed this method by integrating a paper-battery into an electrochemical sensing platform [57] as shown in **Figure 10**. Their integrated battery powered an electrochemical reaction and detection system to detect glucose and hydrogen peroxide in artificial urine samples. Thom *et al.* designed a paper-battery capable of powering a UV LED and demonstrated it in an on-paper fluorescence assay [59]. Their assay detected β -D-galactosidase in a sample in less than 20 minutes. Further, Zheng *et al.* reviewed conductive papers and energy storage mechanisms for paper-based devices [60].

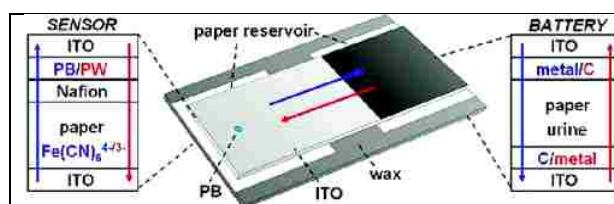


Figure 10. Paper battery for the detection of glucose and hydrogen peroxide in artificial urine samples developed by Liu *et al.* Reprinted with permission from [57]. Copyright 2012 American Chemical Society.

Smart phones as a power source. To date, the majority of smart phone-based technologies have been used for sensing and detection techniques [61, 62] rather than for powering diagnostic devices. The one major exception has been MobiSante's FDA approved ultrasound imaging system that is powered by a dedicated smart phone-based reader [63]. Smart phones have the capability to provide reliable power directly at the POC. For example, the iPhone can output 3.3 V using commercially available pinout connectors such as the PodSocket Breakout from Spark Fun Electronics (Boulder, CO <https://www.sparkfun.com/>). This inexpensive (\$15 retail), reusable device plugs directly into the charging port of an iPhone and can easily create a POC power source.

Using a similar adaptor, the Yager group has designed a lysis system powered only by a mobile electronic device [64].

Heaters. To provide consistent heat to a system, there are two well-developed options suitable for low-resource POC settings. The first is an inexpensive, single-use, flexible thin film heater, shown in **Figure 11**,

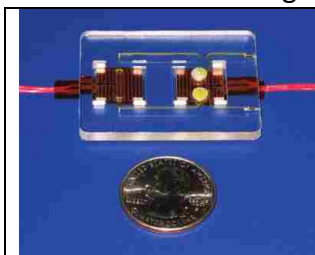


Figure 11. Thin film heater used to power nucleic acid amplification reactions for up to one hour. Reprinted with kind permission from Springer Science + Business Media: [65].

which has been demonstrated to heat disposable plastic cassettes for nucleic acid amplification reactions for up to one hour with minimal power requirements [65]. As an example, a temperature of 40°C requires only 0.15 W of power (~ 0.82 V from a thin film heater, Minco Products, Inc.). This voltage could easily be supplied with a mobile phone or fluidic battery as described above.

The second option eliminates the need for any electrical power by utilizing heat supplied by an exothermic chemical reaction. LaBarre *et al.* have described the use of exothermic chemical reactions activated by the addition of aqueous buffer as the heat generating mechanism for a POC device, achieving constant temperature profiles at 38°C, 55°C, and 63°C (+/- 1°C). Critical to achieving

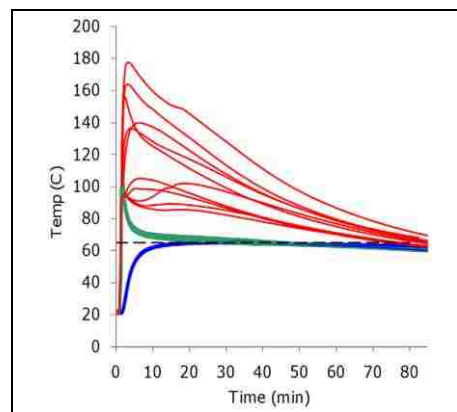


Figure 12. Temperature vs. time of multiple runs (N=10) measured at the exothermic reaction (red), interface with the phase change material (green), and at the nucleic acid amplification reaction (blue) [66].

a robust and stable heating system is coupling the heat generating reaction to a phase-change material, as shown in **Figure 12**. They demonstrated the use of their heating mechanism to power a nucleic acid isothermal amplification reaction (Loop mediated isothermal amplification) in a tube. This reaction ran at 63 +/- 1°C for 38 minutes with detectable signal down to 1 genome copy per microliter [66].

Selected applications for low-resource POC settings

Using many of the above-described tools, multiple groups have developed paper-based devices for low-resource POC applications. Devices have been developed to perform sample preparation, nucleic acid amplification, and assays with extended capabilities such as signal amplification, in a package suitable for use at the POC.

Sample preparation. One of the most challenging aspects of device development for the POC is sample preparation. Multiple groups have developed methods to selectively purify targets of interest utilizing only paper-based systems. Vella *et al.* used paper networks to separate blood plasma from erythrocytes and coupled this process to semi-quantitative, colorimetric detection for two enzymatic markers of liver function, as shown schematically in Figure 13 [67]. Govindarajan *et al.* demonstrated the extraction of bacterial DNA using multiple folding steps in a paper origami device [68]. This device utilized dried lysis buffer

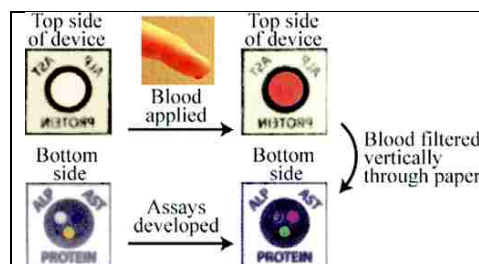


Figure 13. Paper-based sample preparation device used to separate plasma from whole blood and detect enzymatic markers of liver function. Reprinted with permission from [67]. Copyright 2012 American Chemical Society.

that was rehydrated upon assay activation. Cheng *et al.* developed a paper-based ELISA assay to detect the HIV-1 envelope antigen gp41 [69]. This assay significantly reduced the overall assay time from multiple hours using a traditional well-based ELISA to only 1 hour in the paper format. Further, the paper-based assay required a reduced sample volume of 0.5 μL and used a simple-to-read colorimetric detection system. Osborn *et al.* demonstrated multiple mechanisms for paper-based dilution, mixing, and sample separation based on the diffusion of particles through nitrocellulose membranes [70]. Another extremely important sample preparation function for improved limits of detection that is often challenging to perform at the POC, is sample concentration. Golden *et al.* have described the simultaneous purification and concentration of diagnostic biomarkers using poly(N-isopropylacrylamide) (pNIPAAm), a stimuli-responsive polymer, attached via RAFT polymerization onto a porous membrane in a flow-through microfluidic system [71].

Assays with extended capabilities. There is a need for assays with improved limits of detection in a package suitable for use at the POC. One approach that has been recently demonstrated uses signal amplification to achieve the higher sensitivity characteristic of laboratory-based ELISA. Fu *et al.* have developed 2DPNs to incorporate multi-step processes for improved assay sensitivity compared to a standard LFT for hCG detection [73]. In an extension of this work, they developed an automated signal amplified 2DPN for the detection of the malaria protein PfHRP2 [23]. The assay achieved a 4-fold improvement in the limit of detection compared to the assay without the signal amplification step. Fridley *et al.* further extended this work by patterning reagents directly onto the nitrocellulose network in a similar malaria protein assay [41]. Implementation of alternate signal amplification methods using these formats has the potential to produce even greater increases in sensitivity.

Nucleic acid amplification. Another approach to achieve high sensitivity detection is nucleic acid amplification. Until recently, very little work has addressed the ability to amplify nucleic acids within a porous material. Rohrman *et al.* were the first to publish results demonstrating nucleic acid sequence based amplification (Recombinase polymerase amplification) in glass fiber at 10 copy sensitivity using LF detection [74]. More recently, they demonstrated coupled in-tube amplification with quantitative gold nanoparticle detection systems in a lateral flow format as shown schematically in Figure 14. Their results show distinguishable viral loads over the significant clinical range for HIV-1 infection [72]. These promising demonstrations of nucleic acid amplification in a porous material, coupled with the advances described above in equipment-free heating, have the potential to bring high sensitivity nucleic acid amplification assays to low-resource settings.

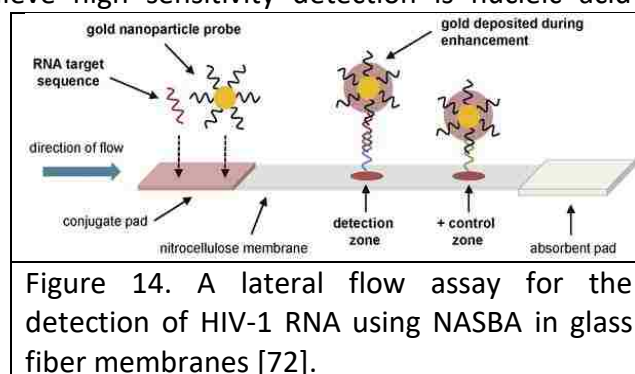


Figure 14. A lateral flow assay for the detection of HIV-1 RNA using NASBA in glass fiber membranes [72].

Field testing for water, food, and drug safety. A set of emerging paper-based demonstrations has focused on the testing of water, food, and drug safety in the field. Shi *et al.* developed filter paper strips combined with screen-printed carbon electrodes to detect lead and cadmium in water supplies. These POC devices utilized a direct electrochemical detection method and were able to detect down to 2.0 and 2.3 ppb of Pb(II) and Cd(II) in water samples, respectively [75]. Zou *et al.* developed a simple LFA for biomonitoring of organophosphorus pesticides. They were able to detect down to 1.0 ng/mL of 3,5,6-trichloropyridinol (TCP), a common concern for in-field POC biomarker testing for humans exposed to pesticides [76]. They utilized quantum dots as the label, which provided quantitative analyte measurements, high sensitivity, resistance to photobleaching, and the potential for multiplexing.

Bajema *et al.* have developed a rapid paper-based card to test for counterfeit drugs such as Panadol [77] (a tradename for acetaminophen), Figure 15. Their system tests for multiple drug components including common additives, the presence or absence of active ingredients, and the proper dosing of active ingredients. This system was able to identify 95% of the counterfeit drug samples from the 460 tested. Though not directly in the field of POC diagnostics development, promising advances in closely related areas including field testing for water, food, and drug safety are relevant and may be utilized for diagnostic devices.

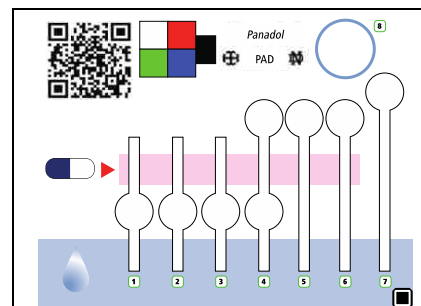


Figure 15. A paper-based device to detect counterfeit Panadol. Lines 1-7 test for important active ingredients and fillers, while line 8 is used for semi-quantitative analysis. Reprinted with kind permission from Springer Science + Business Media: [77].

Future Challenges

Moving forward, a main challenge to the creation of paper-based diagnostic devices for use at the POC is integration to create stand-alone sample-in to result-out devices. As discussed earlier in this article, there has been much activity and progress to date on creating tools for flow control, power and heating methods compatible with low-resource settings, extended readout capabilities with minimal instrumentation, and discrete modules for specific analytical processes. A fully integrated device will include all processes that are required to achieve the performance specifications of the intended application: sample transfer, sample preparation, capture and labeling of the target analyte, detection, and transmission of results. The integration issues relevant to the creation of paper-based diagnostic devices are analogous to the issues in conventional microfluidics-based diagnostics development. Successful device integration can be achieved by a two-part approach composed of (i) a system-level view of the whole device and (ii) individual module development [78]. This approach enables balancing issues of connectivity of the modules and the cost and ease of overall device manufacturing, with potential trade-offs in the performance of the integrated modules, compared to the optimized individual modules; all with the goal of meeting the performance specifications of the intended application and the design constraints of the intended setting.

For example, issues relevant to device integration need to be considered when making a choice of final device material(s). The best performance for the individual modules may be produced when utilizing different substrates in each module. This is because the individual modules may have different functional requirements that translate to a need for different material characteristics for properties such as flow rate, compatibility with specific surface treatments, and propensity for surface adsorption. However, choosing to include multiple materials in the final integrated device requires that the chosen materials be compatible on several levels. First, the material used in a downstream module must be compatible with the upstream processes (e.g., resistant to a solvent used in an upstream process that then flows downstream). Second, the materials need to be compatible with respect to the creation of robust fluidic connections between materials/modules. And third, the disparate materials must be compatible in terms of the existence of a straightforward fabrication process that has the potential to be scaled up. Additionally, the added cost to device manufacturing when using disparate materials should be considered and determined to be reasonable for the intended application, if the device is to have a chance at translation to a commercial product [79]. Down-selection to one material may result in a decrease in performance in one or more modules, but this may be acceptable, if performance specifications for the intended application are still met. Thus, there are multiple trade-offs involved in the final material(s) choice. A thorough understanding of the cost constraints and performance requirements of the end-use application will be needed to optimally balance the issues involved in creating a fully integrated device.

A second main challenge is to fulfill the promise of non-dedicated mobile device use in a POC diagnostic system. Recently there has been much discussion of the expanded use of mobile devices in POC diagnostics; multiple potential functions include (i) directing test operation, (ii) analyzing test results, (iii) interpreting test results, and (iv) transmitting test results to a healthcare provider and instructions back to the patient. A critical requirement for realizing the full potential of mobile device use in POC diagnostics is infrastructure to interface with the existing healthcare system. For example, protocols for the mode of patient interaction with the healthcare provider need to be developed. Specifically, protocols for the use of synchronous (i.e. real-time) or asynchronous (e.g. text messages) communications, procedures for prioritization of these communications based on the nature of patient test results, and mechanisms for ensuring appropriately timely communications between the patient and healthcare provider after the transmission of test results must be developed, tested, and implemented. A further requirement will be to gain acceptance of these within existing medical practice. Future development of POC diagnostics to be compatible with non-dedicated smart phones will require that additional technological and regulatory issues be addressed. For example, given the numerous mobile devices available to the consumer, defining the subset of smart phones that adhere to a common standard, for use with a given diagnostic test, will be required. A significant issue for the non-dedicated smart phone model is to implement a mechanism for keeping abreast of smart phone manufacturer updates to relevant phone models for retesting of compatibility with the diagnostic test. Issues associated with secure transmission of patient information [80] will also have to be addressed by the diagnostic device companies.

Summary

The overall challenge in point-of-care diagnostics development continues to be to create high-performance assays that are appropriate for the various settings relevant for global health applications. For the lowest-resource settings, the requirements for high performance with a rapid, instrument-free, easy to use, and very low cost device brings specific design and implementation challenges. Paper-based microfluidics is especially well suited to addressing these challenges. The development of precise and robust fluidic controls coupled with advances to develop electrical power-free methods and readout with minimal instrumentation underlie the great potential for creating sophisticated assays that are appropriate for low-resource settings.

Acknowledgements

The authors thank Gina Fridley, Carly Holstein, Barry Lutz, and Paul Yager for their helpful comments and suggestions on the manuscript. Research reported in this publication was supported by the National Institute of Allergy and Infectious Disease of the National Institutes of Health under award number R01AI096184. The content is solely the responsibility of the authors and does not necessarily represent the official views of the National Institutes of Health.

